



Catalysis in Cells for Therapeutic Applications

PhD Thesis

submitted to Cardiff University in accordance with the conditions governing candidates for the degree of Doctor of Philosophy (Chemistry)

by

Sophie Rebecca Thomas

October 2021

Cardiff University

Table of Contents

Summary	iv
Acknowledgements	v
1. Metal complexes as anticancer agents	1
1.1. Gold(I) complexes as anticancer agents	2
1.1.1. Auranofin and related gold(I) complexes	2
1.1.2. Gold(I) N-heterocyclic carbene (NHC) complexes	7
1.1.3. Gold(I) Alkynyl complexes	13
1.2. Gold(III) complexes as anticancer agents	17
1.2.1. Gold(III) porphyrin complexes	17
1.2.2. Gold(III) corrole complexes	19
1.2.3. Gold(III) complexes with chelating N donor ligands	20
1.2.4. Gold(III) complexes with dithiocarbamate ligands	22
1.2.5. Gold(III) cyclometalated complexes	23
1.2.5.1. Gold(III) C [^] N complexes	24
1.2.5.2. Gold(III) C [^] N [^] C complexes	27
1.2.5.3. Gold(III) C [^] N [^] N complexes	31
2. Bioorthogonal catalysis in cells	33
2.1. Transition metal catalysts for bioorthogonal reactions	33
2.1.1. Palladium mediated bioorthogonal reactions	34
2.1.1.1. Coupling reactions	34
2.1.1.2. Cyclisation reactions	35
2.1.1.3. Bond-cleaving reactions	36
2.1.2. Gold mediated bioorthogonal reactions	37
2.1.2.1. Au(III) complexes	38
2.1.2.2. Au(I) complexes	45
2.1.2.3. Au(0) nanoparticles	47
3. Gold nanoparticles (AuNPs) stabilised by NHC ligands	50
3.1. AuNPs stabilised by N-heterocyclic carbene (NHC) ligands	52
3.1.1. N-heterocyclic carbenes (NHCs)	52
3.1.2. Synthetic approaches to AuNPs stabilised by NHCs (NHC@AuNPs)	53
3.2. Water-soluble AuNPs stabilised by NHCs	61
3.3. Gold NPs for biomedical applications	67
3.3.1. Drug Delivery	68
3.3.2. Radiotherapy	70
3.3.3. Photothermal Therapy (PTT)	71
3.3.4. Photoacoustic (PA) Imaging	72
3.3.5. Computed Tomography (CT)	73
3.4. Water-Soluble Gold NPs stabilised by NHCs for biomedical applications	74
4. Aims	78
5. C-S Cross-Coupling Reactions mediated by Au(III) Cyclometalated Complexes	79
5.1. Introduction	80

5.2.	Results and Discussion.....	82
5.3.	Summary and Future Outlook	100
5.4.	Materials and Methods.....	102
5.4.1.	General	102
5.4.2.	Synthesis of Au(III) complexes and 2-(phenylthio)pyridine.....	102
5.4.3.	HR-LC-ESI-MS Studies	105
6.	<i>C-P Cross-Coupling Reaction mediated by Au(III) Cyclometalated Complexes.</i>	106
6.1.	Introduction	107
6.2.	Results and Discussion.....	108
6.3.	Summary and Future Outlook	122
6.4.	Materials and Methods.....	124
6.4.1.	General	124
6.4.2.	Synthesis of C-P Reductive Elimination Products	124
6.4.3.	Crystal Formation for XRD analysis.....	127
6.4.4.	³¹ P{ ¹ H} NMR studies	127
7.	<i>C-C Cross-Coupling Reaction Mediated by a Au(III) Cyclometalated Complex: Mechanistic Insights</i>	128
7.1.	Introduction	129
7.2.	Results and Discussion.....	131
7.3.	Summary and Future Outlook	148
7.4.	Materials and Methods.....	150
7.4.1.	General	150
7.4.2.	Synthetic procedures.....	150
7.4.3.	¹ H NMR Reaction Monitoring	153
7.4.4.	Crystal Formation for XRD Analysis	153
8.	<i>Water-Soluble AuNPs stabilised by.....</i>	154
	<i>N-heterocyclic carbenes.</i>	154
8.1.	Introduction	155
8.2.	Results and Discussion.....	157
8.2.1.	Synthesis of water-soluble NHC@AuNPs	157
8.2.2.	Characterisation of water-soluble AuNPs	161
8.2.2.1.	Stability Studies.....	161
8.2.2.2.	¹ H NMR Spectroscopy.....	163
8.2.2.3.	FTIR-ATR Spectroscopy	165
8.2.2.4.	XPS characterisation.....	166
8.2.2.5.	TEM characterisation	168
8.2.2.6.	TGA.....	169
8.2.3.	Catalytic studies of AuNPs.....	170
8.2.3.1.	Reduction of 4-nitrophenol.....	170
8.2.3.2.	Reduction of 2-nitrophenol and 3-nitrophenol	181
8.2.3.3.	Pre-treatment of AuNP-1 with NaBH ₄	181
8.2.4.	Synthesis of supported NHC-stabilised AuNPs.....	184
8.2.5.	Characterisation of supported NHC-stabilised AuNPs	186
8.2.5.1.	XPS	186

8.2.5.2.	TEM.....	188
8.2.6.	Catalytic studies of TiO ₂ supported NHC@AuNPs	190
8.2.6.1.	Pre-treatment of AuNP-1/TiO ₂ with NaBH ₄	192
8.2.6.2.	Recyclability of AuNP-1/TiO ₂ and AuNP-2/TiO ₂	193
8.3.	Summary and Future Outlook	197
8.4.	Materials and Methods	200
8.4.1.	General.....	200
8.4.2.	NHC-L and Au(I) NHC synthesis	200
8.4.3.	NHC@AuNP synthesis	202
8.4.4.	Dialysis procedure	202
8.4.5.	UV-Vis Stability Studies	203
8.4.6.	UV-Vis Kinetic study for 4-nitrophenol reduction reaction	204
8.4.7.	Pre-treatment of AuNP-1 and AuNP-1/TiO ₂	204
8.4.8.	Synthesis of supported NHC@AuNPs	204
9.	<i>Overall Conclusions</i>	206
	<i>Appendix</i>	211
	<i>References</i>	295

Summary

Bioorthogonal reactions templated by metal complexes is a thriving area in medicinal bioinorganic chemistry for applications in therapy and/or imaging. These reactions are commonly catalytic transformations mediated by metal complexes in organic solvents and cannot proceed naturally. However, applying these reactions in physiological conditions is not facile due to the presence of endogenous nucleophiles, e.g. thiols. Palladium complexes have been widely investigated to mediate bioorthogonal reactions; however, they often suffer from lack of chemoselectivity and are limited to certain experimental conditions (e.g. pH and incubation time). Thus, gold complexes have also been considered due to their greater tolerance to aqueous conditions and chemoselectivity.

Therefore, this research aims to explore gold-based catalysts to mediate bioorthogonal reactions using two different approaches. The first part of this thesis investigates the ability of cyclometalated Au(III) C^N complexes to mediate C-S cross-coupling reactions *via* reductive elimination of cysteine residues in different peptides, including pharmacologically relevant zinc finger domains. Following this work, other cross-coupling reactions have been explored in water and/or generally mild reaction conditions, namely C-P and C-C bond formation with different substrates. For example, silver phenylacetylide and vinyl-tri(*n*-butyl)stannane were used as coupling partners to form C(sp²)-C(sp) and C(sp²)-C(sp²) products, respectively. Mechanistic insights into the different cross-coupling reactions were achieved using an integrated investigational approach, including spectroscopic and analytical methods as well as computational studies.

The second part of this thesis incorporates a heterogeneous approach to bioorthogonal reactions by the synthesis and characterisation of water-soluble gold nanoparticles stabilised by N-heterocyclic carbene ligands (NHC@AuNPs) featuring imidazolium scaffolds with sulfonate groups. Gold nanoparticles are widely known for their applications in catalysis. Therefore, we envisaged their use as catalysts in living cells for bioorthogonal reactions, e.g., activating a pro-drug *in situ*. Two types of NHC@AuNPs were synthesised by a bottom-up approach using Au bis-NHC complexes and reducing them with sodium borohydride. Afterwards, the obtained AuNPs were characterised by different methods, including transmission electron microscopy (TEM), which was used to observe the small size of the NPs (ca. 2 nm). The catalytic performance of the nanoparticles was assessed using the model 4-nitrophenol reduction to 4-aminophenol in water, with more biocompatible reactions envisaged in future studies. Moreover, the same NHC@AuNPs can be used in other biomedical applications, including photothermal therapy (PTT) and photoacoustic imaging (PAI).

Acknowledgements

First and foremost, I would like to thank my extraordinary supervisor Prof. Angela Casini. Angela, you have been my biggest inspiration and the best supervisor I could ask for, regardless of us being in different countries for most of the time! I remember the first time I met you when you moved to Cardiff University, I knew instantly that I wanted to work with you, and I made sure I did! Thank you for believing in me and pushing me out of my comfort zone; never would I have believed I would present at International Conferences. On that note, thank you for the amazing opportunities you have given me; I will be forever grateful!

Dr. Riccardo Bonsignore, my academic older brother. You have given me invaluable guidance and support during my PhD, both academically and personally. You have helped me grow as a chemist in both confidence and skill, and I had the best time working with you. I could not have asked for a better Postdoc supervisor, and I hope we can still work together in the future, yet, regardless, you will be a lifelong friend. Thank you so much!

I would also like to thank other members of the Casini research group, past and present, who guided and inspired me during the early months of my PhD. Special mention to Dr. Andreia de Almeida. Andreia, you were instrumental in my decision to pursue a PhD whilst completing my MChem. You were supportive and inspirational, and I loved my project so much that I knew research was the next step for me, so thank you!

I would also like to acknowledge other academics who have been involved in my research, including Dr. Didier Bourissou, Prof. Giampaolo Barone and Dr. Nikolaos Dimitratos. Thank you all for your invaluable guidance; this thesis would not be possible without you. Additionally, I would like to acknowledge the Analytical and Technical Services at Cardiff University who have assisted me over the last three years, thank you for always being on hand to help! I would also like to thank Dom Ward for supplying some great music taste in the lab!

I would also like to acknowledge the EPSRC (EP/L016443/1) and CDT in Catalysis for the funding and opportunity to complete this PhD.

Finally, a massive thank you to my support network, starting with Bek, Marina, Bria and Jess. You are the best friends I could ever ask for, and thank you for always being there to support me. To my family, thank you for always supporting and encouraging me; I could not have done this without you. Lastly, a special thank you to my boyfriend, Ben. You have supported me through these last few years and have been my biggest cheerleader, so thank you, and I hope you're proud.

1. Metal complexes as anticancer agents

The concept of metals in medicine dates back to ancient times when metal compounds, such as mercury sulfide (cinnabar), were used to treat trachoma and venereal diseases.¹ Other metals such as arsenic, gold and copper were also utilised to treat different diseases in early times; however, little was understood about their mechanisms of action and toxicity.¹ Eventually, in the 1960s, Rosenberg *et al.*² discovered the anticancer effects of cisplatin (*cis*-diamminedichloroplatinum(II)), and since then, metal compounds have been truly considered as therapeutic agents (Figure 1, top).¹

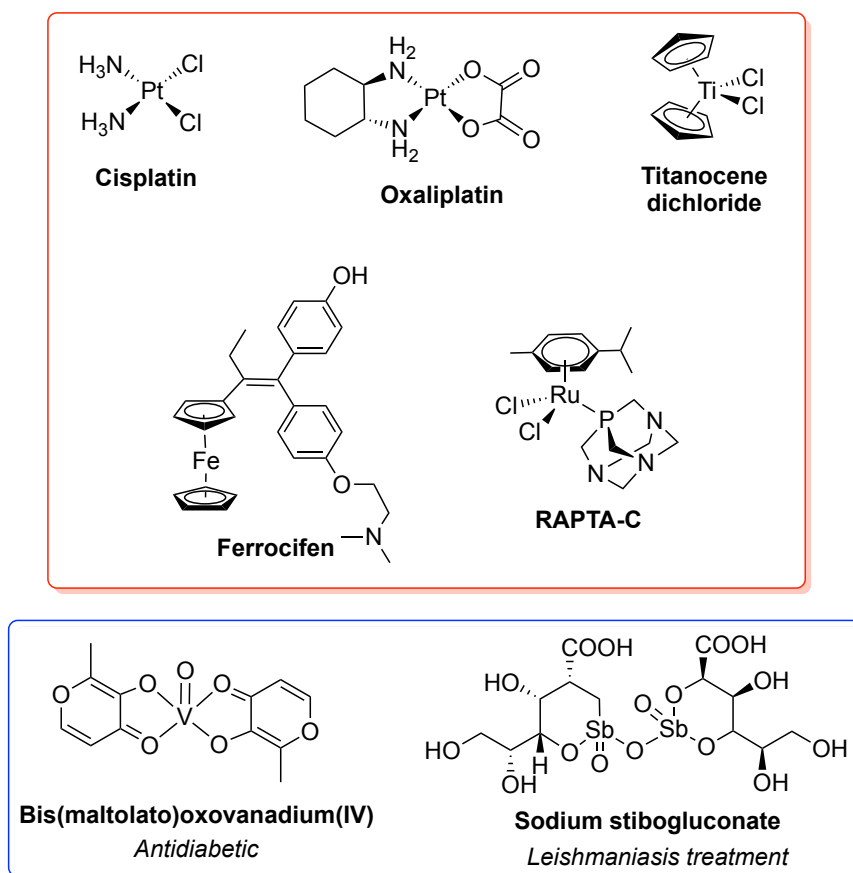


Figure 1 – (Top) Selection of metal-based anticancer complexes. (Bottom) Two metal-based complexes used for treatment of different diseases such as diabetes and leishmaniasis.

However, due to the inherent toxicity of cisplatin and acquired resistance by cancer cells, derivatives were synthesised to overcome these issues, such as oxaliplatin (Figure 1, top).³ Oxaliplatin contains a DACH (diaminocyclohexane) ligand, which, due to its steric bulk, is thought to be responsible for its greater inhibition of DNA synthesis and reduced cross-resistance.⁴ Its exceptional activity against metastatic colorectal cancer has led to its use as a therapeutic in many countries in combination with fluoropyrimidines.⁴ Other metal complexes have also shown anticancer properties such as ferrocifen, titanocene dichloride and RAPTA-C ($[\text{Ru}(\eta^6\text{-}p\text{-cymene})\text{Cl}_2(\text{PTA})]$ (PTA = 1,3,5-triaza-7-

phosphaadamantane and *p*-cymene = 1-methyl-4-(propan-2-yl)benzene)) (Figure 1, top).⁵

Nowadays, metal complexes are not just limited to anticancer treatment; for example, the vanadium complex bis(maltolato)oxovanadium(IV) (Figure 1, bottom) is an insulin-mimetic that can be taken orally as an antidiabetic agent to control glucose levels in the blood.⁶ Additionally, antimonials such as sodium stibogluconate (Figure 1, bottom) have been used for the treatment of leishmaniasis until recently.⁷

1.1. Gold(I) complexes as anticancer agents

1.1.1. Auranofin and related gold(I) complexes

Gold (Au) has played a role in medicine since the early centuries, where it was believed to ward off evil spirits responsible for disease.⁸ The first gold-based drugs featured Au(I) thiolate moieties, such as aurothiomalate and aurothioglucose, which were used to treat tuberculosis between the late 19th and early 20th centuries (Figure 2).^{9–11} However, the treatment induced severe toxicity and eventually also its effectiveness against tuberculosis was questioned.¹⁰ Nevertheless, non-tubercular patients treated with sodium aurothiomalate reported reduced joint pain, which led Forestier to investigate gold compounds as treatment for rheumatoid arthritis.^{10,12} Since then, sodium aurothiomalate (Myochrysine®) has remained in the clinic as an anti-arthritis agent, administered by intramuscular injection.¹⁰

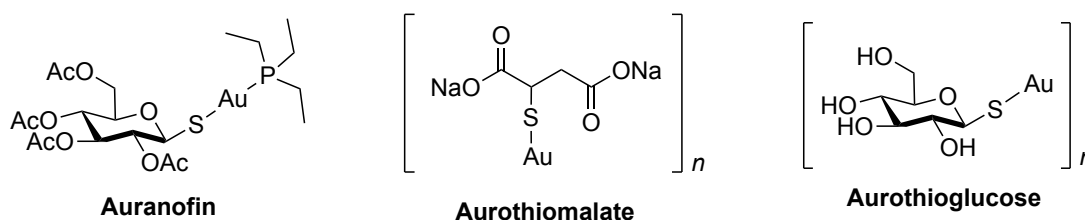


Figure 2 – Structures of antirheumatic gold(I) complexes with anticancer effects.

In 1972, auranofin [2,3,4,6-tetra-*o*-acetyl-L-thio-β-D-glycopyranosato-S-(triethylphosphine)gold(I)] (Figure 2) was tested, along with 12 other alkylphosphine gold complexes, for its anti-arthritic properties.¹³ Auranofin was the most active complex studied and showed less severe side effects compared to gold sodium thiomalate.¹⁰ Due to its hydrophilic nature, auranofin (Ridaura®) could be given as an oral therapeutic in the clinic.¹⁰

Interestingly, in 1979 Simon *et al.*¹⁴ tested the activity of auranofin against cancer cell proliferation in HeLa cells (human cervical cancer cell line). A few years later, Mirabelli *et al.*,¹⁵ evaluated the antitumour activity of auranofin *in vitro* against different tumour cell lines and *in vivo* in different mouse tumour models.¹⁵ Auranofin was found to only be effective against P388 leukaemia *in vivo*, yet was very cytotoxic in a range of

tumour cell types *in vitro*.¹⁵ Further work showed that auranofin derivatives featuring other phosphane groups also possessed the same activity *in vitro* and *in vivo* to the parent compound.¹⁶

However, auranofin was later shown to be inactive against solid tumour models.¹⁷ Additionally, even in mice with the P388 leukaemia model, auranofin was only active when administered by intraperitoneal injection (injection into the body cavity).⁹ Concerning the mechanisms of action, auranofin has also been shown to induce cell apoptosis and inhibition of tumour growth by activation of p38 mitogen-activated protein kinase (p38 MAPK) and inhibition of proteasomal deubiquitinases (DUBs).^{9,18–20}

In terms of pharmacological targets, several studies have reported that auranofin can potently inhibit seleno-containing proteins such as thioredoxin reductase (TrxR).²¹ TrxRs are homodimeric proteins and part of the flavoprotein family.²² They are named as such due to their ability to catalyse the nicotinamide adenine dinucleotide phosphate (NADPH)-dependent reduction of thioredoxins (Trxs) (Figure 3).²² Overall, the thioredoxin system, which includes TrxR, Trx and peroxiredoxin (Prx), are required to regulate the concentration of hydrogen peroxide (H₂O₂) in cells (Figure 3).²¹ Uniquely, mammalian TrxRs contain a C-terminal selenocysteine (Sec) residue that, with an adjacent cysteine (Cys), functions as an additional redox-active site.²² The Sec residue is not found in bacterial TrxRs.²² Of note, there have been several reports of TrxRs and Trxs being overexpressed in cancer cells, making them a suitable target for anticancer treatment.²¹

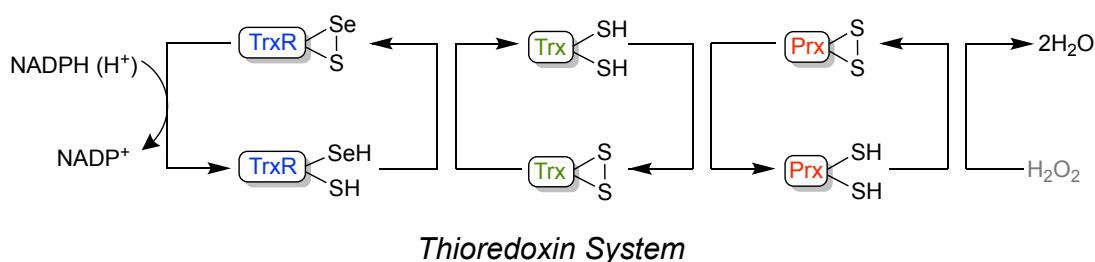


Figure 3 -Thioredoxin pathway to mediate the reduction of hydrogen peroxide. TrxRs catalyse the NADPH-dependent reduction of Trx, which in turn reduces Prx, allowing hydrogen peroxide to be converted to water. Image adapted from ref.²¹

Following the initial studies on auranofin, various families of Au(I) compounds were shown to be potent inhibitors of mammalian TrxRs. This can be explained by the presence of the Sec residue which favours binding to the Au(I) soft Lewis acid leading to TrxR inhibition.²¹ In general, the same gold(I) complexes are 1000-fold less effective in inhibiting human glutathione reductase (GR) and glutathione peroxidase, highlighting the selectivity of these complexes for the seleno-containing enzyme TrxR.^{21,23}

Au(I) complexes usually possess a linear coordination geometry and high reactivity towards sulfur donors (e.g. thiolates of Cys residues) *via* ligand exchange reactions, which may also contribute to the development of side effects.²⁴ With the aim of reducing the reactivity with thiols, several four-coordinated bis-chelated Au(I)-phosphane complexes have also been designed.²⁴ For example, Berners-Price *et al.*²⁵ were the first to report on the antitumoural activity of these complexes, namely [Au(dppe)₂]Cl (dppe = bis(diphenylphosphino)ethane) (Figure 4) in mice tumour models.²⁵ [Au(dppe)₂]⁺ and its derivatives belong to a class of antitumour agents known as delocalised lipophilic cations (DLCs), which accumulate in the mitochondria of cancer cells.²⁶ However, the compounds were not selective for cancer cells causing mitochondrial dysfunction, leading to severe toxicity in preclinical studies on dogs and rabbits.²⁶

In order to modulate the complex to target cancer cells selectively, the lipophilic nature was decreased to avoid membrane permeabilization of healthy cells.²⁴ McKeage *et al.*²⁷ observed that replacing the phenyl groups of [Au(dppe)₂]Cl with pyridyl groups gave a series of complexes with an extensive array of hydrophilic properties, with the general formula, [Au(dnpype)₂]Cl (dnpype = 1,2-bis(di-*n*-pyridylphosphino)ethane, *n* = 2, 3 and 4).²⁷ The 2-pyridyl complex [Au(d2pype)₂]Cl (Figure 4) showed intermediate lipophilic character and significant *in vivo* antitumour activity in colon 38 (MC-38) tumours in mice.^{26,27} The cytotoxic potential of these complexes was also assessed in isolated rat hepatocytes and different cisplatin-resistant human ovarian cancer cell lines.^{26,28} Generally, it was found that increasing the compound's lipophilicity resulted in an increase in cytotoxicity along with a decrease in selectivity towards cancer cells.^{26,28}

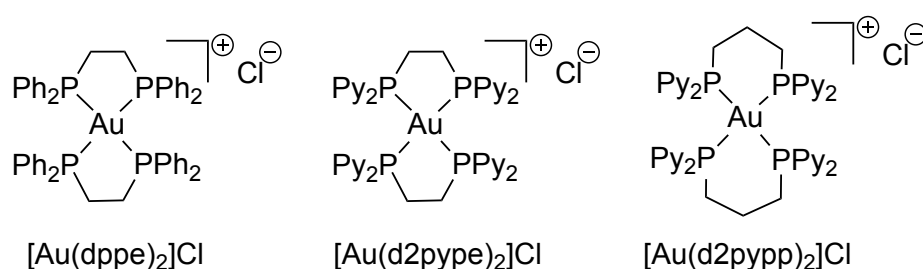


Figure 4 – Structures of Au(I) chelated diphosphine anticancer complexes. Ph = phenyl and Py = 2-pyridyl.

Further work to optimise the lipophilicity of these Au(I) chelated diphosphine complexes involved replacing the ethyl-bridge between the pyridyl phosphine ligands of [Au(d2pype)₂]Cl with a propyl-bridge forming [Au(d2pypp)₂]Cl (d2pypp = 1,3-bis(di-2-pyridylphosphino)propane) (Figure 4).²⁹ The increased length of the alkyl chain increased the lipophilicity, resulting in an octanol-water partition coefficient (log *P*) of the complex to be within an optimal range (increase in log *P* from -0.92 to -0.46 for

$[\text{Au}(\text{d2pype})_2]\text{Cl}$ and $[\text{Au}(\text{d2pypp})_2]\text{Cl}$, respectively).²⁹ It is important to point out that this is still far away from the $\log P$ value of the highly lipophilic parent complex, $[\text{Au}(\text{dppe})_2]^+$ ($\log P = 1.41$).²⁹ Additionally, the complex demonstrated selective cytotoxicity towards triple-negative human breast cancer cells (MDA-MB-468) rather than healthy human mammary epithelial cells (HMEC).²⁹

Further studies showed that the complex could inhibit both Trx and TrxR more effectively in breast cancer cells than healthy cells, which could further account for its selective toxicity.³⁰ It was previously shown that $[\text{Au}(\text{dppe})_2]\text{Cl}$ had low reactivity towards thiols; however, it appears that for $[\text{Au}(\text{d2pypp})_2]\text{Cl}$ this is not the case, which may be due to more facile opening of the six-membered chelate ring, compared to the five-membered ring of the parent complex, allowing it to interact with the protein thiol/selenol groups.³⁰ It was proposed that the Au(I) would irreversibly bind to the Cys/Sec residues in the active site of TrxR1 and TrxR2, causing displacement of the phosphine ligands; therefore, inhibiting the Trx/TrxR system intracellularly (Figure 5).³⁰

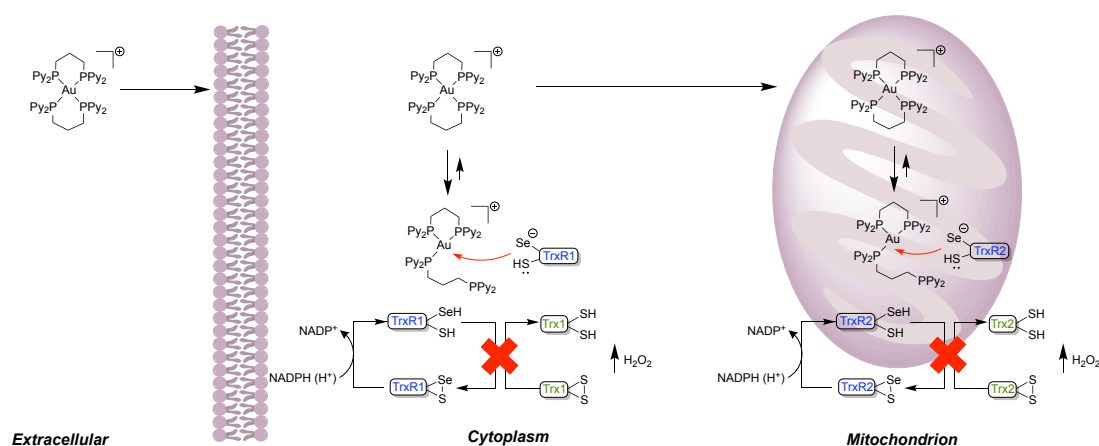


Figure 5 – Schematic representation of $[\text{Au}(\text{d2pypp})_2]\text{Cl}$ uptake in cells leading to its accumulation in the cytoplasm and mitochondria, thus, binding to the corresponding Trx and TrxR isoforms. Image adapted from ref.³⁰

Lipophilic cationic mixed gold phosphine complexes have also been shown to possess anticancer activity; for example, $[\text{Au}(\text{dppp})(\text{PPh}_3)\text{Cl}]$ (dppp = 1,3-bis(diphenylphosphino)propane, PPh_3 = triphenylphosphine) was found to be effective *in vitro* against a range of different cancer cell lines, showing highest toxicity in melanoma cells.³¹ The group later reported mitochondria as the likely target for this complex, inducing mitochondria-mediated apoptosis.³² In solution, the $[\text{Au}(\text{dppp})(\text{PPh}_3)\text{Cl}]$ complex partially decomposes to form the dinuclear cationic species $[\text{Au}_2(\text{dppp})_2\text{Cl}]^+$, which could be the active species responsible for the anticancer activity in the different cell lines.³³

Another interesting gold phosphine complex includes $[\text{Au}(\text{P}(\text{CH}_2\text{OH})_3)_4]\text{Cl}$ (Figure 6a), which shows *in vitro* anticancer properties in a range of different cell lines; most

remarkably, its anticancer effect is exerted in androgen-independent PC-3 human prostate tumour cells, which are rarely inhibited by metal-based drugs.³⁴ Analysis of the cell cycle of HCT-15 cells (human colorectal carcinoma cells), when exposed to the complex, showed elongation of the G1 phase, indicating a cytostatic effect of the drug.³⁴ This effect was also observed *in vivo* for mice bearing syngeneic meth/A sarcoma cells, with an increased survival time when treated with $[\text{Au}(\text{P}(\text{CH}_2\text{OH})_3)_4]\text{Cl}$.³⁴

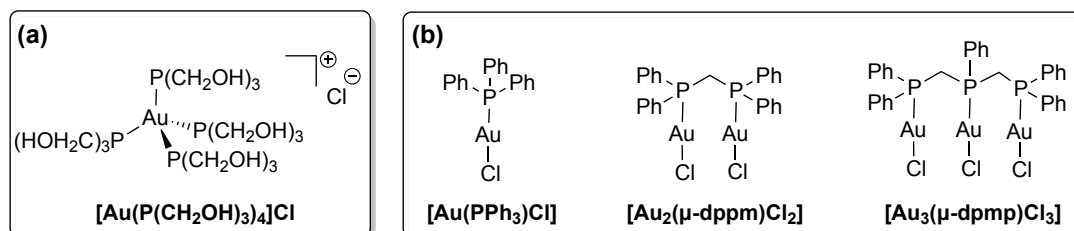
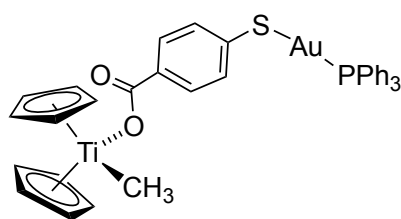


Figure 6 – (a) Structure of the four-coordinate Au(I)-phosphine complex published by Katti and co-workers.³⁴ (b) Au(I)-phosphane complexes capable of inducing autophagy in HeLa cells.³⁵

Che and co-workers later reported a series of Au(I)-phosphines capable of inducing autophagy in HeLa cells, with $[\text{Au}(\text{PPh}_3)\text{Cl}]$, $[\text{Au}_2(\mu\text{-dppm})\text{Cl}_2]$ (dppm = bis(diphenylphosphino)methane) and $[\text{Au}_3(\mu\text{-dpmp})\text{Cl}_3]$ (dpmp = bis(diphenylphosphinomethyl)phenylphosphine) (Figure 6b) producing an accumulation of autophagosomes in the cells as observed by TEM (transmission electron microscopy), which is thought to be associated with cell death.³⁵

In 2015, Contel and co-workers reported the ability of a heterometallic titanocene-gold phosphine complex, $[(\eta\text{-C}_5\text{H}_5)_2\text{TiMe}(\mu\text{-mba})\text{Au}(\text{PPh}_3)]$ (mba = $\text{S-C}_6\text{H}_4\text{-COO}^-$) (Figure 7), to selectively inhibit the growth of human renal cancer cells (Caki-1) against healthy human kidney cell lines, HEK-293T (non-tumourigenic human embryonic kidney cells) and RPTC (human renal proximal tubular cells) *in vitro*.³⁶ Further *in vitro* studies showed that renal cancer growth could be impeded by pathways involving inhibition of TrxR and decreased expression of protein kinases involved in tumour metastasis.³⁶ *In vivo* work was also performed using mice inoculated with Caki-1 cancer cells, which, when treated with the compound for 28 days (3 mg per kg per every other day), saw an impressive 67% decrease in tumour size.³⁶



$[(\eta\text{-C}_5\text{H}_5)_2\text{TiMe}(\mu\text{-mba})\text{Au}(\text{PPh}_3)]$

Figure 7 – Structure of heterometallic titanocene-gold phosphine complex, $[(\eta\text{-C}_5\text{H}_5)_2\text{TiMe}(\mu\text{-mba})\text{Au}(\text{PPh}_3)]$ ($\text{mba} = \text{S-C}_6\text{H}_4\text{-COO}^-$) reported by Contel and co-workers.³⁶

1.1.2. Gold(I) N-heterocyclic carbene (NHC) complexes

In an attempt to reduce the speciation of cytotoxic Au(I) complexes in a biological environment and to control their reactivity with selected targets, numerous recent studies have investigated organometallic Au(I) complexes endowed with increased stability in terms of ligand exchange reactions and redox properties.³⁷ In this context, N-heterocyclic carbene (NHC) ligands have become popular in medicinal inorganic chemistry due to their ease of functionalisation and less toxic nature compared to phosphine ligands.³⁷ NHCs are ideal ligands for gold(I) due to their strong electron-donating ability, providing stability in physiological conditions.³⁷ In 2004, Berners-Price and co-workers^{38,39} presented a series of dinuclear Au(I) cationic complexes (Figure 8) bearing imidazolium-linked cyclophane or cyclophane-like ligands, investigating their ability to induce mitochondrial membrane permeabilization (MMP) in isolated rat liver mitochondria.^{38,39}

Mitochondria are not only needed for ATP (adenosine triphosphate) generation; they are also vital for the control of apoptotic cell death.⁴⁰ Cellular apoptosis can be initiated by the permeabilization of the mitochondrial membrane, which is controlled by the opening of the permeability transition pore in the inner membrane of the mitochondria.⁴¹ However, in diseases such as cancer, mitochondrial apoptosis can be inhibited, allowing cancer to spread.⁴⁰ This led to research into new anticancer complexes capable of targeting the mitochondrial cell death pathway to trigger apoptosis by MMP.³⁹ The significant difference between plasma membrane potentials and mitochondria in cancer cells compared to healthy cells has been exploited as a potential targeted anticancer therapy using compounds with optimal lipophilic character and featuring positive charges (the aforementioned DLCs).³⁹ Although previous work had shown that Au(I) phosphine complexes such as $[\text{Au}(\text{dppe})_2]^+$ could be effective anticancer compounds acting as DLCs,²⁵ the robustness in functionalisation of NHC ligands, together with their reduced toxicity in non-tumourigenic cells with respect to phosphane ligands, has made them attractive alternatives, with easier control of the overall chemico-physical properties.³⁹

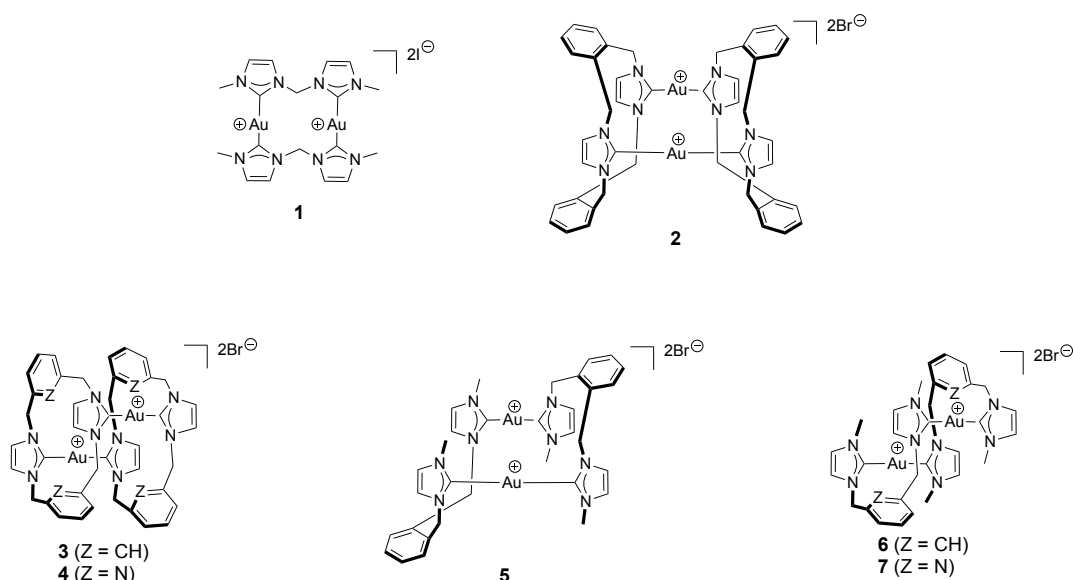


Figure 8 – Series of dinuclear Au(I) NHC complexes bearing imidazolium-linked cyclophanes and related non-cyclophane scaffolds.³⁹

The MMP in the presence of compounds **1-7** (Figure 8) was monitored by mitochondrial swelling, with increased swelling suggesting increased permeabilization.³⁹ Overall, the most active compound was **2** in the presence of Ca^{2+} ,³⁹ however, it still did not exceed the activity of auranofin.⁴²

Two years later, the same group reported five linear mononuclear Au(I) bis-NHC complexes (Figure 9) bearing monodentate dialkylimidazol-2-ylidene ligands, which were varied to alter the lipophilicity of the compound.⁴³ The lipophilic character of the complexes can be tuned to favour rapid uptake in cancer cells compared to healthy cells, specifically in the mitochondria, due to their increased plasma and mitochondrial membrane potentials.⁴³

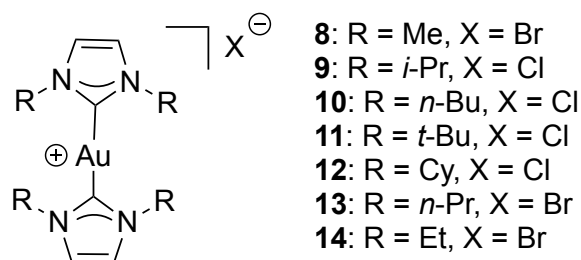


Figure 9 – Structures of Au(I) NHC complexes bearing monodentate dialkylimidazol-2-ylidene ligands altered to tune the lipophilicity of the compound.^{43,44}

Compounds **9-12** showed dose-dependent (1-10 μM) mitochondrial swelling in isolated rat liver mitochondria, whereas the least lipophilic compound (**8**) did not induce significant swelling.⁴³

Following on from this work, Berners-Price and co-workers chose to investigate complex **9** as a potential inhibitor of TrxR due to its intermediate lipophilicity ($\log P = -0.29$), alongside two new derivatives (Figure 9), **13** ($\log P = -0.002$) and **14** ($\log P = -0.84$).⁴⁴ In this study, the cytotoxicity of compounds **9**, **13** and **14** were evaluated against MDA-MB-231 and MDA-MB-468, both of which are highly tumourigenic breast cancer cell lines, and also healthy human mammary epithelial cells (HMEC), to observe any selectivity towards the cancer cell lines.⁴⁴ All three complexes showed selective cytotoxicity for the two breast cancer cell lines over the healthy cells.⁴⁴ However, complex **9**, with the intermediate $\log P$ value, provided the greatest selectivity and cytotoxicity.⁴⁴

To gain more understanding as to whether thiol- and selenol-containing proteins, such as TrxR, are targets for Au(I)-NHC compounds, complex **8** from the previous study, alongside complex **9** (1.7 mM), were incubated with Cys and Sec (8.3 mM) at 37 °C in phosphate-buffered saline (PBS, 0.1 M, pH 7.2).⁴⁴ The reaction was monitored using ¹H NMR (nuclear magnetic resonance), paying close attention to the resonances of the imidazolium H4/H5 protons. It was reported that a two-step process occurs whereby the NHC ligands are exchanged to form either $[\text{Au}(\text{Cys})_2]^-$ or $[\text{Au}(\text{Sec})_2]^-$.⁴⁴ Complex **8** was 2- to 3-times more reactive than complex **9**, which was expected, due to the bulkier wingtip group (*i*Pr) of the latter, providing steric hindrance to the entering ligand. The reactions with Sec for both complexes were also faster compared to Cys, which the authors proposed was due to the difference in pKa values at pH 7.2, as the Sec group would be deprotonated, whereas the Cys would be protonated.⁴⁴ To observe whether these reactions would translate to inhibition of TrxR, complex **9** was incubated with MDA-MB-231 cells over 6 hours with increasing concentrations of **9**. The results showed promise, with TrxR activity inhibited by ca. 50% with 5 μM of **9** with no inhibition of GR, a thiol-containing, Se-free enzyme.⁴⁴

Following on from this work, Ott and co-workers synthesised a series of mono benzimidazol-2-ylidene gold(I) compounds (**15-18**, Figure 10) with the general formula $[\text{Au}(\text{NHC})\text{Cl}]$.⁴⁵ Different substituents on the NHC core were used to alter the lipophilicity and surface volume to interact with the TrxR active site favourably.⁴⁵

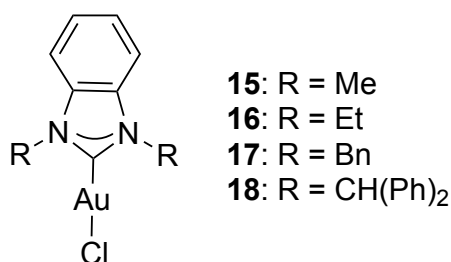


Figure 10 – Series of mono benzimidazol-2-ylidene gold(I) compounds to inhibit TrxR.⁴⁵

also included as a comparison.⁴⁸ In both cell lines, the complexes were cytotoxic, with IC₅₀ values below 10 μM; however, the lowest IC₅₀ values were seen in MCF-7 cells. Complex **20** was the most potent in both cell lines, which could be explained by its high lipophilicity; thus, cellular accumulation.⁴⁸

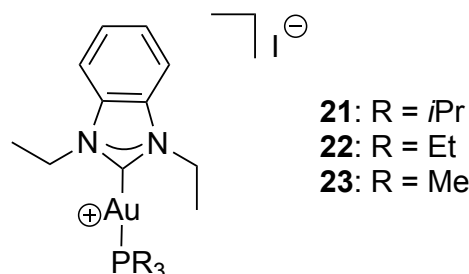


Figure 12 - Structures of Au(I) NHC complexes with different phosphane ancillary ligands.⁴⁸

The potential of the complexes **21-23** to inhibit TrxR was assessed, comparing to the enzyme, GR.⁴⁸ All complexes were effective inhibitors of TrxR, with IC₅₀ values below 1 μM, however complexes **22** and **23**, with the smaller groups on the phosphane ligand, gave the lowest IC₅₀ values.⁴⁸ Importantly, **22** and **23** exhibited a marked selectivity for TrxR inhibition compared to GR inhibition;⁴⁸ however, this is still not enough to exceed the selectivity seen previously by auranofin.^{23,46} The zinc finger protein PARP-1 (poly(ADP-ribose) polymerase-1) was also investigated in this work as another potential target for gold complexes.^{48,49} PARP-1 is responsible for recognising DNA damage and initiating its repair, as well as being involved in cancer cell proliferation.⁵⁰ All complexes (**20-23**) showed exceptional inhibition of the enzyme, with IC₅₀ values 100-fold lower than the benchmark inhibitor 3-aminobenzamide,⁴⁹ with the lowest IC₅₀ value observed for complex **20**.⁴⁸ The authors postulated that this increased activity was due to complex **20** having the lowest BDE value for the Au-PR₃ bond.⁴⁸

Further examples of increasing the potency of the Au(I) NHC complexes have been demonstrated; for example, Contel and co-workers⁵¹ conjugated a Au(I) NHC complex to a titanocene group, resulting in increased cytotoxic activity compared to their corresponding monometallic precursors in prostate and colon cancer cell lines.⁵¹ Targeted drug delivery can also be achieved, as seen by Veige and co-workers, by attachment of a CCRF-CEM-leukaemia specific aptamer sgc8c to a NHC-Au(I) complex.⁵²

Che and co-workers⁵³ demonstrated the advantages of retaining both an NHC and phosphine ligand on the Au(I) for targeting cellular TrxR *in vivo*. The dinuclear complex (**24**, Figure 13) possessed a bridging bis(NHC) ligand to provide stability against cellular thiols, such as glutathione (GSH) and serum albumin, and a diphosphine ligand to allow favourable reactivity towards TrxR.⁵³ *In vivo* studies also showed that the complex could

significantly inhibit tumour growth of HeLa xenografts on mice as well as highly aggressive mouse B16-F10 melanoma. Comprehensive toxicology studies also showed that the complex bears no noticeable side effects in the conditions investigated.⁵³

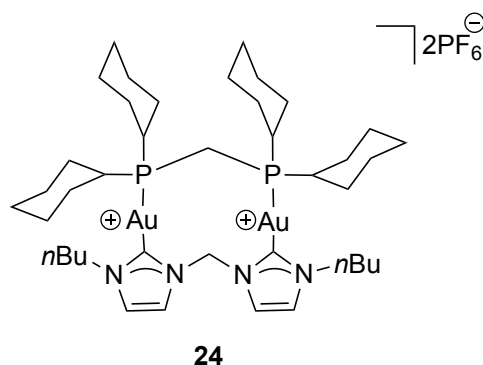


Figure 13 – Dinuclear Au(I) complex investigated as a TrxR inhibitor and anticancer agent by Che and co-workers.⁵³

Au(I) bis-NHC complexes were further investigated for targeting other non-proteinaceous targets, including G-quadruplex (G4) DNA. The formation of G4 structures from single-stranded telomeric DNA can inhibit the enzyme telomerase, which is overexpressed in most cancer cells.⁵⁴ G4 DNA structures are also commonly found in the promoter regions of oncogenes; therefore, stabilisation of these G4 structures can stop the expression of the corresponding oncogene.⁵⁴

Due to the strong Au-C bonds in the Au(I) bis-NHC complex, it was hypothesised that instead of a ligand exchange reaction, the complex would interact with the G4 DNA *via* non-covalent interactions. This was demonstrated by Casini and co-workers,^{55–57} where they used two methylated caffeine ligands to achieve [Au(9-methylcaffeine-8-ylidene)₂]⁺, a potent G-quadruplex stabiliser. The complex also demonstrated selectively by stabilising G4-DNA over duplex DNA.^{55,56} Combined X-ray diffraction (XRD) and atomistic simulations showed that the compound could stack at the top of a G4 unit (Figure 14).⁵⁶ This compound also showed moderate cytotoxicity against the human ovarian cancer cell line A2780 and its cisplatin-resistant variant, A2780/R, with little effect on non-cancerous HEK-293T cells, displaying desirable and selective antiproliferative effects.⁵⁷

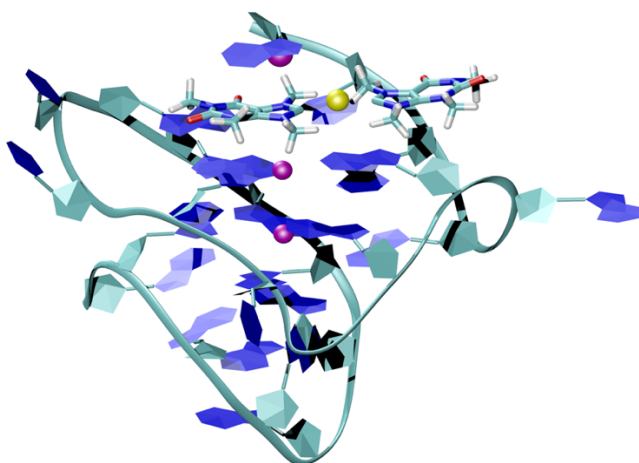


Figure 14 – An adduct of the cationic bis-NHC Au(I) complex $[Au(9\text{-methylcaffeine-8-ylidene})_2]^+$ with promoter G4 structure (cKIT) calculated by multiple collective variable (CV) metadynamics.

Figure generated with VMD software by Dr. Wragg. Reprinted with permission from ref. 59

Copyright (2021) Elsevier.^{56,58,59}

1.1.3. Gold(I) Alkynyl complexes

The use of gold(I) alkynyl complexes for therapeutic applications was first explored in 2009 in two separate papers by the groups of Mohr⁶⁰ and Wong.⁶¹ Mohr and co-workers synthesised Au(I) alkynyl complexes bearing derivatives of known anti-malaria drugs to improve their efficacy (**25-27**, Figure 15).⁶⁰ Unfortunately, the complexes showed low anti-malaria activity when tested on two different strains of *plasmodium falciparum*, with IC₅₀ values several times higher than chloroquine alone.⁶⁰ However, the complexes were also screened as anticancer agents on four different human cancer cell lines and their results were compared to those found for cisplatin. The cytotoxicity was moderate for all complexes, with **27** showing the lowest IC₅₀ values, however still not as active as cisplatin.⁶⁰

Wong and co-workers investigated the anticancer activity of diethynylfluorenes and their Au(I) complexes (**28** and **29**, Figure 15), differing only in a carbonyl group, in three different human cancer cell lines.⁶¹ Remarkably, **28** showed superior anticancer activity compared to cisplatin, at variance to its starting ligand. Due to these promising results, **28** was next investigated *in vivo* against human Hep3B (human liver) carcinoma cells xenografted onto athymic nude mice.⁶¹ Over 10 days, **28** showed no overall change in mean tumour volume; however, the mice treated with the buffer vehicle (placebo) saw a 3-fold increase in tumour volume. Autopsy samples of vital organs from both the mice treated with **28** or the buffer vehicle showed no necrotic features, highlighting a promising toxicology profile of **28**.⁶¹ Investigations into the mechanism of action for **28** led to the discovery that it produces significant intracellular ROS, which the authors proposed as

essential for the cytotoxicity of the compound due to reduction of ROS generation and cytotoxic activity when co-incubated with catalase, a ROS scavenger.^{61,62}

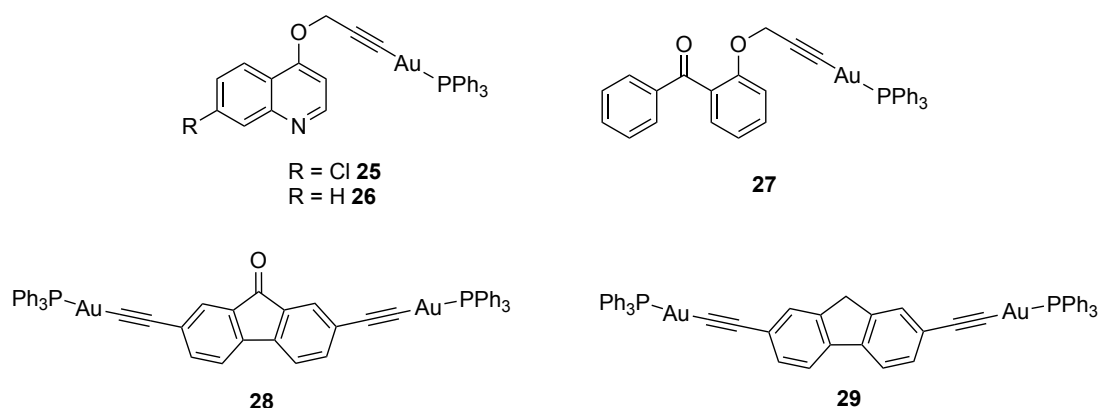


Figure 15 - Au(I) alkynyl complexes bearing triphenylphosphine ligands^{60,61}

The following year, Vergara *et al.*,⁶³ synthesised organometallic alkynyl phosphane Au(I) complexes bearing either PTA or DAPTA (3,7-diacetyl-1,3,7-triaza-5-phosphabicyclo[3.3.1]nonane) as co-ligands to improve the stability and water-solubility of these Au(I) complexes. A series of mono-, di- and trinuclear Au(I) derivatives were formed with a range of alkynyl groups, a selection of which were then tested for their cytotoxicity in A2780 and A2780cisR cell lines.⁶³ The most active compounds are shown in Figure 16 (**30-32**). **30b** showed greater potency compared to cisplatin in both cell lines, with comparable IC₅₀ values to auranofin, suggesting it was capable of overcoming the cisplatin resistance mechanism.⁶³ **31a** and **31b** were both more potent than cisplatin and auranofin in A2780 cells, however, could not outperform auranofin in A2780cisR cells. Trinuclear complexes **32a** and **32b** were again more active than cisplatin however could not match the potency observed for auranofin in either cell line.⁶³

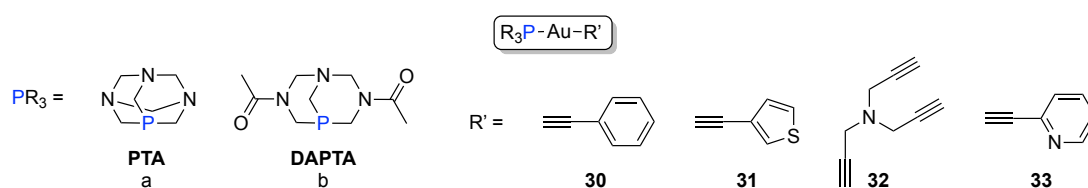


Figure 16 – Organometallic alkynyl Au(I) complexes bearing PTA or DAPTA as a co-ligand.⁶³⁻⁶⁵

More recently, inspired by these results, the groups of Cerrada and Rodriguez-Yoldi,^{64,65} investigated the anticancer effect of complexes **30a**⁶⁴ and **33a**⁶⁵ (Figure 16) on human colorectal carcinoma cells (Caco-2/TC7). Both complexes were able to bind to bovine serum albumin (BSA) more strongly than cisplatin, which was proposed to lead to greater distribution of the complex within the blood.^{64,65} Antiproliferative studies highlighted the high potency of both complexes *in vitro* and their selectivity for cancer cells (Caco-2/TC7

cells which are not at confluence) compared to normal enterocytes (Caco-2/TC7 cells at confluence).^{64,65} However, the mechanism of action of these complexes appeared to be different. **30a** caused inhibition of the enzyme TrxR-1, resulting in increased ROS levels and cell apoptosis. Whereas **33a** showed minimal inhibition of TrxR, but an increase in ROS production, which led to necroptotic cell death in Caco-2/TC7 cells.^{64,65} Therefore **33a** showed promise as a treatment for cancer cells resistant to apoptosis.⁶⁵

Meanwhile, Laguna and co-workers⁶⁶ investigated a series of *s*-propargylthiopyridine phosphane Au(I) complexes coordinated to Cu(I) *via* free nitrogen and sulfur groups for use as anticancer agents for colon cancer. Water-soluble phosphanes (PTA and DAPTA) were also used in this work after the success observed by Vergara *et al.*⁶³ the previous year.⁶⁶ The addition of Cu(I) was anticipated to increase the potency of the complex due to the combination of two cytotoxic metals.⁶⁷ The cytotoxicity of the dimetallic complexes (**35a,b** and **36a,b**, Figure 17) were tested against two clones of the cell line Caco-2: Caco-2/TC7 and Caco-2/PD7, as well as the Au (**34a,b**, Figure 17) and Cu mononuclear precursors.⁶⁶ In all cases, the bimetallic complexes (**35a,b** and **36a,b**) showed significant potency compared to both monometallic precursors. Generally, the complexes bearing two Au atoms and a hexafluorophosphate (PF_6^-) counterion (**35a,b**) exhibited increased cytotoxicity compared to the mono-Au complexes featuring a nitrate (NO_3^-) counterion (**36a,b**), with the exception of **36b** in Caco-2/TC7 cell line.⁶⁶ The bimetallic complexes (**35a,b** and **36a,b**) also showed superior activity compared to cisplatin and auranofin, with a maximum increase in five orders of magnitude for **35a** compared to cisplatin in Caco-2/PD7 cells.⁶⁶ Derivatisation of the propargylthiopyridine to form complexes **37a,b-39a,b** resulted in highly cytotoxic compounds against Caco-2/PD7 and Caco-2/TC7 cell lines, however none were more potent than auranofin. The PTA complexes (**37-39a**) showed greater toxicity than their DAPTA counterparts (**37-39b**) with the most active complex across both cell lines being **37a**, however this was closely followed by **38a** and **39a**.⁶⁶

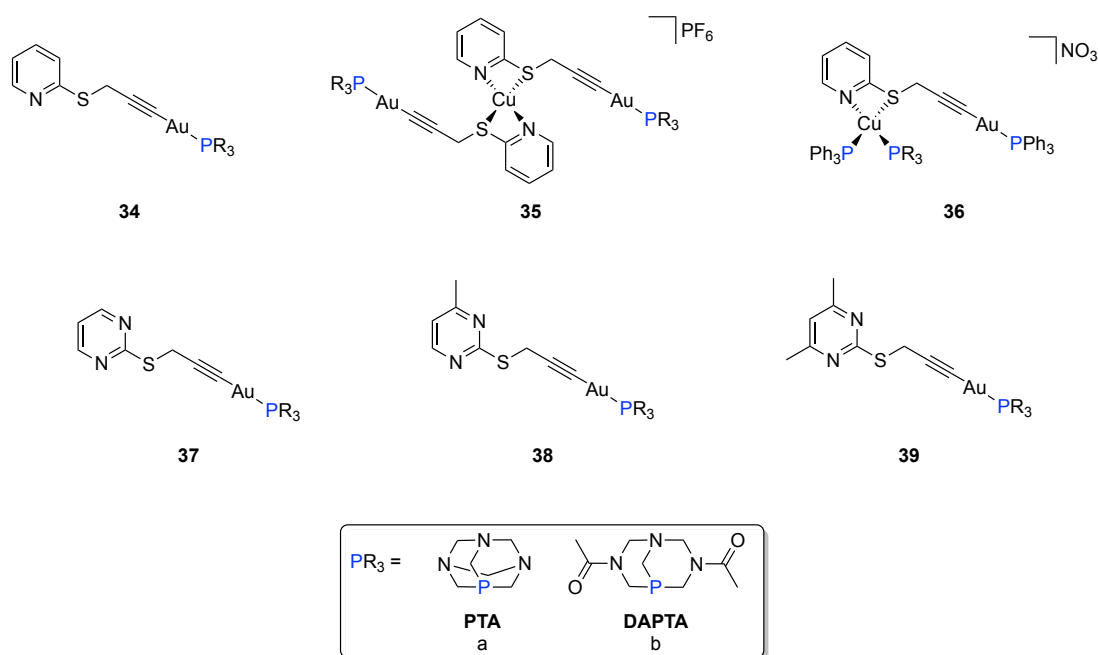


Figure 17 – A series of *S*-propargylthiopyridine phosphane Au(I) complexes with/without Cu(I) coordination.⁶⁶

The group of Ott have also synthesised Au(I) alkynyl complexes for anticancer treatment, bearing a triphenylphosphine (PPh₃) group as the ancillary ligand.⁶⁸ The complexes exhibited IC₅₀ values in the low μM range in MCF-7 and HT-29 cells, with complexes **40** and **41** (Figure 18) being the most successful for TrxR inhibition, with selectivity over GR.⁶⁸ The authors also tested the complexes for anti-angiogenic effects; zebrafish embryos were treated with non-toxic concentrations of **40** and **41** for 48 and 72 h and compared to the known anti-angiogenic drug thalidomide.⁶⁸

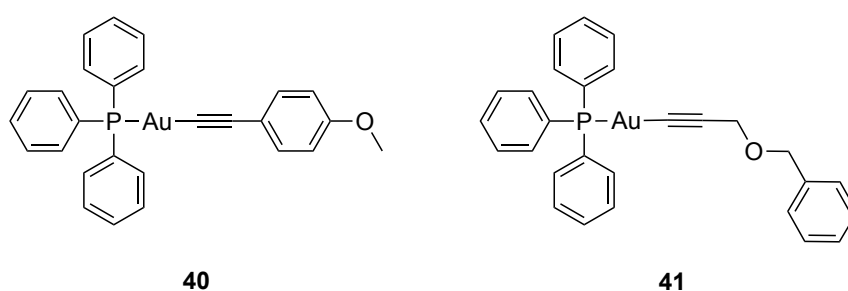


Figure 18 – Au(I) alkynyl complexes bearing a triphenylphosphine ligand synthesised by the Ott group.⁶⁸

Both complexes (**40** and **41**) were shown to be effective anti-angiogenic agents in more than 90% of the embryos treated, whereas thalidomide only affected approximately half

of the embryos.⁶⁸ Interestingly, the corresponding ligands of **40** and **41** showed no anti-angiogenic properties.⁶⁸

Combining the advantages of NHC and alkynyl ligands on Au(I) was first reported by Casini and co-workers⁶⁹ for the NHC-gold(I)-alkynyl complex **42** (Figure 19). The complex was tested against four tumour cell lines such as HCT-116 (p53wt and p53null), MCF-7 and A375 (human melanoma cell line).⁶⁹ Low micromolar IC₅₀ values were obtained across the cell lines, with potential selectivity demonstrated due to little toxicity observed against healthy rat kidney tissue.⁶⁹

Casini, Bonsignore and co-workers⁷⁰ later described a further series of NHC-Au(I)-alkynyl complexes, including complex **43** (Figure 19) where the NHC ligand was derived from a xanthine structure. The complex was tested against three cancer cell lines (A375, SKOV-3 (human ovarian cancer cell line) and MCF-7) and only showed moderate cytotoxicity against the MCF-7 cell line.⁷⁰ Instead, the benzimidazole complexes **44** and **45** (Figure 19) exhibit only moderate cytotoxicity against the same three cell lines.⁷¹

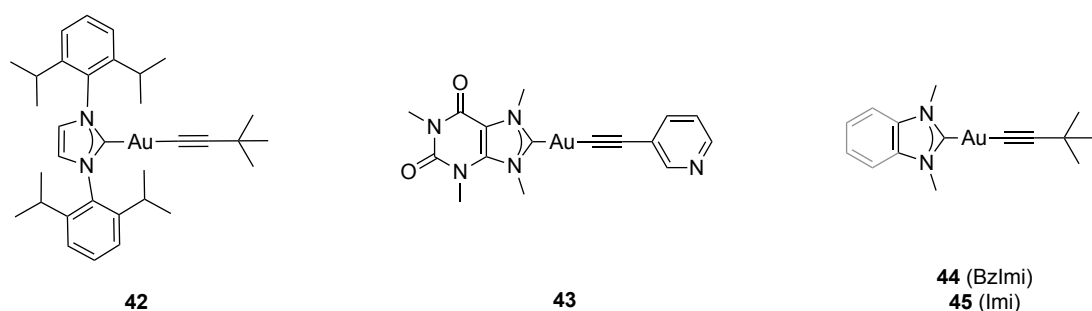


Figure 19 – NHC-Au(I)-alkynyl complexes reported by the Casini group.^{69–71}

1.2. Gold(III) complexes as anticancer agents

1.2.1. Gold(III) porphyrin complexes

Pioneering work by Che and co-workers⁷² sparked interest in this field, describing the ability of a gold(III) tetraphenylporphyrin (TPP) complex (**46**, Figure 20) to exhibit higher potency in human cancer cells compared to the benchmark cisplatin. This included higher potency in cisplatin-resistant cell lines, which indicates a different mechanism of action.⁷² The stability of the complex towards glutathione (2 mM GSH, Tris buffer : Acetonitrile, 19:1 v/v, pH 7.2) was also highlighted using Ultraviolet-Visible (UV-Vis) spectroscopy, with no change observed in the spectrum after several hours. After 48 h, the Soret band did appear to reduce in intensity; however, this could be restored by the addition of acetone, suggesting this change was caused by aggregation of the complex itself.⁷²

Over the years, complex **46** has also shown remarkable cytotoxicity *in vivo* against a range of different cancers, such as: hepatocellular carcinoma (HCC),⁷³ nasopharyngeal carcinoma (NPC),⁷⁴ colon cancer,⁷⁵ neuroblastoma,⁷⁶ NPC metastasis⁷⁷

and melanoma.⁷⁸ Extraordinarily, complex **46** has also been shown to inhibit the development of cancer stem cells *in vivo*, with no significant genotoxicity in nude mice at a dose below 3 mg kg⁻¹.⁷⁹ Additional work by the group also showed that complex **46** was capable of inhibiting both cisplatin sensitive (A2780) and cisplatin-resistant (A2780cisR) ovarian cancers *in vivo*, by using a xenograft model consisting of the two tumours on the same nude mouse.⁸⁰ This was prepared by inoculation of the two types of cancer cells (A2780 and A2780cisR) into either side of the mouse.⁸⁰

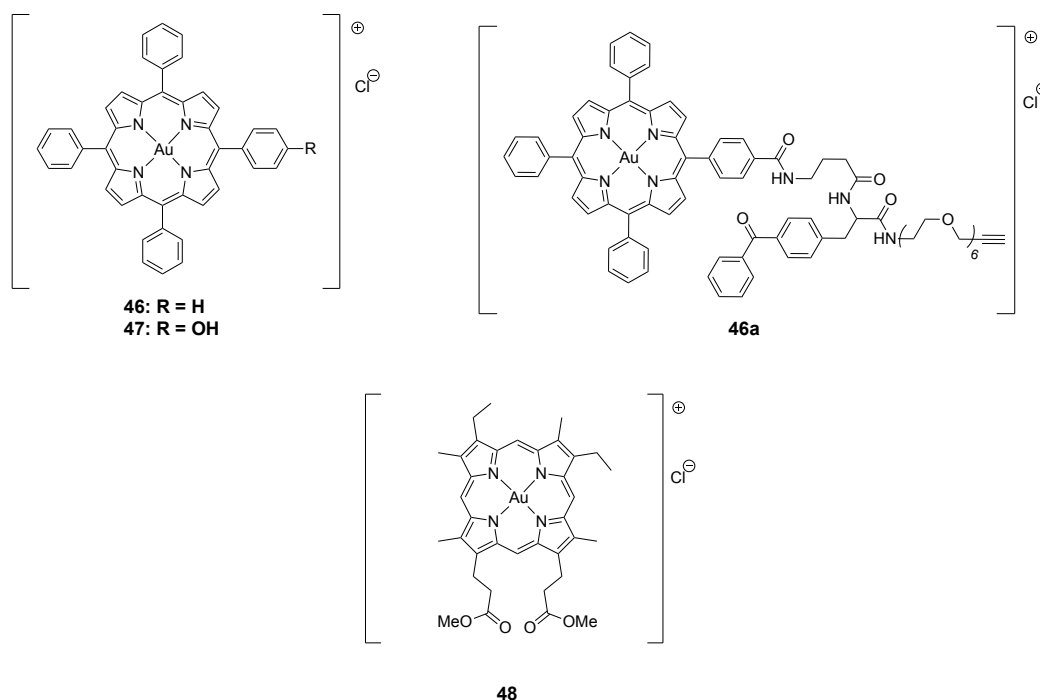


Figure 20 – Cytotoxic Au(III) tetraphenylporphyrin (TPP) complexes (**46**, **47** and **46a**) and Au(III) mesoporphyrin IX dimethyl ester complex (**48**) investigated by the group of Che.^{72,81–83}

Further work by the group of Che⁸⁴ also showed that different peripheral substituents on the *meso*-phenyl rings could influence the properties of the complex; for example, the addition of saccharide conjugations resulted in greater selectivity to cancer cells and enhanced cytostatic activity; however, it reduced the cytotoxicity of the complexes.⁸⁴

The addition of a *meso*-hydroxyl group to the TPP structure (complex **47**, Figure 20) was also reported to improve the water-solubility of complex **46**.⁸¹ Remarkably, complex **47** also showed high cytotoxicity in cancer cells, specifically in human breast cancer cells, with up to 3000-fold greater cytotoxicity compared to cisplatin.⁸¹ *In vivo* work also showed that complex **47** could suppress the growth of breast cancer tumours in nude mice.⁸¹ The authors considered this potency to be partly due to inhibition of the class I histone deacetylase (HDAC) activity which reduced the signalling of Wnt/ β -catenin, a key target of cancer treatment.^{81,85}

In order to gain more insight into the target molecules of the Au porphyrin complexes within cells, Che and co-workers⁸² exploited approaches such as affinity-based proteome profiling, whereby a clickable photoaffinity probe was attached to complex **46** to form complex **46a** (Figure 20). The combination of a linker, clickable tag and photoaffinity tag were required in order to form the complex; however, regardless of these additions, complex **46a** showed comparable cytotoxicity to complex **46**.⁸²

In this work, cancer cells (HeLa) were incubated with complex **46a** for 1 h before irradiation with UV light, initiating the reaction with the azide conjugated Cy5.⁸² The heat-shock protein 60 (Hsp60), a mitochondrial chaperone, was identified as the photo-affinity labelled protein by MALDI-TOF/TOF MS (matrix-assisted laser desorption ionisation-time of flight / time of flight mass spectrometry).⁸² The function of Hsp60 is to refold and reactivate misfolded proteins alongside its co-chaperonin Hsp10;⁸⁶ therefore, to understand if complex **46a** affects its activity, Hsp60 was exposed to denatured malate dehydrogenase (MDH) alongside varying concentrations of **46a** (2-20 μ M).⁸² The authors observed a dose-dependent inhibition of Hsp60 to reactivate MDH, which was also true for complex **46** and **47**. A Pt(II) derivative of **46a** bearing an *N*-substituted pyridine group was also tested for inhibition of Hsp60; however, it did not produce a significant reduction in activity.⁸²

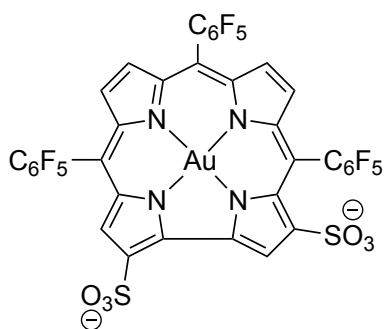
More recently, Che and co-workers⁸³ uncovered the novel reactivity of a gold(III) mesoporphyrin IX dimethyl ester (AuMesolX, complex **48**, Figure 20) due to its ability to react with cysteine residues. Complex **48** forms covalent C-S bonds to the protein's thiols due to the electrophilic methine group, at variance with complex **46** that possess phenyl groups in the *meso*-positions.⁸³ The most common reactivity of gold complexes with thiols is *via* the formation of a Au-S bond; however, in this case the ligand is activated by the electrophilic gold(III), meaning the *meso*-carbon can react with the thiol instead. This work also demonstrated the ability of the complex to inhibit the activity of several anticancer protein targets such as Trxs and DUBs *via* their thiol residues and showed potent cytotoxicity towards cancer cells both *in vitro* and *in vivo*.⁸³ Therefore, this novel reactivity could be exploited to develop new covalent protein inhibitors for anticancer treatment.

1.2.2. Gold(III) corrole complexes

Corrole ligands show interesting coordination chemistry due to their trianionic nature and high electron density, meaning they are able to coordinate to elements in formally high oxidation states such as manganese, iron, cobalt and gallium.⁸⁷

Taking inspiration from similar Au(III) porphyrin complexes, Teo *et al.*,⁸⁸ reported the cytotoxic and cytostatic properties of a water-soluble Au(III) complex of 2,17-bis-sulfonate-5,10,15-tris(pentafluorophenyl)corrole (complex **49**, Figure 21). This ligand has

also been synthesised as a Ga(III) complex, which was found to be cytotoxic towards breast cancer cells.⁸⁹ The cytotoxicity of complex **49** was compared to its Ga analogue in four different cancer cell lines, including DU145 (human prostate), SK-MEL-28 (human melanoma), MDA-MB-231 (human triple-negative breast) and OVCAR-3 (human ovarian).⁸⁸ Remarkably; complex **49** showed superior toxicity across all cancer cell lines compared to the Ga analogue, which was also seen for the cytostatic activity, indicating that the mechanism of action of **49** is *via* cell cycle arrest due to inhibition of DNA replication.⁸⁸



49

Figure 21 – Cytotoxic and cytostatic water-soluble Au(III) corrole complex.⁸⁸

The authors also observed a decrease in binding affinity of complex **49** to human serum albumin (HSA) compared to the Ga complex, which they believe could be responsible for its greater cytotoxicity.⁸⁸

1.2.3. Gold(III) complexes with chelating N donor ligands

Gold(III) can also be stabilised by chelating nitrogen donor ligands (N[^]N), as shown by Messori *et al.*⁹⁰ where they investigated the stability and anticancer properties of these Au(III) complexes (Figure 22). The N donor ligands used to form the Au complexes were: ethylenediamine (en, complex **50**), phenanthroline (phen, complex **51**), diethylenetriamine (dien, complex **52**), terpyridine (terpy, complex **53**) and 1,4,8,11-tetraazacyclotetradecane (cyclam, complex **54**).⁹⁰

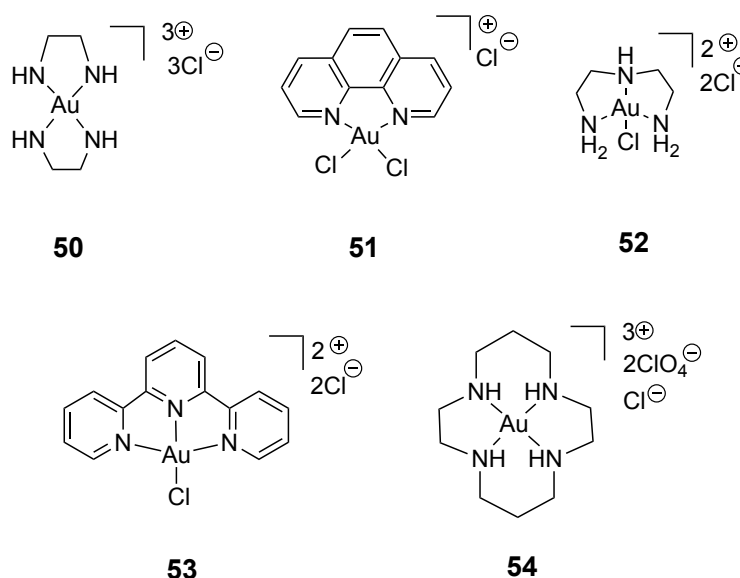


Figure 22 – Series of Au(III) complexes with chelating N donor ligands reported by Messori *et al.*⁹⁰

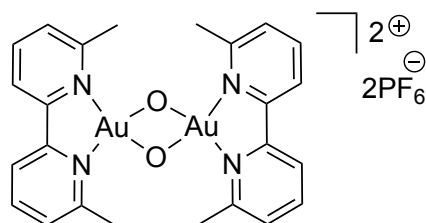
All complexes showed reasonable stability in physiologically relevant buffer over 72 h.⁹⁰ Cytotoxicity studies were performed against the A2780 cell line, both sensitive and resistant to cisplatin, with all complexes apart from Aucyclam (**54**) showing low μM IC₅₀ values in the cisplatin sensitive cell line.⁹⁰ Auterpy (**53**) appeared to be the most toxic across both cell lines; however, the ligand itself was also highly toxic, which suggests loss of the Au(III) centre. Alternatively, Auen (**50**) and Audien (**52**) showed superior toxicity to their corresponding ligands, strongly signifying that their potency is due to the Au(III) centre.⁹⁰

Another key target of Au(III)(NⁿN) complexes are aquaporins (AQPs), which are plasma membrane proteins.^{91,92} There are 13 human isoforms of AQP (AQP0-12), and these can be divided into two groups: orthodox AQPs that transport mainly water, and aquaglyceroporins (AQP3, 7, 9 and 10) that also transport small solutes such as glycerol. They are involved in many physiological processes, including cell proliferation, making them important targets for anticancer treatment.^{91,92} Auphen (**51**) and Audien (**52**) showed superior inhibition of AQP3 activity compared to the other metal complexes tested in the study, with **51** possessing the greatest inhibition.^{91,92} The targeting was also shown to be selective favouring inhibition of AQP3 over AQP1, an orthodox AQP.^{92,93}

A multi-level theoretical study was also performed using the Au(III)(NⁿN) complex [Au(bipy)Cl₂]PF₆ (bipy = 2,2'-bipyridine) as the model inhibitor of AQP3 due to its basic scaffold and ease of functionalisation.⁹⁴ The results concluded that water speciation of the Aubipy complex, where the chloride is replaced by a hydroxide forming [Aubipy(OH)Cl]⁺, is required for interaction with AQP3.⁹⁴

In 2006, Casini *et al.*⁹⁵ reported the synthesis and biological properties of dinuclear oxo-bridged Au(III) complexes bearing bipyridyl ligands. Complex **55** (Figure

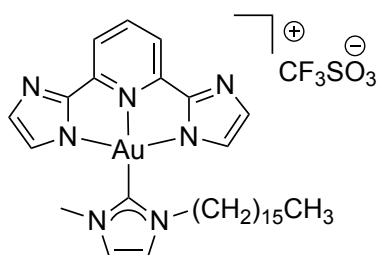
23), bearing two 6,6'-dimethyl-2,2'-bipyridine ligands, showed the highest cytotoxicity against cisplatin sensitive and resistant A2780 cell lines, with a five-fold increase in cytotoxicity compared to cisplatin against the A2780/R cells.⁹⁵ Remarkably, **55** was found to have high selectivity and activity when tested on a panel of thirty six cancer cell lines, with a mode of action predicted by COMPARE analysis to be histone deacetylase (HDAC) inhibition.⁹⁶



55

Figure 23 – Oxo-bridged Au(III) complex bearing two chelating 6,6'-dimethyl-2,2'-bipyridine ligands.⁹⁵

A series of Au(III)-NHC complexes bearing 2,6-bis(imidazol-2-yl)pyridine N[^]N[^]N ligands have been developed as thiol “switch-on” fluorescent probes.⁹⁷ In the presence of thiols such as GSH, the H₂N[^]N[^]N ligand is lost, which is fluorescent and thus quenched when coordinated to the Au(III).⁹⁷ The most cytotoxic compound was **56** (Figure 24), which showed the lowest IC₅₀ values in HeLa cells and also for the inhibition of TrxR, which was correlated to its high lipophilicity. Therefore, this complex was used for *in vivo* studies on nude mice with HeLa xenografts, with a reduction in tumour size observed with no serious side effects.⁹⁷



56

Figure 24 – Au(III) NHC complex bearing a 2,6-bis(imidazol-2-yl)pyridine N[^]N[^]N ligand acting as a fluorescent switch.⁹⁷

1.2.4. Gold(III) complexes with dithiocarbamate ligands

Dithiocarbamate ligands have been shown to decrease the nephrotoxicity of cisplatin without decreasing its anticancer properties,⁹⁸ therefore, it was also investigated as a

ligand for Au(III), which is isoelectronic to Pt(II).⁹⁹ Unsurprisingly, dithiocarbamate ligands have a high affinity to gold and the complexes themselves showed interesting anticancer properties. Fregona and co-workers⁹⁹ demonstrated this by showing that [(DMDT)AuX₂] (DMDT = *N,N*-dimethyldithiocarbamate) (**57**) and [(ESDT)AuX₂] (ESDT = ethylsarcosinedithiocarbamate) (**58**) (Figure 25, X = Cl, Br) complexes possessed greater potency than cisplatin *in vitro* and showed no cross-resistance in cisplatin-resistant cell lines.⁹⁹

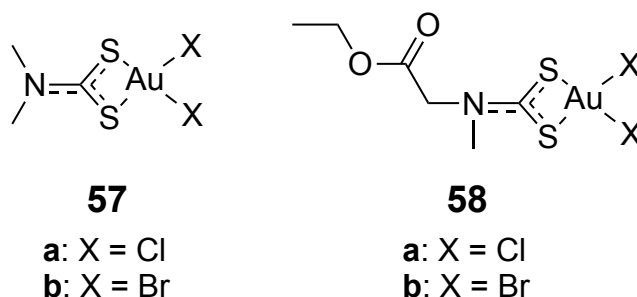


Figure 25 – Series of Au(III) dithiocarbamate complexes investigated as anticancer agents.⁹⁹

The same group later showed that complex **57b** could inhibit proteasome activity *in vitro* and *in vivo*, which have already been highlighted as a key target for anticancer treatment due to their role in tumour growth and survival.^{100,101} Complexes **57a,b** and **58a,b** were also found to be inhibitors of TrxR in HeLa cells.¹⁰² Further investigations into the mechanism of action reported the ability of complex **57a** to affect the mitochondrial functions of PC3 cells (prostate cancer) causing ROS accumulation and inhibition of TrxR, as was previously seen in HeLa cells.^{102,103} *In vivo* studies were also performed on nude mice with PC3 cancer xenografts, with an 85% difference in tumour growth compared to the control after 19 days of treatment with **57a**.¹⁰³ Complex **58b** was also tested *in vivo* on mice implanted with Ehrlich solid carcinoma or Lewis lung carcinoma; in both cases, **58b** showed superior activity to cisplatin and exhibited low toxicity to the mice with reduced nephrotoxicity.¹⁰⁴

1.2.5. Gold(III) cyclometalated complexes

Cyclometalated complexes are popular with late transition metals, including Au(III) ions. Cyclometalation can stabilise this oxidation state and avoid reduction to Au(I) or metallic Au. The process of cyclometalation involves the activation of a C-R bond within a cyclic ligand, which also contains at least one donor (D) atom such as O, N, S, Se or P, to chelate to the metal in at least one other position.¹⁰⁵ Concerning Au(III) cyclometalated compounds, so far, five general scaffolds have been explored (Figure 26) featuring C[^]N, C[^]N[^]N, C[^]N[^]C and N[^]C[^]N ligands. Au(III) cyclometalated complexes will be discussed in the following sections due to their inherent stability in physiological conditions owing

to their strong Au-C bond and interesting reactivity with biomolecules, both of which enhance their anticancer properties.^{106,107}

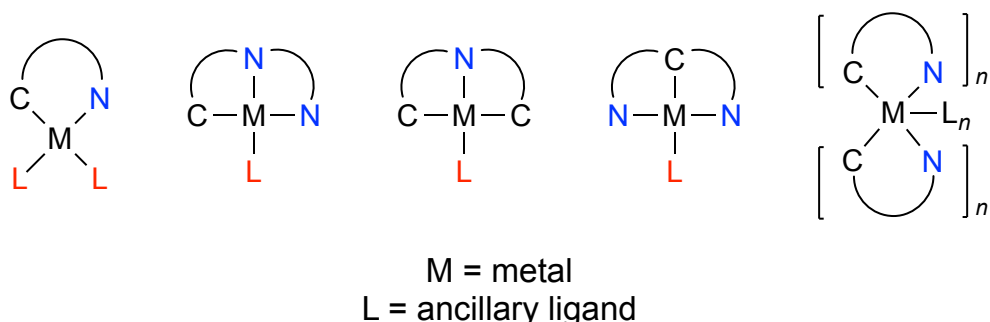


Figure 26 – Five general classes of cyclometalated complexes.

1.2.5.1. Gold(III) CⁿN complexes

The first examples of Au(III) CⁿN complexes as potential anticancer agents were reported in 1996.¹⁰⁸ All compounds contained a 2-[(dimethylamino)methyl]phenyl (damp) ligand which coordinated to Au *via* the C and N atoms of the ligand in order to stabilise the Au(III) centre.¹⁰⁸ The parent complex bearing two chlorides as ancillary ligands [Au(damp)Cl₂], showed *in vitro* cytotoxicity similar to cisplatin, however when transferred to a xenograft ZR-75-1 (human breast cancer) tumour model the toxicity appeared to be less potent as predicted from the *in vitro* studies, which the authors concluded as issues with aqueous solubility.¹⁰⁸

In order to address this problem, Buckley *et al.*¹⁰⁹ investigated different ancillary ligands to improve solubility of the [Au(damp)X₂] complex without loss of its cytotoxicity. The two most successful complexes were X₂ = acetato (complex **59**, Figure 27) and X₂ = malonate (complex **60**, Figure 27), which did not exhibit the cross-resistance seen by cisplatin, suggesting another mechanism of action is present.¹⁰⁹ *In vivo* experiments on mice with implanted HT1376 (human bladder carcinoma) and CH1 (human ovarian carcinoma) xenografts showed that the complexes **59** and **60** had similar toxicity to cisplatin.¹⁰⁹ These compounds have also been reported as potent inhibitors of cathepsin B, a cysteine protease which has been shown to play a role in tumour growth.¹¹⁰

Taking inspiration from this work a further series of Au(III) complexes were synthesised with replacement of the NMe₂ group with a pyridine and the addition of a bridging group between the phenyl and pyridine.¹¹¹ Different bridging groups were tested, including: CH₂, C=O, O, S and NH, as well as different ancillary ligands: monodentate such as chloride or bidentate such as thiosalicylate.¹¹¹ The [Au(C^{CH₂}N)(thiosalicylate)] complex (complex **61**, C^{CH₂}N = benzylpyridine, Figure 27) showed the most promise during *in vitro* studies for the inhibition of cathepsin B and K; however, when tested *in vivo* against a colon HT29 tumour xenograft, the cytotoxicity was comparable to the

parent $[\text{Au}(\text{damp})\text{Cl}_2]$ complex. Again the authors proposed this was due to solubility issues of the complex.¹¹¹

Further work on the 2-benzylpyridine scaffold was performed by Cinellu, Casini and co-workers¹¹² by replacement of one or both of the chloride ligands with PTA or thio- β -D-glucose tetraacetate (GluS^-). The PTA ligand was incorporated to address the issue of water-solubility, whereas the GluS^- ligand was used to target GLUT1 transporters.¹¹² Overall, $[\text{Au}(\text{C}^{\text{CH}_2\text{N}})(\text{PTA})\text{Cl}]\text{PF}_6$ (complex **62**, Figure 27) exhibited the greatest potency *in vitro* and was the most toxic in the HCT116 p53 +/+ cell line.¹¹² In order to gain more insight into the toxicity and transfer mechanisms of complex **62** compared with cisplatin, precision-cut tissue slices (PCTS) from healthy rat kidneys were tested.¹¹³ Toxicity studies showed that complex **62** appeared to be more toxic than cisplatin for the kidney tissue, as well as targeting the distal tubular cells, whereas cisplatin targeted proximal tubular cells in the kidney slices.¹¹³

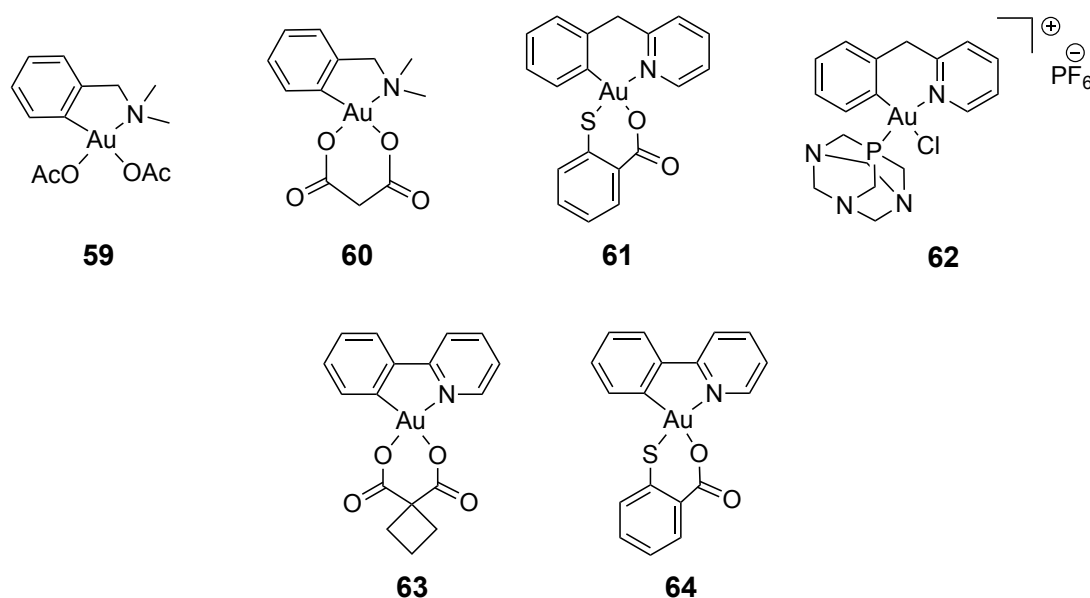


Figure 27 – Structures of AuC^{N} complexes investigated as potential anticancer agents.

$\text{Au}(\text{III})$ complexes bearing 2-phenylpyridine C^{N} ligands have also been reported as anticancer agents. In 2003, Fan *et al.*¹¹⁴ reported four derivatives of the type $[\text{Au}(\text{C}^{\text{N}})\text{X}_2]$ (C^{N} = 2-phenylpyridine) with different carboxylic acid-based ancillary ligands. The most cytotoxic complex was **63** (Figure 27) with significantly lower IC_{50} values in both cell lines investigated (MOLT-4 (human leukaemia cells) and C2C12 (murine myoblast cells)) compared to cisplatin and the other derivatives.¹¹⁴ Interestingly the other carboxylate derivatives were non-toxic in the C2C12 cell line.¹¹⁴

In the same year, the group published further $[\text{Au}(\text{C}^{\text{N}})\text{X}_2]$ derivatives but this time focusing on thiolates (mono- and bidentate) as the ancillary ligands.¹¹⁵ In this work, all complexes showed toxicity in both cell lines (MOLT-4 and C2C12), with all complexes

more potent than cisplatin in the MOLT-4 cell line. Overall the $[\text{Au}(\text{C}^{\wedge}\text{N})(\text{thiosalicylate})]$ complex (**64**, Figure 27) appeared to be most toxic when taking into account both cell lines.¹¹⁵

Che and co-workers¹¹⁶ reported a further derivative of the $[\text{AuC}^{\wedge}\text{N}]$ complex, employing an *n*-butyl moiety to the phenyl group of the scaffold, as well as using biguanide as the ancillary ligand to give a cationic complex (**65**, Figure 28). The *n*-butyl group was added to provide lipophilicity whereas the biguanide was chosen to balance the solubility of the complex.¹¹⁶ Complex **65** showed potency in a number of cancer cell lines outperforming cisplatin and showed less toxicity towards normal lung fibroblast cells.¹¹⁶ The complex specifically induced endoplasmic reticulum (ER) stress, causing ER swelling, as well as displaying angiogenesis inhibition at sub-cytotoxic concentration.¹¹⁶ The following year, the same group modified the ancillary ligand to a diethyldithiocarbamate (DEDT) moiety, which was able to successfully inhibit deubiquitinases (DUB).¹¹⁷ This highlights the diverse biological targets of these $\text{Au}(\text{III})\text{C}^{\wedge}\text{N}$ complexes.

Rubbiani *et al.*¹¹⁸ also reported the cytotoxicity of a $\text{Au}(\text{III})$ 2-phenylpyridine complex, but in this case the ancillary ligands included a PPh_3 group and a 2,4,6-tris(trifluoromethyl)phenyl (FMes) group on the $\text{Au}(\text{III})$ centre (**66**, Figure 28). Complex **66** showed promising cytotoxicity in HeLa cells and inhibited the TrxR enzyme, which was further confirmed by an increase in ROS generation.¹¹⁸

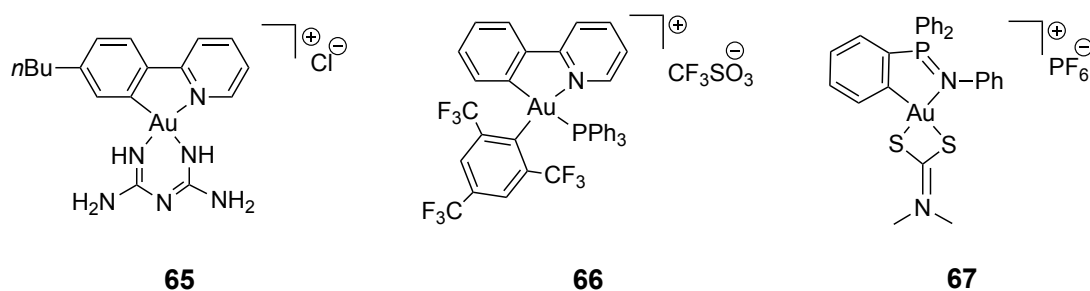


Figure 28 - Structures of further $\text{AuC}^{\wedge}\text{N}$ complexes investigated as potential anticancer agents.

A further derivative of the $\text{C}^{\wedge}\text{N}$ cyclometalated scaffold included iminophosphorane ($2\text{-C}_6\text{H}_4\text{-PPh}_2\text{=NPh}$) ligands.¹¹⁹ Contel and co-workers¹¹⁹ synthesised $\text{Au}(\text{III})$ complexes bearing this pincer ligand and a variety of ancillary ligands. One of the most promising complexes (**67**, Figure 28) contained a dithiocarbamate ancillary ligand and showed high toxicity in HeLa and Jurkat-T (human T lymphocyte) cells *in vitro*.¹¹⁹ No interaction of **67** was observed with calf thymus DNA; therefore the interaction of complex **67** was investigated with two proteins: cytochrome c (used as a model) and TrxR (possible target), respectively. The results showed that an interaction does occur and therefore, the inhibition of these proteins could be responsible for the cytotoxicity of the complex.¹¹⁹

1.2.5.2. Gold(III) C^NC complexes

The synthesis of Au(III) C^NC complexes was first reported by the group of Che in 1998,¹²⁰ specifically using 2,6-diphenylpyridine pincer ligands. The same group later reported a series of such complexes bearing the same 2,6-diphenylpyridine ligand but with varying amounts of gold, $[\text{Au}_m(\text{C}^{\text{N}}\text{C})_m\text{L}]^{n+}$ ($m = 1,3$; $n = 0-3$; L = chloride, N-donor or phosphine ligand).¹²¹ The complexes were unsurprisingly stable in a tris-buffered saline (TBS) / dimethylsulfoxide (DMSO) (9:1) solution in the presence of GSH (2 mM), due to the strong stabilising effect of the C^NC ligand towards the electrophilic Au(III) centre.¹²¹ Modification of the ancillary ligand (L) from the parent complex $[\text{Au}(\text{C}^{\text{N}}\text{C})\text{Cl}]$ (**68**, Figure 29) had a significant effect on the cytotoxicity mechanism of the complexes.¹²¹

The N-donor ligands themselves were non-toxic; however, in combination with the $[\text{Au}_m(\text{C}^{\text{N}}\text{C})_m\text{L}]^{n+}$ structure, the complexes exhibited similar toxicity to cisplatin and other Au(III) cyclometalated complexes as seen in the four cancer cell lines investigated (HeLa, HepG2 (human liver), SUNE1 (human nasopharyngeal carcinoma, cisplatin sensitive) and CNEI (human nasopharyngeal carcinoma, cisplatin-resistant)).¹²¹ Further studies were performed with $[\text{Au}(\text{C}^{\text{N}}\text{C})(1\text{-methylimidazole})]^+$ (**69**, Figure 29) showing the ability of the complex to induce apoptosis in SUNE1 cells. The authors also observed the capability of **69** to bind to DNA by intercalation and that during the S phase of DNA replication it caused cell cycle arrest.¹²¹

This is at variance to the Au(III) C^NC complexes bearing cytotoxic phosphine ligands, such as $[\text{Au}_2(\text{C}^{\text{N}}\text{C})_2(\mu\text{-}1,2\text{-bis}(\text{diphenylphosphino})\text{propane})]^{2+}$ (**70**, Figure 29), that exhibit very potent cytotoxicity; however, do not induce significant DNA binding or induce cell cycle arrest, suggesting a different mechanism of action.¹²¹ It is worth mentioning that the IC₅₀ values of the phosphine derivatives appear to be similar to those of the free phosphine ligands. Therefore, the authors proposed that the $[\text{Au}(\text{C}^{\text{N}}\text{C})]^+$ structure transports the phosphine ligands to the cancer cells due to the overall stability of the complexes, and that the cytotoxicity is due to the release of the phosphine ligands.¹²¹

Further experiments revealed that the cytotoxicity of complex **70** was accompanied by nanomolar inhibition of TrxR, initiation of ER stress and the expression of the death receptor 5 (DR5).¹²² *In vivo* testing of **70** on a nude mice model inoculated with PLC cells (human hepatocellular carcinoma) revealed a greater reduction of tumour growth compared to cisplatin and doxorubicin, with no adverse effects observed.¹²²

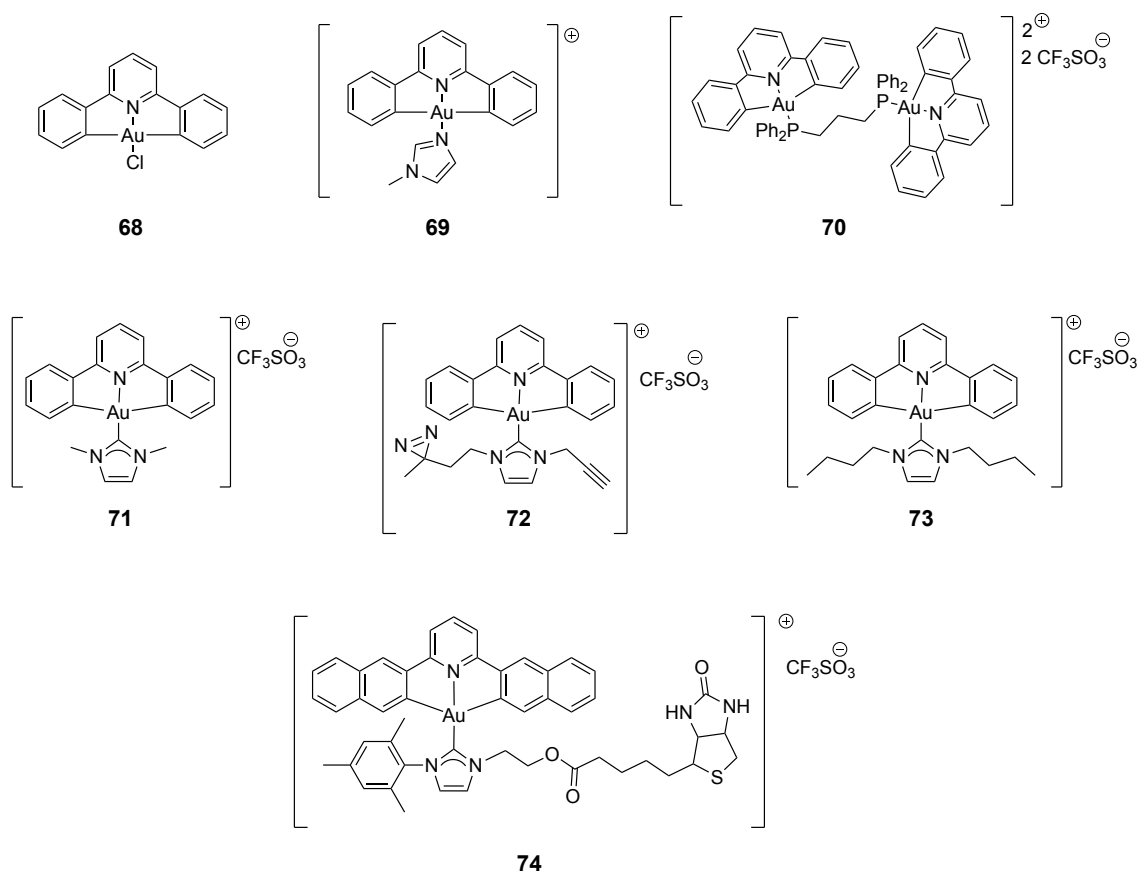


Figure 29 – Au(III) C^NC complexes investigated by the group of Che for anticancer properties.

Following on from their previous work in 2006,¹²¹ Che and co-workers¹²³ synthesised a series of [Au(C^NC)(NHC)]⁺ complexes and investigated their cytotoxic activity. Among the series investigated, [Au(C^NC)(1,3-dimethylimidazol-2-ylidene)]CF₃SO₃ (complex **71**, Figure 29) was the most cytotoxic in the cell lines investigated, showing ca. eighteen- to twenty eight-fold greater cytotoxicity compared to cisplatin.¹²³ *In vivo* cytotoxicity studies were also completed with **71** using nude mice bearing PLC tumours. After 28 days of treatment with **71** at 10 mg/kg/week, there was a reduction in tumour growth by 47%, with no harmful side effects.¹²³ Interestingly, the authors identified the ability of **71** to stabilise topoisomerase I. Topoisomerase I is an enzyme that unfolds DNA; therefore, stabilisation results in DNA strand breakage and thus apoptosis of cells. Therefore, this pathway could be responsible for the potent cytotoxicity of the compound.¹²³

Taking inspiration from complex **71**, Che and co-workers¹²⁴ generated a chemical probe analogue bearing a small photo-activatable diazirine group and a clickable alkyne group on the wingtips of the NHC (complex **72**, Figure 29). Upon irradiation with UV light ($\lambda=365$ nm) the probe covalently bonded to the biomolecule it interacted with due to the loss of nitrogen from the diazirine moiety.¹²⁴ The exposed alkyne group then underwent a click reaction with an azido-biotin complex, which was isolated using a streptavidin-peroxidase conjugate. Upon incubation of **72** with HeLa cells, six biotinylated proteins

could be identified, all of which were known as possible anticancer targets.¹²⁴ In this work the group also formed a series of derivatives of **71** by adding other wingtip groups. A trend was observed upon increase in length of the alkyl chain on the NHC wingtips; complex **73** (Figure 29) bearing two *n*-butyl groups showed increased toxicity from **71**.¹²⁴

Che and co-workers¹²⁵ have also reported the ability of a non-emissive $[\text{Au}(\text{C}^{\wedge}\text{N}^{\wedge}\text{C})(\text{NHC})]^+$ biotin complex (**74**, Figure 29) to become emissive in the presence of avidin, a biotin-binding protein. The Au(III)-avidine conjugate (**74**-conjugate) can then bind to DNA and proteins such as BSA, resulting in an increase in emission intensity as great as 45-fold. Both complex **74** and **74**-conjugate exhibited greater cytotoxicity in HeLa, HepG2 and MDA-MB-231 cell lines compared to cisplatin.¹²⁵

Meanwhile, Bochmann and co-workers¹²⁶ synthesised alternative Au(III) $\text{C}^{\wedge}\text{N}^{\wedge}\text{C}$ complexes by replacing the central pyridine ring with a pyrazine, which resulted in increased photoemission. In total, a series of seven complexes were synthesised, both neutral and ionic; however, the most promising anticancer agent was $[\text{Au}(\text{C}^{\wedge}\text{N}^{\text{pz}\wedge}\text{C})(1,3\text{-dimethylbenzimidazol-2-ylidene})]\text{PF}_6$ (complex **75**, Figure 30).¹²⁷ Its cytotoxicity was tested against numerous cancer cell lines including HL60 (human leukaemia), MCF-7 and A549 (human lung carcinoma); with potency ranging from 0.3 to 8 μM , all of which are superior to cisplatin in the same cell lines.¹²⁷ The selectivity of the complex was also assessed using healthy human fetal lung fibroblast cells (MRC-5); unfortunately, a low IC_{50} value was observed (1.4 μM), highlighting the need for improvements to be made.¹²⁷ Extraordinarily, the replacement of the benzimidazole ligand with a caffeine moiety resulted in a ten-fold decrease in toxicity, which could be assigned to the reduced gold uptake intracellularly observed by ICP-MS (inductively coupled plasma mass spectrometry). This reduced uptake was rationalised by the fact that the caffeine moiety contained more polarity and therefore cannot pass through the cell membrane by passive diffusion as easily as the benzimidazole group.¹²⁷

Complex **75** was also stable towards GSH (10 mM) at room temperature for up to six days in $\text{DMSO-}d_6$ as monitored by ^1H NMR.¹²⁷ Different mechanisms of action were then investigated; interestingly the compound was able to interact strongly with the human telomeric G-quadruplex sequence, with a ΔT_m value of 40 °C, and was also able to stabilise i-motif structures of DNA, both of which were stabilised selectively compared to canonical double helix DNA.¹²⁷ The complex was also able to inhibit mouse double minute 2 homolog (MDM2)-p53 interactions, the first example of a gold complex disrupting this interaction.¹²⁷ This is of particular important for anticancer treatment due to the overexpression of MDM2 proteins in some cancers which can inhibit the p53 tumour suppressor activity by protein-protein interactions.¹²⁸ Therefore, complex **75** showed promise, however further work has to be done to improve its selectivity.

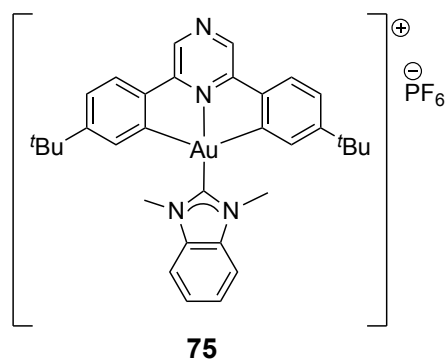


Figure 30 – Structure of a $Au(C^N^{Pz^C})$ complex bearing a NHC ligand by Bochmann and co-workers.¹²⁷

The following year the same group addressed the issue of selectivity by synthesising bioconjugated and binuclear complexes.¹²⁹ The precursor to form these complexes was based on the structure of **75**; however, the NHC ligand had a pentafluorophenyl ester group on one of the NHC wingtips.¹²⁹ This was then reacted with diaminoalkanes with different alkyl chain lengths allowing the conjugation to occur *via* the pendant amine. Three different conjugates (biotin, oestradiol and a Au(I) NHC complex) were used forming complexes **76**, **77** and **78** (Figure 31).¹²⁹

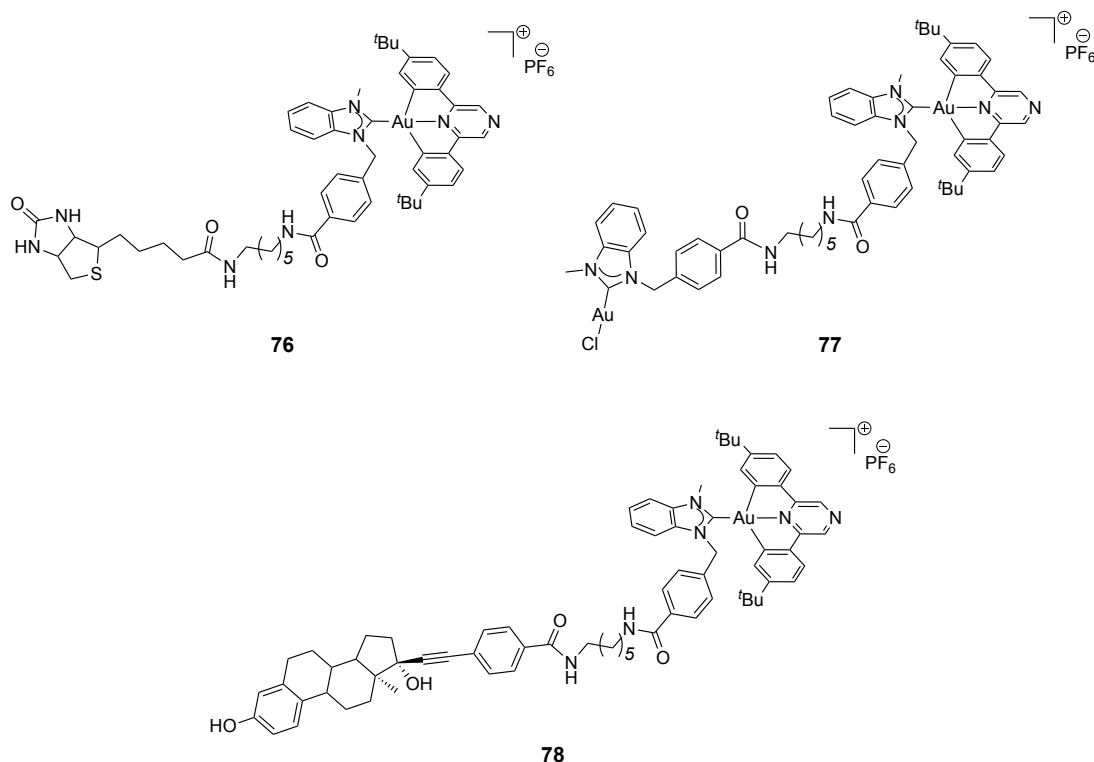


Figure 31 – Structures of bioconjugated and binuclear $[Au(C^N^{Pz^C})(NHC)]$ complexes as potential anticancer agents.¹²⁹

The cytotoxicity of complexes **76** and **78** were tested on cell lines expressing or not expressing biotin receptors and oestrogen receptors, respectively.¹²⁹ However, this did

not have much effect on the IC₅₀ values and overall the precursor complex **75** was more potent compared to **76** and **78**.¹²⁹

1.2.5.3. Gold(III) C^NN complexes

In 2002, Marcon *et al.*¹³⁰ reported the high toxicity of a gold(III) C^NN complex: [Au(bipy^c-H)(OH)][PF₆] (**79**, bipy^c = 6-(1,1-dimethylbenzyl)-2,2'-bipyridine), Figure 32), which showed high stability in physiological buffer at 37 °C and in the presence of ascorbate. The bipyridine analogue, without the organogold bond, is easily reduced with ascorbate.¹³⁰ Complex **79** showed high toxicity in the A2780 cell line in particular, with superior cytotoxicity to cisplatin in the A2780/R cell line, highlighting the potential for an alternative mechanism of action, which was also evidenced by weak interactions with calf thymus DNA.¹³⁰ Further cytotoxicity studies were carried out with 12 other cell lines, although moderate cytotoxicity was observed and no selectivity could be concluded.⁹⁶

Further derivatives of complex **79** were synthesised, such as complex **80** bearing a 2,6-xylylidine ligand instead of the hydroxyl group (Figure 32).¹³¹ In buffer this amine group is easily hydrolysed; however, the bipy^c scaffold remained coordinated to the Au(III) centre.¹³¹ Cytotoxicity studies of complex **80** showed superior toxicity in the various cell lines compared to **79**, as well as exhibiting greater selectivity across a panel of thirty six human tumour cell lines.^{96,131} The mechanism of action of **80** was also postulated using COMPARE analysis, including inhibition of mTOR (mammalian target of rapamycin), proteasome, and/or DNA synthesis.⁹⁶ Remarkably, both complexes **79** and **80** showed inhibition of mitochondrial TrxR and mitochondrial respiration.¹³²

The interaction of complex **79** with various proteins has been investigated over the years, including interactions with BSA,¹³³ cytochrome c, lysosomes¹³⁴ and TrxR.¹³⁵ **79** was also shown to form stable adducts with the copper chaperone Atox-1; however, using high-resolution electrospray ionisation mass spectrometry (HR-ESI-MS) the authors were able to identify the Au in a +1 oxidation state.¹³⁶ This could have been due to the reducing environment the compound was exposed to or due to the interaction with the chaperone; therefore, more research is needed to determine whether **79** could interfere with Atox-1.¹³⁶ **79** has also been identified as an inhibitor of purified 20S proteasome,¹³⁷ as well as the hetero-transmembrane enzyme, Na/K-ATPase.¹³⁸

As discussed above, TrxR was identified as a biological target for both complexes **79** and **80**; however, to further understand the mechanism of inhibition, Casini and co-workers used MALDI-TOF MS experiments on the intact enzyme after incubation with **80**, showing significant enzyme metalation.¹³⁹ At variance to auranofin, which showed coordination to the selenol active site, **80** showed more extensive oxidative protein damage, which could be due to binding to other residues such as methionine and histidine.¹³⁹ More recently, ESI-TOF MS (electrospray ionisation time of flight mass

spectrometry) experiments with complex **79** showed preferential binding to selenocysteines over histidine, cysteine, methionine and glutamate residues.¹⁴⁰

Interestingly, the dinuclear oxo-bridged complex **81** ($[(\text{bipy}^{\text{C}})_2\text{Au}_2(\mu\text{-O})][\text{PF}_6]_2$, Figure 32) can undergo reversible hydrolysis to form two equivalents of **79**.¹⁴¹ However, **81** showed moderate stability in phosphate buffer (10 mM, pH 7.4) and in the presence of reducing agents such as ascorbic acid and glutathione. Remarkably, it only underwent hydrolysis in the presence of model proteins such as lysozyme and cytochrome c.¹⁴¹ The hydrolysis of **81** to **79** was also described by Gratteri *et al.* enabling the stabilisation of non-canonical DNA G-quadruplexes.¹⁴²

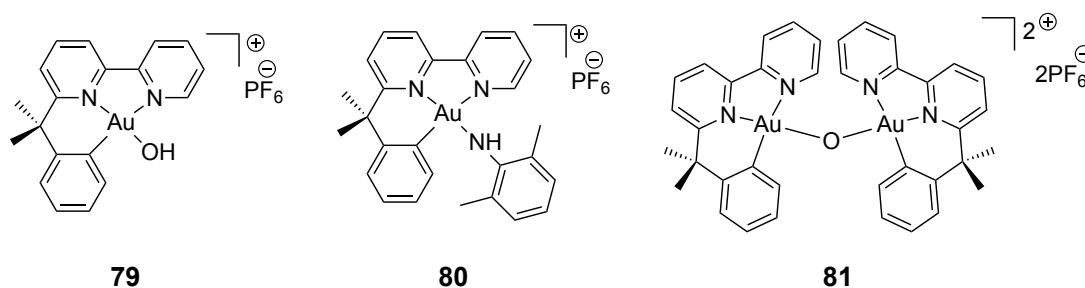


Figure 32 – Structures of mono- and dinuclear Au(III) C^NN complexes as anticancer agents.

More recently, Casini and co-workers¹⁴³ reported on a series of novel (C^NN) cyclometalated Au(III) complexes with the general formula $[\text{Au}(\text{bipy}^{\text{dmb}}\text{-H})\text{X}][\text{PF}_6]$ ($\text{bipy}^{\text{dmb}}\text{-H} = 6\text{-}(1,1\text{-dimethylbenzyl})\text{-}2,2'\text{-bipyridine}$). The complexes featured an array of anionic ligands (X) with C (alkynyl)-, N-, O-, or S-donor atoms, which were found in the fourth coordination position.¹⁴³ The X ligands included: 4-ethynylaniline, saccharine, thio- β -D-glucose tetraacetate, GSH, and a coumarin-substituted amide derived from 4-ethynylaniline. Interestingly, a number of the compounds were found to selectively form adducts with oligonucleotides rather than proteins upon ligand exchange with the monodentate X ligands.¹⁴³ Overall, the obtained results point towards the possibility to selectively target DNA with gold(III) organometallics.

2. Bioorthogonal catalysis in cells

Over the last decade, a thriving area fusing both biologists and chemists has evolved, with interest in modifying and functionalising biomolecules through metal-catalysed bioorthogonal reactions.¹⁴⁴ This term was first defined by Bertozzi and co-workers in 2003,¹⁴⁵ describing the labelling of a glycoprotein with an unnatural azide tag.¹⁴⁵ This field involves the application of conventional organic reactions within a biological setting, and are commonly catalysed by transition metal catalysts.¹⁴⁶ A requirement of the reaction is the non-interference with the surrounding biological environment.¹⁴⁴ The latter is by far the most challenging step to overcome with many biological nucleophiles, such as glutathione (GSH), present in living cells which can deactivate the metal catalyst.¹⁴⁷

Bioorthogonal reactions can open new doors for metal-templated reactions in cells for different applications, including: *i*) labelling of biomolecules with fluorescent tags for intracellular tracking and irreversible modifications of biomolecules *via* coupling to substrates or redox catalysis and *ii*) activation of a prodrug *in situ* by a decaging reaction, for example within cancer cells (Figure 33).¹⁴⁸

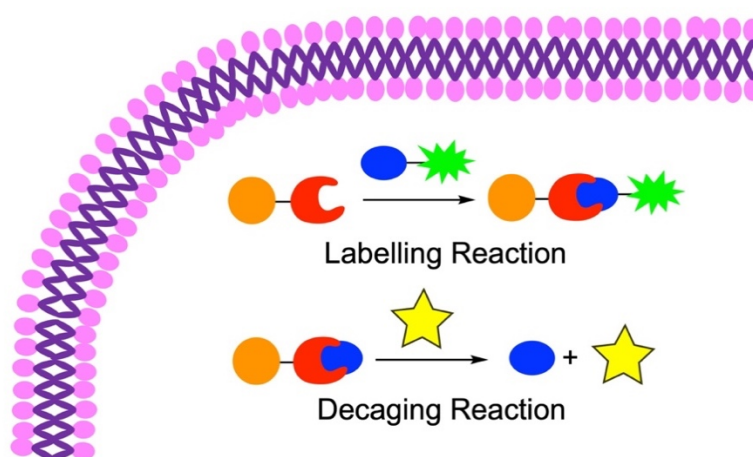


Figure 33 – Examples of bioorthogonal reactions that can be performed in living cells. Image adapted from ref.¹⁴⁹

2.1. Transition metal catalysts for bioorthogonal reactions

The use of transition metal catalysts within these bioorthogonal reactions has stemmed from their natural abundance within nature in the form of metalloproteins.¹⁵⁰ The human proteome contains a large percentage of metalloproteins, making them essential for existence.¹⁵¹ Within a metalloprotein, the metal plays a significant role in the protein's function, influencing both its reactivity and structure.¹⁵¹ An example of an essential metalloprotein is haemoglobin, which contains heme iron and is vital for binding oxygen.¹⁵¹ Therefore, there has been a lot of interest in mimicking metalloproteins by forming artificial versions using different metal active sites; thus, tuning the activity of

these proteins.¹⁵² However, these artificial metalloproteins can be costly, and so an alternative route involves forming small molecules with a metal centre that can catalyse these bioorthogonal reactions.¹⁵²

The area of bioorthogonal chemistry owes its growth to the development of the Copper-Catalysed Azide-Alkyne Cycloaddition (CuAAC) reaction, which was independently published by Rostovtsev *et al.*¹⁵³ and Tornøe *et al.*¹⁵⁴ both in 2002. The reaction requires a copper(I) catalyst to achieve reasonable reaction rates, which can be increased with ligands that are specific for Cu(I).¹⁵⁵ Within a year of the reaction discovery, three groups, Wang *et al.*¹⁵⁶, Speers *et al.*¹⁵⁷ and Link and Tirrell,¹⁵⁸ published work involving CuAAC in biological contexts. However, the cytotoxicity of Cu(I) has remained a barrier in using these catalysts in living cells.¹⁵⁵

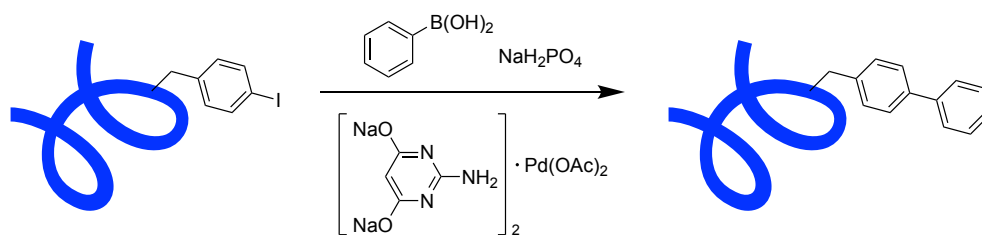
Pioneering work by Streu and Meggers paved the way for the use of organometallic transition metal complexes in bioorthogonal reactions.¹⁵⁹ They reported the ability of Ru(II) complexes to mediate the cleavage of an allylcarbamate group to expose the respective amine within living HeLa cells (human cervical cancer cell line) with the final aim to activate a prodrug molecule.¹⁵⁹

2.1.1. Palladium mediated bioorthogonal reactions

Palladium catalysis has been at the forefront of cross-coupling reactions, with the Nobel Prize awarded in 2010 for the exceptional work by Heck, Negishi and Suzuki.¹⁶⁰ These reactions can also be interesting in the field of bioorthogonal chemistry, such as the formation of C-C bonds to form an active compound *in situ* or the activation of an inert C-H bond of a biomolecule.¹⁶⁰ However, these cross-coupling reactions are usually performed in organic solvents; therefore, research is needed to perform such reactions in biologically relevant media.¹⁶¹

2.1.1.1. Coupling reactions

In 2012, Davis and co-workers¹⁶² demonstrated the ability of a Pd(II) catalyst to mediate a Suzuki-Miyaura cross-coupling reaction within a biological environment. The coupling was performed on the cell surface of *Escherichia coli* (*E. coli*) by targeting an aryl halide moiety, introduced in a porin channel, with boronic acid as the coupling agent in the presence of a Pd(OAc)₂ catalyst (Scheme 1). However, this system has shown disadvantages due to unwanted reactions with intracellular thiols such as GSH.¹⁶²



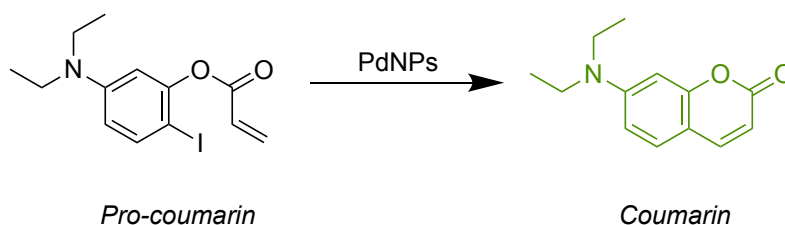
Scheme 1 – Suzuki-Miyaura cross-coupling reaction between an aryl iodide tagged porin channel in *Escherichia coli* with boronic acid, mediated by a Pd(II) catalyst with a 2-amino-4,6-dihydroxyprimidine ligand.¹⁶²

Nevertheless, the group of Bradley¹⁵⁰ showed that Pd(0) nanoparticles (PdNPs) supported on polystyrene microspheres could be used to perform a Suzuki-Miyaura cross-coupling reaction in HeLa cells. This involved the coupling of two non-fluorescent substrates to form a fluorescent product.¹⁵⁰ One of the substrates contained a lipophilic triphenylphosphine (PPh₃) group that could facilitate cell uptake and target the mitochondria.¹⁵⁰ These PdNPs have also been shown to favour the Suzuki-Miyaura coupling reaction of two non-cytotoxic precursors to form an anticancer prodrug in cancer cells *in situ*.¹⁶³ The PdNPs could also be targeted by conjugation to a cyclic peptide, cRGD, which is a potent antagonist of the $\alpha_v\beta_3$ receptor, overexpressed in tumour cells.¹⁶⁴ Not only did the peptide conjugated PdNPs selectively accumulate in glioblastoma cells, but they could also simultaneously form two anticancer agents *in situ*, one by a Suzuki-Miyaura cross-coupling reaction mentioned above, and the other by prodrug activation involving the cleavage of the propargyl group of 5-fluoro-1-propargyl uracil (Pro-5FU), yielding 5-Fluorouracil (5FU).¹⁶⁴

Finally, Sonogashira cross-coupling reactions in physiological conditions have also been mediated by palladium(II) complexes, with the group of Lin demonstrating the versatility of aminopyrimidine Pd(II) complexes without the need for toxic Cu(I) salts.^{165–167} Such bioorthogonal reactions have been used for the labelling of proteins in *E. coli* and on mammalian cell surfaces.^{165,167}

2.1.1.2. Cyclisation reactions

Palladium is less known for its ability to perform cyclisation reactions, with Weissleder and co-workers¹⁶⁸ reporting one of the only examples within living cells. A Pd(II) precatalyst (PdCl₂(TFP)₂, TFP = tri(2-furyl)phosphine) was encapsulated into a poly(lactic-co-glycolic acid)-*b*-polyethyleneglycol formulation to form NP type species. These NPs were used to mediate the intramolecular Heck coupling reaction of a coumarin precursor, 5-diethylamino-2-iodophenyl ester, which can be monitored within HT1080 (human fibrosarcoma) cells by formation of a fluorescent signal (Scheme 2).¹⁶⁸



Scheme 2 – PdNP catalysed intramolecular Heck coupling of 5-diethylamino-2-iodophenyl ester to form the fluorescent compound coumarin.¹⁶⁸

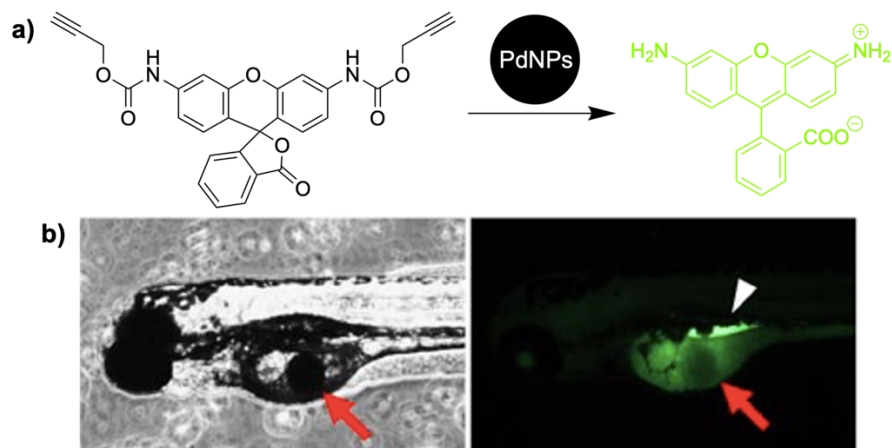
2.1.1.3. Bond-cleaving reactions

The papers already discussed above have described the use of palladium catalysts to cleave allyl/alloc groups.^{150,168} For example, Yusop *et al.*¹⁵⁰ described the ability of their PdNPs to mediate not only the Suzuki-Miyaura cross-coupling reaction within HeLa cells, but also the allylcarbamate cleavage of bis-*N,N'*-allyloxycarbonyl rhodamine 110 to form fluorescent rhodamine 110.¹⁵⁰ Miller *et al.*¹⁶⁸ also reported the ability of their PdNPs to mediate the allylcarbamate cleavage of a prodrug (pro-doxorubicin) to form the anticancer drug doxorubicin within HT1080 cells. The activated drug could then induce DNA damage and apoptosis over 72 h, resulting in an IC₅₀ value of 26 ± 1 nM.¹⁶⁸

More recently, Martínez-Calvo *et al.*¹⁶⁹ described the ability of palladium(II) complexes bearing phosphine ligands, designed to balance optimal stability and reactivity properties, to perform deallylation and depropargylation reactions in HeLa cells successfully. Bradley and co-workers¹⁷⁰ have also described the ability of a Pd(II)-carbene complex conjugated to a cell-penetrating peptide for the depropargylation reaction of *N, N'*-bis(propargyloxycarbonyl)rhodamine 110 (pro-rhodamine 110) to rhodamine 110 in PC-3 cells (human prostate cancer cell line).

The group of Chen have been essential contributors to this field, reporting the ability of Pd(II) catalysts to perform depropargylation reactions to degrade lysine residues.¹⁷¹ The same group then went on to study the same reaction but for the *in situ* generation of neuramic acid (Neu) on cell-surface glycans.¹⁷² In this work, Pd(0)NPs were more efficient catalysts than the Pd(II) complexes previously used by the group.^{171,172}

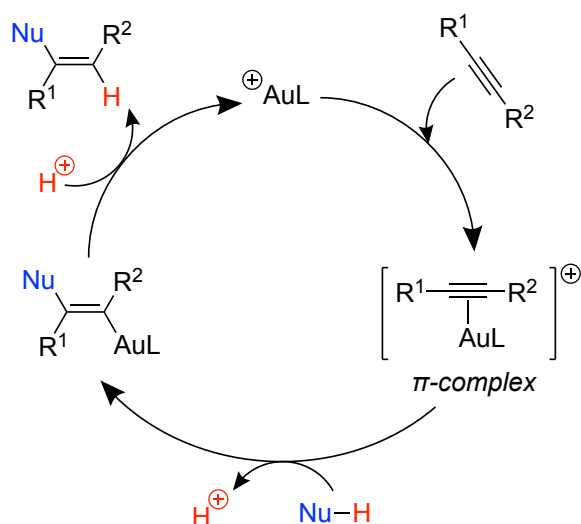
Unciti-Broceta, Bradley and co-workers¹⁷³ demonstrated the versatility of their PdNPs, reporting the propargylcarbamate cleavage of the protected fluorophore, proc-rhodamine 110 (Scheme 3a). The PdNPs were implanted in the yolk of zebrafish embryos 24 h after fertilisation and then the pro-dye was added after a subsequent 24 h.¹⁷³ Fluorescence from the rhodamine 110 was observed within the yolk sac after 24 h incubation due to successful *in vivo* propargylcarbamate cleavage (Scheme 3b). A fluorescent signal was also observed in the gastrointestinal tract (Scheme 3b), with or without the PdNPs due to cleavage by digestive enzymes; therefore, proc-rhodamine 110 should not be administered orally.¹⁷³



Scheme 3 – a) Propargylcarbamate cleavage of *N,N'*-bis(propargyloxycarbonyl)rhodamine 110 mediated by PdNPs to form rhodamine 110 in zebrafish embryos, b) Images to show the position of the PdNP, which is indicated with a red arrow. Confocal microscopy images (right) showed successful *in vivo* propargylcarbamate cleavage due to the strong fluorescent signal surrounding the NP. The gastrointestinal tract is also fluorescent as indicated with a white arrowhead. Figure partially reproduced (b) with permission from ref 173. Copyright 2014, Springer, Nature, <http://creativecommons.org/licenses/by-nc-sa/3.0/>.¹⁷³

2.1.2. Gold mediated bioorthogonal reactions

More recently, gold complexes have been recognised as suitable bioorthogonal catalysts due to several advantages over conventional Pd(II) complexes, including biocompatibility in physiological media and mild reaction conditions.^{174,175} The field began in the area of sensing probes for gold ions in physiological environment due to the carbophilicity of Au(I) and Au(III) ions to coordinate and thus activate unsaturated bonds.^{147,176} The general scheme for a nucleophilic addition reaction involving a nucleophile and alkyne is shown in Scheme 4.¹⁷⁷ The first step is the formation of the π -complex whereby the cationic AuL^+ species activates the alkyne. This then allows for the concerted addition of the nucleophile to form the alkene species, followed by the protodeauration reaction to release the cationic Au catalyst. This mechanism is typical for many processes involving alkynes activated by LAu^+ species, including hydration, hydroamination and hydrocarboxylation reactions, to name only a few.¹⁷⁷



Scheme 4 – A typical catalytic cycle for the nucleophilic addition reaction between a nucleophile and an alkyne, which has first been activated by a cationic AuL^+ species to form the π -complex.

Image adapted from ref.¹⁷⁷

The ability of gold complexes, particularly Au(III), to mediate cross-coupling reactions in organic solvents has only been recognised over the last few years.¹⁷⁴ Therefore transforming these reactions into biological conditions is still in its infancy. However, there have been recent examples of selective modifications of biomolecules *via* C-X (X = heteroatom) or C-C bond formation reactions which will be discussed in the following sections.¹⁷⁸

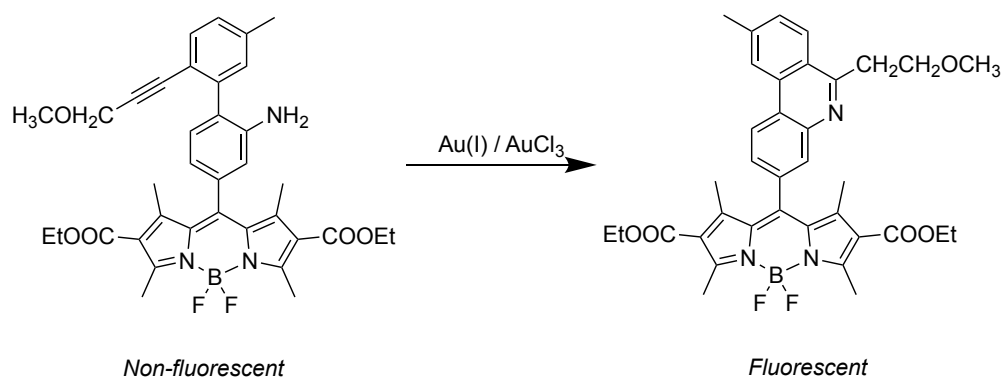
2.1.2.1. Au(III) complexes

2.1.2.1.1. Heterocyclization reactions

To the best of my knowledge, the first example of using Au(III) salts to mediate bioorthogonal reactions was published by Jou *et al.* in 2009,¹⁷⁹ where AuCl_3 was shown to mediate the intramolecular cyclisation of a rhodamine-alkyne derivative transforming a propargylamide moiety to an oxazolecarbaldehyde group. This resulted in a colorimetric change from colourless to pink, alongside a considerable enhancement in fluorescence, defining the complex as a 'chemodosimeter' for Au(III) ions.¹⁷⁹ This activity has also been reported for Pd(II) salts, although in that case, a stoichiometric amount of oxidant was also needed.¹⁸⁰ Localisation of the fluorescence was observed within the cells after 1 h incubation of the rhodamine probe with the Au salt, highlighting great promise for these reactions within living systems.¹⁷⁹

Yang *et al.*¹⁸¹ published a similar rhodamine probe for Au(III) ions, whereby an irreversible Au(III)-promoted cyclisation reaction of the rhodamine amide produced a pink fluorescence. This was also observed in HeLa cells after incubation with AuCl_3 and subsequent incubation with the probe.¹⁸¹

In 2012, Wang *et al.*¹⁸² reported the ability of a BODIPY (boron-dipyrromethene, 4,4-difluoro-4-bora-3a,4a-diaza-s-indacene) derivative to undergo an intramolecular hydroamination reaction in the presence of Au(III) and Au(I) ions (Scheme 5), at variance to the examples above where only Au(III) ions were detected. The BODIPY derivative is initially non-fluorescent due to photoinduced electron transfer (PET) from the aniline to the BODIPY group. However, upon detection of Au(III) or Au(I) ions, the intramolecular hydroamination reaction is mediated, converting the 2'-ethynyl biphenylamine to a phenanthridine group.¹⁸² This results in inhibition of the PET mechanism due to the removal of the amino group. Although Au(I) could also promote this reaction, it was less effective, showing lower reaction rates.¹⁸² Nevertheless, interference studies showed that the probe could be 'turned on' by Hg(II) and Pd(II) ions, albeit at a lower fluorescence intensity. The reaction was also performed in HeLa cells to demonstrate its applicability in physiological environments.¹⁸²



Scheme 5 – Non-fluorescent BODIPY derivative undergoes an intramolecular hydroamination reaction in the presence of Au(I) and Au(III) ions producing a fluorescent product.¹⁸²

Seo *et al.*¹⁸³ addressed the drawbacks of previous work using rhodamine alkyne derivatives as probes,^{179,181} due to side reactions associated with the alkyne activation mediated by the gold ions, including alkyne hydration.¹⁸³ Previous work by the same group attempted to overcome this by separating the reaction part of the probe from the signalling part, thereby reducing the fluorescence interference by side reactions; however, the ester moieties present in the probe were susceptible to the esterase enzyme in living systems.¹⁸⁴

In more recent work, the group investigated different ways of modifying the initial rhodamine alkyne derivative.¹⁸³ Steric strain was added to the lactam group by addition of an *N*-(2-ethynylphenyl) moiety, resulting in the promotion of the gold mediated ring-opening of the rhodamine due to an increase in ground state energy. This work also included the synthesis of a novel FRET (Förster resonance energy transfer) probe consisting of the rhodamine-alkyne moiety as the FRET acceptor and a naphthalimide dye acting as the FRET donor.¹⁸³ FRET systems are advantageous in cell studies due

to a larger pseudo-Stokes shift and less influence from environmental factors due to two emission intensities at different wavelengths.¹⁸⁵ Fluorescence microscopy was used to evaluate the FRET system in N2A cells (murine neuroblastoma cell line); the probe alone emitted green fluorescence, then in the presence of Au(III), red fluorescence was observed, overlap of these images demonstrated the key advantages to these systems.¹⁸³

2.1.2.1.2. Carbocyclization reactions

An apocoumarin probe has also been used as a Au(III) sensor with a relative fluorescence response of 60% due to a hydroarylation reaction mediated by gold(III) ions between the alkyne, acting as a Michael acceptor, and the phenyl with a dialkylamino moiety located in the *para* position.¹⁸⁶ This was demonstrated in HaCaT cells (human epidermal keratinocyte cell line) with initial incubation with Au(III) ions and then the addition of the pre-fluorescent complex. Fluorescence microscopy of the cells showed localised fluorescence within the cytoplasm, with sensitivity studies demonstrating the ability of the probe to detect toxic concentrations of Au(III) (40 ppm). The fluorophore was also sensitive to Ag(I) ions; however, this fluorescence response was only 4.6% and therefore should have minimal effect.¹⁸⁶

2.1.2.1.3. Ester amidation reactions

The first *in vivo* study of a gold mediated reaction was published by Tsubokura *et al.*,¹⁸⁷ involving an organ-targeted Au(III) cyclometalated complex capable of mediating amide bond formation between propargyl ester probes and amino groups on the surface of the target organ (Figure 34).¹⁸⁷ Two glycoalbumins were used to target the liver and intestine: α (2-6)-disialoglycoalbumin (Sia) and galactosylglycoalbumin (Gal), respectively.^{188–190} These were complexed with a coumarin-Au conjugate due to the strong binding affinity of coumarin in the binding pocket of albumin,¹⁹¹ allowing the formation of two complexes: Glyco-Au(Sia) and Glyco-Au(Gal).¹⁸⁷ The *in vivo* studies on live mice first involved the introduction of the complexes intravenously, allowing time to reach their target organ. A second injection was then administered containing the fluorescently labelled propargyl ester probe. Subsequently, this underwent a Au(III)-mediated amide bond formation with an amino group on the surface of the targeting organ, generating a localised fluorescence (Figure 34).¹⁸⁷ This work provides very promising results in therapeutic applications due to its impressive organ targeting and ability to be performed *in vivo*; hopefully, this can be extended to tumour tissue over the next few years.

Kung *et al.*¹⁹⁵ were the first to describe the use of a Au(III) cyclometalated complex to mediate cysteine arylation *via* a C-S reductive elimination reaction. A series of Au(III) organometallic complexes were investigated, three of which contained an msen chelating group as the ancillary ligand (msen = *N,N'*-bis(methanesulfonyl)ethylenediamine), whilst one other possessed two chloride ligands.¹⁹⁵ The initial investigations involved the incubation of the [Au(C^{CH₂N})(msen)] (C^{CH₂N} = 2-benzylpyridine) complex (Figure 35B) with different cysteine-containing peptides in phosphate-buffered saline (PBS, pH 7.4): DMSO (dimethylsulfoxide) (9:1) at 25 °C for 2 h. In all cases, the conversion to cysteine arylation was above 90%, as determined by LC-MS (liquid chromatography-mass spectrometry) analysis.¹⁹⁵ The excellent chemoselectivity of this complex was observed when reacting with cysteine-free peptides, as no conversion was detected. However, when the reaction was performed with the [Au(C^{CH₂N})Cl₂] complex, an N-terminal modification was observed, which could be due to the inherent hardness of both the N-terminal α-amino group (RNH₂) and the chloride ligands, favouring this reaction.¹⁹⁵

Investigations into the cysteine arylation ability of the two additional complexes, [Au(C^{CO}N)(msen)] and [Au(C[^]N)(msen)] (C[^]N = 2-phenylpyridine), revealed that in the latter cysteine arylation could not be achieved, as only adducts of the type [Au(C[^]N)-Cys] could be detected, whereas [Au(C^{CO}N)(msen)] could efficiently mediate the reaction similarly to the C^{CH₂N} analogue.¹⁹⁵ Attempts to expand the scope of the cysteine arylation were successful using a dansyl-functionalised (dansyl = 5(dimethylamino)naphthalene-1-sulfonyl) gold(III) cyclometalated complex (10 eq.) to arylate the single surface-exposed cysteine in both bovine serum albumin (BSA) and human serum albumin (HSA), as confirmed by LC-MS/MS (liquid chromatography-mass spectrometry/mass spectrometry) analysis.¹⁹⁵

Messina *et al.*¹⁹⁶ were next to publish work on Au(III)-mediated cysteine arylation *via* reductive elimination. However, in this work, an oxidative addition Au(III) complex, [(Me-DalPhos)Au(tolyl)Cl][SbF₆] (Me-DalPhos = (Ad₂P(*o*-C₆H₄))NMe₂), Figure 35B), was employed as the catalyst, showing quantitative arylation of GSH after only a few minutes in water (H₂O) : acetonitrile (CH₃CN) (80:20) at 25 °C.¹⁹⁶ The reaction was tested in a variety of conditions, including an extensive pH range, different buffers and in the presence of tris(2-carboxyethyl)phosphine (TCEP), a disulfide reducing agent, and guanidine·HCl, a protein denaturing agent.¹⁹⁶ Derivatives of the lead catalyst were also prepared by addition of different substrates, replacing the tolyl group. This included biorelevant groups such as heterocycles, a fluorescent tag, a drug molecule, an affinity label and a poly(ethylene glycol) polymer (PEG) moiety, which resulted in a water-soluble Au catalyst. Remarkably, all derivatives were successful for cysteine arylation of GSH and more complex peptide substrates.¹⁹⁶

The lead complex was also able to mediate cysteine arylation of DARPin (designed ankyrin repeat protein), and the PEG derivative could arylate the cysteine of FGF2 (fibroblast growth factor 2).¹⁹⁶ Due to the success of these Au(III) catalysts, their activity was challenged against a Pd(II) complex, [Ru(Phos)Pd(tolyl)Cl], previously reported for cysteine arylation.¹⁹⁴ The Au(III) catalyst was most successful for the arylation of GSH, with ca. 92% conversion to the corresponding product, demonstrating that the gold-mediated arylation was a faster reaction compared to the palladium-mediated reaction.¹⁹⁶

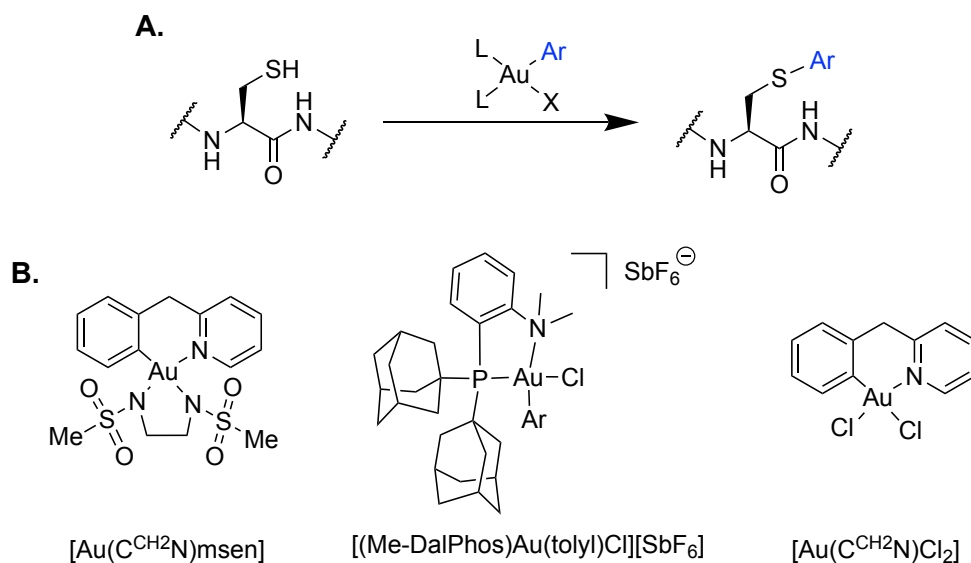


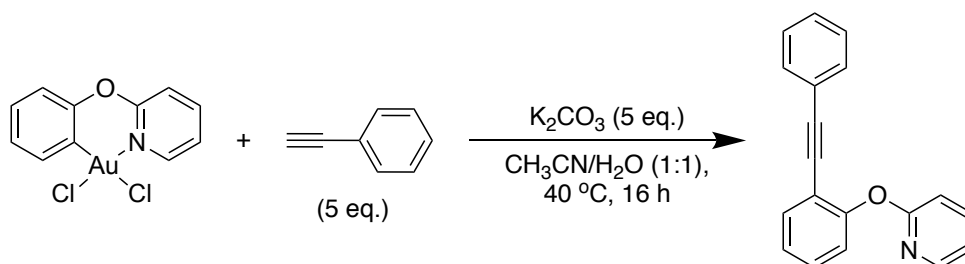
Figure 35 – **A)** Schematic representation of a cysteine arylation reaction; **B)** Au(III) cyclometalated complexes capable of mediating cysteine arylation.^{195–197}

A few years later, Farrell and co-workers¹⁹⁷ reported the ability of the Au(III) cyclometalated complex, [Au(C^{H2}N)Cl₂] (Figure 35B), to arylate the cysteines of the full-length zinc finger (ZF) of HIV-1 nucleocapsid protein NCp7 with a ZnCys₃His coordination sphere, as well as its single C-terminal finger. The reaction was not limited to this type of ZF, with cysteine arylation also observed with the Cys₂His₂ ZF of the Sp1 human transcription factor.¹⁹⁷ Three other Au(III) complexes were investigated bearing N-donor ligand scaffolds (2,2'-bipyridine, 4,4'-dimethyl-2,2'-bipyridine and 1,10-phenanthroline); however, these were ineffective for cysteine arylation, highlighting the importance of the C^{H2}N cyclometalated scaffold to provide stability to the Au(III) centre. It should be noted that in these experiments, the conditions for incubation of the complexes and ZF peptides were far from physiological, with cysteine arylation occurring only after 48 h.¹⁹⁷

Alternatively, as mentioned in 1.2.1, a gold(III) mesoporphyrin IX dimethyl ester complex (AuMesolX) can also be used to modify cysteine residues by covalent C-S bond formation to the electrophilic methine group of the porphyrin scaffold.¹⁹⁸

2.1.2.1.5. C-C cross-coupling reactions

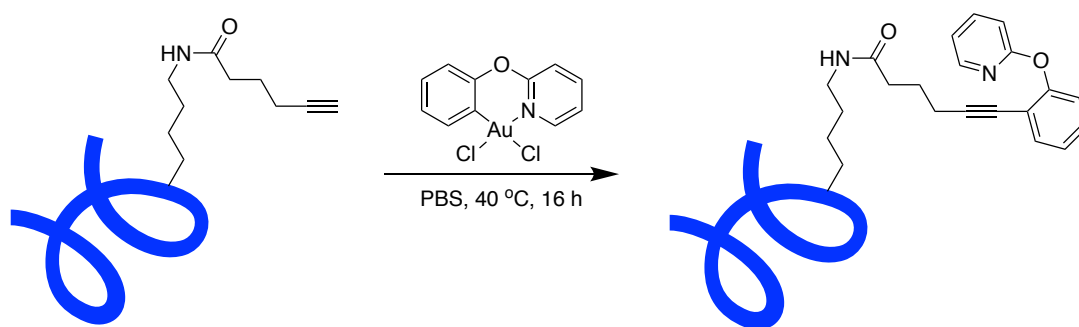
More recently, Wong and co-workers¹⁹⁹ reported the ability of cyclometalated Au(III) complexes to mediate a C-C cross-coupling reaction in a biological environment *via* an alkylation reaction. The reaction was achieved using the Au(III) cyclometalated complex, $[\text{Au}(\text{C}^{\text{O}}\text{N})\text{Cl}_2]$ ($\text{C}^{\text{O}}\text{N}$ = 2-phenoxyphenylpyridine) (1 eq.), which was coupled with phenylacetylene (5 eq.) in the presence of K_2CO_3 (potassium carbonate) (5 eq.) in a $\text{CH}_3\text{CN}:\text{H}_2\text{O}$ (1:1) mixture at 40 °C for 16 h (Scheme 6), yielding the product (82%).¹⁹⁹



Scheme 6 – C-C bond formation mediated by the Au(III) cyclometalated complex $[\text{Au}(\text{C}^{\text{O}}\text{N})\text{Cl}_2]$.¹⁹⁹

The reaction scope was further expanded by using a series of other Au(III) cyclometalated complexes with different groups between the pyridyl and aryl rings, as well as introducing electron-donating and withdrawing groups on the phenylacetylene.¹⁹⁹ Unsurprisingly, the five-membered cyclometalated complex, $[\text{Au}(\text{C}^{\wedge}\text{N})\text{Cl}_2]$, was unable to yield any product.¹⁹⁹

Proof-of-concept experiments were then performed to showcase the ability of these complexes to mediate the reaction in a biological system.¹⁹⁹ In detail, an alkyne tethered to a model peptide was reacted with $[\text{Au}(\text{C}^{\text{O}}\text{N})\text{Cl}_2]$ or $[\text{Au}(\text{C}^{\text{O}}\text{N})\text{Cl}_2]$ (5 eq.) in a PBS (pH 7.4, 50 mM):DMSO (9:1) solution at 40 °C for 4 h, resulting in a >99% conversion for both complexes.¹⁹⁹ To perform this reaction in living cells, selectivity is essential. Therefore, an alkyne was tethered to lysine residues in a lysozyme model protein to selectively couple with $[\text{Au}(\text{C}^{\text{O}}\text{N})\text{Cl}_2]$ (10 eq.) in PBS (pH 7.4, 50 mM) at 40 °C for 16 h (Scheme 7). Product formation was confirmed by LC-MS/MS analysis of the digested peptide sequences.¹⁹⁹ The versatility of this reaction was demonstrated by attaching either a dansyl or BODIPY group to the cyclometalated Au(III) scaffold to achieve fluorescent labelling of a model protein. These reactions were again performed in PBS (pH 7.4, 50 mM) at 40 °C for 16 h and involved the reaction between the fluorescent Au(III) cyclometalated complex (10 eq.) and the alkyne tethered lysozyme, resulting in successful product formation.¹⁹⁹ This work provides great promise for utilising Au(III) cyclometalated complexes for *in vivo* fluorescent labelling of target proteins.



Scheme 7 – C-C cross-coupling reaction between an alkyne tethered to a lysine residue in a lysozyme with the cyclometalated Au(III) complex in PBS.¹⁹⁹

2.1.2.2. Au(I) complexes

2.1.2.2.1. Cyclisation reactions

There are far fewer examples of Au(I) complexes to mediate reactions in living cells, and those that do usually can still be mediated by Au(III) complexes, albeit at a slower rate. The standard method for Au sensing, as described above in section 2.1.2.1.1, involves a non-fluorescent molecule comprising of a fluorophore and organic molecule, which within the presence of Au ions undergoes a structural change forming a fluorescent probe.¹⁸² However, in 2012 Patil *et al.*²⁰⁰ reported a new approach involving the ‘anchoring and unanchoring’ of a fluorophore. In detail, on addition of the fluorescent fluorophore to the organic substrate, its fluorescence is masked; however, in the presence of Au(I) and Au(III) ions, the fluorescence is restored. Interestingly the reaction with Au(III) ions occurred at a slower rate compared to Au(I) ions.²⁰⁰ A549 cells (human lung carcinoma) were incubated with the organic substrate fluorophore conjugate, and upon addition of Au(I) ions, green fluorescence was observed which appeared concentrated in certain areas of the cells. Unfortunately, the images were not of sufficient quality to allow conclusions to be undoubtedly drawn.²⁰⁰

In 2018, Mascareñas and co-workers²⁰¹ reported the ability of simple Au(I) coordination complexes to mediate a carbocyclization reaction *via* hydroarylation of a pro-coumarin derivative to form the fluorescent coumarin product (Figure 36). A range of different Au(I) and Au(III) complexes were tested to mediate this reaction; however, the most successful were the coordination complexes with the general formula $[\text{Au}^{\text{I}}(\text{L})\text{Cl}]$ (L = phosphane ligand, complexes **1-4**, Figure 36).²⁰¹ Starting from the $[\text{Au}(\text{PTA})\text{Cl}]$ (PTA = 1,3,5-triaza-7-phosphaadamantane, **1**) complex, the hydroarylation reaction was initially performed in water; however, due to scarce solubility of the pro-coumarin derivative, a co-solvent (CH_3CN) was required (8:2, $\text{H}_2\text{O}:\text{CH}_3\text{CN}$). It is important to mention that using CH_3CN alone also did not result in any activity, which the authors proposed was due to water being needed to form the active catalyst.²⁰¹

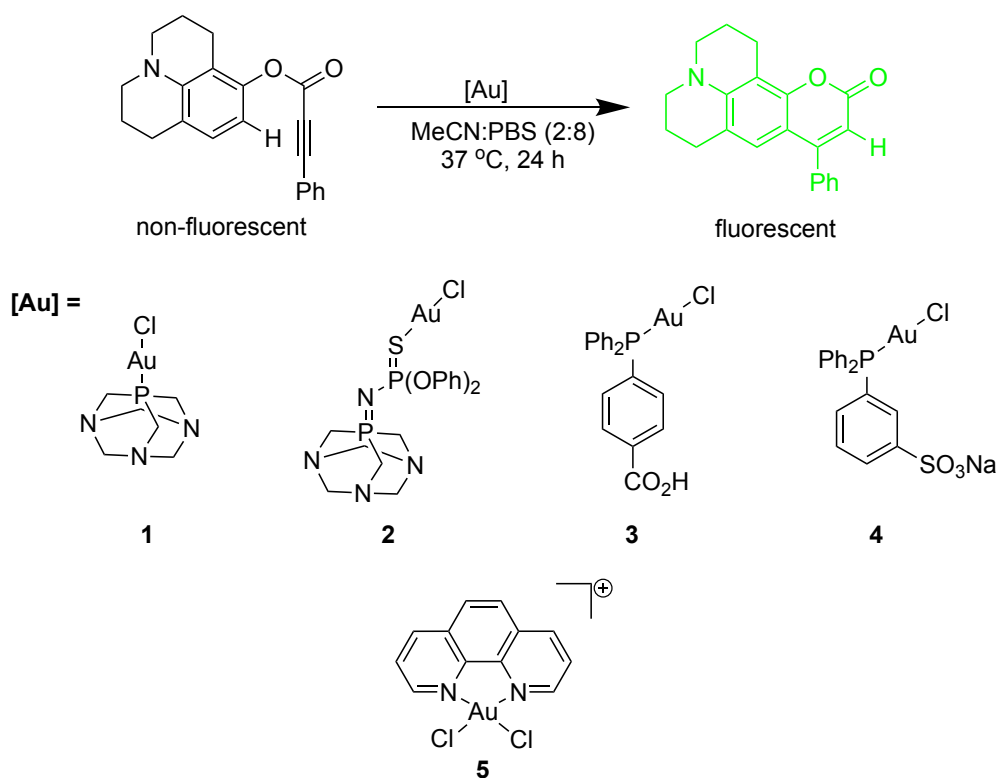


Figure 36 – Schematic representation of the carbocyclization reaction via hydroarylation of a pro-coumarin derivative to form the fluorescent coumarin product, mediated by Au(I) and Au(III) coordination complexes (1-5).²⁰¹

Other [Au^I(L)Cl] catalysts (2-4) were also very active, except for [Au(PPh₃)Cl], which was due to its low solubility in the reaction mixture.²⁰¹ Overall, it was concluded that facile hydrolysis of the chloride ligands helped facilitate this reaction. Out of the three Au(III) coordination complexes studied, only the one bearing a 1,10-phenanthroline scaffold, [Au(phen)Cl]PF₆ (5, Figure 36) was capable of successfully mediating this reaction.²⁰¹ The [Au(PTA)Cl] complex was the least cytotoxic and therefore was used in fluorescent microscopy images within HeLa cells along with the pro-coumarin derivative. The fluorescent coumarin product was found to accumulate within the lysosomes of the HeLa cells.²⁰¹

Unfortunately, the catalytic activity of the [Au(PTA)Cl] complex was inhibited in the presence of excess thiols, including GSH and cysteine, both ubiquitous in physiological media.²⁰¹ Therefore, to translate this work *in vivo*, greater protection from speciation is required.²⁰¹ However, it should be highlighted that the reaction can be performed concurrently with the previously reported¹⁵⁰ Ru-mediated deallylation reaction within HeLa cells.²⁰¹ The reactions were performed with the same substrates, with infrared fluorescence detected for the deallylation product and a green and blue emission for the hydroarylation product. This example is a first of its kind, highlighting the significant chemoselectivity and bioorthogonal manner of these transition metal catalysts.²⁰¹

2.1.2.3. Au(0) nanoparticles

In attempts to overcome speciation issues and unwanted reactions with thiols, commonly observed for homogenous gold catalysts in the cellular environment, Unciti-Broceta and co-workers²⁰² reported the first example of an uncaging reaction mediated by gold nanoparticles (AuNPs) in living systems. The AuNPs themselves were embedded within a polyethylene glycol (PEG)-grafted low-cross-linked polystyrene matrix, similar to the matrix the authors used to embed PdNPs,¹⁵⁰ providing greater protection against large thiol molecules whilst still allowing small molecules to enter and react.²⁰² The AuNPs were first tested for the *O*-depropargylation reaction of a non-fluorescent rhodamine 110 derivative to form the fluorescent rhodamine 110 product. The reactions were performed in physiologically relevant conditions, with and without serum. Interestingly, in both cases, fluorescent rhodamine 110 was formed, with the addition of serum increasing the yield by ca. 25%.²⁰²

To explore this phenomenon further, GSH was added to the AuNPs and rhodamine 110 derivative at varying concentrations.²⁰² It was found that up to physiological concentrations of GSH the reaction was promoted; however, once this was surpassed (over 50 μM) the fluorescence intensity decreased.²⁰² Therefore the authors concluded that the Au-S bonding of GSH to the NP surface could facilitate the dealkylation reaction when GSH concentration was below the threshold; however, once this was surpassed, the GSH then blocked most of the active sites on the surface of the NPs meaning the gold-alkyne could not interact and the depropargylation reaction was not performed.²⁰²

In vitro studies were next performed in A549 cells to evaluate the reaction in more physiological conditions; in this case, protected anticancer drugs (prodrugs) were used.²⁰² Remarkably, this was successful with cell viability measured after incubation with both the AuNPs and prodrugs alone, both of which had no cytotoxic effect; yet, when combined cytotoxicity was observed.²⁰²

Due to this success, the authors then envisaged using these embedded AuNPs as implants for localised tumours within the brain or prostate, for example, offering *in situ* transformation of the prodrug to an active anticancer agent in a specific area.²⁰² Therefore, *in vivo* proof-of-concept experiments involving the AuNPs and non-fluorescent rhodamine 110 derivative (pro-dye) were performed within the cranium of zebrafish embryos (Figure 37). The AuNPs were first implanted into the brain of zebrafish larvae before the addition of the lipophilic pro-dye to the embryo media, which was taken up through the skin and/or by ingestion.²⁰² Extraordinarily, fluorescence was only observed once the pro-dye had reached the AuNPs, as observed by the strong green fluorescence localised in the area of the AuNPs (Figure 37).²⁰² This work paves the way

for heterogeneous gold catalysts as bioorthogonal reagents, overcoming issues of speciation and unwanted thiol reactions whilst demonstrating the ability of AuNPs to successfully activate prodrugs *in situ*, reducing harm to healthy tissues, an ever-present challenge with using chemotherapeutics.²⁰²

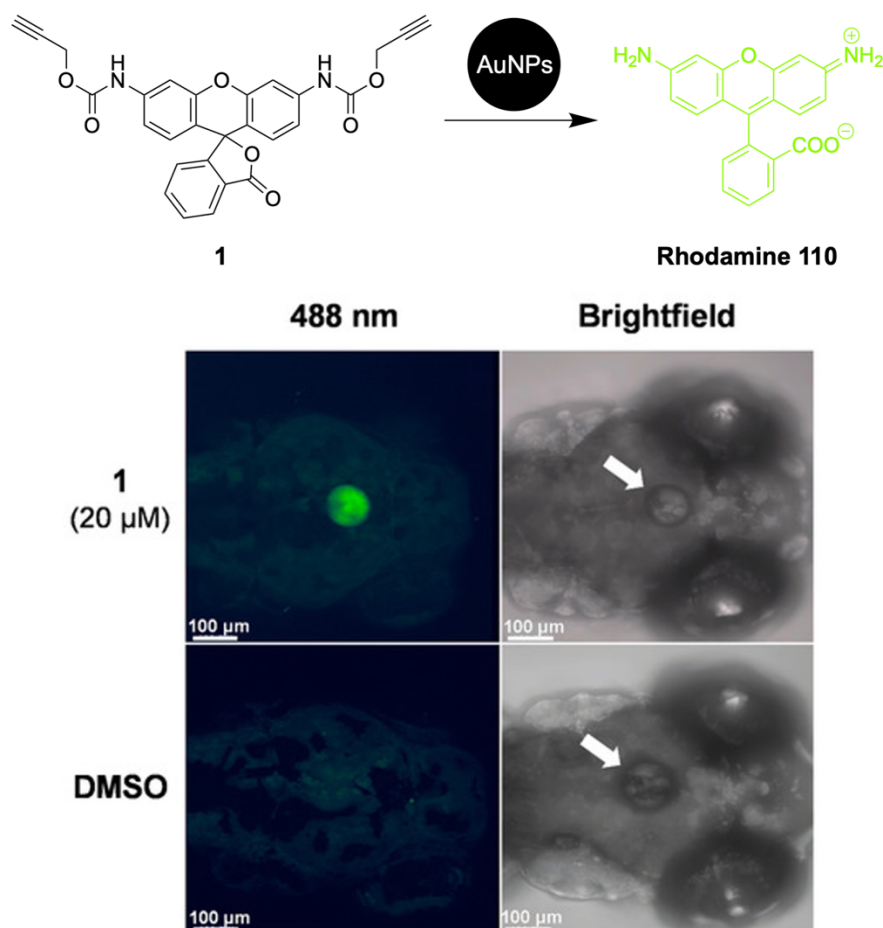


Figure 37 - O-depropargylation reaction of **1** mediated by AuNPs to form the green fluorescent Rhodamine 110 in the brain of zebrafish embryos. The white arrow in the brightfield image shows the presence and location of the AuNPs. Figure partially reproduced from ref 202.

Copyright 2017, John Wiley and Sons, *Angewandte Chemie International Edition*,

<http://creativecommons.org/licenses/by/4.0/>.²⁰²

Motivated by this success, the same group recently published the ability of similar AuNPs to activate the prodrug of Panobinostat, which has been approved for the treatment of multiple myeloma.^{203,204} The AuNPs were formed using a similar method to before,²⁰² except trisodium citrate was used as a more biocompatible reducing and stabilising agent to replace tetrakis(hydroxymethyl)phosphonium chloride (THPC).²⁰³ *In vitro* studies were performed in non-small-cell lung cancer (NSCLC) A549 cells and showed successful depropargylation of the Panobinostat prodrug by the AuNPs. The AuNPs

were also demonstrated to be re-usable, with sufficient activity over three successive cycles.²⁰³

3. Gold nanoparticles (AuNPs) stabilised by NHC ligands

Nanomaterials such as inorganic nanoparticles are identified as such due to their dimension being within the nanometre scale (1-100 nm).²⁰⁵ They possess different chemical and physical properties compared to small molecules and bulk materials, showing increased reactivity due to a large surface area to volume ratio.²⁰⁶ This latter property makes metal nanoparticles (MNPs) natural choices for new catalysts. The advantages of these systems surpasses the benefit of metal economy as the restriction of electrons within a nanoscale domain can improve the activity and selectivity of these catalysts.²⁰⁷ In fact, MNPs also have distinct optical properties due to the presence of a surface plasmon resonance (SPR) band.^{208,209} This is due to the excitation of free electrons of the MNPs when exposed to the electromagnetic field of light, causing them to oscillate collectively away from the lattice of positive ions.²¹⁰ The frequency of oscillation is the same as the incident light, forming localised surface plasmons (LSPs), as shown in Figure 38.^{210,211} This in turn gives strong SPR bands due to light scattering, thus enhancement of local electromagnetic fields.^{209,210} The properties of the SPR bands (frequency and intensity) allow the material to be identified.²⁰⁹

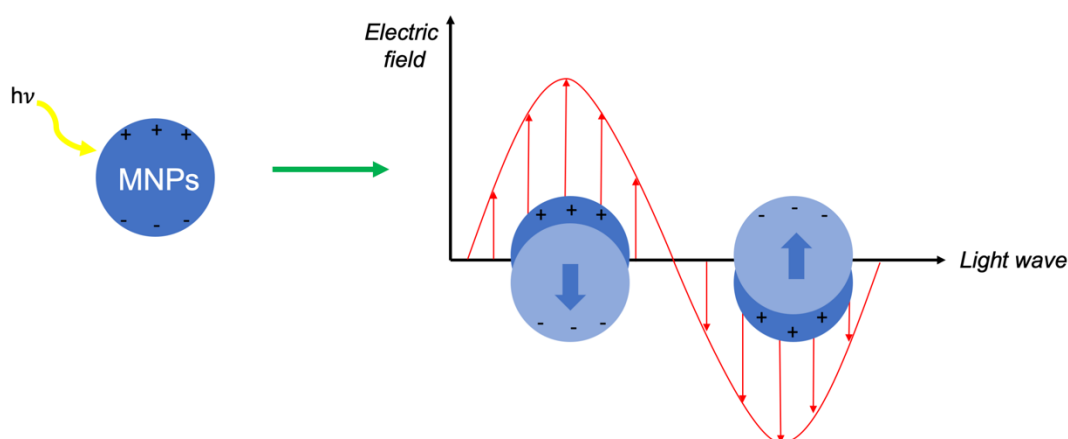


Figure 38 - Excitation of free electrons of MNPs by light forming localised surface plasmons, adapted from ref.²¹¹

Gold nanoparticles (AuNPs) are one of the most well-researched MNPs and can be produced from a range of different synthetic methods, all of which can affect the size, shape, and stability of the NPs. The preparative methods can be divided into two main types: physical and chemical.^{206,212} The former, which is less common, usually produces NPs of larger size obtained by grinding, evaporation or milling.^{206,212} The chemical method generally involves a reducing agent, such as sodium borohydride (NaBH_4), which is added to the Au ions in a chosen solvent with the addition of a protecting

agent/stabiliser to reduce agglomeration of AuNPs. Altering the ratios of these reagents can affect the size and morphology of the NPs.²¹²

The diverse colour of AuNPs was first discovered by Michael Faraday who presented a reaction involving the reduction of an aqueous solution of a gold salt, sodium tetrachloroaurate (NaAuCl_4), with a solution of phosphorus in carbon disulfide.²¹³ A colour change of the yellow NaAuCl_4 solution to deep ruby was observed after a few minutes of reduction due to the formation of AuNPs.²¹³ In fact, as light scattered from AuNPs is within the visible region of the electromagnetic spectrum, this yields an array of colours characteristic of the type of AuNPs.²¹⁴ The sensitivity of the plasmon frequency of AuNPs means that the wavelength of the SPR band can be indicative of the environment the AuNP is in, see Figure 39.²¹⁴ For example, aggregation of NPs increases the amount of light scattered, rather than absorbed, increasing the wavelength of the SPR band, resulting in the ruby red colloidal solution becoming more purple.²¹⁴

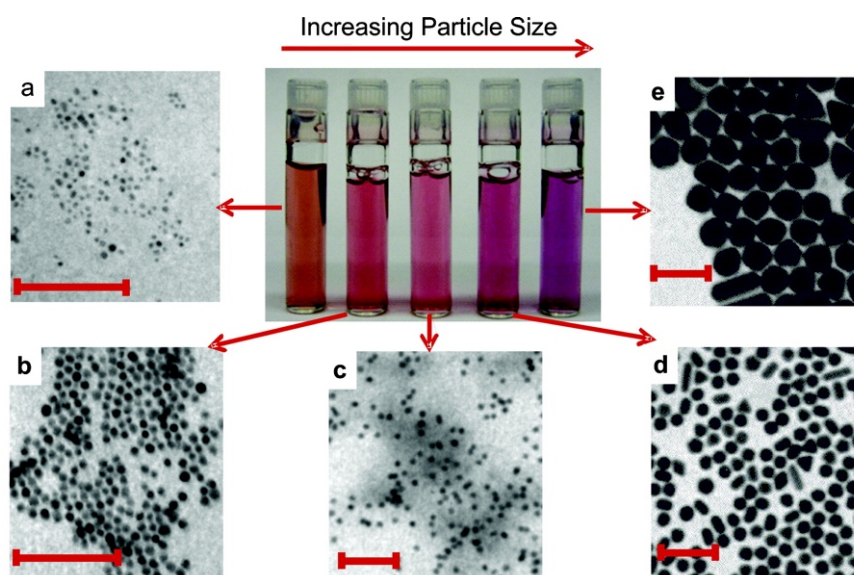


Figure 39 – Central image showing colour change observed upon increasing size of gold nanoparticles in an aqueous solution from 4 to 40 nm (a-e), with corresponding transmission electron microscopy images of the nanoparticles, scale bars are 100 nm. Reprinted with permission from ref 214. Copyright (2008) American Chemical Society.²¹⁴

There have been many applications of AuNPs over the years in different areas, such as catalysis, biological sensing, clinical imaging and drug delivery.^{206,208,214,215} This is mostly due to the unique optical properties of AuNPs, but also to their biocompatibility and relatively low toxicity, which have made them a popular choice in biomedical applications among the possible nanomaterials.²⁰⁶

As mentioned above, stabilisers are needed to inhibit irreversible agglomeration of metal NPs, and among the different types, ligands containing donor atoms, polymers or surfactants can be used for these purposes.²⁰⁷ Stabilisers can function either sterically

or electrostatically, both preventing the encounter of distinct NPs.²⁰⁷ The choice of stabiliser can influence different properties of the NPs such as size, shape and structure.²¹⁶ In 1994, the first example of thiol stabilised AuNPs was reported by Brust *et al.*²¹⁷ using the alkanethiol, dodecanethiol, due to the aurophilic nature of thiols. This yielded AuNPs with a small size distribution ranging between 1-3 nm, thus remained a popular choice for NP synthesis.²¹⁷ Thioethers have also been explored as a stabiliser for AuNPs,^{218,219} as well as phosphines,²²⁰ however these ligands do not bind to Au as strongly as thiols.²²¹ The stabilising ligand can occupy further roles such as functionalisation of the NP surface by the addition of various groups including biocompatible targeting ligands, and to increase the solubility of the NPs.²²²

The following sections will be focused on AuNPs stabilised by N-heterocyclic carbene (NHC) ligands, however it should be noted that the literature is teeming with examples of NHC stabilised Au materials²²³ such as: nanocrystals,^{224–226} nanoclusters^{227–229} and monolayers.^{230–235}

3.1. AuNPs stabilised by N-heterocyclic carbene (NHC) ligands

3.1.1. N-heterocyclic carbenes (NHCs)

The field of NHCs was developed following the isolation of the stable carbene IAd (1,3-bis(adamantyl)imidazol-2-ylidene) (Figure 40a) in 1991.²³⁶ NHCs have become a popular choice over the years due to their high stability and facile synthesis, with the ability to functionalise multiple positions of the structure over a short period of time.²³⁷

NHCs possess a singlet ground state electron configuration, where the carbenic carbon is considered formally as having an sp^2 -hybridised lone pair as the highest occupied molecular orbital (HOMO) and the lowest unoccupied molecular orbital (LUMO) being an unoccupied p orbital (Figure 40b).²³⁷ The presence of the adjacent N atoms help to stabilise the structure electronically as they act as σ -electron-withdrawing groups (green arrows, Figure 40b), lowering the energy of the occupied σ orbital, as well as π -electron-donating groups, donating electron density to the empty p orbital (red arrows, Figure 40b).²³⁷ The reactivity and stability of NHCs is affected by both electronic and steric factors. For example, IAd contains two bulky adamantyl groups constituting the N-anchored wingtips, which sterically disfavour the NHC dimerization (Figure 40a).²³⁷ Replacement of these groups with other substituents greatly affects the steric properties of the NHC. The cyclic structure of the NHC also favours the more stable singlet ground state on the carbenic carbon by imposing a more bent structure.²³⁷ Modification of the backbone itself can also affect the electronic properties of the NHC by the addition of different substituents, for example a carbonyl group on the NHC backbone can cause the NHC to be less electron-donating.²³⁸

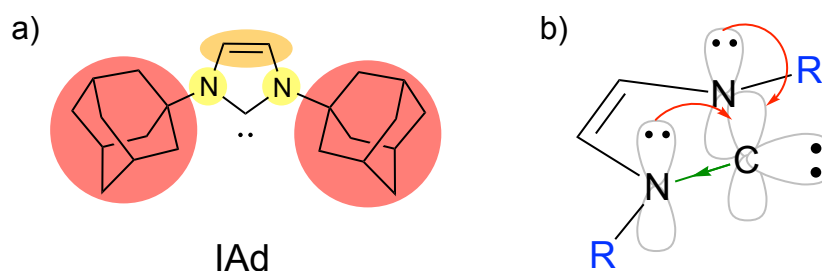


Figure 40 - (a) Structure of IAd (1,3-bis(adamantyl)imidazol-2-ylidene), (b) Representation of singlet ground state electronic structure of imidazol-2-ylidene-type NHC. Adapted from ref.²³⁷

NHC ligands are known to be strong σ -donors and weak π -acceptors, similar to phosphine ligands.²³⁷ However, phosphines, at variance with NHCs, often suffer from decomposition at high temperatures.²³⁷ In 1995, Herrmann *et al.*²³⁹ were the first to describe a transition metal complex bearing an NHC ligand to be used as a homogenous catalyst.²³⁹

Within this framework, organometallic gold complexes featuring NHC ligands have raised interest over the years for applications in catalysis, such as enyne cycloisomerisation,²⁴⁰ hydration of nitriles to amides²⁴¹ and C-H activation by carboxylation,²⁴² to name just a few. Also, due to their high affinity for binding to metals in the oxidation state 0, NHCs were also explored for applications in heterogeneous catalysis, and in 2009, the first examples of AuNPs stabilised by NHCs were reported.^{243,244}

3.1.2. Synthetic approaches to AuNPs stabilised by NHCs (NHC@AuNPs)

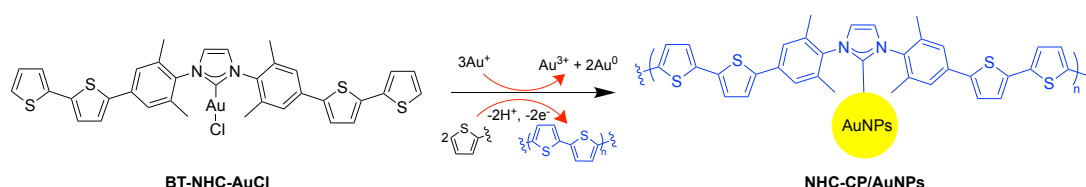
Hurst *et al.*²⁴³ were the first to report the synthesis of AuNPs stabilised with NHCs (NHC@AuNPs) *via* a ligand exchange method, which has been named as the 'top-down' approach. Generally, this approach involves the replacement of a weaker ligand from the AuNP, such as a thioether ligand, with an NHC ligand. For example, bis-*tert*-butylimidazol-2-ylidene was first prepared by deprotonation of the corresponding imidazolium salt using KO^tBu (potassium *tert*-butoxide), before the addition to the AuNPs stabilised with dodecyl sulfide in benzene.²⁴³ The NHC@AuNPs then precipitated out of solution after ca. 12 h. Although the NPs were stable at -4 °C in their solid form for months, in solvents including DMSO (dimethylsulfoxide), CH₃CN (acetonitrile) and CH₂Cl₂ (dichloromethane), the NPs were only stable for ca. 12 h before a precipitate was formed. The instability of such AuNPs was attributed to the large sterics of the NHC ligand.²⁴³

In the same year, Vignolle and Tilley²⁴⁴ reported a different so-called 'bottom-up' approach for the formation of NHC@AuNPs which involved the direct reduction of the corresponding NHC-Au(I) starting complex. Specifically, this work used a Au(I) NHC complex as the starting material, featuring the less sterically demanding ^tPr₂Im (1,3-

diisopropylimidazol-2-ylidene) NHC ligand.²⁴⁴ After reduction with KBET_3H (potassium triethylborohydride) in THF (tetrahydrofuran) a brown solution was formed. Unfortunately, due to the small size of the spherical AuNPs (2.19 ± 0.47 nm) and similar solubility to the NHC-Au(I) starting complex, purification of these NPs could not be achieved.²⁴⁴

This study then moved towards NHC ligands with longer $\text{C}_{14}\text{H}_{29}$ alkyl chains as wingtip groups on the NHC scaffold, which again were reduced using KBET_3H in THF.²⁴⁴ The synthesised AuNPs produced a ruby red solution with an SPR band around 525 nm. The purified NPs were stable as solids or in apolar organic solvents, excluding chlorinated solvents.²⁴⁴ TEM (transmission electron microscopy) analysis showed mainly spherical NPs with a larger size of 6.8 ± 1.8 nm. The effect of the reducing agent was next investigated by replacement with a weaker reducing agent, 9-BBN (9-borabicyclo[3.3.1]nonane).²⁴⁴ The NPs formed were more triangular or rhombic in shape, with a lower size distribution and overall smaller size (5.75 ± 0.49 nm) compared to those formed with KBET_3H .²⁴⁴ Compared to the work by Hurst *et al.*,²⁴³ this work showed the formation of more stable AuNPs, albeit with different NHC ligands and preparation methods.²⁴⁴

Using the same 'bottom-up' approach as Vignolle and Tilley,²⁴⁴ Song *et al.*²⁴⁵ explored AuNPs with NHC ligands attached to π -conjugated polymers or conducting polymers (CPs).²⁴⁵ Interestingly, when starting from the bithiophene-NHC-Au(I) precursor (BT-NHC-AuCl, Scheme 8), replacement of the chloride with triflate, which binds more weakly, resulted in disproportionation of Au(I) to Au(III) and Au(0). The Au(III) immediately induced oxidative polymerisation through the thiophene groups and the Au(0) initiated growth of AuNPs.²⁴⁵ This afforded NHC-based CP/AuNP hybrids, where the NHC ligands were significant for the dispersion of the AuNPs in the polymer matrix.²⁴⁵ The catalytic applicability of these NHC-CP/AuNPs was then demonstrated for the reduction of 4-nitrophenol (4-NP) to 4-aminophenol (4-AP) using NaBH_4 in H_2O . The reduction was completed within 510 s showing significant activity.²⁴⁵ Hybrid composites of CP and NPs can be used as materials in many areas including optoelectrics.²⁴⁶



Scheme 8 - Synthesis of NHC functionalised conducting polymer/AuNP hybrids from the bithiophene-NHC Au(I) precursor by concurrent disproportionation of Au(I) to Au(III) and Au(0) and oxidative polymerisation of the thiophene groups.²⁴⁵

In 2014, further work on the 'top-down' method was reported by Richter *et al.*²⁴⁷ with a focus on forming stable PdNPs with NHC ligands; however an example using AuNPs was also included.²⁴⁷ This involved the ligand exchange reaction in a two-phase solvent system of CH₃CN and hexane, with thioether stabilised AuNPs and a long alkyl chain imidazolium salt (1,3-dimethyl-4,5-diundecyl-1*H*-imidazol-3-ium), in the presence of *t*BuONa (sodium tert-butoxide).²⁴⁷ The authors described the ligand exchange on the AuNPs as successful, forming stable AuNPs with long-chain NHC ligands. Unfortunately, very little information was given on the stability of the AuNPs synthesised in this work.²⁴⁷

In the same year, Richeter and co-workers²⁴⁸ also used the 'top-down' method to produce stable NHC@AuNPs; however, they focused solely on AuNPs.²⁴⁸ In this work, two benzimidazol-2-ylidene derivatives (**1a** and **1b**, Figure 41) were used to try and improve the lack of stability observed previously when using imidazolium derivatives.^{243,248} The starting thioether-coated AuNPs were reacted with the carbene, formed *in situ* by the addition of *t*BuONa to the corresponding NHC salt (**1a** and **1b**).²⁴⁸ This led to the formation of the AuNPs as a precipitate. The NHC@AuNPs formed from **1a** were two times smaller than the starting thioether NPs (2.8 ± 0.6 nm vs. 5.8 ± 1.2 nm, respectively) and more aggregated, as seen by the broad SPR band at λ_{max} ~552 nm, compared to 510 nm for the thioether NPs.²⁴⁸ Investigations showed that the corresponding bis-NHC Au(I) complexes were formed alongside the NPs, as well as NHC ligands remaining present on the NP surface, which was also seen previously.^{243,248} This was additionally observed for **1b** and **1c**.²⁴⁸

In 2016, the same group continued this work by comparing the stabilisation ability of **1d** (*N,N*-dibenzylbenzimidazol-2-ylidene, Figure 41) to those previously reported.^{248,249} Benzyl groups were chosen to further stabilise the AuNPs through π-interactions with the surface.²⁴⁹ Unfortunately, enhanced stability was not achieved, with the bis-NHC Au(I) complex once again being the predominant species, with small aggregated NPs also present.^{248,249}

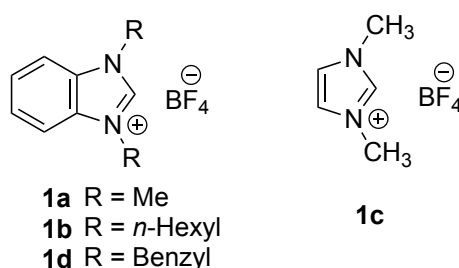


Figure 41 - Structure of benzimidazol-2-ylidene derivatives used in work by Richeter and co-workers.^{248,249}

The size of the AuNPs can be important for biomedical applications, for example, ultrasmall NPs (UNPs) have a size ranging between 1 to 2 nm and can be used for

intracellular drug delivery²⁵⁰ or as a contrast agent for *in vivo* fluorescence imaging of tumour cells.²⁵¹ The first example of NHC@AuUNPs was reported by Richeter and co-workers²⁵² in 2014. In this work, two types of Au(I) C₆F₅ complexes were used as the precursors for the formation of AuUNPs (Figure 42).²⁵² The first was an anionic complex with an imidazolium cation, [C₁₈H₃₇-MIM][Au(C₆F₅)₂] (C₁₈H₃₇-MIM = 1-methyl-3-octadecyl-imidazolium) (**2**, Figure 42), and the second was a neutral complex with an imidazol-2-ylidene ligand, [Au(C₆F₅)(C₁₈H₃₇-NHC)] (C₁₈H₃₇-NHC = 1-methyl-3-octadecyl-imidazol-2-ylidene) (**3**, Figure 42).²⁵²

In order to synthesise UNPs that have a small size distribution and high stability, high temperature thermolysis was used to ensure a fast nucleation step.²⁵² This synthetic method can be considered as a 'bottom-up' approach due to reduction of the Au(I) NHC species to the Au(0) NPs, using the C₆F₅⁻ ligands attached to the Au(I) NHC. After heating under air at 285 °C for 10 min, AuUNPs of **2** were formed, containing a mixture of UNPs and larger polyhedral nanocrystals.²⁵² Next, AuUNPs of **3** were formed by thermolysis at 285 °C, albeit in this case the NPs were formed after only 3 min and of slightly smaller size, with no nanocrystals. Reducing the temperature for the thermolysis of **3** to 250 °C, paired with a longer reaction time, gave UNPs as well as larger NPs of ~15 nm in size. The authors proposed that in the case of **2**, two steps are required to reach the UNPs, both mediated by the C₆F₅⁻ ligands.²⁵² Firstly, the C₆F₅⁻ ligands deprotonate the MIM cation to form complex **3** *in situ* and secondly, the C₆F₅⁻ ligands act as reductive elimination agents to reduce Au(I) to Au(0). However, when starting with **3** only the reductive elimination step is required. Therefore, this suggests that in the case of **2**, larger NPs are seen alongside the UNPs due to the extra step needed to first form **3**, meaning the nucleation step is slower.²⁵²

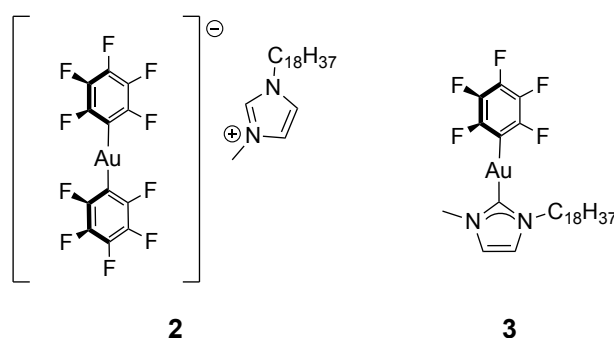


Figure 42 – Structures of complexes [C₁₈H₃₇-MIM][Au(C₆F₅)₂] (C₁₈H₃₇-MIM = 1-methyl-3-octadecyl-imidazolium) (**2**) and [Au(C₆F₅)(C₁₈H₃₇-NHC)] (C₁₈H₃₇-NHC = 1-methyl-3-octadecyl-imidazol-2-ylidene) (**3**).²⁵²

To assess the catalytic ability of these UNPs, NPs of **3** were supported on aminopropyl-functionalised silicon dioxide to improve water-solubility and subsequently tested for the

ethanol was added as the polar solvent to the AuNPs in THF to solubilise the TEG group.²⁵⁴ Water formed small aggregates with an SPR band of 555 nm, whereas ethanol formed larger ensembles as seen by the SPR band shift to 580 nm. The stability of the NP aggregates formed in water was assessed against excess glutathione (GSH).²⁵⁴ GSH is ubiquitous in human cells and therefore, resistance to its nucleophilic power is vital for biological applications.²⁵⁷ After 24 h there was only a 10% decrease in intensity of the SPR band, which shows moderate stability towards GSH, however due to the formation of aggregates it is unlikely that these systems can be used for biological applications.²⁵⁴

In 2018, the same group²⁵⁸ reported the first example of AuNPs stabilised by bis-NHC ligands (Figure 7). This work investigated if the addition of alkyl groups to the benzimidazole scaffold (**R**), or an increase in chain length (**L**) between the NHC ligands, would effect NP stability (Figure 44A).²⁵⁸ Interestingly, the synthesis of the NPs was conducted using the ‘top-down’ and ‘bottom-up’ approaches to observe possible changes in stability due to the preparation method (Figure 44A).²⁵⁸

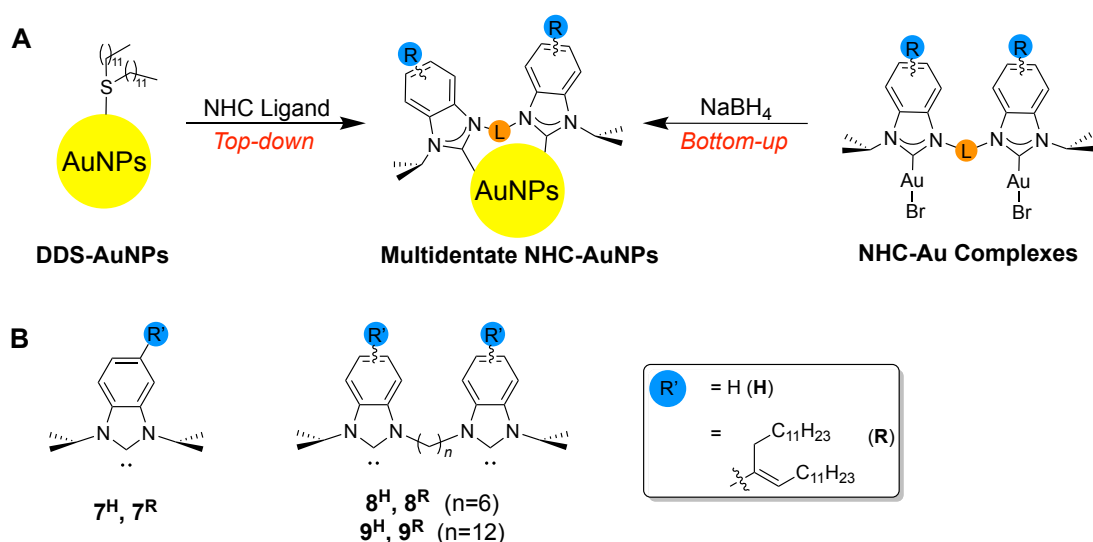
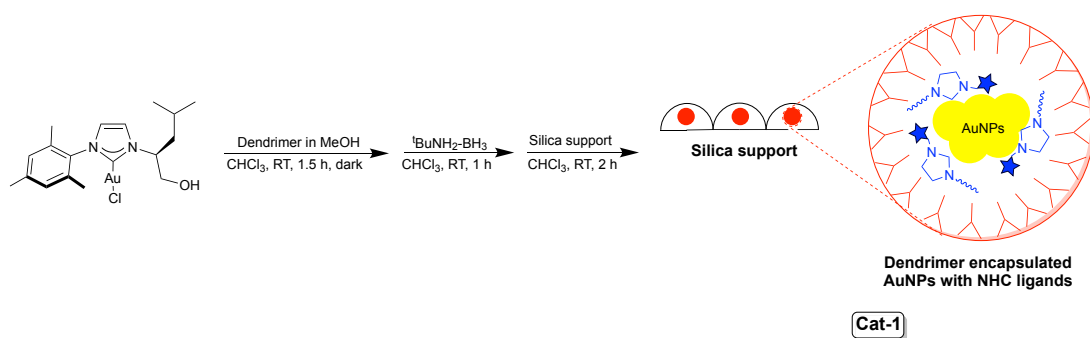


Figure 44 – (A) Synthetic routes used to form multidentate NHC@AuNPs (‘top-down’ and ‘bottom-up’ approaches). (B) Structures of monodentate (**7^H** and **7^R**) and bidentate (**8-9^H** and **8-9^R**) NHC ligands used to stabilise multidentate AuNPs against external thiols by Crudden and co-workers, adapted from ref.²⁵⁸

The stability of the AuNPs possessing both mono- (**7**) and bi-dentate (**8**, **9**) NHC ligands were investigated, featuring (**R**), or not (**H**), alkyl groups on the benzimidazole scaffold (Figure 44B).²⁵⁸ Overall, the bidentate NHC ligands with the alkyl groups, synthesised using the ‘top-down’ approach, produced the most stable NPs (**8^R AuNP^{TD}** and **9^R AuNP^{TD}**) with respect to high temperature and thiols (e.g. dodecanethiol).²⁵⁸ This result is surprising considering previous reports of unstable NPs produced by the ‘top-down’ approach,^{243,248,249} and could be ascribed to the inherent stability of the bidentate



*Scheme 10 - Dendrimer encapsulated gold nanoparticles with NHC ligands supported on silica forming **Cat-1**.²⁶⁰*

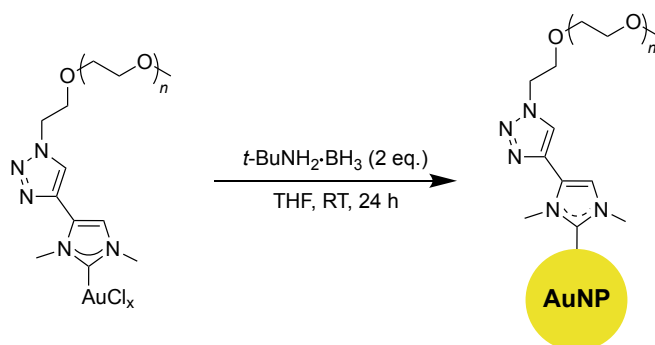
The catalytic activity of **Cat-1** was challenged against the intramolecular lactonization reaction of allenes,²⁶⁰ which has previously been catalysed by Au(I) complexes dispersed in silica.²⁶¹ **Cat-1** catalysed the reaction in deuterated DCM (CD_2Cl_2) at 20 °C after 22 h, requiring 100 °C and deuterated toluene to reach full conversion.²⁶⁰ In this work, techniques such as XPS (X-ray photoelectron spectroscopy) suggested the presence of a Au(I)-NHC monolayer around the Au(0) core of **Cat-1**, which the authors acknowledged as a potential catalytic active site. The NHC ligands not only activated the AuNPs as catalysts but also provided chirality, resulting in an enantiomeric excess (e.e.) of 16% for the reaction.²⁶⁰ A control experiment using the mono Au(I)-NHC as the catalyst showed no reactivity, however this does not prove that the Au(I)-NHC monolayer on the AuNPs is not responsible for the catalytic activity in this reaction, although does suggest that the heterogeneous nature of the catalyst plays a significant role in its catalytic activity.²⁶⁰

More recently, Lomelí-Rosales *et al.*²⁶² investigated the difference in AuNP formation using either Au(I) or Au(III) complexes as precursors, all featuring NHC ligands. The AuNPs were formed by direct reduction of the complexes with an aqueous solution of NaBH_4 added dropwise in ethanol.²⁶² For the mono and bis-Au(I)NHCs, addition of NaBH_4 formed black solutions, showing uncontrollable reduction and therefore, instability of the resulting NPs regardless of the ligand to metal ratio.²⁶² However, reduction of the neutral mono-Au(III)NHC complexes showed controlled NP formation, evidenced by purple colloidal suspensions after addition of NaBH_4 , which authors claim to remain stable over an undefined period of time. TEM analysis showed these NPs were spherical and small (average size ca. 3-5 nm).²⁶² Therefore, the authors suggested that the oxidation state of the AuNHC precursor was accountable for the stability of the resulting AuNPs, with Au(III) being the most suitable when using neutral Au(III) mono-NHCs as precursors.²⁶² Nevertheless, further work is needed in this area, such as exploring the NP formation starting from charged Au(III) bis-NHC complexes and variation of NHC ligands used. More in-depth analysis into the stability of the AuNPs

formed from the Au(III) complexes is also required, such as in the presence of exogenous thiols.

3.2. Water-soluble AuNPs stabilised by NHCs

For the application of AuNPs in biological systems or green chemistry, their solubility in an aqueous environment is an essential feature; however, it was not until 2015 that MacLeod and Johnson reported the first example of water-soluble NHC@AuNPs.²⁶³ Their work was focused on the applicability of water-soluble AuNPs for biomedical purposes, where stability is essential for function. Therefore, a hydrophilic NHC poly(ethylene glycol) (PEG) ligand was selected to provide steric stability to the AuNPs, with *N*-methyl substituents.²⁶³ The NPs were formed by reduction of the corresponding Au(I)/Au(III) NHC complexes with $t\text{-BuNH}_2\cdot\text{BH}_3$ in THF at room temperature (Scheme 11) before dialysis against water. Unfortunately, issues of separation during the synthesis of the AuNHC complex meant a mixture of Au(I) and Au(III) NHC complexes were used to form the AuNPs.²⁶³



*Scheme 11 - Synthesis of water-soluble AuNPs stabilised by hydrophilic NHC PEG ligands formed by the reduction of corresponding Au(I) and Au(III) NHC complexes.*²⁶³

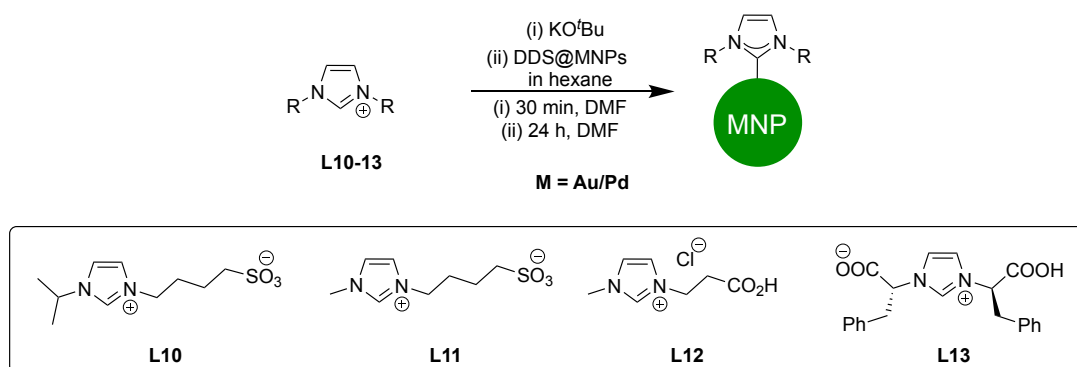
TEM analysis showed spherical AuNPs with an average diameter (D_{TEM}) of 4.2 ± 0.7 nm, whilst DLS (dynamic light scattering) measurements showed an average hydrodynamic diameter (D_h) of 16.2 ± 0.1 nm in an aqueous solution, indicating the presence of a core-shell structure.²⁶³ Next, the stability of the NPs in aqueous solutions was assessed based on the SPR band; the NPs were stable for at least 3 months at room temperature and tolerated extreme high and low temperatures (95 and -78 °C) for 5 h. The pH tolerance of the NPs was also investigated and showed high stability over 24 h, independent of the pH.²⁶³ After 2 days, only particles at pH 1 showed signs of aggregation. Exceptionally, after 8 weeks, NP solutions with a pH >3 did not show any change, whilst at pH 3 there was only a small decrease and red shift of the SPR band.²⁶³ Solutions of pH 1 and 2 were visibly aggregating with a large decrease in the SPR band. To mimic more

biological conditions, the stability of the NPs in saline solution was also assessed and showed that the AuNPs were stable for 6 h.²⁶³

The AuNPs were also tested in other solutions including buffers of varying pH: after 3 days there was only a small shift in the SPR bands and after 7 weeks the NPs had no visible aggregation.²⁶³ The NPs were also stable in cell culture medium containing fetal bovine serum (FBS) after 26 h at either room temperature or 37 °C.²⁶³

Finally, the AuNPs were exposed to two thiol-based reducing agents, namely 2-mercaptoethanol (BME) and GSH.²⁶³ NPs exposed to BME exhibited immediate broadening of the SPR band, although over 3 h this remained mostly unchanged. After 26 h, the BME exposed NPs had completely aggregated.²⁶³ However, the GSH exposed NPs only suffered a small shift in the SPR band. Treatment of the NPs with excess PEG-SH resulted in ligand exchange with the NHC ligand, but also the release of Au(I)/(III) NHC complexes. Unfortunately, no further biological data was reported for these NPs.²⁶³

Later that year, Ferry *et al.*²⁶⁴ continued the work on water-soluble NHC stabilised PdNPs and AuNPs. Thus, different negatively charged NHC ligands bearing either sulfonate or carboxylate groups to improve water-solubility and stabilisation by electrostatic interactions were reported (**L10-13**, Scheme 12).²⁶⁴ The ‘top-down’ approach was employed in this work, beginning with the *in situ* formation of the reactive NHCs in DMF (dimethylformamide) by the addition of KO^tBu to their corresponding imidazolium salts (**L10-13**), followed by the addition of didodecylsulfide (DDS) stabilised Pd or AuNPs in hexane (Scheme 12).²⁶⁴



Scheme 12 - Reaction scheme to form MNPs (M = Au/Pd) from imidazolium salts (**L10-13**), by Ferry *et al.*²⁶⁴

Ligand exchange was confirmed by phase transfer of the NPs in non-polar hexane into polar DMF, leaving behind excess DDS in hexane.²⁶⁴ After purification by dialysis the NPs were stable over 3 months. NHC@PdNPs were formed with **L10-13**, whereas NHC@AuNPs were formed with **L10-12**, due to previous work using **L13** for Au complexes.^{264,265} TEM analysis of the NHC@PdNPs compared to the DDS@PdNPs showed very little variation; however, the NHC@AuNPs showed a significant decrease

in size upon ligand exchange, for example, DDS@AuNPs had a mean size of 8.5 ± 1.7 nm, whereas **L10**@AuNPs had a mean size of 4.7 ± 1.6 nm.²⁶⁴ This had also been seen previously for the 'top-down' method, as reported above,^{243,248,249} by loss of corresponding Au(I)-NHC complexes, deeming the NPs unstable.²⁶⁴ However, NMR (nuclear magnetic resonance) and ESI-MS (electrospray ionisation mass spectrometry) analysis confirmed that before purification by dialysis, Au(I)-NHC species were present, however after dialysis these species were successfully removed yielding the pure NPs, which showed no further decrease in size after dialysis.²⁶⁴

To further investigate their stability, the Pd and AuNPs were subjected to acidic pH solutions between pH 1 and 4.²⁶⁴ Stability of the NPs was attributed to the charged group on the NHC ligand, sulfonated ligands (**L10** and **L11**) gave stable NPs at pH 4, whereas the NPs with the carboxylate ligands (**L12** and **L13**) aggregated. This can be explained due to partial protonation of the carboxylate group, reducing its charge and therefore electrostatic repulsion to neighbouring NPs, resulting in aggregation.²⁶⁴ This aggregation was reversible for **L12** Pd and AuNPs by adjusting the pH to 10 for 3 cycles, although the NPs did not tolerate acidic conditions for longer than 30 min. Lastly, the catalytic ability of the PdNPs was investigated for the hydrogenation of olefins, showing high chemoselectivity and reactivity, as well as the ability to be recycled.²⁶⁴

Following on from the work of Ferry *et al.*,²⁶⁴ further investigations into sulfonated imidazolium salts as stabilisers for water-soluble AuNPs was reported in 2017 by Monti *et al.*²⁶⁶ The AuNPs were formed *in situ* by addition of an aqueous solution of the imidazolium salts (**L14-16**, Figure 45) to HAuCl₄ (chloroauric acid), before the addition of hydrazine, producing AuNPs almost immediately.²⁶⁶

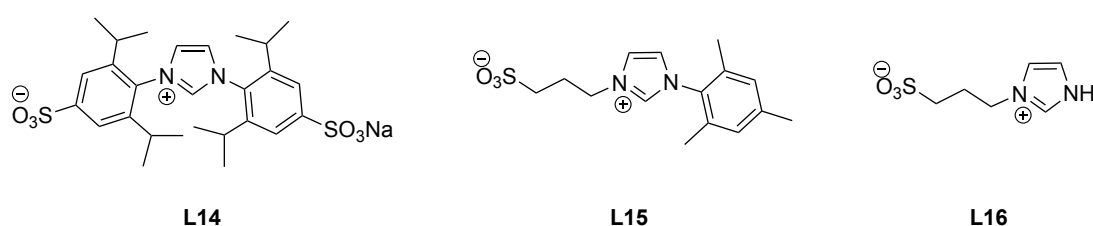


Figure 45 – Structures of sulfonated imidazolium salts (**L14-16**) used as stabilisers for water-soluble AuNPs by Monti *et al.*²⁶⁶⁻²⁶⁸

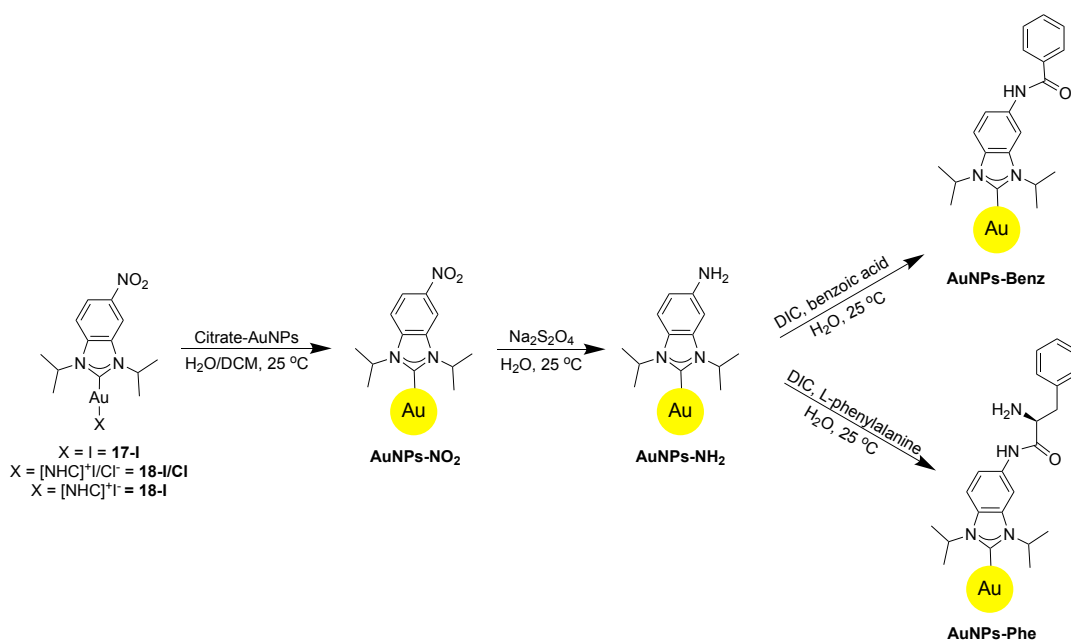
TEM analysis was used to determine the average diameter of the NPs, with **L14** giving the smallest NPs (9 ± 2 nm) and **L15** giving the largest (15 ± 2 nm).²⁶⁶ Negative zeta potential values were seen for all NPs, which led the authors to hypothesise that the AuNP surface interacts with the positively charged imidazolium ring, meaning that the negatively charged sulfonate groups point away from the surface.²⁶⁶

Additional investigations by the group showed that the interaction between the imidazolium ring and AuNP surface was electrostatic, with the strength of interaction

dictated by the orientation of the alkyl chain and sulfonate groups.²⁶⁷ Therefore, the stronger the interaction, the more stability the AuNPs had in water. **L14** possessed bulky isopropyl groups which reduced the interaction with the NP surface, making them less stable.²⁶⁷ Whilst **L15** and **L16** showed only small differences, the orientation and coverage of the ligands appeared to be different, with **L16** showing a stronger interaction of the imidazole ring with the NP surface compared to **L15**, which could be attributed to more steric impedence on **L15**.²⁶⁷

The catalytic ability of the NPs for reduction of 1,4-dinitrobenzene (DNB) to 4-nitroaniline (NA) was also assessed.²⁶⁷ The reaction was performed in water at room temperature with the addition of hydrazine and monitored by absorption spectra. All NPs showed activity after 30 min.²⁶⁷ To further explore the difference in reactivity between the AuNPs of **L15** and **L16**, the rate constant (k) of the reaction was determined for each NP by varying the apparent rate constant (k_{app}) with DNB concentration.²⁶⁸ AuNPs of **L16** showed a greater k value, which was recognised to be due to less compaction and steric hinderance of the stabilising NHC ligands, providing easier access of the DNB molecules to react with the AuNP surface.²⁶⁸ The recyclability of the NPs of **L15** and **L16** was also assessed, with the conversion determined after each recovery and re-use of the NPs. After each cycle the conversion of DNB dropped for both NPs.²⁶⁸ The authors hypothesised that the loss in conversion could be due to loss of AuNP during recovery, or increased occupied/modified active sites after each cycle, meaning less active sites for DNB molecules to compete for.²⁶⁸

Recent work published by DeJesus *et al.*²⁶⁹ described the formation in aqueous conditions of AuNPs stabilised by NHC ligands bearing protic groups; the synthesised AuNPs had an average diameter >15 nm.²⁶⁹ AuNPs larger than 10 nm have been reported as advantageous in areas such as *in vivo* biological applications to avoid rapid excretion by the kidneys.^{269,270} The authors aimed to utilise the reactions of amine functional groups in amide coupling reactions.²⁶⁹ However, due to the incompatibility of amines with typical reaction conditions for NP formation, a nitro group was initially attached to the NHC precursor complex (Scheme 13, **17-I**, **18-I/CI** and **18-I**).²⁶⁹ Mono (**17-I**) and bis (**18-I/CI** and **18-I**) AuNHC complexes were initially formed and isolated before addition of the NHC complex in CH₂Cl₂ to an aqueous solution of citrate-capped AuNPs. After 10 min, spontaneous functionalisation of the AuNPs produced **AuNPs-NO₂** (Scheme 13).²⁶⁹ Post-synthetic modification of the nitro group on the **AuNPs-NO₂** was achieved by reduction with Na₂S₂O₄ (sodium dithionite) to form the amino group functionalised NPs, **AuNPs-NH₂** (Scheme 13).²⁶⁹



Scheme 13 - Synthesis of AuNPs stabilised by NHC ligands bearing a nitro group (**AuNPs-NO₂**) via the ligand exchange method, which could then be reduced to form **AuNPs-NH₂**, allowing further derivatisation by formation of an amide bond (**AuNPs-Benz** and **AuNPs-Phe**) (DIC = *N,N'*-diisopropylcarbodiimide).²⁶⁹

The amino group was then functionalised further to form a carboxylic acid group via amide coupling (Scheme 13).²⁶⁹ Benzoic acid was first reacted with DIC (*N,N'*-diisopropylcarbodiimide) in water, before the addition of **AuNPs-NH₂**, resulting in successful amide bond formation to produce **AuNPs-Benz** (Scheme 13). L-phenylalanine was chosen for bioconjugation to the NPs, successfully yielding **AuNPs-Phe** after only 10 min (Scheme 13).²⁶⁹ This work describes a robust procedure to form large NHC@AuNPs with protic functional groups, which can be further functionalised for applications in many different areas, including medicine. Unfortunately, no stability tests in physiological conditions were performed for these NPs.²⁶⁹

In the same year, Pleixats and co-workers²⁷¹ reported the ability of water-soluble AuNPs, stabilised with PEG-tagged imidazolium salts (Figure 46), to be used as recyclable catalysts for two organic reactions.²⁷¹ The effect of the counterion was explored for stabiliser **19**, using either a bromide (**19A**) or tetrafluoroborate (**19B**) anion, and **19A** and **20** were used to compare the effect of the cation.²⁷¹

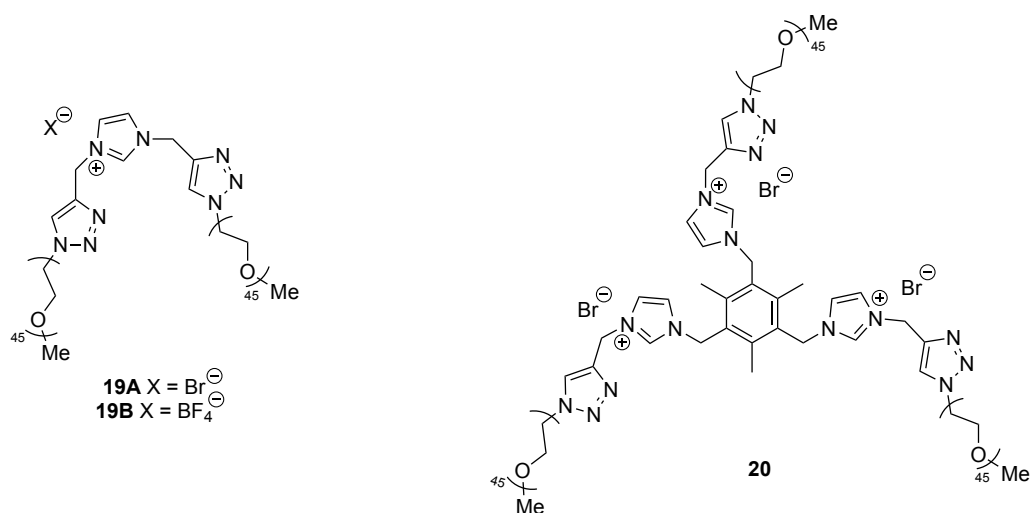


Figure 46 – Structures of the PEG-tagged imidazolium stabilisers (**19A**, **19B** and **20**) used to stabilise the water-soluble AuNPs reported by Pleixats and co-workers.²⁷¹

The AuNPs were prepared by the ‘bottom-up’ approach involving the reduction of tetrachloroauric acid trihydrate using NaBH₄ in the presence of the stabiliser (**19A**, **19B** or **20**, Figure 46) in water at room temperature.²⁷¹ The NPs formed varied slightly in size, with **19A** and **19B** producing NPs with a mean diameter of 5.2 ± 3 nm and 4.5 ± 2 nm, respectively, and **20** yielding NPs of a narrower size distribution of 5.6 ± 1.5 nm. XPS studies revealed that NPs of stabiliser **20** contained two valence states of Au (Au(0) and Au(I)).²⁷¹ The authors suspected that not all of the Au(III) precursor had been fully reduced to Au(0). Therefore, the synthesis was repeated with increased equivalents of NaBH₄; however, this surprisingly resulted in the Au(I) signals being slightly higher in intensity. The XPS studies for NPs of **19A** and **19B** also showed evidence of the two Au valence states; however, Au(0) dominated.²⁷¹ The presence of Au-NHC-Cl species, formed due to deprotonation of the imidazolium hydrogen by a hydride anion from the excess reducing agent, could be responsible for the Au(I) valence states, although this was not proven in this work. Additionally, ¹H NMR of **19B** showed the presence of the imidazolium proton of the stabiliser, whereas for **19A** and **20** this was not seen along with other protons near the centre of the stabiliser, indicating a strong interaction of the stabiliser to the gold surface.²⁷¹

The catalytic ability of the AuNPs was assessed *via* two organic transformations, the first reaction being the A³ coupling between aldehydes, terminal alkynes and amines to yield propargylamines in neat conditions at 100 °C for 24 h.²⁷¹ The second, a less common transformation catalysed by AuNPs, the cycloisomerisation of γ -alkynoic acids to afford enol lactones in toluene/water at room temperature for 50 min to 48 h, depending on the NP used.²⁷¹ The best performing NPs were with stabiliser **20**, showing the highest catalytic performance and the ability to be recycled for both reactions for four and six runs for the A³ coupling and cycloisomerisation, respectively.²⁷¹

3.3. Gold NPs for biomedical applications

AuNPs have received significant attention over the last two decades, especially in the area of nanomedicine.²⁷² One of the first examples of AuNPs in medicine, specifically as radiotracers, was reported in the 1950s by Sherman and Ter-Pogossian, using radioactive colloidal Au¹⁹⁸.²⁷³ Nowadays, the unique properties of AuNPs are accountable for their use in various diagnostic techniques such as optical imaging, as well as in therapeutic techniques including radiotherapy.²⁷² The enhanced permeability and retention (EPR) effect has been reported to increase accumulation of nanomaterials, including AuNPs at a cancer site, making them ideal systems for targeted drug delivery.²⁷⁴ The latter property, together with the biocompatibility and large surface area of AuNPs has led to more *theranostic* applications, with conjugation of the AuNPs to various drug molecules, targeting ligands and imaging probes.^{272,275}

Finally, it is also worth mentioning that AuNPs have emerged as popular choices as bio-sensors due to their optoelectronic properties and their ease of synthesis.²⁷⁶ The characteristic strong absorbance of AuNPs, due to their SPR band, can be applied in colorimetric studies for the interaction of an analyte with the NP causing a colorimetric change.²⁰⁸ The different possible applications of AuNPs in medicine are summarised in Figure 47 and will be discussed in more detail in the following sections.

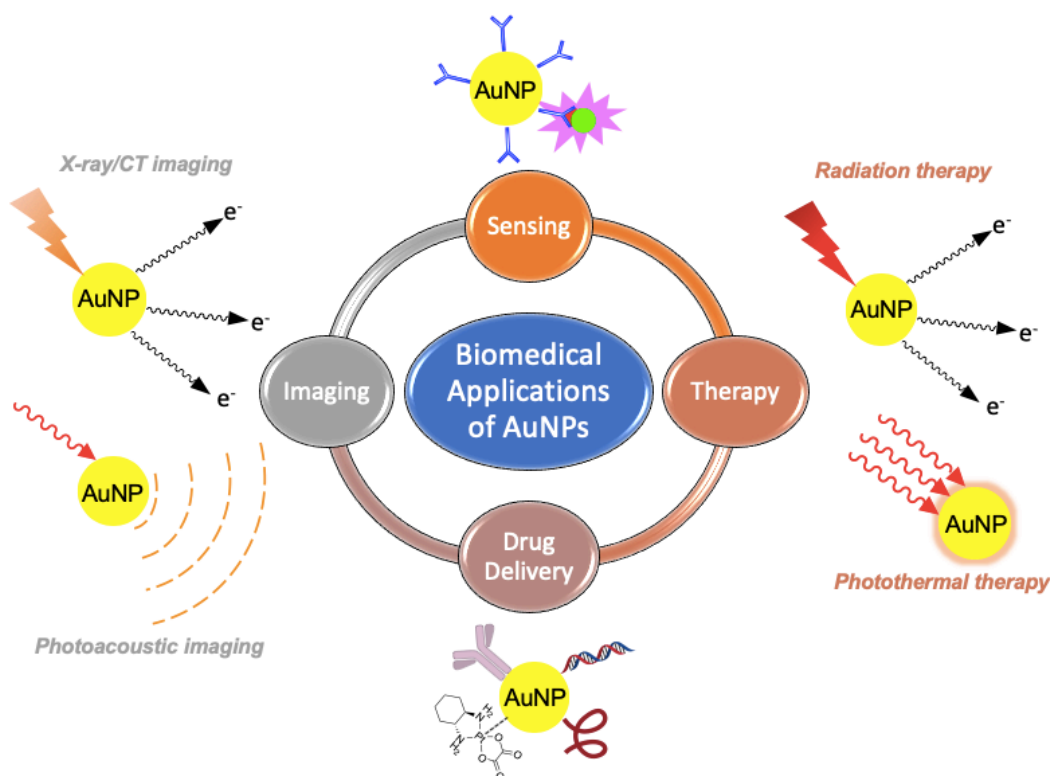


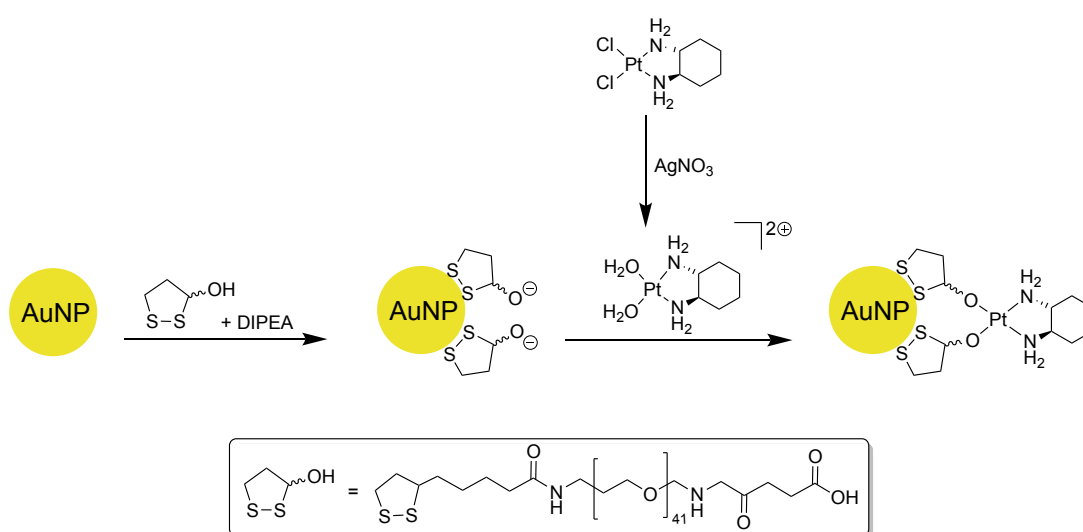
Figure 47 – The wide array of biomedical applications of AuNPs, adapted from ref.²⁷⁴

3.3.1. Drug Delivery

AuNPs have become popular drug delivery systems as they are relatively non-toxic, they possess a large surface-to-volume ratio and their surface chemistry can be altered by changing the charge, hydrophilicity and functionality of the surface ligands.²⁷⁷ Specifically, these drug delivery systems have been widely explored in anticancer therapy due to their preferential accumulation at the tumour site *via* the so-called EPR effect.^{275,278}

AuNPs are not just **drug** delivery systems, they can also be used to deliver other compounds, such as imaging agents that exhibit low solubility and poor pharmacokinetics, or compounds that are intrinsically prone to enzymatic degradation, as well as those that display poor intracellular penetration (e.g., siRNA).²⁷⁵ The ability to tune the size of AuNPs, as well as ease of functionalisation has also led to successful delivery of large biomolecules, such as peptides, proteins, genes or nucleic acids.²⁷⁹

As an example of AuNPs delivering cytotoxic metallodrugs, Brown *et al.*²⁸⁰ reported the conjugation of an activated oxaliplatin complex, [Pt(*R,R*-dach)Cl₂] (dach = diaminocyclohexane) to AuNPs (Scheme 14).²⁸⁰ In order to anchor the metallodrug to the NPs, a PEG linker was first attached to the NPs *via* bonding to the cyclic disulfide group. This linker possessed a terminal carboxylic acid group, which was initially deprotonated with DIPEA (*N,N*-diisopropylethylamine) to bind to Pt(II).²⁸⁰ The compound used in this work is the activated form of the original oxaliplatin structure within cells after hydrolysis to [Pt(*R,R*-dach)(H₂O)₂]. The water ligands are then displaced by the carboxylate groups of the PEG linker. Notably, the Pt-tethered AuNPs were shown to be specifically targeted to the nucleus of lung cancer cells.²⁸⁰



Scheme 14 - Chemical synthesis of AuNPs conjugated to the active component of oxaliplatin via a PEG linker with a cyclic disulfide group, to bind to the AuNPs, and a carboxylic acid group which can bind the [Pt(*R,R*-dach)(H₂O)₂], after deprotonation with DIPEA (*N,N*-diisopropylethylamine).²⁸⁰

In 2004, Rotello and co-workers²⁸¹ reported AuNPs able to bind and inhibit the enzyme β -galactosidase (β -gal), which was chosen due to its overall negative surface charge. They showed that this inhibition could be reversed causing release of the enzyme in the presence of intracellular concentrations of GSH (Figure 48A).²⁸¹ The AuNPs were coated with a mixed monolayer (MM) functionalised with positively charged trimethylammonium groups providing electrostatic interactions to the anionic enzyme, leading to enzyme inhibition.²⁸¹ This interaction caused inhibition of the enzyme meaning it could not catalyse the hydrolysis of the chromogenic substrate, ONPG (*o*-nitrophenyl- β -D-galactopyranoside) upon increase of AuNP concentration.²⁸¹

To demonstrate that electrostatic interactions were responsible for the enzyme inhibition, agarose gel electrophoresis was used to demonstrate the loss in charge of the enzyme upon addition of NPs.²⁸¹ The enzyme alone migrated to the positive pole due to its negative charge, whereas when the AuNPs were added there was a significant decrease in the movement of the enzyme. This was attributed to an increase in size of the enzyme upon AuNP binding and a decrease in the negative surface charge of the enzyme due to the positively charged groups of the AuNP monolayer.²⁸¹ The ability of GSH to reactivate the enzyme after inhibition is due to the presence of its negative charge, which can mitigate against the positive charge of the AuNP monolayer, thus reducing the electrostatic interaction causing release of the enzyme.²⁸¹

Increasing the length of the alkyl chains of the monolayer (MM1 vs. MM2) prevents release of the enzyme by GSH (Figure 48B), which the authors attributed to an insufficient interaction of the GSH with the longer alkyl chain monomer (MM2), meaning it cannot mitigate its charge.²⁸¹ This concept provides promise for reversible inhibition of enzymes *in vivo*, which could be applied to other concepts such as release of drugs or proteins in certain intracellular conditions using the addition and mitigation of electrostatic interactions.²⁸¹ Unfortunately, no *in vitro* or *in vivo* work was included in the scope of this study; however, it provides proof-of-concept to how these reactions could occur for biomedical applications.²⁸¹

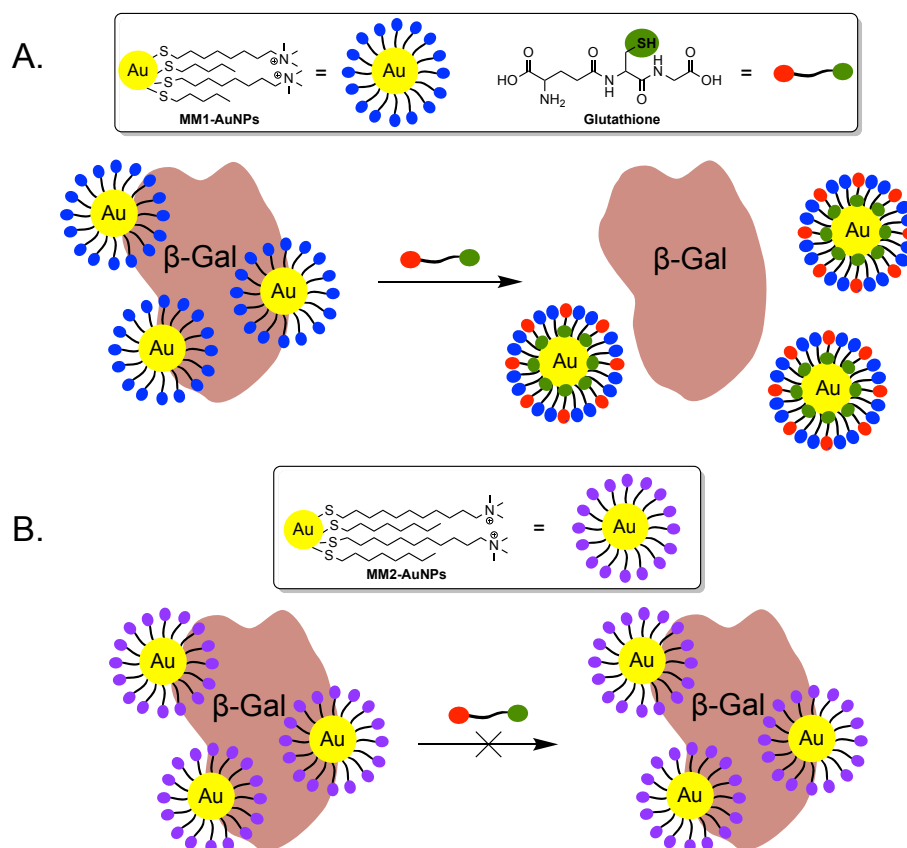


Figure 48 – (A) Inhibition of β -galactosidase enzyme by binding of MM1-AuNPs, enzyme is released and active in the presence of GSH. (B) Inhibition of β -galactosidase enzyme by binding of MM2-AuNPs; however, due to the longer alkyl chain of MM2 the enzyme cannot be released with GSH. Image adapted from ref.²⁸¹

3.3.2. Radiotherapy

As mentioned above, radioactive Au^{198} colloids were utilised in the 1950s as radiotracers;²⁷³ however, non-radiolabelled AuNPs are generally applied in radiotherapy simply to enhance the dose of the radiation. The increased radiotherapy efficiency seen in combination with AuNPs is due to the interaction of the ionising radiation with the electrons in the NP, which can cause excitation of an inner shell electron and subsequent emission of an Auger electron.²⁸² Auger electrons can then damage the DNA itself or produce reactive species such as hydroxyl radicals ($\cdot\text{OH}$) by interaction with water, eventually leading to cell damage.²⁸²

In 1998, Regulla *et al.*²⁸³ reported the ability of gold foil to enhance the dose of radiation *in vitro*, which was later confirmed by Herold *et al.*²⁸⁴, who reported radiation dose enhancement by AuNPs *in vitro*. However, it wasn't until 2004 that the first report on the use of AuNPs for radiation dose enhancement *in vivo* was published by Hainfeld *et al.*²⁸⁵ The AuNPs (1.9 ± 0.1 nm, Nanoprobes Inc.) were injected into syngeneic mouse mammary EMT-6 (experimental mammary tumour-6) tumours and irradiated with X-rays.²⁸⁵ The difference in tumour size between those treated with just radiation and those

treated with radiation and AuNPs was significant. Nine out of ten mice receiving both AuNPs and radiation were tumour-free over 30 days, with the tenth mouse showing a decrease in tumour size.²⁸⁵

3.3.3. Photothermal Therapy (PTT)

Photothermal therapy (PTT) is a therapeutic technique using photon energy, which is converted to heat by NPs to kill cancer cells.²⁸⁶ It is less damaging than typical anticancer chemotherapy due to the localised heating of the cancer cells in the early stage of tumour growth.²⁷² Spherical AuNPs have been used in PTT for treatment of shallow tumours, such as skin cancer.²⁸⁶ This is due to the SPR band of the AuNPs absorbing in the visible region, which is also absorbed by tissues.²⁸⁶ To target tumours within the body for *in vivo* therapy, near-infrared (NIR) light is needed to penetrate tissues.²⁸⁶ AuNPs can absorb NIR light when their size is above 50 nm.²⁷²

Gold nanorods (AuNRs) are the most common NIR PTT agents, with their first application *in vitro* by El-Sayed and co-workers in 2006.²⁸⁷ In this work, the AuNRs were attached to anti-epidermal growth factor receptor (anti-EGFR) monoclonal antibodies to target malignant cells due to their overexpression of EGFR on their cytoplasmic membrane.²⁸⁷ Following treatment with the NRs, cells were then exposed to a NIR laser at 800 nm, before a further laser, with different energies, was used to destroy the cells. Due to increased uptake of the NRs in cancer cells, half of the energy was required to destroy them compared to the non-malignant cells, showing a good selectivity.²⁸⁷

The advantage of using AuNRs for PTT is due to the strong absorption band in the NIR region from the oscillation of electrons along the longitudinal length of the rod (Figure 49).²⁸⁶ This longitudinal wavelength undergoes red shift with increase in aspect ratio (length/width) of the rod. The transverse band is weak and appears in the visible region, it is unaffected by the aspect ratio of the rod (Figure 49).²⁸⁶ The size of AuNRs can vary for different applications, however, the width is usually between 10-20 nm and the length can be up to 300 nm depending on the synthesis conditions.²⁷⁵ Nanorods with a high aspect ratio (larger length compared to width) and small volume are favoured for use as photo-absorbers, whereas NRs with high aspect ratio and large volume are better scattering contrast agents for bioimaging.²⁸⁸

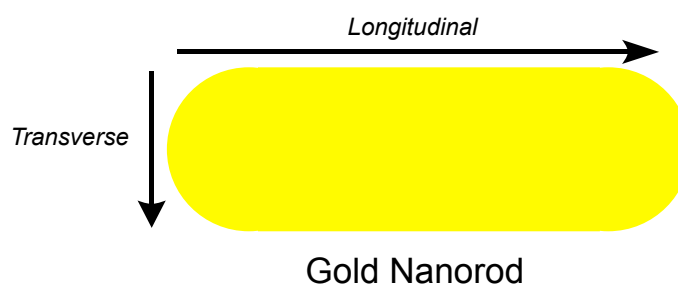


Figure 49 - Diagram of a gold nanorod showing longitudinal and transverse direction.

3.3.4. Photoacoustic (PA) Imaging

Photoacoustic (PA) imaging involves exposure of target organs to short pulses of NIR laser light which is absorbed by the different tissue components present, such as haemoglobin, lipids and water (Figure 50).²⁸⁹ The latter then undergo thermoelastic expansion, emitting ultrasound signals which can be detected by an ultrasound transducer, providing information on tissue composition, such as the presence of tumours (Figure 50).²⁸⁹

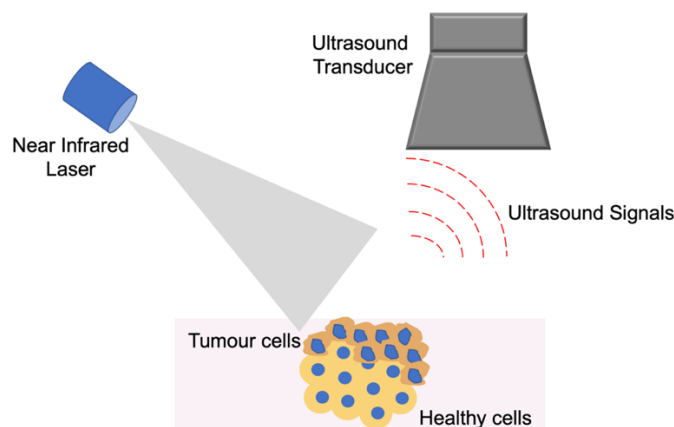


Figure 50 – The principle of photoacoustic imaging. Image adapted from ref.²⁸⁹

AuNPs in particular have been previously utilised as probes for photoacoustic imaging, enhancing the depth of tissue that can be imaged.²⁹⁰ This is due to the SPR band of the AuNPs which leads to far superior optical absorption compared to organic dyes previously used.²⁹¹ Additionally, the EPR effect plays a role in identifying tumours by accumulation of AuNPs at the tumour site, which can be detected by PA imaging.²⁹¹ However, as mentioned above, AuNPs generally have a typical absorbance in the UV-Vis (ultraviolet-visible) region (around 520 nm), which is also similar to the absorbance of blood, reducing the contrast.²⁹¹ Therefore, AuNRs have also been utilised in PAI.²⁹¹ Eghtedari *et al.*²⁹² demonstrated the ability of a highly sensitive laser optoacoustic imaging system to detect AuNRs *in vivo* at concentrations as low as 1.25 pM within tissue.²⁹²

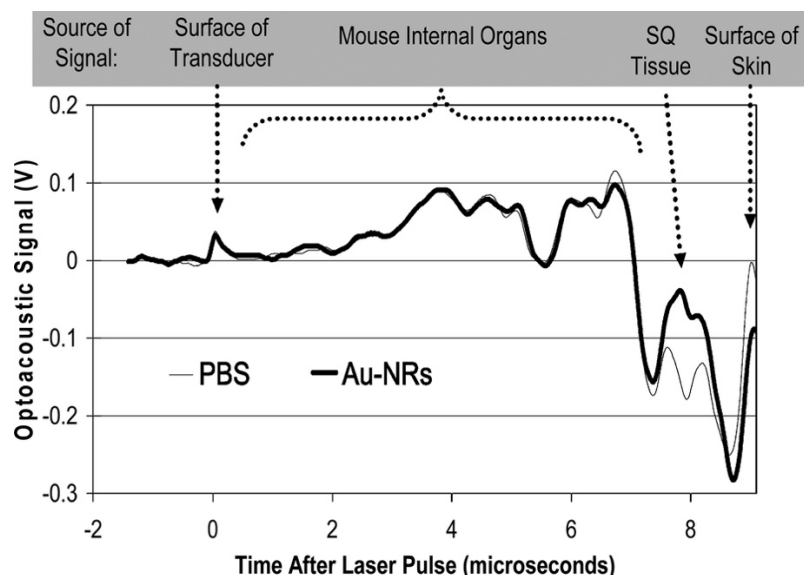


Figure 51 – Detection of AuNRs *in vivo* in nude mice using single optoacoustic transducer. AuNR suspension (25 μL at a concentration of 1.25 μM) or PBS solution (25 μL) was injected into the abdominal area of the mouse subcutaneously (SQ) to enhance optoacoustic signal. Signal was then detected via a transducer on the back of the mouse. Reprinted with permission from ref 292. Copyright (2007) American Chemical Society.²⁹²

The laser pulse was administered at $-2.5 \mu\text{s}$ and arrived at the transducer at time zero, which can be seen as the first peak in the graph (Figure 51).²⁹² The AuNRs were administered subcutaneously (SQ), meaning just under the skin, in the abdominal area of the mouse. There was very little difference between injecting the NRs or PBS (phosphate-buffered saline), until ca. 8 μs where the AuNRs enhanced the amplitude of the optoacoustic signal by increasing the light absorption in the local subcutaneous area (SQ) where the injection was given. The optoacoustic signal increased proportionally with AuNR concentration.²⁹²

To increase the selectivity towards breast cancer cells, the AuNRs could also be functionalised by attaching monoclonal antibodies which bind to Her2/neu receptors (human epidermal growth factor receptor-2).²⁹³ These receptors are commonly overexpressed in breast cancer cells.²⁹³

3.3.5. Computed Tomography (CT)

Computed tomography (CT) was presented in 1972 and has been a common technique for imaging ever since.²⁹⁴ Its discovery enabled production of 3D images instead of 2D radiographs (X-rays), which often had shadowing and overlap of different components, making diagnostic imaging challenging.²⁹⁴ CT exploits the difference in electron density of the different tissues it is targeting by emission of X-ray photons.^{208,272} However, due to similar electron density between tissues, the images can experience poor contrast.²⁷² AuNPs have been used to enhance contrast due to their high electron density.²⁷² The

first example of AuNPs as contrast agents was seen in the work by Hainfeld *et al.*²⁸⁵ that focused on enhanced radiotherapy by AuNPs as described above, but also included a radiograph with increased contrast of the tumour when treated with AuNPs.²⁸⁵ Over the years many more examples of AuNPs as x-ray contrast agents have been published with improved contrast enhancement to allow more in-depth images to be seen.²⁹⁴ An example of this has been published by Reuveni *et al.*²⁹⁵ where they demonstrated the use of targeted AuNPs by conjugation of an anti-epidermal growth factor *in vivo* to identify cancer molecular markers rather than the actual tumour itself with CT imaging, which could lead to earlier diagnosis.²⁹⁵ Remarkably, this allowed identification of a small tumour that could not be seen using conventional anatomical CT, as seen in Figure 52.²⁹⁵

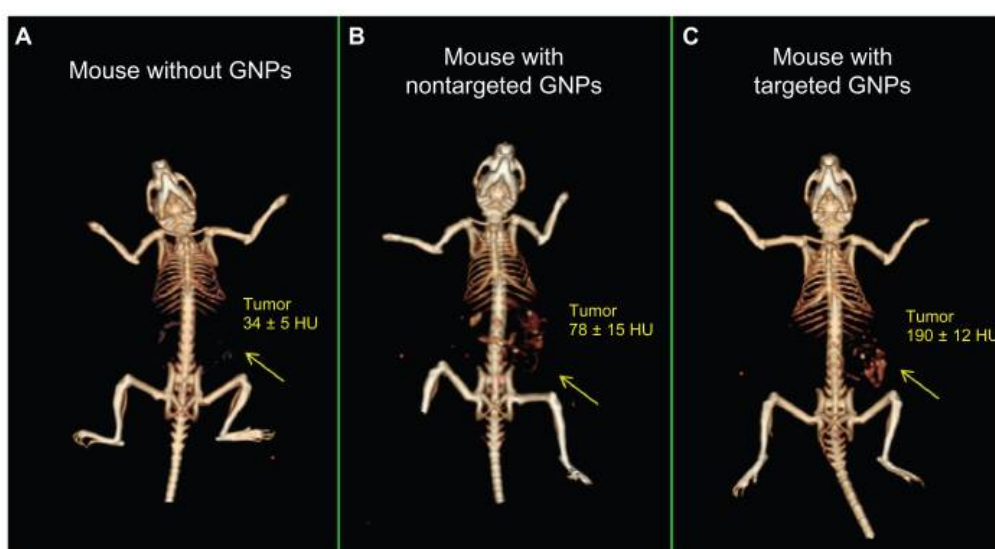


Figure 52 – *In vivo* X-ray computer tomography (CT) images of (A) mouse without AuNPs (GNPs), (B) mouse treated with nonspecific immunoglobulin G AuNPs, 6 h post-injection, and (C) mouse treated with anti-epidermal growth factor receptor (EGFR)-coated AuNPs that target squamous cell carcinoma head and neck tumours, 6 h post-injection. Targeted AuNPs (C) show contrast enhancement of the tumour (yellow arrow), which is absent in the mouse with no AuNPs (A, yellow arrow). The CT numbers represent the average Hounsfield units (HU) of each tumour area, with (C) showing the highest CT number for the tumour due to the high density of AuNPs attached to the tumour. All scans performed using a clinical CT at 80 kVp, 500 mAs, collimation 0.625 x 64 mm and 0.521 pitch size (64 detector CT scanner, LightSpeed VCT; GE Healthcare, Little Chalfont, UK). Figure reproduced with permission from ref 295. Copyright (2011), Targeted gold nanoparticles enable molecular CT imaging of cancer: an *in vivo* study, Reuveni T *et al*, *International Journal of NanoMedicine*, Dove Medical Press, <http://creativecommons.org/licenses/by-nc/3.0/>.²⁹⁵

3.4. Water-Soluble Gold NPs stabilised by NHCs for biomedical applications

In 2017, Crudden and co-workers²⁹⁶ presented water-soluble NHC@AuNPs formed by the 'bottom-up' approach.²⁹⁶ The [Au(NHC)Cl] (21, Figure 53A) complex and

corresponding bis-complex [(NHC)₂Au]OTf (**22**, Figure 53A) were reduced by NaBH₄ in an aqueous solution of NaOH (sodium hydroxide). NaOH was necessary to deprotonate the carboxylate group on the NHC ligand, resulting in a negatively charged surface, thus water-soluble AuNPs.²⁹⁶

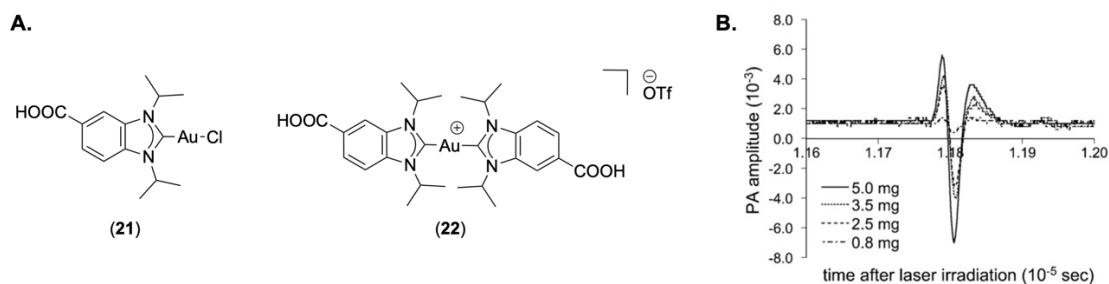


Figure 53 – (A) Structures of Au(I) NHC complexes (**21** and **22**) used for the formation of water-soluble AuNPs. (B) Acoustic wave signal recorded after irradiation of an aqueous solution of **22** at 532 nm using a pulsed laser beam. Image (B) adapted with permission from ref. 296.

Copyright (2017) John Wiley and Sons, *Angewandte Chemie International Edition*.²⁹⁶

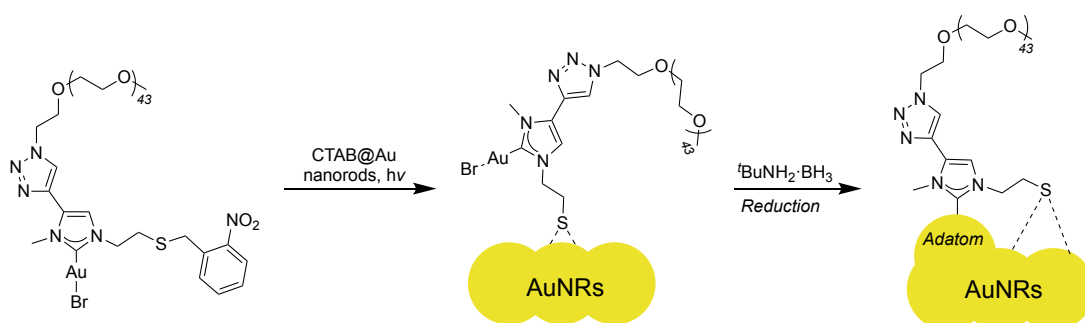
The charged surface was exploited using polyacrylamide gel electrophoresis (PAGE) to determine the purity and monodispersity of the AuNPs due to size separation.²⁹⁶ NPs from **21** were formed almost immediately on addition of NaBH₄, maintaining high monodispersity even after 5 h. Conversely, AuNPs formed from the reduction of **22** required more time (at least 1 h).²⁹⁶ PAGE showed that after 5 h reaction time, AuNPs of **21** and **22** were similar in size (ca. 2.4 nm). Therefore, due to the more facile synthesis of **22** compared to **21** and the similar size of the NPs formed, the authors decided to only investigate the bis-NHC NPs (**22**). Increasing reaction time correlated to an increase in particle size.²⁹⁶

The stability of the NPs was assessed in pH 8 and pH 10 solutions for 2 months, which resulted in only minor changes in the UV-Vis spectra for both pH solutions, indicating that the NPs were stable.²⁹⁶ A sodium chloride (NaCl) solution (150 mM) was next used to mimic more biological media, which resulted in a slight sharpening of the SPR band of the AuNPs after 7 days; however, this was very minimal.²⁹⁶ The AuNPs were then exposed to an excess of GSH (2 mM) in a slightly basic solution. Over 24 h there was a drop in absorbance of the SPR band; however, it was still centred around 515 nm, showing some stability in the presence of excess GSH.²⁹⁶

Lastly, the NPs were tested as possible probes for PA imaging, the first report of NHC@AuNPs for biological applications.²⁹⁶ Preliminary experiments involved the preparation and irradiation of an aqueous solution of AuNPs with a pulsed laser beam (532 nm). A photoacoustic signal was recorded for the AuNPs, despite their weak SPR bands, with a linear increase in signal observed as AuNP concentration increased

(Figure 53B). Subsequent *in vitro* work is needed to evaluate the feasibility of this application.²⁹⁶

In 2019, MacLeod *et al.*²⁹⁷ reported the ability of bidentate NHC-thiolate ligands to form AuNRs for application in PTT.²⁹⁷ As described above, AuNRs exhibit enriched plasmonic properties compared to spherical NPs due to elongation, meaning that they can absorb NIR light, which can be exploited for use in bioimaging.²⁹⁸ Nanorod formation usually involves an intermediate stabilising ligand, such as cetyl trimethylammonium bromide (CTAB) in water, before ligand exchange with a more robust and stable thiol ligand.²⁹⁷ In this work, the authors exploited this concept by starting from the CTAB-stabilised gold nanorods and adding a bidentate thiolate masked Au(I) NHC complex (Scheme 15).²⁹⁷



Scheme 15 - Formation of NHC stabilised Au nanorods, (i) firstly the bidentate thiolate NHC ligand is photogenerated *in situ* to exchange with CTAB ligands to stabilise the Au nanorods, (ii) then the Au(I) complex is reduced with ^tBuNH₂·BH₃ to form the NHC stabilised Au nanorods.²⁹⁷

The Au(I) complex with the bidentate thiolate NHC ligand was firstly activated by *in situ* photogeneration (365 nm) of the thiolate by removal of the *ortho*-nitrobenzyl group, which could then undergo ligand exchange with the CTAB@AuNRs (Scheme 15).²⁹⁷ A *tert*-butylamine borane complex was then used as a mild reducing agent, resulting in addition of the Au atom on the NHC ligand to the surface of the nanorod as an adatom, forming NHC-stabilised nanorods (Scheme 15).²⁹⁷ The synthesis of these nanorods can be considered as a mixture of the 'top-down' and 'bottom-up' approaches. The first step follows the 'top-down' approach as ligand exchange occurs between the CTAB ligands and the thiol, then the second step, whereby the Au(I)-NHC complex is reduced, can be considered as the 'bottom-up' approach.²⁹⁷ The nanorods were stable over a range of different pH solutions, temperatures and salt concentrations, also showing outstanding stability when treated with 4 mM of GSH in water over 6 days.²⁹⁷

Due to these promising results, the use of these nanorods in PTT was assessed, whereby the nanorods were irradiated with a laser to produce local heating, resulting in cell death.²⁹⁷ Preliminary tests in MCF7 cells (human breast cancer cell line) showed that when irradiation was given in absence of the AuNR, no effect on cell viability was

observed (0 μg , + $h\nu$, Figure 54). This was also true when 38 or 75 $\mu\text{g ml}^{-1}$ of AuNR was given with no irradiation (3.8 μg , - $h\nu$ and 7.5 μg , - $h\nu$, Figure 54).²⁹⁷ However, there was a significant decrease in cell viability when the cells were exposed to irradiation and 38 or 75 $\mu\text{g ml}^{-1}$ of AuNR (3.8 μg , + $h\nu$ and 7.5 μg , + $h\nu$, Figure 54), showing that both the irradiation and the AuNRs are essential for cell death.²⁹⁷ This work highlights the significance of the nanorod structure and its applicability in therapy, although the study has been performed only *in vitro*.²⁹⁷

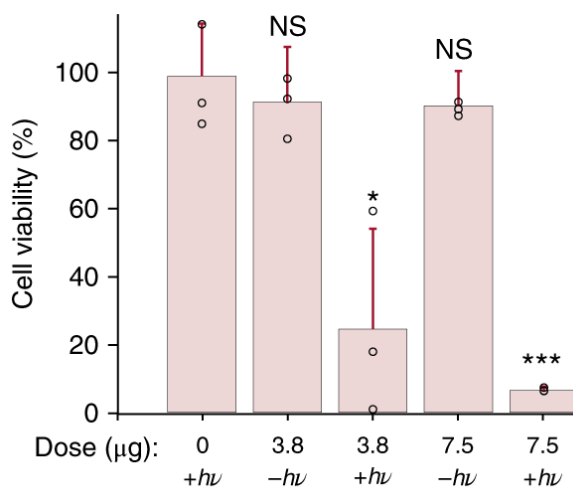


Figure 54 – Graph to show the MCF-7 cell viability studies *in vitro* determined by CellTiter-Glo. Statistical significance was assessed by a two-tailed *t*-test with 3 independent samples. NS, not significant, * $P < 0.05$, *** $P < 0.001$. Image reproduced with permission from ref. 297. Copyright (2018) Springer Nature, Nature Chemistry.²⁹⁷

4. Aims

The overall aim of this work is to explore different gold-based catalysts to mediate bioorthogonal reactions in living cells for applications in therapy and/or imaging. Therefore, in the first part of the project (*Chapter 5* to *Chapter 7*), we envisaged that gold(III) compounds could be used for metal-templated reactions in living cells, leading either to *i*) the chemoselective modification of a biomolecule (protein) affecting its function, or *ii*) the *in situ* synthesis of a therapeutic drug. The first approach has exploited organometallic gold(III) compounds, featuring cyclometalated C^N ligands, that are able to template C-S cross-coupling reactions in physiological conditions *via* reductive elimination. This work was inspired by previous work in our group involving the ability of a [Au(C^N)Cl₂] complex to interact with model zinc finger domains by displacement of the zinc cation with the gold(III) whilst retaining its C^N scaffold.²⁹⁹ Interestingly, initial mechanistic insights into the title reaction has enabled broadening of the scope to other types of C-X bond forming reactions, namely C-P (*Chapter 6*) and C-C (*Chapter 7*) cross-couplings, in mild conditions.

The second part of this thesis has instead focused on the synthesis of water-soluble gold nanoparticles stabilised by NHC ligands (NHC@AuNPs) as a heterogeneous approach to both biomedicine and catalysis (*Chapter 8*). The NHC@AuNPs are evaluated by different techniques, including ¹H NMR (nuclear magnetic resonance) spectroscopy, XPS (X-ray photoelectron spectroscopy), FTIR-ATR (Fourier-transform infrared attenuated total reflectance) spectroscopy, TEM (transmission electron microscopy) and TGA (thermogravimetric analysis). Moreover, their stability in physiologically relevant media is studied to ensure their suitability for future biomedical applications, e.g. photothermal therapy (PTT) and photoacoustic imaging (PAI). The catalytic performance of the NHC@AuNPs is also challenged using the reduction of 4-nitrophenol to 4-aminophenol as a model reaction. The maintenance of the AuNPs catalytic behaviour in aqueous environment can hold promise for future biocompatible catalysis.

5. C-S Cross-Coupling Reactions mediated by Au(III) Cyclometalated Complexes.

This chapter is based on the following papers:

Cyclometalated Au^{III} Complexes for Cysteine Arylation in Zinc Finger Protein Domains: towards Controlled Reductive Elimination

Margot N. Wenzel⁺, Riccardo Bonsignore⁺, **Sophie R. Thomas**, Didier Bourissou, Giampaolo Barone and Angela Casini

[⁺] *Authors contributed equally to this work.*

DOI: 10.1002/chem.201901535

&

Exploring the Chemoselectivity towards Cysteine Arylation by Cyclometallated Au^{III} Compounds: New Mechanistic Insights

Sophie R. Thomas⁺, Riccardo Bonsignore⁺, Jorge Sánchez Escudero, Samuel M. Meier-Menches, Christopher M. Brown, Michael O. Wolf, Giampaolo Barone, Louis Y. P. Luk and Angela Casini

[⁺] *Authors contributed equally to this work.*

DOI: 10.1002/cbic.202000262

5.1. Introduction

The selective modification of biomolecules, such as proteins, has become an important tool for researchers to investigate biosynthetic pathways and gain an understanding of the natural function of proteins.³⁰⁰ The modification can be performed by functionalisation of the protein with a tag, such as a fluorophore for *in vivo* live cell imaging, or can involve a reaction to disrupt the protein function, such as blocking of the active site for therapeutic applications.³⁰⁰ These reactions are commonly synthetic chemistry reactions that would otherwise not occur naturally, and so are defined as 'bioorthogonal reactions'.¹⁴⁸

However, these reactions are not facile: they need to be selective towards the biomolecule (protein) of interest, whilst avoiding interactions with other intracellular substrates.³⁰¹ The use of transition metal complexes for bioorthogonal protein labelling reactions was first demonstrated using copper(I),^{153,154} however due to issues of toxicity, other transition metal catalysts have been since explored including Ru, Ir, Fe and Pd.³⁰¹

Palladium complexes are well-known for their ability to catalyse cross-coupling reactions, particularly C-C, therefore it comes to no surprise that there are many examples in the literature of palladium-catalysed reactions to selectively modify proteins *in vitro* and *in vivo*.³⁰² An example of which was reported by Buchwald and co-workers for the arylation of a cysteine (cys) residue by a palladium aryl complex.¹⁹⁴ Cysteine is commonly targeted for selective modification due to its strong nucleophilic behaviour and relatively low natural abundance.³⁰³ *N*-methylmaleimide cysteine ligation has been used as a metal-free alternative route in the past, however the maleimide adducts suffer with instability in biologically relevant conditions, therefore transition metal catalysts were investigated.¹⁹³ Nevertheless, issues also arise when using palladium complexes as they often suffer with unwanted interactions with endogenous biomolecules in living cells,¹⁹³ meaning other alternatives are still needed.

This has led to the emergence of gold complexes to mediate reactions in living cells due to their high reactivity and chemoselectivity, ability to tolerate aqueous conditions, as well as their capability to perform these reactions under mild conditions.^{174,175} Wong and co-workers¹⁹⁵ were pioneers in the area of C-S cross-coupling *via* reduction elimination, reporting the ability of a Au(III) cyclometalated C^{CH₂}N (C^{CH₂}N = 2-benzylpyridine) complex, featuring a *N,N'*-bis(methanesulfonyl)-ethylene (msen) ancillary ligand (Figure 55), to selectively arylate cysteine residues. Preliminary reactions involved the incubation of different peptidic domains with equimolar amounts of the [Au(C^{CH₂}N)(msen)] complex at 37 °C for 24 h in phosphate-buffered saline (PBS) : dimethyl sulfoxide (DMSO) (9:1) solution.¹⁹⁵ The adducts were then identified by liquid chromatography-mass spectrometry (LC-MS) and showed exclusive cysteine

modification.¹⁹⁵ The authors also demonstrated the ability of a Au(III) C[^]N dansyl (dansyl = 5-(dimethylamino)naphthalene-1-sulfonyl) functionalised cyclometalated complex to mediate the C-S cross-coupling reaction of a single cysteine residue exposed in bovine and human serum albumin (BSA and HSA).¹⁹⁵

Further work in this area was reported by Messina *et al.*¹⁹⁶ who demonstrated the ability of an oxidative addition complex [(Me-DalPhos)Au(tolyl)Cl][SbF₆] (Me-DalPhos = adamantyl₂P(*o*-C₆H₄)NMe₂, Figure 55) to mediate cysteine arylation of GSH (glutathione) *via* reductive elimination. The complex was also further derivatised by replacing the tolyl group with biorelevant moieties, including a drug molecule.¹⁹⁶

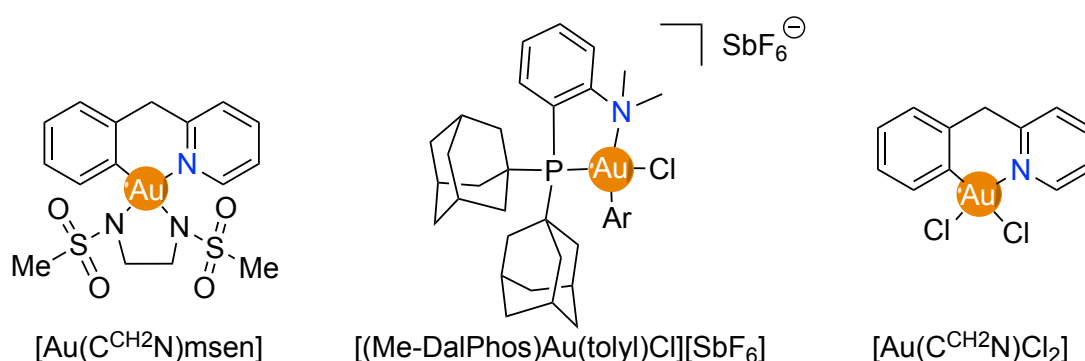


Figure 55 – Representative Au(III) organometallic complexes able to mediate cysteine arylation *via* reductive elimination.

Targeting of cysteine residues can be particularly useful for developing therapeutic protein binders where the cysteine residues play a role in the activity and function of the protein, such as zinc finger proteins (ZFP). ZFPs can be classified into different families depending on the structural motif of its domain, which plays important roles in the protein function.³⁰⁴ All domains possess a central Zn²⁺ ion that maintains its tetrahedral structure when coordinated to a combination of cysteine and histidine residues, or just cysteine residues. The three classical ZF domains are: Cys₂His₂ (CCHH), Cys₃His (CCHC) and Cys₄ (CCCC).³⁰⁴

In 2018, Farrell and co-workers¹⁹⁷ investigated the interaction of the [Au(C^{CH2}N)Cl₂] complex (Figure 55) with the full length ZF (Cys₂HisCys) of HIV nucleocapsid protein NCp7. In this work, in addition to classical ZF-Au(C^{CH2}N) adducts, cysteine arylation was observed after 48 h incubation by mass spectrometry.¹⁹⁷ In the same year, our group studied the interaction of Au(III) complexes (organometallic and coordination) with the zinc finger domain PARP-1 (poly(ADP-ribose)polymerase-1) by a hyphenated liquid chromatography mass spectrometry (LC-MS) approach, which was supported by quantum mechanics/molecular mechanics (QM/MM) calculations.²⁹⁹ PARP-1 contains the CCHC domain (Cys₃His) and is involved in DNA repair as well as

in cisplatin resistance mechanisms, making it a popular pharmacological target.³⁰⁴ Overall, the $[\text{Au}(\text{C}^{\text{CH}_2\text{N}})\text{Cl}_2]$ complex showed the greatest selectivity and reactivity towards the ZF domain Cys₂HisCys in the presence of another Cys₂His₂ model peptide, forming mostly adducts of the type apo-ZF- $[\text{Au}(\text{C}^{\text{CH}_2\text{N}})]$, with no reductive elimination observed.²⁹⁹ Conversely, the Au(III) coordination complex Auphen ($[\text{Au}(\text{phen})\text{Cl}_2]\text{Cl}$ (phen = 1,10-phenanthroline), with a chelating N^N ligand, did not exhibit such selectivity towards the different model peptides and formed adducts of the type apo-ZF- $[\text{Au}(\text{I})]$ with both peptides due to loss of the N^N ligand and displacement of the Zn ion.²⁹⁹

Intrigued by the reactivity of the cyclometalated Au(III) C^N complexes with the ZF domains, we decided to investigate a series of Au(III) C^N complexes with a model peptide of the Cys₂His₂ zinc finger domain to investigate whether derivatives of the C^N scaffold would induce the cysteine arylation reaction.

5.2. Results and Discussion

Circular dichroism experiments were performed by Dr. Riccardo Bonsignore. Computational analysis was completed by Prof. Giampaolo Barone. Synthesis of AC, C and L peptides was completed by Jorge Sánchez Escudero. Online tandem MS analysis was completed by Dr. Samuel M. Meier-Menches. 2-(phenylthiol)pyridine was synthesised and characterised by Dr. Christopher Brown. Dr. Thomas Williams helped with the MS studies.

The Au(III) cyclometalated complexes chosen for this study, alongside the $[\text{Au}(\text{C}^{\text{CH}_2\text{N}})\text{Cl}_2]$ complex, were: $[\text{Au}(\text{C}^{\text{CO}}\text{N})\text{Cl}_2]$ (C^{CO}N = 2-benzoylpyridine), $[\text{Au}(\text{C}^{\text{NH}}\text{N})\text{Cl}_2]$ (C^{NH}N = N-phenylpyridin-2-amine) and $[\text{Au}(\text{C}^{\wedge}\text{N})\text{Cl}_2]$ (C[^]N = 2-phenylpyridine) (Figure 56). The model Cys₂His₂ zinc finger peptide was constituted by incubation of the peptide sequence with DTT (dithiothreitol) and zinc acetate in (NH₄)₂CO₃ buffer (25 mM, pH 7.4). Each of the compounds were then incubated separately with the peptide for 10 min and 24 h in a ratio of 3:1 (complex : ZF) in (NH₄)₂CO₃ buffer, before analysing with high-resolution liquid chromatography electrospray ionization mass spectrometry (HR-LC-ESI-MS), following a procedure that was previously reported by our group.²⁹⁹

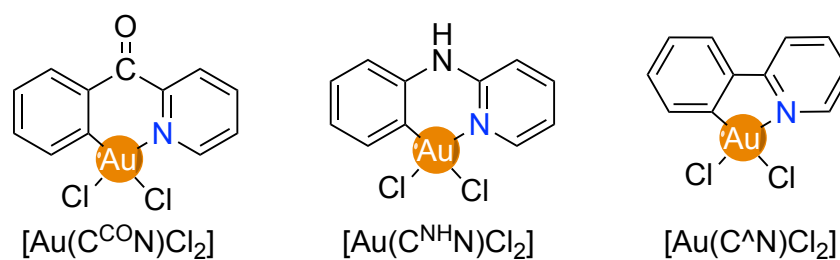


Figure 56 – Series of cyclometalated Au(III) C^AN complexes investigated in this work to mediate cysteine arylation.³⁰⁵

The HR-LC-ESI-MS results showed that after 10 min all four compounds had formed the classical coordination adduct with the ZF domain (apo-ZF-[AuC^AN]), where the Zn²⁺ ion has been displaced by the Au complex due to the aurophilic nature of the thiol functional group in a cysteine residue. The Au complex loses its two labile chloride ligands whilst retaining the C^AN scaffold due to the strong organometallic bond and chelating effect. It should be noted that multiple binding sites must be present in the model peptide, not just cysteine residues, as after 10 min, adducts of the type [Apo-ZF+2AuC^AN]⁷⁺ were observed for the three six-membered Au(III) cyclometalated complexes, with [Au(C^{CH₂}N)Cl₂] and [Au(C^{NH}N)Cl₂] also forming the [Apo-ZF+3AuC^AN]⁷⁺ adduct.

The [Au(C^{CO}N)Cl₂] complex was found to be the most reactive, as even after only 10 min incubation, the C-S cross-coupling product was observed by HR-LC-ESI-MS in combination with the coordination adduct [Apo-ZF+(AuC^{CO}N)+(C^{CO}N)]^{7+/6+} (Figure 57a), which was not seen for the other complexes.

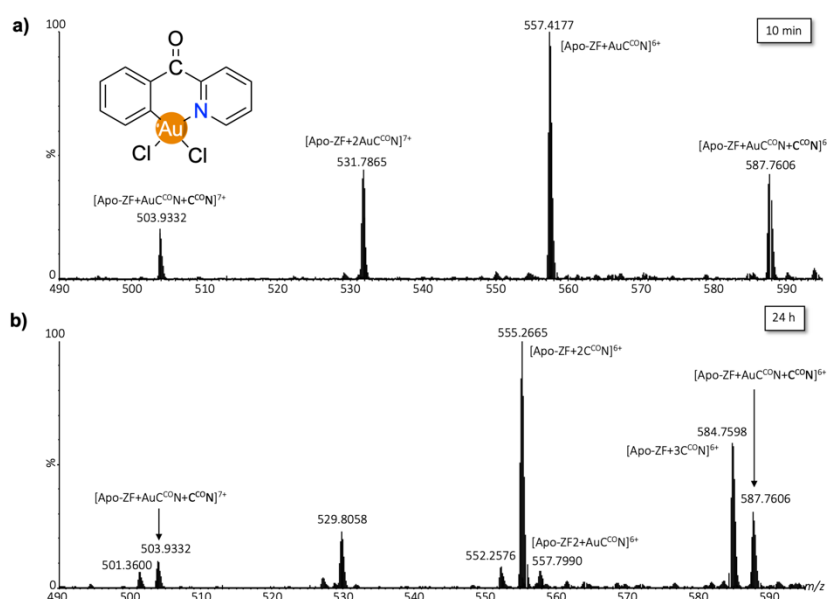


Figure 57 - HR-LC-ESI-MS spectra for the incubation of $[\text{Au}(\text{C}^{\text{CO}})\text{Cl}_2]$ with the model ZF domain in a 3:1 ratio after **a)** 10 min and **b)** 24 h incubation at 37 °C in $(\text{NH}_4)_2\text{CO}_3$ buffer (25 mM, pH 7.4). Figure modified from ref 305. Copyright 2019, John Wiley and Sons
<https://creativecommons.org/licenses/by/4.0/>.³⁰⁵

After 24 h, the $[\text{Au}(\text{C}^{\text{CO}})\text{Cl}_2]$ complex (Figure 57b) showed multiple adducts of the C-S arylated product, including a peak for the $[\text{Apo-ZF}+3\text{C}^{\text{CO}}]^{6+}$ adduct, providing evidence that other residues could not only be potential binding sites for gold, but also arylation sites if both cysteines have been arylated. This is further corroborated by previous tandem MS studies, which showed that the fragmentation pattern of the $[\text{Apo-ZF}+\text{Au}(\text{C}^{\text{CH}_2\text{N}})]$ adduct involved coordination to Cys4, Cys7 and His24.²⁹⁹

The two other six membered cyclometalated complexes showed similar reactivity after 24 h (Figure 58a and b), including a mixture of classical coordination and C-S product adducts, highlighting their reduced reactivity compared to the $[\text{Au}(\text{C}^{\text{CO}})\text{Cl}_2]$ complex. The $[\text{Au}(\text{C}^{\text{CH}_2\text{N}})\text{Cl}_2]$ complex showed slightly greater reactivity than the NH analogue due to less classical coordination adducts present. Remarkably the five membered $[\text{Au}(\text{C}^{\wedge}\text{N})\text{Cl}_2]$ complex showed only the classical coordination adducts, even after 24 h (Figure 58c).

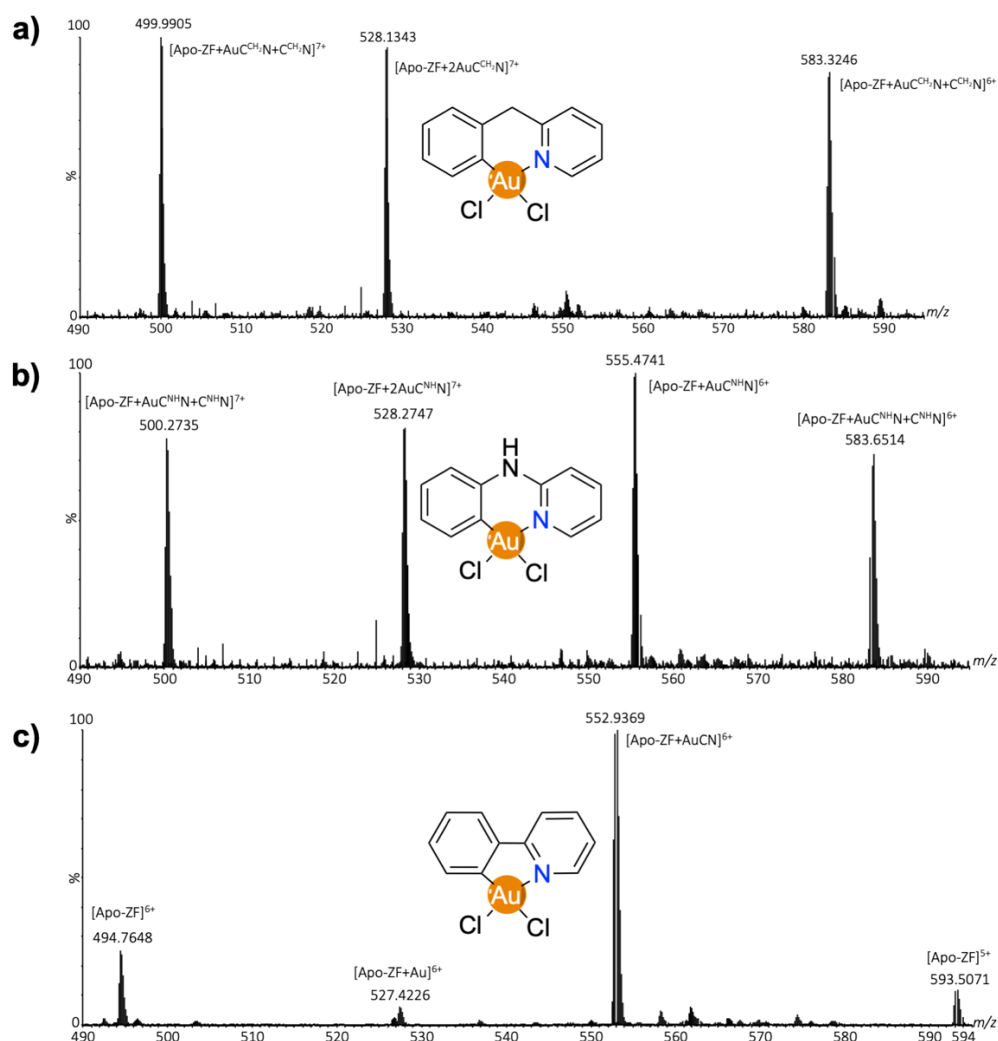


Figure 58 - HR-LC-ESI-MS spectra for the incubation of the complex **a**) $[\text{Au}(\text{C}^{\text{CH}_2\text{N}})\text{Cl}_2]$, **b**) $[\text{Au}(\text{C}^{\text{NH}})\text{Cl}_2]$ and **c**) $[\text{Au}(\text{C}^{\text{N}})\text{Cl}_2]$ with the model ZF domain in a 3:1 ratio after 24 h incubation at 37 °C in $(\text{NH}_4)_2\text{CO}_3$ buffer (25 mM, pH 7.4). Figure modified from ref 305. Copyright 2019, John Wiley and Sons <https://creativecommons.org/licenses/by/4.0/>.³⁰⁵

The reactions were repeated under the same conditions using a free cysteine molecule. Interestingly, the compounds could not mediate cysteine arylation in this case, which suggests the peptide structure is required to template the reaction, potentially due to the multiple binding sites.

It should also be noted that circular dichroism (CD) spectroscopy was performed to confirm the presence of the folded holo-zinc finger³⁰⁶ formed with DTT and zinc acetate, as well as the loss of this secondary structure upon addition of the $[\text{Au}(\text{C}^{\text{CO}}\text{N})\text{Cl}_2]$ complex in buffered solution over 1 h (Figure 59). Upon addition of the complex, the loss of ellipticity was immediate (grey line vs. red line, Figure 59), indicating loss of the Zn^{2+} ion and interaction of the peptide with the complex. However, the type of interaction

cannot be confirmed by CD spectra, therefore the interaction could be total arylation, coordination, or a mixture of the two.

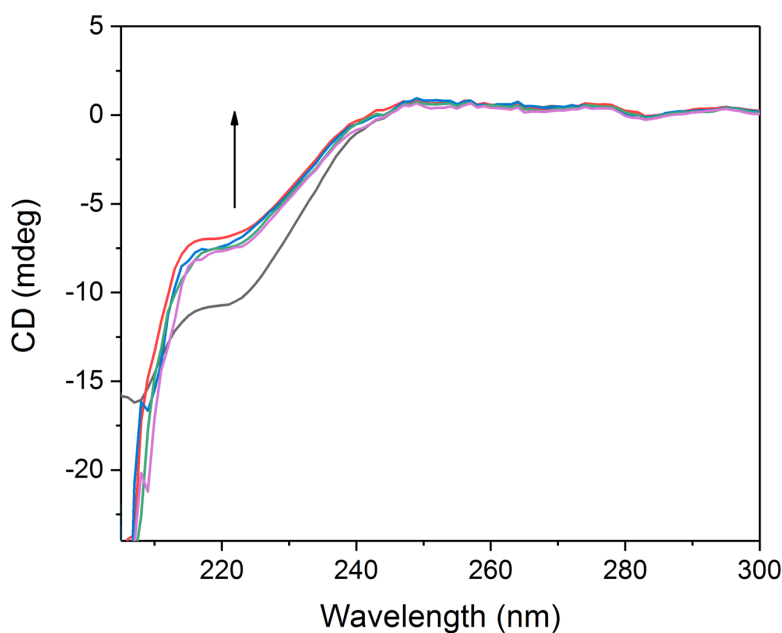
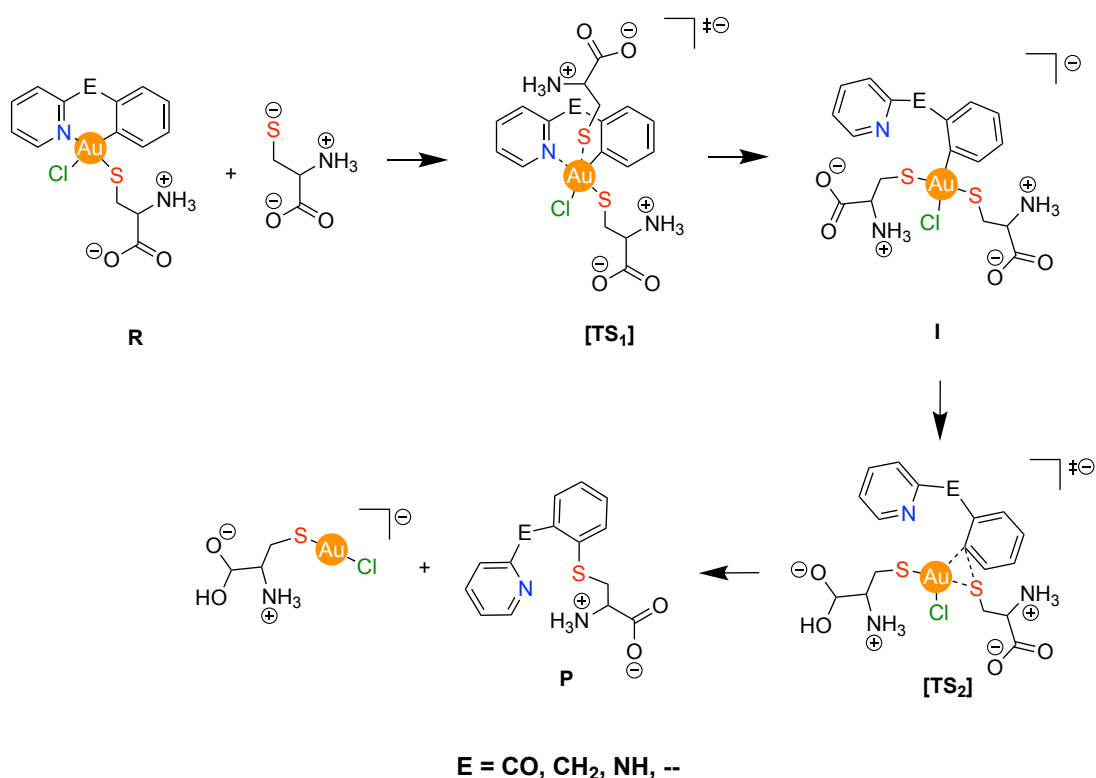


Figure 59 - CD spectra of the Zn-ZF domain ($25 \mu\text{M}$ in $\text{NH}_4\text{CH}_3\text{COO}^-$, 5 mM , $\text{pH} = 7.4$) without (grey line) and in presence of 3 equiv. of $[\text{Au}(\text{C}^{\text{O}}\text{N})\text{Cl}_2]$ after 0 min (red line), 10 min (blue line), 30 min (green line) and 60 min (magenta line). Figure from ref 305. Copyright 2019, John Wiley and Sons <https://creativecommons.org/licenses/by/4.0/>.³⁰⁵

In order to obtain a greater understanding of our experimental results, DFT calculations for all four complexes with two cysteinate groups were performed by Prof. Giampaolo Barone, which allowed us to hypothesise a potential reaction mechanism (Scheme 16).



Scheme 16 – Hypothesised mechanism for the C-S cross-coupling reaction mediated by Au(III) cyclometalated complexes resulting in cysteine arylation.³⁰⁵

The reactant (**R**) is proposed as the first species to be formed, with a cysteinatate bound *trans* to the pyridyl nitrogen. This is not only necessary due to the preference of reductive elimination to occur between two groups that are *cis* to each other, but also the stronger *trans* influence of the C compared to N, meaning that **R** is the thermodynamically favoured species.^{175,307} This could also be observed when comparing the standard Gibbs formation free energy (ΔG°) values of both diastereomers for each complex, with the *E* conformation of the cysteinatate (*trans* to N) being lower in energy, therefore more thermodynamically favoured. The structure and energies of the $[\text{Au}(\text{C}^{\text{CO}}\text{N})(\text{Cys})\text{Cl}]$ diastereomers are shown in Figure 60, however all complexes follow this same trend.

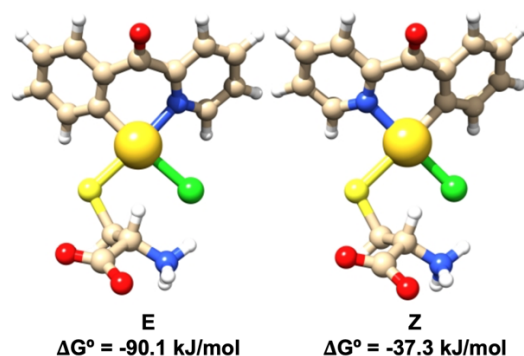


Figure 60 – Structures and ΔG° of the E and Z $[\text{Au}(\text{C}^{\text{CO}}\text{N})(\text{Cys})\text{Cl}]$ adducts obtained by DFT calculations. Figure modified from ref 305. Copyright 2019, John Wiley and Sons

<https://creativecommons.org/licenses/by/4.0/>.³⁰⁵

In order for the reaction to progress from the **R** species, the aryl group must rotate from its coplanar position with the Au atom, to allow coupling with the adjacent S atom. Therefore, to initiate the aryl group rotation, the pyridyl N must be decoordinated from the Au, which can be promoted by the apical approach of a second cysteinate residue. This results in the formation of the bis-cysteinate intermediate species (**I**) *via* the first transition state (**TS1**). A second transition state (**TS2**) then proceeds *via* a three coordinate species to form the C-S reductive elimination product (**P**) and the Au(I) side product $[\text{CysAuCl}]$.

The four complexes each showed differences in relative energies across the reaction pathway, as can be seen graphically in Figure 61, including the activation energy barriers to overcome the two transition states. The values for the relative energies and activation energy barriers for all four compounds can be found in Table 1. Beginning with the three six-membered Au(III) cyclometalated complexes, all reaction pathways appear quite similar: the steps from **R** to **I** and **I** to **P** are exergonic in nature, meaning a more thermodynamically stable product is formed for both steps (**I** and **P**) and the 1st activation energy barrier is lower than the 2nd. Nevertheless, even though a similar trend is observed, the differences in energy to overcome the two activation energy barriers could be responsible for the disparities in reactivity observed. Of note, the energy to overcome the 1st activation energy barrier was related to the trend in reactivity; the $[\text{Au}(\text{C}^{\text{CO}}\text{N})\text{Cl}_2]$ complex was most reactive and required lower energy to overcome the 1st activation energy, whereas the opposite was true for the $[\text{Au}(\text{C}^{\text{NH}}\text{N})\text{Cl}_2]$ complex. This same trend was also observed for the 2nd activation energy barrier, with an increase in energy in the order $[\text{Au}(\text{C}^{\text{CO}}\text{N})\text{Cl}_2] < [\text{Au}(\text{C}^{\text{CH}_2}\text{N})\text{Cl}_2] < [\text{Au}(\text{C}^{\text{NH}}\text{N})\text{Cl}_2]$.

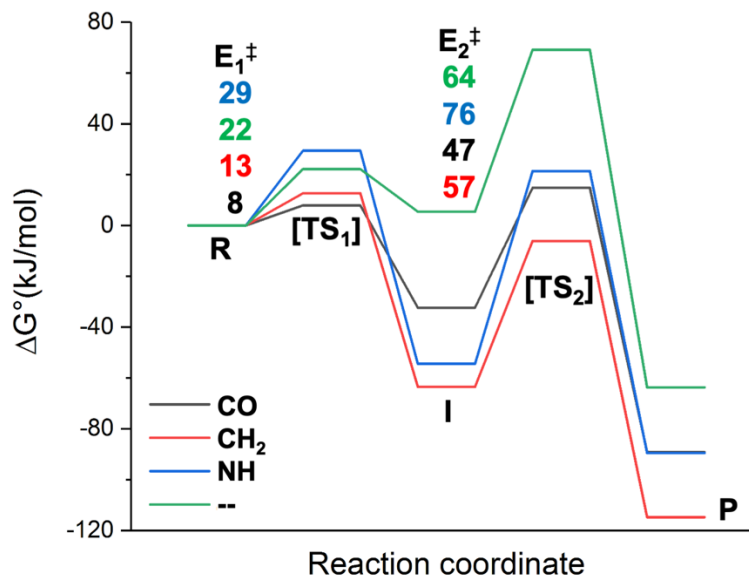


Figure 61 – Calculated relative energy profiles for the four Au(III) cyclometalated complexes with activation energies (E_1^\ddagger and E_2^\ddagger).³⁰⁵

The five-membered phenylpyridine complex (--) showed a different reaction pathway (Figure 61, green trace), which was not surprising due to the absence of its reductive elimination product in the HR-LC-ESI-MS studies. The first activation energy barrier is within the range of the other three Au complexes, however the energy of the **I** species is slightly higher than the **R**, meaning this step would not be thermodynamically favourable, making **I** fairly unstable. This could be explained by the stronger chelating effect of the phenylpyridine ligand compared to the other ligands with a group between the phenyl and pyridine, therefore, the decoordination of the N is less favoured. However, even if **I** with low stability is formed, the activation energy barrier to form **P** is large (63.8 kJ/mol), which could be explained by the greater steric shielding of the pyridine group directly attached to the aryl, meaning rotation of the aryl group cannot be performed. Overall this corroborates our experimental results.

Table 1 – Calculated relative standard Gibbs free energy values (kJ/mol) and calculated 1st and 2nd activation energy barriers (kJ/mol) of the species involved in the cysteine arylation mechanism.³⁰⁵

	Compounds				
	CO	CH ₂	NH	--	CO/ZF
R	0.0	0.0	0.0	0.0	0.0
TS1 = E₁[‡]	7.9	12.7	29.4	22.2	4.1
I	-32.4	-63.5	-54.4	5.4	-36.2
TS2	14.8	-6.1	21.4	69.2	37.2
E₂[‡]	47.3	57.4	75.8	63.8	73.4
P	-89.2	-114.8	-89.5	-63.7	-81.3

QM/MM calculations were also performed with the [Au(C^{CO}N)Cl₂] complex and a ZF model to mimic the binding and reactivity in a more biologically relevant system. The relative energy values of the reaction species can be found in Table 1 (**CO/ZF**). It is interesting to see that regardless of the peptide structure, the relative energies of the reaction species are comparable to those found with the two cysteinates (Table 1, **CO**).

Comparing the overall results obtained from both HR-LC-ESI-MS and DFT calculations, a trend in reactivity was confirmed for the cysteine arylation reaction, increasing in the order: [Au(C^{NH}N)Cl₂] < [Au(C^{CH₂}N)Cl₂] < [Au(C^{CO}N)Cl₂]. Therefore, we envisaged that differences in the C^N scaffold could be responsible for the difference in stability of **R** and **I**. The electronic effects of the bridging groups were initially thought to have an effect on the donating strength of the pyridyl N. However, this cannot be the case since the C=O group is an electron withdrawing group and as such would not decrease the donor strength of the pyridyl N as it is not in the meta position. This would not result in more thermodynamically favourable decoordination of the N to Au, which is observed in the relative energy values, i.e. the intermediate **I** given by [Au(C^{CO}N)Cl₂] is the least thermodynamically stable compared to the other intermediates.

Other factors which could be responsible for the difference in stability of the intermediate **I** could involve the π-conjugation of the different C^N scaffolds and its effect on the N decoordination. Consequently, natural bond orbital (NBO) analysis of **R** (one cysteinate bound *trans* to the pyridyl N) for the [Au(C^{CO}N)Cl₂] and [Au(C^{CH₂}N)Cl₂] complexes was performed. Unfortunately, no conclusive differences in the donating strength of the pyridyl N or π-conjugation strength of the scaffolds could be identified, with the N-Au distance and bond strength similar for both **R**. Steric effects were also considered as a possible difference between the scaffolds, therefore non-covalent interaction (NCI) plots of the CO and CH₂ **I** (N decoordination with Au bound to two cysteinates) were performed. However, this analysis also did not unveil any conclusive

difference in the sterics or non-covalent interactions between the I. Advanced computational experiments are currently in progress to try and understand these differences in reactivity.

Intrigued by the results of this work, the reactivity of three other Au(III) cyclometalated complexes (Figure 62) with the ZF model peptide were investigated, two C[^]N complexes featuring either a O or S bridging group: [Au(C^SN)Cl₂] (C^SN = 2-(phenylthiol)pyridine) and [Au(C^ON)Cl₂] (C^ON = 2-phenoxy pyridine), and a C[^]N[^]N complex [Au(C[^]N[^]N)Cl][PF₆] (C[^]N[^]N = 6-(1,1-dimethylbenzyl)-2,2'-bipyridine).

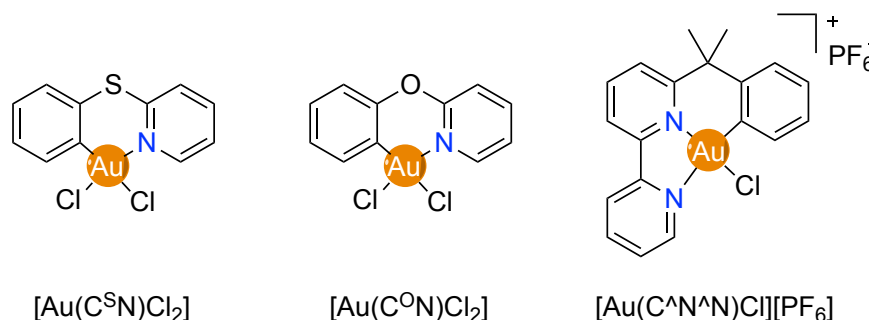


Figure 62 – Structures of the three cyclometalated Au(III) complexes (C[^]N and C[^]N[^]N) investigated in this work to mediate cysteine arylation via reductive elimination.³⁰⁸

The same conditions were used as described above (3 eq. Au complex, (NH₄)₂CO₃ buffer (25 mM, pH 7.4), 37 °C), however in this work the two incubation times used were 30 min and 24 h. The [Au(C^ON)Cl₂] complex was also included in these studies to allow comparison with the new complexes investigated.

After 30 min, HR-LC-ESI-MS analysis (Table 2) identified the classical coordination adduct [Apo-ZF+AuC[^]N+4H]⁶⁺ and the cysteine arylated adduct [Apo-ZF+C[^]N+5H]⁶⁺ for the three AuC[^]N complexes, whereas the AuC[^]N[^]N complex only showed coordination adducts of the type [Apo-ZF+2AuC[^]N[^]N+2H]⁶⁺. The [Au(C^ON)Cl₂] and [Au(C^SN)Cl₂] complexes appeared more reactive than the [Au(C^ON)Cl₂] complex as more Au coordination adducts were observed in the latter. Interestingly, adducts of the type [Apo-ZF+2C[^]N+4H]⁶⁺ could also be identified, even after 30 min, highlighting the presence of at least two binding sites on the peptide, which are most likely the two cysteine residues.

Table 2 - Experimental (M_{exp}) and theoretical (M_{theor}) masses of the detected species at specific retention times (RT) during the individual HR-LC-ESI-MS experiment of Cys₂His₂ model peptide after 30 min incubation.³⁰⁸

Compound	RT (mins)	Species	M_{exp}	M_{theor}	Δppm
Au(C ^{CO} N)	3.96	[Apo-ZF+AuC ^{CO} N+4H] ⁶⁺	557.5768	557.5846	13.99
		[Apo-ZF+C ^{CO} N+5H] ⁶⁺	524.9214	524.9248	6.48
	4.25	[Apo-ZF+2C ^{CO} N+4H] ⁶⁺	555.2608	555.2673	11.71
Au(C ^S N)	4.03	[Apo-ZF+C ^S N+5H] ⁶⁺	525.5815	525.5876	11.61
		[Apo-ZF+AuC ^S N+4H] ⁶⁺	558.2365	558.2474	19.52
	4.39	[Apo-ZF+2C ^S N+4H] ⁶⁺	556.5881	556.5930	8.80
Au(C ^O N)	3.74	[Apo-ZF+AuC ^O N+4H] ⁶⁺	555.5796	555.5846	9.00
		[Apo-ZF+C ^O N+5H] ⁶⁺	523.0834	523.0919	16.25
	3.91	[Apo-ZF+AuC ^O N+C ^O N+3H] ⁶⁺	583.7609	583.7601	1.37
	4.02	[Apo-ZF+2C ^O N+4H] ⁶⁺	551.0939	551.1003	11.61
		[Apo-ZF+AuC ^O N+C ^O N+3H] ⁶⁺	583.9191	583.9271	13.70
		[Apo-ZF+AuC ^O N+Au ^I +3H] ⁶⁺	588.2609	588.2444	28.05
Au(C ^{^N^N})	3.86	[Apo-ZF+2AuC ^{^N^N} +2H] ⁶⁺	650.9475	650.9465	1.54

After 24 h, both the [Au(C^SN)Cl₂] and [Au(C^ON)Cl₂] complexes had retained some of the coordination adducts, whereas the [Au(C^{CO}N)Cl₂] complex showed full conversion to the reductive elimination adduct. However, the [Au(C^{^N^N})Cl][PF₆] complex preserved its coordination adduct throughout. It should be noted that the adduct formation was never quantitative in all cases as the free ZF peptide could be observed in the chromatogram.

The chemoselectivity towards cysteine arylation was next explored using a model peptide with only one cysteine residue and the sequence ANGELACASINI (AC). The same experimental conditions as the ZF peptide were used, except a lower ratio of 1:1 for the complex and AC peptide. This was due to the high reactivity of the peptide in preliminary studies, which resulted in peptide decomposition with the Au complexes. After 30 min incubation, HR-LC-ESI-MS analysis detected four different adducts with the AuC^{^N} complexes; the mono Au adduct [AC+AuC^{^N}N]²⁺, the bis Au adduct [AC+2AuC^{^N}N-2H]²⁺, the reductive elimination adduct [AC+C^{^N}N+1H]²⁺ and their co-existence [AC+AuC^{^N}N+C^{^N}N-1H]²⁺, an example of which can be seen for the [Au(C^ON)Cl₂] complex at 854.8404 m/z in Figure 63. Therefore, regardless of only one cysteine residue present, the peptide can still offer a second Au binding site that is not a cysteine. The [Au(C^{^N^N})Cl][PF₆] complex formed the classical coordination adduct seen with the ZF peptide, however only one molecule of complex was coordinated to the peptide, rather than two, which suggests a strong chemoselectivity for cysteine, which has been observed previously.³⁰⁹

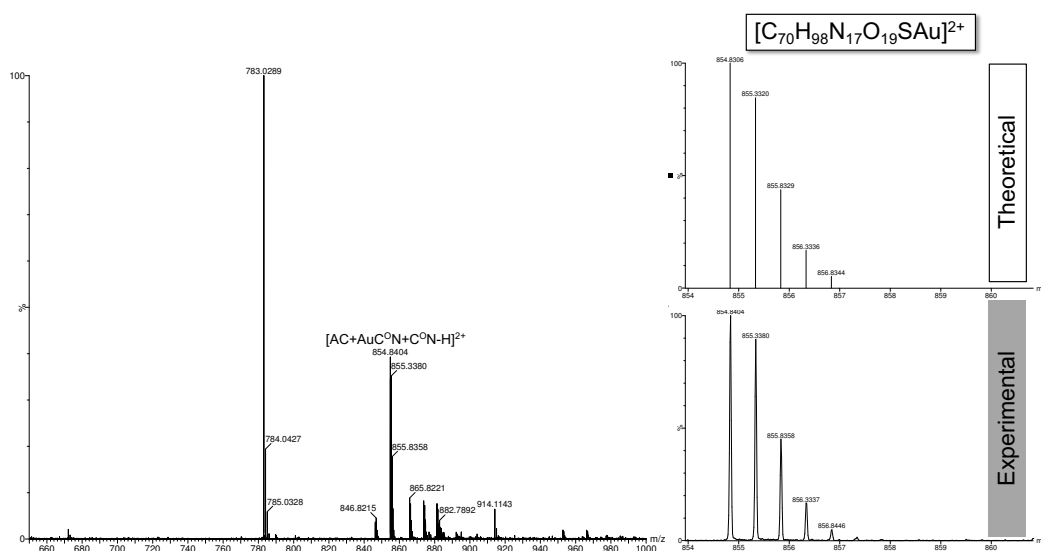


Figure 63 – HR-LC-ESI-MS analysis for the reaction of the $[Au(C^O)Cl_2]$ complex with AC model peptide (1 : 1 ratio) after 30 min incubation at 37 °C, recorded at retention time 6.60 min. Comparison between the experimental isotopic patterns of a representative adduct with the theoretical values is also shown. Figure from ref 308. Copyright 2020, John Wiley and Sons <https://creativecommons.org/licenses/by/4.0/>.³⁰⁸

After 24 h, even though a ratio of 1:1 was used for the complex and peptide, the CO complex still initiated peptide decomposition, which has been previously reported for Pt(II) and Pd(II) complexes due to hydrolysis of the amide backbone.³¹⁰ Conversely, the $[Au(C^S N)Cl_2]$ and $[Au(C^O N)Cl_2]$ complexes retained their $[AC+AuC^N+C^N-1H]^2+$ adducts, whilst the $C^N N$ complex adduct remained the same (Table 3).

Table 3 - Experimental (M_{exp}) and theoretical (M_{theor}) masses of the detected species at specific retention times (RT) during the individual HR-LC-ESI-MS experiment of the AC model peptide after 24 h incubation.³⁰⁸

Compound	RT (mins)	Species	M_{exp}	M_{theor}	Δppm
$Au(C^S N)$	6.53	$[AC+2AuC^S N-2H]^2+$	968.7899	968.7870	2.99
		$[AC+AuC^S N+C^S N-1H]^2+$	870.8113	870.8077	4.13
$Au(C^O N)$	6.43	$[AC+AuC^O N+C^O N-1H]^2+$	854.8404	854.8306	11.46
$Au(C^N N)$	4.80	$[AC+AuC^N N]^2+$	821.8527	821.8434	11.32

Next, the position of the cysteine residue for cysteine arylation was investigated using an N-terminal cysteine peptide sequence, CASINI (C). These experiments were also carried out with a 1:1 ratio of complex : peptide to allow comparison to the AC peptide. The results after 30 min can be seen in Table 4, where all four complexes have formed the classical coordination adduct. Interestingly, the $C^O N$ complex also formed a $[C+2AuC^O N-3H]^+$ adduct indicating that a secondary Au binding site could also be found

in this peptide. After 24 h the classical coordination adducts remained with no reductive elimination products, demonstrating that the position of the cysteine plays an important role in the reductive elimination mechanism.

Table 4 - Experimental (M_{exp}) and theoretical (M_{theor}) masses of the detected species at specific retention times (RT) during the individual HR-LC-ESI-MS experiment of C model peptide after 30 min incubation.³⁰⁸

Compound	RT (mins)	Species	M_{exp}	M_{theor}	Δppm
Au(C ^{CO} N)	5.20	[C+AuC ^{CO} N-1H] ⁺	996.3513	996.3353	16.06
Au(C ^{CO} N)	5.29	[C+AuC ^{SN} N-1H] ⁺	1000.3221	1000.3124	9.70
Au(C ^{ON})	5.19	[C+AuC ^{ON} N-1H] ⁺	984.3491	984.3353	14.02
	6.89	[C+2AuC ^{ON} N-3H] ⁺	1349.3585	1349.3467	8.72
Au(C ^{AN} N)	4.78	[C+AuC ^{AN} N-1H] ⁺	1087.4188	1087.4138	4.60

The complexes were also incubated with GSH, a physiologically relevant reducing agent containing one cysteine residue.³¹¹ The incubation was carried out in a 3:1 ratio (complex : peptide) and analysed after 24 h (Table 5).

Table 5 - Experimental (M_{exp}) and theoretical (M_{theor}) masses of the detected species at specific retention times (RT) during the individual HR-LC-ESI-MS experiment of GSH after 24 h incubation.³⁰⁸

Compound	RT (mins)	Species	M_{exp}	M_{theor}	Δppm
Au(C ^{CO} N)	9.65	[GSH+C ^{CO} N] ⁺	489.1411	489.1444	6.75
Au(C ^{CO} N)	11.58	[GSH+C ^{SN} N] ⁺	493.1254	493.1216	7.71
Au(C ^{ON})	10.85	[GSH+AuC ^{ON} N-1H] ⁺	673.1104	673.1031	10.84
	11.02	[GSH+C ^{ON} N] ⁺	477.1422	477.1444	4.61
		[GSH+AuC ^{ON} N-1H] ⁺	673.1104	673.1031	10.84
Au(C ^{AN} N)	9.65	[GSH+AuCNN-1H] ⁺	776.1815	776.1817	0.26

As expected, the three AuC^{AN} complexes were capable of mediating cysteine arylation, whereas the AuC^{AN}N complex could only form the classical coordination adduct at 776.1815 m/z (Figure 64).

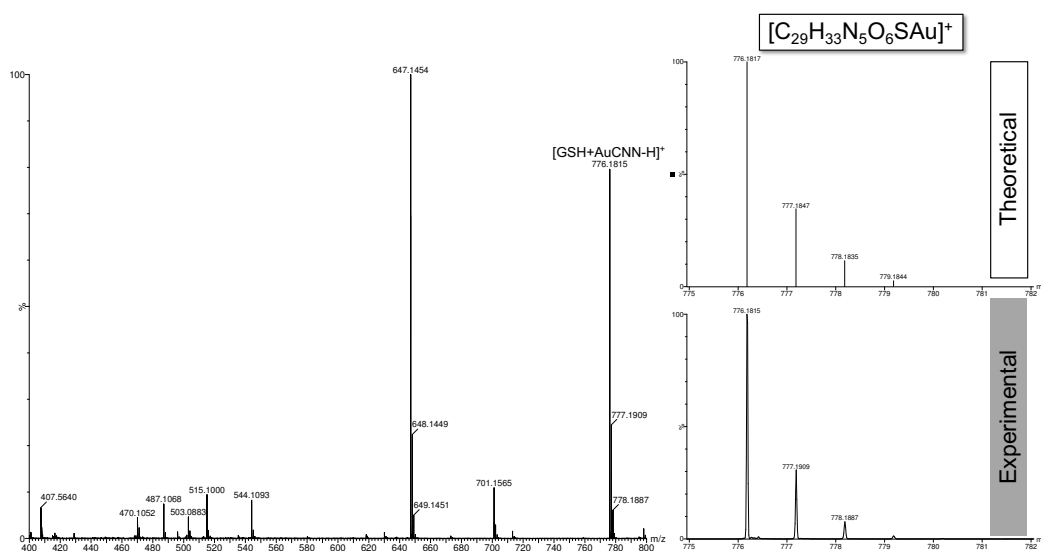


Figure 64 – HR-LC-ESI-MS analysis for the reaction of $[Au(C^N^N)Cl][PF_6]$ with GSH (3 : 1 ratio) after 24 h incubation at 37 °C. Comparison between the experimental isotopic patterns of a representative adduct with the theoretical values is also shown. Figure from ref 308. Copyright 2020, John Wiley and Sons <https://creativecommons.org/licenses/by/4.0/>.³⁰⁸

The chemoselectivity of the cysteine arylation was next investigated with a cysteine-free peptide with the sequence LFRANALK (L). Similar results were observed at 30 min and 24 h, with the AuC^N complexes forming mainly the classic coordination adduct of the type $[L+AuC^N]^{2+}$, with no reductive elimination (Table 6). The AuC^ON complex also exhibited an adduct of the type $[L+Au^I+H]^{2+}$, where the gold centre had been reduced from Au(III) to Au(I). Interestingly, no adducts were observed for the AuC^N^N complex, even after 24 h, demonstrating its preference to bind to cysteine residues only, as described earlier.³⁰⁹

Table 6 - Experimental (M_{exp}) and theoretical (M_{theor}) masses of the detected species at specific retention times (RT) during the individual HR-LC-ESI-MS experiment of L model peptide after 24 incubation.³⁰⁸

Compound	RT (mins)	Species	M_{exp}	M_{theor}	Δppm
Au(C ^O N)	4.27-4.64	$[L+AuC^ON]^{2+}$	654.8054	654.8018	5.50
	4.74-4.93	$[L-NH_4+AuC^ON]^{2+}$	645.8030	645.7845	28.65
Au(C ^S N)	4.25+4.76	$[L+AuC^SN]^{2+}$	656.7945	656.7903	6.40
Au(C ^O N)	4.69	$[L+AuC^ON]^{2+}$	648.8228	648.8018	32.37
	4.91	$[L+Au^I+1H]^{2+}$	564.2738	564.2753	2.66

Another cysteine-free peptide was included in this study, $[Leu^5]$ Enkephalin (LE), which is part of the enkephalin family that can act as agonists at opiate receptors.³¹² They were originally isolated from pig and cow brains and possess the amino acid sequence: Tyr-

Gly-Gly-Phe-Leu (YGGFL).³¹² This peptide was investigated due to the absence of classical nucleophilic sites for coordination to the Au(III) complexes, that were present in L. However, regardless of this, the adducts formed were very similar to L (Table 7), with coordination adducts formed for the AuC^{^N} complexes, and no reactivity with the AuC^{^N^N} complex.

Table 7 - Experimental (M_{exp}) and theoretical (M_{theor}) masses of the detected species at specific retention times (RT) during the individual HR-LC-ESI-MS experiment of the LE model peptide after 24 h incubation.³⁰⁸

Compound	RT (mins)	Species	M_{exp}	M_{theor}	Δppm
Au(C ^{CO} N)	5.22-5.39	[LE-NH ₄ +OH+AuC ^{CO} N-2H] ⁺	932.3184	932.2808	40.33
	6.50	[LE+AuC ^{CO} N-1H] ⁺	933.2914	933.3124	22.50
	6.92	[LE-NH ₄ +AuC ^{CO} N-1H] ⁺	915.2888	915.2781	11.69
Au(C ^S N)	5.27+6.87	[LE+AuC ^S N-1H] ⁺	937.2682	937.2896	22.83
Au(C ^O N)	5.22+6.75	[LE+AuC ^O N-1H] ⁺	921.2922	921.3124	21.92

Therefore, to elucidate the binding sites of the AuC^{^N} complexes, tandem MS (MS/MS) studies were analysed by Dr. Samiel M. Meier-Menches using an online top-down software, Apm²s, developed by Dyson and co-workers.³¹³ The tandem MS technique involves performing an initial ESI-MS to identify the ion of interest before further fragmentation of this signal. The conventional nomenclature for peptide fragmentation can be seen in Figure 65a.

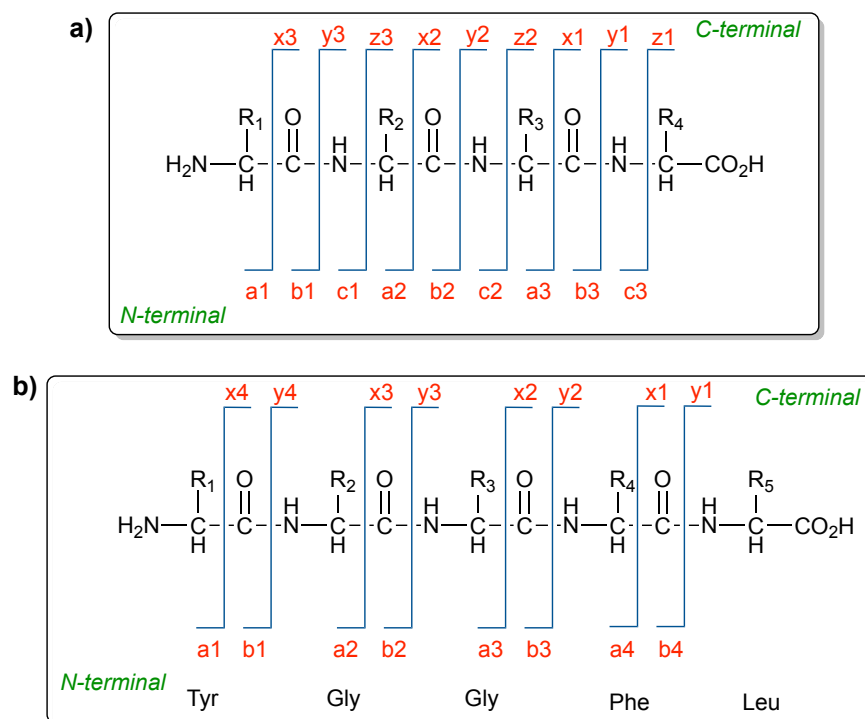


Figure 65 – a) Diagram of conventional nomenclature used for peptide fragment positive ions as reported by Biemann,³¹⁴ b) Diagram of LE peptide with expected fragmentation pattern from collision induced dissociation.³⁰⁸

In this work the fragmentation was carried out by collision-induced dissociation (CID) on the $[\text{LE}+\text{AuC}^{\text{CO}}\text{N}-\text{H}]^+$ adduct with a m/z of 933. CID experiments usually generate b and y fragment ions due to cleavage of the peptide backbone at the C-N bond;³¹⁵ the nomenclature used can be seen in Figure 65b. However, in this work, only b fragments were observed with associated high energy a -fragments, the results of which can be seen in Figure 66. Overall, the postulated binding sites of the $[\text{Au}(\text{C}^{\text{CO}}\text{N})\text{Cl}_2]$ complex can be seen in gold circles in Figure 66, the first being the N-terminal coordination to Tyr1 (tyrosine1), as these metalated a and b fragments were abundant in the spectrum. The second binding site was predicted to be the amide backbone of the Gly3Phe4 (glycine3 phenylalanine4) fragment due to the identification of two internal fragments, a_4y_3 and a_3y_3 .

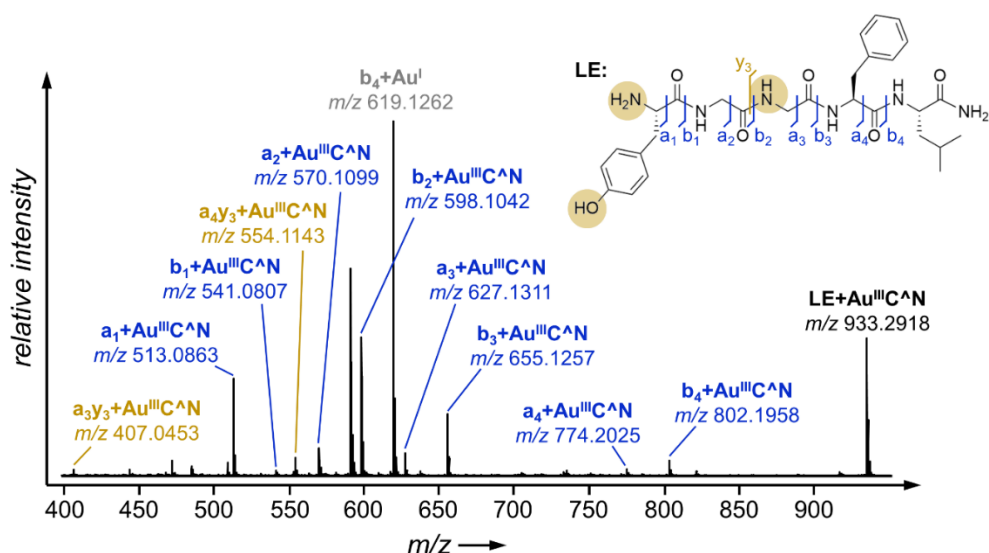


Figure 66 - Fragment-mass spectrum of the $[LE+Au^{CO}N-H]^+$ adduct (m/z 933) showing the identified metalated *a*-, *b*- (*N*-terminal) and *ay*- (internal) fragments. The fragmentation positions and the most likely binding sites (golden circles) are indicated in the structure of LE in the top right corner. Figure from ref 308. Copyright 2020, John Wiley and Sons

<https://creativecommons.org/licenses/by/4.0/>.³⁰⁸

In addition, to further complement these experimental results, computational analysis was performed by Prof. Giampaolo Barone. Firstly, DFT calculations were used to determine the standard formation Gibbs free energy values of mono adducts of the type $[Au(C^{CO}N)Cl(X)]$, where X = amino acid with binding site. As expected, using hard-soft acid-base (HSAB) theory, the most stable adduct contained the cysteine residue, followed by the N-containing side chain residues (arginine, asparagine and glutamine). O-containing side chain residues (tyrosine and serine) showed similar values to the N-containing side chains, which also provided further evidence to support the tandem MS studies for the potential binding of the Au complex to Tyr1.

DFT calculations were also used to postulate a reaction mechanism between the $[Au(C^{CO}N)Cl_2]$ complex and the AC peptide to elucidate the importance of the cysteine residue position for reductive elimination to occur. We predicted that the binding of the complex to the peptide would involve bidentate coordination due to the previous mechanism hypothesised using the Cys₂His₂ model peptide (Scheme 16). Therefore, due to the presence of only one cysteine residue in the AC peptide, a secondary binding site that it not a cysteine must be involved.

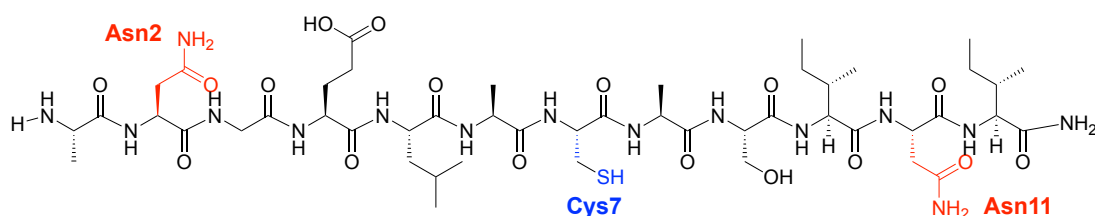
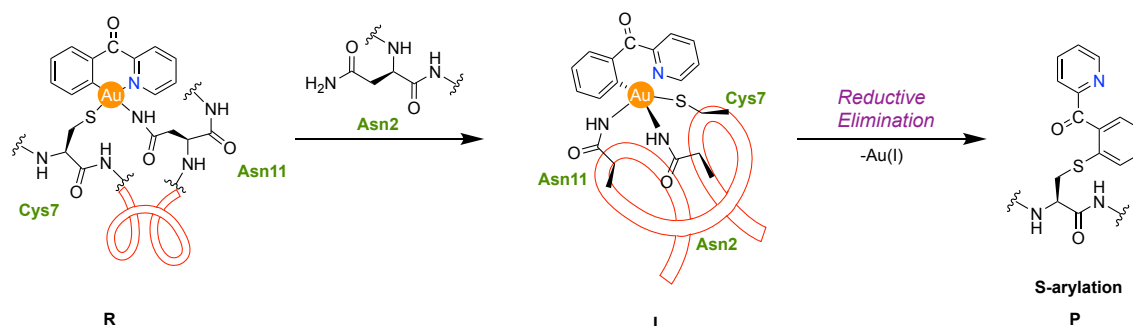


Figure 67 – ANGELACASINI model peptide structure with the potential binding sites for the Au complex highlighted: Cys7, Asn11 and Asn2.³⁰⁸

Modelling of the complex and AC peptide identified two other possible binding sites for the Au complex, Asn2 and Asn11, which were located on either side of the Cys7 (Figure 67). This is supported by the favourable mono adduct formation energy calculated between the $[\text{Au}(\text{C}^{\text{CO}}\text{N})\text{Cl}_2]$ complex and asparagine ($\Delta G^\circ = -42.0$ kJ/mol), as described above. The first step in the hypothesised mechanism (Scheme 17) involved the formation of the reactant (**R**), whereby the two chloride ligands were displaced by the Cys7 and Asn11 side chains. The formation of the intermediate (**I**) then proceeded by the addition of the second asparagine (Asn2) which resulted in the decoordination of the pyridyl N, as observed in our previously proposed mechanism (Scheme 16) using a second cysteine residue. The formation of **I** was thermodynamically favoured as it was 114 kJ/mol more stable than **R**. DFT calculations then showed that two types of cross-coupling reactions could be observed *via* reductive elimination, both of which are exergonic in nature, namely cysteine (S)-arylation or asparagine (N)-arylation. Surprisingly, the N-arylated product is ca. 20 kJ/mol more thermodynamically stable than the S-arylated product shown in Scheme 17. However, it should be highlighted that the product is also comprised of the Au(I) side product, which possessed Asn2 and Asn11 ligands in the S-arylation reaction, and Cys7 and Asn2 ligands for the N-arylation. Therefore, the N-arylation Au(I) side product could be responsible for the increased stability.



Scheme 17 – Proposed mechanism for the reaction of the $[\text{Au}(\text{C}^{\text{CO}}\text{N})\text{Cl}_2]$ complex with the model AC peptide forming the cysteine arylation product via reductive elimination.³⁰⁸

Unfortunately our MS data cannot discriminate between the two arylation sites, however the feasibility of this second arylation site does potentially provide insights into the adducts formed with the $[\text{Au}(\text{C}^{\text{S}}\text{N})\text{Cl}_2]$ and $[\text{Au}(\text{C}^{\text{O}}\text{N})\text{Cl}_2]$ complexes and the AC peptide. For example, adducts of the type $[\text{AC}+\text{AuC}^{\text{A}}\text{N}+\text{C}^{\text{A}}\text{N}-\text{H}]^{2+}$ were identified, meaning there must be more than one binding site other than Cys7 for reductive elimination to occur, which could potentially be the Asn11 residue suggested by the DFT calculations. In fact, the C peptide contained a secondary binding site as evidenced by the ability of the $[\text{AuC}^{\text{A}}\text{N}]$ complexes to form classical coordination adducts, however the absence of reductive elimination could be more related to the fact that the coordination environment surrounding the cysteine did not allow stabilisation of the intermediate. The importance of the coordination environment can also be seen with the GSH peptide, as although it is a short sequence, the residues surrounding the cysteine allow reductive elimination to occur with the $\text{AuC}^{\text{A}}\text{N}$ complexes.

5.3. Summary and Future Outlook

To conclude, this work has provided thorough investigations into the propensity for Au(III) cyclometalated complexes to mediate cysteine arylation, with a total of seven complexes evaluated across the two studies, allowing initial structure activity relationships (SARs) to be established. However, an explanation for these SARs is not as straight forward as one would expect, as initial computational analysis (NBO and NCI) could not provide conclusive evidence for the greater reactivity of the $[\text{Au}(\text{C}^{\text{O}}\text{N})\text{Cl}_2]$ complex compared to the $[\text{Au}(\text{C}^{\text{CH}_2}\text{N})\text{Cl}_2]$ complex. DFT calculations were also used to help hypothesise a mechanism for the cysteine arylation *via* reductive elimination, which first begins with the displacement of a chloride by a cysteinyl group *trans* to the pyridyl N. A second cysteinyl group can then approach and bind to the Au(III), causing the Au-N bond to break, forming the intermediate (I) species $[\text{Au}(\text{III})(\text{C}^{\text{A}}\text{N})(\text{Cys})_2\text{Cl}]^-$. This step is crucial to allow the aryl group to rotate to facilitate reductive elimination.

Our second study delved further into the chemoselectivity of the cysteine arylation, concluding that the intermediate I does not necessarily require a second cysteine to form, but can take place in the presence of any nucleophilic group within the peptide chain, which is available for coordination to Au(III). Therefore, the possibility of forming intermediate I is strongly dependent on the coordination environment surrounding the cysteine residue (AC vs. C peptide). This means that the reactivity of Au(III) complexes with peptides cannot be predicted solely on their affinity for binding certain residues, but is modulated by the overall protein folding and residue exposure. The structure of the Au(III) cyclometalated complex is also an important factor to consider; the $[\text{Au}(\text{C}^{\text{A}}\text{N}^{\text{A}}\text{N})\text{Cl}][\text{PF}_6]$ only formed the coordination complex (displacement

of the chloride by the cysteine residue) with the cysteine containing peptides and showed no adduct formation with the L and LE peptides. This high chemoselectivity was not observed with the $[\text{Au}(\text{C}^{\wedge}\text{N})\text{Cl}_2]$ complexes.

The future outlook of this project is currently being pursued in our group, and includes exploring proteomic profiling of the $[\text{Au}(\text{C}^{\wedge}\text{N})\text{Cl}_2]$ complexes for cysteine arylation in bacteria,³¹⁶ as well as the conjugation of therapeutic and imaging agents to the cyclometalated ligand scaffold.

5.4. Materials and Methods

5.4.1. General

Circular dichroism experiments were performed by Dr. Riccardo Bonsignore. Computational analysis was completed by Prof. Giampaolo Barone. Synthesis of AC, C and L peptides was completed by Jorge Sánchez Escudero. Online tandem MS analysis was completed by Dr. Samuel M. Meier-Menches. 2-(phenylthio)pyridine was synthesised and characterised by Dr. Christopher Brown. $[\text{Au}(\text{C}^{\wedge}\text{N}^{\wedge}\text{N})\text{Cl}][\text{PF}_6]$ ($\text{C}^{\wedge}\text{N}^{\wedge}\text{N}$ = 6-1,1-dimethylbenzyl)-2,2'-bipyridine) was available in the group. Dr. Thomas Williams helped with the MS studies.

Solvents and reagents (reagent grade) were all commercially available and used without further purification. The zinc finger precursor peptide was obtained from Peptide Specialty Laboratories GmbH and had the sequence ${}^1\text{PYKCPECGKSFSQKSDLVKHQRTHTG}^{26}$ (ZF). ${}^1\text{H}$ NMR (nuclear magnetic resonance) spectra were recorded in $\text{DMSO-}d_6$, $\text{acetone-}d_6$ and CD_2Cl_2 with TMS as an internal reference, on Bruker Avance 400 or 500 MHz NMR spectrometers. HR-LC-ESI-MS spectra were recorded on Synapt G2-Si time-of-flight (TOF) mass spectrometer (Waters) by high-pressure liquid chromatography (HPLC). Mass spectra were acquired and processed using MassLynx V4.1 (Waters). The purity of the compounds was confirmed by elemental analysis which showed purity >98%.

5.4.2. Synthesis of Au(III) complexes and 2-(phenylthio)pyridine

$[\text{Au}(\text{C}^{\text{O}}\text{N})\text{Cl}_2]$ was synthesised by modification of a literature procedure.¹¹¹

A mixture of NaAuCl_4 (400 mg, 1 mmol, 1 eq.) and 2-benzoylpyridine (184 mg, 1 mmol, 1 eq.) in deionised (DI) H_2O (15 mL) was stirred at room temperature for 20 min before the addition of a solution of AgNO_3 (340 mg, 2 mmol, 2 eq.) in DI H_2O (5 mL). The orange/brown suspension was then stirred for 10 min at room temperature before increasing the temperature to reflux for 3 days. The mixture was then filtered whilst hot and the light brown precipitate was collected and dried before recrystallisation using propionitrile. A white precipitate was then filtered to yield the clean product (170 mg, 0.37 mmol, 37%).

${}^1\text{H}$ NMR (400 MHz, $\text{DMSO-}d_6$) δ 9.48 (d, J = 5.7 Hz, 1H), 8.60 – 8.51 (m, 1H), 8.41 – 8.33 (m, 1H), 8.09 (ddd, J = 7.6, 5.9, 1.7 Hz, 1H), 7.79 – 7.72 (m, 1H), 7.73 – 7.65 (m, 1H), 7.51 – 7.43 (m, 2H).

[Au(C^{CH₂}N)Cl₂] was synthesised following a literature procedure.¹¹²

NaAuCl₄ (400 mg, 1 mmol, 1 eq.) was added to a flask and dissolved in DI H₂O (24 mL). Benzylpyridine (160 μ L, 1 mmol, 1 eq.) was then added, forming a yellow precipitate. The mixture was refluxed overnight until the precipitate had turned from yellow to white. The mixture was then filtered and the precipitate was washed with methanol, followed by recrystallisation from a dichloromethane/diethyl ether mixture to yield the pure product (320 mg, 0.74 mmol, 74%).

¹H NMR (400 MHz, Acetone-*d*₆) δ 9.33 – 9.27 (m, 1H), 8.31 (td, *J* = 7.7, 1.5 Hz, 1H), 8.06 (d, *J* = 7.8 Hz, 1H), 7.75 (t, *J* = 6.9 Hz, 1H), 7.49 (dd, *J* = 8.0, 1.2 Hz, 1H), 7.32 – 7.24 (m, 1H), 7.18 (td, *J* = 7.3, 1.2 Hz, 1H), 7.08 (td, *J* = 7.7, 1.8 Hz, 1H), 4.68 (d, *J* = 15.4 Hz, 1H), 4.41 (d, *J* = 15.1 Hz, 1H).

[Au(C^{NH})Cl₂] was synthesised following a literature procedure.³¹⁷

A mixture of NaAuCl₄ (398 mg, 1 mmol, 1 eq.) and 2-anilinopyridine (170 mg, 1 mmol, 1 eq.) in DI H₂O (30 mL) was stirred at room temperature for 1 h, before increasing the temperature to reflux for a further 3 h. The precipitate was filtered after cooling and then washed with water, collected and dried in air. The product was then recrystallised using hot acetone and the solution was concentrated to yield a light brown precipitate. This was then filtered and washed with a little acetone to yield the pure product (200 mg, 0.46 mmol, 46%).

¹H NMR (400 MHz, DMSO-*d*₆) δ 10.70 (s, 1H), 8.81 (d, *J* = 6.5 Hz, 1H), 7.97 (ddd, *J* = 8.6, 7.0, 1.6 Hz, 1H), 7.56 (dd, *J* = 8.2, 1.3 Hz, 1H), 7.40 (d, *J* = 8.6 Hz, 1H), 7.26 (td, *J* = 7.5, 1.3 Hz, 1H), 7.19 – 7.06 (m, 2H), 7.06 – 6.97 (m, 1H).

[Au(C[^]N)Cl₂] was synthesised by combining two literature procedures.^{111,318}

A mixture of NaAuCl₄ (400 mg, 1 mmol, 1 eq.) and 2-phenylpyridine (0.14 mL, 0.98 mmol, 1 eq.) in DI H₂O (15 mL) was stirred at room temperature for 20 min. The addition of the 2-phenylpyridine caused a yellow precipitate to be formed. A solution of AgNO₃ (340 mg, 2 mmol, 2 eq.) in DI H₂O (5 mL) was then added. This was then stirred for 10 min at room temperature before increasing the temperature to reflux for 3 days producing an off-white suspension. The mixture was then filtered whilst hot and the off-white precipitate was collected and dried before recrystallisation using propionitrile. A white precipitate was then filtered to yield the clean product (80 mg, 0.19 mmol, 20%).

¹H NMR (400 MHz, DMSO-*d*₆) δ 9.57 – 9.49 (m, 1H), 8.44 – 8.36 (m, 2H), 8.01 – 7.94 (m, 1H), 7.82 (dd, *J* = 8.1, 1.2 Hz, 1H), 7.77 (td, *J* = 6.3, 2.4 Hz, 1H), 7.52 – 7.45 (m, 1H), 7.42 – 7.35 (m, 1H).

[Au(C¹³N)Cl₂] was synthesised by modification of a literature procedure.³¹⁹

A mixture of NaAuCl₄ (200 mg, 0.5 mmol, 1 eq.) and 2-phenoxy pyridine (86 mg, 0.5 mmol, 1 eq.) in DI H₂O (8 mL) was stirred at room temperature for 20 min. On addition of the 2-phenoxy pyridine to the aqueous gold solution, a yellow precipitate was formed. A solution of AgNO₃ (170 mg, 1 mmol, 2 eq.) in DI H₂O (2 mL) was then added causing the formation of an orange precipitate. This was then stirred for 10 min at room temperature before increasing the temperature to reflux for 2 days producing a light grey suspension. The mixture was then filtered whilst hot and the precipitate was collected and dried before recrystallisation using propionitrile. A yellow precipitate was then filtered to yield the clean product (154 mg, 0.35 mmol, 69%).

¹H NMR (400 MHz, DMSO-*d*₆) δ 9.06 (d, *J* = 6.1 Hz, 1H), 8.42 (t, *J* = 7.7 Hz, 1H), 7.86 (d, *J* = 8.2 Hz, 1H), 7.69 (t, *J* = 6.8 Hz, 1H), 7.59 (d, *J* = 8.0 Hz, 1H), 7.37 (q, *J* = 8.5 Hz, 2H), 7.28 – 7.19 (m, 1H).

Au(C¹³S)Cl₂] was synthesised by modification of a literature procedure.³¹⁹

A mixture of NaAuCl₄ (210 mg, 0.53 mmol, 1 eq.) and 2-(phenylthio)pyridine (100 mg, 0.53 mmol, 1 eq.) in DI H₂O (15 mL) was stirred at room temperature for 20 min. A solution of AgNO₃ (180 mg, 1 mmol, 2 eq.) in DI H₂O (2 mL) was then added causing the formation of a dark orange precipitate. This was then stirred for 10 min at room temperature before increasing the temperature to reflux for 3 days producing a light brown suspension. The mixture was then filtered whilst hot and the precipitate was collected and dried before recrystallisation using propionitrile. A white precipitate was then filtered to yield the clean product (57 mg, 0.12 mmol, 23%).

¹H NMR (400 MHz, DMSO-*d*₆) δ 9.17 (dd, *J* = 6.5, 1.2 Hz, 1H), 8.32 – 8.20 (m, 2H), 7.78 (td, *J* = 6.7, 1.7 Hz, 1H), 7.61 – 7.56 (m, 1H), 7.49 – 7.42 (m, 1H), 7.30 – 7.21 (m, 2H).

C¹³N Ligand (2-(phenylthio)pyridine) – *Synthesised by Dr. Chris Brown*

Prepared using a procedure adapted from Ma *et al.*³²⁰

To a dried Schlenk bomb, diphenyl disulfide (3.40 g, 15.6 mmol, 1 eq.) and NaOH (0.936 g, 24.4 mmol, 1.5 eq.) were added and placed under an N₂ atmosphere. DMSO (50 mL) and 2-bromopyridine (2.48 mL, 26 mmol, 1.67 eq.) were added before the vessel was sealed. The reaction mixture was heated to 130 °C and stirred for 18 h before the solution was allowed to cool to room temperature, following this the DMSO was reduced in volume to ~5 mL *in vacuo* and then diluted with brine (100 mL). The crude product was extracted with CH₂Cl₂ (3 x 50 mL) before purification of the yellow oil *via* column chromatography (CH₂Cl₂) and the second fraction (*R*_f = 0.28) was collected. The pure product was isolated as a light-yellow oil (3.56 g, 19 mmol, 78%).

^1H NMR (400 MHz, CD_2Cl_2) δ 8.39 (ddd, $J = 4.9, 1.9, 0.9$ Hz, 1H), 7.63 – 7.56 (m, 2H), 7.50 – 7.42 (m, 4H), 7.01 (ddd, $J = 7.5, 4.9, 1.0$ Hz, 1H), 6.93 (dt, $J = 8.1, 1.0$ Hz, 1H). ESI-MS calcd. for $\text{C}_{11}\text{H}_{10}\text{NS}$: 188.0534; found: 188.0533 $[\text{M}+\text{H}]^+$.

5.4.3. HR-LC-ESI-MS Studies

HPLC was performed with an Acquity UPLC system (Waters) and using an Acquity UPLC protein BEH C4 column (300 Å, 1.7 μm , 2.1 mm \times 100 mm) for ZF peptide and an Acquity UPLC CSH C18 column (130 Å, 1.7 μm , 2.1 mm \times 100 mm) for the remaining peptides. The instrumental parameters for HPLC-MS were as follows: 2.85 kV capillary voltage, 120 °C source temperature, 350 °C desolvation temperature, 90 $\text{L}\cdot\text{h}^{-1}$ cone gas, 900 $\text{L}\cdot\text{h}^{-1}$ desolvation gas and 6 bar nebulizer. A linear gradient from 95% to 5% water (0.1% FA), while proportionally increasing acetonitrile (0.1% FA), in 8 min was used. The flow rate was 300 $\mu\text{L}\cdot\text{min}^{-1}$, the column was held at 40 °C and the autosampler at 20 °C.

Solutions of L and LE were prepared by dissolving the peptides in $(\text{NH}_4)_2\text{CO}_3$ buffer solution (25 mM, pH = 7.4) at 37 °C. The peptides ZF, AC and C were first incubated with DTT (3 eq., 3 h) in $(\text{NH}_4)_2\text{CO}_3$ buffer solution (25 mM, pH = 7.4) at 37 °C. The ZF peptide was reconstituted to its holo-form according to a previously published procedure³²¹ by further incubation with zinc acetate (3 eq., 30 min) at 37 °C. The formation of the ZF was confirmed by a mass shift in the resulting mass spectrum. Stock solutions of the gold compounds were freshly prepared in DMSO at a concentration of 10 mM and diluted to the final concentration using $(\text{NH}_4)_2\text{CO}_3$ (25 mM, pH = 7.4). The individual experiments between the gold compounds and the peptides were performed at a molar ratio of 3:1 or 1:1 (gold complex : peptide) with the peptide reaching a final concentration of 10 μM . The compounds were incubated at 37 °C for 10 min/30 min and 24 h.

ESI-MS/MS were obtained in a HPLC-MS setup by selecting the desired mass signal and fragmenting the parent ions at 18–34 eV.

6. C-P Cross-Coupling Reaction mediated by Au(III) **Cyclometalated Complexes.**

This chapter is based on the following paper:

Carbon-Phosphorus Coupling from C[^]N Cyclometalated Au^{III} Complexes

Riccardo Bonsignore⁺, **Sophie R. Thomas**⁺, Wim T. Klooster, Simon J. Coles, Robert L. Jenkins, Didier Bourissou, Giampaolo Barone and Angela Casini

[⁺] *Authors contributed equally to this work.*

DOI: 10.1002/chem.201905392

6.1. Introduction

Gold homogenous catalysis has become a thriving topic over the last few years; however, this has not always been the case. It was not until ground-breaking work was published in 1998 by Teles *et al.*,³²² that gold was considered to truly be an active catalyst.³²³ Since then, gold has been used for many organic synthesis reactions, including total synthesis of natural products.^{324–328} The advantages of using gold in homogeneous catalysis compared to other transition metals includes: its high atom economy, increased orthogonal reactivity, high functional group tolerance and compatibility in aqueous medium.³²⁵ Au(I) complexes have been used extensively in homogenous catalysis, with most reactions performed in air.¹⁷⁴ However, compared to metallic gold nanoparticles, both Au(I) and Au(III) species can precipitate from the reaction over time due to reduction of the Au centre; this is seen especially with Au(III) complexes.¹⁷⁴ Nevertheless, Au(I) and Au(III) catalysts are most commonly used in catalysis for activation of alkynes or heteroatoms due to their Lewis acidity.³²⁹

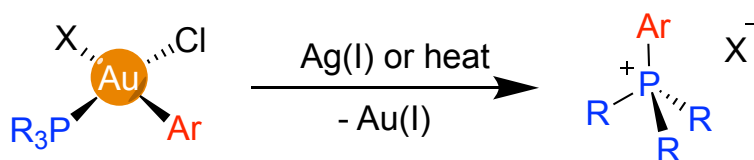
Another area of gold homogenous catalysis involves the ability of the gold complex to template cross-coupling reactions.³³⁰ The latter can be mediated by transition metals and generally proceed through three distinct steps: (i) an oxidative addition reaction of the metal, e.g. Au(I) to Au(III); (ii) transmetalation with a co-catalyst, often involving the transfer of an organic group; and (iii) reductive elimination to release the product with concurrent reduction of the metal, e.g. Au(III) to Au(I).³³⁰ This topic is still very much in its infancy; however, due to the high redox potential of the Au(I)/Au(III) couple, oxidative addition reactions can be particularly problematic and slow with Au(I) complexes.¹⁷⁵ Conversely, reductive elimination at Au(III) is more facile and can be used to form carbon-carbon and carbon-heteroatom bonds, including C-S, C-O and C-halide.³³⁰ Nevertheless, it should be noted that the carbon-carbon and carbon-heteroatom reductive elimination steps can be competitive, leading to poor selectivity for the desired product.³³⁰

Insights into the mechanism of the gold-catalysed cross-coupling reactions remain rare in the literature due to the requirement to isolate reaction intermediates which are often short-lived and highly reactive.³³¹ Therefore, ligands that can stabilise the Au(III) centre are required, such as cyclometalated ligands of the type: C[^]N, C[^]N[^]N, C[^]N[^]C and N[^]C[^]N, as described in Chapter 1.³³¹

The ability of cyclometalated Au(III) C[^]N complexes to mediate C-S bond formation *via* reductive elimination has been described by us in previous work^{305,308} and Chapter 5. Therefore, following these promising results, we decided to investigate a different type of reductive elimination reaction, namely carbon-phosphorus bond formation. Organophosphorus compounds are found in a wide array of different fields,

including: material science,³³² catalysis,³³³ medicine³³⁴ and chemical synthesis.³³⁵ Typically, organophosphorus compounds are formed by a C-P cross-coupling reaction catalysed by a transition metal complex, which is most commonly palladium,³³⁶ although nickel³³⁷ and copper³³⁸ have also been reported to effectively catalyse this reaction.

To the best of my knowledge, Toste and co-workers³³⁹ were the first authors to report a C-P reductive elimination reaction mediated by a gold(III) catalyst (Scheme 18). Several Au(III) complexes with the general formula [(R₃P)Au(aryl)ClX] (X = halide) were shown to undergo irreversible reductive elimination to form a phosphonium salt by C_{aryl}-P bond formation when reacted with silver salts or by thermolysis.³³⁹ Toste and co-workers also reported in earlier work that dual gold and photoredox catalysis could be used for C_{aryl}-P bond formation between aryldiazonium salts and *H*-phosphonates to yield arylphosphonates.³⁴⁰



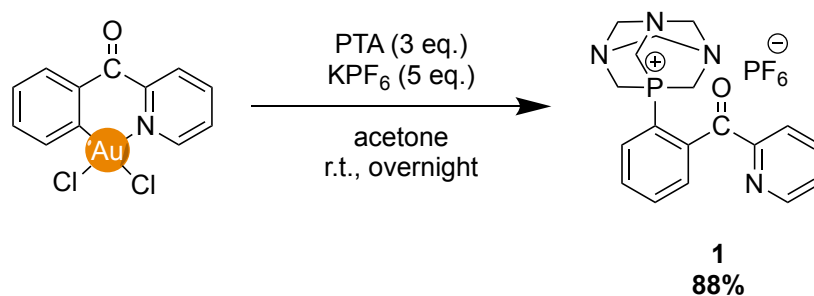
Scheme 18 – General reductive elimination reaction to form a C-P product mediated by a Au(III) aryl complex, reported by Toste and co-workers.³³⁹

At variance to the work by Toste and co-workers,³³⁹ we applied a similar approach that was used for our C-S reductive elimination work^{305,308} and remained in mild reaction conditions with Au(III) C^N cyclometalated complexes. Moreover, to gain more insight into the mechanism of this reaction we used *in situ* ³¹P{¹H} nuclear magnetic resonance (NMR) and high-resolution electrospray ionisation mass spectrometry (HR-ESI-MS) combined with density functional theory (DFT) calculations.

6.2. Results and Discussion

Computational analysis was completed by Prof. Giampaolo Barone. XRD (X-ray diffraction) analysis was performed by Dr. Wim T. Klooster. Dr. Robert L. Jenkins assisted in the ³¹P{¹H} NMR monitoring studies at 15 °C.

In this study, the [Au(C^ON)Cl₂] complex was first explored for C-P reductive elimination due to its previously reported ability to efficiently promote C-S cross-coupling reactions.³⁰⁵ The compound was reacted with 3 eq. of 1,3,5-triaza-7-phosphaadamantane (PTA) and 5 eq. of potassium hexafluorophosphate (KPF₆) in acetone at room temperature for 24 h (Scheme 19). After purification by column chromatography the clean product (**1**) was isolated with a yield of 88% and fully characterised by ¹H, ³¹P{¹H}, ¹³C{¹H} NMR, HR-ESI-MS and elemental analysis.



Scheme 19 – C-P bond formation via reductive elimination of a cyclometalated [Au(III)(C^{CO}N)Cl₂] complex with PTA in mild conditions.³⁴¹

Reducing the amount of PTA to 2 and 1 eq. resulted in a decrease in the yield of **1** to 49% and ca. 10%, respectively. Interestingly, the addition of 4 eq. of PTA did not improve the yield of **1**, suggesting that 3 eq. of PTA are involved in the reaction mechanism. The same optimised reaction was also explored with different counter ions, including BF₄⁻ (tetrafluoroborate), NO₃⁻ (nitrate) and B(C₆F₅)₄⁻ (tetrakis(pentafluorophenyl)borate). The results showed that the yield of product **1** decreased significantly with all anions compared to PF₆⁻. In detail, the yields decreased in the order: B(C₆F₅)₄⁻ (<20%) > BF₄⁻ (10%) > NO₃⁻ (<1%). A straightforward explanation could not be drawn for the trend observed, and many factors had to be considered, including: coordinating ability, sterics and solubility, to name a few. However, one explanation for the very poor performance of the nitrate counter ion could be that it is the most coordinating anion³⁴² investigated; thus, it could influence the reaction mechanism and prevent product formation. Nevertheless, more work is needed to investigate the role of the counter ion in this reaction and to provide an explanation for the overall trend observed.

Additionally, product **1** was obtained as colourless, needle-shaped crystals, grown from a solution of dichloromethane (CH₂Cl₂) and *n*-pentane. The resulting crystals were analysed by XRD studies to yield the expected structure of **1**, as can be seen in Figure 68. It should be noted that the distance from the oxygen to the phosphorus is quite short (2.752(2) Å),³⁴³ which is due to the quasi-coplanar position of the *ortho* C=O bond; therefore this could result in a O→P interaction as already observed in a palladium benzoyl phosphonium complex.³⁴⁴

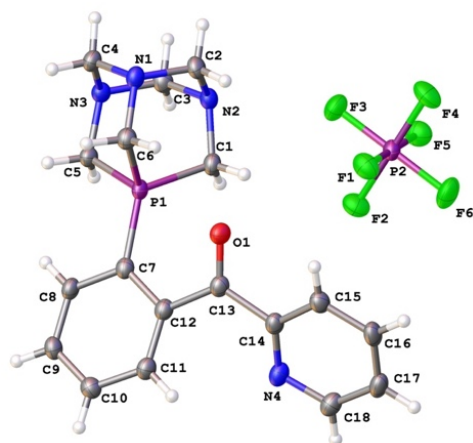


Figure 68 – Oak Ridge Thermal Ellipsoid Plot (ORTEP) to present the crystal structure of the phosphonium product **1**. Thermal ellipsoids are shown in 50% probability. Figure from ref 341.

Copyright 2020, John Wiley and Sons <https://creativecommons.org/licenses/by/4.0/>.³⁴¹

In order to gain an understanding of the mechanism involved for this reductive elimination reaction, the reaction was monitored by $^{31}\text{P}\{^1\text{H}\}$ NMR to provide simple, yet informative spectra. This was performed by adding the $[\text{Au}(\text{C}^{\text{O}}\text{N})\text{Cl}_2]$ (1 eq.) in acetone- d_6 to an NMR tube, along with PTA (3 eq.) and KPF_6 (5 eq.). Once the reagents had been suspended the NMR spectrum was immediately acquired; further spectra were measured after 1 h, then every 3 h for the subsequent 18 h, followed by a final measurement at 24 h (Figure 69).

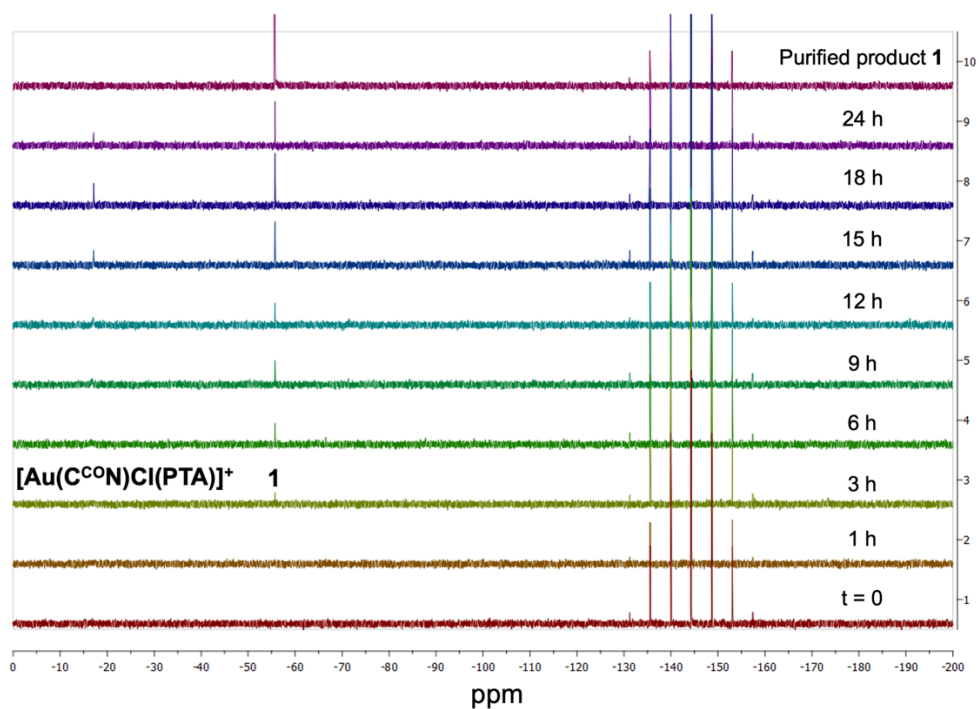


Figure 69 – $^{31}\text{P}\{^1\text{H}\}$ NMR spectra monitoring the reaction of $[\text{Au}(\text{C}^{13}\text{O})\text{Cl}_2]$ with PTA (3 eq.) and KPF_6 (5 eq.) in acetone- d_6 over 24 h at room temperature. The spectrum for the purified product **1** is also included for comparison. Figure reproduced from ref 341. Copyright 2020, John Wiley and Sons <https://creativecommons.org/licenses/by/4.0/>.³⁴¹

It should be noted that the heptet peak present across all spectra at -144.3 ppm corresponds to the PF_6^- counter ion. Comparing the spectrum of the purified product (**1**) to the $^{31}\text{P}\{^1\text{H}\}$ monitoring spectra (Figure 69), it can be seen that after 3 h the product is formed with a singlet peak at -55.7 ppm. This peak continues to increase in intensity over the reaction time. Additionally, another singlet peak can be identified at -17.1 ppm, which can be assigned as the $[\text{Au}(\text{C}^{13}\text{O})\text{Cl}(\text{PTA})]^+$ coordination product with the PTA ligand displacing the chloride, forming a bond to the Au atom. This was assigned as such due to the isolation of the similar $[\text{Au}(\text{C}^{\text{CH}_2}\text{N})\text{Cl}(\text{PTA})]^+$ coordination complex previously in our group.¹¹² After the 24 h reaction, the mixture was also directly measured by HR-ESI-MS (Figure 70). This further confirmed the presence of the reaction product (**1**) at 339.1515 m/z , as well as the coordination complex $[\text{Au}(\text{C}^{13}\text{O})\text{Cl}(\text{PTA})]^+$ at 571.0737 m/z .

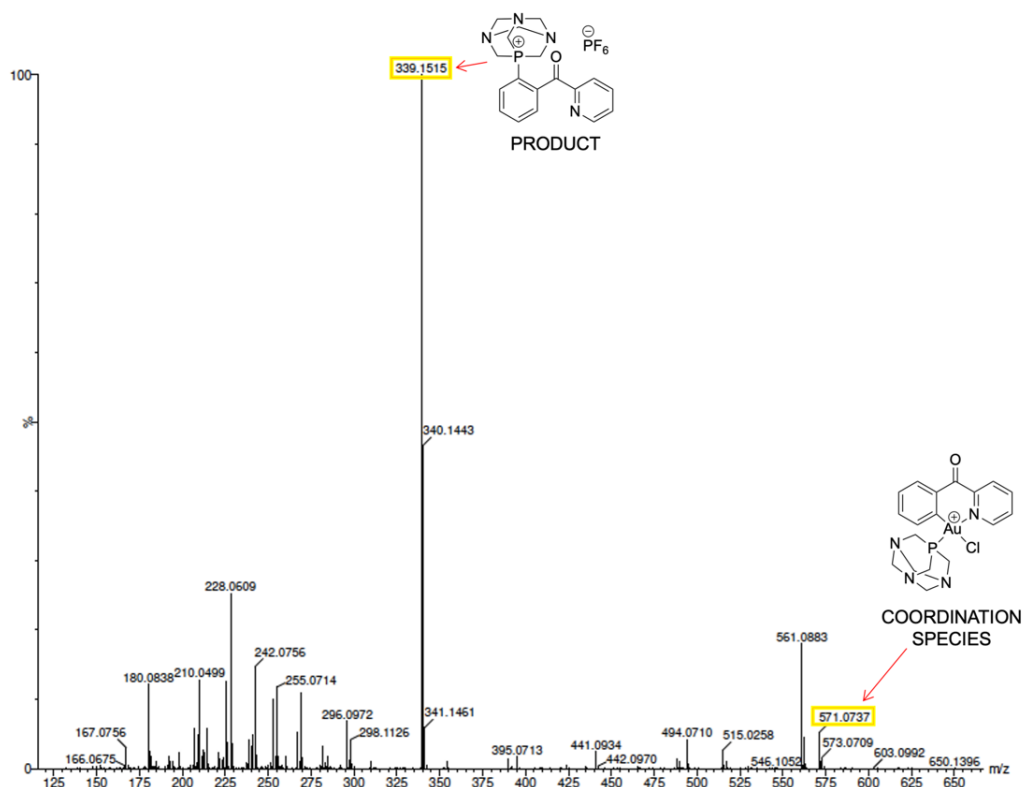


Figure 70 – HR-ESI-MS spectrum of the reaction mixture of $[\text{Au}(\text{C}^{\text{O}}\text{N})\text{Cl}_2]$ with PTA (3 eq.) and KPF_6 (5 eq.) in acetone- d_6 over 24 h. Figure reproduced from ref 341. Copyright 2020, John Wiley and Sons <https://creativecommons.org/licenses/by/4.0/>.³⁴¹

Additionally, the reaction was performed in water to test the potential of this reaction in even milder conditions, which could provide promise for future biocompatible transformations. Remarkably, the product (**1**) was formed over 24 h with a yield of 70% after column chromatography, which is only a slight decrease compared to the yield obtained in acetone (88%).

In order to rationalise the mechanism to form **1**, DFT calculations were performed by Prof. Giampaolo Barone in acetone for the reaction between the $[\text{Au}(\text{C}^{\text{O}}\text{N})\text{Cl}_2]$ complex and PTA, the PF_6^- counter ion was not included. Using the knowledge we had gained from our previous C-S reductive elimination work,³⁰⁵ and the experimental results obtained by the $^{31}\text{P}\{^1\text{H}\}$ NMR monitoring experiment and subsequent HR-ESI-MS; the first step was predicted to involve the coordination of the PTA to the gold(III) centre by displacement of a chloride ligand forming the coordination complex $[\text{Au}(\text{C}^{\text{O}}\text{N})\text{Cl}(\text{PTA})]^+$. As previously observed,³⁰⁵ the stereoisomer with substitution of the chloride *trans* to the pyridyl N is the more thermodynamically stable product (**R1** SP-4-4, Figure 71) by -52.3 kJ/mol. This arrangement also favours the desired reductive elimination product (**1**), where the aryl group and phosphine are *cis* to each other.

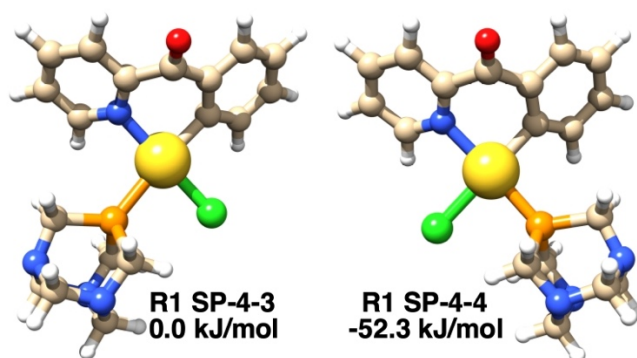


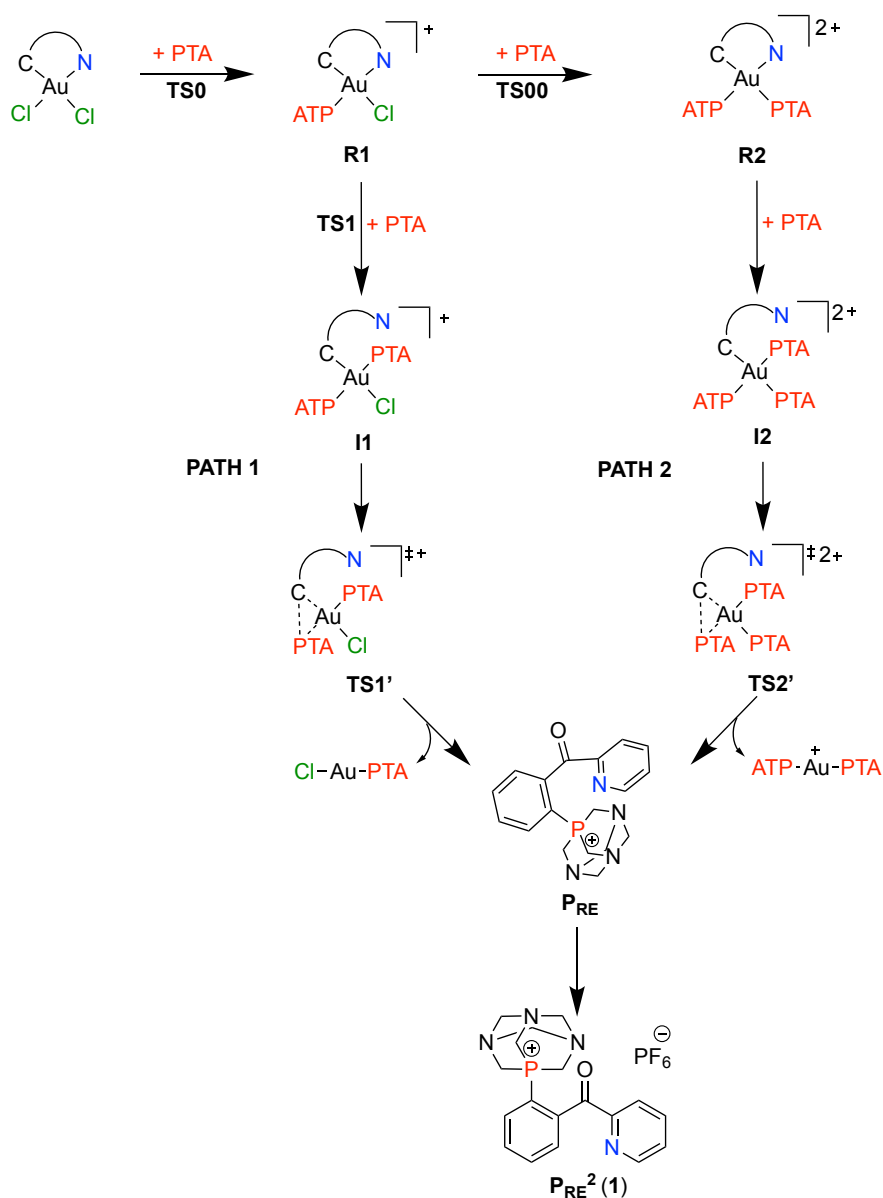
Figure 71 – Structure and relative stability of the two possible stereoisomers of the $[Au(C^{CO}N)Cl(PTA)]^+$ complexes (**R1**) in acetone, attained by DFT calculations. Figure from ref 341. Copyright 2020, John Wiley and Sons <https://creativecommons.org/licenses/by/4.0/>.³⁴¹

The proposed mechanism for C-P formation can be seen in Scheme 20. As described above, the first step involves the substitution of the chloride, *trans* to the pyridyl N, with a molecule of PTA to form **R1**. This step is exergonic and proceeds *via* **TS0** with an activation energy barrier of only 13 kJ/mol to form **R1** and Cl⁻, which is -71.4 kJ/mol more thermodynamically stable than the Au(III) precursor, $[Au(C^{CO}N)Cl_2]$.

Following the formation of **R1**, the next step can progress *via* two different pathways, both involving the addition of another molecule of PTA. Path 1 proceeds *via* **TS1** with a very low activation energy barrier ($E_1^\ddagger = 0.4$ kJ/mol) to form **I1**, involving the coordination of the 2nd PTA that instigates decoordination of the pyridyl N. This is also exergonic in nature ($\Delta E = -61.3$ kJ/mol) and therefore favourable. Path 2 involves the substitution of the 2nd chloride ligand with the 2nd PTA to form **R2** *via* **TS00**, which has a low activation barrier of only 8 kJ/mol. **R2** is slightly more stable than **R1** ($\Delta E = -4.3$ kJ/mol), suggesting its formation is more favoured in excess of PTA. **R2** can then form **I2** upon coordination of a 3rd PTA molecule by an exergonic reaction ($\Delta E = -45.1$ kJ/mol), which results in decoordination of the pyridyl N.

Interestingly, a transition state could not be identified for the formation of **I2** from **R2**. However, it should be noted that the absence of an activation energy barrier for a reaction step is not uncommon, especially for metal complexes, and could be explained by a number of factors, including: elevated leaving group lability, a favourable interaction energy between the two atoms being coupled, and large strain and steric effects between substituents in a transition state.^{345–348}

Nevertheless, both **I1** and **I2** can form the reductive elimination product (**1**) *via* **TS1'** and **TS2'**, respectively; however, the activation energy barrier is considerably higher for **TS1'** ($E_1'^\ddagger = 89.2$ kJ/mol and $E_2'^\ddagger = 55.5$ kJ/mol), suggesting that it is less favoured.



Scheme 20 – A hypothesised mechanism for the C-P reductive elimination reaction between $[Au(C^{C^O}N)Cl_2]$ and PTA to form **1**.³⁴¹

The reductive elimination product initially formed (P_{RE}) must undergo rotation of the CO-phenyl bond as can be seen in Figure 72, to yield the desired product **1** that was identified by X-ray crystallography (Figure 68). This rotation formed the more thermodynamically stable conformer P_{RE}^2 ($\Delta E = -18.3$ kJ/mol, Figure 72) with a calculated distance of 2.66 Å between the oxygen and phosphorus, which is comparable to the distance observed in the XRD structure (Figure 68).

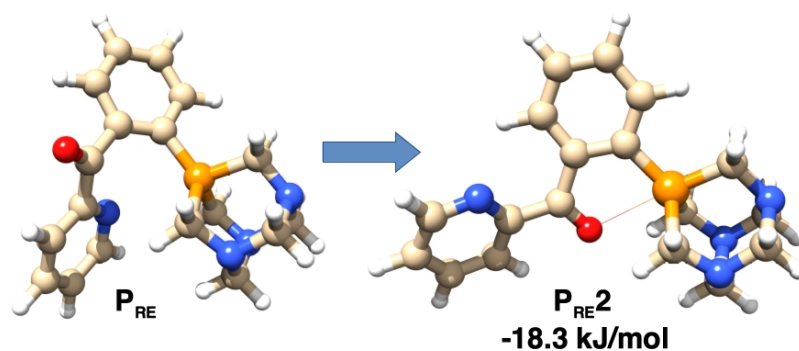


Figure 72 – Structure and relative stability obtained by DFT calculations after rotation of the CO-phenyl bond in P_{RE} to form P_{RE}^2 (**1**). Figure from ref 341. Copyright 2020, John Wiley and Sons <https://creativecommons.org/licenses/by/4.0/>.³⁴¹

It should be highlighted that the relative energy of P_{RE} obtained by each pathway also includes the Au(I) side product formed. In the case of pathway 1, the relative energy of P_{RE} and $[Au(PTA)Cl]$ is -99.8 kJ/mol, whereas for pathway 2, the relative energy of P_{RE} and $[Au(PTA)_2]^+$ is -153.5 kJ/mol, highlighting that the product of pathway 2 is more thermodynamically favoured. The overall energies and structures of the species involved in the two reaction pathways can be seen in Figure 73, which led us to conclude that pathway 2 was more favourable, as not only was **R2** more thermodynamically stable than **R1**, but the rest of the steps and species formed were of lower energy, apart from the **I2** species.

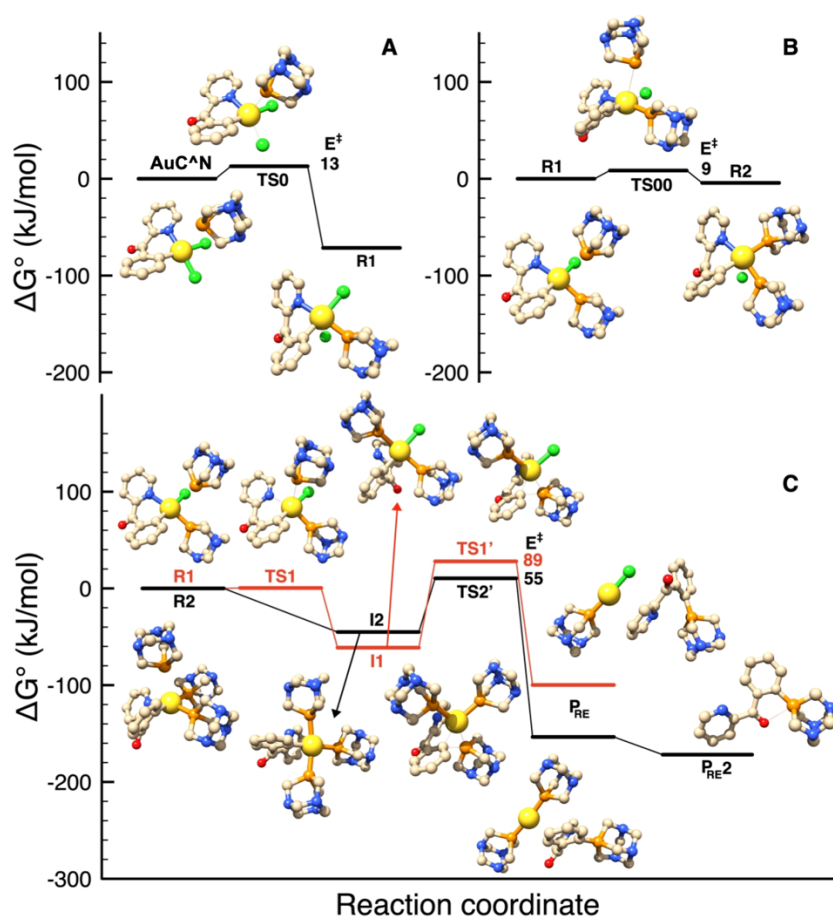
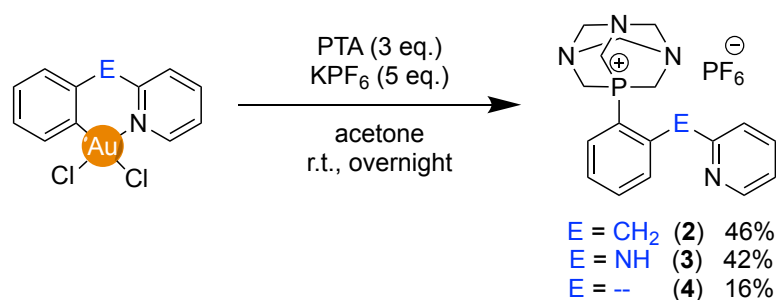


Figure 73 – Relative energies and structures, obtained by DFT calculations, of the species involved in the C-P cross-coupling reaction via reductive elimination, beginning with the Cl/PTA substitution of $[\text{Au}(\text{C}^{\text{O}}\text{N})\text{Cl}_2]$ to form (A) R1 or (B) R2, (C) which can both then undergo reductive elimination to yield the product P_{RE}^2 (1). Figure reproduced from ref 341. Copyright 2020, John Wiley and Sons <https://creativecommons.org/licenses/by/4.0/>.³⁴¹

Furthermore, to evaluate the reaction scope of the C-P cross-coupling reaction, three other Au(III) C^N cyclometalated complexes were tested to mediate this reaction with PTA, namely: $[\text{Au}(\text{C}^{\text{CH}_2\text{N}})\text{Cl}_2]$ ($\text{C}^{\text{CH}_2\text{N}}$ = 2-benzylpyridine), $[\text{Au}(\text{C}^{\text{NH}^{\text{N}}})\text{Cl}_2]$ ($\text{C}^{\text{NH}^{\text{N}}}$ = *N*-phenylpyridin-2-amine) and $[\text{Au}(\text{C}^{\text{N}})\text{Cl}_2]$ (C^{N} = 2-phenylpyridinato), which were also evaluated in the C-S cross-coupling reaction (Chapter 5).³⁰⁵ Each of the complexes were reacted in the same conditions used for the $[\text{Au}(\text{C}^{\text{O}}\text{N})\text{Cl}_2]$ complex and purified by column chromatography after 24 h (Scheme 21).



Scheme 21 - C-P cross-coupling reaction via reductive elimination with PTA, KPF₆ and different Au(III) cyclometalated C^N complexes to yield the products **2-4** in mild conditions.³⁴¹

In all cases the phosphonium products were formed (**2-4**) and fully characterised, including X-ray diffraction analysis for products **2** and **3** (Figure 74). Interestingly, a second species could be identified with the crystals of **2**: the Au(I) side product [Au(PTA)₂][PF₆], which we postulated to be the Au(I) side product of the more thermodynamically favoured pathway **2**, providing further evidence for its preference. However, the yield of product (**2-4**) varied across the three complexes. The [Au(C^{CH₂N})Cl₂] complex showed the greatest yield of 46%; which decreased slightly to 42% for the [Au(C^{NH}N)Cl₂] complex, and lastly, the [Au(C^N)Cl₂] complex showed an even larger drop in yield to 16%. This follows the same trend in reactivity observed for the C-S reductive elimination reaction.³⁰⁵

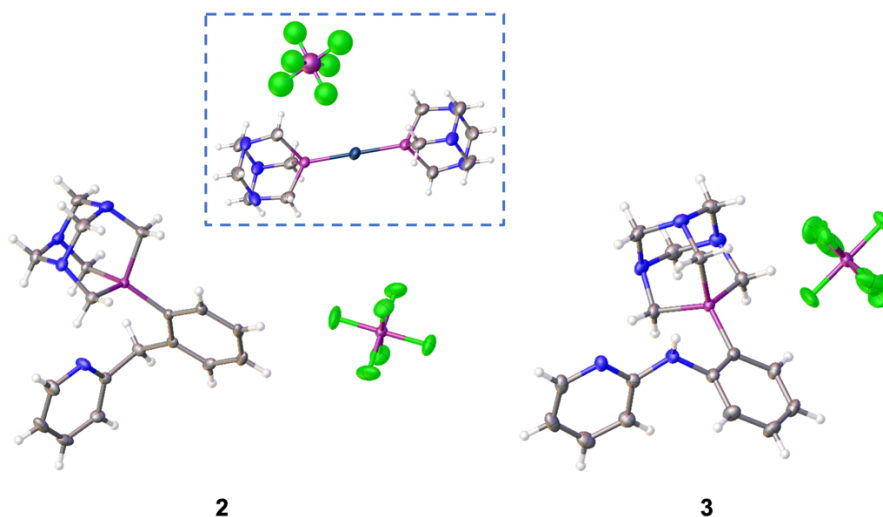


Figure 74 - ORTEP to present the crystal structure of the phosphonium products **2** and **3**. Insert: [Au(PTA)₂][PF₆] side product obtained in combination with **2**. Thermal ellipsoids are shown in 50% probability. Figure reproduced from ref 341. Copyright 2020, John Wiley and Sons

<https://creativecommons.org/licenses/by/4.0/>.³⁴¹

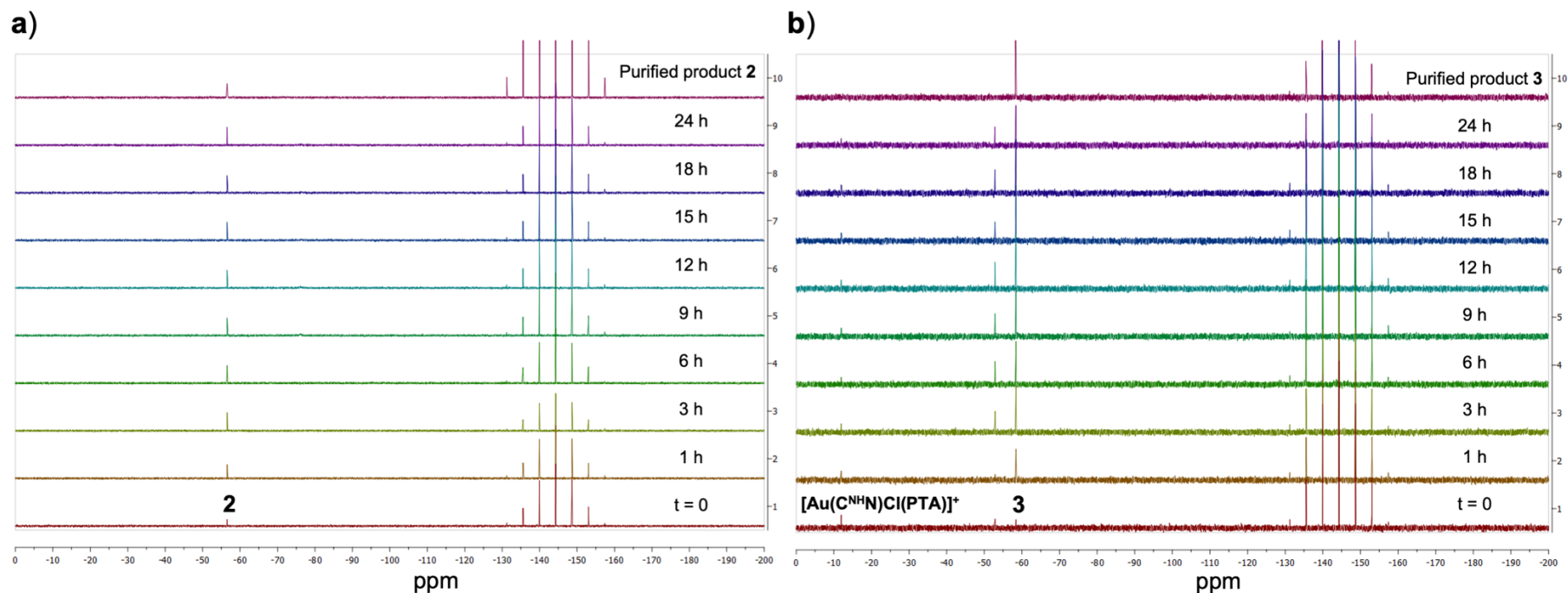


Figure 75 - $^{31}\text{P}\{^1\text{H}\}$ NMR spectra monitoring the reaction of a) $[\text{Au}(\text{C}^{\text{CH}_2\text{N}})\text{Cl}_2]$ and b) $[\text{Au}(\text{C}^{\text{NH N}})\text{Cl}_2]$, with PTA (3 eq.) and KPF_6 (5 eq.) in acetone- d_6 over 24 h at room temperature. The spectrum of the purified product is also included in both spectra for comparison. Partial figure reproduced from ref 341. Copyright 2020, John

Wiley and Sons <https://creativecommons.org/licenses/by/4.0/>.³⁴¹

The $^{31}\text{P}\{^1\text{H}\}$ NMR monitoring experiment was also performed with the $[\text{Au}(\text{C}^{\text{CH}_2}\text{N})\text{Cl}_2]$ and $[\text{Au}(\text{C}^{\text{NH}}\text{N})\text{Cl}_2]$ complexes (Figure 75) using the same procedure previously used. Remarkably, the reaction of $[\text{Au}(\text{C}^{\text{CH}_2}\text{N})\text{Cl}_2]$ with 3 eq. of PTA (Figure 75a) formed the phosphonium product **2** (-56.6 ppm) almost instantaneously at time 0, and remained the only peak present in the spectra over 24 h, apart from the PF_6^- peak at -144.3 ppm.

The $^{31}\text{P}\{^1\text{H}\}$ NMR monitoring experiment with the $[\text{Au}(\text{C}^{\text{NH}}\text{N})\text{Cl}_2]$ complex (Figure 75b) showed two other species, in addition to the peak for the product (**3**) at -58.4 ppm and PF_6^- . The peak at -11.9 ppm could be assigned to the coordination species $[\text{Au}(\text{C}^{\text{NH}}\text{N})\text{Cl}(\text{PTA})]^+$, which was also observed with the $[\text{Au}(\text{C}^{\text{CO}}\text{N})\text{Cl}_2]$ complex and with $[\text{Au}(\text{C}^{\text{CH}_2}\text{N})\text{Cl}_2]$ previously.¹¹² The other peak at -52.9 ppm appeared at time 0, increased in concentration up to 3 h, then remained stable over the 24 h. The environment of this phosphorus appeared to be similar to the product **3**, suggesting that it is not bound to Au, as is observed for the coordination product at -11.9 ppm. In order to try and understand the identity of the specie, HR-ESI-MS was performed on both reaction mixtures (Figure 76).

The HR-ESI-MS spectrum for the reaction of $[\text{Au}(\text{C}^{\text{CH}_2}\text{N})\text{Cl}_2]$ and PTA (Figure 76a) showed **2** as the predominant species at 325.1707 m/z , as well as an additional peak at 511.1231 m/z , which was identified as the $[\text{Au}(\text{PTA})_2]^+$ side product of the reaction proceeding *via* pathway 2 and isolated as a crystal (Figure 74) in the presence of **2**. Conversely, the HR-ESI-MS spectrum for the reaction of $[\text{Au}(\text{C}^{\text{NH}}\text{N})\text{Cl}_2]$ and PTA (Figure 76b) showed product **3** in a relatively low amount (326.1561 m/z), as well as the coordination complex $[\text{Au}(\text{C}^{\text{NH}}\text{N})\text{Cl}(\text{PTA})]^+$ at 558.0894 m/z . Unfortunately, the species present in the $^{31}\text{P}\{^1\text{H}\}$ NMR spectrum at -52.9 ppm could not be identified.

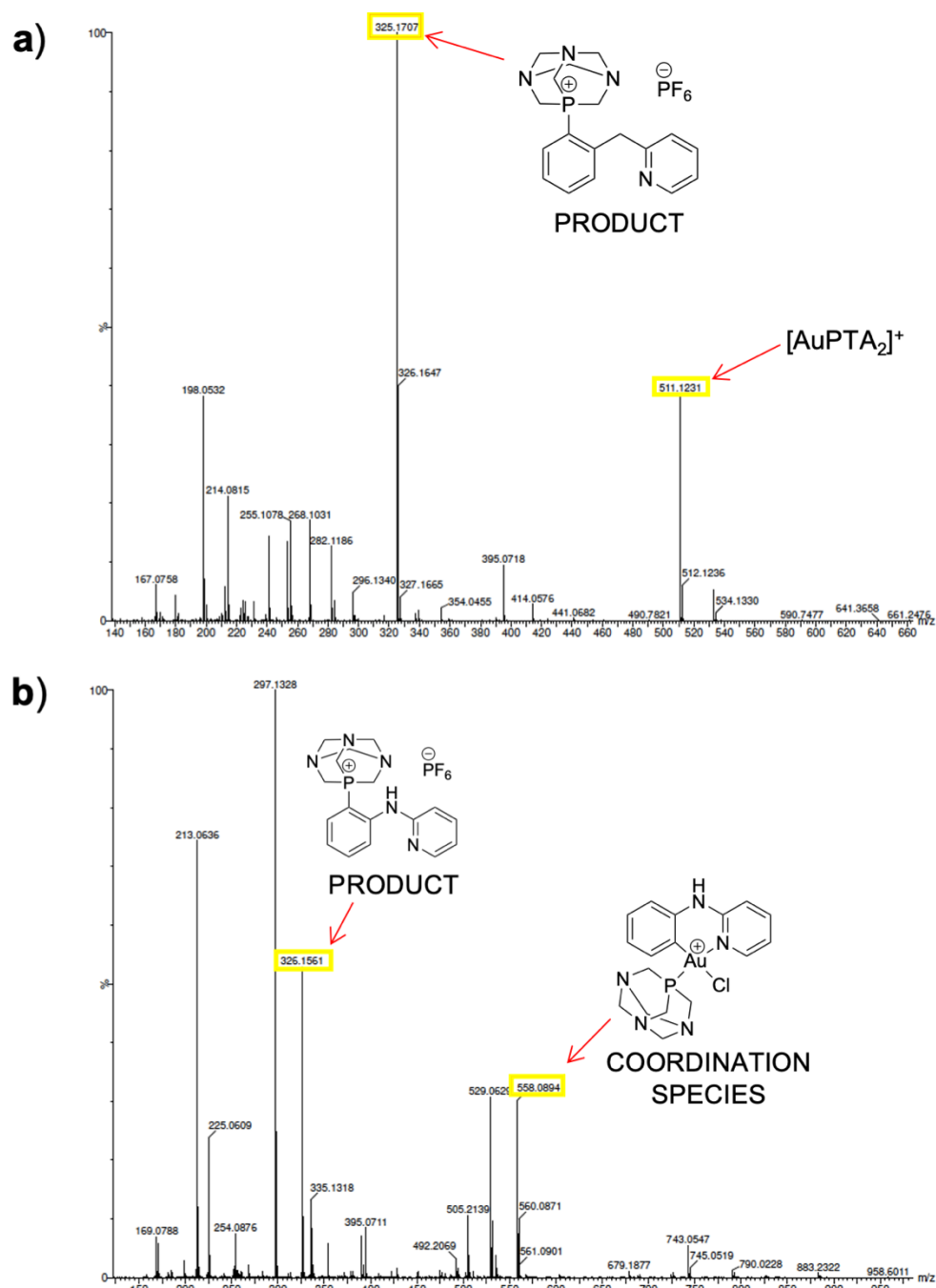


Figure 76 - HR-ESI-MS spectrum of the reaction mixture of **a)** $[\text{Au}(\text{C}^{\text{CH}_2\text{N}})\text{Cl}_2]$ and **b)** $[\text{Au}(\text{C}^{\text{NH}})\text{Cl}_2]$ with PTA (3 eq.) and KPF_6 (5 eq.) in acetone- d_6 over 24 h. Partial figure reproduced from ref 341. Copyright 2020, John Wiley and Sons
<https://creativecommons.org/licenses/by/4.0/>.³⁴¹

To further elucidate the intermediates present in the $[\text{Au}(\text{C}^{\text{CH}_2\text{N}})\text{Cl}_2]$ and PTA reaction, the $^{31}\text{P}\{^1\text{H}\}$ NMR monitoring experiment was repeated at a lower temperature (15 °C), and the spectra were obtained with shorter time intervals (every 5 min over 100 min). The resulting spectra (Figure 77) showed an additional species present at -16.1 ppm at time 0, which can be confidently assigned as the coordination complex, $[\text{Au}(\text{C}^{\text{CH}_2\text{N}})\text{Cl}(\text{PTA})]^+$, previously reported.¹¹² The coordination complex decreased in intensity over time, whereas the C-P product peak (**2**) increased, providing further

evidence that the coordination peak is an intermediate to form the final product (Figure 77). This was also confirmed by synthesising and isolating the $[\text{Au}(\text{C}^{\text{CH}_2\text{N}})\text{Cl}(\text{PTA})]^+$ complex following the literature procedure,¹¹² and then reacting it with PTA (2 eq.) and KPF_6 (5 eq.) in acetone for 24 h. This resulted in the formation of the C-P product (**2**) with a 74% yield, which is greater than the yield obtained using the original synthetic approach (46%), and no further purification was required.

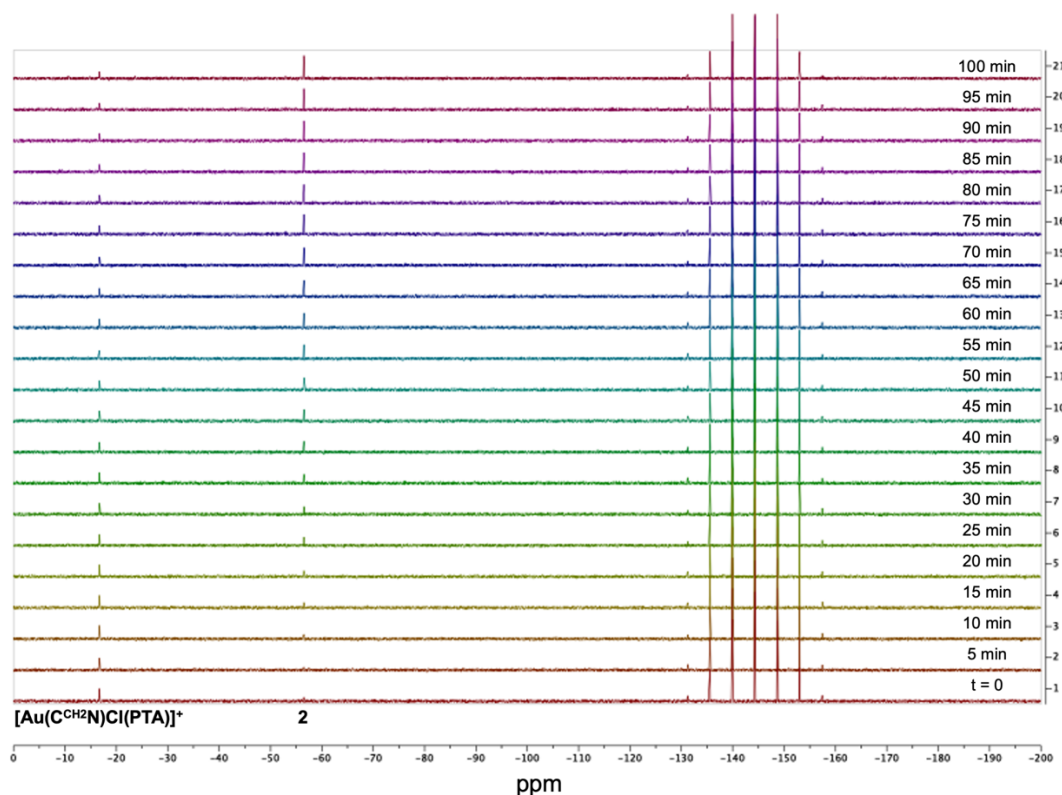


Figure 77 - $^{31}\text{P}\{^1\text{H}\}$ NMR spectra monitoring the reaction of $[\text{Au}(\text{C}^{\text{CH}_2\text{N}})\text{Cl}_2]$ with PTA (3 eq.) and KPF_6 (5 eq.) in acetone- d_6 over 100 min at 15 °C. Figure reproduced from ref 341. Copyright 2020, John Wiley and Sons <https://creativecommons.org/licenses/by/4.0/>.³⁴¹

Additional studies were also performed to extend the scope of the reaction to different phosphines. Preliminary experiments were performed using other tertiary phosphines, namely: triphenylphosphine, tri-*n*-butylphosphine and tris(hydroxypropyl)phosphine; which were reacted in 3 eq. with the $[\text{Au}(\text{C}^{\text{CO}}\text{N})\text{Cl}_2]$ complex (1 eq.) and KPF_6 (5 eq.) in acetone for 24 h at room temperature. The C-P reductive elimination product was observed with all phosphines by $^{31}\text{P}\{^1\text{H}\}$ NMR and HR-ESI-MS. In addition, HR-ESI-MS also showed the presence of different Au intermediates. However, the purification of the products proved challenging in all cases due to the low yield of reductive elimination products formed and the similar hydrophilic/lipophilic character of the product and intermediates, meaning separation by chromatography could not be achieved. Therefore, the C-P reductive elimination reaction with different phosphines requires

further optimisation. Nevertheless, the C-P reductive elimination products can be clearly identified by $^{31}\text{P}\{^1\text{H}\}$ NMR,³⁴⁹ as can be seen in Figure 78, with the corresponding product structure.

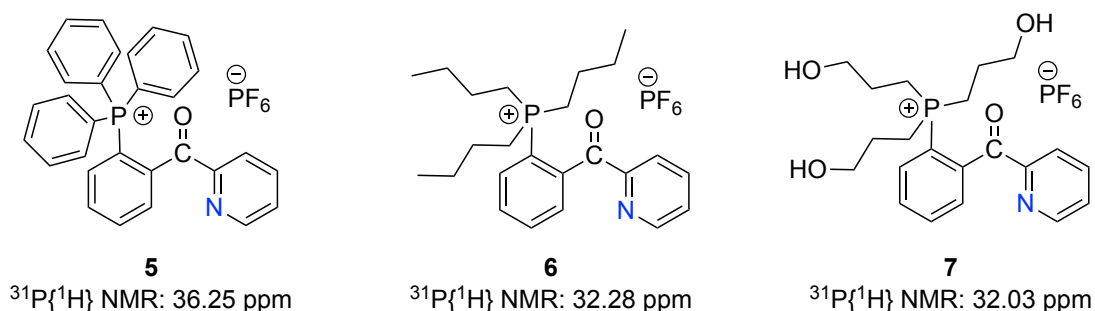


Figure 78 - Structures of the C-P reductive elimination products obtained using triphenylphosphine (**5**), tri-*n*-butylphosphine (**6**) and tris(hydroxypropyl)phosphine (**7**), as well as their corresponding peak identified by $^{31}\text{P}\{^1\text{H}\}$ NMR.³⁴¹

Interestingly, during the reaction with triphenylphosphine to form **5**, a crystal of the intermediate $[\text{Au}(\text{C}^{\text{O}}\text{N})\text{Cl}(\text{PPh}_3)_2][\text{PF}_6]$, with nitrogen decoordination, was isolated and analysed by XRD to obtain the structure shown in Figure 79. A species of this type (**11**) was postulated to be formed during pathway 1, as seen in Scheme 20 and Figure 73.

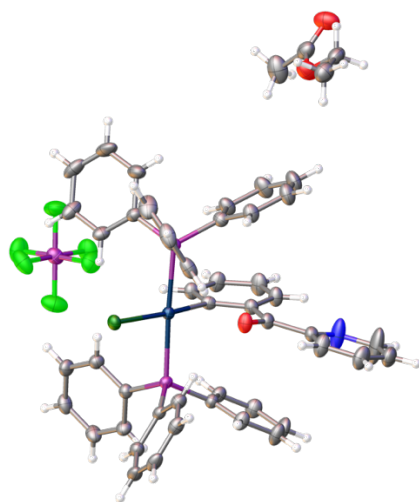


Figure 79 - ORTEP of intermediate **11** $[\text{Au}(\text{C}^{\text{O}}\text{N})\text{Cl}(\text{PPh}_3)_2][\text{PF}_6]$ with a molecule of ethyl acetate. Thermal ellipsoids drawn at the 50% probability level. Figure from ref 341. Copyright 2020, John Wiley and Sons <https://creativecommons.org/licenses/by/4.0/>.³⁴¹

6.3. Summary and Future Outlook

Overall, in this work we have provided further evidence for the effectiveness of Au(III) C[^]N cyclometalated complexes in cross-coupling reactions, namely C-P bond formation *via* reductive elimination. This reaction was optimised for the coupling of $[\text{Au}(\text{C}^{\text{O}}\text{N})\text{Cl}_2]$

and PTA, with KPF_6 as a counter ion source, which resulted in a high yield of the phosphonium product in mild conditions, including in water. Using DFT calculations, $^{31}\text{P}\{^1\text{H}\}$ NMR monitoring and HR-ESI-MS we could identify possible intermediates of the reaction, and a hypothesis on the overall mechanism could be made.

Additionally, we further explored the effect of the different ligand scaffold on the reactivity of the gold C^N complexes, which was found to follow the same trend observed in our previous work for C-S cross-coupling.³⁰⁵ Although further optimisation is required, we have demonstrated that this reaction can be applied to other tertiary phosphines generating phosphonium salts. The synthesis of phosphonium salts is relatively scarce in the literature, mostly involving group 10 metals such as copper,³⁵⁰ whereas metal catalysed C-P bond formation generally results in the synthesis of phosphines, phosphites and phosphinates.^{351–353}

The future outlook of this project involves further exploration into the different factors involved in the reaction, including: the cyclometalated ligand scaffold, counter-ion, solvent and phosphorus source, and how each of these can affect the overall efficiency of this reaction. Furthermore, employing a C-P cross-coupling reaction within biological media could be envisaged, such as C-P bond formation between two non-toxic substrates *in situ* to form a toxic drug molecule, as many clinical drugs contain carbon-phosphorus bonds.³⁵⁴

6.4. Materials and Methods

6.4.1. General

Computational analysis was completed by Prof. Giampaolo Barone. XRD analysis was performed by Dr. Wim T. Klooster. Dr. Robert L. Jenkins assisted in the $^{31}\text{P}\{^1\text{H}\}$ NMR monitoring studies at 15 °C.

Solvents and reagents (reagent grade) were all commercially available and used without further purification. ^1H , $^{13}\text{C}\{^1\text{H}\}$ and $^{31}\text{P}\{^1\text{H}\}$ NMR spectra were recorded in acetone- d_6 solution, with TMS as an internal reference, on Bruker Avance (400-500 MHz) NMR spectrometers. HR-ESI-MS spectra were recorded on a Synapt G2-Si time-of-flight (TOF) mass spectrometer (Waters). Mass spectra were acquired and processed using MassLynx V4.1 (Waters). The synthesis of the Au(III) cyclometalated complexes: $[\text{Au}(\text{C}^{\text{CO}}\text{N})\text{Cl}_2]$, $[\text{Au}(\text{C}^{\text{CH}_2}\text{N})\text{Cl}_2]$, $[\text{Au}(\text{C}^{\text{NH}}\text{N})\text{Cl}_2]$ and $[\text{Au}(\text{C}^{\text{N}})\text{Cl}_2]$ can be found in Chapter 5.

6.4.2. Synthesis of C-P Reductive Elimination Products

The $\text{Au}(\text{C}^{\text{N}})\text{Cl}_2$ complex (40 mg, 0.09 mmol, 1 eq.) was suspended in acetone (6 mL), before the addition of KPF_6 (84 mg, 0.44 mmol, 5 eq.) and PTA (43 mg, 0.27 mmol, 3 eq.). This mixture was then stirred overnight at room temperature. Once the reaction was complete, the solvent was removed under vacuum, prior to re-suspension of the crude product in CH_2Cl_2 . This was then filtered and the filtrate was purified by flash column chromatography ($\text{CH}_2\text{Cl}_2:\text{CH}_3\text{OH}$) (CH_3OH = methanol) gradient from 100:0 to 85:15, respectively) to obtain the product.

1 (Yellow solid, 38 mg, 88%)

^1H NMR (400 MHz, Acetone- d_6) δ 8.87 – 8.80 (m, 2H, ar), 8.31 – 8.26 (m, 1H, ar), 8.20 (td, J = 7.7, 1.7 Hz, 1H, ar), 8.08 – 8.00 (m, 3H, ar), 7.80 (ddd, J = 7.6, 4.7, 1.3 Hz, 1H, ar), 5.17 (d, J = 6.7 Hz, 6H, CH_2), 4.84 – 4.69 (m, 6H, CH_2).

$^{13}\text{C}\{^1\text{H}\}$ NMR (126 MHz, Acetone- d_6) δ 194.32 (d, J = 2.2 Hz, CO), 154.08 (s, ar), 149.85 (s, ar), 139.65 (d, J = 4.2 Hz, ar), 138.82 (s, ar), 137.29 (d, J = 8.2 Hz, ar), 136.22 (d, J = 9.4 Hz, ar), 135.08 (d, J = 3.3 Hz, ar), 134.92 (d, J = 12.8 Hz, ar), 128.78 (s, ar), 126.70 (s, ar), 122.28 (d, J = 56.7 Hz, ar), 72.65 (d, J = 10.0 Hz, CH_2), 51.78 (d, J = 32.3 Hz, CH_2).

$^{31}\text{P}\{^1\text{H}\}$ NMR (162 MHz, Acetone- d_6) δ -55.67 (s, PTA), -144.26 (hept, J = 707.6 Hz, PF_6)

ESI-MS (CH_3CN , pos. mode) for $[\text{C}_{18}\text{H}_{20}\text{N}_4\text{OP}]^+$: exp. 339.1375 (calc. 339.1382). Elemental analysis for $\text{C}_{18}\text{H}_{22}\text{F}_6\text{N}_4\text{O}_2\text{P}_2$ (**1**+ H_2O): exp. C 43.30%, H 3.90%, N 11.30% (calc. C 43.04%, H 4.41%, N 11.15%).

2 (White solid, 20 mg, 46%).

^1H NMR (400 MHz, Acetone- d_6) δ 8.76 – 8.73 (m, 1H, ar), 7.98 (ddd, $J = 14.3, 7.9, 0.8$ Hz, 1H, ar), 7.84 (td, $J = 7.7, 1.8$ Hz, 1H, ar), 7.75 – 7.66 (m, 1H, ar), 7.63 – 7.59 (m, 1H, ar), 7.59 – 7.53 (m, 2H, ar), 7.33 (ddd, $J = 7.6, 4.9, 1.2$ Hz, 1H, ar), 5.26 (d, $J = 6.3$ Hz, 6H, CH₂), 4.77 (s, 6H, CH₂), 4.29 (s, 2H, CH₂).

$^{13}\text{C}\{^1\text{H}\}$ NMR (126 MHz, Acetone- d_6) δ 159.23 (s, ar), 150.46 (s, ar), 146.12 (d, $J = 8.0$ Hz, ar), 138.79 (s, ar), 135.57 (d, $J = 3.5$ Hz, ar), 133.09 (d, $J = 25.4$ Hz, ar), 133.07 (d, $J = 3.0$ Hz, ar), 128.65 (d, $J = 12.7$ Hz, ar), 124.52 (s, ar), 123.27 (s, ar), 120.56 (d, $J = 58.6$ Hz, ar), 72.46 (d, $J = 9.8$ Hz, CH₂), 52.10 (d, $J = 31.0$ Hz, CH₂), 43.32 (d, $J = 3.4$ Hz, CH₂).

$^{31}\text{P}\{^1\text{H}\}$ NMR (162 MHz, Acetone- d_6) δ -56.55 (s, PTA), -144.32 (hept, $J = 707.4$ Hz, PF₆). ESI-MS (CH₃CN, pos. mode) for [C₁₈H₂₂N₄P]⁺: exp. 325.2334 (calc. 325.1582). Elemental analysis for C₁₈H₂₂F₆N₄P₂: exp. C 45.98%, H 4.40%, N 11.75% (calc. C 45.97%, H 4.71%, N 11.91%)

3 (Brown solid, 18 mg, 42%)

^1H NMR (400 MHz, Acetone- d_6) δ 8.30 (s, 1H, NH), 8.24 (d, $J = 3.9$ Hz, 1H, ar), 7.89 (dd, $J = 13.8, 7.8$ Hz, 1H, ar), 7.81 (ddd, $J = 9.2, 3.2, 1.6$ Hz, 1H, ar), 7.77 – 7.70 (m, 1H, ar), 7.59 – 7.44 (m, 2H, ar), 6.97 (dd, $J = 7.5, 4.4$ Hz, 2H, ar), 4.97 (d, $J = 6.8$ Hz, 6H, CH₂), 4.71 – 4.56 (m, 6H, CH₂).

$^{13}\text{C}\{^1\text{H}\}$ NMR (126 MHz, Acetone- d_6) δ 158.61 (s, ar), 148.48 (s, ar), 147.30 (s, ar), 139.74 (s, ar), 136.82 (d, $J = 3.1$ Hz, ar), 133.40 (d, $J = 9.9$ Hz, ar), 128.76 (s, ar), 127.46 (d, $J = 12.3$ Hz, ar), 118.78 (s, ar), 117.81 (s, ar), 111.78 (s, ar), 72.42 (d, $J = 9.9$ Hz, CH₂), 50.96 (d, $J = 32.9$ Hz, CH₂).

$^{31}\text{P}\{^1\text{H}\}$ NMR (162 MHz, Acetone- d_6) δ -58.38 (s, PTA), -144.24 (hept, $J = 707.7$ Hz, PF₆). ESI-MS (CH₃CN, pos. mode) for [C₁₇H₂₁N₅P]⁺: exp. 326.1535 (calc. 326.1563). Elemental analysis for C₁₇H₂₁F₆N₅P₂: exp. C 43.23%, H 4.45%, N 14.20% (calc. C 43.32%, H 4.49%, N 14.86%).

4 (White solid, 7 mg, 16%)

^1H NMR (400 MHz, Acetone- d_6) δ 9.20 – 9.15 (m, 1H, ar), 8.23 (dd, $J = 6.8, 5.1$ Hz, 1H, ar), 8.17 (d, $J = 8.1$ Hz, 1H, ar), 8.07 (td, $J = 8.0, 1.7$ Hz, 1H, ar), 7.88 – 7.77 (m, 2H, ar), 7.71 – 7.65 (m, 1H, ar), 7.61 (ddd, $J = 7.5, 4.9, 1.0$ Hz, 1H, ar), 4.91 (d, $J = 6.4$ Hz, 6H, CH₂), 4.59 (q, $J = 13.3$ Hz, 6H, CH₂).

$^{13}\text{C}\{^1\text{H}\}$ NMR (126 MHz, Acetone- d_6) δ 153.93 (s, ar), 149.09 (s, ar), 144.45 (d, $J = 3.8$ Hz, ar), 140.45 (s, ar), 136.34 (d, $J = 10.7$ Hz, ar), 135.99 (d, $J = 3.4$ Hz, ar), 131.18 (d,

$J = 13.1$ Hz, ar), 129.76 (d, $J = 9.3$ Hz, ar), 126.16 (s, ar), 122.70 (s, ar), 118.36 (d, $J = 62.8$ Hz, ar), 72.77 (d, $J = 9.9$ Hz, CH₂), 54.26 (d, $J = 34.9$ Hz, CH₂).

³¹P{¹H} NMR (162 MHz, Acetone-*d*₆) δ -60.55 (s, PTA), -144.25 (hept, $J = 707.5$ Hz, PF₆). ESI-MS (CH₃CN, pos. mode) for [C₁₇H₂₀N₄P]⁺: exp. 311.1500 (calc. 311.1425). Elemental analysis for C₂₃H₃₂F₆N₄O₂P₂ (4+2CH₃COCH₃): exp. C 48.66%, H 5.63%, N 9.79% (calc. C 48.70%, H 5.58%, N 9.79%).

[Au(C^{CH₂N)Cl(PTA)][PF₆]} was formed following a literature reported procedure.¹¹²

[Au(C^{CH₂N)Cl₂] (50 mg, 0.115 mmol, 1 eq.) and KPF₆ (106 mg, 0.573 mmol, 5 eq.) were suspended in acetone (5 mL), prior to the addition of PTA (18 mg, 0.115 mmol, 1 eq.) at room temperature. The reaction was stirred for 1.5 h, before partial removal of the solvent. CH₂Cl₂ was then added before filtration of the solution over Celite®, resulting in a yellow/orange solution. The solvent was then fully removed under reduced pressure to yield the crude product which was purified by recrystallisation using a CH₂Cl₂/*n*-pentane mixture. The purified product was obtained as an off-white solid (59 mg, 78%).}

¹H NMR (500 MHz, Acetone-*d*₆) δ 9.01 – 8.97 (m, 1H, ar), 8.28 (td, $J = 7.7, 1.1$ Hz, 1H, ar), 8.02 (d, $J = 7.8$ Hz, 1H, ar), 7.87 (ddd, $J = 7.9, 3.5, 1.2$ Hz, 1H, ar), 7.78 (t, $J = 6.6$ Hz, 1H, ar), 7.48 (dd, $J = 7.5, 2.0$ Hz, 1H, ar), 7.33 (t, $J = 7.3$ Hz, 1H, ar), 7.26 – 7.20 (m, 1H, ar), 4.96 (d, $J = 3.7$ Hz, 6H, PTA), 4.82 (dt, $J = 13.8, 1.4$ Hz, 3H, PTA), 4.61 (d, $J = 11.5$ Hz, 4H, CH₂, PTA), 4.41 (d, $J = 14.8$ Hz, 1H, CH₂).

³¹P{¹H} NMR (202 MHz, Acetone-*d*₆) δ -16.61, -144.23 (hept, $J = 707.6$ Hz, PF₆).

Synthesis of **2** from **[Au(C^{CH₂N)Cl(PTA)][PF₆]}**

[Au(C^{CH₂N)Cl(PTA)][PF₆]} (40 mg, 0.057 mmol, 1 eq.) was added to acetone (6 mL) along with KPF₆ (52 mg, 0.285 mmol, 5 eq.). PTA (18 mg, 0.114 mmol, 2 eq.) was then added at room temperature and after a few min stirring the solution was fully solubilised. This was then left to stir overnight at room temperature where a white precipitate was formed. The solvent was then removed under reduced pressure and re-suspended in CH₂Cl₂ before filtering to obtain the product as a white solid (20 mg, 74%).

¹H NMR (400 MHz, Acetone-*d*₆) δ 8.78 – 8.70 (m, 1H, ar), 7.97 (ddd, $J = 14.3, 7.8, 1.3$ Hz, 1H, ar), 7.84 (td, $J = 7.7, 1.9$ Hz, 1H, ar), 7.73 – 7.64 (m, 1H, ar), 7.64 – 7.50 (m, 3H, ar), 7.32 (ddd, $J = 7.7, 4.9, 1.3$ Hz, 1H, ar), 5.25 (d, $J = 6.3$ Hz, 6H, CH₂), 4.76 (s, 6H, CH₂), 4.28 (s, 2H, CH₂).

³¹P{¹H} NMR (162 MHz, Acetone-*d*₆) δ -56.55 (s, PTA), -144.23 (hept, $J = 707.7$ Hz, PF₆).

Characterisation aligns with product 2.

The procedure to form the C-P product with the other phosphines (triphenylphosphine, tri-*n*-butylphosphine and tris(hydroxypropyl)phosphine) was the same as the procedure

used to form **1-4**, except in the case of tri-*n*-butylphosphine and tris(hydroxypropyl)phosphine, inert conditions were used (dry acetone, nitrogen environment).

6.4.3. Crystal Formation for XRD analysis

Suitable crystals of complex **1** were obtained from a mixture of CH₂Cl₂ and *n*-pentane. Complexes **2** and **3** formed crystals by slow evaporation at room temperature of acetone. The [Au(PTA)₂]⁺ crystal was formed in combination with **2**. Additionally, crystals of [Au(C^{CO}N)Cl(PPh₃)₂]⁺ were grown in a mixture of ethyl acetate and hexane.

6.4.4. ³¹P{¹H} NMR studies

The reactions to synthesise **1-3** were monitored over 24 h by NMR spectroscopy on a Bruker Avance (400 MHz). The reaction mixtures were prepared by suspending [Au(C^N)Cl₂] (2 mg, 1 eq.), KPF₆ (4 mg, 5 eq.) and PTA (2.1 mg, 3 eq.) in acetone-*d*₆ (0.7 mL) in an NMR tube. Initial spectra were performed at room temperature at different time intervals (after the first hour, every 3 h for the subsequent 18 h and a final measurement at 24 h). The reaction yielding **2** was also studied at 15 °C collecting spectra every 5 min over 100 min.

7. C-C Cross-Coupling Reaction Mediated by a Au(III) Cyclometalated Complex: Mechanistic Insights

This chapter is based on the following paper:

C-C Cross-Couplings from a Cyclometalated Au(III) Complex: Mechanistic Insights and Synthetic Developments

Riccardo Bonsignore⁺, **Sophie R. Thomas**⁺, Mathilde Rigoulet, Christian Jandl, Alexander Pöthig, Didier Bourissou, Giampaolo Barone and Angela Casini

[⁺] *Authors contributed equally to this work.*

DOI: 10.1002/chem.202102668

7.1. Introduction

Taking inspiration from our previous work on C-S^{305,308} and C-P³⁴¹ cross-coupling reactions *via* reductive elimination, we next set our sights on the more investigated, although challenging, C-C cross-coupling reaction. The ability of a Au(III) alkyl complex to mediate C-C bond formation *via* reductive elimination was first reported by the groups of Schmidbaur,³⁵⁵ Kochi^{356,357} and Tobias³⁵⁸ in the early 1970s. Since then, the area of C-C cross-coupling through Au(I)/Au(III) redox cycles has thrived.^{359–365} It has been observed that the hybridisation of the C atoms involved in the C-C reductive elimination is generally responsible for the rate of reactions, namely C(sp³)-C(sp³) is slower than C(sp²)-C(sp²) or C(sp)-C(sp).³⁶⁶

In 2014, Toste and co-workers reported the ability of a *cis*-diaryl-Au(III) complex to mediate a fast C(sp²)-C(sp²) cross-coupling reaction to form the 4,4'-difluorobiphenyl complex, even at -52 °C.³⁵⁹ Alternatively, in the same year, Nevado and co-workers investigated the C(sp²)-C(sp²) reductive elimination reaction with a *cis*-diaryl-Au(III) complex, [Au(C₆F₅)₂(PPh₃)Cl] (PPh₃ = triphenylphosphine), however in this work the reaction was slow, even at 150 °C.³⁶⁷ In 2017, Kang *et al.* reported an in-depth study into the C(sp²)-C(sp²) cross-coupling reaction involving a series of *cis*-diaryl-Au(III) complexes.³⁶⁸ The study also investigated the steric and electronic effects of the ligands on the reaction.³⁶⁸ An example of C(sp)-C(sp) cross-coupling mediated by a Au(III) catalyst was reported by Corma and co-workers³⁶¹ in 2015 for the homogenous coupling of terminal alkynes. The reaction began with the oxidative addition of the Au(I) phosphine complex using the sacrificial oxidant selectfluor under basic conditions, which then underwent transmetalation of the alkyne, resulting in the fast reductive elimination reaction of the 4-coordinate Au(III) complex.³⁶¹

Nevertheless, detailed mechanistic understanding of gold catalysed cross-coupling reaction steps, particularly reductive elimination, are still lacking. Isolation of intermediates within the reaction remain challenging due to the fast kinetics and instability of high-valent gold intermediates; therefore more groups are turning to cyclometalated Au(III) complexes to reduce the reaction rates due to their redox and thermodynamic stability.^{107,331}

In 1990, Vicente and co-workers reported the C(sp²)-C(sp²) reductive elimination reaction using a Au(III) C[^]N cyclometalated complex bearing an aryl group (Figure 80).³⁶⁹ PPh₃ was also required to aid the decoordination of the nitrogen donor to form the C-C product.³⁶⁹ More recently, You and co-workers³⁷⁰ demonstrated a phosphine-free C(sp²)-C(sp²) coupling reaction by *ortho*-arylation of arylpyridines with arylboronic acids, using a [Au(C[^]N)Br₂] catalyst (Figure 80). However, high temperatures (130 °C) are needed for these reactions to proceed.³⁷⁰

Rocchigiani *et al.*³⁷¹ included both C(sp²)-C(sp²) and C(sp²)-C(sp³) cross-coupling in their work, which was mediated by AuC^N cyclometalated cations derived from a C^N pincer Au(III) complex by protodeauration with a strong acid (Figure 80). The addition of a second ligand (L) is required to enable the decoordination of the pyridyl N, allowing reductive elimination to take place through a four coordinate transition state.³⁷¹ The type of L used dictates the reactivity of the complex; if L = OEt₂ (etherate) C-C coupling cannot be seen, however if a stronger donor L is used such as SMe₂ (dimethylsulfide) or P(*p*-tol)₃ (tri(*p*-tolyl)phosphine) the reaction can proceed. The R group used to form the C-C bond also affects the rate of C-C coupling, with a decrease in rate following the sequence R = vinyl > aryl >> C₆F₅ > Me.³⁷¹

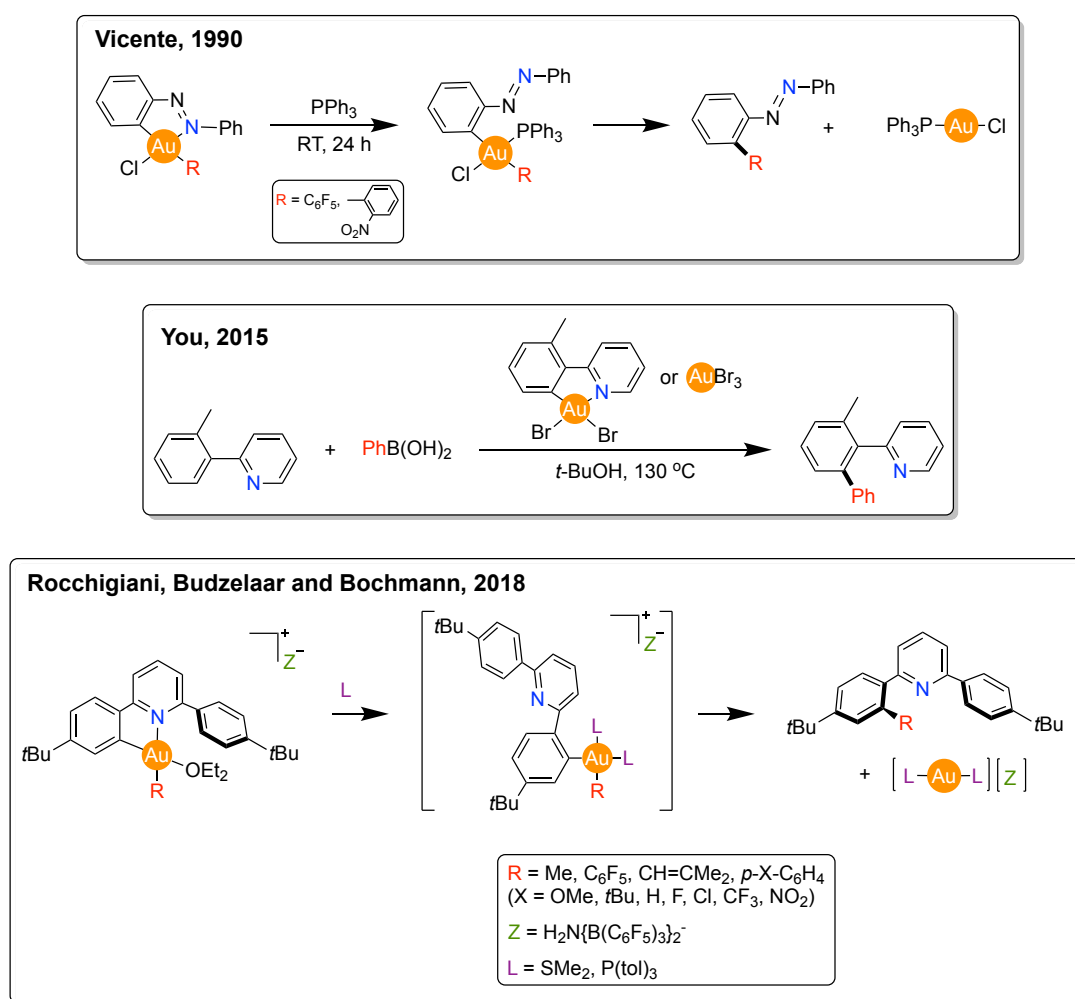
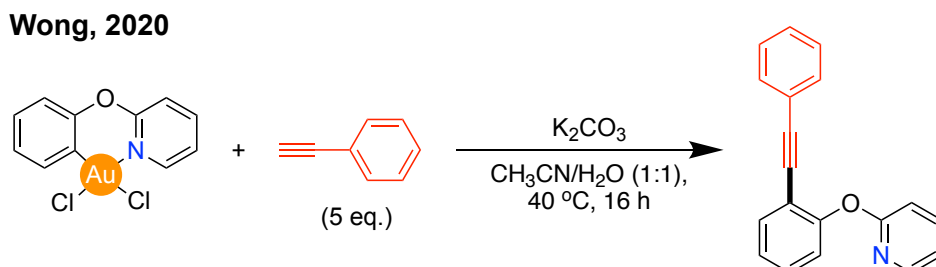


Figure 80 – Examples of C(sp²)-C(sp²) and C(sp²)-C(sp³) cross-coupling reactions templated by Au(III) cyclometalated C^N complexes.^{369–371}

An example of C(sp²)-C(sp) cross-coupling templated by a Au(III) cyclometalated complex was reported in 2020 by Wong and co-workers for the reaction of Au(III) cyclometalated C^N complexes with phenylacetylene and a base (Scheme 22).¹⁹⁹ The reaction involving [Au(C^ON)Cl₂] (C^ON = 2-phenoxy-pyridine, 1 eq.) and phenylacetylene

(5 eq.) resulted in a C-C product yield of 82%, which outcompetes the alternative C(sp)-C(sp) homocoupling of the phenylacetylene, isolated with a yield of ca. 17%. The authors also explored the reaction with the five-membered $[\text{Au}(\text{C}^{\wedge}\text{N})\text{Cl}_2]$ complex ($\text{C}^{\wedge}\text{N}$ = 2-phenylpyridine); however no product was formed as we observed in the C-S reaction³⁰⁵, with only a small yield in the C-P³⁴¹ reductive elimination reaction.¹⁹⁹



Scheme 22 - C(sp²)-C(sp) cross-coupling reaction templated by $[\text{Au}(\text{C}^{\text{O}}\text{N})\text{Cl}_2]$ ($\text{C}^{\text{O}}\text{N}$ = 2-phenoxyphenylpyridine) involving phenylacetylene (5 eq.) and K_2CO_3 .¹⁹⁹

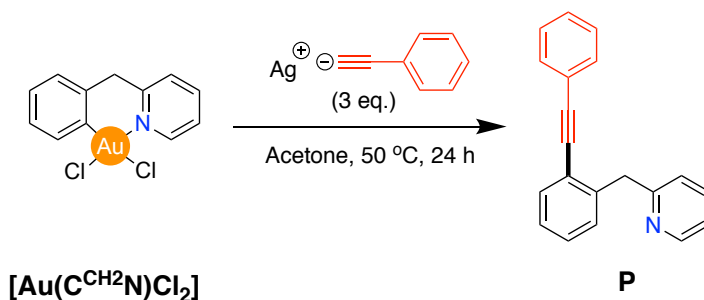
Nevertheless, despite the investigations reported above there is still very little mechanistic understanding of the C-C reductive elimination reaction. Therefore, in our work we combined multiple approaches to help elucidate the mechanism, including: ¹H NMR (nuclear magnetic resonance) monitoring, X-ray crystallography and DFT (density functional theory) calculations; as well as using the knowledge we have gained in our previous cross-coupling work.^{305,341}

7.2. Results and Discussion

P4, (2-thienyl)zinc chloride, **R3** and **P5** were synthesised by Mathilde Rigoulet. X-ray diffraction (XRD) studies were performed by Christian Jandl. Computational analysis was performed by Prof. Giampaolo Barone.

Initial experiments involved the optimisation of the reaction between $[\text{Au}(\text{C}^{\text{CH}_2}\text{N})\text{Cl}_2]$ (1 eq.) and silver phenylacetylide (AgPhCC , 3 eq.) in acetone to form the C(sp²)-C(sp) cross-coupling product (**P**) (Scheme 23). A yield of 33% of **P** was obtained after column chromatography when reacting in 25 mL acetone at 50 °C for 24 h. This yield could be increased to 73% on addition of an extra equivalent of AgPhCC and reacting for a further 24 h. **P** was fully characterised by ¹H, ¹³C{¹H} and 2D NMR, along with HR-ESI-MS (High-Resolution Electrospray Ionisation Mass Spectrometry). The homo-coupled alkyne side product formed by C(sp)-C(sp) coupling was observed in trace amounts, as reported by Wong and co-workers.¹⁹⁹ Furthermore, Lauterbach *et al.*³⁷² described the ability of Pd contaminants to catalyse Sonogashira cross-coupling between aryl iodides and terminal alkynes, rather than the gold catalysts themselves. However, using Inductively Coupled

Plasma Mass Spectrometry (ICP-MS), we proved that **P** was formed in the absence of Pd.



Scheme 23 - C(sp²)-C(sp) cross-coupling reaction templated by [Au(C^{CH₂N})Cl₂] (C^{CH₂N} = 2-benzylpyridine) with silver phenylacetylide.³⁷³

Additionally, the reaction was attempted with the five-membered cyclometalated complex [Au(C^N)Cl₂]; due to its insolubility in acetone the reaction was performed in DMSO-*d*₆ in an NMR tube. AgPhCC (3 eq.) was added and the tube was heated in an oil bath to 50 °C for 24 h. Once completed, an NMR spectrum was recorded, however no reactivity was observed, which aligns with the results observed by Wong and co-workers.¹⁹⁹

The C(sp²)-C(sp) reaction with [Au(C^{CH₂N})Cl₂] (1 eq.) and AgPhCC (3 eq.) at 50 °C for 24 h was also explored in different solvents, including: methanol (CH₃OH), dimethylformamide (DMF), water (H₂O), acetonitrile (CH₃CN) and dimethyl sulfoxide (DMSO) (Table 8). Due to the challenging removal of DMSO from the reaction mixture, the reaction was performed directly in the NMR tube with the same conditions (3 eq. of AgPhCC, 50 °C, 24 h), but on a smaller scale and with DMSO-*d*₆. The yield of reaction in DMSO-*d*₆ was estimated using the internal standard, benzylether, which showed the largest **P** yield of 70% (Table 8). DMF and water showed only traces of product, as observed by recording the ¹H spectrum of the crude reaction mixture. This is most likely due to insolubility of the reagents in these solvents. Furthermore, after purification, CH₃CN showed the next highest yield of **P** (63%), followed by CH₃OH (49%) (Table 8).

Table 8 – Yield of product formed by C(sp²)-C(sp) cross-coupling reaction templated by [Au(C^{CH}₂N)Cl₂] (1 eq.) with AgPhCC (3 eq.) in different solvents (25 mL) at 50 °C for 24 h.³⁷³

*Performed in NMR tube using DMSO-d₆ with yield estimated by internal standard.

Solvent	Yield
Acetone	33%
CH ₃ OH	49%
DMF	traces
Water	Traces
CH ₃ CN	63%
DMSO*	70%

Next, we focused our attention on identification of the intermediates within the reaction by ¹H NMR spectroscopy, which required the reaction to be slow enough to observe all the possible species. Acetone was the chosen solvent due to the relatively low yield of product produced, although the conditions were altered slightly to slow down the reaction rate further (2 eq. of AgPhCC, 1 mL acetone-d₆, which corresponds to 14 mL acetone if performed in batch, and room temperature). A spectrum was recorded every 30 min for the first h, followed by every 2 h from 2 h up to 12 h, then every 4 h until 24 h was reached.

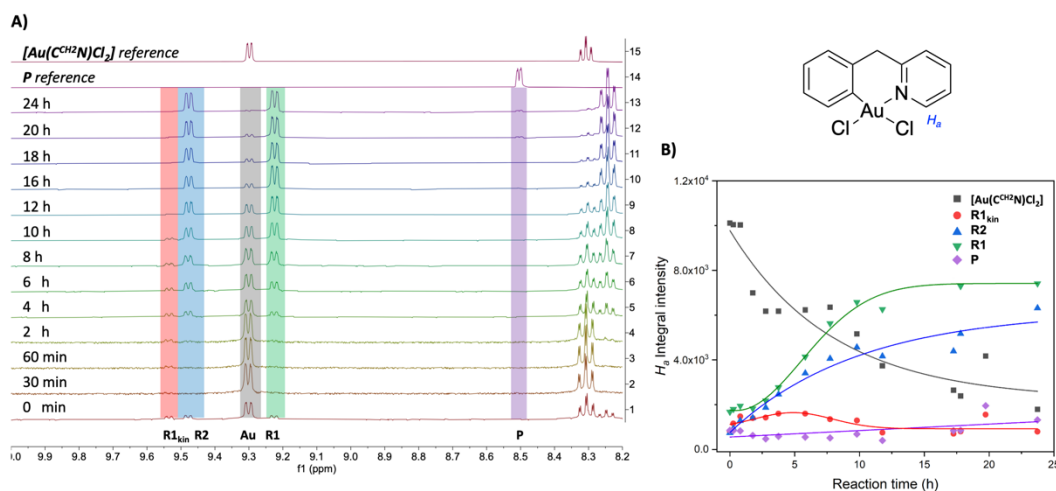
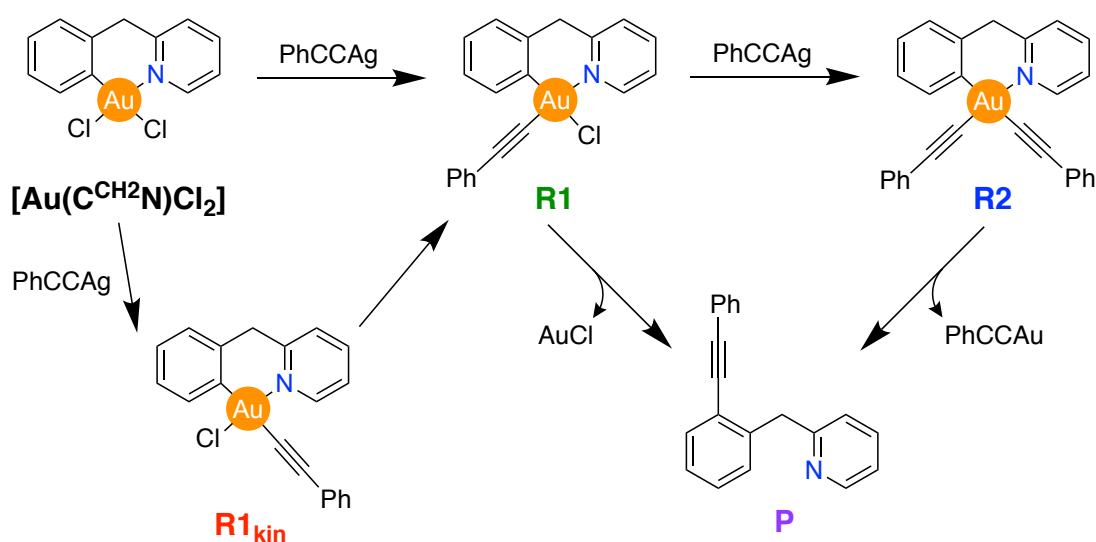


Figure 81 – **A)** ¹H NMR spectra (between 8.2 and 10 ppm) of the reaction between [Au(C^{CH}₂N)Cl₂] (1 eq.) and AgPhCC (2 eq.) at r.t. over 24 h in acetone-d₆. The spectra of [Au(C^{CH}₂N)Cl₂] and **P** are shown for comparison. The H_a signals of various species have been assigned, the structure of [Au(C^{CH}₂N)Cl₂] is shown highlighting the H_a proton, ortho to the pyridyl N. **B)** Evolution of the intensities of the different H_a integrals over 24 h, fitting lines included to help visualise the trend. Figure modified from ref 373. Copyright 2021, John Wiley and Sons

<https://creativecommons.org/licenses/by/4.0/>³⁷³

The ^1H NMR spectra over 24 h can be seen in Figure 81A, where the proton *ortho* to the pyridyl nitrogen (H_a) is monitored over the reaction as it is a diagnostic signal for the coordination or absence of the Au centre to the pyridyl N. Figure 81B provides the H_a integral intensity of each of the species identified over time. The spectra of the $[\text{Au}(\text{C}^{\text{CH}_2\text{N}})\text{Cl}_2]$ complex and **P** are given in Figure 81A for comparison and allow both to be immediately identified and monitored. As expected, $[\text{Au}(\text{C}^{\text{CH}_2\text{N}})\text{Cl}_2]$ decreased in intensity over time (Figure 81A and B, grey lines), whilst **P** is formed in traces due to the reduction in rate (Figure 81A and B, purple lines).

Three additional species are present in the spectra (Figure 81A and B) and all show a H_a signal in the typical ppm range for Au(III) cyclometalated C^N species. Therefore, tentative assignments were made for the identity of these species using previous knowledge we have gained from our C-S³⁰⁵ and C-P³⁴¹ cross-coupling mechanisms, and the ppm of the H_a signals compared to $[\text{Au}(\text{C}^{\text{CH}_2\text{N}})\text{Cl}_2]$ and **P**. The proposed mechanism is shown in Scheme 24, starting with the mono-substitution of a chloride *cis* or *trans* to the pyridyl N with AgPhCC to form **R1_{kin}**/**R1** ($[\text{Au}(\text{C}^{\text{CH}_2\text{N}})(\text{CCPh})\text{Cl}]$), respectively. While substitution of the chloride *cis* to the pyridyl N is expected to be the kinetically favoured species **R1_{kin}** due to the stronger *trans* effect of C vs. N,³⁷⁴ substitution of the chloride *trans* to the pyridyl N is expected to be the thermodynamically favoured species, **R1**. The third species in the NMR spectra has been tentatively assigned as the bis-substituted complex, **R2** (Scheme 24, $[\text{Au}(\text{C}^{\text{CH}_2\text{N}})(\text{CCPh})_2]$).

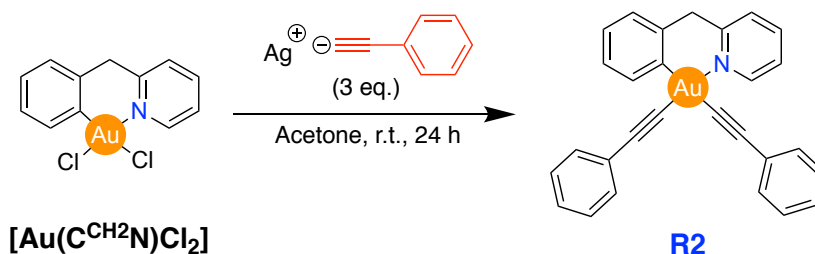


Scheme 24 – Proposed reaction mechanism for the C(sp^2)-C(sp) cross-coupling reaction templated by $[\text{Au}(\text{C}^{\text{CH}_2\text{N}})\text{Cl}_2]$ with AgPhCC.³⁷³

Figure 81A and B show that all three unknown species appear almost immediately from mixing, with two species (red and blue lines) exhibiting a similar H_a shift (9.54 and 9.48

ppm, respectively). The H_a peaks of these species are more downfield than that of $[\text{Au}(\text{C}^{\text{CH}_2\text{N}})\text{Cl}_2]$, therefore we proposed that these H_a peaks could correspond to **R1_{kin}** and **R2** as both possess an alkynyl group *cis* to the pyridyl N (Figure 81A and B, Scheme 24). It should be noted that the red line (**R1_{kin}**) is short-lived, providing further evidence for its identification as a kinetic species. The third H_a peak (green line, Figure 81A and B) has a similar shift to the H_a of $[\text{Au}(\text{C}^{\text{CH}_2\text{N}})\text{Cl}_2]$, and so can be cautiously assigned as **R1**, as both retain a chloride *cis* to the pyridyl N (Figure 81A and B, Scheme 24). ^1H NMR monitoring studies were also carried out in other deuterated solvents in the same conditions, including: $\text{DMSO-}d_6$, $\text{CH}_3\text{OH-}d_4$, $\text{DMF-}d_7$ and $\text{CH}_3\text{CN-}d_3$. All solvents exhibited the same intermediates as in acetone- d_6 and followed a similar pathway. However, to confirm the assignments made above, isolation of the intermediates was required.

In an attempt to isolate the intermediate **R2**, the reaction conditions used in the ^1H NMR monitoring were optimised to push the reaction towards **R2**, but not **P**. This was done by increasing the equivalents of AgPhCC to 3 from 2, as used in ^1H NMR monitoring studies. Therefore, $[\text{Au}(\text{C}^{\text{CH}_2\text{N}})\text{Cl}_2]$ (1 eq.) was reacted in acetone (14 mL) with AgPhCC (3 eq.) at room temperature for 24 h (Scheme 25). After purification by column chromatography, the species was isolated as the bis-substituted complex **R2** with a yield of 48%.



Scheme 25 – Formation of **R2** by reaction of $[\text{Au}(\text{C}^{\text{CH}_2\text{N}})\text{Cl}_2]$ with 3 eq. of AgPhCC at room temperature in acetone (14 mL) for 24 h.³⁷³

This was confidently assigned with HR-ESI-MS and NMR data; specifically, 2D HMBC (heteronuclear multiple bond correlation) and HSQC (heteronuclear single quantum coherence) experiments. $^1\text{H-}^{13}\text{C}$ HMBC NMR in particular was very useful for assigning **R2** due to the coupling of C14 with H_j , C22 with H_m , C8 with H_i and H_h , and C7 with H_f and H_g (Figure 82). It should be noted that the H_a of the **R2** isolated species corresponded to the blue trace in the ^1H NMR in acetone- d_6 at room temperature (Figure 81A and B).

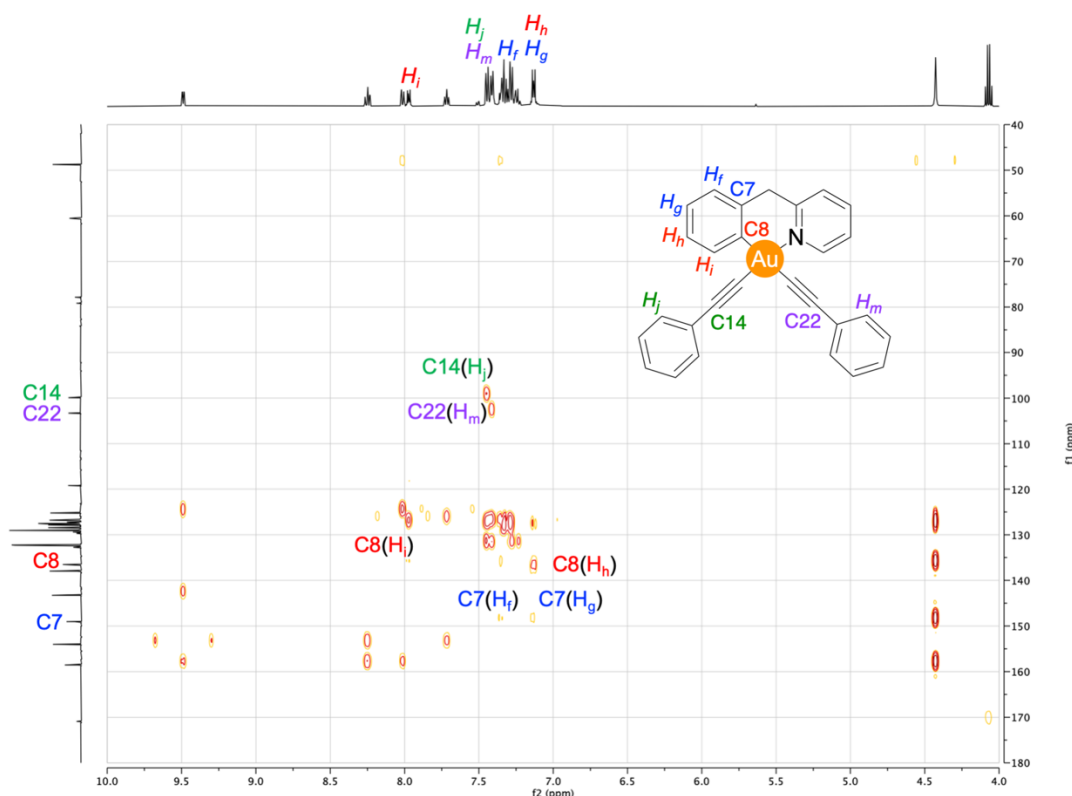
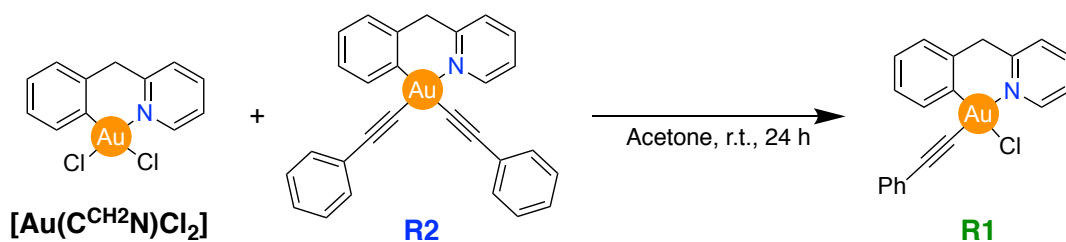


Figure 82 – ^1H - ^{13}C HMBC NMR spectrum of **R2** in acetone- d_6 . Figure modified from ref 373.

Copyright 2021, John Wiley and Sons <https://creativecommons.org/licenses/by/4.0/>.³⁷³

Additionally, the HR-ESI-MS of the crude mixture forming **P** from $[\text{Au}(\text{C}^{\text{CH}_2\text{N}})\text{Cl}_2]$ and AgPhCC at 50 °C showed the presence of **R2** in a small amount, providing evidence that **R2** is indeed an intermediate to form **P**. An intermediate species of this type was also observed in previous C-S³⁰⁵ and C-P³⁴¹ cross-coupling experiments with C[^]N cyclometalated Au(III) complexes. This was further evidenced by reacting **R2** with AgPhCC (2 eq.) in acetone (25 mL) at 50 °C for 48 h, resulting in the formation of **P** with a yield of 80% after column chromatography. Interestingly, **R2** can also evolve into **P** in the absence of AgPhCC when heated to 50 °C.

Next, attempts were made to isolate the mono-substituted species $[\text{Au}(\text{C}^{\text{CH}_2\text{N}})(\text{PhCC})\text{Cl}]$, **R1**. Efforts were made to modify the procedure used to form **R2** by reducing the equivalents of AgPhCC, however **R2** was still formed, albeit in a lower amount. Therefore, taking inspiration from the chloride/aryl exchange reaction reported by Toste and co-workers using a Au(III) species, a redistribution experiment was performed.³³⁹ This involved mixing equimolar amounts of $[\text{Au}(\text{C}^{\text{CH}_2\text{N}})\text{Cl}_2]$ and **R2** in acetone at room temperature for 24 h (Scheme 26). After column chromatography the **R1** species was isolated with a yield of 85% and fully characterised by NMR and MS experiments.



Scheme 26 - Formation of **R1** by reaction of equimolar amounts of $[\text{Au}(\text{C}^{\text{CH}_2\text{N}})\text{Cl}_2]$ and **R2** at room temperature in acetone for 24 h.³⁷³

The H_a proton of **R1** overlaps as expected with the green trace in Figure 81A and B at 9.22 ppm, which was predicted to be the more thermodynamically stable product with the chloride substitution *trans* to the pyridyl N. To provide further evidence for this, DFT calculations were performed to assess the stability of **R1** and **R1_{kin}**. As expected, **R1** was lower in energy than **R1_{kin}**, with a difference of 59.4 kJ/mol (Figure 83), confirming that **R1** is the more thermodynamically stable product.

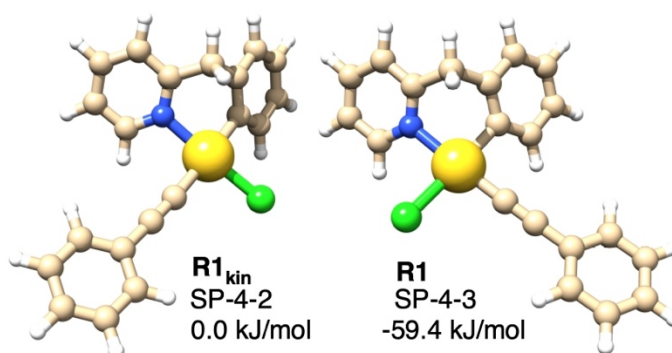


Figure 83 – Structure and relative stability of the possible stereoisomers of $[\text{Au}(\text{C}^{\text{CH}_2\text{N}})(\text{PhCC})\text{Cl}]$ (**R1_{kin}** and **R1**) in acetone, attained by DFT calculations. Figure from ref 373. Copyright 2021, John Wiley and Sons <https://creativecommons.org/licenses/by/4.0/>.³⁷³

Furthermore, the relative energy (ΔG°) of the redistribution reaction between $[\text{Au}(\text{C}^{\text{CH}_2\text{N}})\text{Cl}_2]$ and **R2** to form **R1** was found to be downhill in energy by 31 kJ/mol per Au atom, therefore is thermodynamically favoured, as calculated by the following equation:

$$\Delta G^\circ = \{ 2 \times G^\circ[\text{R1}] - G^\circ[\text{R2}] - G^\circ[\text{Au}(\text{C}^{\text{CH}_2\text{N}})\text{Cl}_2] \} / 2 \quad \text{Equation 1}$$

To further confirm the identity and conformation of the alkynyl group of **R1**, crystal formation was attempted. This was performed by layering *n*-pentane on top of a diluted chloroform solution of **R1**, resulting in the formation of a milky interface. After 24 h crystal formation was observed allowing single crystal XRD analysis to be completed by

Christian Jandl. Two polymorphs of **R1** were found, as can be seen in Figure 84, the difference between them is due to the disorder of the alkynyl group in the first polymorph across three orientations of the phenyl group, whereas the second polymorph does not exhibit any disorder of the alkynyl group. Therefore, due to the similarity in geometry, only the second polymorph will be discussed in detail.

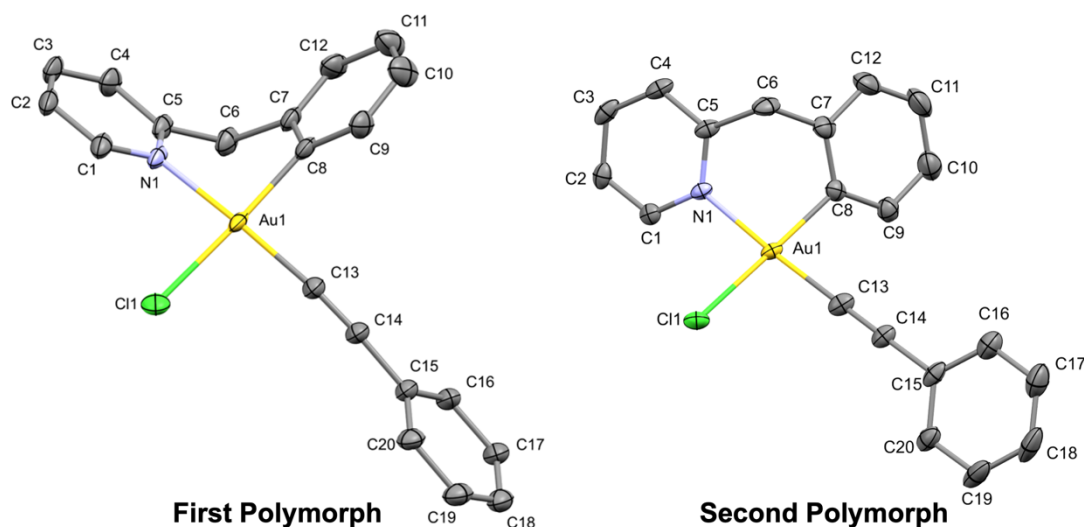


Figure 84 – Two polymorphs of **R1** found in the solid state with ellipsoids at 50% probability, H atoms omitted for clarity. Figure adapted from ref 373. Copyright 2021, John Wiley and Sons <https://creativecommons.org/licenses/by/4.0/>.³⁷³

As shown in Figure 84, the alkynyl ligand is bound *trans* to the pyridyl N, as expected due to the higher thermodynamic stability of this conformation (Figure 83). **R1** also exhibits a typical square planar geometry, which can be evidenced by a small τ_8 value of 0.03.^{375,376} Figure 85 shows the difference in τ_8 values across different 4-coordinate geometries, ranging from ideal tetrahedral ($\tau_8 = 1$) to ideal square planar ($\tau_8 = 0$).³⁷⁵

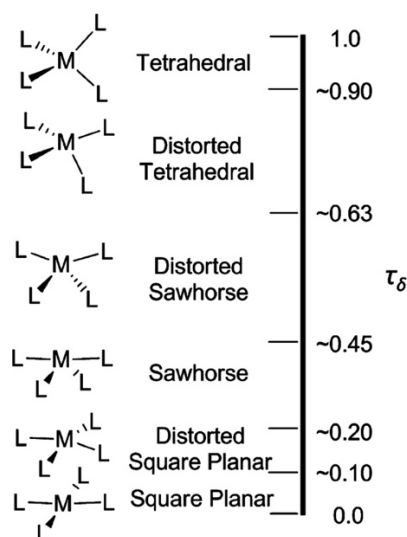


Figure 85 – Examples of τ_8 values and corresponding 4-coordinate structures ranging between ideal tetrahedral and ideal square planar geometries. Reprinted with permission from ref 375.

Copyright (2015) American Chemical Society.³⁷⁵

The bond distances between Au1 and C11, N1 or C8 are similar to those reported in the literature for complexes of a similar type, with 1,3,5-triaza-7-phosphaadamantane (PTA) or PPh_3 replacing the alkynyl group.^{112,377} However, the bite angle of N1-Au1-C8 in the C^N scaffold does appear to be slightly larger than the complexes in the literature.^{112,377} The second polymorph of **R1** also features a boat-like conformation of the C^{CH₂N} ligand coordinated to Au1 (Figure 86), where the (N1 Au1 C8) plane and (C5 C6 C7) plane are in a similar range to the literature reported values.^{112,377}

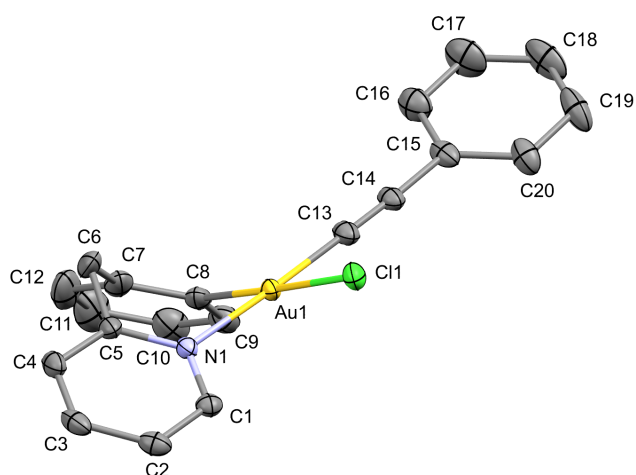


Figure 86 – Molecular structure of the second polymorph of **R1** in the boat-like conformation with ellipsoids at 50% probability. H atoms omitted for clarity. Figure adapted from ref 373.

Copyright 2021, John Wiley and Sons <https://creativecommons.org/licenses/by/4.0/>.³⁷³

Remarkably, during the crystallisation of **R1**, two zwitterionic Au(I) vinyl complexes **P3a** and **P3b** were also co-crystallised, the structures of which can be seen in Figure 87. **P3a** and **P3b** were found in a disordered mixture with a ratio of ca. 62:38, and were constitutional isomers of **R1** at the same position. Bond lengths and angles were difficult to compare to the literature due to the level of disorder present. The formation of **P3a** and **P3b** involved the formation of a C(sp²)-C(sp) bond *via* cross-coupling, as observed for **P**, together with a C-N coupling reaction. A similar di-functionalisation reaction of alkynyl bonds with C-C and C-N bond formation has also been observed previously by a visible light mediated reaction with a Au(I) catalyst.³⁷⁸

In both **P3a** and **P3b** the pyridyl N binds to the alkynyl bond, the position of the binding dictates the structure formed, as can be seen in Figure 87 with the red and black curly arrows. **P3a** is formed by coordination of the N to the alkynyl C closest to the C[^]N scaffold, forming a six-membered ring, whereas **P3b** is formed by coordination of the N to the other alkynyl C, resulting in a seven-membered ring (Figure 87). Nevertheless, both complexes feature the pyridyl N and Au *trans* to the alkene formed, due to *anti*-nucleophilic attack of the pyridyl N to the π-activated alkyne bond. Unfortunately, **P3a** and **P3b** could not be identified in the NMR studies; however, their presence in crystallography certainly provides inspiration for future studies between [Au(C^{CH}2N)Cl₂] and AgPhCC.

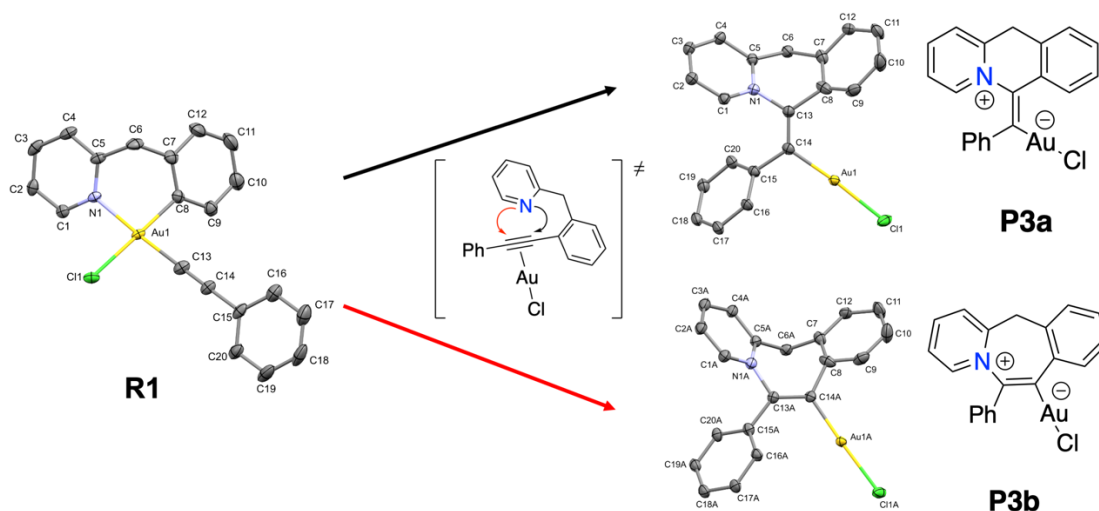
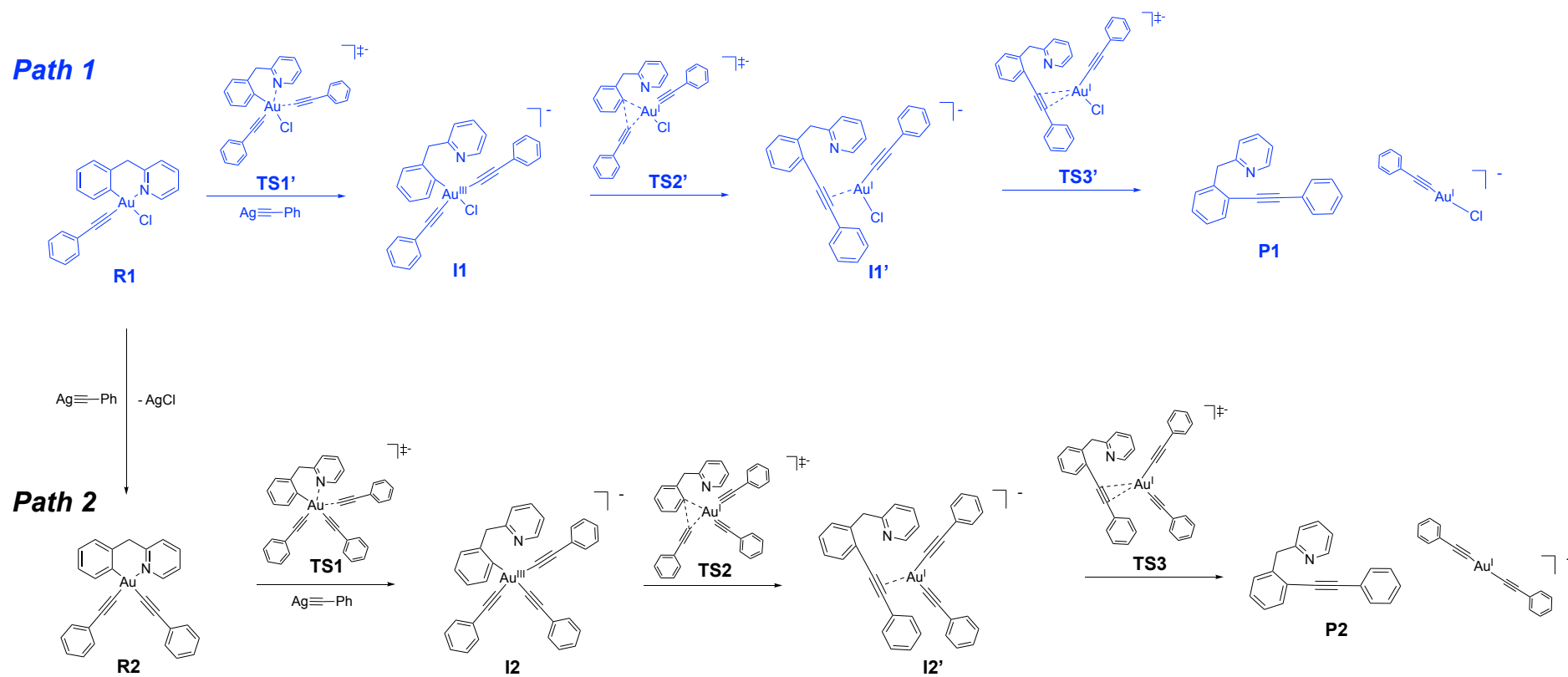


Figure 87 – Molecular structures for the formation of insertion products **P3a** and **P3b** from **R1**, with corresponding Chemdraw structures on the right. Chemdraw of the postulated transition state is also shown. Ellipsoids are shown at 50% probability with H atoms omitted for clarity.

Figure adapted from ref 373. Copyright 2021, John Wiley and Sons

<https://creativecommons.org/licenses/by/4.0/>.³⁷³



Scheme 27 – Two proposed reaction pathways, including transition states, for the C(sp²)-C(sp) cross-coupling reaction resulting in reductive elimination, as obtained by DFT calculations.³⁷³

Returning to Scheme 24, both **R2** and **R1** had been isolated and fully characterised, leaving **R1_{kin}** as the only unconfirmed intermediate from the ¹H NMR monitoring studies in Figure 81A,B (red trace). Unfortunately, attempts to isolate it were not successful; however, this could be expected due to its transient nature before converting to **R1** and **R2**. The ¹H NMR resonance of the H_a signal (9.54 ppm) also further corroborates its identity, as previously discussed, with a similar H_a signal to **R2** (9.48 ppm) as both possess an alkynyl group *cis* to the pyridyl N.

Furthermore, DFT calculations were performed by Prof. Giampaolo Barone to support the experimental results obtained, which were also performed in our C-S and C-P cross-coupling work with cyclometalated Au(III) C[^]N complexes.^{305,308,341} In all cases the decoordination of the pyridyl N was vital for the reductive elimination reaction to occur due to rotation of the phenyl ring.^{305,341} Therefore, in this work following Scheme 24, DFT calculations were performed using the PhCC⁻ anion, rather than AgPhCC, to simplify the reactant model, leading to the proposed mechanism as seen in Scheme 27. Initial calculations were performed on the reaction profiles from [Au(C^{CH2}N)Cl₂] and PhCC⁻ to **R1**, from **R1** and PhCC⁻ to **R2**, from **R1** and PhCC⁻ to **I1** and from **R2** and PhCC⁻ to **I2**. The relative standard Gibbs free energy values (ΔG°) and activation energy barriers (E^\ddagger) are shown in Table 9 and Figure 88A-D. All four steps exhibited low activation energy barriers (up to 15 kJ/mol) and were exergonic in nature with stabilisation energies greater than 100 kJ/mol in all cases, meaning they are highly favourable. The formation of **R2** from **R1** and PhCC⁻ involved a small activation energy barrier (E_{00}^\ddagger) of 13.8 kJ/mol, however **R2** was more stable than **R1** ($\Delta G^\circ = -104.3$ kJ/mol), meaning its formation was favourable.

Table 9 – Calculated relative standard Gibbs free energy values (ΔG°) and activation energy barriers (E^\ddagger) of the species involved in the C(sp²)-C(sp) cross-coupling reaction of [Au(C^{CH2}N)Cl₂] and PhCC⁻ to **I1/I2** via pathway 1 or 2 in acetone.³⁷³

Pathway 1		Pathway 2	
Species	ΔG° (kJ/mol)	Species	ΔG° (kJ/mol)
[Au(C ^{CH2} N)Cl ₂] + PhCC ⁻	0.0	R1 + PhCC ⁻	0.0
TS0 = E_0^\ddagger	5.3	TS00 = E_{00}^\ddagger	13.8
R1 + Cl ⁻	-162.8	R2 + Cl ⁻	-104.3
R1 + PhCC ⁻	0.0	R2 + PhCC ⁻	0.0
TS1' = E_1^\ddagger	15.4	TS1 = E_1^\ddagger	7.3
I1	-116.6	I2	-125.1

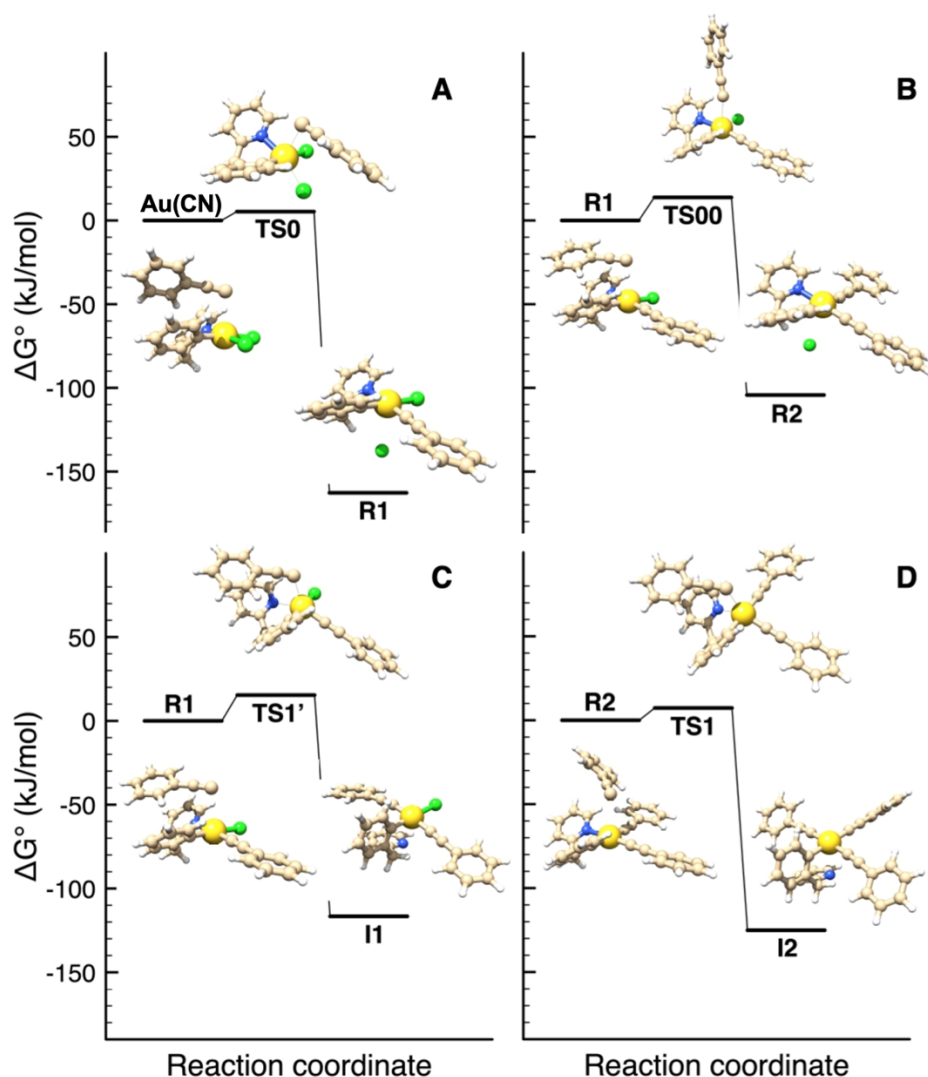


Figure 88 – Reaction coordinates of **A)** $[\text{Au}(\text{C}^{\text{CH}_2\text{N}})\text{Cl}_2]$ and PhCC^- to **R1**, **B)** **R1** and PhCC^- to **R2**, **C)** **R1** and PhCC^- to **I1** and **D)** **R2** and PhCC^- to **I2**. The structures and energy values were calculated using DFT calculations. Figure adapted from ref 373. Copyright 2021, John Wiley and Sons <https://creativecommons.org/licenses/by/4.0/>.³⁷³

Next, following Scheme 24 and Scheme 27, the intramolecular reaction takes place beginning with **I1** or **I2** leading to the cross-coupling products **P1** ($\text{P} + [\text{Au}(\text{I})\text{Cl}(\text{PhCC})]^-$) or **P2** ($\text{P} + [\text{Au}(\text{I})(\text{PhCC})_2]^-$), respectively. The energies of which can be seen in Table 10 and Figure 89. In both cases, the anionic intermediates (**I1** and **I2**) proceeded through a three-coordinate transition state (**TS2'** and **TS2**) to form the second intermediate species (**I1'** and **I2'**) by the reductive elimination reaction forming the $\text{C}(\text{sp}^2)\text{-C}(\text{sp})$ bond and a $\text{Au}(\text{I})$ species. The resulting π -complexes (**I1'** and **I2'**) feature the alkynyl bond π -coordinated to Au in the same plane to maximise the $\text{Au} \rightarrow \pi^*(\text{CC})$ backdonation. The activation energy barrier to form **I2'** and **I1'** is greater for **I2** than **I1**, respectively (85.8 vs. 67.1 kJ/mol), however in both pathways this step is exergonic, thus favourable.

Table 10 - Calculated relative standard Gibbs free energy values (ΔG°) and activation energy barriers (E^\ddagger) of the species involved in the intramolecular reaction from **I1** or **I2** to **P1** or **P2** via pathway 1 or 2 in acetone, respectively.³⁷³

Pathway 1		Pathway 2	
Species	ΔG° (kJ/mol)	Species	ΔG° (kJ/mol)
I1	0.0	I2	0.0
TS2' = E₂[‡]	67.1	TS2 = E₂[‡]	85.8
I1'	-110.4	I2'	-79.9
TS3'	-90.5	TS3	-67.3
E₃[‡]	19.9	E₃[‡]	12.6
P1	-168.9	P2	-197.1

The last step to form the products **P1** or **P2**, requires dissociation of the alkyne from the Au(I) complex via **TS3'** or **TS3**. In both cases this step is exergonic, forming the more thermodynamically stable products with a low activation energy barrier of 19.9 kJ/mol for **E₃[‡]** and 12.6 kJ/mol for **E₃[‡]**, respectively.

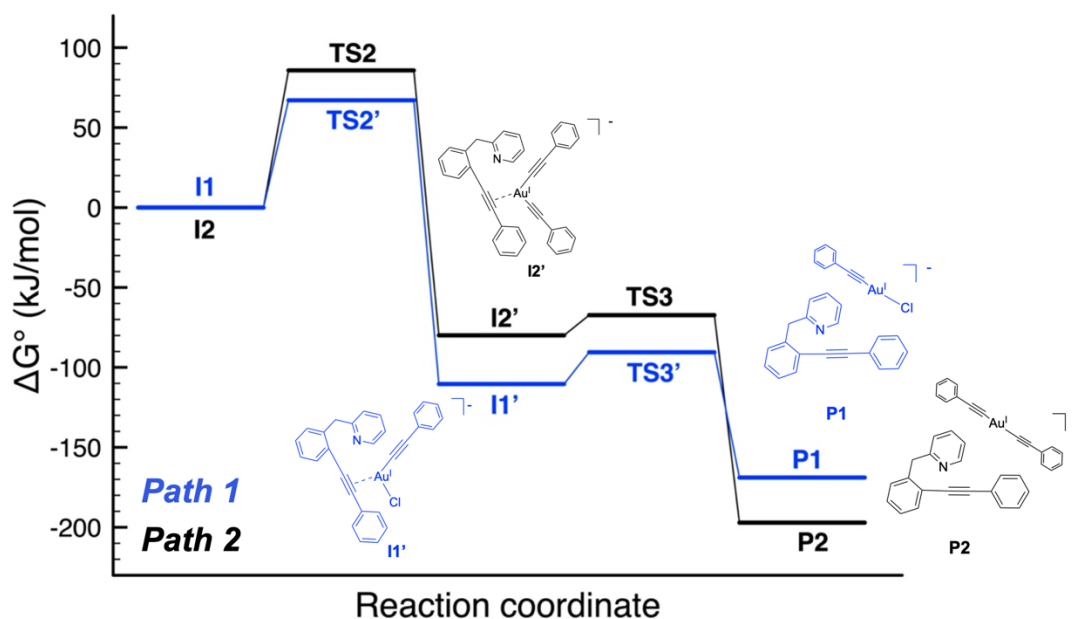


Figure 89 – Comparison of energy values between the two pathways forming **P1** or **P2** from **I1** or **I2**, respectively. Chemdraw structures included for **I1'**, **I2'**, **P1** and **P2**. Results obtained by DFT calculations. Figure adapted from ref 373. Copyright 2021, John Wiley and Sons

<https://creativecommons.org/licenses/by/4.0/>.³⁷³

The overall comparison in energy of the two pathways beginning with **I1** or **I2** can be seen in Figure 89. Both pathways show a similar reaction profile, with only small differences in Path 1 along the different steps. For example, the energy of the transition state **TS2'** is ca. 19 kJ/mol lower than **TS2**, meaning the formation of **I1'** will be kinetically

favoured. Nevertheless, the activation energy of **TS3** is ca. 7.3 kJ/mol lower than **TS3'** and **P2** is more thermodynamically stable than **P1**, by ca. 28 kJ/mol. The greater stability of **P2** must be due to the increased stability of the Au(I) co-product, [Au(I)(PhCC)₂]⁻.

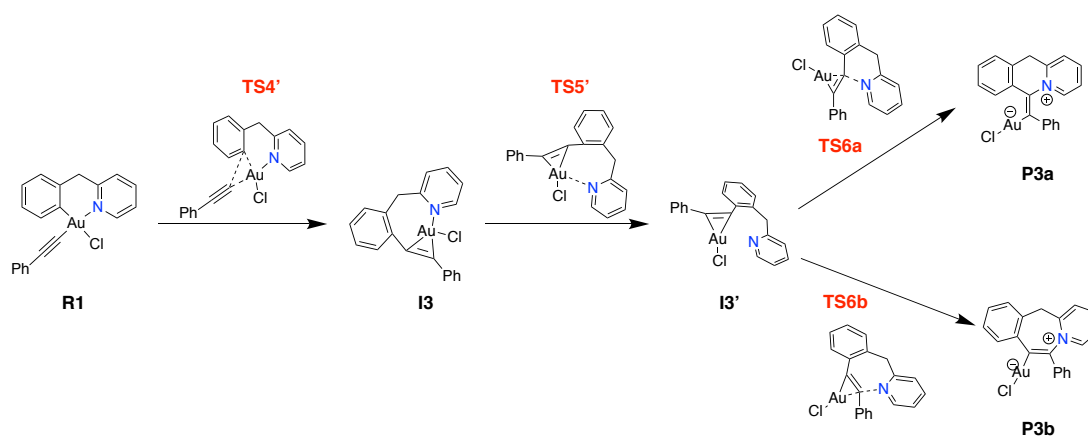
Comparisons were also made with the C-P cross-coupling reaction we previously studied.³⁴¹ Interestingly, the activation energy barriers were comparable for both C-C and C-P cross-coupling using the same level of theory.

Experimentally, we were able to show that the reductive elimination reaction could be observed directly by heating the bis-alkynyl complex **R2**, therefore DFT calculations were performed to evaluate the energy required. The results can be seen in Table 11, concluding that an activation energy (E_4^\ddagger) of at least 80.7 kJ/mol is required to form the C(sp²)-C(sp) bond, which supports our experimental results.

Table 11 - Calculated relative standard Gibbs free energy values (ΔG°) and activation energy barriers (E^\ddagger) of the species involved in the C(sp²)-C(sp) cross-coupling from **R2**.³⁷³

Species	ΔG° (kJ/mol)
R2	0.0
TS4 = E₄[‡]	80.7
I4	-126.3
TS5	-122.1
E₅[‡]	4.3
I4'	-139.9

DFT calculations were also performed to help elucidate the mechanism for the formation of **P3a** and **P3b** from **R1**, as all three were found as crystals in the sample of **R1**. The proposed mechanism can be seen in Scheme 28 and the resulting energies with activation energy barriers in Table 12. The steps from **R1** to **I3'** remain the same to form both **P3a** and **P3b** and involve the formation of the C(sp²)-C(sp) bond by reductive elimination of the Au(III) centre, as well as decoordination of the pyridyl N. The first activation energy barrier (E_4^\ddagger) to form **I3** from **R1** is relatively high, which can be expected as it involves the C(sp²)-C(sp) coupling step, with a value of 87.9 kJ/mol, although this step is exergonic as **I3** is 115.6 kJ/mol more stable than **R1**. The next step to form **I3'** involves the decoordination of the pyridyl N and exhibits a lower activation energy barrier (E_5^\ddagger) of 26.9 kJ/mol. However, this step is less favourable as **I3'** is slightly higher in energy compared to **I3**.



Scheme 28 – Proposed mechanism to form Au(I) vinyl species **P3a** and **P3b** from **R1**, calculated by DFT calculations, including transition states.³⁷³

Next, **I3'** can proceed *via* two steps to form either **P3a** or **P3b**. The activation energy barriers to form both products are very similar, and the thermodynamics of the products formed have very little difference, therefore this could explain why both products were found as a mixture, co-crystallised. The formation of **P3a** and **P3b** is considered to be 'parasitic' as the activation energy barrier from **I3** to **TS4'** is over 200 kJ/mol and so the formation of **I3** from **R1** is irreversible. This means that **R1** is consumed from the pathway to form **P**.

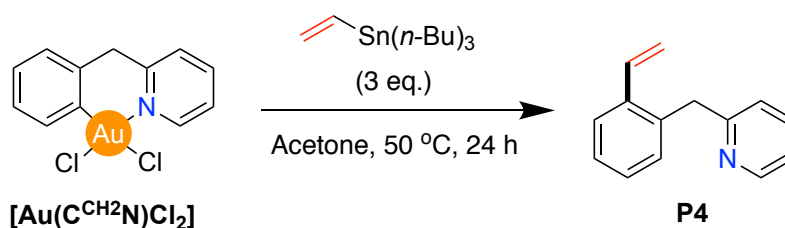
Table 12 - Calculated relative standard Gibbs free energy values (ΔG°) and activation energy barriers (E^\ddagger) of the species to form **P3a** and **P3b** from **R1**.³⁷³

Species		ΔG° (kJ/mol)	
R1		0.0	
TS4' = E₄[‡]		87.9	
I3		-115.6	
TS5'		-88.7	
E₅[‡]		26.9	
I3'		-101.9	
Species	ΔG° (kJ/mol)	Species	ΔG° (kJ/mol)
TS6a	-62.8	TS6b	-60.0
E₆[‡]	39.1	E₇[‡]	41.9
P3a	-145.0	P3b	-142.9

After our thorough investigation into C(sp²)-C(sp) cross-coupling with C(sp) alkynyl substituents, we questioned whether similar reaction conditions could be used with C(sp²)-based nucleophiles to form C(sp²)-C(sp²) cross-coupling products. These reactions are very rare with cyclometalated Au(III) C[^]N complexes, to the best of our knowledge there is only one example in the literature by the group of You, using

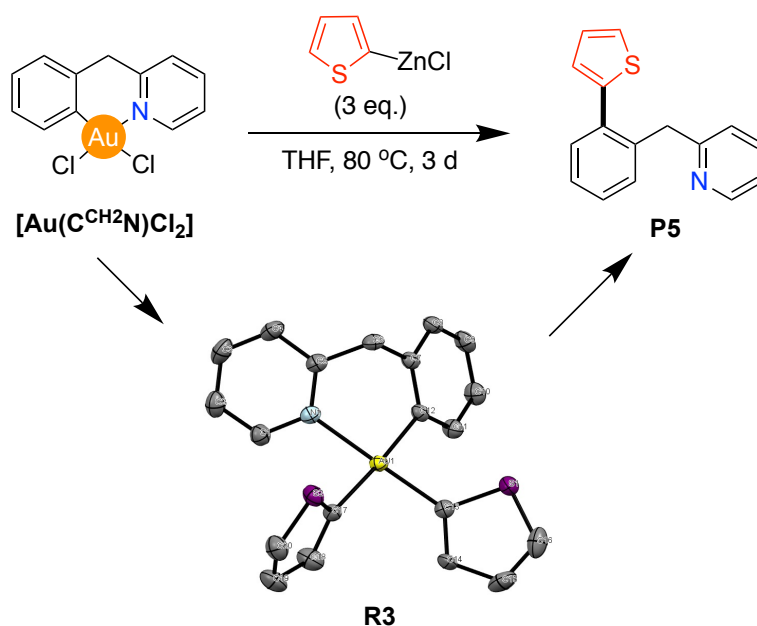
arylboronic acid as coupling partners and harsh, oxidising conditions.³⁷⁰ The following reactions were performed by Mathilde Rigoulet.

A mild organometallic complex, vinyl-tri(*n*-butyl)stannane, was chosen as the first coupling partner and was reacted in similar conditions used to form **P**: 3 eq. of vinyl-tri(*n*-butyl)stannane with $[\text{Au}(\text{C}^{\text{CH}_2\text{N}})\text{Cl}_2]$ (1 eq.) at 50 °C in acetone, overnight (Scheme 29). After column chromatography, **P4** was obtained in a mixture with (*n*-Bu)₃SnCl, which was then removed by extraction to yield **P4** as an oil (44%).



Scheme 29 – C(sp²)-C(sp²) cross-coupling of $[\text{Au}(\text{C}^{\text{CH}_2\text{N}})\text{Cl}_2]$ with vinyl-tri(*n*-butyl)stannane in acetone.³⁷³

After the success of the vinyl stannane complex, the heteroaryl nucleophile, (2-thienyl)zinc chloride, was evaluated as another coupling partner to form the C(sp²)-C(sp²) product with $[\text{Au}(\text{C}^{\text{CH}_2\text{N}})\text{Cl}_2]$. This reaction required slightly harsher conditions (THF (tetrahydrofuran) as a solvent, 80 °C and a reaction time of 3 d) (Scheme 30); however, the same equivalents of the coupling partner and Au(III) C[^]N complex were used as above to form **P** and **P4**. After 3 days, **P5** was isolated with a 71% yield after column chromatography. Interestingly, the bis(2-thienyl) C[^]N Au(III) intermediate **R3** could be synthesised and characterised by reacting $[\text{Au}(\text{C}^{\text{CH}_2\text{N}})\text{Cl}_2]$ (1 eq.) with (2-thienyl)zinc chloride (3 eq.) in THF at room temperature for 2 h. Crystals of **R3** were grown by slow evaporation of dichloromethane (CH₂Cl₂) (Scheme 30), and XRD analysis confirmed that the structure of **R3** was very similar to **R2**.



Scheme 30 - C(sp²)-C(sp²) cross-coupling of [Au(C<sup>CH₂N)Cl₂] with (2-thienyl)zinc chloride in THF to form **P5**. The molecular structure of the bis(2-thienyl) Au(III) complex **R3** is also present, ellipsoids are shown at 50% probability with H atoms omitted for clarity. Partial figure adapted from ref 373. Copyright 2021, John Wiley and Sons
<https://creativecommons.org/licenses/by/4.0/>.³⁷³</sup>

7.3. Summary and Future Outlook

To summarise, this work has delved into the viability of C-C cross-coupling reactions mediated by a cyclometalated Au(III) C^N complex, as well as the mechanistic details of this reaction, which remains sparse in the literature. In detail, we have investigated the C(sp²)-C(sp) cross-coupling between [Au(C^{CH₂N)Cl₂] and AgPhCC in relatively mild conditions, similar to our previous C-P cross-coupling work.³⁴¹ The reaction was then studied using ¹H NMR in different solvents and conditions to elucidate the most efficient way to identify the intermediates. The optimised conditions led us to identify intermediates involved in the cross-coupling reaction and we were then able to isolate and fully characterise two of these by different methods including: 2D NMR and XRD studies. The XRD analysis also led us to a serendipitous identification of ‘parasitic’ Au(I) vinyl complexes, which are capable of consuming the **R1** intermediate irreversibly. Furthermore, we demonstrated the versatility of the cross-coupling reaction with [Au(C^{CH₂N)Cl₂] by successfully performing the C(sp²)-C(sp²) reaction with vinyl tin and heteroaryl zinc reagents.}}

Overall, the combination of experimental studies and DFT calculations have led us to propose a mechanism for the C(sp²)-C(sp) cross-coupling reaction which can hopefully help improve the understanding of Au(III)-mediated catalytic reactions in the future. Future work in this area includes expanding the library of Au(III) cyclometalated

C[^]N complexes to perform these reactions, as seen in our C-S and C-P cross-coupling work,^{305,308,341} to identify possible structure-activity relationships.

7.4. Materials and Methods

7.4.1. General

P4, (2-thienyl)zinc chloride, **R3** and **P5** were synthesised by Mathilde Rigoulet. X-ray diffraction studies were performed by Christian Jandl. Computational analysis was performed by Prof. Giampaolo Barone.

Solvents and reagents (reagent grade) were commercially available and used without purification. ^1H , $^{13}\text{C}\{^1\text{H}\}$ and 2D NMR spectra were recorded on Bruker Avance (300-500 MHz) NMR spectrometers in acetone- d_6 solution, with TMS as an internal reference. They were analysed using MestReNova v.14 by MestreLab Research S.L. Benzylether was used as an internal standard to determine the reaction yield in DMSO- d_6 . Additionally, hexamethylbenzene was used as an internal standard to determine the reaction yield of the coupling reaction with stannanes in acetone- d_6 . HR-ESI-MS spectra were recorded on a Synapt G2-Si time-of-flight (TOF) mass spectrometer (Waters). Mass spectra were recorded and processed using MassLynx V4.1 (Waters). The synthesis of the Au(III) cyclometalated complex $[\text{Au}(\text{C}^{\text{CH}_2\text{N}})\text{Cl}_2]$ is reported in Chapter 5.

7.4.2. Synthetic procedures

Synthesis of silver phenylacetylde

*Synthesised following a literature procedure.*³⁷⁹

A solution of silver nitrate (170 mg, 1 mmol, 1.1 eq.) in a mixture of acetonitrile and triethylamine (2:1, 5 mL : 3.4 mL, respectively) was added to a stirred solution of phenylacetylene (100 μl , 0.91 mmol, 1 eq.) in acetonitrile (6.4 mL) at room temperature. This was left to stir in darkness for 3 h. The resulting precipitate was collected and washed with acetonitrile. After leaving to dry protected from light the product was isolated (183 mg, 0.876 mmol, 96%).

Synthesis of P

$[\text{Au}(\text{C}^{\text{CH}_2\text{N}})\text{Cl}_2]$ (50 mg, 0.11 mmol, 1 eq.) was suspended in acetone (25 mL) before the addition of silver phenylacetylde (71 mg, 0.34 mmol, 3 eq.). The mixture was then stirred at 50 °C overnight. Subsequently, the resulting suspension was then filtered and the filtrate was purified *via* flash chromatography (*n*-hexane : ethyl acetate, 85:15). The desired product was formed as a yellow oil (10 mg, 0.037 mmol, 33%).

^1H NMR (400 MHz, Acetone- d_6) δ 8.52 (d, J = 5.8 Hz, 1H), 7.66 (td, J = 7.7, 1.9 Hz, 1H), 7.59 – 7.50 (m, 3H), 7.47 – 7.37 (m, 3H), 7.39 – 7.27 (m, 3H), 7.25 (d, J = 7.9 Hz, 1H), 7.18 (ddd, J = 7.6, 4.8, 1.2 Hz, 1H), 4.43 (s, 2H).

$^{13}\text{C}\{^1\text{H}\}$ NMR (126 MHz, Acetone- d_6) δ 160.42, 149.23, 141.75, 136.26, 132.05, 131.37, 130.15, 128.68, 128.54, 128.48, 126.54, 123.22, 122.95, 122.85, 121.23, 93.25, 88.08, 42.76.

HR-ESI-MS (CH₃CN, pos. mode) for C₂₀H₁₆N⁺: exp. 270.1307 (calc. 270.1283).

Synthesis of R2

[Au(C^{CH₂}N)Cl₂] (48 mg, 0.11 mmol, 1 eq.) was suspended in acetone (14 mL) before the addition of silver phenylacetylide (71 mg, 0.34 mmol, 3 eq.). The mixture was stirred overnight at room temperature and the resulting suspension was then filtered. The filtrate was purified *via* flash chromatography (CH₂Cl₂ : CH₃OH 100→98%) to yield the desired product as a yellow solid (31 mg, 0.055 mmol, 48%).

^1H NMR (500 MHz, Acetone- d_6) δ 9.48 (d, J = 5.0 Hz, 1H), 8.24 (td, J = 7.7, 1.6 Hz, 1H), 8.01 – 7.99 (m, 1H), 7.99 – 7.96 (m, 1H), 7.70 (ddd, J = 7.4, 5.8, 1.5 Hz, 1H), 7.46 – 7.40 (m, 4H), 7.36 – 7.22 (m, 7H), 7.15 – 7.11 (m, 2H), 4.41 (s, 2H).

$^{13}\text{C}\{^1\text{H}\}$ NMR (126 MHz, Acetone- d_6) δ 158.55, 154.01, 149.04, 143.27, 137.97, 136.53, 132.28, 132.22, 129.04, 128.96, 128.43, 127.85, 127.64, 127.51, 127.40, 127.22, 126.79, 125.22, 119.20, 103.29, 99.91, 79.16, 77.85, 48.75.

HR-ESI-MS (CH₃CN, pos. mode) for C₂₈H₂₀NNa⁺: exp. 590.1146 (calc. 590.1159).

Synthesis of R1

Compound **R2** (61.7 mg, 0.11 mmol, 1 eq.) was dissolved in acetone (16 mL) before the addition of an equimolar amount of [Au(C^{CH₂}N)Cl₂] (48 mg, 0.11 mmol, 1 eq.). The suspension was stirred overnight and formed a pale-yellow solution. Purification was performed *via* flash chromatography (*n*-hexane : ethyl acetate, 40:60) to afford the desired product as an off-white solid (51 mg, 0.1 mmol, 85%).

^1H NMR (400 MHz, Acetone- d_6) δ 9.22 (dd, J = 5.8, 1.6 Hz, 1H), 8.24 (td, J = 7.7, 1.6 Hz, 1H), 7.98 (d, J = 7.5 Hz, 1H), 7.80 (dd, J = 7.7, 1.3 Hz, 1H), 7.72 (ddd, J = 7.5, 5.8, 1.5 Hz, 1H), 7.43 – 7.36 (m, 2H), 7.40 – 7.26 (m, 5H), 7.20 (t, J = 7.3 Hz, 1H), 7.11 (t, J = 7.6 Hz, 1H), 4.47 (s, 1H).

$^{13}\text{C}\{^1\text{H}\}$ NMR (126 MHz, Acetone- d_6) δ 157.40, 152.19, 143.31, 139.95, 136.54, 134.87, 132.30, 129.58, 129.05, 128.61, 128.10, 128.02, 127.92, 126.65, 126.59, 125.37, 125.09, 98.94, 81.67, 47.52.

HR-ESI-MS (CH₃CN, pos. mode) for C₂₀H₁₅AuN⁺: exp. 466.0833 (calc. 466.0870).

Elemental analysis for C₄₁H₄₄Au₂Cl₄N₂O₆ (**2R1**·6H₂O·CH₂Cl₂): exp. C 41.04 %, H 3.43 %, N 2.87 % (calc. C 41.16 %, H 3.71 %, N 2.34 %).

Synthesis of P4

Synthesised by Mathilde Rigoulet

[Au(C^{CH₂}N)Cl₂] (43 mg, 0.10 mmol, 1 eq.) was suspended in acetone (10 mL) before the addition of vinyl-tri(*n*-butyl)stannane (88 μ L, 0.30 mmol, 3 eq.). The mixture was then stirred at 50 °C overnight before purification *via* flash chromatography (*n*-pentane : ethyl acetate, 85:15). This resulted in a mixture of the product and (*n*-Bu)₃SnCl. Thus, CH₃CN (10 mL) was used to dissolve the mixture allowing (*n*-Bu)₃SnCl to be extracted with *n*-pentane (3 x 10 mL). CH₃CN was removed under vacuum to yield the desired product as an oil (8.5 mg, 0.044 mmol, 44%). A reaction was also performed in an NMR tube (starting from 0.01 mmol of [Au(C^{CH₂}N)Cl₂]) with hexamethylbenzene as an internal standard in acetone-*d*₆, which resulted in a quantitative NMR yield (> 99%).

¹H NMR (300 MHz, Acetone-*d*₆) δ 8.51-8.47 (m, 1H), 7.64 (td, *J* = 7.7, 1.9 Hz, 1H), 7.60-7.53 (m, 1H), 7.31-7.20 (m, 3H), 7.20-7.15 (m, 1H), 7.14 (dd, *J* = 17.4, 11.0 Hz, 1H), 7.11-7.07 (m, 1H), 5.65 (dd, *J* = 17.4, 1.5 Hz, 1H), 5.23 (dd, *J* = 11.0, 1.5 Hz, 1H), 4.23 (s, 2H).

¹³C{¹H} NMR (75 MHz, Acetone-*d*₆) δ 161.65, 149.93, 137.92, 137.84, 137.32, 135.84, 131.59, 128.77, 127.74, 126.49, 123.65, 122.06, 115.79, 42.38.

EI-MS for C₁₄H₁₁N: exp. 195.25 (calc. 195.10).

Synthesis of (2-thienyl)zinc chloride

Synthesised by Mathilde Rigoulet

To a solution of 2-bromothiophene (194 μ L, 2 mmol) in THF (4 mL, 0.5 M), *n*-BuLi (1.5 mL, 1.46 M, 1.1 eq.) was added dropwise at -78 °C. This was then left to stir for 1 h. After stirring, a freshly prepared solution of ZnCl₂ (300 mg, 2 mL of THF, 1.1 eq.) was added dropwise at -78 °C. The mixture was then allowed to warm to room temperature for 1 h whilst stirring, before the solution was titrated using a THF solution of I₂.

Synthesis of R3

Synthesised by Mathilde Rigoulet

[Au(C^{CH₂}N)Cl₂] (43 mg, 0.10 mmol, 1 eq.) was suspended in THF (9 mL) before the addition of (2-thienyl)zinc chloride (1.1 mL of solution in THF, C = 0.26 M, 0.30 mmol, 3 eq.) at 0 °C. This was then stirred at room temperature for 2 h before purification *via* flash chromatography (*n*-pentane : ethyl acetate, 70:30) to yield **R3** as a white solid (22.1 mg, 42% yield).

¹H NMR (500 MHz, CD₂Cl₂) δ 8.55-8.51 (m, 1H), 7.89 (td, *J* = 7.7, 1.7 Hz, 1H), 7.66 (d, *J* = 7.7, 1H), 7.47 (dd, *J* = 4.8, 0.8 Hz, 1H), 7.41 (dd, *J* = 5.1, 1.0 Hz, 1H), 7.28-7.24 (m, 2H), 7.23 (dd, *J* = 7.3, 1.5 Hz, 1H), 7.16 (dd, *J* = 4.8, 3.3 Hz, 1H), 7.08 (dd, *J* = 5.1, 3.3

Hz, 1H), 7.03 (td, $J = 7.3, 1.5$ Hz, 1H), 6.98 (td, $J = 7.3, 1.6$ Hz, 1H), 6.96 (dd, $J = 3.4, 1.0$ Hz, 1H), 6.90 (dd, $J = 3.3, 0.8$ Hz, 1H), 4.38 (s, 2H).

$^{13}\text{C}\{^1\text{H}\}$ NMR (126 MHz, CD_2Cl_2) δ 163.95, 159.10, 157.72, 152.00, 141.46, 137.27, 136.49, 131.08, 130.72, 128.32, 127.94, 127.72, 127.54, 127.16, 127.10, 126.63, 126.27, 125.79, 124.02, 49.30.

EI-MS for $\text{C}_{16}\text{H}_{13}\text{AuNS}$: exp. 448.0 (calc. 448.04).

Synthesis of P5

Synthesised by Mathilde Rigoulet

$[\text{Au}(\text{C}^{\text{CH}_2}\text{N})\text{Cl}_2]$ (88 mg, 0.20 mmol, 1 eq.) was suspended in THF (17 mL) before the addition of (2-thienyl)zinc chloride (2.8 mL of solution in THF, $C = 0.22$ M, 0.60 mmol, 3 eq.) at 0 °C. The mixture was then stirred at 80 °C for 3 days. The reaction mixture was quenched with addition of an aqueous solution of HCl and extracted with CH_2Cl_2 . The organic layers were combined and washed with brine, then dried over Na_2SO_4 . After filtration, the solution was purified *via* flash chromatography (*n*-pentane : ethyl acetate, 80:20) to yield the desired product (35.7 mg, 71% yield).

^1H NMR (300 MHz, CDCl_3) δ 8.53 (d, $J = 4.3$ Hz, 1H), 7.51 (td, $J = 7.8, 1.9$ Hz, 1H), 7.46-7.41 (m, 1H), 7.32-7.25 (m, 4H), 7.11-7.04 (m, 1H), 7.02 (dd, $J = 5.1, 3.5$ Hz, 1H), 6.96 (dd, $J = 3.5, 1.2$ Hz, 1H), 6.88 (d, $J = 7.8$ Hz, 1H), 4.30 (s, 2H).

$^{13}\text{C}\{^1\text{H}\}$ NMR (75 MHz, CDCl_3) δ 161.21, 149.39, 142.56, 137.79, 136.48, 134.72, 131.39, 131.02, 128.39, 127.23, 126.86, 126.73, 125.57, 123.23, 121.19, 42.29.

DCI/ NH_3 -MS for $\text{C}_{16}\text{H}_{13}\text{NS}$: exp. 252.2 (calc. 252.1).

7.4.3. ^1H NMR Reaction Monitoring

The cross-coupling reactions to yield product **P** were monitored at room temperature over 24 h by ^1H NMR spectroscopy, on a Bruker Avance (400 MHz). The samples were prepared by suspending 1 eq. of $[\text{Au}(\text{C}^{\text{CH}_2}\text{N})\text{Cl}_2]$ and 2 eq. of AgPhCC in 1 mL of the deuterated solvent in an NMR tube. The reactions were carried out in acetone- d_6 , methanol- d_4 , acetonitrile- d_3 , DMF- d_7 and DMSO- d_6 . The spectra were collected and analysed using the Reaction Monitoring plugin in MestReNova v.14 (Mestrelab Research S.L.).

7.4.4. Crystal Formation for XRD Analysis

R1, **P3a** and **P3b** were co-crystallised by layering *n*-pentane on a saturated solution of **R1** in CH_2Cl_2 . Crystals of **R3** were obtained by slow evaporation of a CH_2Cl_2 solution.

8. Water-Soluble AuNPs stabilised by
N-heterocyclic carbenes.

8.1. Introduction

Gold nanoparticles (AuNPs) are amongst the most explored type of nanomaterials due to their vast array of applications in many fields, including: catalysis, energy and medicine.³⁸⁰ The unique surface plasmon resonance (SPR) band of AuNPs can be identified by irradiation with light at specific frequencies, which is dependent on many factors including size and shape of the NPs.²¹⁴

AuNPs require stabilisation by ligands to avoid irreversible aggregation due to van der Waals interactions between the AuNP metallic core and their high surface energies.³⁸¹ A vast array of ligands have been reported in the literature; most common are the organosulfur ligands, including thiols and sulfides, due to their aurophilic nature and large packing density, as well as steric and electrostatic stabilisers (e.g. PVA (polyvinyl alcohol), PVP (polyvinylpyrrolidone) and citrate).^{222,381} However, such stabilisers are not always ideal due to the lack of oxidative and thermal stability of the Au-S bond, as well as difficulties in derivatisation preventing further functionalisation of the AuNPs.³⁸¹ Therefore, researchers began investigating different stabilising ligands, including N-heterocyclic carbenes (NHCs).

To date, the most common application of NHCs in materials science is to stabilise metal NPs and surfaces due to the strong NHC-M bond.²²³ The electronic structure of NHCs is responsible for the enhanced sigma-donor properties of the carbonic centre.²²³ So far, two main synthetic procedures have been employed to form NHC stabilised AuNPs (NHC@AuNPs): the 'top-down' and 'bottom-up' approaches (Figure 90), respectively.³⁸⁰ The 'top-down' approach typically involves the addition of the deprotonated imidazolium precursor, which is often formed *in situ*, to AuNPs possessing a weaker stabilising ligand that is replaced by ligand exchange at the NP surface (Figure 90A).³⁸⁰ Conversely, the 'bottom-up' approach involves the direct reduction of pre-formed Au(I) NHC complexes (Figure 90B).³⁸⁰

The first example of NHC@AuNPs formed by the 'top-down' method was reported by Chechik and co-workers in 2009, which involved the ligand exchange of didodecyl sulfide (DDS) to bis-*tert*-butylimidazol-2-ylidene.²⁴³ In the same year, the first example of the 'bottom-up' approach was demonstrated by Vignolle and Tilley, involving the reduction of mono-NHC Au(I) complexes using two different reducing agents (KBEt₃H (potassium triethylborohydride) and 9-BBN (9-borabicyclo[3.3.1]nonane)).²⁴⁴

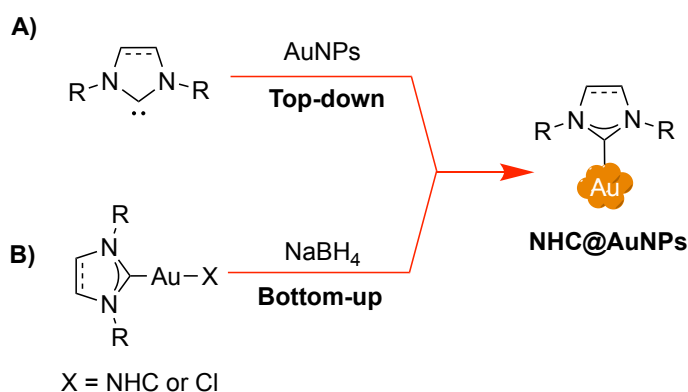


Figure 90 – Two general procedures to form NHC stabilised AuNPs: **A)** ‘top-down’ approach and **B)** ‘bottom-up’ approach, respectively.

Over the years, these methods have been employed and adapted to form NHC@AuNPs of different types, including ultra-small NHC@AuNPs,²⁵² NHC functionalised conducting polymer/AuNP hybrids,²⁴⁵ amphiphilic AuNPs,²⁵⁴ chiral amino acid-derived NHC@AuNPs²⁵⁹ and dendrimer encapsulated NHC@AuNPs.²⁶⁰

However, for use in biomedical applications, the NHC@AuNPs require aqueous-solubility and stability, the latter often being challenging, especially in the presence of biologically relevant compounds such as glutathione (GSH). The first example of water-soluble NHC@AuNPs was reported by MacLeod and Johnson in 2015.²⁶³ These PEGylated NHC@AuNPs were formed by the ‘bottom-up’ approach and showed stability in various biologically relevant conditions, including in the presence of GSH.²⁶³

Later that year, Glorius and co-workers used the ‘top-down’ approach to form water-soluble AuNPs with sulfonated imidazolium ligands, which displayed stability over months in aqueous solution with a pH >4.²⁶⁴ Afterwards, the same group published the first example of NHC stabilised bimetallic NPs formed from an Au-Pd alloy by the ‘top-down’ approach.³⁸² These bimetallic NPs were also water-soluble and demonstrated their catalytic performance in both oxidation and hydrogenation reactions.³⁸² Considering that typical Au/Pd bimetallic nanoparticles are often utilised for catalytic reactions, including hydrogenation, oxidation of alkanes, alcohols, polyols, C-C coupling,³⁸³ it can be envisaged that the development of new NHC stabilisers may have an impact on a wide variety of catalytic processes. More recently, DeJesus *et al.*²⁶⁹ reported the post-synthetic modification of nitro-groups on NHC@AuNPs to form amine groups for amide coupling; unfortunately, the stability and biological evaluation of the NPs were not investigated.²⁶⁹

Taking inspiration from their previous work,²⁵⁹ Reithofer and co-workers³⁸⁴ reported the synthesis of water-soluble histidine-2-ylidene@AuNPs by the ‘bottom-up’ approach and their stability in biologically relevant solutions, including a 2 mM aqueous GSH solution.³⁸⁴ The ‘bottom-up’ approach was also used by Pleixats and co-workers²⁷¹

to synthesise PEG-tagged NHC@AuNPs, which were used as recyclable catalysts for the synthesis of propargylamines by A^3 coupling of aldehydes, terminal alkynes and amines, as well as the cycloisomerisation of γ -alkynoic acids.²⁷¹

One of the few examples of water-soluble NHC@AuNPs for biomedical applications was published by Crudden and co-workers in 2017.²⁹⁶ In this study, NHC@AuNPs featuring carboxylate groups in the NHC scaffold were synthesised.²⁹⁶ The NPs had an average particle size of 4.2 ± 0.7 nm and exhibited moderate stability in biologically relevant conditions, including a 2 mM GSH solution.²⁹⁶ They also showed potential as possible probes for photoacoustic imaging.²⁹⁶

Of note, the use of NHC stabilising ligands is not just limited to spherical AuNPs, MacLeod *et al.*²⁹⁷ reported the first example of gold nanorods (NHC@AuNRs) with a length of 42.6 ± 6.7 nm and width of 9.9 ± 1.3 nm, synthesised by a combined 'top-down' and adatom approach, and demonstrated their extraordinary applicability for *in vitro* photothermal therapy.²⁹⁷

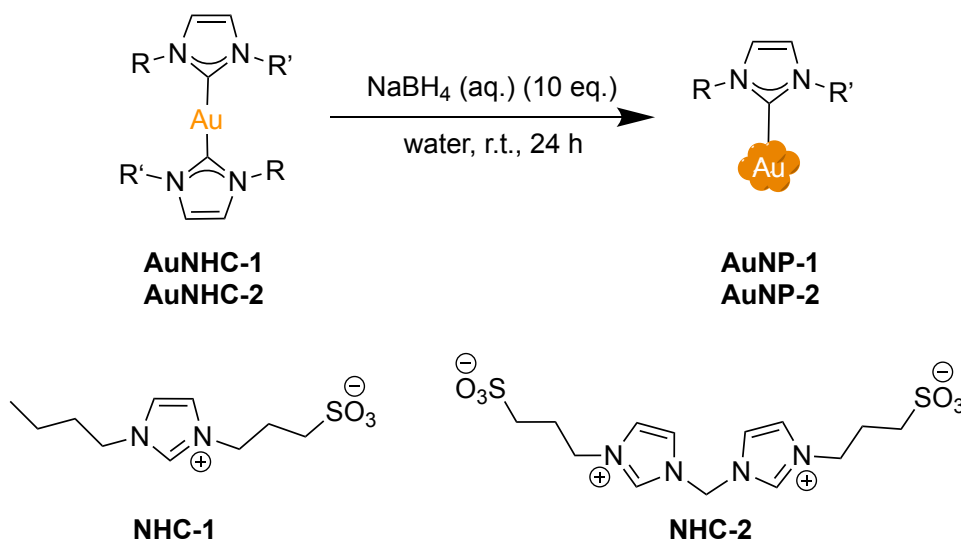
Overall, aside from these seminal examples, the use of NHC@AuNPs for catalysis and biomedical applications is still in its infancy, with no reports to date of NHC@AuNPs being used for catalysis in living cells for therapy or further biomedical applications. Nevertheless, the use of AuNPs to catalyse bioorthogonal reactions in the brains of zebrafish has been demonstrated by Unciti-Broceta and co-workers, bringing great motivation to this area.²⁰² Therefore, the aim of this work is to explore the ability of water-soluble/dispersible NHC@AuNPs to catalyse reactions in aqueous environment, for future applications in bioorthogonal transformations in cells.

8.2. Results and Discussion

TG measurements were performed by Dr. Greg Shaw. XPS was performed by Dr. David Morgan. TEM was performed by Dr. Thomas Davies. ICP-MS studies were performed by Mr. Simon Waller.

8.2.1. Synthesis of water-soluble NHC@AuNPs

The chosen synthetic approach to form NHC@AuNPs was the 'bottom-up' method, inspired by the work of Salorinne *et al.*²⁹⁶ Initially, the synthesis of the water-soluble NHC ligands and corresponding Au(I) NHC complexes was performed. One of the Au(I) NHC complexes investigated was previously reported by our group and features sulfonate groups to enhance hydrophilicity.³⁸⁵



Scheme 31 – Formation of NHC@AuNPs in aqueous conditions from their corresponding Au(I)NHC complexes in the presence of sodium borohydride (NaBH₄).

The ligands (**NHC-1** and **NHC-2**, Scheme 31) were synthesised by a straightforward nucleophilic addition reaction between the corresponding imidazole and 1,3-propanesultone.^{386,387} Subsequently, the Au(I) NHC complexes (**AuNHC-1** and **AuNHC-2**, Scheme 31) were formed *via* transmetalation of the respective Ag(I) bis-NHC complex in the presence of the Au(I) precursor, [Au(SMe₂)Cl] (SMe₂ = dimethylsulfide).^{385,388} The NHC@AuNPs were then formed by dissolving the Au(I) complexes in water before the fast addition of an aqueous fresh solution of excess NaBH₄ (Scheme 31). The solution was then stirred for 24 h to ensure full reduction and narrow size distribution, as described by Salorinne *et al.*,²⁹⁶ where they concluded that longer reaction time gave slightly larger NPs with a small particle size distribution. The formation of the NHC@AuNPs was monitored by Ultra Violet-Visible (UV-Vis) spectroscopy, which can give important details on the NP size and shape due to their inherent SPR band.³⁸⁹ The maximum wavelength (λ_{max}) of the SPR band increases with increasing particle diameter, and broadening of the SPR band can be indicative of aggregate formation.³⁸⁹ Overall, the characterisation techniques used to confirm NHC@AuNP formation, as well as properties including size and stability were: UV-Vis spectroscopy, ¹H NMR (nuclear magnetic resonance) spectroscopy, XPS (X-ray photoelectron spectroscopy), FTIR-ATR (Fourier-transform infrared attenuated total reflectance) spectroscopy, TEM (transmission electron microscopy) and TGA (thermogravimetric analysis).

In a first series of studies, the aqueous AuNP solution obtained from the 'bottom-up' approach was centrifuged to remove any insoluble material before being lyophilised. UV-Vis spectroscopy was first used to check for the presence of an SPR band and its position, as well as the stability of the NPs in aqueous solution over time. Therefore, to obtain the spectra shown in Figure 91: 0.43 mg of **AuNP-1** and 4 mg of **AuNP-2** were solubilised in 500 μL unbuffered MilliQ water and their stability was monitored over 15 h.

Both NPs feature an SPR band around 500 nm, with **AuNP-1** exhibiting a more intense band. The broader band seen for **AuNP-2** could indicate that there are multiple species present, also due to partial reduction of the Au(I) precursor. However, the **AuNP-2** solution becomes very dark during the reduction, which is indicative of NP formation. Unfortunately, due to the lack of Au(I) absorption bands in the visible region as well as the intense absorbance of the NHC ligand below 400 nm, remaining Au(I) species cannot be detected by spectrophotometry.

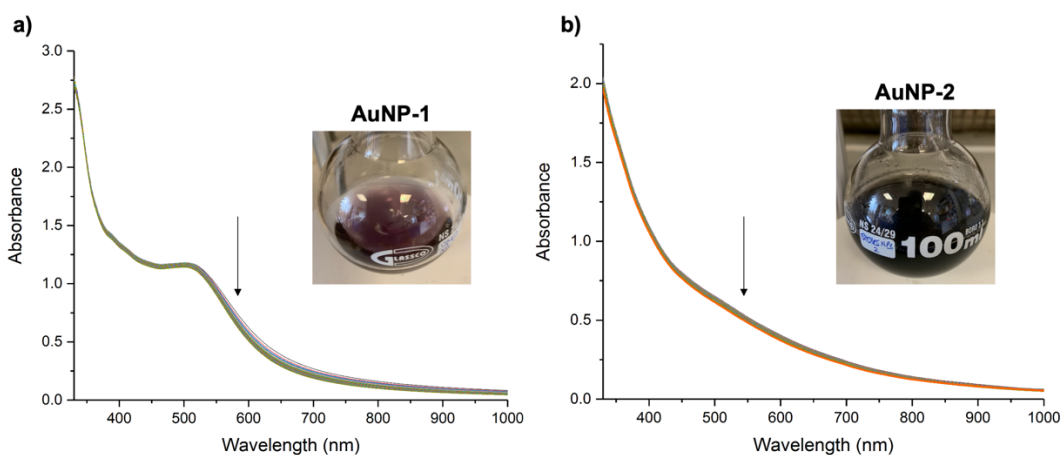


Figure 91 - UV-Vis Spectra of **a) AuNP-1** and **b) AuNP-2** in MilliQ water over 15 h. Spectra recorded every 15 min for the first hour and then every 30 min until 15 h. Insert: Images of the NHC@AuNP solutions after reduction.

TEM characterisation of the NHC@AuNPs indicated that organic material was still present on the surface of the NPs due to very small particles buried with poor contrast making them difficult to visualise, as well as large aggregates (Figure 92).

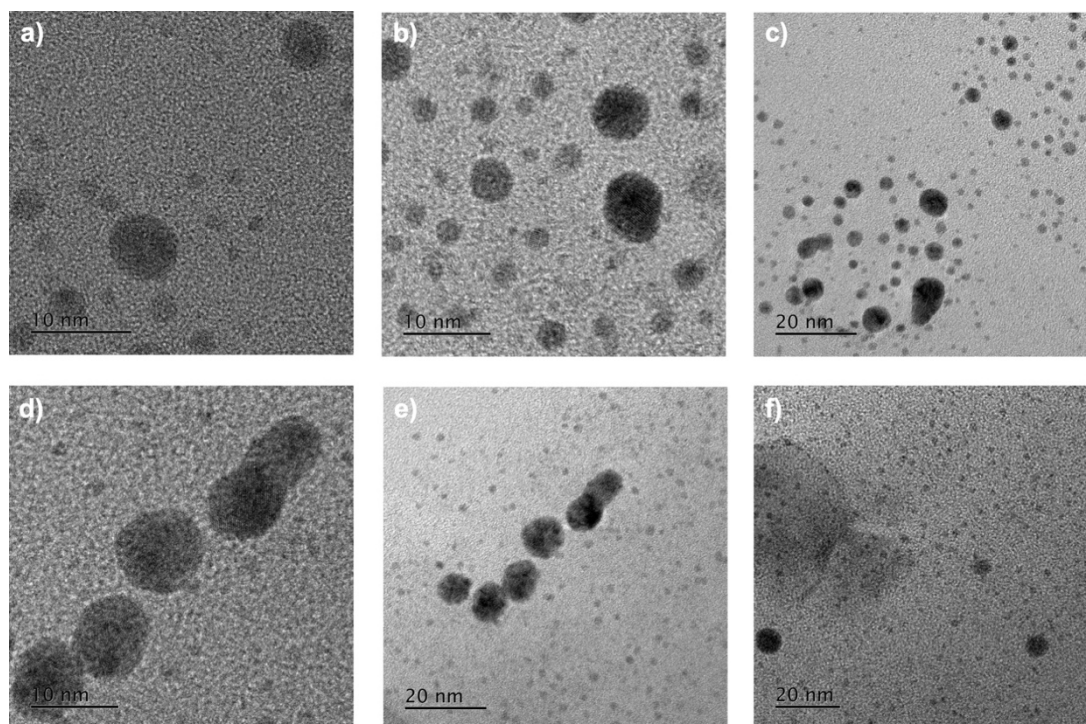


Figure 92 – TEM images of NHC@AuNPs after lyophilisation: a)-c) **AuNP-1** and d)-f) **AuNP-2**. Scale bars included in each image.

The average particle size was determined over a large statistical data set. In total, 596 particles were measured for **AuNP-1** over 3 images with an average diameter of 1.89 ± 1.39 nm, and 767 particles for **AuNP-2** over 2 images with an average diameter of 1.29 ± 0.94 nm (Figure 93). As shown in Figure 93, there is quite a large range in size distribution of both NPs, particularly **AuNP-1**.

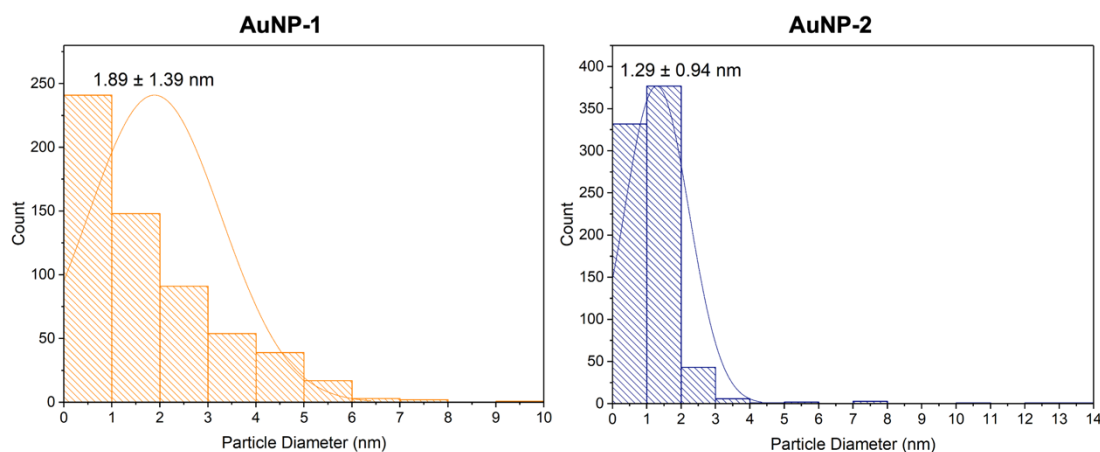


Figure 93 – Particle size histograms of NHC@AuNPs before dialysis: **AuNP-1** displayed an average size of 1.89 ± 1.39 nm and **AuNP-2** displayed an average size of 1.29 ± 0.94 nm.

In addition, XPS analysis (Table 13) showed that there is a higher concentration of Au(I) present compared to Au(0) on the NP surface for both NHC@AuNPs, suggesting that some of the Au(I) NHC complex could still be present, as speculated for **AuNP-2** from

the broad SPR band (Figure 91b). It is worth mentioning that similar results were obtained by Pleixats and co-workers²⁷¹ who tried to enhance the percentage of Au(0) by increasing the amount of NaBH₄. Unfortunately, this made very little difference to the amount of Au(I) present. Therefore, the authors proposed that a mixture of Au(0) and Au(I) species were forming the NP surface.²⁷¹

Table 13 - XPS data (binding energy (BE) and composition) for **AuNP-1** and **AuNP-2** before dialysis.

Peak	AuNP-1		AuNP-2	
	BE (eV)	%At Conc.	BE (eV)	%At Conc.
Au 4f (Au(I))	84.99	0.33	85.18	0.11
Au 4f (Au(I))	88.66	0.24	88.85	0.08
Au 4f (Au(0))	82.98	0.06	83.07	0.07
Au 4f (Au(0))	86.65	0.04	86.74	0.05
B 1s	191.44	10.42	191.72	17.19
C 1s	284.8	25.71	284.8	11.3
C 1s	286.13	8.73	286.09	3.36
C 1s	288.52	3.49	288.2	2.11
F 1s	687.77	0.82	688.16	0.46
N 1s	400.6	2.45	400.76	0.86
N 1s	398.72	0.73	399.03	0.49
Na 1s	1070.84	11.76	1071.02	16.9
O 1s	531.03	33.39	531.27	45.83
S 2p	167.56	1.22	167.92	0.79
S 2p	168.77	0.61	169.17	0.39

Consequently, we opted for purification of the NPs surface by dialysis rather than increasing the NaBH₄ amount. The dialysis was carried out straight after reduction with NaBH₄ as described in the experimental section. Once the dialysis was complete the AuNP solutions were filtered. This was essential in the case of **AuNP-1** as aggregation had occurred meaning the AuNPs were precipitating out of solution. The subsequent aqueous filtrates were then lyophilised and characterised fully as described in the following sections.

8.2.2. Characterisation of water-soluble AuNPs

8.2.2.1. Stability Studies

Stability studies of the NPs after dialysis was performed by UV-Vis spectroscopy as described above. The UV-Vis spectra of both NPs in unbuffered MilliQ water appeared

very similar to the spectra measured before dialysis (Figure 91a and b). In detail, **AuNP-1** possessed an intense SPR band centred around 515 nm, which remained relatively stable over 15 h exhibiting a minimal loss in absorbance of ca. 4% (Figure 94a). In MilliQ water, **AuNP-2** showed a relatively broad SPR band around 520 nm, indicating that some Au(I) species could still be present despite dialysis. The **AuNP-2** remained very stable over 15 h in water with only a 0.5% decrease in absorbance of the SPR band at 520 nm (Figure 94b).

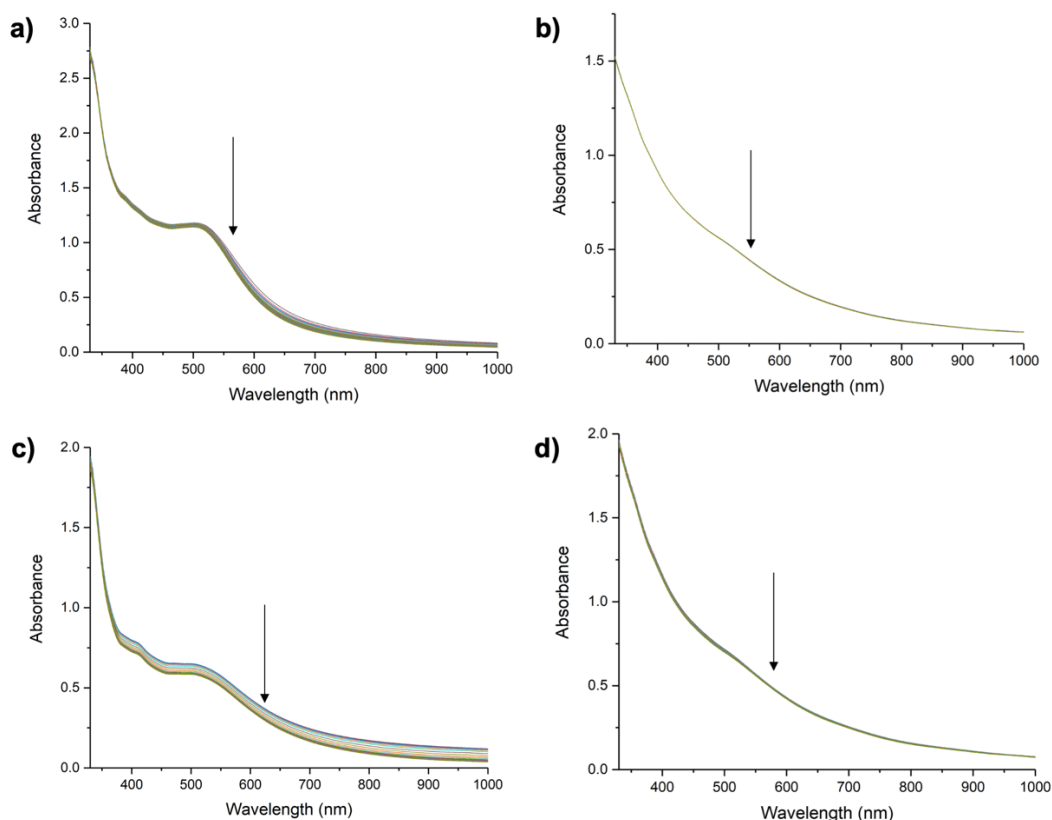


Figure 94 – UV-Vis Spectra of **a) AuNP-1** and **b) AuNP-2** in MilliQ water; and **c) AuNP-1** and **d) AuNP-2** in PBS 1x (pH 7.4) over 15 h after dialysis. Spectra recorded every 15 min for the first hour and then every 30 min until 15 h.

Stability in biological conditions is paramount for the use of AuNPs in biomedical applications, therefore the stability of the NPs in PBS 1x (phosphate buffered solution) was assessed over 15 h (Figure 94c and d), which showed a similar trend to that observed in water. The biological compatibility was then explored further by the addition of an aqueous 2 mM solution of GSH to PBS 1x. GSH is ubiquitous in living cells and therefore stability towards it and similar thiols is very important.²⁵⁷ Most living cells have a GSH concentration between 1-2 mM,³¹¹ therefore, the upper range of 2 mM was chosen to evaluate the NP stability. The results obtained by absorption spectroscopy are depicted in Figure 95a and b, where both NPs show high stability with very little difference in the UV-Vis spectra over time.

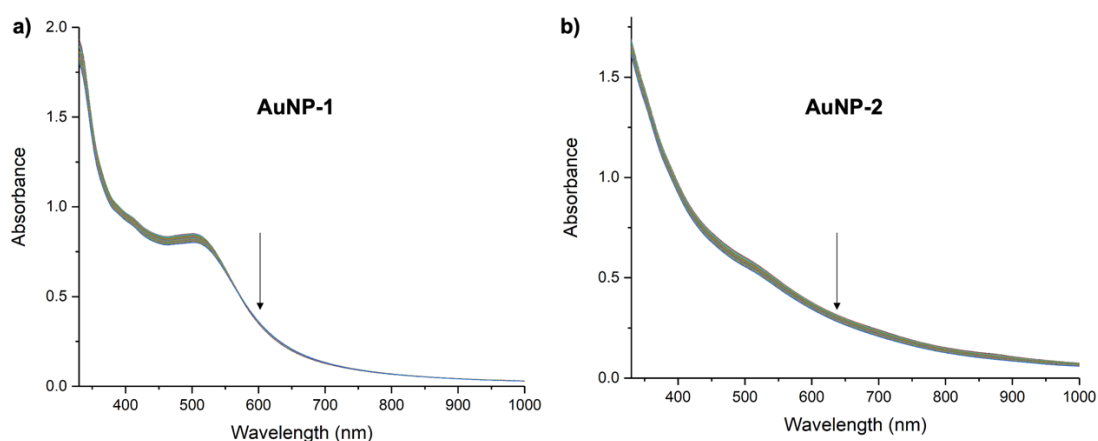


Figure 95 - UV-Vis Spectra of **a) AuNP-1**, **b) AuNP-2** in PBS 1x (pH 7.4) + GSH (2mM) after dialysis, recorded every 10 min for the first hour, then every 30 min until 23 h.

To summarise, both NHC@AuNPs have an SPR band ranging from 515-520 nm (Table 14), providing evidence for nanoparticle formation. Both NPs show high stability in the conditions evaluated (Table 14), especially **AuNP-2**, holding promise for future biological applications.

Table 14 – Summary of AuNP stability and SPR band position (nm) in different conditions over time.

AuNPs	Conditions	Time (h)	SPR band (nm)	Loss in Abs over time (%)
AuNP-1	MilliQ H ₂ O	15	515	3.4
	PBS 1x	15	515	10.1
	PBS 1x and 2 mM GSH	23	515	5.8
AuNP-2	MilliQ H ₂ O	15	520	0.4
	PBS 1x	15	520	2.6
	PBS 1x and 2 mM GSH	23	520	8.2

8.2.2.2. ¹H NMR Spectroscopy

NMR spectroscopy is not commonly used for the characterisation of AuNPs, however ¹H NMR especially, can provide invaluable information on the ligand structure retained on the AuNP surface. Therefore, after dialysis and lyophilisation, **AuNP-1** and **AuNP-2** were dissolved in D₂O and the NMR experiments were performed. The ¹H NMR of **AuNP-1** overlapped with its respective compound and ligand as can be seen in Figure 96, which confirms the absence of the imidazolium proton (H_a at 8.83 ppm) in both the Au complex and NPs highlighting binding to Au.

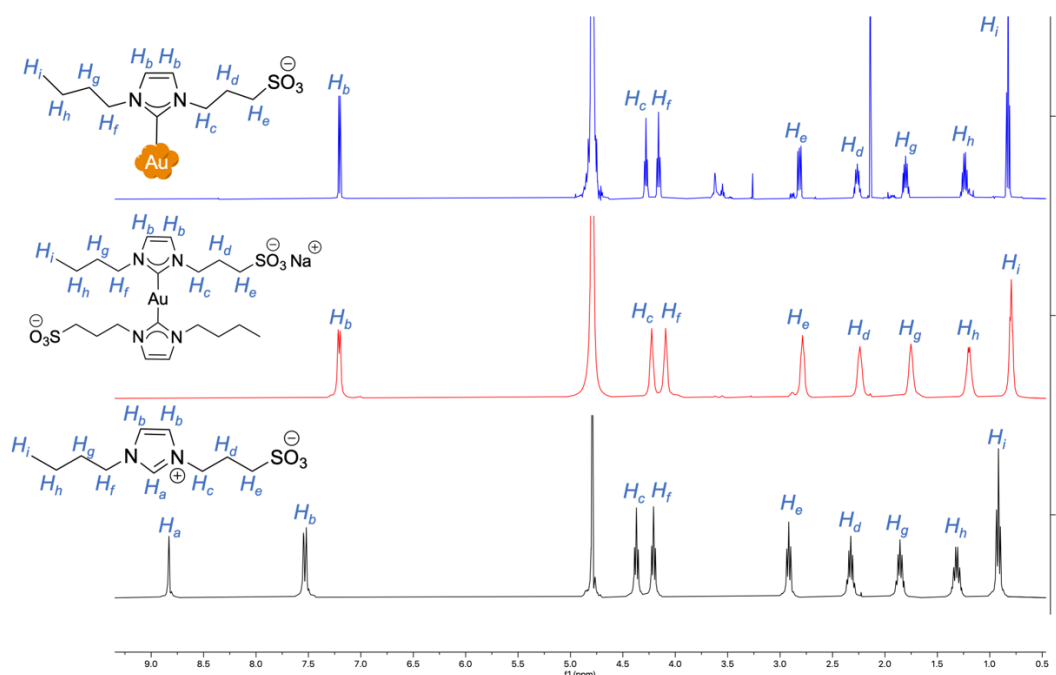


Figure 96 - ^1H NMR spectra of ligand **NHC-1** (bottom, black), complex **AuNHC-1** (middle, red) and **AuNP-1** (top, blue) in D_2O .

The ^1H NMR overlap of **AuNP-2** with its respective compound and ligand can be seen in Figure 97. The spectrum of **AuNP-2** shows two or more species present. However, the main species overlaps with the peaks of **AuNHC-2**. Furthermore, the imidazolium proton (H_a at 9.35 ppm) present in the ligand is not observed in the **AuNP-2** or **AuNHC-2**, highlighting the binding to the Au centre.

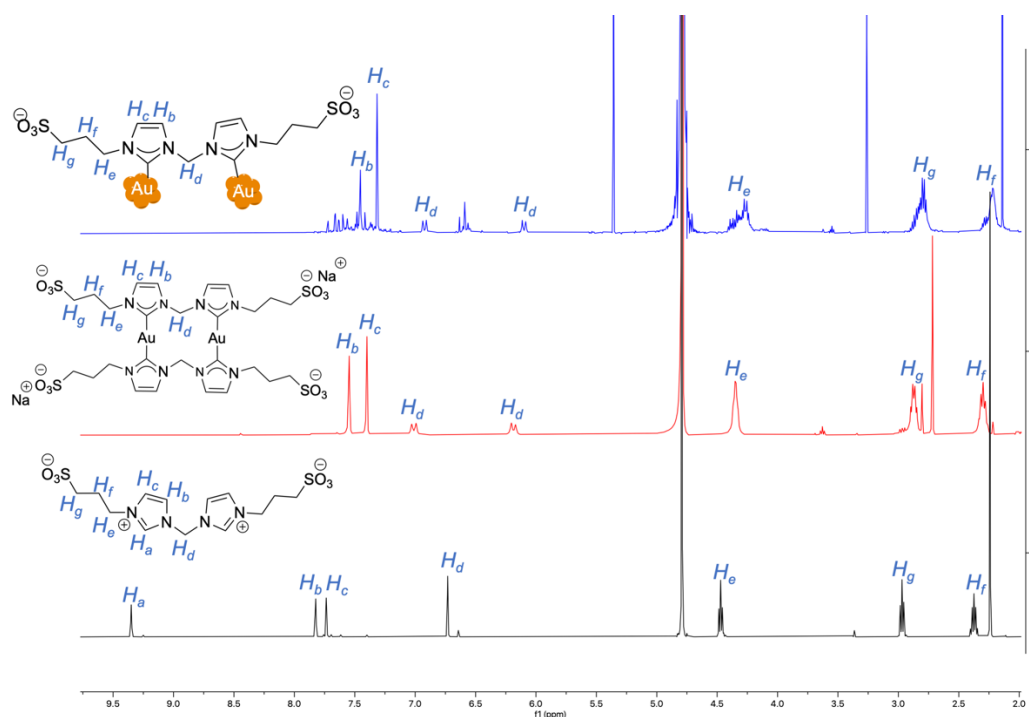


Figure 97 - ^1H NMR spectra of ligand **NHC-2** (bottom, black), complex **AuNHC-2** (middle, red) and **AuNP-2** (top, blue) in D_2O .

8.2.2.3. FTIR-ATR Spectroscopy

Fourier-transform IR spectroscopy is most commonly used nowadays compared to traditional IR due to the much faster speed and less tedious analysis.³⁹⁰ FTIR radiates a number of molecules at once with their characteristic IR radiation, whereas traditional IR spectrophotometers require selection of specific IR radiations to determine specific functional groups.³⁹⁰ However, adapted sample preparation is required for solids in FTIR, including the formation of potassium bromide (KBr) pellets by grinding the solid with KBr salt; a Nujol mull by grinding the solid with Nujol (2-(3,4,5-trihydroxyphenyl)cheomenylium-3,5,7-triol chloride), a mineral oil, which is then pressed between two plates; or dissolving the solid in a solvent.³⁹⁰ However, all of these techniques can interfere with the IR spectra and so the use of an attenuated total reflection (ATR) attachment is preferred as the sample can be placed directly on the ATR crystal without any pre-treatment.³⁹⁰

In this work, FTIR-ATR was used to corroborate the ¹H NMR data that there was an absence of the imidazolium precursors in the NPs. A comparison of the IR spectra was made between the NHC ligands, Au(I) NHC compounds and corresponding AuNPs to highlight the absence of the imidazolium ring stretch. A background spectrum was collected prior to analysis of each sample and each spectrum was averaged from 32 scans.

The IR spectrum of **AuNP-1** (Figure 98) and its corresponding Au(I) NHC complex lack the characteristic peak at 1623.13 cm⁻¹ of the corresponding imidazolium ligand (**NHC-1**). This can be tentatively assigned as the vibrational band of the imidazolium C-H ring stretch which is commonly observed between 1500-1620 cm⁻¹.³⁹¹ This peak was also observed at ~1576 cm⁻¹ by MacLeod and Johnson in their NHC@AuNPs.²⁶³

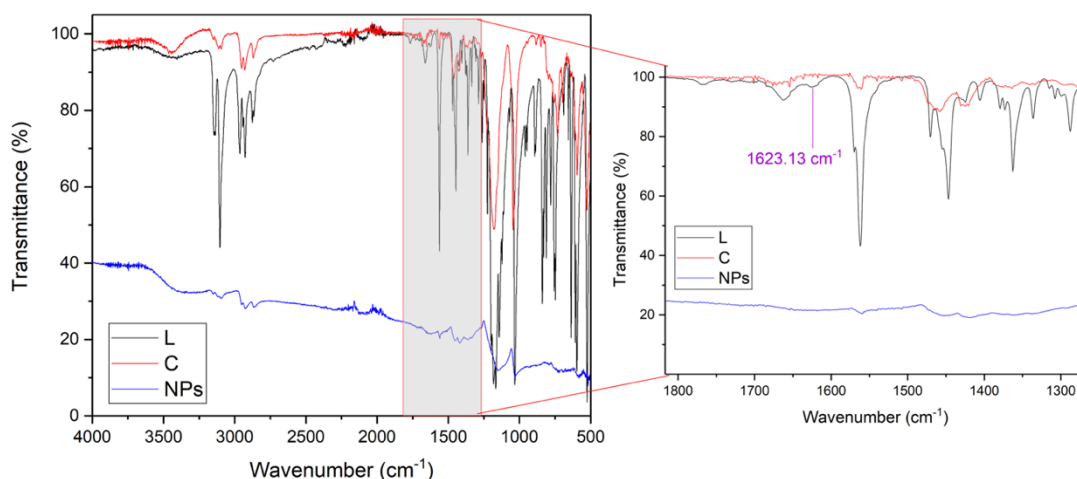


Figure 98 – FTIR-ATR spectra of **NHC-1** (L, black trace), **AuNHC-1** (C, red trace) and **AuNP-1** (NHC@AuNPs, blue trace); zoom in to show presence of the imidazolium C-H ring stretch signal (1623.13 cm^{-1}) in the free imidazolium ligand but not in the corresponding Au(I) NHC complex and NHC@AuNPs.

Similarly, the spectrum for **AuNP-2** also showed the absence of the related bis-imidazolium C-H ring stretch at 1551.76 cm^{-1} (Figure 99), providing further evidence for the absence of imidazolium precursors in the NHC@AuNPs.

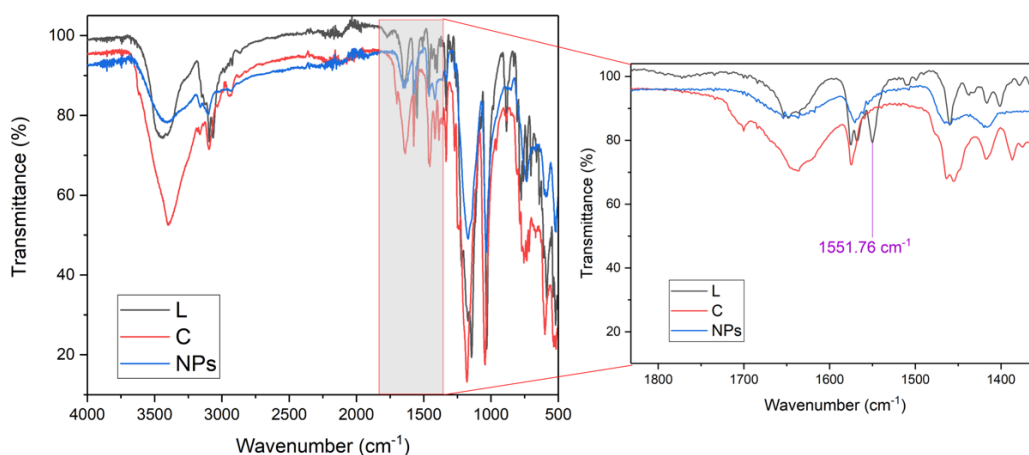


Figure 99 – FTIR-ATR spectra of ligand **NHC-2** (L, black trace), complex **AuNHC-2** (C, red trace) and **AuNP-2** (NHC@AuNPs, blue trace); zoom in to show presence of the imidazolium C-H ring stretch signal (1551.76 cm^{-1}) in the free imidazolium ligand but not in the corresponding dinuclear Au(I) NHC complex and NHC@AuNPs.

8.2.2.4. XPS characterisation

XPS is a powerful technique for the characterisation of NPs, providing information on the surface coverage of the material, including atoms present, their concentration at that point, as well as the oxidation state of possible metals at the surface.³⁹² Previous reports have used XPS to provide evidence for NHC ligands bound to the surface of the AuNPs

by looking at the BE of the C 1s and N 1s signals,^{254,258} as well as some information from the Au 4f signals.^{393,394} The results obtained for **AuNP-1** and **AuNP-2** after dialysis can be found in Table 15.

Beginning with the C 1s peaks, both NPs show three characteristic peaks at around 285, 286 and 288/289 eV (rounded to the nearest whole number). The peaks at 285 and 286 eV can be confidently assigned to the C-C and C-N bonds of the corresponding ligands respectively, which is in line with the literature.^{393,394} The peaks at 288.69 and 288.28 eV for **AuNP-1** and **AuNP-2**, respectively, have a lower concentration compared to the other C 1s peaks. These binding energies were also observed by Bridonneau *et al.*,³⁹³ and assigned to the $\pi \rightarrow \pi^*$ transition originating from the photoelectron excitation within the heterocycle, forming a 'satellite peak'.³⁹³ There is only one N 1s peak found in both NPs with a binding energy around 401 eV, which is in line with the values previously reported for the N atoms within the NHC structure.^{254,258,393,394}

Table 15 – XPS data (BE and composition) for **AuNP-1** and **AuNP-2**.

Peak	AuNP-1		AuNP-2	
	BE (eV)	%At Conc.	BE (eV)	%At Conc.
Au 4f (Au(I))	85.23	0.18	85.13	1.07
Au 4f (Au(I))	88.9	0.13	88.8	0.8
Au 4f (Au(0))	83.91	0.45	83.44	0.66
Au 4f (Au(0))	87.58	0.34	87.11	0.49
C 1s	284.8	61.53	284.92	39.6
C 1s	286.3	10.04	286.28	17.64
C 1s	288.69	6.18	288.28	3.51
N 1s	400.88	1.2	401.08	6.67
Na 1s			1071.98	0.92
O 1s	533.29	7.12	532.88	7.6
O 1s	531.94	11.97	531.59	15.91
S 2p (SO _x)	168.08	0.87	167.78	5.13

The other interesting peaks originate from Au 4f; however, in both cases two oxidation states were present, which we also saw before dialysis (Table 13). This was also observed by Young *et al.*³⁹⁴ and can be assigned to two of the different oxidation states of Au (Au(0) and Au(I)). Two peaks are present for each oxidation state of gold due to the two spin-orbit split of Au 4f into Au 4f_{7/2} and Au 4f_{5/2} and are separated by 3.7 eV.^{394,395} The difference in BE between the two oxidation states of Au provides further evidence for their assignment: compared to the BE of Au(0) 4f peaks, a Δ BE of ~2.0 eV is

characteristic of Au(I), whereas a ΔBE of ~ 3.3 eV is expected for Au(III).^{394,395} Therefore, in this work, the oxidised form can be confidently assigned to Au(I) rather than Au(III) due to a ΔBE of 1.32 eV for **AuNP-1** and 1.69 eV for **AuNP-2**, respectively, when compared to the Au(0) oxidation state.

Young *et al.*³⁹⁴ postulated that due to the nature of forming the NPs by reduction of the Au(I) NHC species, it is common for some Au(I) species to remain in the NPs, whereas this is not the case when the NPs are formed from the imidazolium haloaurate salts.³⁹⁴ Figure 100 shows the overall composition of the Au 4f states, suggesting that **AuNP-2** contains more Au(I) species than **AuNP-1**. The percentage of Au(I) and Au(0) can be estimated based on the percentage concentration of the peaks in Table 15. **AuNP-1** consisted of 28% Au(I) and 72% Au(0), whereas **AuNP-2** had 62% Au(I) and 38% Au(0). Overall, it is pivotal to assess whether the Au(I) species affects the ability of the NPs to catalyse reactions.

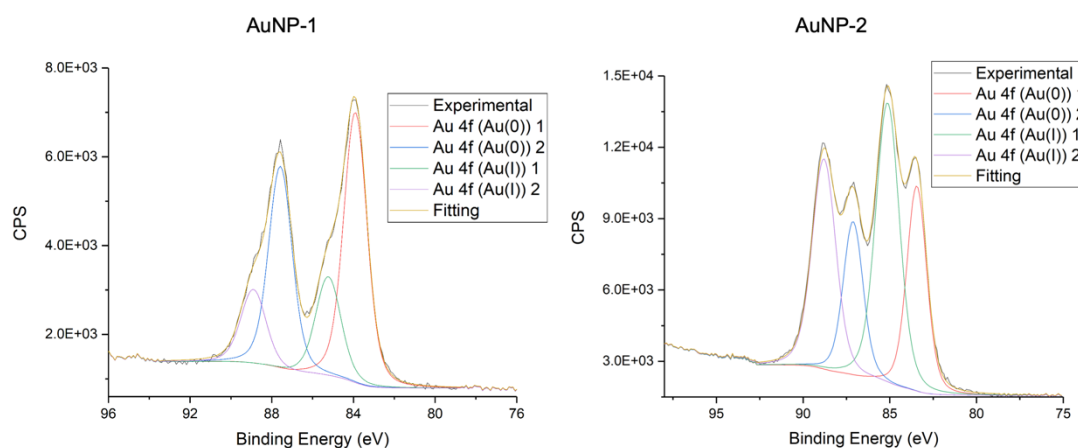


Figure 100 – XPS spectra of the Au 4f region for **AuNP-1** (left) and **AuNP-2** (right).

8.2.2.5. TEM characterisation

TEM is a staple technique used for the characterisation of metal nanoparticles, especially those used for catalysis, as the performance of the nanoparticles can ultimately be linked to their size and shape.³⁸⁹ TEM can be used to measure each particle size directly, allowing the mean particle size and particle size distribution to be derived. High contrast TEM images of **AuNP-1** and **AuNP-2** proved difficult due to the very small size of the NPs, which is close to the maximum resolution of the microscope. Additionally, there was still some organic matter located on the surface of the NPs despite dialysis, which can hamper the overall contrast of the images.

Nevertheless, TEM images could be obtained and an average particle size was determined over a large statistical data set. In addition, comparing to the TEM images of the AuNPs before dialysis (Figure 92), the NPs appear more uniform in size and well distributed (Figure 101). In total, 391 particles were measured for **AuNP-1** over 6 images,

and 507 particles for **AuNP-2** over 5 images. As shown in Figure 101, both NHC@AuNPs have an average size of ca. 2 nm. However, a rather large particle size distribution of ± 1.1 nm and ± 1.18 nm for **AuNP-1** and **AuNP-2**, respectively, is observed. This could be explained by the presence of organic material on the surface of the NPs as described above. Alternatively, the use of acetone to deposit the NPs onto the carbon grid for TEM analysis could also be responsible for the slight aggregation as the NPs are insoluble in acetone leading to a large particle size distribution. Future studies should include TEM analysis without solvent to ensure no solvent effects are involved. Overall, the TEM analysis clearly highlights the small size of the AuNPs, which could also be predicted from the λ_{\max} of the SPR band.³⁸⁹

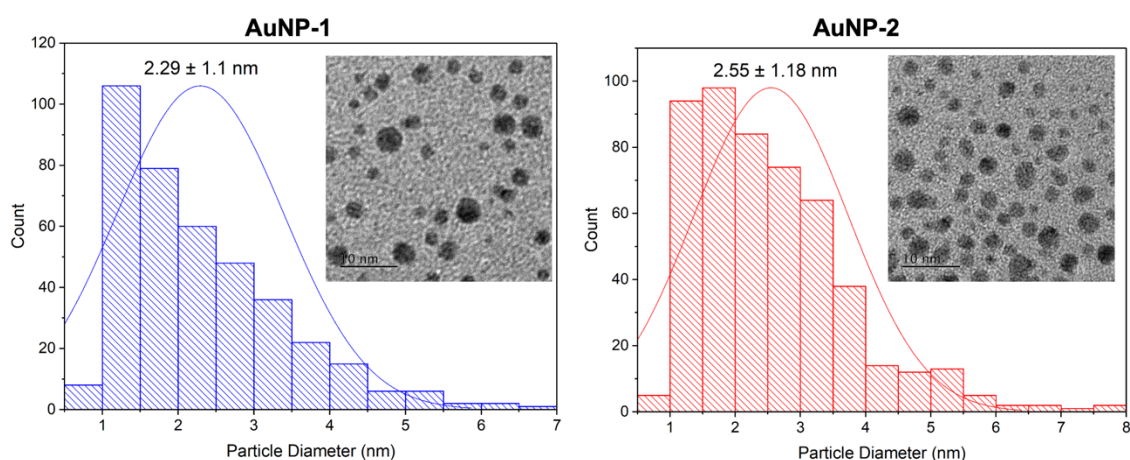


Figure 101 – Particle size histograms of NHC@AuNPs with representative TEM image: **AuNP-1** (left) displayed an average size of 2.29 ± 1.1 nm and **AuNP-2** (right) displayed an average size of 2.55 ± 1.18 nm. Scale bar: 10 nm.

8.2.2.6. TGA

Thermogravimetric analysis (TGA) involves heating a sample of known mass and monitoring the percentage drop in mass as the sample decomposes. Volatile compounds, physisorbed water and solvents evolve first below 150 °C, whereas chemisorbed water and low molecular weight organic materials are lost between 150 °C and 250 °C.³⁹⁶ Above 250 °C, other organic matter decomposes leaving the metal core.³⁹⁶ TGA was performed on the NHC@AuNPs and corresponding NHCs to estimate the degree of AuNP ligand functionalisation. The measurement was recorded in a nitrogen environment at 20 mL/min and the samples were heated with a ramp rate of 5 °C/min from 30 to 800 °C.

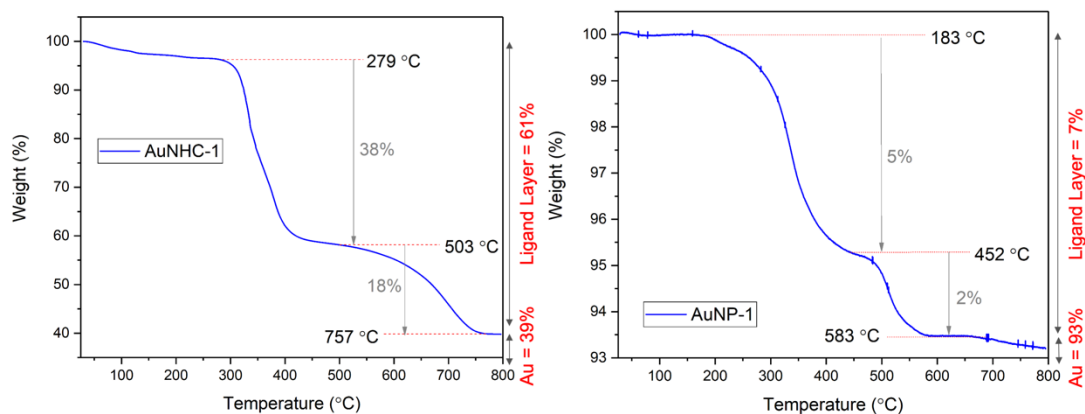


Figure 102 – TG curves of **AuNHC-1** (left) and **AuNP-1** (right).

The TG curves of **AuNP-1** and its corresponding Au(I) NHC complex (**AuNHC-1**) can be seen in Figure 102. The ligand layer of **AuNP-1** is a lot lower than its corresponding **AuNHC-1** (7% vs. 61%, respectively), indicating low ligand functionalisation of the NPs. The TG curves of **AuNP-2** and its corresponding Au(I) NHC complex (Figure 103) appear a lot more alike compared to **AuNP-1**. This suggests that **AuNP-2** has high ligand coverage over the gold core and still contains a significant amount of **AuNHC-2**, which was also observed in the XPS data with a significant amount of Au(I) species.

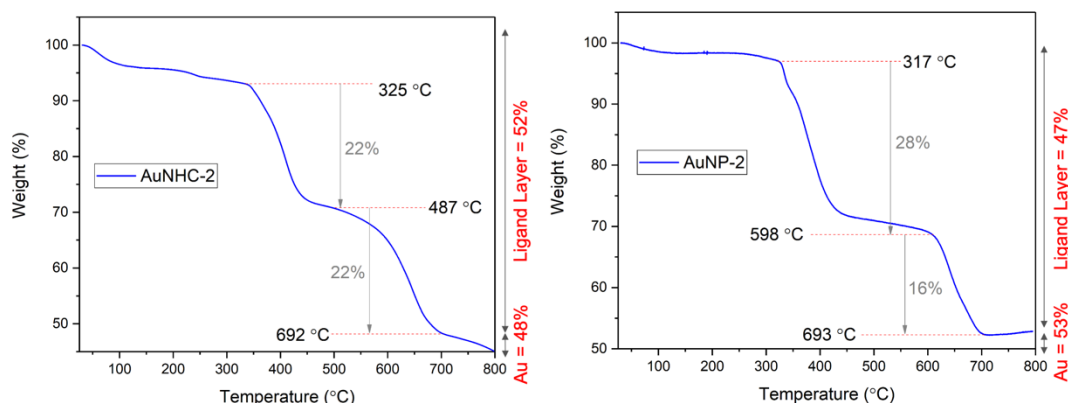


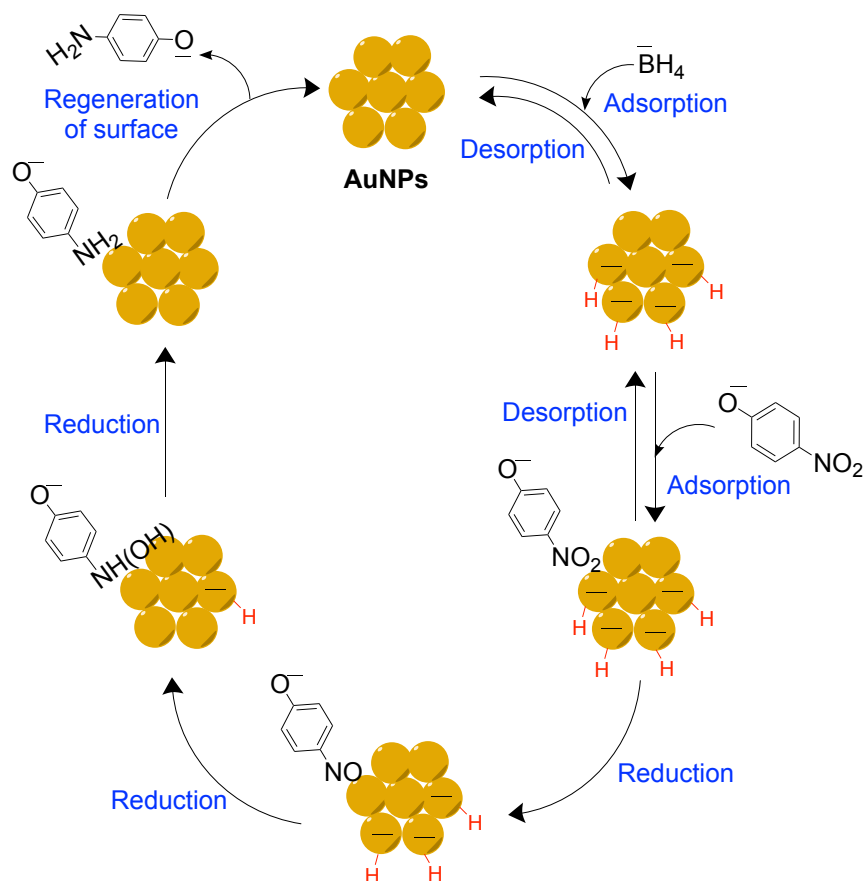
Figure 103 – TG curves of **AuNHC-2** (left) and **AuNP-2** (right).

8.2.3. Catalytic studies of AuNPs

8.2.3.1. Reduction of 4-nitrophenol

The catalytic performance of the NHC@AuNPs was next investigated for the reduction of 4-nitrophenol to 4-aminophenol in the presence of excess NaBH₄. This catalytic reaction is very popular for screening the catalytic performance of AuNPs as the reaction can be monitored by UV-Vis spectroscopy as a function of reaction time. This is due to the reduction of the peak around 400 nm, corresponding to 4-nitrophenol, with the concurrent increase in absorbance of the peak around 300 nm, corresponding to 4-aminophenol. Moreover, it has been demonstrated that the only product for this reaction

at these experimental conditions is 4-aminophenol. The exact mechanism of this reaction has not yet been defined; however, a postulated mechanism is shown in Scheme 32 as described by de Oliveira *et al.*³⁹⁷ The first step in the reduction of 4-nitrophenol is proposed to be the rate-limiting step, involving the B-H bond cleavage of NaBH₄ to activate the hydrides on the AuNP surface.³⁹⁷ The activated hydrides can then be transferred to the nitro group resulting in the reduction to aminophenol over three reduction steps. It should be noted that an excess of NaBH₄ is vital in this reaction as a considerable amount of activated hydrides are lost from the NP surface as gaseous H₂.³⁹⁷ An excess of NaBH₄ compared to 4-nitrophenol also means that this reaction can be considered as *pseudo*-first-order allowing the rate constant to be determined using a first-order rate equation.



Scheme 32 – Postulated reaction mechanism for the reduction of 4-nitrophenol catalysed by AuNPs in the presence of sodium borohydride. Image adapted from ref.³⁹⁷

The typical experimental protocol for the reaction was the following: the AuNPs (**AuNP-1**: 0.2 mg and **AuNP-2**: 0.275 mg) were added directly to a UV-Vis cuvette, followed by addition of 1.9 mL of MilliQ water and 100 μ L of 4-nitrophenol aqueous solution (3 mM). Afterwards, 1 mL of a freshly prepared NaBH₄ solution (0.03 M) was added to the cuvette. The absorption spectra were then recorded every 30 sec until the reaction was

complete. In all cases, full conversion could not be achieved, which we propose to be due to the NaBH₄ being fully converted or hydrolysed before all of the 4-nitrophenol had reacted. This could be identified by a plateau in absorbance of the bands at 400 nm.

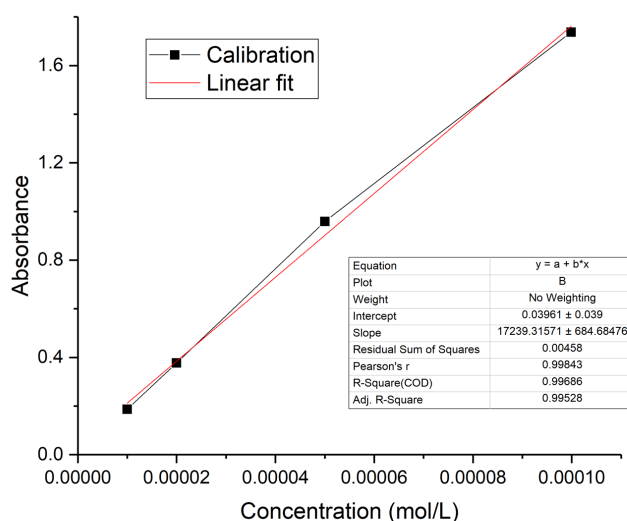


Figure 104 – Calibration plot for 4-nitrophenol.

In order to obtain the rate constant of the reaction, a calibration plot of 4-nitrophenol was first measured by plotting the absorbance at 400 cm⁻¹ (Figure 104) of different concentrations of 4-nitrophenol (0.01 mM, 0.02 mM, 0.05 mM and 0.1 mM). 400 cm⁻¹ was chosen as it is the λ_{max} of 4-nitrophenol. Therefore, the slope of this line was equal to the molar extinction coefficient (ε), which was then used to plot the concentration (C) of 4-nitrophenol over time using the rearranged Beer-Lamber law (Equation 2):

$$C = \frac{A}{\epsilon L} \text{ Equation 2}$$

[A = absorbance at 400 cm⁻¹, ε = molar extinction coefficient (17239.32 M⁻¹ cm⁻¹) and L = path length of the cuvette used (1 cm)]. The change in concentration over time was then used to plot the conversion as a percentage over time using the following equation:

$$\text{Conversion (\%)} = \left[\frac{C_0 - C_t}{C_0} \right] \times 100 \quad \text{Equation 3}$$

[C₀ = concentration of 4-nitrophenol at time zero and C_t = concentration at each time point]. The rate constant (k) of the reaction was then calculated by plotting the natural logarithm for the change in concentration over time. A straight line is fitted for these points and the gradient of the slope is equal to -k due to the following equation:

$$\ln[C] = -kt + \ln[C_0] \quad \text{Equation 4}$$

The UV-Vis kinetic study of **AuNP-1** can be seen in Figure 105a, which illustrates the speed of the reaction, with the largest drop in absorbance of the 4-nitrophenol band from 0.5 to 1 min. It is also clear from the plot in Figure 105b that the concentration of 4-nitrophenol started to plateau after 1.5 min. This is also illustrated in Figure 105c where the conversion reaches 81% after 1.5 min, only increasing to 84% after 2.5 min.

The UV-Vis kinetic study of **AuNP-2** is reported in Figure 105d, as well as the concentration of 4-nitrophenol vs. time (Figure 105e), and the conversion of 4-nitrophenol vs. time (Figure 105f).

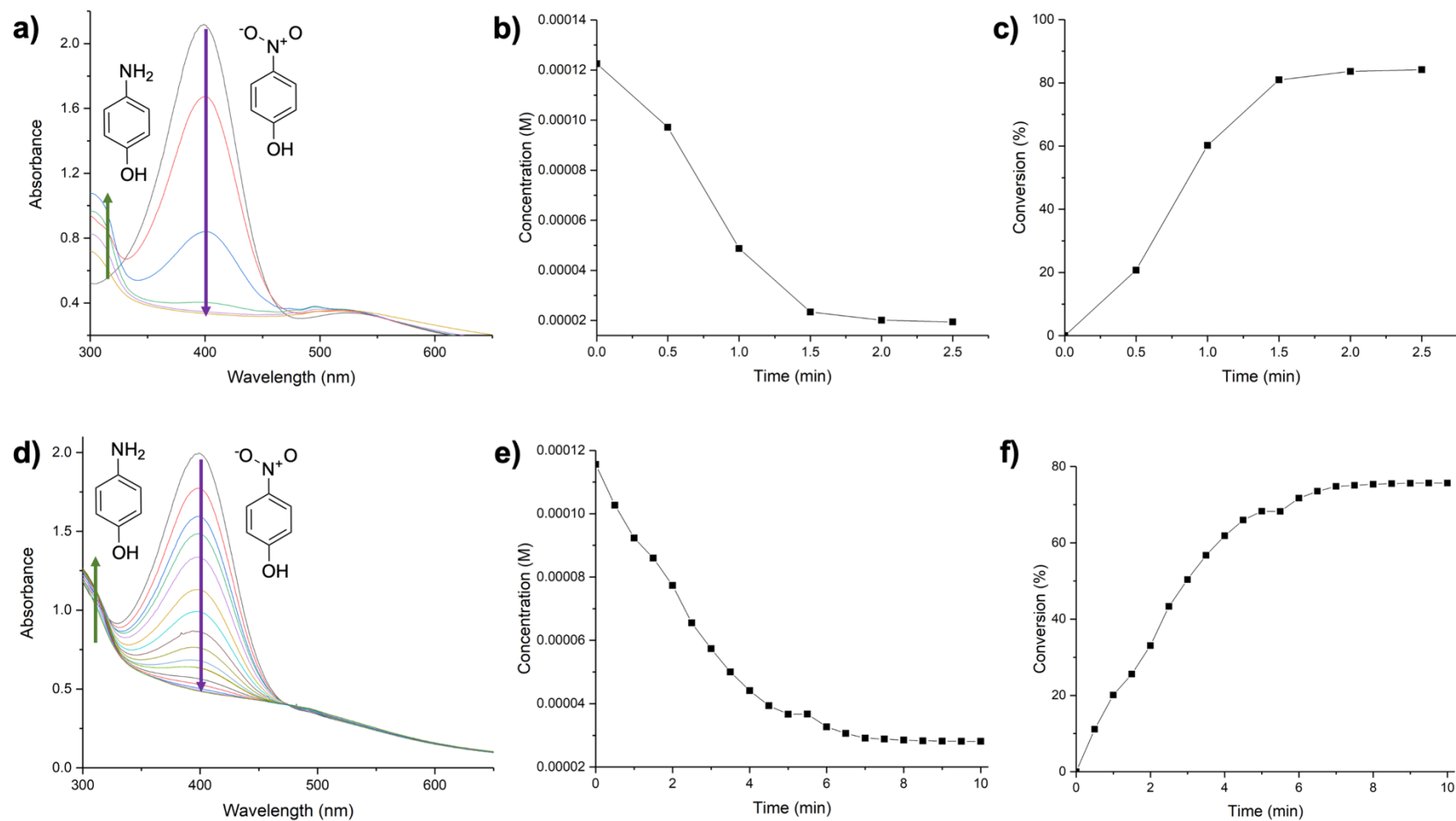


Figure 105 - Representative UV-Vis kinetic study for the reduction of 4-nitrophenol into 4-aminophenol catalysed by **a) AuNP-1** over 2.5 min, with a spectrum recorded every 30 sec, **d) AuNP-2** over 10 min, with a spectrum recorded every 30 sec. Plots of concentration vs. time for **b) AuNP-1** and **e) AuNP-2**. Plots of substrate conversion vs. time at 400 cm^{-1} for **c) AuNP-1** and **f) AuNP-2**, respectively.

Figure 106a displays the plot of the natural logarithm for the change in concentration over time beginning from 0 min for **AuNP-1**. Of note, from 0 to 0.5 min an induction period can be detected; in other words, the rate is a lot slower, whereas from 0.5 to 1.5 min the rate is faster following a straight line. Therefore, in order to calculate the apparent rate constant, after the induction period, the time points from 0.5 to 1.5 min were plotted, as shown in Figure 106b. These points follow a straight line displaying a rate constant of 1.42 min^{-1} per 0.2 mg of **AuNP-1**, compared to 1.13 min^{-1} when the induction period was considered. The existence of the induction period was also observed when this reaction was repeated.

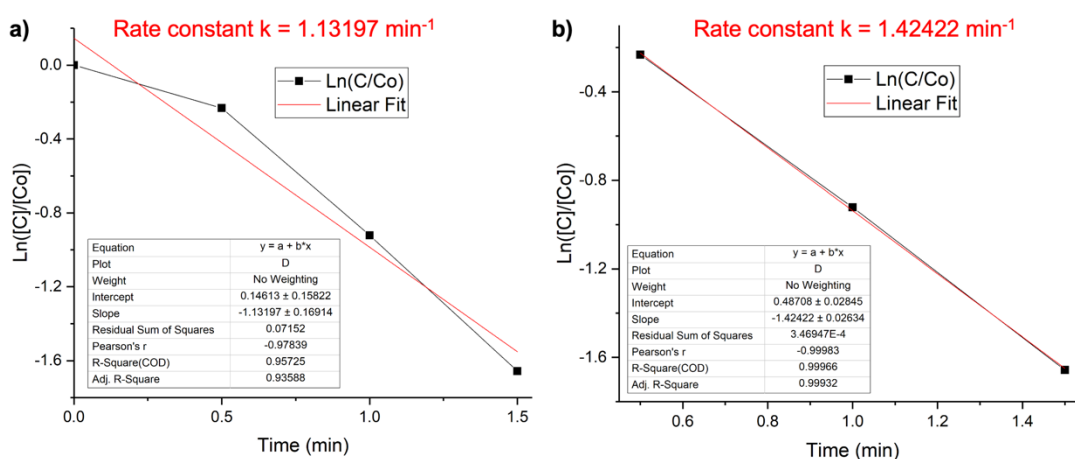


Figure 106 - Plots of $\text{Ln}([C]/[C_0])$ vs. time for the reduction of 4-nitrophenol to calculate the rate constant for the **AuNP-1** catalyst, **a)** from 0 to 1.5 min and **b)** from 0.5 to 1.5 min.

The natural logarithm (\ln) of the concentration vs. time was also plotted to determine the rate constant for **AuNP-2**, as shown in Figure 107. In this representative plot the points are taken from 0 to 7 mins as after this time the reaction plateaus, giving a rate constant of 0.21 min^{-1} per 0.275 mg of **AuNP-2**. At variance to **AuNP-1**, no induction period was observed for **AuNP-2**.

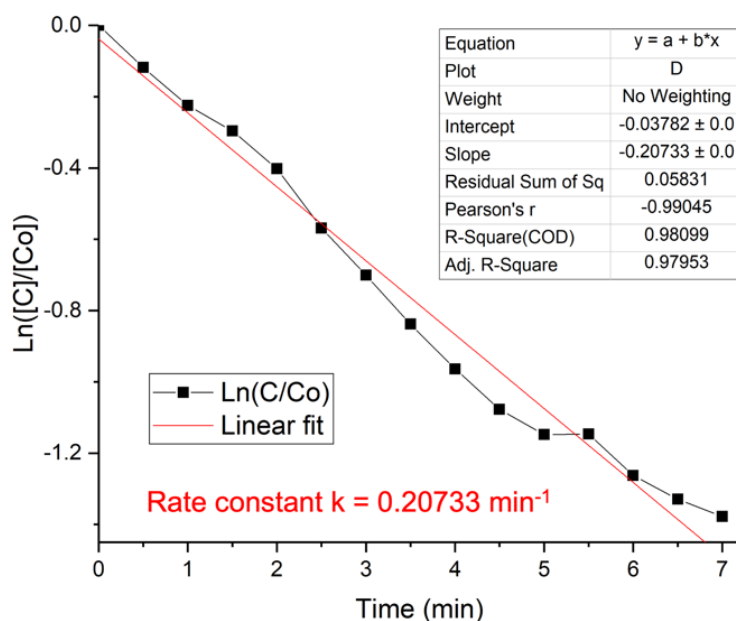


Figure 107 – Plot of $\text{Ln}([C]/[Co])$ vs. time for the reduction of 4-nitrophenol to calculate the rate constant for the **AuNP-2** catalyst.

It should be noted that the rate constants calculated above are based upon the mass of the catalyst. However, to draw an overall conclusion of which was most efficient, the mass of Au in each catalyst should be considered, as this is the proposed active site of the reaction. Therefore, ICP-MS (inductively coupled plasma mass spectrometry) studies were performed to determine the mass of ^{197}Au in each catalyst. **AuNP-1** contained 0.0126 mg of Au per 0.1 mg of catalyst, making 12.6% of the sample Au, whereas **AuNP-2** contained 0.029 mg of Au per 0.1 mg of catalyst, thus 29% of the sample was Au.

An explanation for **AuNP-1** being more active despite the lower overall Au percentage could be supported by the XPS results, which showed that in **AuNP-1** 72% of Au was present in the Au(0) oxidation state, whereas only 38% of Au in **AuNP-2** was Au(0). Therefore, despite 0.1 mg of **AuNP-2** containing ca. 2.3 times more Au than 0.1 mg **AuNP-1**, the mass of Au(0) remains fairly similar: ca. 0.011 mg of Au(0) for 0.1 mg of **AuNP-2** and ca. 0.0091 mg of Au(0) for 0.1 mg of **AuNP-1**. This can also be evidenced by the TG data (Figure 102 and Figure 103) showing that **AuNP-1** have less ligand functionalisation compared to **AuNP-2**. The high surface functionalisation of **AuNP-2** could also mask a potential induction period since the overall rate of reaction is lower. However, more experiments are needed to confirm this hypothesis.

Repeats of the experiments were also performed, however in these cases the mass of catalyst was not the same, therefore further studies are required to obtain an average rate constant. A summary of the results for the 4-nitrophenol reduction reactions, including the rate constants, is reported in Table 16. The moles of ^{197}Au per catalyst were obtained by ICP-MS, allowing the mmol ratio of 4-nitrophenol (4-NP) to Au and NaBH_4 to Au to be calculated. Thus, it can be concluded that for both AuNPs a lower

mass of catalyst resulted in a higher rate constant. This is to be expected as the moles of the 4-nitrophenol and NaBH₄ remained the same in all experiments, therefore the mmol ratio of reagents and Au increased when the mass of catalyst was lower.

Table 16 – Summary of 4-nitrophenol reduction reactions using AuNP-1 and AuNP-2 with corresponding rate constants. Mass of Au obtained by ICP experiments to calculate the mmol ratio of 4-nitrophenol (NP) to Au, and NaBH₄ to Au. Moles of 4-nitrophenol in cuvette = 0.003 mmol, moles of NaBH₄ in cuvette = 0.03 mmol.

Catalyst	Repeat	Mass of catalyst (mg)	Mass of Au (mg)	Moles of Au (mmol)	4-NP: Au mmol ratio	NaBH ₄ : Au mmol ratio	Rate constant (min ⁻¹)
AuNP-1	1	0.2	0.0253	1.3E-4	23.08	230.8	1.42422
	2	0.8	0.1011	5.1E-4	5.88	58.8	0.90134
AuNP-2	1	0.275	0.080	4.1E-4	7.32	73.2	0.20733
	2	0.5	0.145	7.4E-4	4.05	40.5	0.16617
	3	0.6	0.174	8.8E-4	3.41	34.1	0.13916

Preliminary studies were also performed to assess the recyclability of the water-soluble AuNPs. Ideally the NPs would be washed with water after each cycle to remove excess reagents and products from the previous cycle, however due to their water-solubility this could not be achieved. The 4-nitrophenol reduction reactions were performed with the same conditions as previously with **AuNP-1** and **AuNP-2**, before the removal of the solvent by reduced pressure. A ¹H NMR spectrum was then recorded using D₂O as the solvent to observe any changes in the ligand structure. The D₂O was then removed before re-suspension in MilliQ water and the second nitrophenol reduction reaction was performed. Another ¹H NMR spectrum was then recorded after replacement of MilliQ water with D₂O.

The stacked ¹H NMR of **AuNHC-1**, **AuNP-1**, **AuNP-1** after the 1st and 2nd 4-nitrophenol reduction reactions and 4-nitrophenol can be seen in Figure 108. The most downfield proton in the **AuNP-1** and **AuNHC-1** spectra (ca. 7.2 ppm) disappeared after the 4-nitrophenol reduction reaction, with only a very small aromatic peak present around that ppm due to an impurity from the 4-nitrophenol (as can be seen in Figure 108). This can be explained by the formation of a black solid after removal of the solvent following the 1st nitrophenol reduction reaction, which could not be re-solubilised in D₂O. Nevertheless, the ¹H NMR was still performed to observe if any free NHC ligand could be seen indicating loss from the NP itself, however only the peaks from the nitrophenol and NaBH₄ were observed. This points towards aggregation of the NPs once the water was removed due to destabilisation, which must have been caused by the 4-nitrophenol

or NaBH₄ as this insolubility was not observed when aqueous solutions of the NPs were dried prior to the reaction.

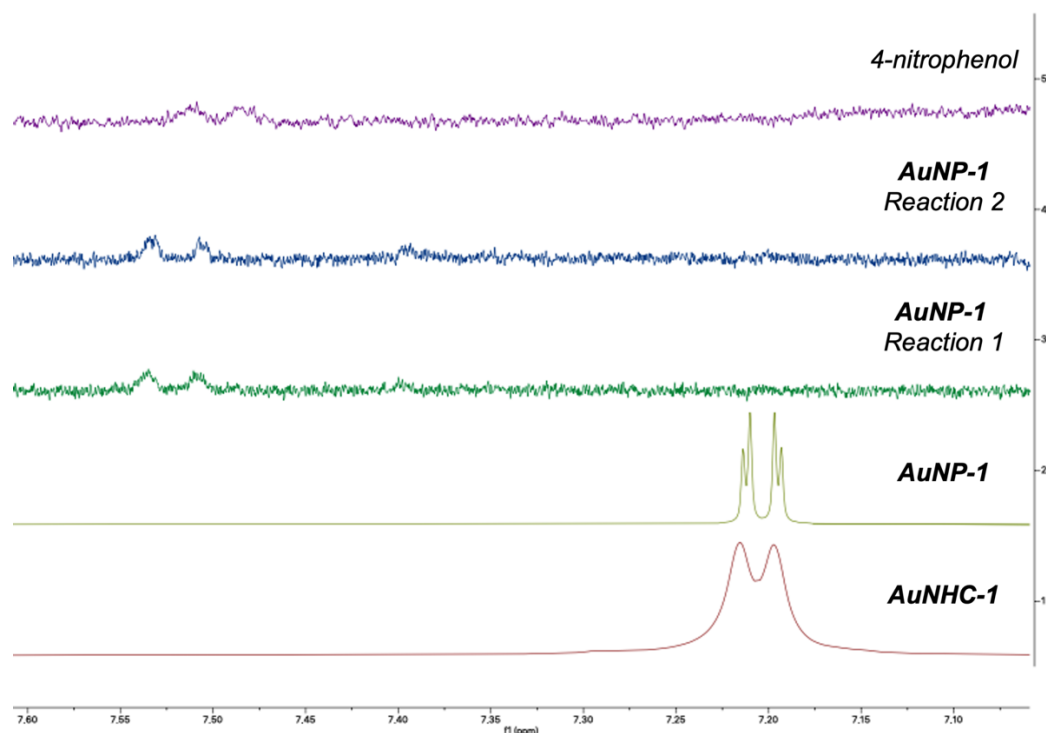


Figure 108 - Stacked ¹H NMR in D₂O of **AuNHC-1** (complex, red), **AuNP-1** (NPs, light green), **AuNP-1** after 1st 4-nitrophenol reduction (green), **AuNP-1** after 2nd 4-nitrophenol reduction (blue) and 4-nitrophenol (reagent, purple).

Nevertheless, the 2nd cycle could still be carried out with the black precipitate and the rate constant was compared to cycle 1 showing a significant decrease in catalytic performance as expected, with the presence of an induction period for 11 min before any conversion was observed (Figure 109a). The ln of concentration vs. time is shown in Figure 109b. As previously described, the rate constant does not consider the induction period. Nevertheless, the rate constant is still significantly reduced compared to that of cycle 1 (Figure 109c).

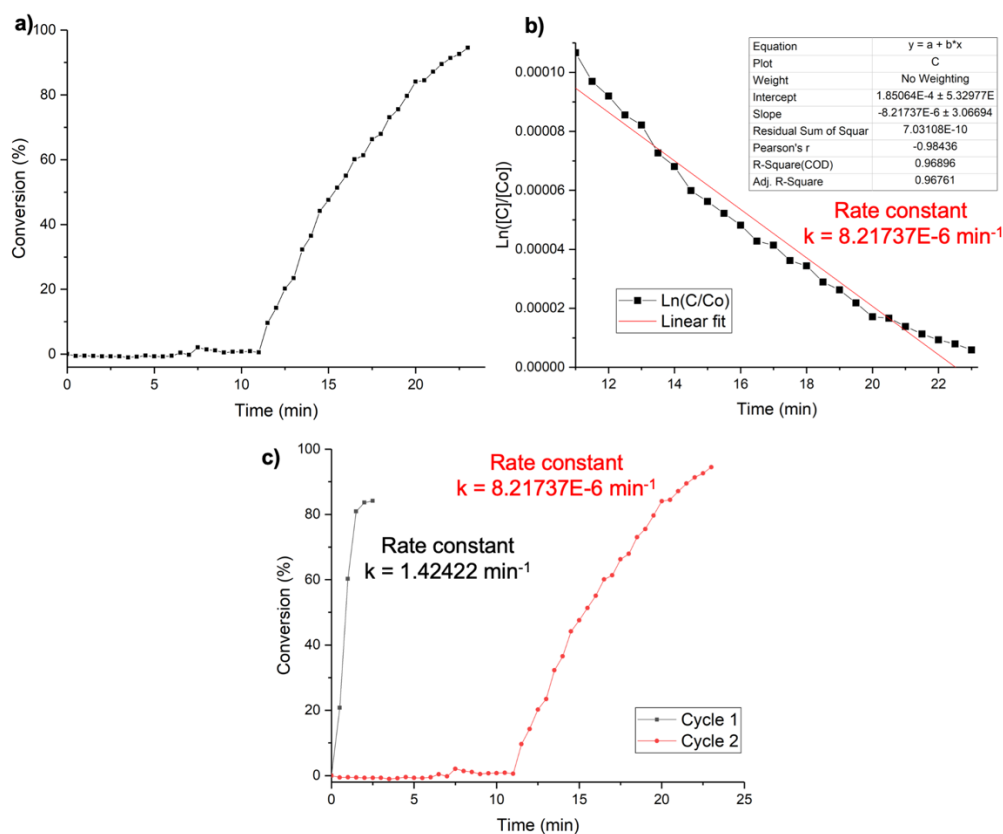


Figure 109 – Plots for the 2nd cycle of the 4-nitrophenol reduction reaction using **AuNP-1**: **a)** conversion against time and **b)** $\ln([C]/[Co])$ vs. time, **c)** Comparison of the conversion of 4-nitrophenol over time catalysed by **AuNP-1** for the 1st cycle (black dots) and the 2nd cycle (red circles).

The stacked ¹H NMR of the **AuNHC-2**, **AuNP-2**, **AuNP-2** after the 1st and 2nd 4-nitrophenol reduction reactions and 4-aminophenol (reduction product) can be seen in Figure 110. There is also an additional spectrum of the **AuNP-2** with NaBH₄. This was simply ca. 2 mg of **AuNP-2** with 0.9 mL of MilliQ water and 1 mL of NaBH₄ aqueous solution (0.03 M) mixed and then left to sit for 1 hour allowing time for the excess NaBH₄ to be hydrolysed. It appears that after the pre-treatment with NaBH₄ or reaction with 4-nitrophenol and NaBH₄, the **AuNP-2** were more similar to the NHC in the **AuNHC-2** ¹H NMR (red dashed line to show this, Figure 110). NaBH₄ could be responsible for this as even when 4-nitrophenol is not involved (**AuNP-2** with NaBH₄) this is still observed. Further investigations into the surface structure after exposure to NaBH₄ are needed.

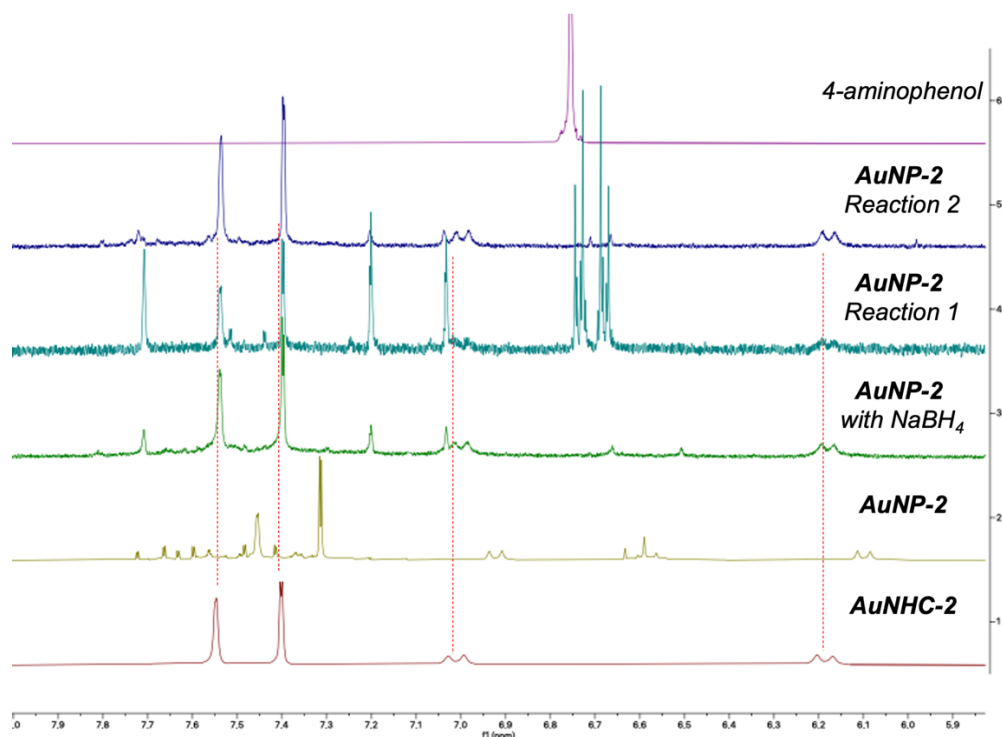


Figure 110 – Stacked ^1H NMR in D_2O of **AuNHC-2** (complex, red), **AuNP-2** (NPs, light green), **AuNP-2** after pre-treatment with NaBH_4 (green), **AuNP-2** after 1st 4-nitrophenol reduction (green/blue), **AuNP-2** after 2nd 4-nitrophenol reduction (blue) and aminophenol (reaction product, purple).

The plot of \ln concentration vs. time (Figure 111a) to determine the rate constant, k , for the second cycle revealed a three-fold increase in reaction rate compared to the first cycle (0.21 min^{-1} vs. 0.58 min^{-1} , cycle 1 vs. cycle 2, respectively) (Figure 111b). The increased rate could be linked to the removal of some of the ligands/Au(I) complexes from the surface of **AuNP-2** with NaBH_4 . The TGA showed a high ligand functionalisation for **AuNP-2**, very similar to the corresponding Au(I) NHC complex, which could potentially slow down the reaction rate as seen in the 1st cycle.

The only consideration to be made for the second cycle is that the conversion of 4-nitrophenol does appear to be lower, which could be due to other experimental factors such as presence of reagents from the previous cycle remaining and consuming some of the NaBH_4 , meaning that full conversion cannot be achieved. Comparing the ^1H NMR of the **AuNP-2** after the first and second 4-nitrophenol reduction (Figure 110), an increase in intensity of the NHC peaks does seem to be more evident after the 2nd cycle. This could be due to the addition of more NaBH_4 , resulting in further alterations to the NP surface which also positively increase the catalytic performance of the NPs. These reactions should be completed with more cycles to understand the capability of these NPs.

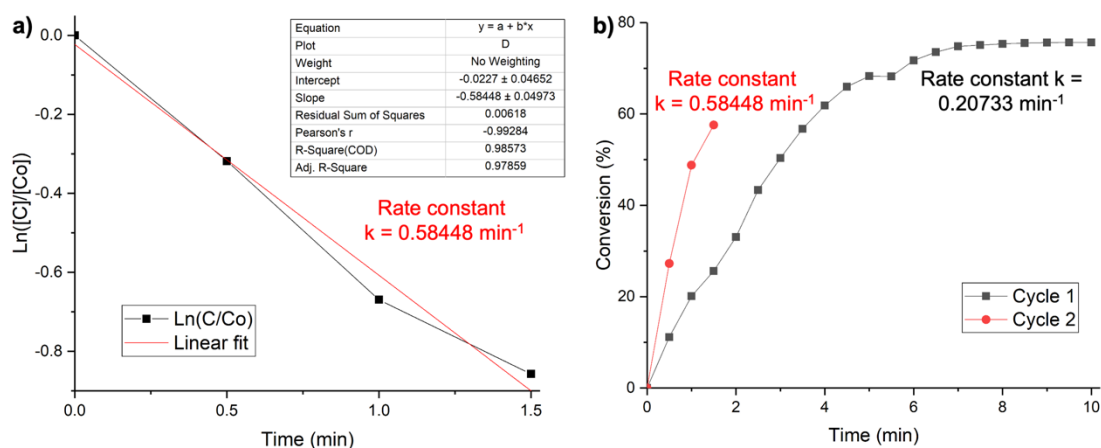


Figure 111 - a) Plot of $\ln([C]/[Co])$ vs. time for the 2nd cycle of the 4-nitrophenol reduction to calculate the rate constant and the reusability of AuNP-2, b) Plot to compare conversion of 4-nitrophenol over time catalysed by AuNP-2 for the 1st cycle (black dots) and the 2nd cycle (red circles), respectively.

8.2.3.2. Reduction of 2-nitrophenol and 3-nitrophenol

In order to explore the versatility of the catalysts, preliminary reactions for the reduction of 2-nitrophenol and 3-nitrophenol were completed. It was clear to see that despite the same conditions as the 4-nitrophenol reduction, the conversions to their respective aminophenol species were a lot lower. Only 17% and 16% of 3-nitrophenol was converted by AuNP-1 and AuNP-2, respectively, whereas for the reduction of 2-nitrophenol, AuNP-1 converted 40% and AuNP-2 converted 33%. Therefore, due to the poor conversion, the rate constants will not be discussed in detail here. However, it is important to note that despite this, both catalysts showed relatively similar rate constants. It should also be mentioned that the induction period observed for the reduction of 4-nitrophenol with AuNP-1 was also present in the reduction of 2- and 3-nitrophenol.

8.2.3.3. Pre-treatment of AuNP-1 with NaBH₄

As discussed, an induction period in the catalytic performance was only observed for AuNP-1. However, it is a phenomenon commonly observed for ligand stabilised NPs in catalytic reactions that take place on the NP surface, such as the 4-nitrophenol reduction reaction.²⁶⁸ The presence of an induction period has been previously described in the literature, and a number of factors contribute to it: *i*) the diffusion time needed for the 4-nitrophenol to reach the NP surface, *ii*) the time required to reconstruct the NP surface by the adsorption of reactants to make it active, or *iii*) the time required to remove surface oxides before the reaction can begin.²⁶⁸ The reconstruction of the NP surface has been described as the creation of catalytically active sites, such as corner or edges, by the reorganisation of surface atoms.³⁹⁸

Due to this induction period only being present in **AuNP-1**, we began by investigating if the reconstruction of the NP surface was involved. Wunder *et al.*³⁹⁹ previously reported that the induction period they observed for the 4-nitrophenol reduction reaction was in response to the surface restructuring of the AuNPs, due to adsorption of the 4-nitrophenol on the NP surface.³⁹⁹ Monti *et al.*²⁶⁸ also concluded that surface reconstruction was responsible for the induction period observed for the AuNP catalysed 1,4-dinitrobenzene reduction, due to activation energies within the range of 10 to 60 kJ/mol, which correlated with those previously reported.⁴⁰⁰ However, the activation energies for this surface reconstruction can depend on the size and type of NPs investigated.^{399,401} Interestingly in this work imidazolium salts were used as stabilisers, however the authors did not explore the induction period in any more detail.²⁶⁸

The literature is rife with contrasting opinions on what causes the induction period, with the ligands themselves also being deemed responsible. Ansar *et al.*⁴⁰² reported the ability of NaBH₄ to act as a 'detergent' by removing the stabilising ligands on AuNPs, including organothiols and polymers such as PVP to yield active NPs.⁴⁰² Whereas, more recently, it has been reported that dissolved oxygen could also play a role in the induction period, with the oxygen concentration showing a sharp decrease with the simultaneous ending of the induction period.⁴⁰³ The length of the induction period was correlated to the binding strength of the stabilising ligands, thus, the stronger the ligand, the longer the induction period.⁴⁰³ Therefore, they concluded that both the stabilising ligand and dissolved oxygen should be considered responsible for the induction period.⁴⁰³

However, it should also be mentioned that in the literature described above, NHC ligands have not been used as stabilising ligands. Therefore, in the case of **AuNP-1** the short induction period could be because of the low ligand functionalisation on the surface of **AuNP-1** observed by TGA. In order to investigate this for **AuNP-1**, 0.4 mg of catalyst was added to a cuvette along with 0.9 mL of MilliQ water and 1 mL of NaBH₄ aqueous solution (0.03 M). A UV-Vis kinetic study was then performed to measure any changes in the SPR band of the **AuNP-1** over 16 mins (Figure 112a). The pre-treatment of **AuNP-1** appears to show a broadening of the SPR band after 16 mins (Figure 112a), which could be related to aggregation of the NPs due to the loss of the stabilising ligands.

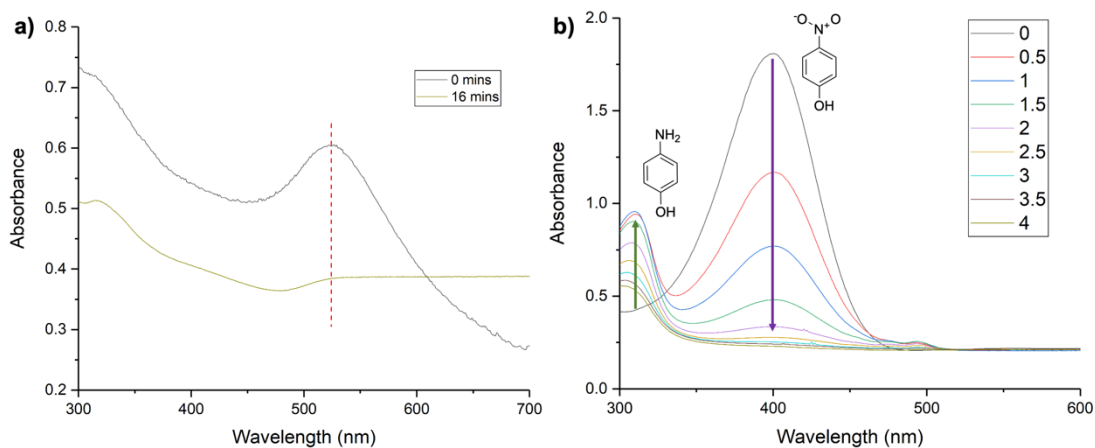


Figure 112 – Pre-treatment of **AuNP-1** with NaBH_4 , **a**) UV-Vis study of **AuNP-1** SPR band from 0 to 16 min in the presence of NaBH_4 , **b**) UV-Vis kinetic study for the reduction of 4-nitrophenol into 4-aminophenol catalysed by pre-treated **AuNP-1**.

However, more importantly, we wanted to observe if there had been any change in the catalytic performance and if the induction period was still present. Therefore, to ensure any excess NaBH_4 had been hydrolysed before addition of 4-nitrophenol, the cuvette was left for 1 h with the lid removed to allow the hydrogen to be released. After this time, 100 μL of the 4-nitrophenol aqueous solution (3 mM) was added before the fast addition of 1 mL of a freshly prepared NaBH_4 solution (0.03 M). A UV-Vis kinetic study was performed as before (Figure 112b), showing a 4-nitrophenol conversion of 87% over 4 mins, with the first 2.5 mins showing the largest conversion.

The rate constant, k , could also be calculated assuming a first order reaction by plotting the \ln of the 4-nitrophenol concentration vs. time (Figure 113a). The rate constant determined per 0.4 mg of catalyst was 0.776 min^{-1} . Although a direct comparison of the rate constant for the 4-nitrophenol reduction reaction with the untreated **AuNP-1** cannot be made as a different starting mass of catalyst was used (0.2 mg for untreated vs. 0.4 mg for pre-treated) the pre-treatment does appear to reduce the rate constant over three-fold per 0.1 mg of catalyst. However, the overall conversion is greater and the induction period is no longer present (Figure 113b).

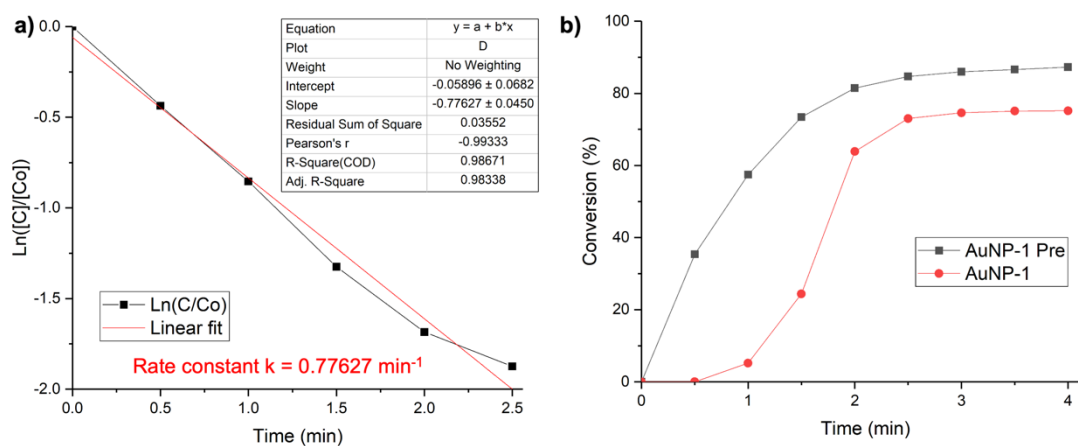


Figure 113 – a) Plot of $\ln([C]/[C_0])$ vs. time for the reduction of 4-nitrophenol to calculate the rate constant for the **AuNP-1** catalyst pre-treated with NaBH_4 from 0 to 2.5 min, b) Plot to compare conversion of 4-nitrophenol over time for the pre-treated **AuNP-1** (black dots) and non-treated **AuNP-1** (red circles), respectively.

In order to observe if any changes had occurred in the overall NP structure after the pre-treatment and subsequent 4-nitrophenol reduction reaction, the solvent was removed under reduced pressure and the solid was resuspended in D_2O . The previously water-soluble NPs had now formed a black solid that appeared insoluble in D_2O , as seen in the recyclability studies in section 8.2.3.1., indicating that destabilisation had occurred.

8.2.4. Synthesis of supported NHC-stabilised AuNPs

Supports are often utilised in AuNP synthesis due to their ability to reduce aggregation of the AuNPs and provide stabilisation, as well as potentially improving their catalytic performance, indirectly or directly.⁴⁰⁴ To the best of my knowledge there is only one example in the literature of supported NHC-stabilised AuNPs, which reported the spontaneous decomposition of Au(I) NHC complexes by reduced graphene oxide, forming AuNPs functionalised with NHC ligands deposited on graphene.⁴⁰⁵ The supported NPs were tested for the hydrogenation reaction of internal and terminal alkynes and showed no loss in activity over five consecutive runs.⁴⁰⁵ However, after these five runs a decrease in activity was observed which was attributed to leaching of the NHC@AuNP from the support.⁴⁰⁵ The group also followed this up in a more recent paper, describing the role that the aryl group attached to the imidazole plays in π -stacking towards the graphene support.⁴⁰⁶ They concluded that the smaller the aryl group, the less π -stacking would be observed and therefore the NHC@AuNP would have a higher propensity for leaching during the recyclability studies.⁴⁰⁶

Instead, in our work we opted for an adapted colloidal method⁴⁰⁷ using the AuNPs already formed. Therefore, instead of forming the colloids and then directly adding the support, as reported by Rogers *et al.*,⁴⁰⁷ the water-soluble AuNPs were synthesised as before and then redissolved in MilliQ water before addition of the support. The two

supports chosen were activated carbon and titania, both of which are commonly used in the literature with different advantages.⁴⁰⁴

Often when supporting colloid solutions the initial Au precursor will be the commercial salt, therefore the Au concentration can easily be determined. However, in this work the NPs had already been formed and so preliminary experiments to synthesise supported NPs were performed with 10 wt.% of the AuNPs compared to the support. As previously mentioned, firstly the water-soluble AuNPs were dissolved in MilliQ water with stirring before addition of the support. This was then left to stir vigorously overnight. In the case of titania, the white support became lilac after a couple of minutes, which is indicative of NP immobilisation. Conversely, the carbon support did not immobilise the AuNPs overnight, which was determined due to a brown coloured filtrate when the AuNP and support mixture was filtered. Thus, in a second attempt, a few drops of concentrated sulfuric acid were added after the addition of support and this was left to stir overnight. It should be noted that the addition of acid may protonate the sulfonate groups of the stabilising ligands, and therefore, could affect the AuNPs. However, the acid facilitated the immobilisation of the NPs and so further investigations were carried out. Once the NPs were supported, they were filtered and washed with water, before being left to dry on the filter paper in air, overnight. In the case of the carbon supported NPs, washing proceeded until the filtrate reached a neutral pH.

The rate of adsorption depends on the isoelectric point (IEP) of the support and the charge of the stabilising ligands, therefore the interaction can be varied depending on the pH of the solution.⁴⁰⁸ For example, activated carbon (X40S) favours electrostatic interaction below a pH of 3, as it is positively charged at this pH and so can favourably interact with AuNPs with a PVA stabiliser as they are negatively charged.⁴⁰⁸ Titania (P25) on the other hand becomes positively charged below pH 6,⁴⁰⁹ therefore in the case of **AuNP-1** and **AuNP-2**, this pH could be sufficient for immobilisation. Future studies should involve determination of the zeta potential of the AuNPs to ensure maximum immobilisation with the supports at the appropriate pH due to opposite charges. However, it should be mentioned that ICP-MS experiments were also performed on the filtrates from the titania supported NPs to elucidate the amount of Au supported; the filtrate from **AuNP-1/TiO₂** contained 0.5 mg of Au and the filtrate from **AuNP-2/TiO₂** contained 1.8 mg. In these experiments 7.5 mg and 7.6 mg of **AuNP-1** and **AuNP-2** were used respectively; therefore, ca. 7% of **AuNP-1** was lost in the filtrate, and ca. 24% of **AuNP-2** was lost. This highlights that the immobilisation of the AuNPs could be improved by further optimisation, including the use of acid when using the titania support as maybe a lower pH is required for better interaction with the AuNPs.

8.2.5. Characterisation of supported NHC-stabilised AuNPs

The characterisation of the supported NPs was carried out to ensure the AuNPs had been immobilised and to observe whether this had altered the composition or morphology of the NPs. The two techniques used for this were: XPS and TEM. TGA was performed for **AuNP-2/TiO₂** and **AuNP-2/C**; however, the data was noisy with very little drop in mass which could be due to the lack of sensitivity of the instrument due to the large amount of support used to immobilise the nanoparticles.

8.2.5.1. XPS

The XPS data confirms the presence of the AuNPs on the support, as can be seen in Table 17 and Table 18. Interesting results were observed for **AuNP-1** on both supports due to the absence of peaks corresponding to the Au(I) oxidation state, as can be seen in Figure 114.

Table 17 - XPS data (BE and composition) for **AuNP-1** and **AuNP-2** supported on activated carbon.

Peak	AuNP-1/C		AuNP-2/C	
	BE (eV)	%At Conc.	BE (eV)	%At Conc.
Au 4f (Au(I))			84.57	0.15
Au 4f (Au(I))			88.25	0.11
Au 4f (Au(0))	83.58	3.41	83.72	0.78
Au 4f (Au(0))	87.28		87.4	0.58
C 1s	283.98	87.63	283.98	88.02
N 1s	400.88	0.8	400.28	1.92
O 1s	532.38	8.21	532.38	7.37
S 2p (SO _x)	168.18	0.23	167.78	1.08

Table 18 - XPS data (BE and composition) for **AuNP-1** and **AuNP-2** supported on titania.

Peak	AuNP-1/TiO ₂		AuNP-2/TiO ₂	
	BE (eV)	%At Conc.	BE (eV)	%At Conc.
Au 4f (Au(I))			84.96	0.03
Au 4f (Au(I))			88.63	0.02
Au 4f (Au(0))	82.93	0.06	83.44	0.44
Au 4f (Au(0))	86.63	0.05	87.12	0.33
C 1s	284.58	41.08	284.8	25.53
C 1s			286.24	5.57
C 1s			288.65	3.72
N 1s			400.2	0.88
O 1s (Ti-O)	529.51	31.65	529.68	36.33
O 1s	531.7	10.9	531.69	8.69
O 1s	533.24	1.64	533.47	0.99
S 2p (SO _x)			167.78	0.55
Ti 2p	458.28	14.63	458.5	16.92

In the case of **AuNP-1/TiO₂**, the absence of Au(I) could be explained by the relatively low concentration of the sample measured, with the Au(0) peaks being very low in concentration, as can be seen in Figure 114b, as well as the absence of the N 1s and S 2p peaks. This suggests that the low immobilisation of the AuNPs on TiO₂ could be responsible and therefore the immobilisation method requires more optimisation. However the same conclusion does not seem likely for **AuNP-1/C** as the Au(0) peak present is at a relatively high concentration (Figure 114a) and the immobilisation was more successful due to the addition of acid. Therefore, optimisation and repeats of this synthesis are required to draw further conclusions on whether the Au(I) has been removed.

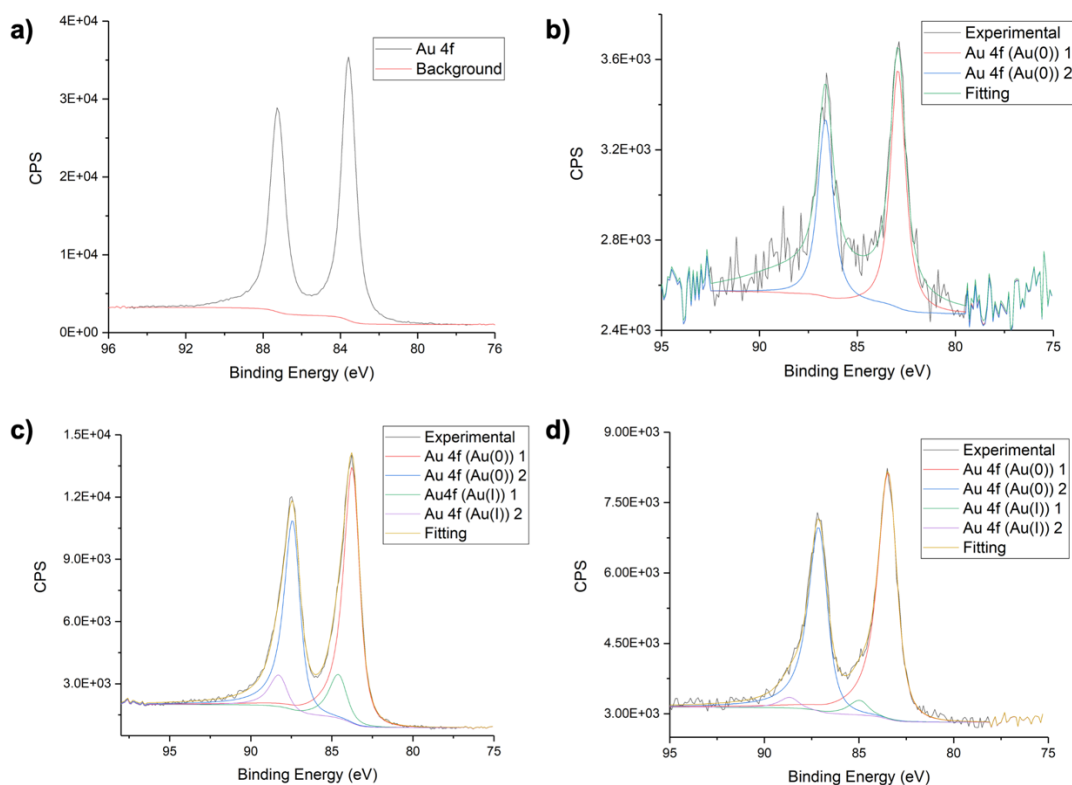


Figure 114 - XPS spectra of the Au 4f region for a) **AuNP-1/C**, b) **AuNP-1/TiO₂**, c) **AuNP-2/C** and d) **AuNP-2/TiO₂**.

8.2.5.2. TEM

TEM analysis was performed on all four catalysts, providing information on the differences of the two supports. On both supports, **AuNP-1** appeared larger than expected, especially with the activated carbon (Figure 115, top) and poor dispersion of the AuNPs was observed. Activated carbon is known to form large aggregates of AuNPs when supported by the deposition-precipitation method;⁴¹⁰ therefore, if a carbon support is required for future studies, a different procedure for immobilisation should be considered which does not result in such aggregation, such as magnetron sputtering.⁴¹⁰ **AuNP-1/TiO₂** do not appear to aggregate as much as on carbon; however, they are not very well dispersed (Figure 115, bottom).

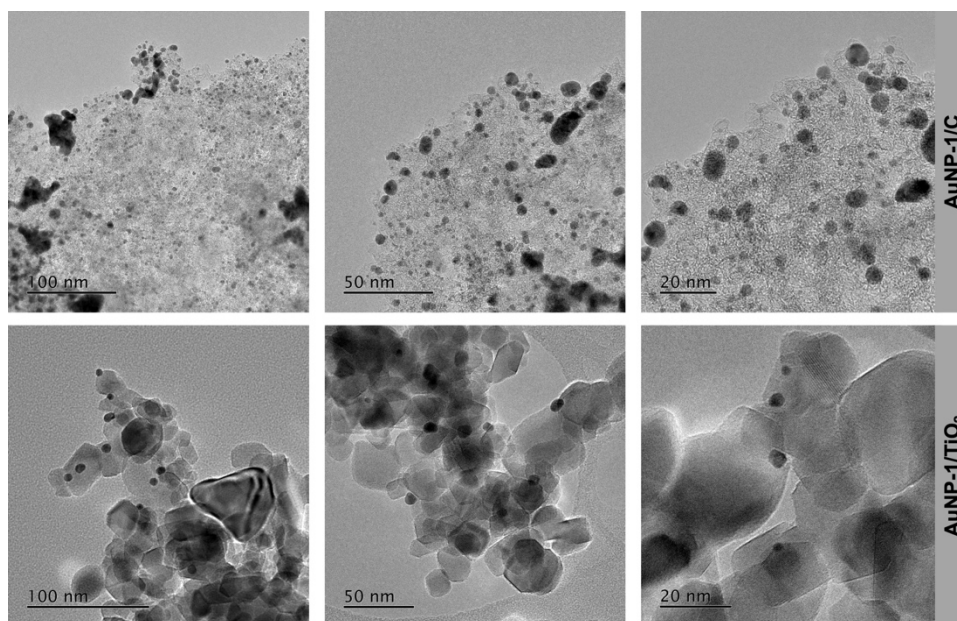


Figure 115 - TEM Images of **AuNP-1/C** (top) and **AuNP-1/TiO₂** (bottom). Scale bars are included in each image.

Concerning the supported **AuNP-2** (Figure 116), the key difference observed between the supports was the large aggregation observed on carbon, which was also seen with **AuNP-1/C**. However, at variance to **AuNP-1/TiO₂**, **AuNP-2/TiO₂** appeared to be well distributed retaining their small size and narrow particle size distribution, evidenced by the small value of deviation (± 0.36 nm) observed in Figure 117.

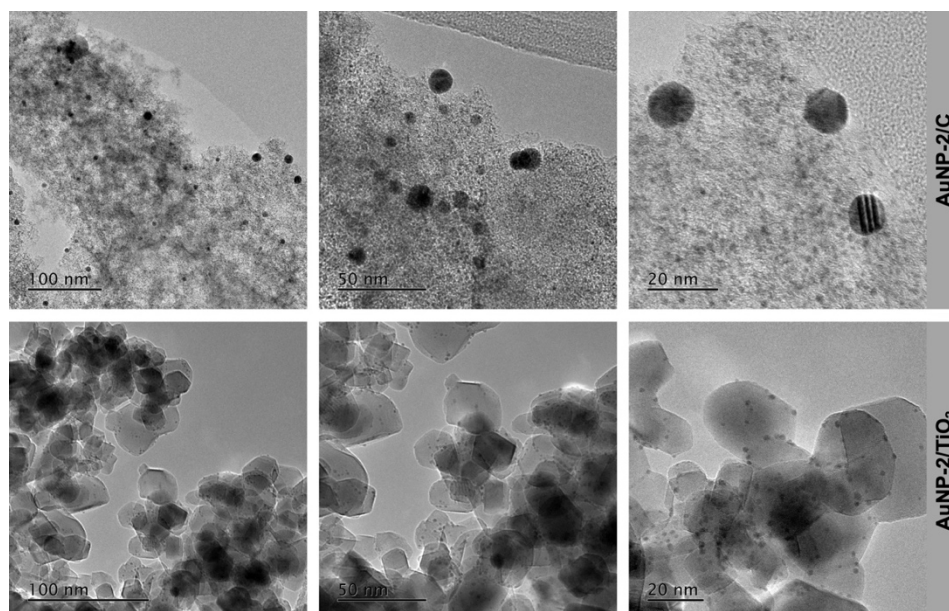


Figure 116 – TEM Images of **AuNP-2/C** (top) and **AuNP-2/TiO₂** (bottom). Scale bars are included in each image.

Although these images allow us to observe the overall distribution and size of NPs, it is difficult to obtain accurately the average size and count of the NPs due to poor contrast, especially for the activated carbon. Activated carbon and titania supports both have a relatively low atomic number (Z), as well as the AuNPs themselves, meaning that there is not a significant difference in the diffraction of the electron beam, providing poor contrast.⁴¹¹ Nevertheless, an average size count of the NPs supported on titania could be achieved. **AuNP-1/TiO₂** had an average size of 6.7 ± 2.03 nm across 27 images and 116 NPs (Figure 117), which is considerably higher compared to the unsupported **AuNP-1** (2.29 ± 1.1 nm). This could be due to the effect of Ostwald ripening, which has been observed with other AuNPs on oxide supports.⁴¹² It involves the growth of larger NPs, which take material from the smaller NPs, causing them to shrink to an even smaller size.⁴¹² This could also explain the large size distribution observed for **AuNP-1/TiO₂**.

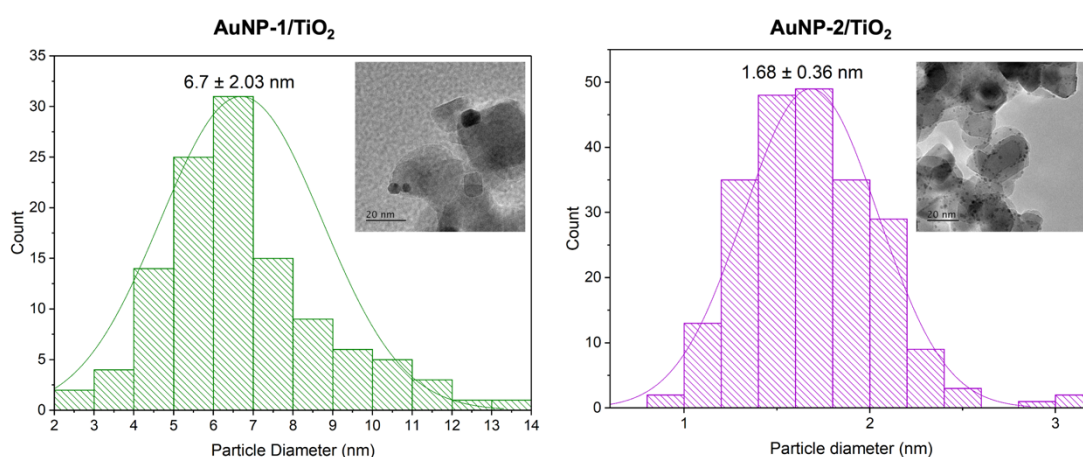


Figure 117 – Particle size histogram of NHC@AuNPs/TiO₂ with representative TEM images: **AuNP-1/TiO₂** displayed an average size of 6.7 ± 2.03 nm and **AuNP-2/TiO₂** displayed an average size of 1.68 ± 0.36 nm. Scale bar: 20 nm.

On the other hand, **AuNP-2/TiO₂** had an average size of 1.68 ± 0.36 nm across 9 images and 226 NPs (Figure 117), which corresponds to a decrease in size compared to the unsupported **AuNP-2** (2.55 ± 1.18 nm). However, the large standard deviation observed with the unsupported NPs means that there is still uncertainty on the average AuNPs size. In conclusion, the addition of a support seems to have improved the overall particle size distribution of the NPs.

8.2.6. Catalytic studies of TiO₂ supported NHC@AuNPs

The catalytic performance of the supported NPs was also assessed using the 4-nitrophenol reduction, in this case only the AuNPs/TiO₂ were evaluated due to the high aggregation of the AuNPs/C. The same concentrations of 4-nitrophenol and NaBH₄ were used as seen in section 8.2.3, with 2.4 mg of supported catalyst. Interestingly, supporting

the AuNPs fostered a decrease in their reactivity, which was unexpected as often supporting AuNPs improves performance due to reduced aggregation.⁴¹³ However, it has also been reported that when attributing the performance of the catalysts to the mass of the gold in each sample, colloidal AuNPs are more active.⁴¹⁴

Remarkably, **AuNP-1/TiO₂** showed a significant induction period of ca. 15.5 min before any product formation was observed (Figure 118), which is a lot larger than the induction period observed for **AuNP-1**. A total conversion of 73% was reached over 28.5 min (Figure 118a). However, even when excluding the induction period, the rate constant was still relatively low at 0.12567 min⁻¹ per 2.4 mg of catalyst (Figure 118b). This decrease in reaction rate for **AuNP-1/TiO₂** compared to **AuNP-1** can be clearly reflected in the increase in average size of the NPs; as generally the greater the size, the lower the reactivity.⁴¹⁵

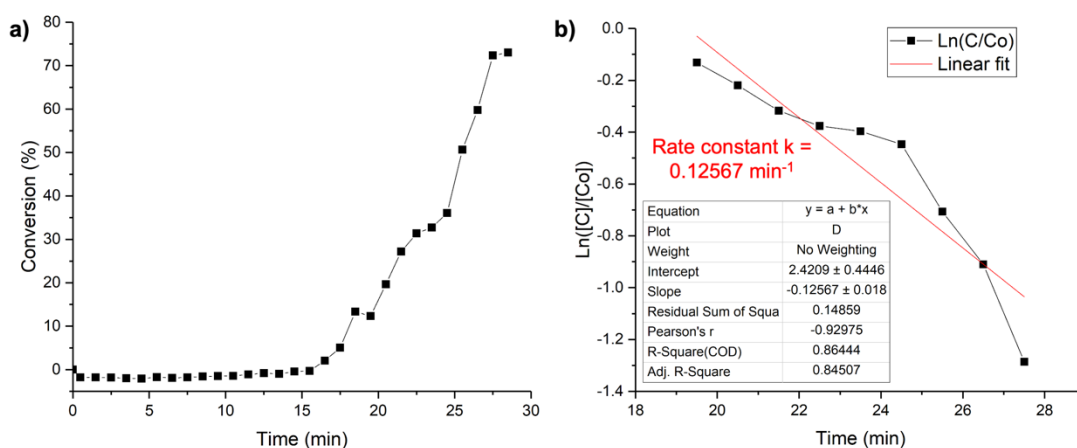


Figure 118 - Plots for the 4-nitrophenol reduction reaction using **AuNP-1/TiO₂**: a) conversion against time and b) Ln([C]/[Co]) vs. time.

AuNP-2/TiO₂ reached a conversion of 78% after 17 min, with a rate constant of 0.08805 min⁻¹ per 2.4 mg of catalyst. Figure 119a shows that the conversion of 4-nitrophenol follows a near linear trend over time with a similar performance to **AuNP-2** as no induction period was observed in Figure 119b.

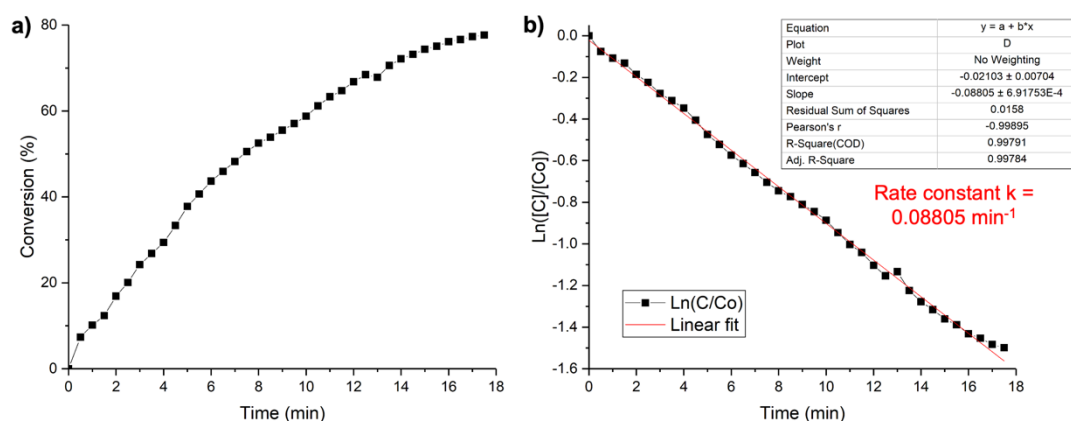


Figure 119 – Plots for the 4-nitrophenol reduction reaction using **AuNP-2/TiO₂**: a) conversion against time and b) $\text{Ln}([C]/[C_0])$ vs. time.

The ICP-MS results, (along with the data of the filtrate from the immobilisation step) allow the actual percentage of Au loaded onto titania to be calculated. Therefore, considering that **AuNP-1/TiO₂** used in the 4-nitrophenol reduction reaction contained 0.14088 mg of Au per 2.4 mg of supported catalyst, the amount of Au in 7.5 mg of **AuNHC-1** that was supported would be 0.44 mg. However, the filtrate from the support reaction contained 0.5 mg of Au. Therefore, while the 100% theoretical loading of Au should be 0.94 mg, we can conclude that only 46.8% of Au catalyst was immobilised onto **AuNP-1/TiO₂**. Through similar calculations, it was possible to assess that **AuNP-2/TiO₂** catalysts used in the 4-nitrophenol reduction only contained 0.044 mg of Au per 2.4 mg of catalyst, corresponding to only 7% of the theoretical loading (1.94 mg). To conclude, regardless of the lower loading of gold in **AuNP-2/TiO₂** the rate constant was higher compared to **AuNP-1/TiO₂**.

8.2.6.1. Pre-treatment of **AuNP-1/TiO₂** with **NaBH₄**

Interestingly, pre-treatment of **AuNP-1/TiO₂** with **NaBH₄** resulted in a longer induction and reaction time compared to the untreated AuNPs (Figure 120). The longer induction time was not observed when the unsupported **AuNP-1** were pre-treated, as shown in section 8.2.3.3.

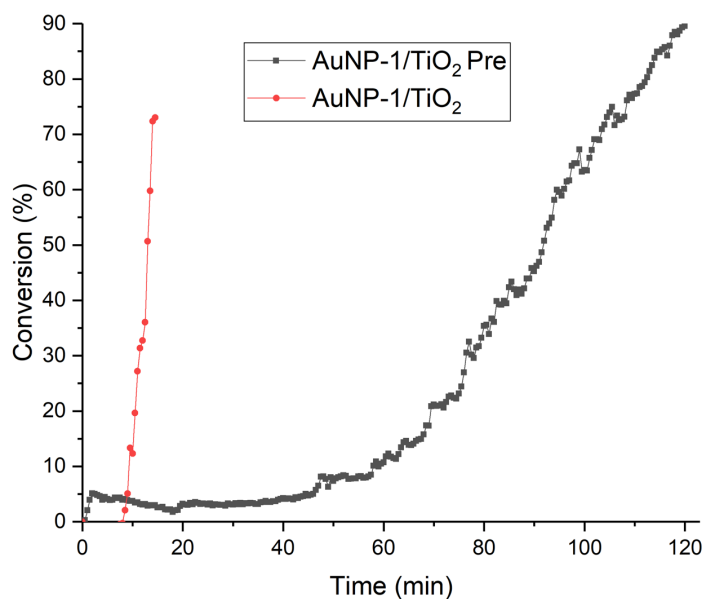


Figure 120 – Conversion of 4-nitrophenol over time for the pre-treated **AuNP-1/TiO₂** (black dots) and non-treated **AuNP-1/TiO₂** (red circles).

8.2.6.2. Recyclability of AuNP-1/TiO₂ and AuNP-2/TiO₂

The recyclability of the TiO₂ supported AuNPs was assessed using the same conditions as before (2.4 mg of catalyst). However, after each cycle the filtrate in the cuvette was removed and the NPs at the bottom of the cuvette were washed with MilliQ water before leaving to dry overnight. The reaction was then performed again with addition of fresh 4-nitrophenol and NaBH₄ solutions. A total of three cycles were performed for the supported NPs.

The recyclability of **AuNP-1/TiO₂** was determined considering both its induction period as well as the reaction rates for each cycle. Surprisingly, the induction period decreased over the cycles and the reaction rate constant (k), excluding the induction times, decreased from cycle 1 to 2, but then increased from cycle 2 to 3, as can be seen in Figure 121a-d. Although, it should be noted that the k value of cycle 3 was still ca. 4-fold less than cycle 1; therefore, more repeats are needed to conclude whether the increase from cycle 2 to cycle 3 is significant.

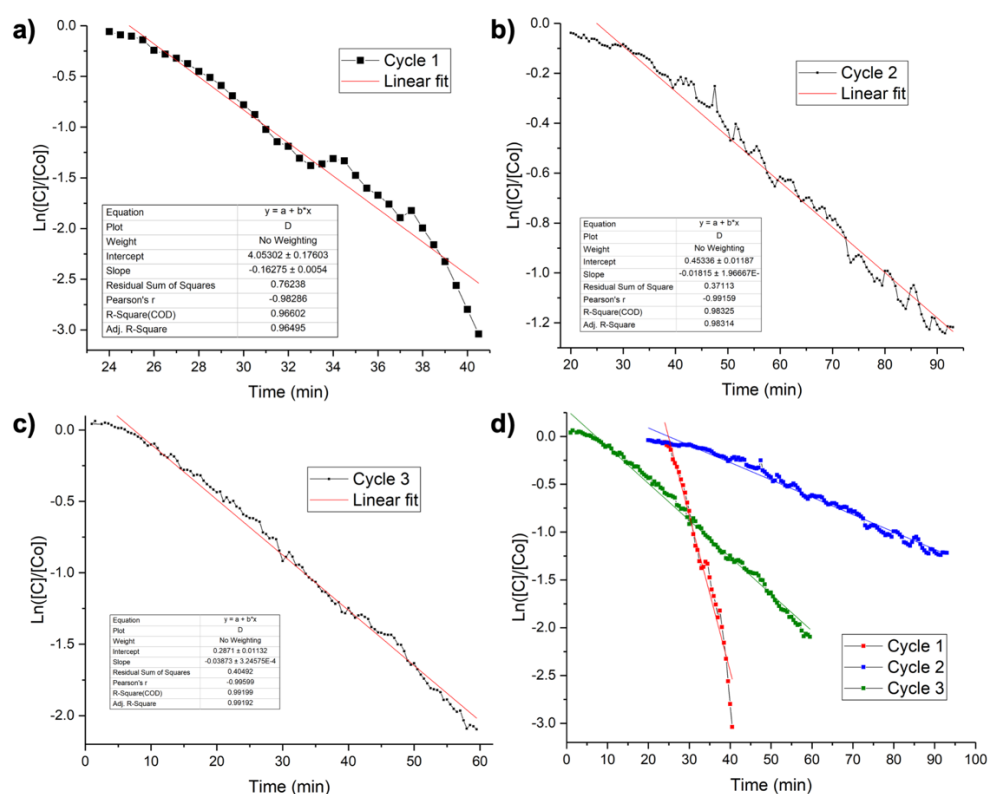


Figure 121 - Plots of $\text{Ln}([C]/[C_0])$ vs. time for the 4-nitrophenol reduction reaction using **AuNP-1/TiO₂** across 3 cycles: **a)** cycle 1, **b)** cycle 2, **c)** cycle 3 and **d)** comparison of all three cycles.

After each cycle the NPs were washed, as mentioned above, and the filtrate of the reaction and wash were submitted for ICP-MS experiments. This is to elucidate if any unsupported Au(0) or Au(I) had leached from the NPs. The results showed only a small loss of Au after the 1st cycle (0.19 mg/l), suggesting that leaching does not appear to play a role for the decrease in rate. This can also be further evidenced from the XPS of the NPs after the third reaction cycle (Table 19), with Au 4f still present around the same concentration.

Table 19 - XPS data (BE and composition) for **AuNP-1/TiO₂** before and after three 4-nitrophenol reduction reactions.

Peak	Before Reaction		After Reactions	
	BE (eV)	%At Conc.	BE (eV)	%At Conc.
Au 4f (Au(0))	82.93	0.06	82.71	0.08
Au 4f (Au(0))	86.63	0.05	86.41	0.06
C 1s	284.58	41.08	284.58	27.59
O 1s (Ti-O)	529.51	31.65	529.19	32.42
O 1s	531.7	10.9	531.27	15.6
O 1s	533.24	1.64	533.67	0.7
Ti 2p	458.28	14.63	457.98	15.12

The decrease in induction time over the cycles could be due to the pre-treatment-like nature of the previous cycle(s) due to a reconstruction caused by the NaBH_4 , however unlike the unsupported **AuNP-1**, aggregation does not appear to affect the catalysis due to immobilisation.

However, if only the overall conversion is considered as described by Monti *et al.*²⁶⁸ and Rogers *et al.*⁴⁰⁷ the conversion percentage of **AuNP-1/TiO₂** over the three cycles (Figure 122, orange bars) does not vary greatly, independent of the reaction time.

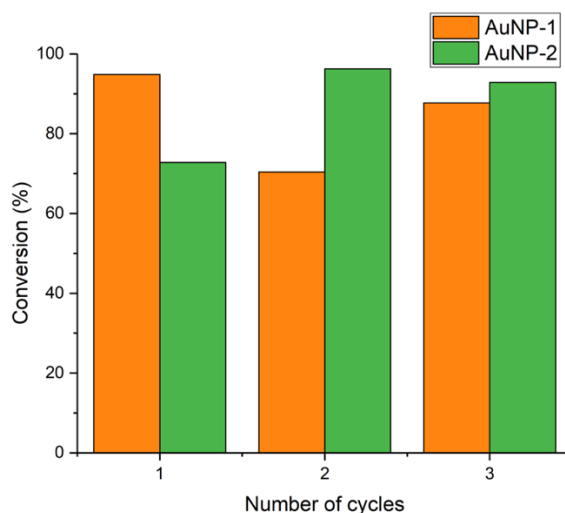


Figure 122 – Conversion percentage for the reduction of 4-nitrophenol using **AuNP-1/TiO₂** (orange bars) and **AuNP-2/TiO₂** (green bars) as catalysts across three cycles.

Interestingly, **AuNP-2/TiO₂** showed an induction period, at variance to its unsupported counterpart, with a significant increase from cycle 2 to cycle 3, as can be seen in Figure 123. The presence of the induction period could be more reflective of what is happening in section 8.2.3.1 due to the unmasking of the induction period; however, repeats are needed to clarify whether this is true.

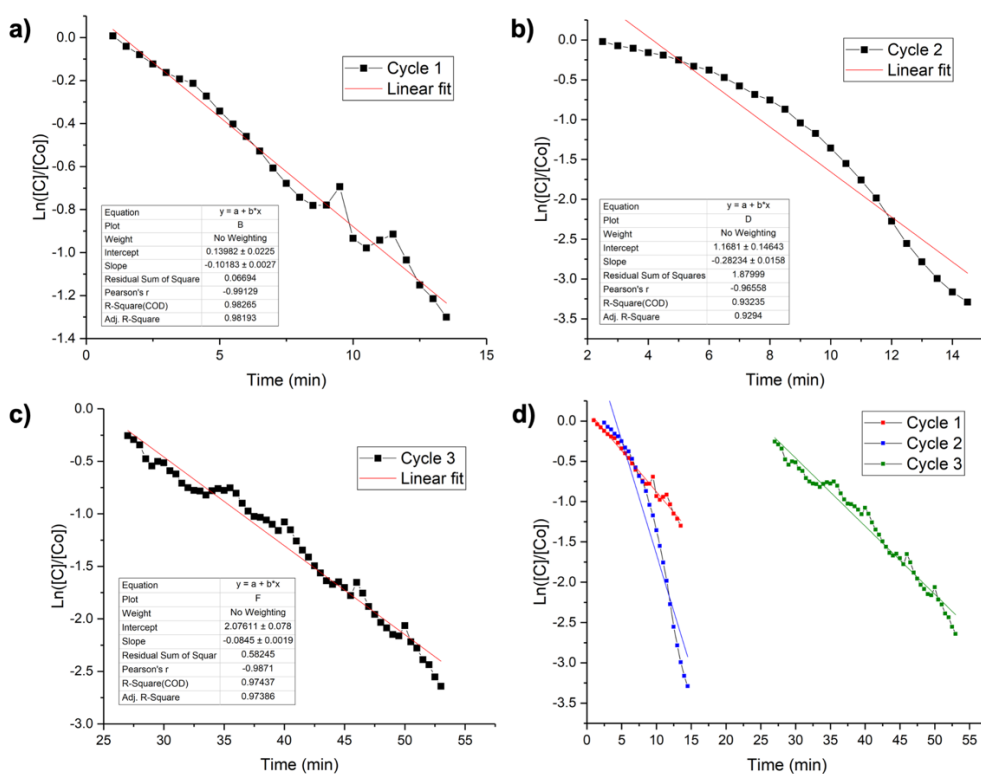


Figure 123 – Plots of $\text{Ln}([C]/[C_0])$ vs. time for the 4-nitrophenol reduction reaction using **AuNP-2/TiO₂** across 3 cycles: **a)** cycle 1, **b)** cycle 2, **c)** cycle 3 and **d)** comparison of all three cycles.

The ICP-MS results for the filtrate and wash after the first cycle with **AuNP-2/TiO₂** contained 14.43 mg/l of Au, meaning that there is significant leaching of the AuNPs from the support. Interestingly this improved the reaction rate for cycle 2 compared to cycle 1 (excluding the induction time in both cases) with the rate constant (k) increasing from 0.10183 min^{-1} to 0.28234 min^{-1} . It could be speculated that the Au leaching from the first cycle could have been Au(I) covering the NP surface, which once removed resulted in an increased reaction rate. Another explanation could be that the Au(I) species leached from the surface could subsequently be reduced in the reducing environment, meaning they could still act as catalysts increasing the reaction rate. The induction period for cycle 3 had significantly increased compared to the first two cycles and the overall reaction rate was slower (0.0845 min^{-1}). The overall instability of the catalyst combined with Au leaching could be responsible for the slow reaction rate and long induction time observed for the third cycle, since after this last reaction, XPS analysis showed no Au 4f species on the catalyst surface (Table 20).

Table 20 - XPS data (BE and composition) for **AuNP-2/TiO₂** before and after three cycles of 4-nitrophenol reduction reactions.

Peak	Before Reactions		After Reactions	
	BE (eV)	%At Conc.	BE (eV)	%At Conc.
Au 4f (Au(I))	84.96	0.03		
Au 4f (Au(I))	88.63	0.02		
Au 4f (Au(0))	83.44	0.44		
Au 4f (Au(0))	87.12	0.33		
C 1s	284.8	25.53	284.78	35.74
C 1s	286.24	5.57		
C 1s	288.65	3.72		
Na 1s			1071.38	3.37
N 1s	400.2	0.88		
O 1s (Ti-O)	529.68	36.33	529.57	33.46
O 1s	531.69	8.69	531.75	11.51
O 1s	533.47	0.99	533.47	0.83
S 2p (SO _x)	167.78	0.55		
Ti 2p	458.5	16.92	458.28	15.09

The conversion of **AuNP-2/TiO₂** across the three cycles can be seen in Figure 122, (green bars). Overall, the conversion increases from cycle 1 to 2 (73% to 96%) which could be reflected in the loss of Au from the NP surface, then, from cycle 2 to 3, there is only a small loss in conversion which could be within the experimental error (96% to 93%). This indicates that the NPs are not deactivated, albeit take longer to react due to concurrent Au leaching.

8.3. Summary and Future Outlook

In conclusion, this work has described the synthesis and characterisation of two water-soluble NHC@AuNPs formed by the 'bottom-up' approach from the bis-NHC Au(I) precursors, one of which is a di-gold complex. The thorough characterisation of these AuNPs has demonstrated their stability in water and biologically relevant media (PBS 1x and GSH), as well as their small size (ca. 2 nm). Additionally, the catalytic performance of the NHC@AuNPs was demonstrated for the reduction of 4-nitrophenol, with exceptional performance seen with **AuNP-1**. However, as mentioned, repeats of the 4-nitrophenol reduction reaction are necessary using the same mass of catalyst throughout to obtain an average rate constant.

Furthermore, attempts to immobilise the NHC@AuNPs on two types of support (activated carbon and titania) were performed. The titania support was able to immobilise

some of the AuNPs by stirring in MilliQ water, however the loading was quite low. Whereas the AuNPs supported on carbon required the addition of acid; nevertheless, this did result in good immobilisation.

To summarise:

- The synthesis of NHC@AuNPs *via* the 'bottom-up' approach was achieved, leading to small NPs, similarly to other colloidal methods (e.g. 2 nm).
- The NHC@AuNPs showed high stability in biologically relevant media.
- Some differences between the two NHC@AuNPs were identified, such as the amount of Au(I) species remaining absorbed on the surface, and their catalytic performance, with **AuNP-1** showing superior results.
- Differences between the AuNPs/TiO₂ were also identified, such as the smaller particle size of **AuNP-2/TiO₂** which improved the particle size distribution, resulting in a greater catalytic performance compared to **AuNP-1/TiO₂**.

Challenges to overcome in future work:

- Au(I) species could still be identified by XPS for the AuNPs despite dialysis. This could be improved by varying the amount of ligand present, the amount of reducing agent, the type of reducing agent (e.g. milder reagents such as formic acid, citrate) or the method of synthesis. *In situ* ¹H NMR for the reduction of the Au(I) NHCs could also be useful to identify any possible intermediates.
- The induction time present in **AuNP-1** could also be removed by varying the addition sequence of the reagents. This has been reported by Chakraborty *et al.*⁴¹⁴ who found that by adding 4-nitrophenol and NaBH₄ to the aqueous solution before the AuNPs, both reagents could adsorb together onto the NP surface avoiding the induction time.
- Future work should optimise the immobilisation of the titania catalysts by different methods such as addition of acid. However, it should be noted that immobilisation of the NHC@AuNPs did not increase the catalytic performance compared to the unsupported NPs as expected, especially for **AuNP-1/TiO₂**. Nevertheless, **AuNP-2/TiO₂** did show NPs of smaller size and greater particle size distribution compared to **AuNP-1/TiO₂**.
- **AuNP-2/TiO₂** also suffered with Au leaching during the recycling of the AuNPs for the reduction of 4-nitrophenol. Therefore, to improve the stability of the AuNPs on titania, metal-support interactions can be enhanced by heating the sample,⁴¹⁶ although the temperature used must be carefully balanced to avoid removal of all surface ligands.

Future perspectives for these NHC@AuNPs include improving the catalyst stability and gaining a greater understanding of the role that the NHC ligand plays. This can be explored by characterising the AuNPs under their operating conditions, including *in situ/operando* studies to help understand the reaction mechanism, immobilisation process and leaching of the AuNPs.³⁸⁹

Another area that we are keen to explore involves investigating the catalytic performance of the NHC@AuNPs in more biologically relevant reactions, such as bioorthogonal uncaging reactions, and also investigating the effect of altering the NP shape e.g. nanorod for bioimaging applications. Studies into the biological activity of **AuNP-2** as PTT agents is currently underway with collaborators.

8.4. Materials and Methods

8.4.1. General

Solvents and reagents (reagent grade) were all commercially available and used without further purification. ^1H and $^{13}\text{C}\{^1\text{H}\}$ NMR spectra were recorded in D_2O solution on Bruker Avance (400-500 MHz) NMR spectrometers. ESI-MS spectra were recorded on Synapt G2 Si time-of-flight (TOF) mass spectrometer (Waters). UV-Vis spectra were recorded on a Cary 60 UV-Vis spectrometer from Agilent Technologies. Fourier-transform infrared attenuated total reflectance (FTIR-ATR) spectroscopy was carried out on a Shimadzu IRAffinity-1S FT-IR spectrophotometer equipped with an ATR unit. TG measurements were performed on a PerkinElmer Pyris TGA by Dr. Greg Shaw. XPS was performed on a Thermo K-alpha⁺ X-ray photoelectron spectrometer by Dr. David Morgan and analysis was performed using CasaXPS software Version 2.3.21 (rev1.0W). TEM images were obtained on a JEOL 2100 Transmission Electron Microscope by Dr. Thomas Davies, and the images were then analysed using ImageJ software.⁴¹⁷ ICP-MS was performed on a Agilent 7900 by Mr. Simon Waller.

8.4.2. NHC-L and Au(I) NHC synthesis

NHC-L1 was formed according to a literature procedure.³⁸⁶

1-butylimidazole (1.28 mL, 0.97 mmol, 1 eq.) and 1,3-propane sultone (5.92 g, 4.85 mmol, 5 eq.) were added to a flask under nitrogen, before the addition of dry acetone (25 mL). This was then left to stir under nitrogen at room temperature for 24 h, producing an off-white precipitate. The precipitate was then separated by filtration and washed with acetone (~50 mL). The clean product was obtained in a 95% yield (2.2819 g).

^1H NMR (400 MHz, D_2O) δ 8.83 (s, 1H), 7.57 – 7.50 (m, 2H), 4.41 – 4.33 (m, 2H), 4.25 – 4.17 (m, 2H), 2.96 – 2.88 (m, 2H), 2.39 – 2.27 (m, 2H), 1.92 – 1.80 (m, 2H), 1.38 – 1.25 (m, 2H), 0.92 (t, $J = 7.4$ Hz, 3H).

$^{13}\text{C}\{^1\text{H}\}$ NMR (101 MHz, D_2O) δ 135.40, 122.56, 122.26, 49.38, 47.71, 47.17, 31.14, 25.05, 18.73, 12.58.

HR-ESI-MS (H_2O , pos. mode) for $\text{C}_{10}\text{H}_{19}\text{N}_2\text{O}_3\text{S}^+$: exp. 247.1437 (calc. 247.1116).

NHC-L2 was formed by slight modification of a literature procedure.³⁸⁷

Bis(imidazol-1-yl)methane (296 mg, 2 mmol, 1 eq.) was added to a flask along with acetone (30 mL). This was left to stir at 0 °C, whilst in another flask 1,3-propane sultone (546 mg, 4.4 mmol, 2 eq.) and acetone (30 mL) were added. The propane sultone solution was then slowly added to the cold bis(imidazol-1-yl)methane solution. Upon completion, the reaction mixture was allowed to warm to room temperature before increasing the temperature to 50 °C. This was then left to stir for 5 d. The solvent was then removed under reduced pressure to afford a white solid which was then re-

suspended in methanol (~20 mL) before filtering. The resulting solid was subsequently washed with acetone to yield the product in 66% yield (517 mg).

^1H NMR (500 MHz, D_2O) δ 9.35 (s, 2H), 7.82 (d, $J = 1.4$ Hz, 2H), 7.73 (d, $J = 1.5$ Hz, 2H), 6.73 (s, 2H), 4.47 (t, $J = 7.2$ Hz, 4H), 2.97 (t, $J = 7.3$ Hz, 4H), 2.41 – 2.34 (m, 4H).

$^{13}\text{C}\{^1\text{H}\}$ NMR (101 MHz, D_2O) δ 137.19, 123.80, 122.26, 58.90, 48.48, 47.14, 24.75.

HR-ESI-MS (H_2O , pos. mode) for $\text{C}_{13}\text{H}_{21}\text{N}_4\text{O}_6\text{S}_2^+$: exp. 393.1096 (calc. 393.0902).

AuNHC-1 was formed by modification of a literature procedure.³⁸⁸

A mixture of **NHC-L1** (240 mg, 1 mmol, 1 eq.) and Ag_2O (230 mg, 1 mmol, 1 eq.) were added to a flask under nitrogen, before the addition of dry MeOH (6 mL). This was stirred at 50 °C in darkness, overnight and under nitrogen. NaCl (58 mg, 1 mmol, 1 eq.) was then added, and the mixture was left to stir at room temperature for 30 min. This was then passed through a short Celite® pad until a clear, yellow solution was obtained. The solution was then added to a flask along with $\text{Au}(\text{SMe}_2)\text{Cl}$ (145 mg, 0.5 mmol, 0.5 eq.) and this was left to stir overnight at room temperature in darkness. The mixture was then passed through another Celite® pad, followed by vacuum evaporation of the solvent. The crude product was purified by precipitation of impurities from a concentrated aqueous solution with addition of methanol. The pure product was obtained as an off-white solid with a yield of 34% (119 mg).

^1H NMR (500 MHz, D_2O) δ 7.21 (d, $J = 9.0$ Hz, 4H), 4.22 (t, $J = 6.9$ Hz, 4H), 4.09 (t, $J = 7.0$ Hz, 4H), 2.79 (t, $J = 7.8$ Hz, 4H), 2.31 – 2.17 (m, 4H), 1.75 (t, $J = 7.1$ Hz, 4H), 1.28 – 1.12 (m, 4H), 0.79 (t, $J = 7.4$ Hz, 6H).

$^{13}\text{C}\{^1\text{H}\}$ NMR (126 MHz, D_2O) δ 182.72, 121.88, 121.54, 50.69, 49.17, 47.81, 32.90, 26.43, 19.17, 12.96.

HR-ESI-MS (H_2O , pos. mode) for $\text{C}_{20}\text{H}_{35}\text{AuN}_4\text{NaO}_6\text{S}_2^+$: exp. 711.1613 (calc. 711.1561).

AuNHC-2 was formed by modification of a literature procedure.³⁸⁵

NHC-L2 (209 mg, 0.53 mmol, 1 eq.) was dissolved in deionised water (10 mL), and Ag_2O (123 mg, 0.53 mmol, 1 eq.) was added. After the suspension was stirred at 50 °C for 2 h, NaCl (34 mg, 0.58 mmol, 1.1 eq.) was added and the mixture was stirred for a further 30 min at room temperature. After filtration over Celite®, $\text{Au}(\text{SMe}_2)\text{Cl}$ (157 mg, 0.53 mmol, 1 eq.) was added to the clear solution and this was stirred at room temperature overnight. The solvent was then removed and this procedure was repeated once more assuming only one Au-NHC complex had been formed. The solvent was then removed at 45 °C under reduced pressure, before the addition of DI H_2O (~5 mL) and a large excess of methanol (~20-30 mL). This was then left in the fridge for 2 days before

filtering. The filtrate was then evaporated to yield the product as an off-white solid (146 mg, 45%).

^1H NMR (400 MHz, D_2O) δ 7.55 (s, 2H), 7.40 (d, $J = 2.1$ Hz, 4H), 7.01 (d, $J = 14.0$ Hz, 2H), 6.19 (d, $J = 13.4$ Hz, 2H), 4.39 – 4.30 (m, 8H), 2.92 – 2.82 (m, 8H), 2.35 – 2.24 (m, 8H).

$^{13}\text{C}\{^1\text{H}\}$ NMR (126 MHz, D_2O) δ 183.21, 122.83, 121.35, 62.98, 49.88, 47.57, 26.20.

HR-ESI-MS (H_2O , pos. mode) for $\text{C}_{26}\text{H}_{39}\text{Au}_2\text{N}_8\text{O}_{12}\text{S}_4^+$: exp. 1177.0804 (calc. 1177.0901).

8.4.3. NHC@AuNP synthesis

The same 'bottom-up' method was employed to form both the gold nanoparticles: **AuNP-1** and **AuNP-2**.

The starting Au(I) NHC complex (50 mg, 1 eq.) was dissolved in deionised H_2O (5 mL) at room temperature with medium stirring. A freshly prepared aqueous NaBH_4 solution (10 eq., 1 mL) was added quickly resulting in a darkening of the reaction solution. This was then left to stir for 24 h at room temperature. The resulting aqueous solution of AuNPs were then purified by dialysis using treated cellulose dialysis membrane (Sigma-Aldrich, D9652) (see 8.4.4.) with a molecular weight cut off of 14,000 Da.

AuNP-1

^1H NMR (500 MHz, D_2O) δ 7.21 (d, $J = 1.9$ Hz, 2H), 7.19 (d, $J = 1.9$ Hz, 2H), 4.28 (t, $J = 6.7$ Hz, 4H), 4.16 (t, $J = 6.8$ Hz, 4H), 2.84 – 2.79 (m, 4H), 2.31 – 2.22 (m, 4H), 1.85 – 1.76 (m, 4H), 1.29 – 1.18 (m, 4H), 0.83 (t, $J = 7.4$ Hz, 6H).

$^{13}\text{C}\{^1\text{H}\}$ NMR (126 MHz, D_2O) δ 182.90, 121.72, 121.35, 50.62, 49.09, 47.78, 32.78, 26.32, 19.06, 12.88.

AuNP-2

^1H NMR (500 MHz, D_2O) δ 7.72 (d, $J = 2.2$ Hz, 1H), 7.66 (d, $J = 2.1$ Hz, 1H), 7.63 (d, $J = 2.2$ Hz, 1H), 7.60 (d, $J = 2.2$ Hz, 1H), 7.56 (d, $J = 1.3$ Hz, 1H), 7.48 (d, $J = 2.1$ Hz, 1H), 7.46 (d, $J = 2.1$ Hz, 7H), 7.41 (d, $J = 2.1$ Hz, 1H), 7.31 (d, $J = 2.0$ Hz, 13H), 6.92 (d, $J = 14.0$ Hz, 6H), 6.65 – 6.53 (m, 10H), 6.10 (d, $J = 14.1$ Hz, 6H), 4.42 – 4.20 (m, 10H), 2.90 – 2.73 (m, 11H), 2.32 – 2.16 (m, 8H).

$^{13}\text{C}\{^1\text{H}\}$ NMR (126 MHz, D_2O) δ 183.20, 122.81, 121.33, 62.98, 49.88, 47.56, 26.18.

8.4.4. Dialysis procedure

The procedure for dialysis was adapted from a visual tutorial reported by Low and Bansal.⁴¹⁸ The dialysis membranes (Sigma-Aldrich) chosen had a typical molecular weight cut off of 14,000 Da, however they required treating prior to their use. The dialysis membrane was first cut to its desired length depending on the amount of NP solution (~

10 cm for 5 mL solution). The membrane was then placed in a 1 L beaker $\frac{3}{4}$ filled with MilliQ H₂O which was vigorously stirred to remove glycerol. The water was changed every hour, four times. In order to remove sulfur compounds, the membranes were treated with a 0.3% (w/v) solution of sodium sulfide at 80 °C for 1 min, before transfer into a beaker of MilliQ H₂O at 60 °C for 2 min. The membranes were next acidified with 0.2% (v/v) solution of sulfuric acid at room temperature, before transferring into another beaker of MilliQ H₂O at 60 °C to remove the acid. All steps required stirring of the membranes in the solutions.

The aqueous NP solution could then be transferred to the treated membranes, by firstly adding a dialysis clip to one end and then filling with the solution. The second dialysis clip was then added to the other end to create a dialysis bag. This was then placed in a 1L beaker $\frac{3}{4}$ filled with MilliQ H₂O and left to stir for 6 h or overnight (Figure 124). After this time the MilliQ H₂O was replenished and this was repeated three times. The AuNP solution was then removed from the dialysis bag, filtered and then lyophilised.

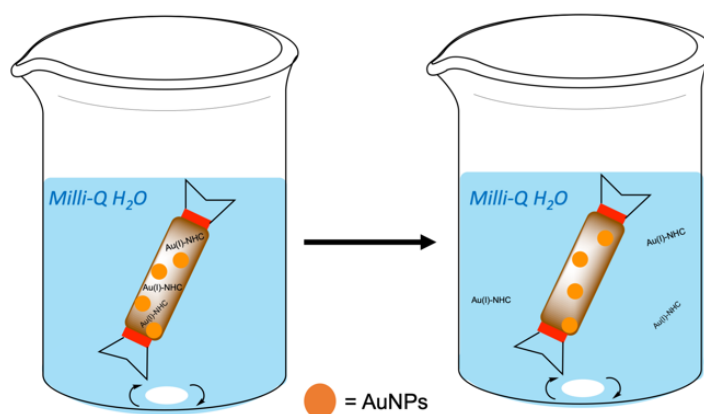


Figure 124 – Dialysis procedure to remove Au(I)NHC complexes from the NHC@AuNPs.

8.4.5. UV-Vis Stability Studies

Stability studies were recorded from 1000-330 nm with an average time of 0.1 sec, interval of 0.5 nm and scan rate of 300 nm/min. The studies were performed using 0.43 – 0.6 mg of **AuNP-1** and 0.29 – 0.34 mg of **AuNP-2** to achieve an absorbance ca. 0.8 for the SPR band. The stability studies were completed in MilliQ water (500 μ L), PBS 1x (500 μ L, pH 7.4) and PBS 1x (500 μ L) with 2 mM GSH. A background of the solutions without the AuNPs were performed prior to the study. The stability studies were obtained using the advanced collect function on the Cary scanning kinetics software. Studies in MilliQ water and PBS 1x were performed with 2 stages and 33 cycles. Stage 1 had a cycle of 15 min and stopped at 60 min; stage 2 had a cycle of 30 min and stopped after 900 min. Studies in PBS 1x with 2 mM GSH were monitored for longer with 2 stages and 51 cycles. Stage 1 had a cycle of 10 min for 60 min; stage 2 had a cycle of 30 min and

stopped after 1380 min. After the stability study was performed the cuvette was shaken to redissolve any precipitate formed over time. A single scan was then performed using the same set-up to observe the effects of this.

8.4.6. UV-Vis Kinetic study for 4-nitrophenol reduction reaction

Nitrophenol reduction reactions were monitored by UV-Vis spectroscopy from 820-370/300 nm with an average time of 0.1 s, interval of 1 nm and scan rate of 600 nm/min. The experiments were performed using 0.2 mg of **AuNP-1** and 0.275 mg of **AuNP-2**, respectively. A background scan of MilliQ water was performed and the UV-Vis kinetic study was set up to measure every 30 sec over 360 min, however this was stopped once the 400 nm peak was no longer decreasing in absorbance. A 4-nitrophenol aqueous solution of 3 mM (4 mg in 10 mL) was then prepared and 100 μ L of this was added to a cuvette containing the NPs and 1.9 mL of MilliQ water. An aqueous 30 mM (11.3 mg in 10 mL) solution of NaBH₄ was then freshly prepared and 1 mL was quickly added to the cuvette whilst starting the analysis. The overall concentration of nitrophenol and NaBH₄ in the cuvette was 0.1 mM and 10 mM, respectively. The reduction reactions of 2- and 3-nitrophenol were performed using the same method and using ~0.5 mg of NPs. The TiO₂ supported AuNPs were also monitored using this method with 2.4 mg of catalyst.

Calibration plots of 3- and 2-nitrophenol were also obtained by plotting the absorbance at 385 cm⁻¹ and 415 cm⁻¹, respectively, at different concentrations (0.01 mM, 0.02 mM, 0.05 mM and 0.1 mM). The same equations were then used as seen in 8.2.3.1. to determine the rate constant.

8.4.7. Pre-treatment of AuNP-1 and AuNP-1/TiO₂

AuNP-1 (0.4 mg) was added to the cuvette along with 0.9 mL of MilliQ water and 1 mL of a 30 mM aqueous NaBH₄ solution. A UV-Vis kinetic study was then set up to measure every 30 sec over 16 min. After this time the cuvette was left uncovered for 1 h. The 4-nitrophenol reduction reaction was then performed directly on this solution by the addition of 100 μ L of 4-nitrophenol aqueous solution (3 mM) and the fast addition of 1 mL of a freshly prepared NaBH₄ solution (30 mM). Again, the UV-Vis kinetic study was set up to measure every 30 sec over 360 min, however was stopped once the 400 nm peak had flattened. The same procedure was followed for the pre-treatment of **AuNP-1/TiO₂** except 2.4 mg of catalyst was used.

8.4.8. Synthesis of supported NHC@AuNPs

The supported NHC@AuNPs were formed by dissolving in MilliQ water with stirring before addition of the support, the quantities of which can be found in Table 21.

Table 21 – Quantities of NHC@AuNP and support (TiO₂ or activated C) required to form supported NPs, along with volume of MilliQ water used as the solvent.

NHC@AuNP		Support		MilliQ H ₂ O Volume (mL)
Type	Mass (mg)	Type	Mass (mg)	
AuNP-1	7.5	TiO ₂	75	30
AuNP-1	2	Act. C	20	10
AuNP-2	7.6	TiO ₂	76	30
AuNP-2	4.1	Act. C	41	20

The NPs supported on carbon also required the addition of a few drops of sulfuric acid to facilitate the immobilisation. The mixtures were then left to stir overnight at room temperature before filtering. The NPs were then washed with water and left to dry in air overnight. Due to the addition of acid for the carbon supported NPs, the washing proceeded until a neutral pH of the filtrate was achieved.

9. Overall Conclusions

The overall aim of this research was to explore the topic of metal-templated reactions in aqueous environment by gold-based catalysts for future applications in chemical biology, therapy and/or imaging. Part A of this thesis focused on a series of organometallic Au(III) cyclometalated complexes to template cross-coupling reactions in mild/biological conditions. In part B, a heterogenous catalysis approach has been selected, whereby water-soluble gold nanoparticles stabilised by N-heterocyclic carbene (NHC) ligands have been investigated for potential use in both biomedicine and catalysis.

Part A

Chapter 5 is based on two publications^{305,308} and included the exploration of Au(III) cyclometalated complexes to mediate the C-S cross-coupling reaction *via* reductive elimination, resulting in cysteine (cys) arylation with peptide substrates. The first series of complexes of general formula $[\text{Au}(\text{C}^{\wedge}\text{N})\text{Cl}_2]$ ($\text{C}^{\wedge}\text{N} = \text{C}^{\text{CO}}\text{N}$ (2-benzoylpyridine), $\text{C}^{\text{CH}_2}\text{N}$ (2-benzylpyridine), $\text{C}^{\text{NH}}\text{N}$ (*N*-phenylpyridin-2-amine) and $\text{C}^{\wedge}\text{N}$ (2-phenylpyridine)), were studied for their interactions with different peptidic domains, including zinc finger peptides, using high-resolution liquid chromatography electrospray ionisation mass spectrometry (HR-LC-ESI-MS). The reactivity of the complexes towards cysteine arylation increased in the order $\text{C}^{\wedge}\text{N} < \text{C}^{\text{NH}}\text{N} < \text{C}^{\text{CH}_2}\text{N} < \text{C}^{\text{CO}}\text{N}$. To understand the mechanism of this reaction, density functional theory (DFT) and quantum mechanics/molecular mechanics (QM/MM) calculations were also used, whose suggestions aligned well with the experimental results. The mechanism proposed by DFT calculations revealed that the decoordination of the pyridyl nitrogen from the Au(III) centre, producing the intermediate (I) $[\text{Au}(\text{III})(\text{C}^{\wedge}\text{N})(\text{Cys})_2\text{Cl}]^-$, was essential to template the formation of the C-S bond *via* reductive elimination.

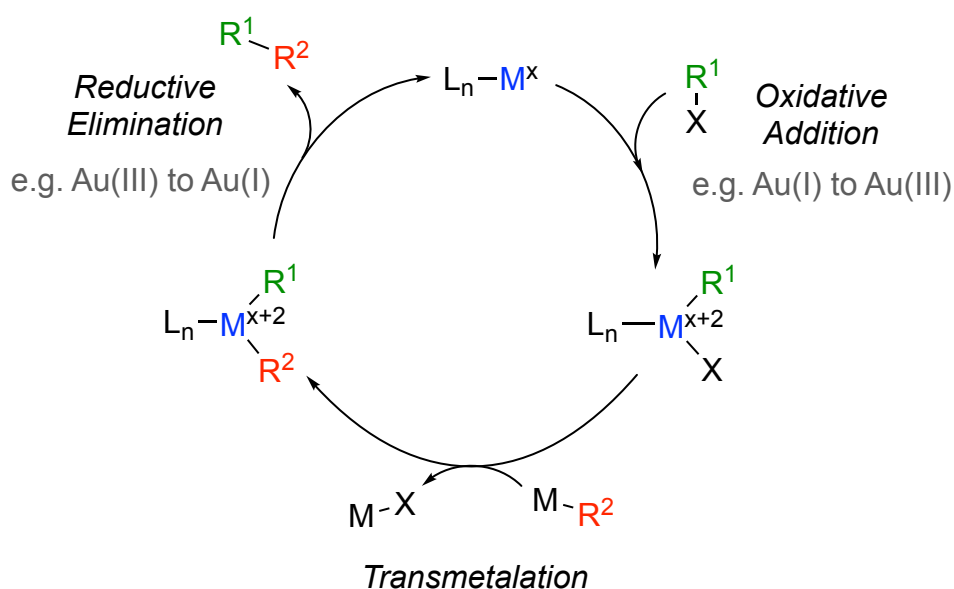
The second study included in *Chapter 5* enlarged the library of cyclometalated Au(III) complexes to include bidentate $[\text{Au}(\text{C}^{\text{S}}\text{N})\text{Cl}_2]$ ($\text{C}^{\text{S}}\text{N} = 2$ -(phenylthiol)pyridine), $[\text{Au}(\text{C}^{\text{O}}\text{N})\text{Cl}_2]$ (2-phenoxy pyridine), but also tetradentate $[\text{Au}(\text{C}^{\wedge}\text{N}^{\wedge}\text{N})\text{Cl}][\text{PF}_6]$ ($\text{C}^{\wedge}\text{N}^{\wedge}\text{N} = 6$ -(1,1-dimethylbenzyl)-2,2'-bipyridine) compounds. Different peptides were also investigated to determine whether the complexes displayed any chemoselectivity towards cysteine residues, including their positioning within the peptide chain. This was proven to be the case, with the $[\text{Au}(\text{C}^{\wedge}\text{N})\text{Cl}_2]$ complexes exhibiting cysteine arylation with the ANGELACASINI peptide, but not with the CASINI peptide featuring an N-terminal cysteine residue. Of note, the $[\text{Au}(\text{C}^{\wedge}\text{N}^{\wedge}\text{N})\text{Cl}][\text{PF}_6]$ complex only formed coordination adducts of the type $[\text{peptide}+\text{Au}(\text{C}^{\wedge}\text{N}^{\wedge}\text{N})]$. The chemoselectivity of the Au(III) compounds was investigated further using the peptides LFRANKALK and $[\text{Leu}^5]\text{Enkephalin}$, lacking cysteine residues. The obtained results showed that, whilst Au(III) coordination adducts

of the type [peptide+(AuC[^]N)] could be formed, none of the compounds could lead to C-X (X = N, O) cross-coupling reactions with other amino acidic residues.

Inspired by the success of the Au(III) cyclometalated C[^]N complexes to template C-S reductive elimination, we set our sights on another cross-coupling reaction, namely C-P bond formation described in *Chapter 6*. The obtained results were also recently published.³⁴¹ The reaction was first optimised with the most reactive complex from the C-S studies, [Au(C^{CO}N)Cl₂]. The latter was added to 1,3,5-triaza-7-phosphaadamantane (PTA) in acetone at room temperature, yielding the expected phosphonium product in a high yield. Remarkably, the reaction could also efficiently proceed in water at room temperature. The mechanism of the reaction, including the identification of key intermediates, was then explored using ³¹P{¹H} NMR (nuclear magnetic resonance) monitoring studies, HR-ESI-MS and DFT calculations. The results were in line with the hypothesis made in the case of the C-S cross-coupling, with the initial coordination of the PTA *trans* to the pyridyl N, before the approach of a second PTA ligand to induce N decoordination from the Au(III) centre prior to reductive elimination. The reaction was also studied with other Au(III) cyclometalated complexes, [Au(C[^]N)Cl₂] (C[^]N = C^{CH₂}N, C^{NH}N), and followed the same trend in reactivity as seen for the C-S cross-coupling work, with [Au(C^{CO}N)Cl₂] showing the highest propensity to undergo reductive elimination, followed by [Au(C^{CH₂}N)Cl₂] and [Au(C^{NH}N)Cl₂].

Finally, the Au(III) cyclometalated complex [Au(C^{CH₂}N)Cl₂] was challenged to mediate the C(sp²)-C(sp) cross-coupling reaction with silver phenylacetylide (AgPhCC) in mild conditions. The obtained results are included in *Chapter 7* and also recently published.³⁷³ Using the knowledge we had gained from the C-S and C-P cross-coupling work, the mechanism and intermediates of reaction were also investigated using ¹H NMR monitoring studies. After identification of three unknown intermediates from the ¹H NMR, isolation of the key species was attempted by adapting the C-C cross-coupling procedure. This led to the identification of two of the intermediates, confirmed by ¹H, ¹³C, 2D NMR, HR-ESI-MS and X-ray diffraction (XRD) analysis. Of note, the mechanism of C-C cross-coupling featured a substantial difference with respect to the C-S and C-P reactions. This is due to the formation of an additional π-complex intermediate in the C-C cross-coupling reaction after the reductive elimination step, whereby the C≡C is π-coordinated to the Au(I) co-product. The product is then released by dissociation of the alkyne, which is thermodynamically favoured, featuring a relatively low activation energy barrier. The experimental data was also supported by DFT calculations, further contributing to the understanding of the reductive elimination process and possible reaction coordinates. Additionally, the [Au(C^{CH₂}N)Cl₂] was able to successfully perform a C(sp²)-C(sp²) reaction with a vinyl tin and heteroaryl zinc complex.

Overall, part A has demonstrated the great versatility of organometallic Au(III) cyclometalated complexes to template different cross-coupling reactions in mild reaction conditions. Presently, our group is also working on the applicability of the same Au(III) complexes for C-Se cross-coupling reactions. These would be relevant to selectively target seleno-enzymes involved in cancer cells redox metabolism. It should also be highlighted that the Au(III) templated reactions addressed in this work are not catalytic in nature. In fact, only the reductive elimination process is taken into account and stoichiometric amounts of Au(III) complexes are necessary. A typical cross-coupling reaction relies on the principle that the metal involved can cycle between at least two oxidation states, e.g. Au(I/III) or Pd(0/II), and involves several elemental steps including: oxidative addition, transmetalation and reductive elimination, as shown in Scheme 33.⁴¹⁹

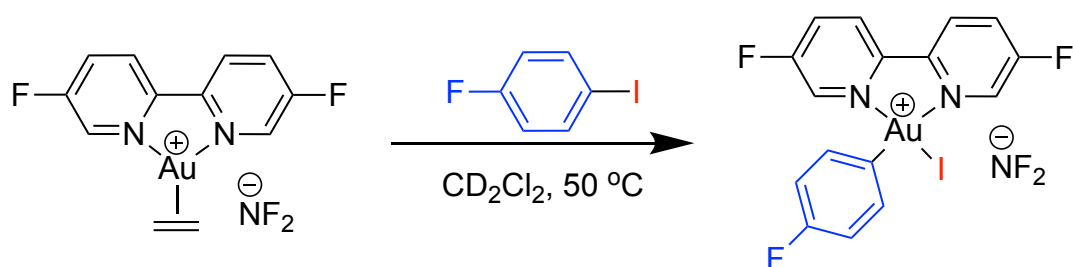


Scheme 33 - Typical transition-metal-catalyzed cross-coupling reaction, adapted from ref. ⁴¹⁹

Although Au(I/III) and Pd(0/II) are isoelectronic and share the same number of d electrons, the redox potential of the Au(III/I) couple is much higher compared to the Pd(II/0) couple ($E^0(\text{Au}^{\text{III/I}}) = 1.41 \text{ V vs. } E^0(\text{Pd}^{\text{II/0}}) = 0.92 \text{ V}$).⁴¹⁹ This results in the higher propensity for Au(III) to be reduced to Au(I) or metallic Au, favouring reductive elimination, whilst oxidative addition from Au(I) to Au(III) is more thermodynamically challenging.⁴²⁰

Although examples of oxidative addition with Au(I) are rare, in recent years there have been more reports on the controlled oxidation by halogens or sacrificial oxidants, such as As(V) salts or I(III) reagents, of oxidative addition at Au(I) centers.⁴²⁰ More recently, the use of bidentate ligands to coordinate Au(I) with a tight bite angle of ca. 90° has proven to be efficient to allow Ar-X oxidative addition to occur, as reported by the groups of Bourissou^{421–423} and Russell.^{424–426} See Scheme 34 for an example of this

Au(III)/Au(I) catalysis. An alternative method has also been described by Toste and co-workers whereby oxidative addition of CF_3I to Au(I) can be photoinitiated by near-ultraviolet (UV) light ($\lambda_{\text{max}} = 313 \text{ nm}$).⁴²⁷ These successful examples hold promise for future applications of Au homogenous catalysts in cross-coupling reactions to not only replicate the well-known Pd catalysts, but to offer a difference in reactivity and chemoselectivity. In general, Au has greater tolerance to different functional groups and performs catalysis under milder conditions than Pd; therefore, this can result in a greater versatility of substrates, as well as variations in selectivity of the products formed.⁴²⁴

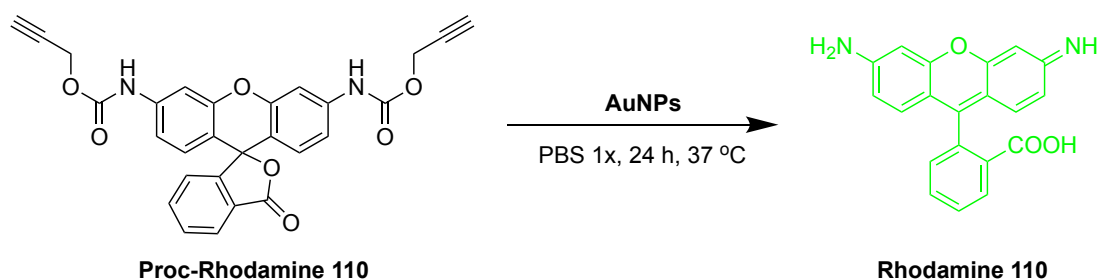


Scheme 34 – Example of an oxidative addition reaction using $[\text{bipyAu}(\text{C}_2\text{H}_4)][\text{NTf}_2]$ and Ar-X , as reported by Russell and co-workers.⁴²⁴

Part B

Chapter 8 involved the ‘bottom-up’ synthesis of water-soluble gold nanoparticles stabilised by NHC ligands (NHC@AuNPs). To this aim, first the synthesis of two water-soluble Au(I) NHC complexes featuring imidazolium scaffolds with sulfonate groups was achieved. The two formed nanoparticles, **AuNP-1** and **AuNP-2**, were purified by dialysis before extensive characterisation. The latter included techniques to assess the size, shape and composition of the NPs, as well as their stability in biologically relevant media. The catalytic performance of the AuNPs was also evaluated for the reduction of 4-nitrophenol. Attempts to immobilise the water-soluble NHC@AuNPs on two types of support (activated carbon and titania) were also performed; however, this did not result in an increase in catalytic performance. Preliminary ongoing studies in our group are also evaluating the potential of NHC@AuNPs to perform more biocompatible catalysis. For example, we have recently explored the reactivity of **AuNP-2** to activate the non-fluorescent proc-rhodamine 110 (bis-*N,N'*-propargyloxycarbonyl-rhodamine 110) to form rhodamine 110, a fluorescent dye, by *O*-depropargylation (Scheme 35). This was inspired by the work of Unciti-Broceta and co-workers, who successfully performed the reaction with their solid-supported AuNPs in physiologically relevant conditions.²⁰² Unfortunately, preliminary studies using **AuNP-2** and supported **AuNP-2/TiO₂** have been

unsuccessful. Thus, further work is needed to assess whether this is an issue of optimisation or catalytic performance.



Scheme 35 – O-depropargylation reaction of bis-N,N'-propargyloxycarbonyl-rhodamine 110 to form rhodamine 110, mediated by AuNPs as reported by Unciti-Broceta and co-workers.²⁰²

Overall, this work has demonstrated the great potential of these water-soluble NHC@AuNPs for catalytic reactions, in particular bioorthogonal reactions, due to their high stability in biologically relevant media. However, future work should focus on improving the stability of the AuNPs against leaching during catalysis, which could be due to the formation of a Au(I) layer on the surface, particularly evident for **AuNP-2**. Instability of AuNPs formed by the 'bottom-up' approach due to the formation of a Au(I) layer has already been reported,^{260,263,394} including by Crudden and co-workers²⁵⁸.

During our study, we also speculated that a change in composition of the AuNPs was occurring during the catalytic reaction; therefore, *in situ* characterisation methods should be applied in future studies, such as environmental transmission electron microscopy (TEM) or *in situ* Fourier-transform infrared (FT-IR) spectroscopy.³⁸⁹ Furthermore, other characterisation techniques can be utilised to investigate the binding of the NHC to the AuNP surface, such as surface-enhanced Raman spectroscopy (SERS), which has been pioneered by Camden, Jenkins and co-workers.^{428,429}

Another area to be considered in the future is the formation of NHC@AuNP with different shapes, such as Au nanorods (AuNRs). To the best of my knowledge, Johnson and co-workers²⁹⁷ published the first and only example of AuNRs stabilised by NHC ligands, which have great potential in biomedicine. This is particularly true in areas such as photothermal therapy (PTT) due to the ability of AuNRs to absorb light in the near-infrared range (NIR), which is less damaging than UV light, yet can still penetrate tissues *in vivo*.²⁸⁷ Ongoing collaborative studies are in progress to assess the suitability of our NHC@AuNPs for PTT applications.

Appendix

Supplementary Material: Chapter 5

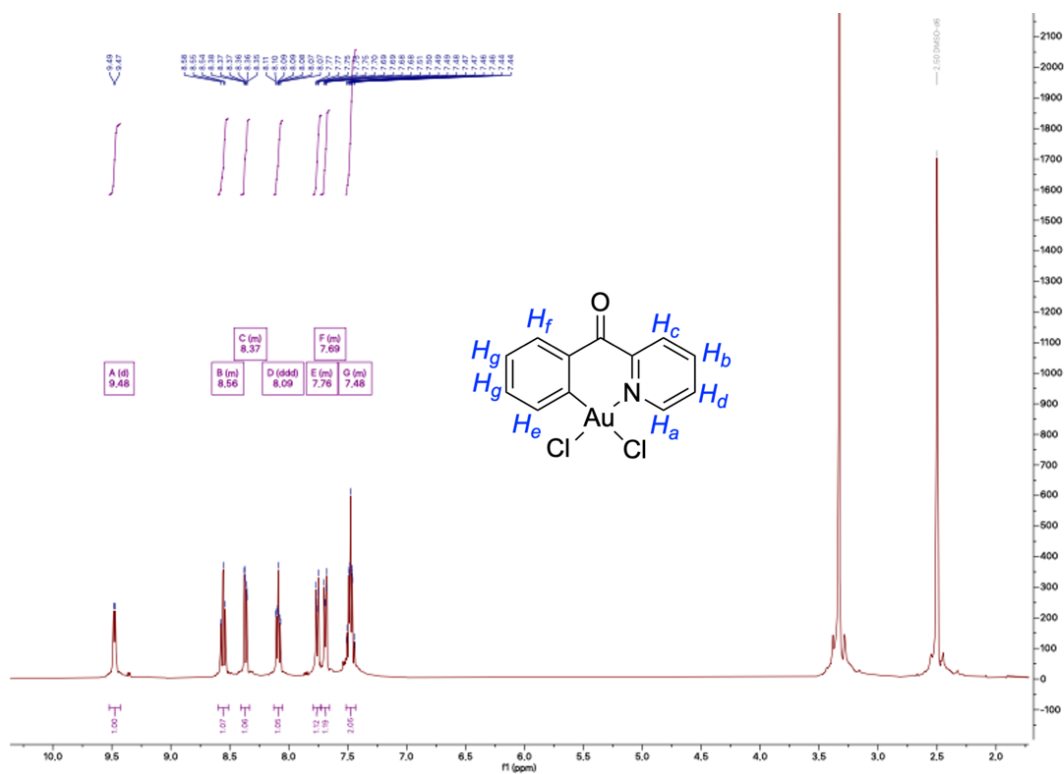


Figure S1 - ^1H NMR of $[\text{Au}(\text{C}^{\text{O}}\text{N})\text{Cl}_2]$ in $\text{DMSO-}d_6$.

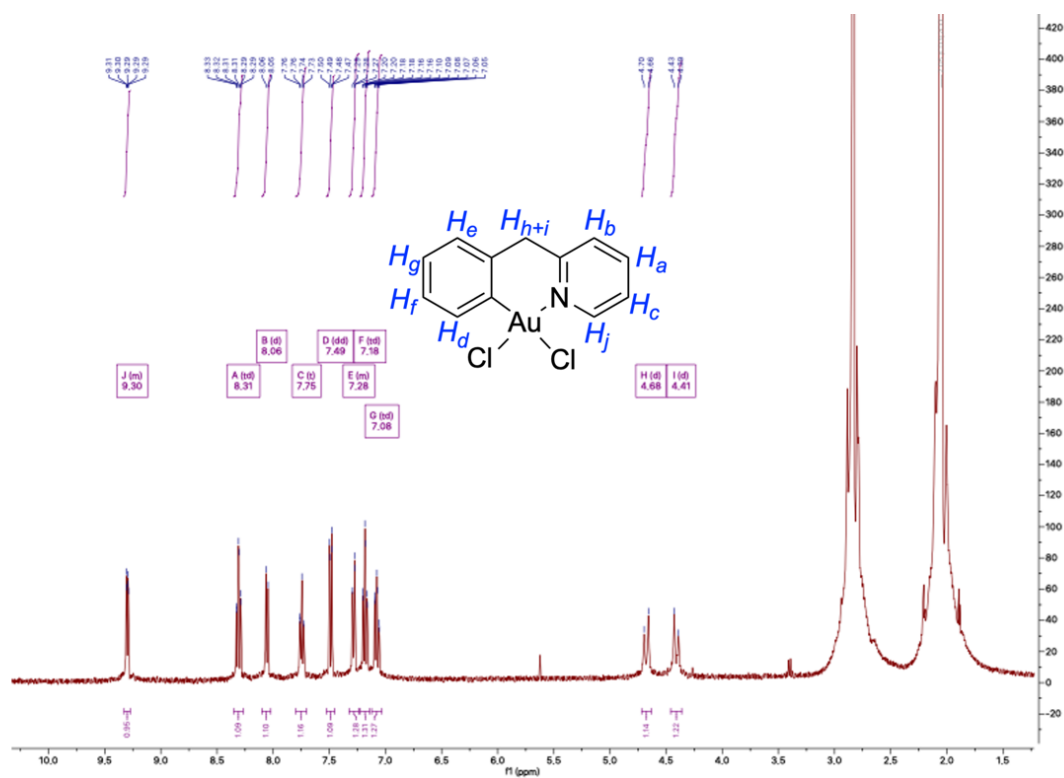


Figure S2 - ^1H NMR of $[\text{Au}(\text{CH}_2\text{N})\text{Cl}_2]$ in $\text{acetone-}d_6$.

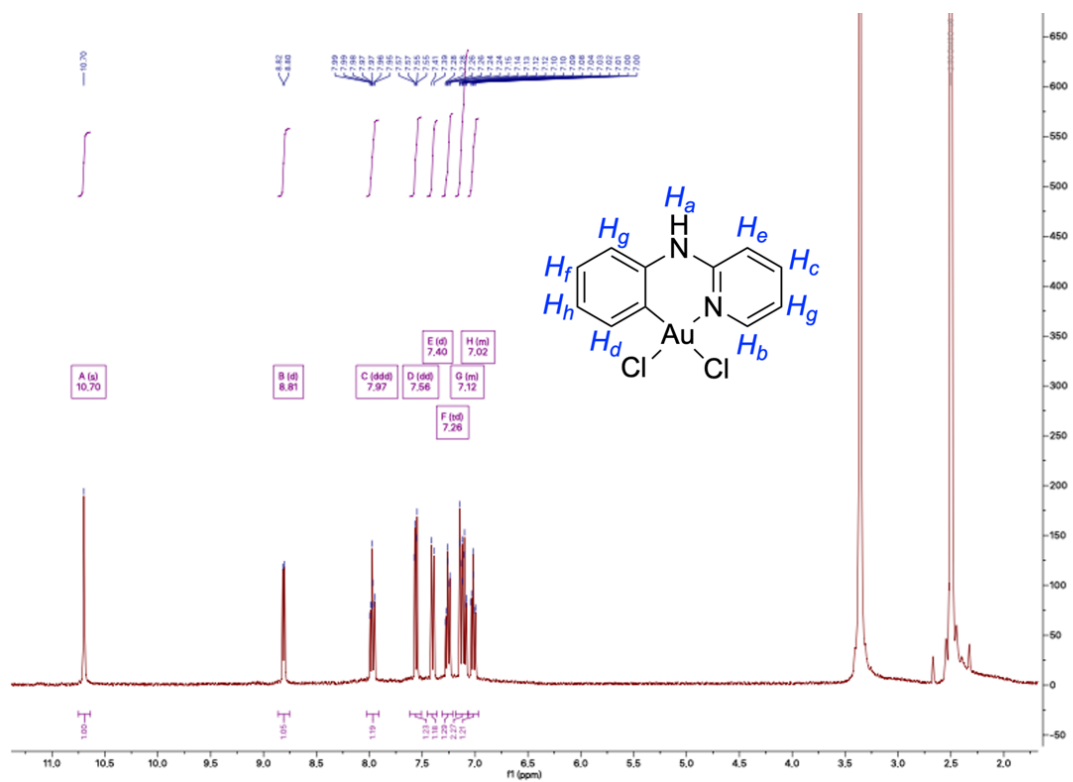


Figure S3 - ^1H NMR of $[\text{Au}(\text{C}^{\text{NH}})\text{Cl}_2]$ in DMSO-d_6 .

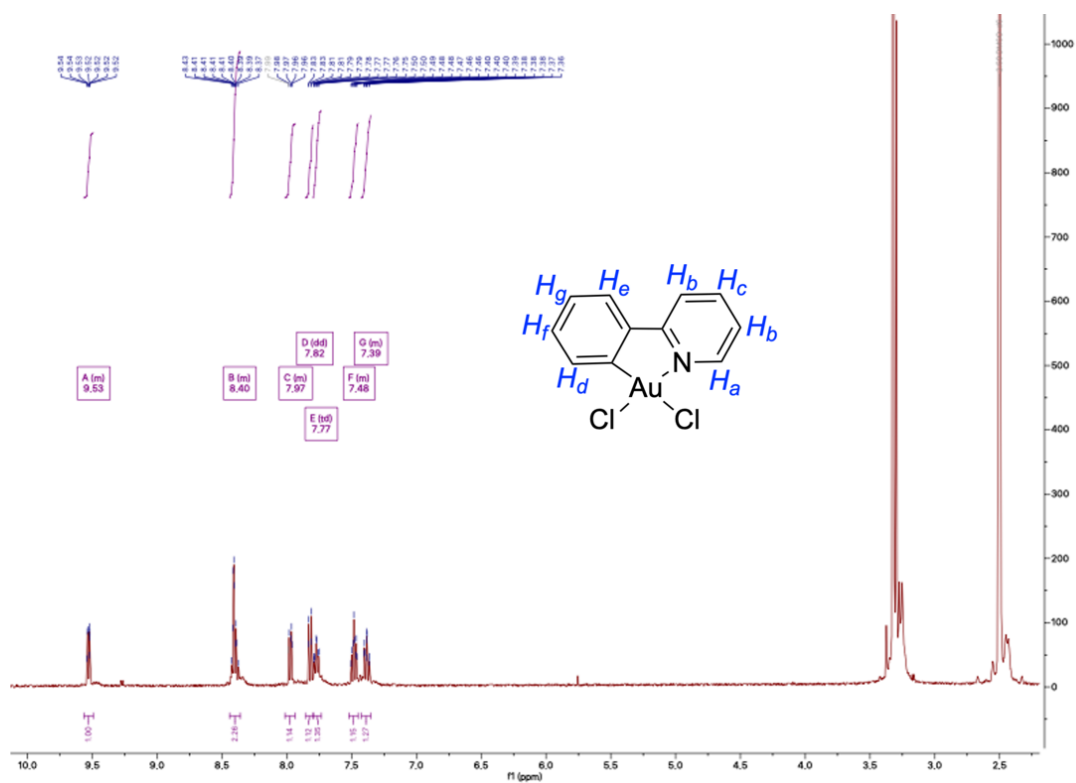


Figure S4 - ^1H NMR of $[\text{Au}(\text{C}^{\text{N}})\text{Cl}_2]$ in DMSO-d_6 .

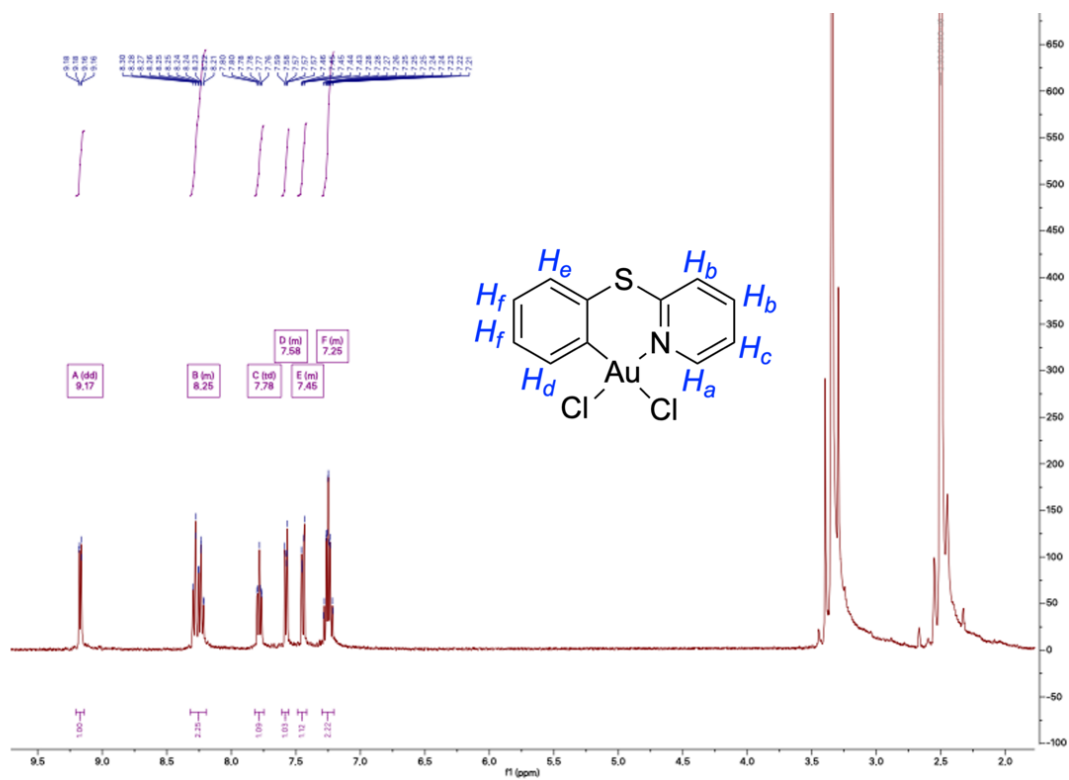


Figure S5 - 1H NMR of $[Au(C^S N)Cl_2]$ in $DMSO-d_6$.

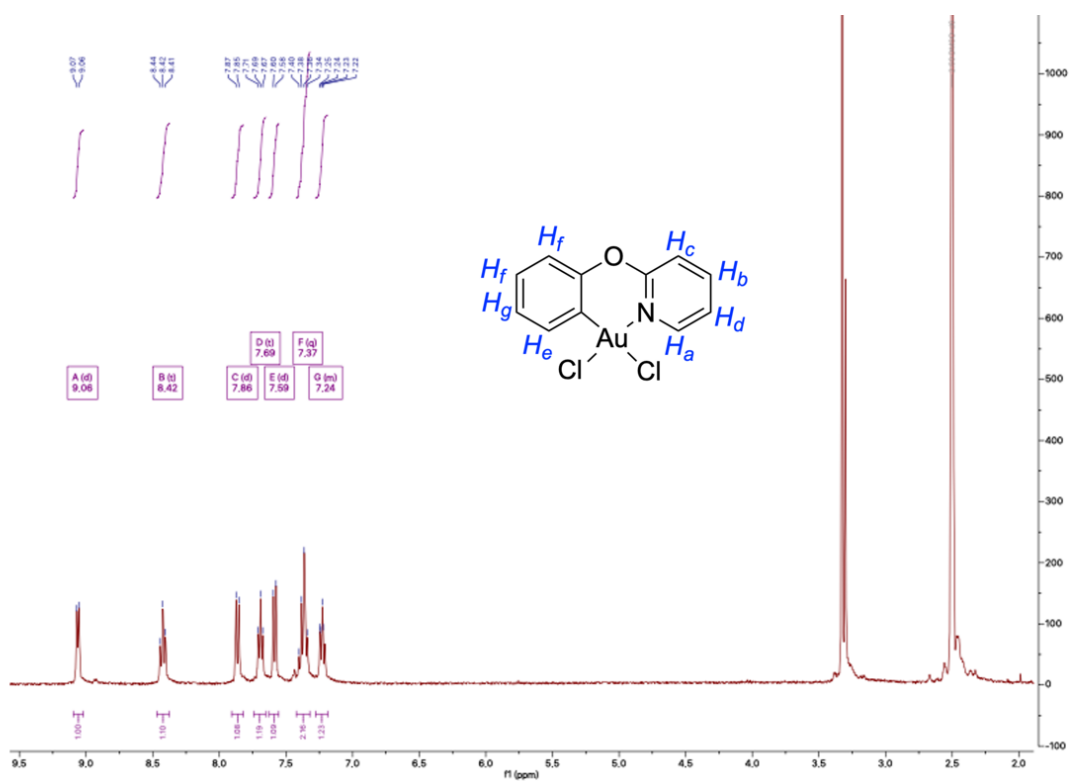


Figure S6 - 1H NMR of $[Au(C^O N)Cl_2]$ in $DMSO-d_6$.

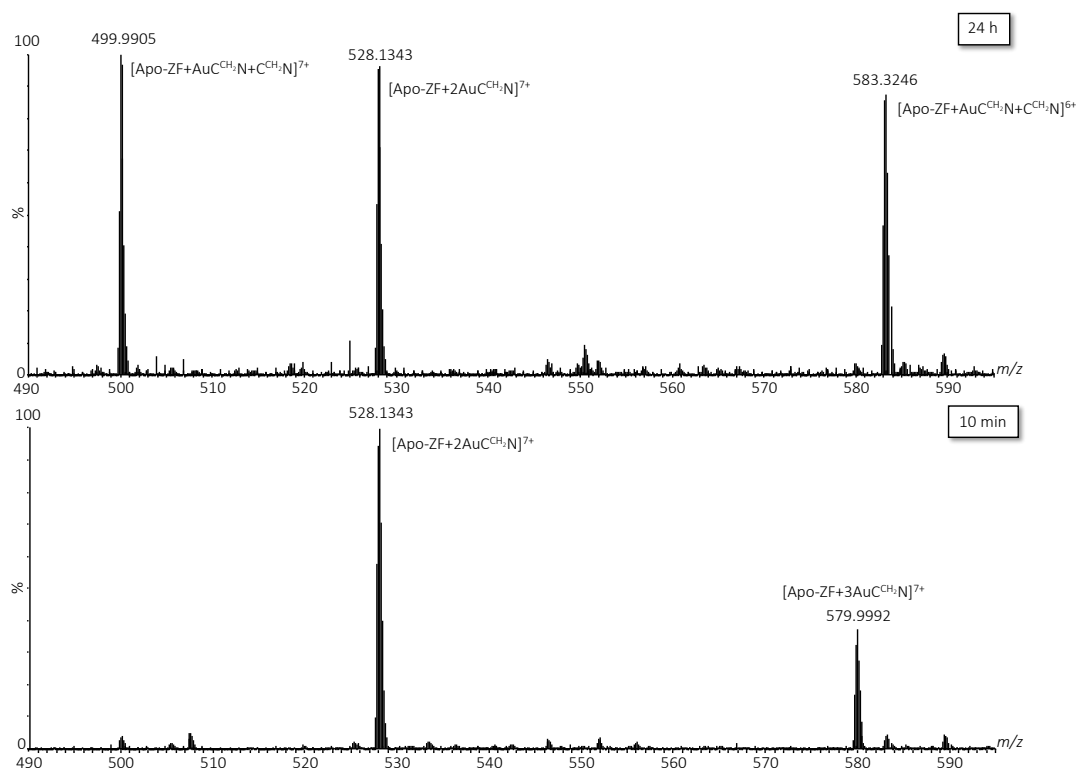


Figure S7 - HPLC-ESI-MS spectra of the reaction of $[\text{Au}(\text{C}^{\text{CH}_2\text{N}})\text{Cl}_2]$ with the Zn-ZF domain (3:1 ratio) after 10 min or 24 h incubation at 37°C in $(\text{NH}_4)_2\text{CO}_3$ buffer (25 mM, pH 7.4). Figure from ref 305. Copyright 2019, John Wiley and Sons <https://creativecommons.org/licenses/by/4.0/>.³⁰⁵

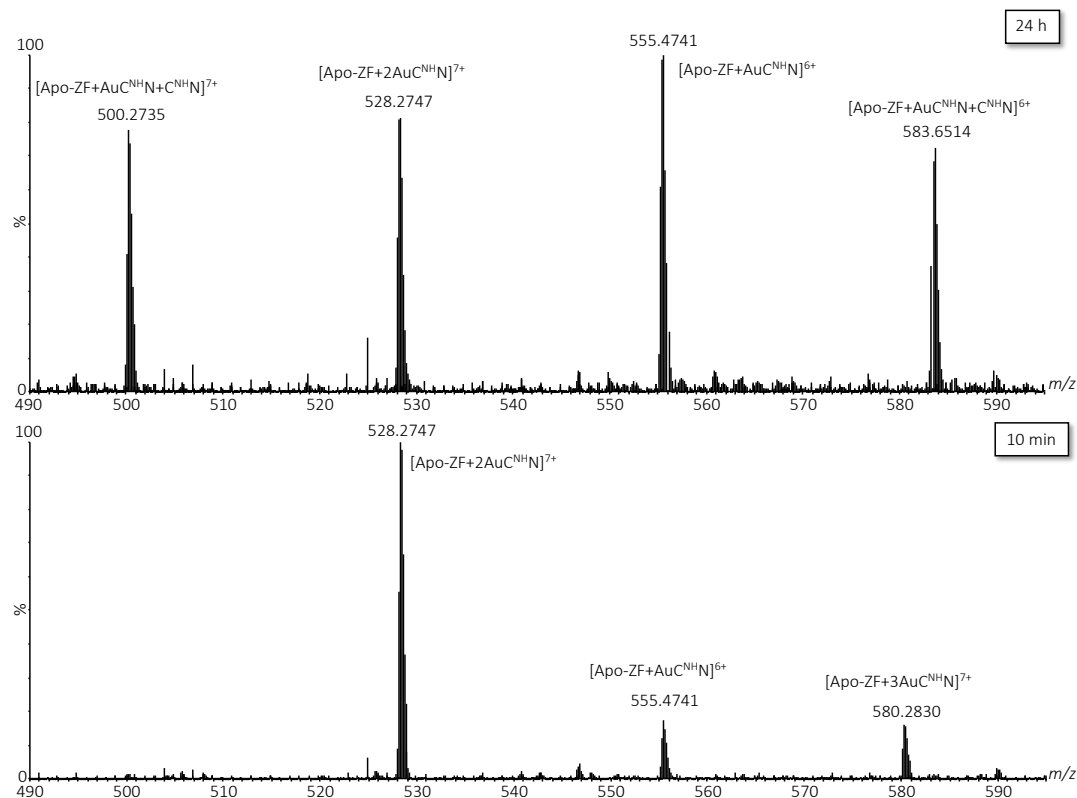


Figure S8 - HPLC-ESI-MS spectra of the reaction of $[\text{Au}(\text{C}^{\text{NH}}\text{N})\text{Cl}_2]$ with the Zn-ZF domain (3:1 ratio) after 10 min or 24 h incubation at 37°C in $(\text{NH}_4)_2\text{CO}_3$ buffer (25 mM, pH 7.4). Figure from ref 305. Copyright 2019, John Wiley and Sons <https://creativecommons.org/licenses/by/4.0/>.³⁰⁵

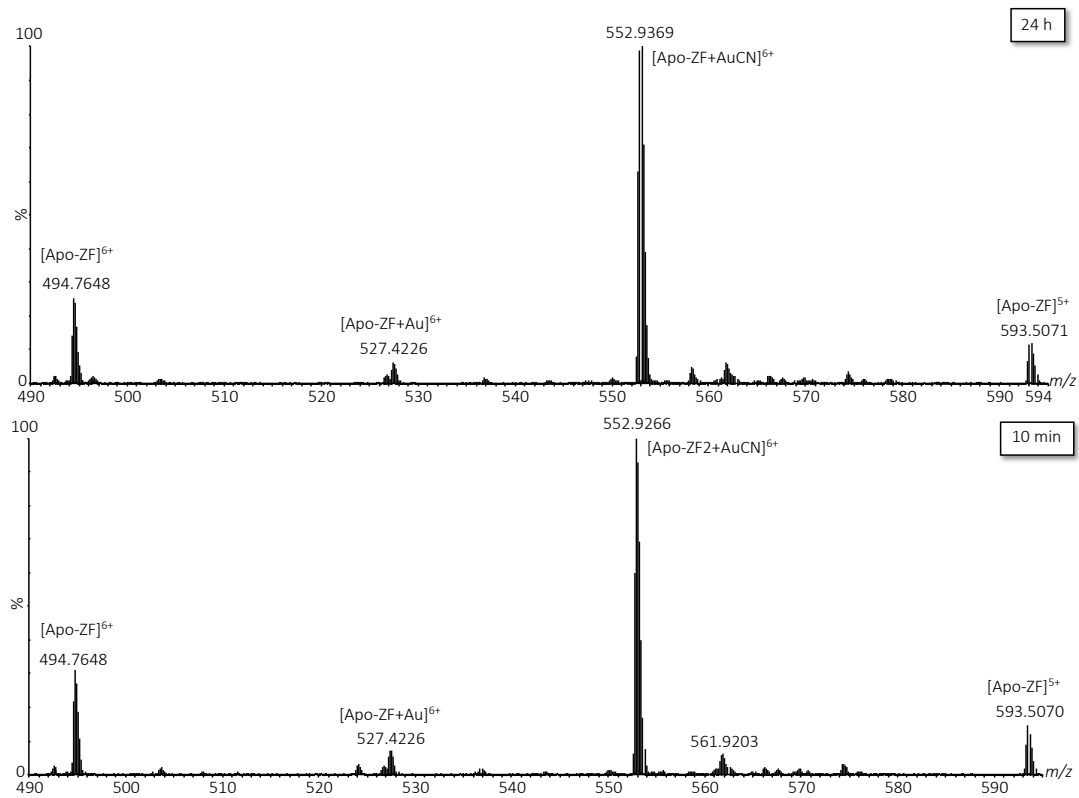


Figure S9 – HPLC-ESI-MS spectra of the reaction of $[Au(C^N)Cl_2]$ with the Zn-ZF domain (3:1 ratio) after 10 min or 24 h incubation at 37°C in $(NH_4)_2CO_3$ buffer (25 mM, pH 7.4). Figure modified from ref 305. Copyright 2019, John Wiley and Sons <https://creativecommons.org/licenses/by/4.0/>.³⁰⁵

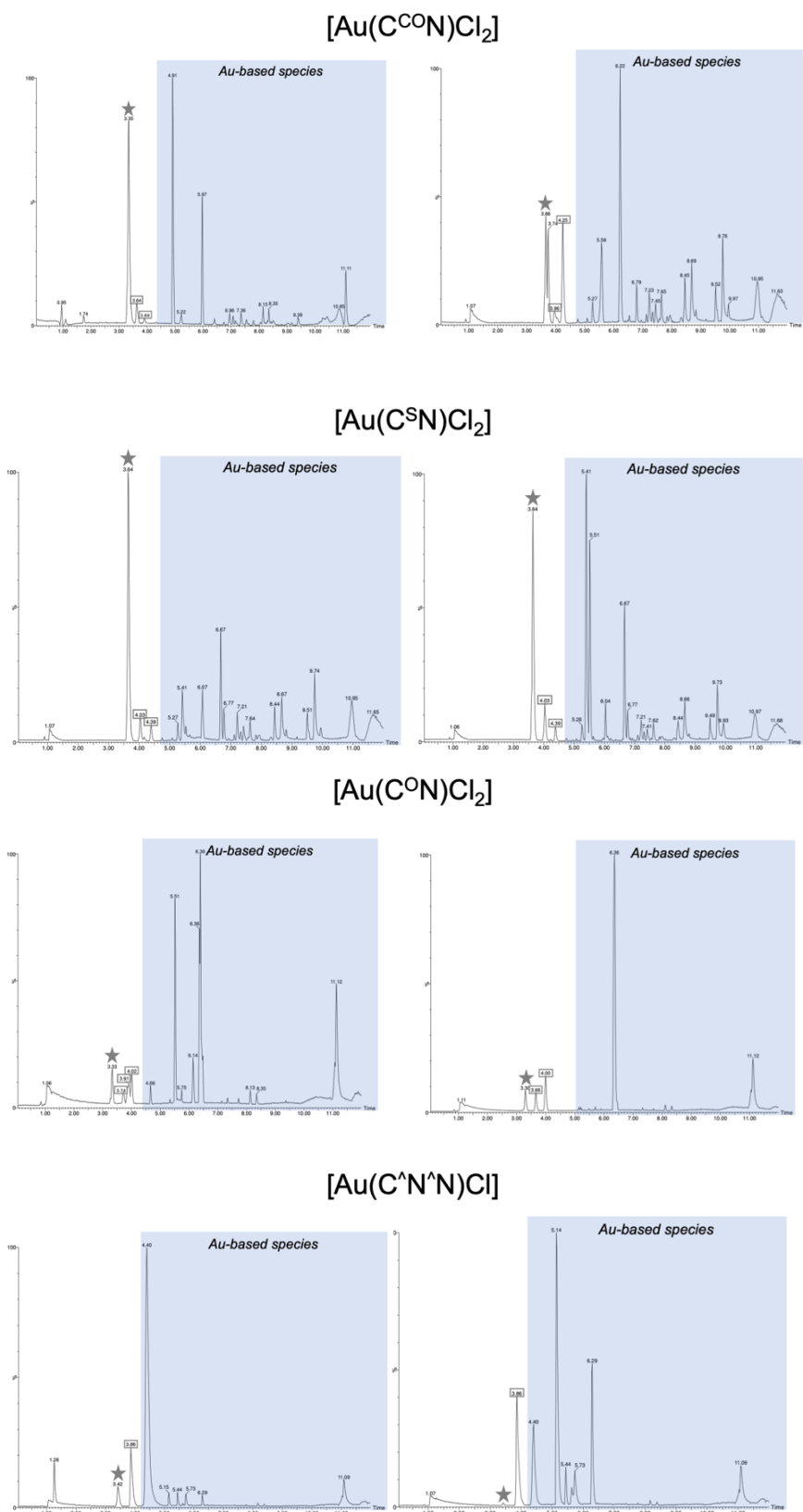


Figure S10 - Representative chromatograms of the individual HPLC-ESI-MS experiments of Cys₂His₂ with each Au(III) complex in a 1:3 ratio for either 30 min (left) or 24 h (right) incubation at 37 °C. The 'star' labelled peaks correspond to the free peptide, while the 'square' labelled peaks correspond to the analysed Au complex/peptide adducts. Figure modified from ref 308. Copyright 2020, John Wiley and Sons <https://creativecommons.org/licenses/by/4.0/>.³⁰⁸

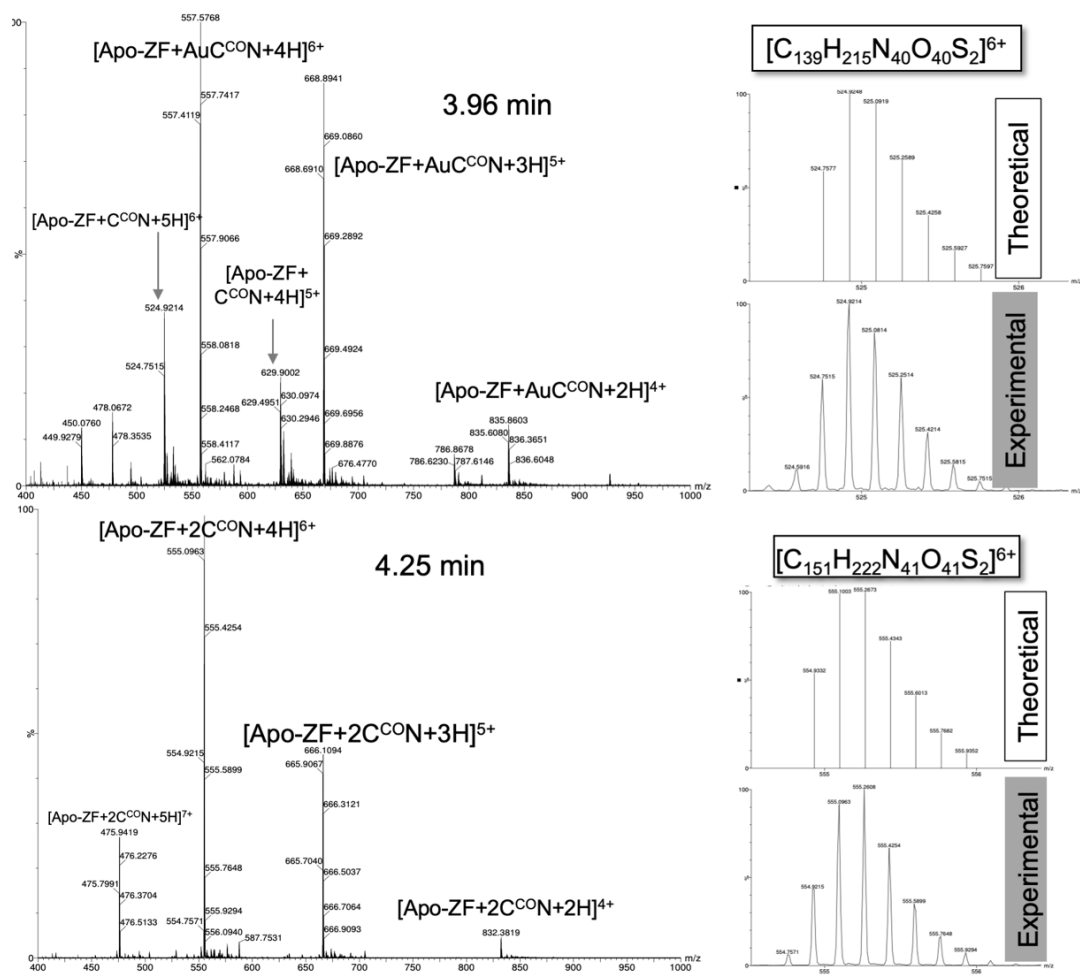


Figure S11 - HPLC-ESI-MS analysis of the reaction of $[Au(C^{CO})Cl_2]$ with the ZF Cys_2His_2 model peptide (3 : 1 ratio) after 30 min incubation at 37 °C recorded at retention times (RTs) 3.96 min and 4.25 min. Comparison between the experimental isotopic patterns of representative adducts with the theoretical values.³⁰⁸

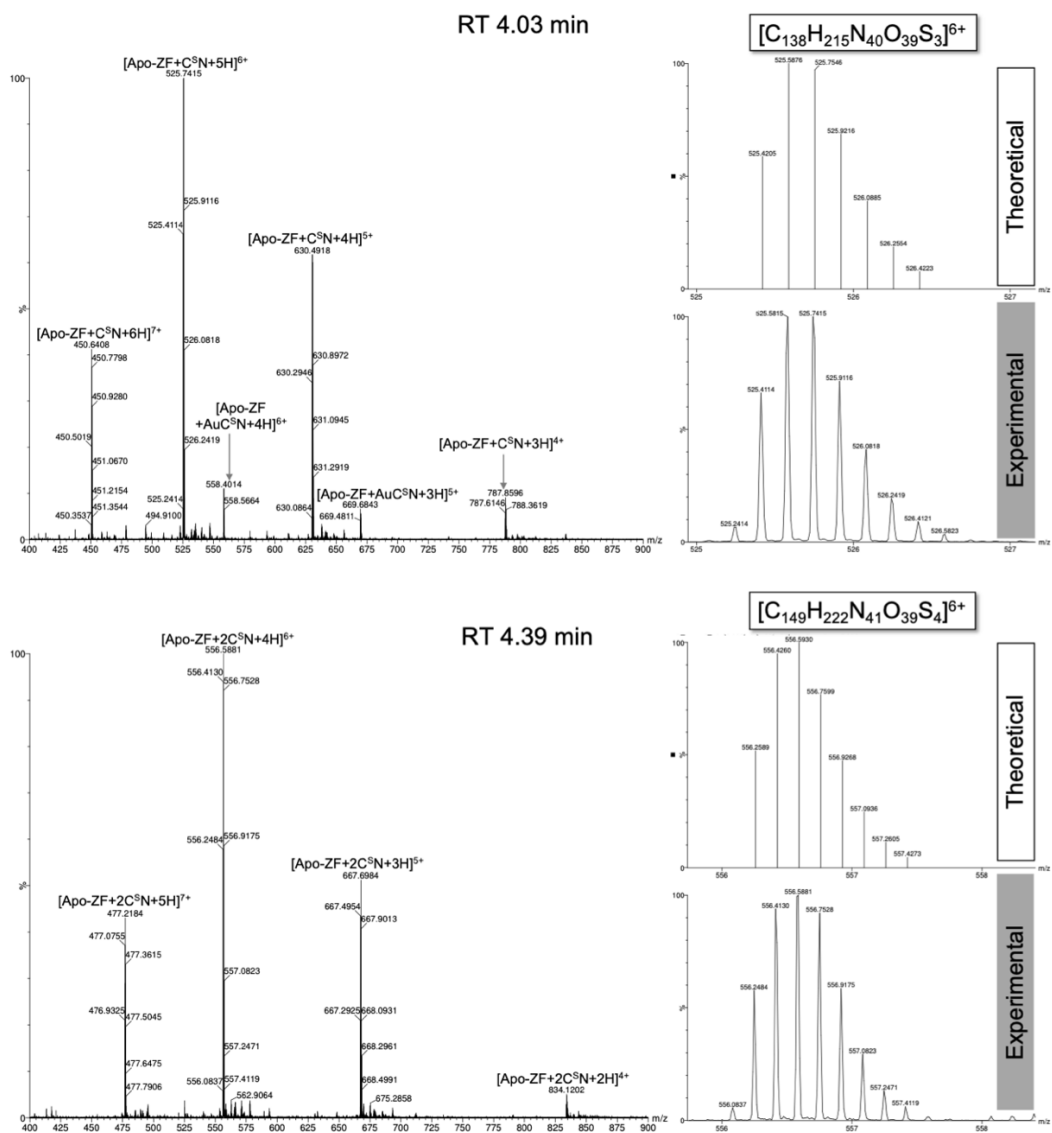


Figure S12 - HPLC-ESI-MS analysis of the reaction of $[Au(C^S N)Cl_2]$ with the ZF Cys₂His₂ model peptide (3 : 1 ratio) after 30 min incubation at 37 °C recorded at retention times (RTs) 4.03 min and 4.39 min. Comparison between the experimental isotopic patterns of representative adducts with the theoretical values. Figure modified from ref 308. Copyright 2020, John Wiley and Sons <https://creativecommons.org/licenses/by/4.0/>.³⁰⁸

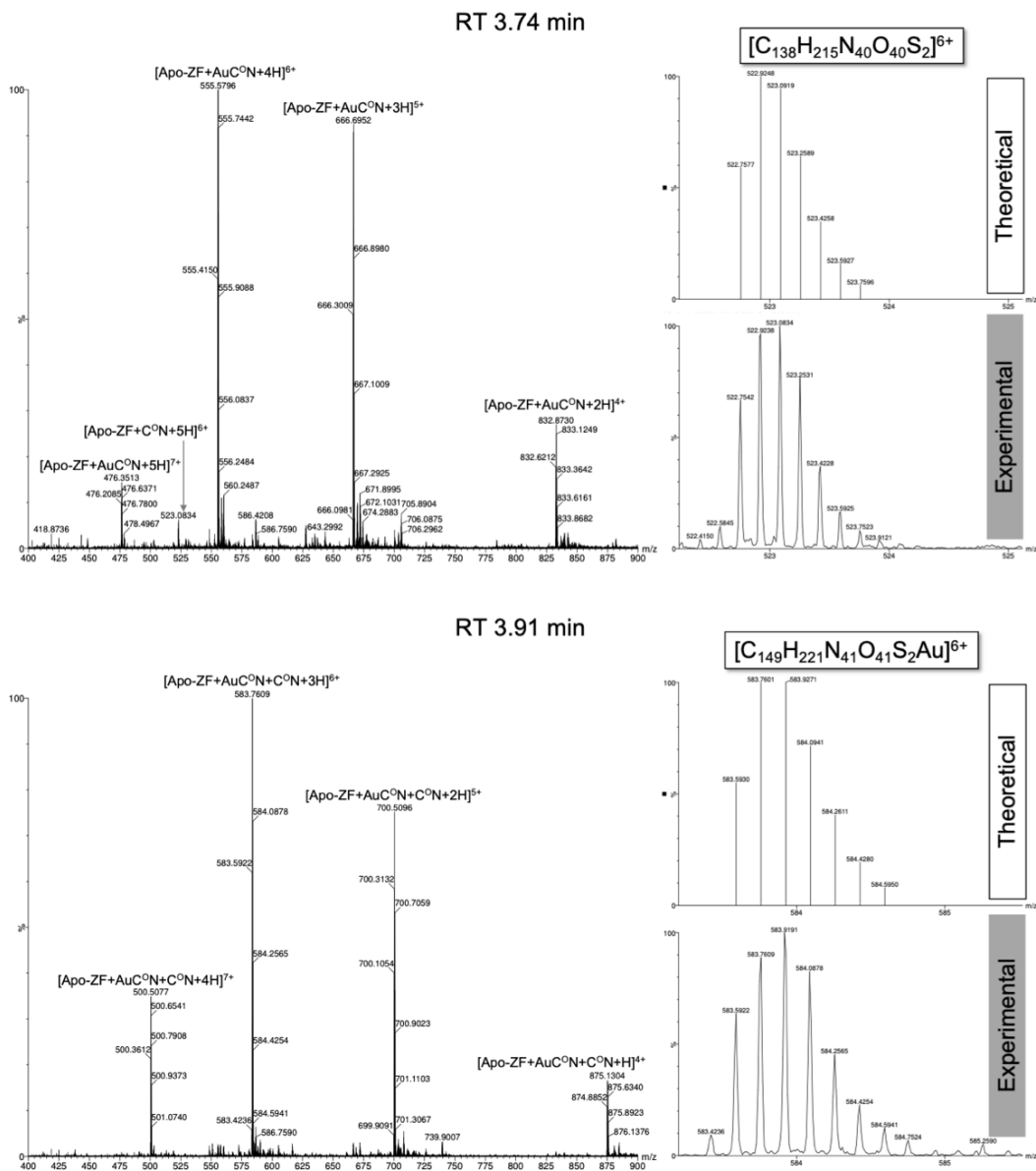


Figure S13 - HPLC-ESI-MS analysis of the reaction of $[Au(C^O)Cl_2]$ with the ZF Cys₂His₂ model peptide (3 : 1 ratio) after 30 min incubation at 37 °C recorded at retention times (RTs) 3.74 min and 3.91 min. Comparison between the experimental isotopic patterns of representative adducts with the theoretical values. Figure modified from ref 308. Copyright 2020, John Wiley and Sons <https://creativecommons.org/licenses/by/4.0/>.³⁰⁸

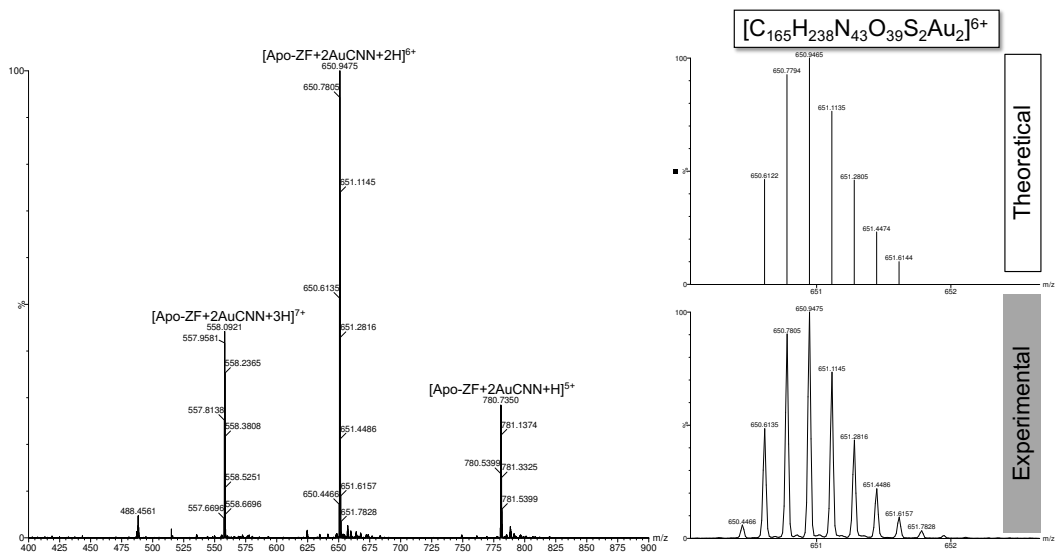


Figure S14 - HPLC-ESI-MS analysis of the reaction of $[Au(C^N^N)Cl]$ with the ZF Cys₂His₂ model peptide (3 : 1 ratio) after 30 min incubation at 37 °C recorded at retention time 3.86 min. Comparison between the experimental isotopic patterns of representative adducts with the theoretical values. Figure from ref 308. Copyright 2020, John Wiley and Sons <https://creativecommons.org/licenses/by/4.0/>.³⁰⁸

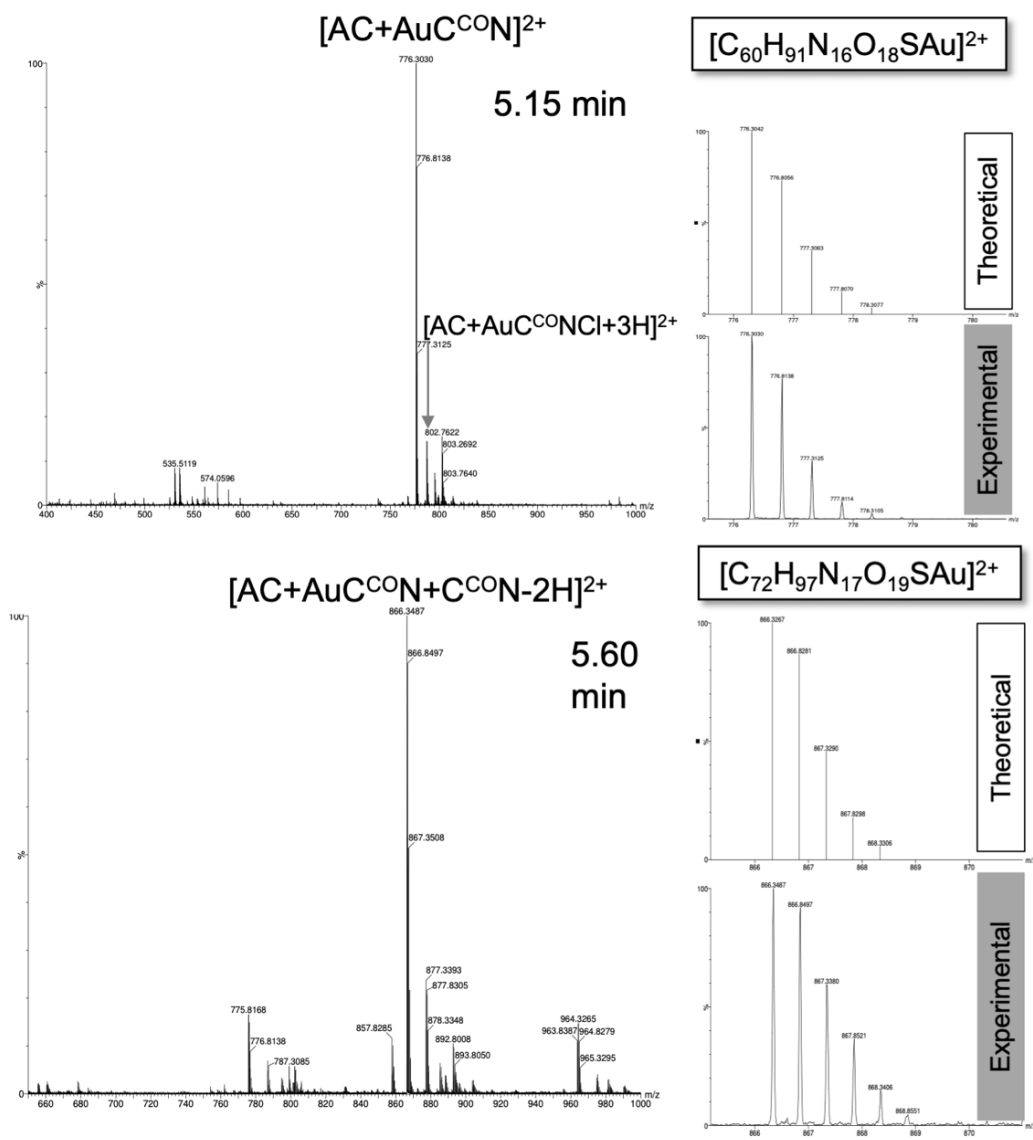


Figure S15 - HPLC-ESI-MS analysis of the reaction of $[Au(C^{CO})Cl_2]$ with AC model peptide (1 : 1 ratio) after 30 min incubation at 37 °C recorded at retention times (RTs) 5.15 min and 5.60 min. Comparison between the experimental isotopic patterns of representative adducts with the theoretical values.³⁰⁸

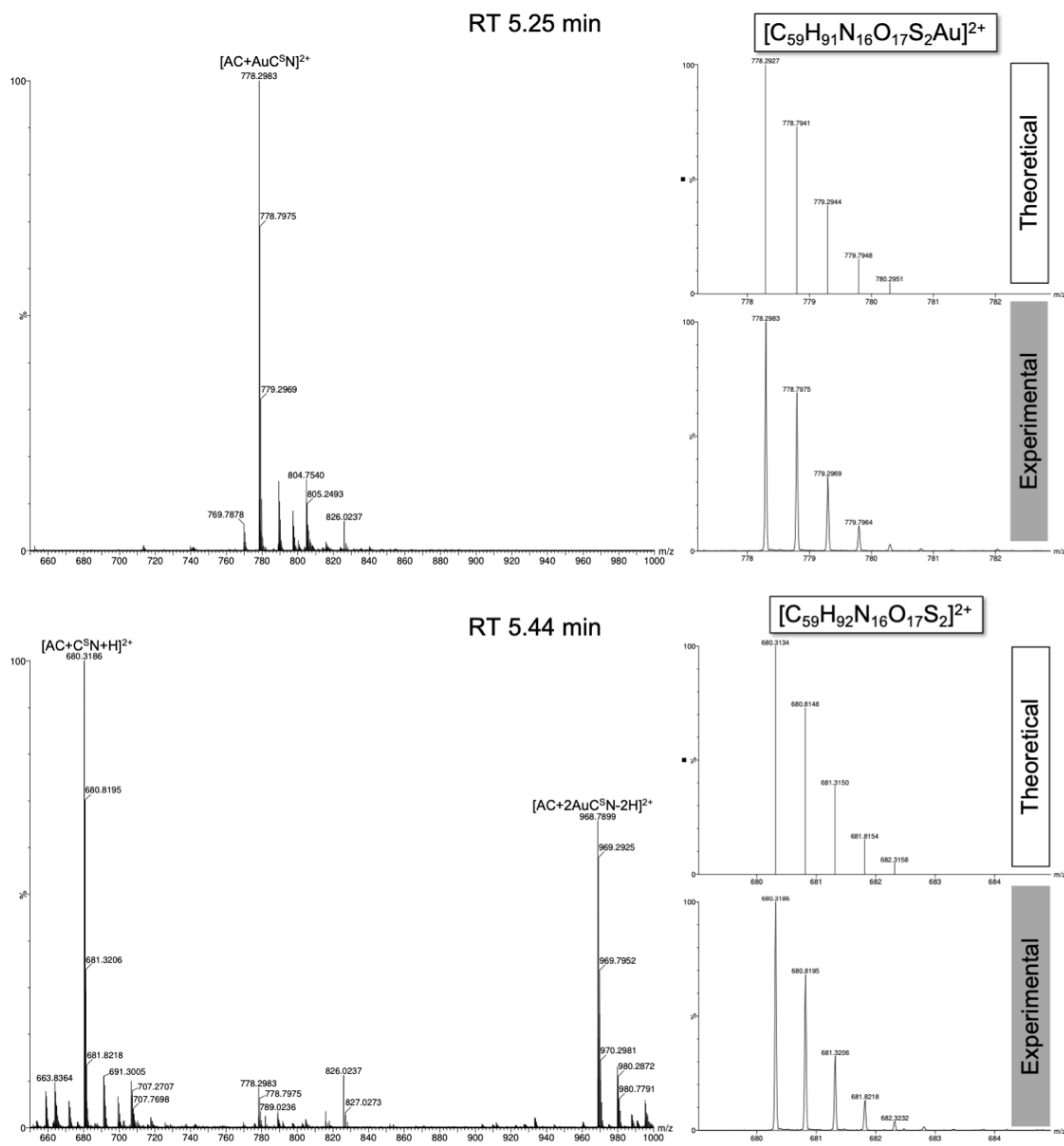


Figure S16 - HPLC-ESI-MS analysis of the reaction of $[Au(C^S N)Cl_2]$ with AC model peptide (1 : 1 ratio) after 30 min incubation at 37 °C recorded at retention times (RTs) 5.25 min and 5.44 min. Comparison between the experimental isotopic patterns of representative adducts with the theoretical values. Figure modified from ref 308. Copyright 2020, John Wiley and Sons <https://creativecommons.org/licenses/by/4.0/>.³⁰⁸

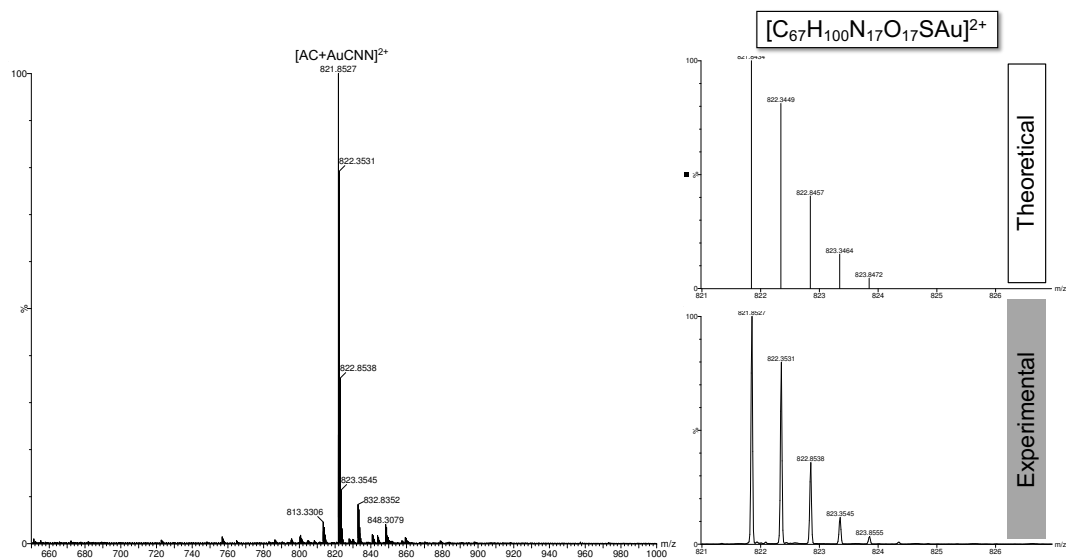


Figure S17 - HPLC-ESI-MS analysis of the reaction of $[Au(C^N^N)Cl]$ with AC model peptide (1 : 1 ratio) after 30 min incubation at 37 °C recorded at retention time 4.78 min. Comparison between the experimental isotopic patterns of representative adducts with the theoretical values. Figure from ref 308. Copyright 2020, John Wiley and Sons
<https://creativecommons.org/licenses/by/4.0/>.³⁰⁸

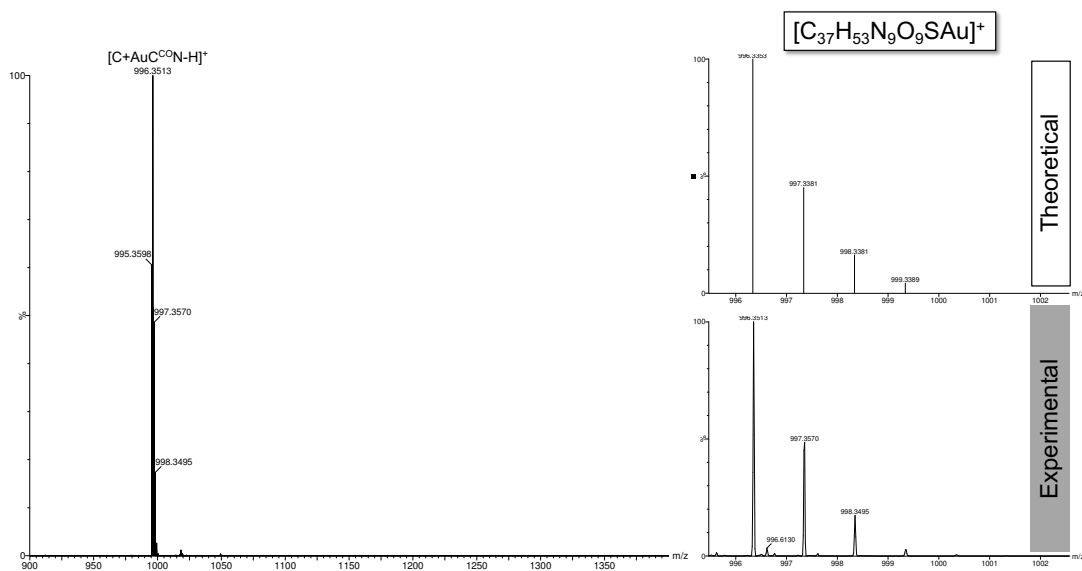


Figure S18 - HPLC-ESI-MS analysis of the reaction of $[Au(C^{CO})Cl_2]$ with C model peptide (1 : 1 ratio) after 30 min incubation at 37 °C recorded at retention time 5.20 min. Comparison between the experimental isotopic patterns of representative adducts with the theoretical values. Figure from ref 308. Copyright 2020, John Wiley and Sons
<https://creativecommons.org/licenses/by/4.0/>.³⁰⁸

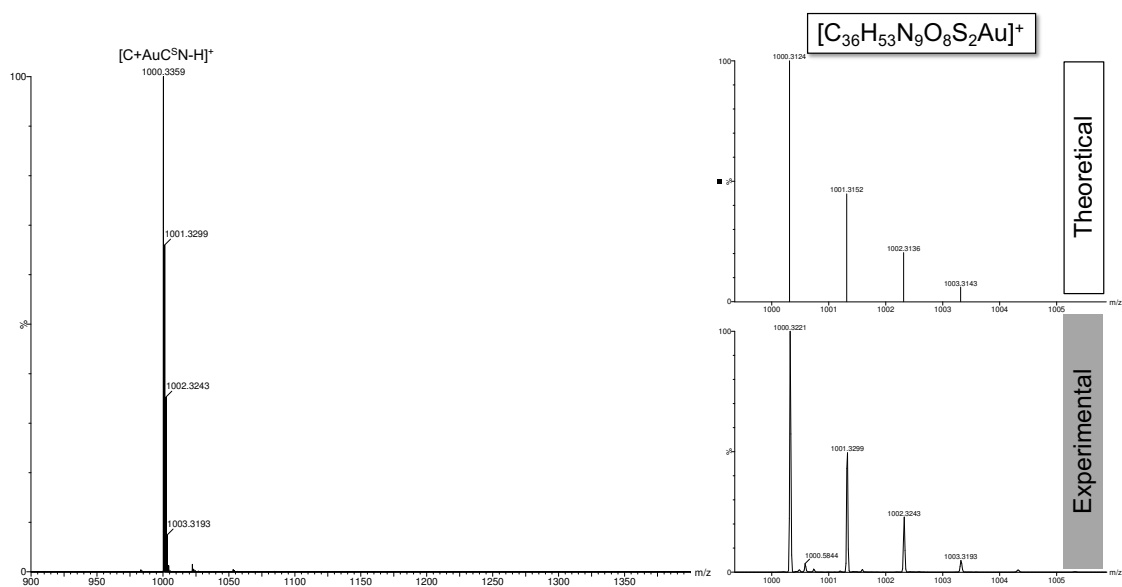


Figure S19 - HPLC-ESI-MS analysis of the reaction of $[\text{Au}(\text{C}^{\text{S}}\text{N})\text{Cl}_2]$ with C model peptide (1 : 1 ratio) after 30 min incubation at 37 °C recorded at retention time 5.29 min. Comparison between the experimental isotopic patterns of representative adducts with the theoretical values. Figure from ref 308. Copyright 2020, John Wiley and Sons <https://creativecommons.org/licenses/by/4.0/>.³⁰⁸

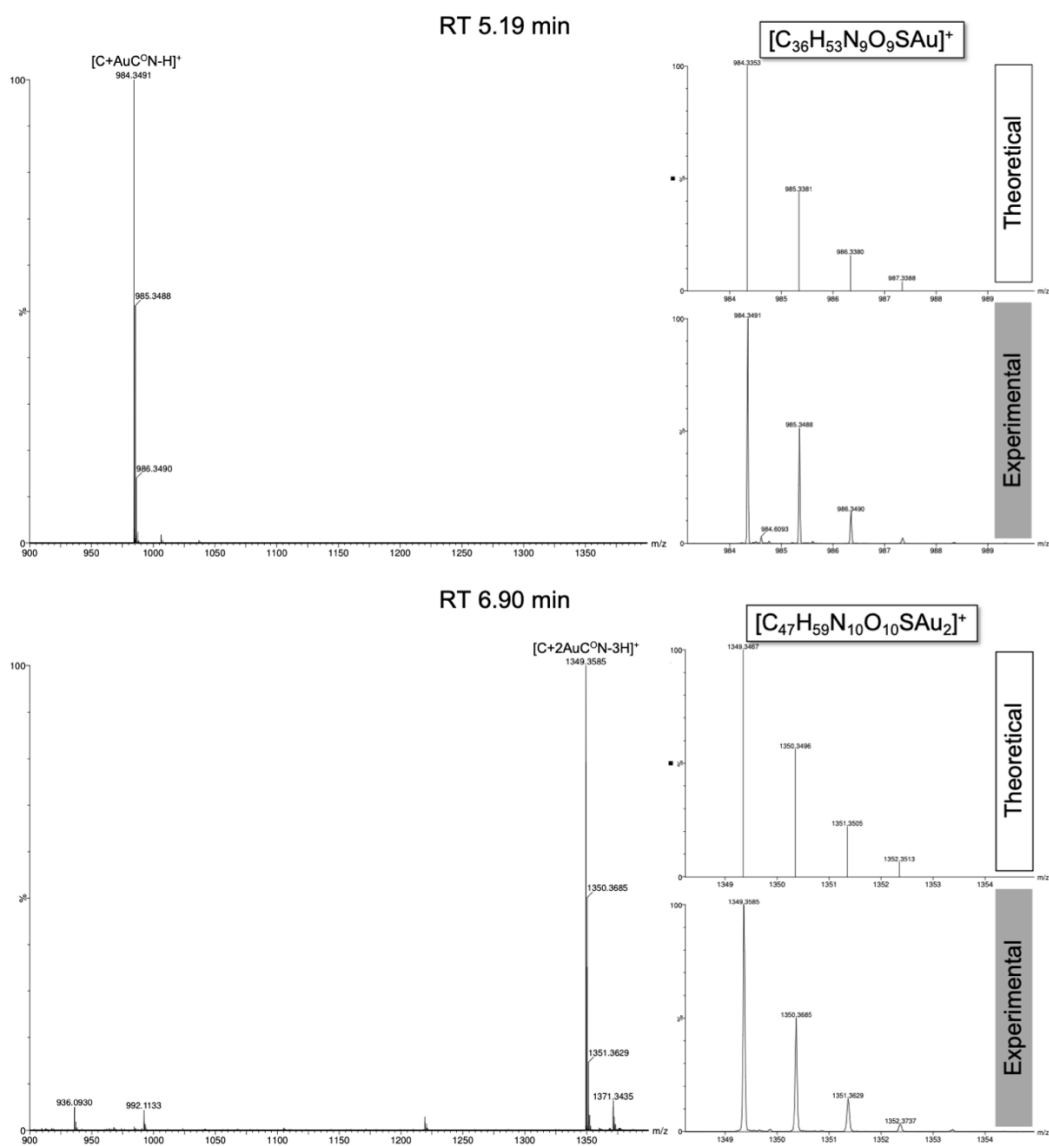


Figure S20 - HPLC-ESI-MS analysis of the reaction of $[Au(C^0N)Cl_2]$ with C model peptide (1 : 1 ratio) after 30 min incubation at 37 °C recorded at retention times (RTs) 5.19 min and 6.90 min. Comparison between the experimental isotopic patterns of representative adducts with the theoretical values. Figure from ref 308. Copyright 2020, John Wiley and Sons <https://creativecommons.org/licenses/by/4.0/>.³⁰⁸

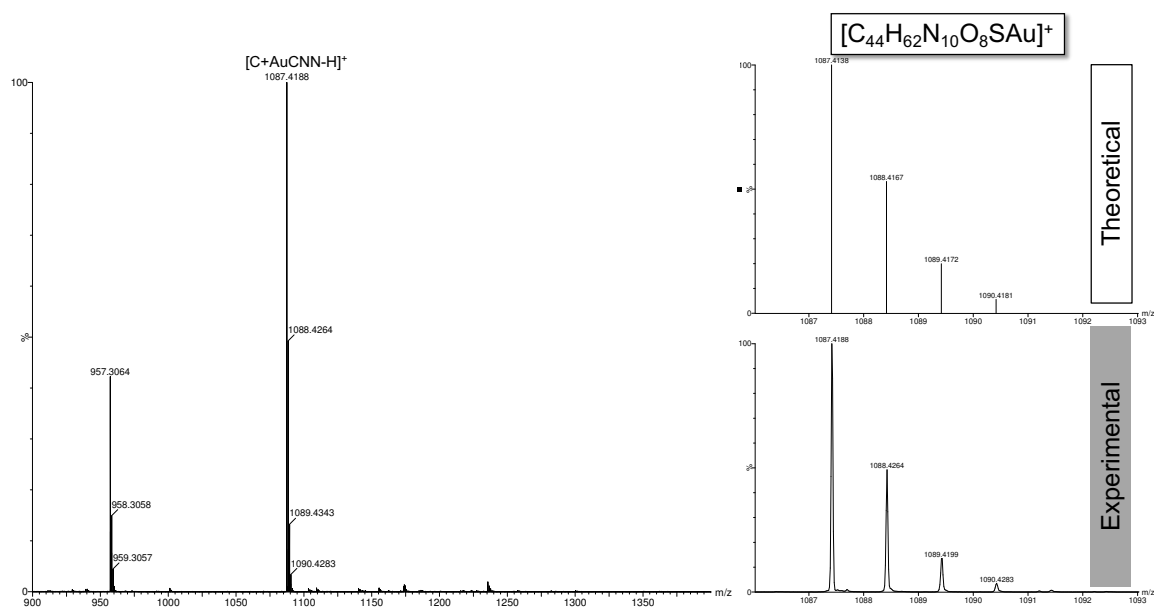


Figure S21 - HPLC-ESI-MS analysis of the reaction of $[Au(C^N^N)Cl]$ with C model peptide (1 : 1 ratio) after 30 min incubation at 37 °C recorded at retention time 4.78 min. Comparison between the experimental isotopic patterns of representative adducts with the theoretical values. Figure from ref 308. Copyright 2020, John Wiley and Sons <https://creativecommons.org/licenses/by/4.0/>.³⁰⁸

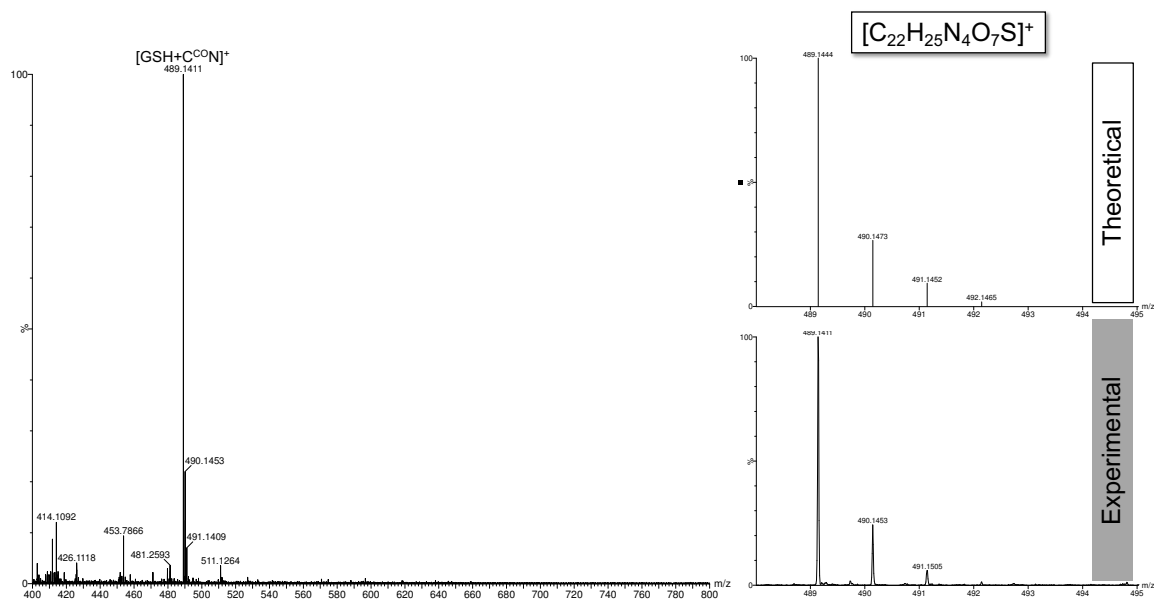


Figure S22 - HPLC-ESI-MS analysis of the reaction of $[Au(C^O^N)Cl_2]$ with GSH (3 : 1 ratio) after 24 h incubation at 37 °C. Comparison between the experimental isotopic patterns of representative adducts with the theoretical values. Figure from ref 308. Copyright 2020, John Wiley and Sons <https://creativecommons.org/licenses/by/4.0/>.³⁰⁸

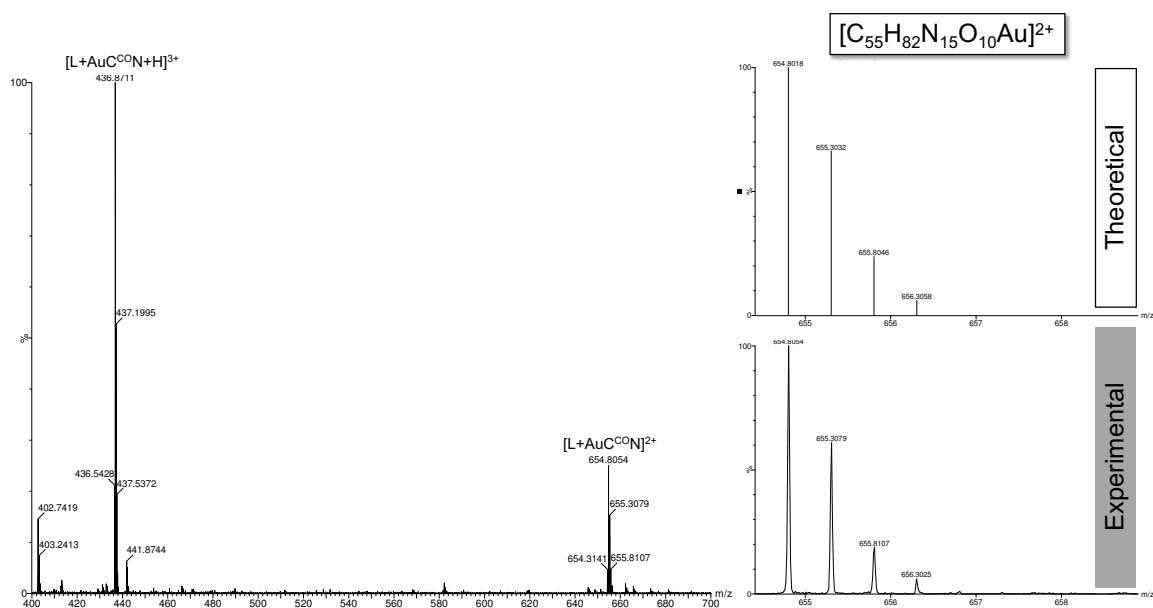


Figure S23 - HPLC-ESI-MS analysis of the reaction of $[Au(C^O N)Cl_2]$ with L model peptide (3 : 1 ratio) after 30 min incubation at 37 °C recorded at retention time 4.37 min. Comparison between the experimental isotopic patterns of representative adducts with the theoretical values. Figure from ref 308. Copyright 2020, John Wiley and Sons <https://creativecommons.org/licenses/by/4.0/>.³⁰⁸

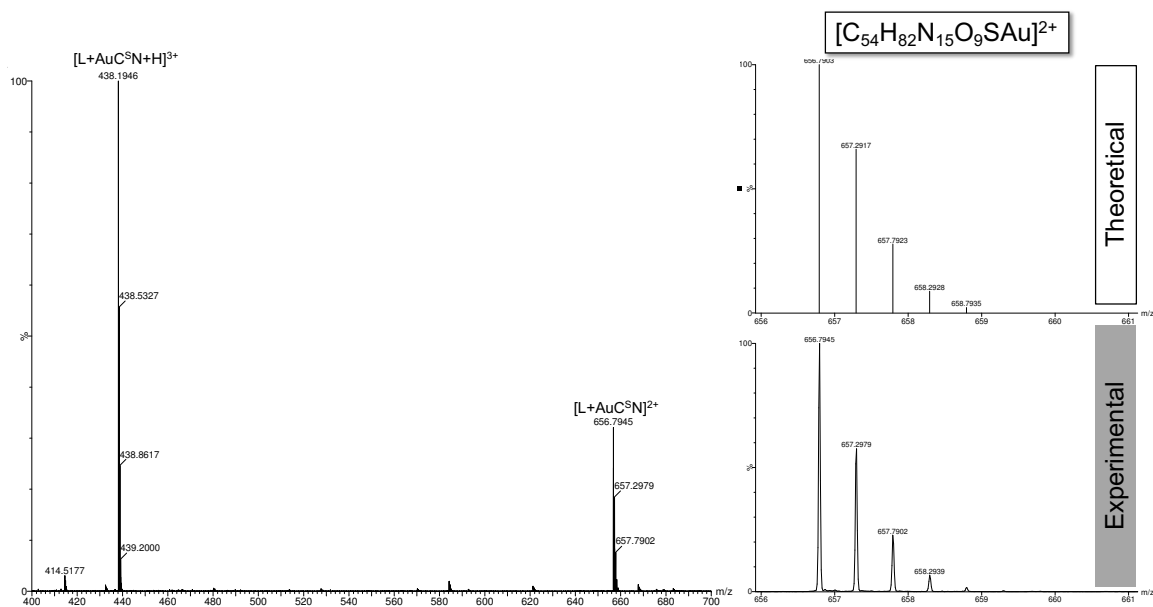


Figure S24 - HPLC-ESI-MS analysis of the reaction of $[Au(C^S N)Cl_2]$ with L model peptide (3 : 1 ratio) after 30 min incubation at 37 °C recorded at retention time 4.51 min. Comparison between the experimental isotopic patterns of representative adducts with the theoretical values. Figure from ref 308. Copyright 2020, John Wiley and Sons <https://creativecommons.org/licenses/by/4.0/>.³⁰⁸

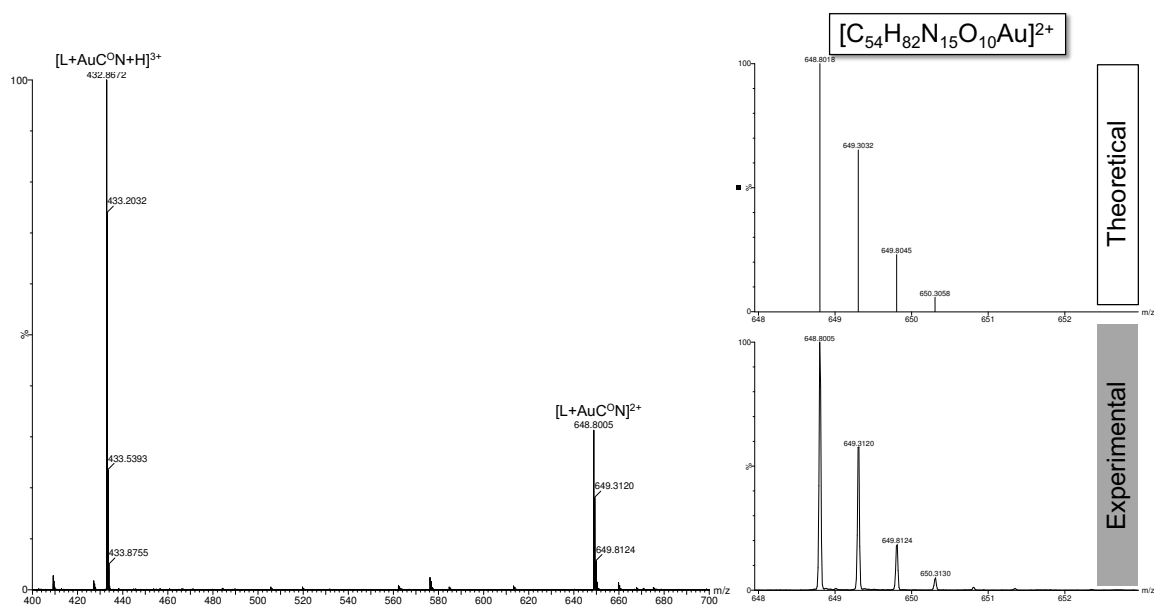


Figure S25 - HPLC-ESI-MS analysis of the reaction of $[\text{Au}(\text{C}^{\text{O}}\text{N})\text{Cl}_2]$ with L model peptide (3 : 1 ratio) after 30 min incubation at 37 °C recorded at retention time 4.39 min. Comparison between the experimental isotopic patterns of representative adducts with the theoretical values. Figure from ref 308. Copyright 2020, John Wiley and Sons <https://creativecommons.org/licenses/by/4.0/>.³⁰⁸

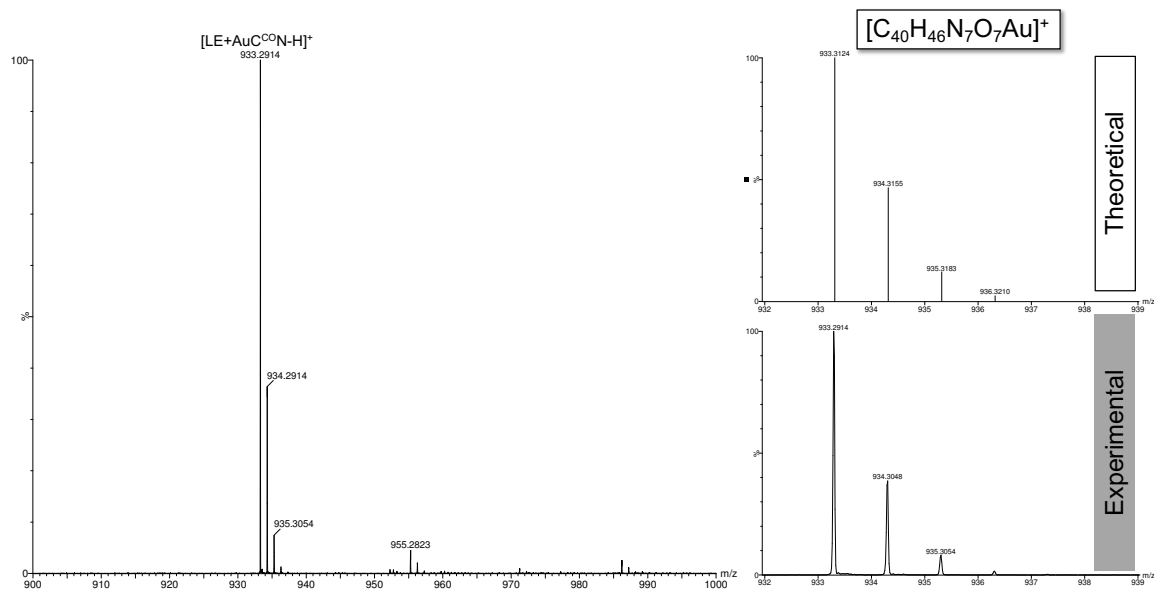


Figure S26 - HPLC-ESI-MS analysis of the reaction of $[\text{Au}(\text{C}^{\text{O}}\text{N})\text{Cl}_2]$ with LE model peptide (3 : 1 ratio) after 30 min incubation at 37 °C recorded at retention time 6.62 min. Comparison between the experimental isotopic patterns of representative adducts with the theoretical values. Figure from ref 308. Copyright 2020, John Wiley and Sons <https://creativecommons.org/licenses/by/4.0/>.³⁰⁸

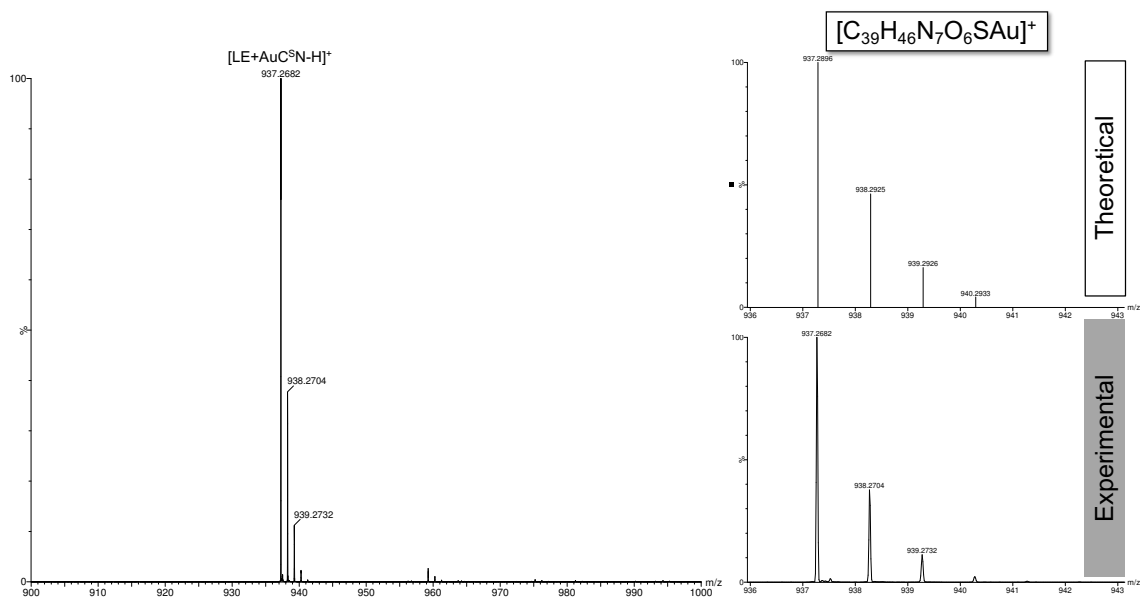


Figure S27 - HPLC-ESI-MS analysis of the reaction of $[Au(C^S N)Cl_2]$ with LE model peptide (3 : 1 ratio) after 30 min incubation at 37 °C recorded at retention time 5.44 min. Comparison between the experimental isotopic patterns of representative adducts with the theoretical values. Figure from ref 308. Copyright 2020, John Wiley and Sons <https://creativecommons.org/licenses/by/4.0/>.³⁰⁸

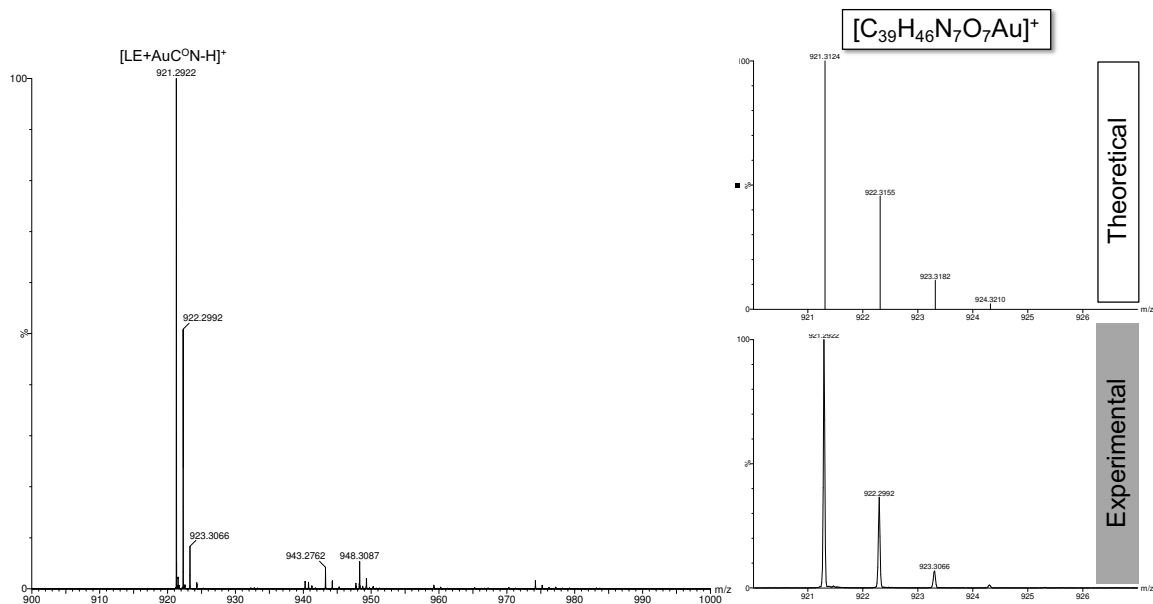


Figure S28 - HPLC-ESI-MS analysis of the reaction of $[Au(C^O N)Cl_2]$ with LE model peptide (3 : 1 ratio) after 30 min incubation at 37 °C recorded at retention time 6.84 min. Comparison between the experimental isotopic patterns of representative adducts with the theoretical values. Figure from ref 308. Copyright 2020, John Wiley and Sons <https://creativecommons.org/licenses/by/4.0/>.³⁰⁸

Table S1 – List of the different adducts detected by HPLC-ESI-MS after 10 min and 24 h incubation of the ZF and the Au(III) cyclometalated complexes. The oxidation state of Au is +3 unless specified.³⁰⁵

Complex	Time	Adduct	Molecular Formula	<i>m/z</i> experimental	<i>m/z</i> theoretical	Charge State
[Au(C^{CH₂N})Cl₂]	10 min	Apo-ZF+2AuC ^{CH₂N}	C ₁₅₁ H ₂₁₈ N ₄₁ O ₃₉ S ₂ Au ₂	528.1343	528.0781	7+
		Apo-ZF+3AuC ^{CH₂N}	C ₁₆₃ H ₂₂₆ N ₄₂ O ₃₉ S ₂ Au ₃	579.9992	579.9453	7+
	24 h	Apo-ZF+AuC ^{CH₂N} +C ^{CH₂N}	C ₁₅₁ H ₂₁₉ N ₄₁ O ₃₉ S ₂ Au	499.9905	499.9453	7+
				583.3246	583.2656	6+
[Au(C^{N^HH})Cl₂]	10 min	Apo-ZF+2AuC ^{N^HH}	C ₁₄₉ H ₂₁₆ N ₄₃ O ₃₉ S ₂ Au ₂	528.2747	528.2266	7+
		Apo-ZF+AuC ^{N^HH}	C ₁₃₈ H ₂₀₉ N ₄₁ O ₃₉ S ₂ Au	555.4741	555.4219	6+
		Apo-ZF+3AuC ^{N^HH}	C ₁₆₀ H ₂₂₆ N ₄₅ O ₃₉ S ₂ Au ₃	580.2830	580.2266	7+
	24 h	Apo-ZF+AuC ^{N^HH} +C ^{N^HH}	C ₁₄₉ H ₂₁₇ N ₄₃ O ₃₉ S ₂ Au	500.2735	500.2266	7+
				583.6514	583.6016	6+
			Apo-ZF+2AuC ^{N^HH}	C ₁₄₉ H ₂₁₆ N ₄₃ O ₃₉ S ₂ Au ₂	528.2747	528.2266
[Au(C^{CO}N)Cl₂]	10 min	Apo-ZF+AuC ^{CO} N+C ^{CO} N	C ₁₅₁ H ₂₁₄ N ₄₁ O ₄₁ S ₂ Au	503.9332	503.9375	7+
				587.7606	587.7578	6+
		Apo-ZF+2AuC ^{CO} N	C ₁₅₁ H ₂₁₂ N ₄₁ O ₄₁ S ₂ Au ₂	531.7865	531.7891	7+
	24 h	Apo-ZF+AuC ^{CO} N	C ₁₃₉ H ₂₀₇ N ₄₀ O ₄₀ S ₂ Au	557.4177	557.4141	6+
		Apo-ZF+AuC ^{CO} N+C ^{CO} N	C ₁₅₁ H ₂₁₅ N ₄₁ O ₄₁ S ₂ Au	503.9332	503.9375	7+
				587.7606	587.7578	6+
			Apo-ZF+2C ^{CO} N	C ₁₅₁ H ₂₁₆ N ₄₁ O ₄₁ S ₂	555.2665	555.2656
	Apo-ZF+3C ^{CO} N	C ₁₆₃ H ₂₂₀ N ₄₂ O ₄₂ S ₂	584.9181	584.9375	6+	
[Au(C[^]N)Cl₂]	10 min	Apo-ZF	C ₁₂₇ H ₂₀₂ N ₃₉ O ₃₉ S ₂	494.7648	494.7500	6+
				593.5070	593.5000	5+
		Apo-ZF+Au	C ₁₂₇ H ₂₀₁ N ₃₉ O ₃₉ S ₂ Au	527.4226	527.4063	6+
	24 h	Apo-ZF+AuC [^] N	C ₁₃₈ H ₂₁₁ N ₄₀ O ₃₉ S ₂ Au	552.9266	552.9219	6+
		Apo-ZF	C ₁₂₇ H ₂₀₂ N ₃₉ O ₃₉ S ₂	494.7648	494.7500	6+
				593.5071	593.5000	5+
Apo-ZF+Au	C ₁₂₇ H ₂₀₁ N ₃₉ O ₃₉ S ₂ Au	527.4226	527.4063	6+		
Apo-ZF+AuC [^] N	C ₁₃₈ H ₂₁₁ N ₄₀ O ₃₉ S ₂ Au	552.9369	552.9219	6+		

Table S2 - Experimental (M_{exp}) and theoretical (M_{theor}) masses of the detected species during the individual HPLC-ESI-MS experiment of Cys₂His₂ model peptide after 24 h incubation. The oxidation state of Au is +3 unless specified.³⁰⁸

Compound	RT (mins)	Species	M_{exp}	M_{theor}	Δppm
[Au(C ^{CO} N)Cl ₂]	3.64	[Apo-ZF+C ^{CO} N+5H] ⁶⁺	524.9178	524.9248	13.33
	3.89	[Apo-ZF+2C ^{CO} N+4H] ⁶⁺	555.0999	555.1003	0.72
[Au(C ^{SN})Cl ₂]	4.03	[Apo-ZF+C ^{SN} N+5H] ⁶⁺	525.7515	525.7546	5.90
	4.39	[Apo-ZF+AuC ^{SN} N+4H] ⁶⁺	558.4117	558.4144	4.83
[Au(C ^{ON})Cl ₂]	3.66	[Apo-ZF+2C ^{ON} N+4H] ⁶⁺	556.5881	556.5930	8.80
		[Apo-ZF+C ^{ON} N+5H] ⁶⁺	522.9238	522.9248	1.91
	4.00	[Apo-ZF+AuC ^{ON} N+4H] ⁶⁺	555.5796	555.5846	9.00
[Au(C ^{AN} ^N)Cl] ₊	3.86	[Apo-ZF+2AuCNN+2H] ⁶⁺	551.2681	551.2673	1.45
			650.9475	650.9465	1.54

Table S3 - Experimental (M_{exp}) and theoretical (M_{theor}) masses of the detected species during the individual HPLC-ESI-MS experiment of AC model peptide after 30 min incubation. The oxidation state of Au is +3 unless specified.³⁰⁸

Compound	RT (mins)	Species	M_{exp}	M_{theor}	Δppm
[Au(C ^{CO} N)Cl ₂]	5.15	[AC+AuC ^{CO} N] ²⁺	776.3030	776.3042	1.55
		[AC+AuC ^{CO} NCl+3H] ²⁺	795.2873	795.3004	16.47
	5.32	[AC+C ^{CO} N+1H] ²⁺	678.3282	678.3248	5.01
[Au(C ^{SN})Cl ₂]	5.25	[AC+AuC ^{SN} N] ²⁺	778.2983	778.2927	7.19
	5.44	[AC+C ^{SN} N+1H] ²⁺	680.3186	680.3134	7.64
		[AC+2AuC ^{SN} N-2H] ²⁺	968.7899	968.7870	2.99
[Au(C ^{ON})Cl ₂]	6.28	[AC+2AuC ^{ON} N-2H] ²⁺	952.8157	952.8099	6.09
	6.60	[AC+AuC ^{ON} N+C ^{ON} N-1H] ²⁺	854.8404	854.8306	11.46
[Au(C ^{AN} ^N)Cl] ₊	4.78	[AC+AuCNN] ²⁺	821.8527	821.8434	11.32

Table S4 - Experimental (M_{exp}) and theoretical (M_{theor}) masses of the detected species during the individual HPLC-ESI-MS experiment of C model peptide after 24 h incubation. The oxidation state of Au is +3 unless specified.³⁰⁸

Compound	RT (mins)	Species	M_{exp}	M_{theor}	Δppm
[Au(C ^{CO} N)Cl ₂]	4.98	[C+AuC ^{CO} N-1H] ⁺	996.3513	996.3353	16.06
[Au(C ^{SN})Cl ₂]	5.09	[C+AuC ^{SN} N-1H] ⁺	1000.3221	1000.3124	9.70
[Au(C ^{ON})Cl ₂]	5.02	[C+AuC ^{ON} N-1H] ⁺	984.3491	984.3353	14.02
[Au(C ^{AN} ^N)Cl] ₊	4.95	[C+AuCNN-1H] ⁺	1087.4332	1087.4138	17.84

Table S5 - Experimental (M_{exp}) and theoretical (M_{theor}) masses of the detected species during the individual HPLC-ESI-MS experiment of L model peptide after 30 min incubation. The oxidation state of Au is +3 unless specified.³⁰⁸

Compound	RT (mins)	Species	M_{exp}	M_{theor}	Δppm
[Au(C ^{CO} N)Cl ₂]	4.37+4.83	[L+AuC ^{CO} N] ²⁺	654.8054	654.8018	5.50
	4.51	[L-NH ₄ +OH+AuC ^{CO} N-H] ²⁺	654.3141	654.2859	43.10
	5.1	[L-NH ₄ +AuC ^{CO} N] ²⁺	645.8030	645.7845	28.65
[Au(C ^S N)Cl ₂]	4.51+4.98	[L+AuC ^S N] ²⁺	656.7945	656.7903	6.40
[Au(C ^O N)Cl ₂]	4.39	[L+AuC ^O N] ²⁺	648.8005	648.8018	2.00
	4.90	[L+AuC ^O N] ²⁺	648.8116	648.8018	15.10
	5.10	[L+Au ^I +1H] ²⁺	564.2738	564.2753	2.66

Table S6 - Experimental (M_{exp}) and theoretical (M_{theor}) masses of the detected species during the individual HPLC-ESI-MS experiment of LE model peptide after 30 min incubation. The oxidation state of Au is +3 unless specified.³⁰⁸

Compound	RT (mins)	Species	M_{exp}	M_{theor}	Δppm
[Au(C ^{CO} N)Cl ₂]	5.44-5.63	[LE-NH ₄ +OH+AuC ^{CO} N-2H] ⁺	932.3051	932.2808	26.06
	6.62	[LE+AuC ^{CO} N-1H] ⁺	933.2914	933.3124	22.50
	6.97	[LE-NH ₄ +AuC ^{CO} N-1H] ⁺	915.2888	915.2781	11.69
[Au(C ^S N)Cl ₂]	5.44	[LE+AuC ^S N-1H] ⁺	937.2682	937.2896	22.83
[Au(C ^O N)Cl ₂]	5.37+6.84	[LE+AuC ^O N-1H] ⁺	921.2922	921.3124	21.92

Table S7 - List of identified metalated peptide fragments from online MS/MS experiments of the [LE+Au(C^{CO}N)-2H]⁺ adduct (m/z 933). The similarity score takes into account the convergence of the experimental and the theoretical isotopic distribution and mass accuracy. The oxidation state of Au is +3 unless specified.³⁰⁸

Modification	Type	M_{exp}	M_{theor}	Similarity	Charge	Intensity [%]	Δppm
AuC ^{CO} N	parent mass	933.2886	933.2881	95	1	30	4.0
AuC ^{CO} N	b4	802.1958	802.1935	94	1	26	3.0
AuC ^{CO} N	a4	774.2025	774.1985	95	1	1	5.2
AuC ^{CO} N	b3	655.1257	655.1250	96	1	11	0.9
AuC ^{CO} N	a3	627.1311	627.1301	95	1	4	1.5
AuC ^{CO} N	b2	598.102	598.1036	94	1	20	1.0
AuC ^{CO} N	a2	570.1099	570.1087	87	1	6	2.2
AuC ^{CO} N	a4y3	554.1143	554.1137	80	1	4	0.9
AuC ^{CO} N	b1	541.0807	541.0821	66	1	1	2.6
AuC ^{CO} N	a1	513.0863	513.0872	96	1	15	1.8
AuC ^{CO} N	a3y3	407.0453	407.0453	84	1	1	0.1
Au(I)	b4	619.1262	619.1256	n.a.	1	100	0.6

Supplementary Material: Chapter 6

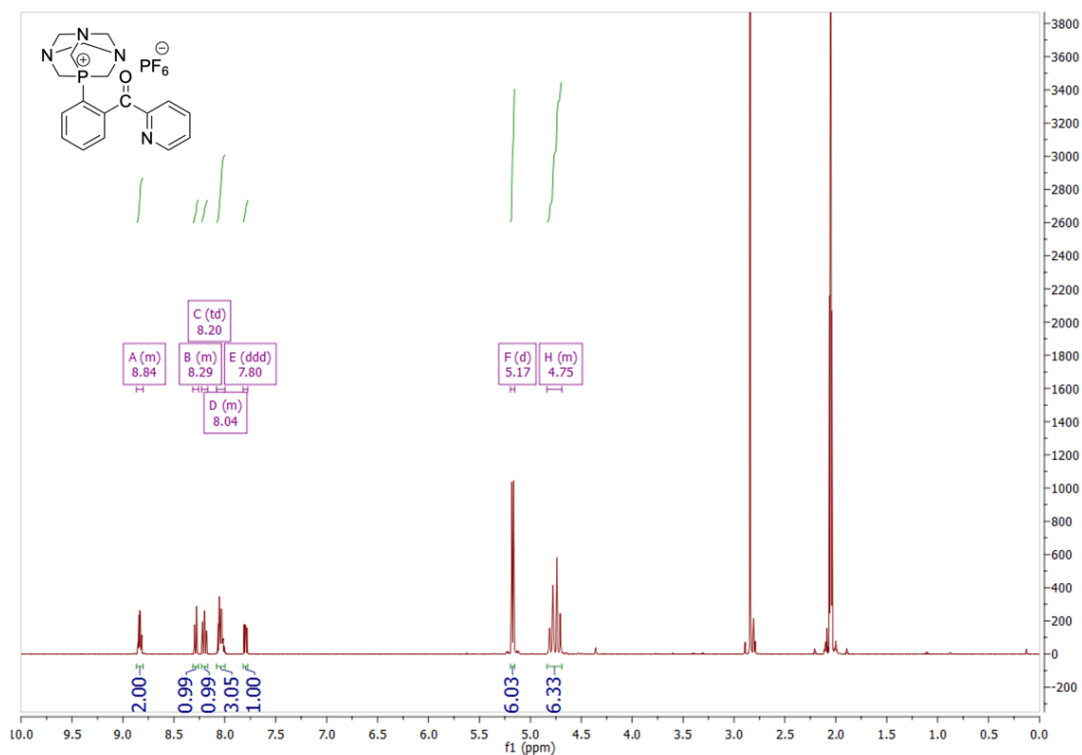


Figure S29 - ^1H NMR spectrum of **1** in acetone- d_6 . Figure modified from ref 341. Copyright 2020, John Wiley and Sons <https://creativecommons.org/licenses/by/4.0/>.³⁴¹

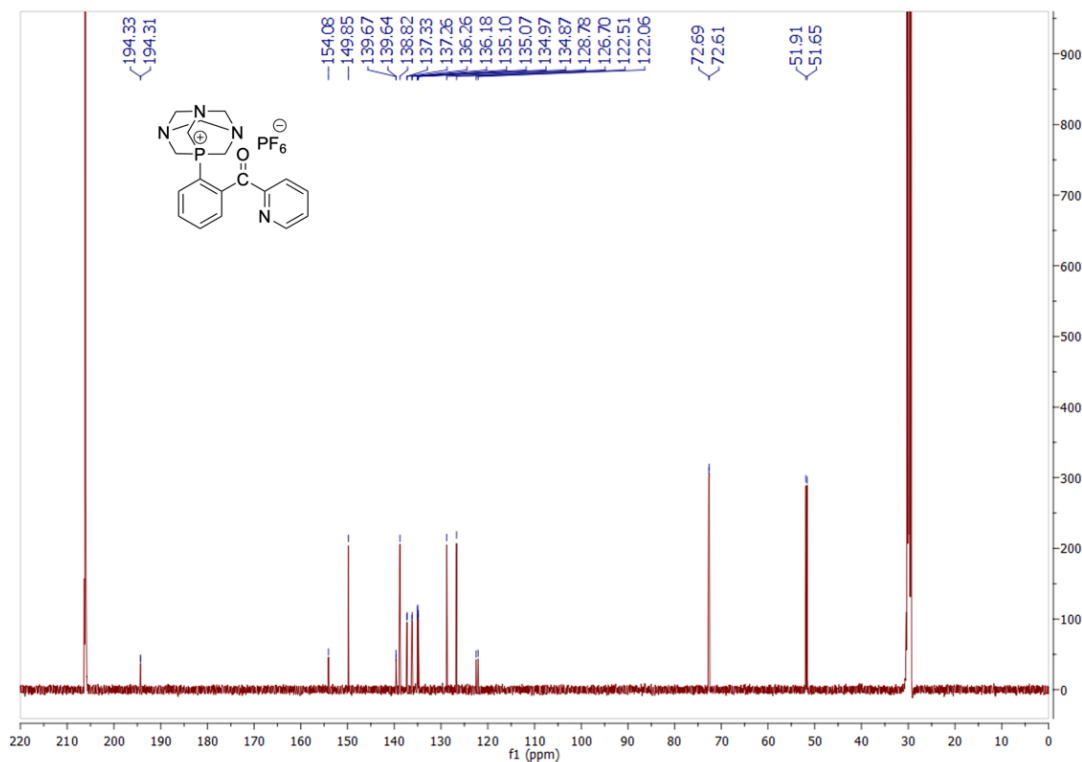


Figure S30 - $^{13}\text{C}\{^1\text{H}\}$ NMR spectrum of **1** in acetone- d_6 . Figure modified from ref 341. Copyright 2020, John Wiley and Sons <https://creativecommons.org/licenses/by/4.0/>.³⁴¹

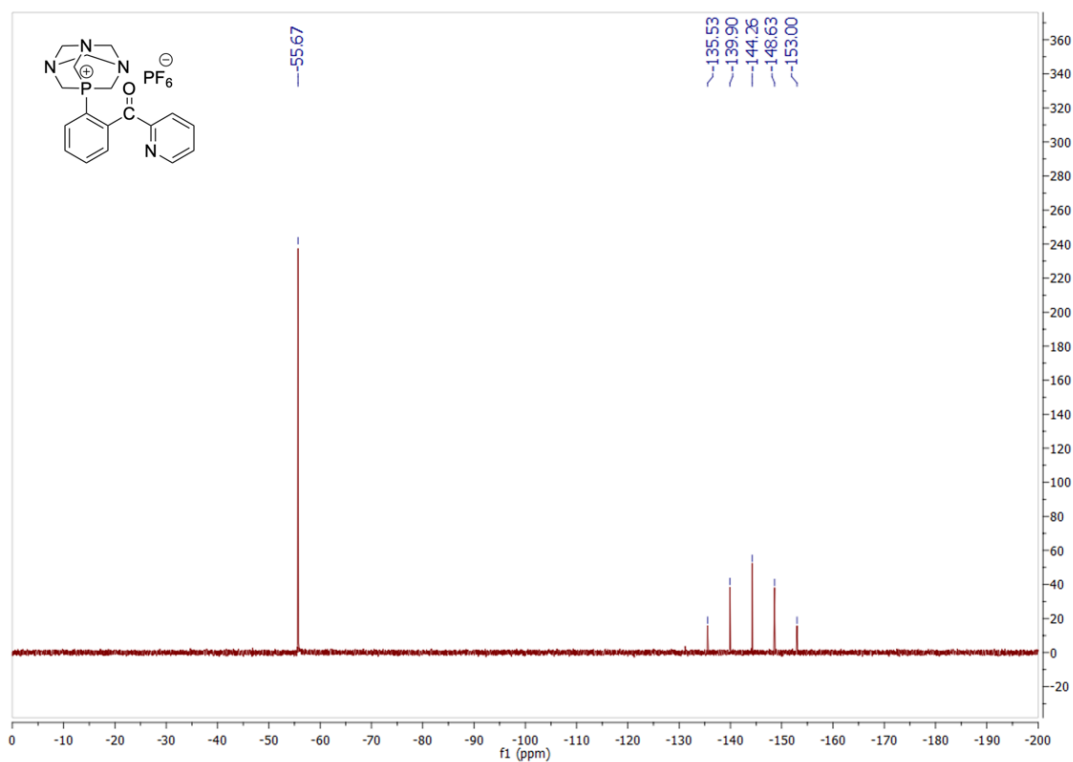


Figure S31 - $^{31}\text{P}\{^1\text{H}\}$ NMR spectrum of **1** in acetone- d_6 . Figure modified from ref 341. Copyright 2020, John Wiley and Sons <https://creativecommons.org/licenses/by/4.0/>.³⁴¹

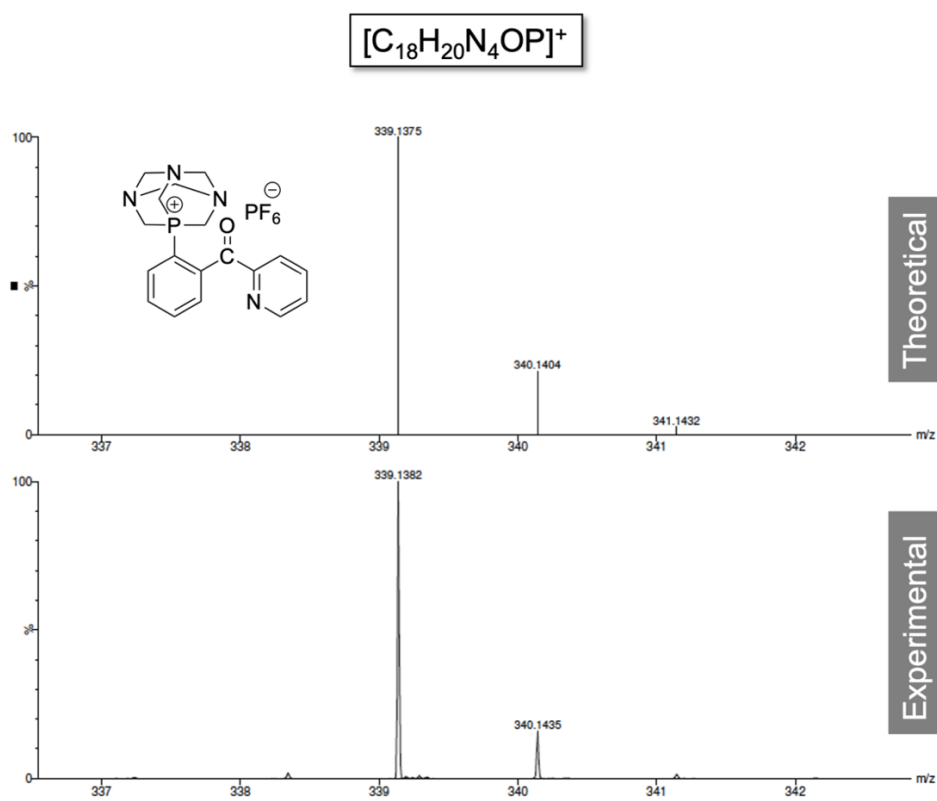


Figure S32 - HR-ESI-MS theoretical (top) and experimental (below) spectra of **1**.³⁴¹

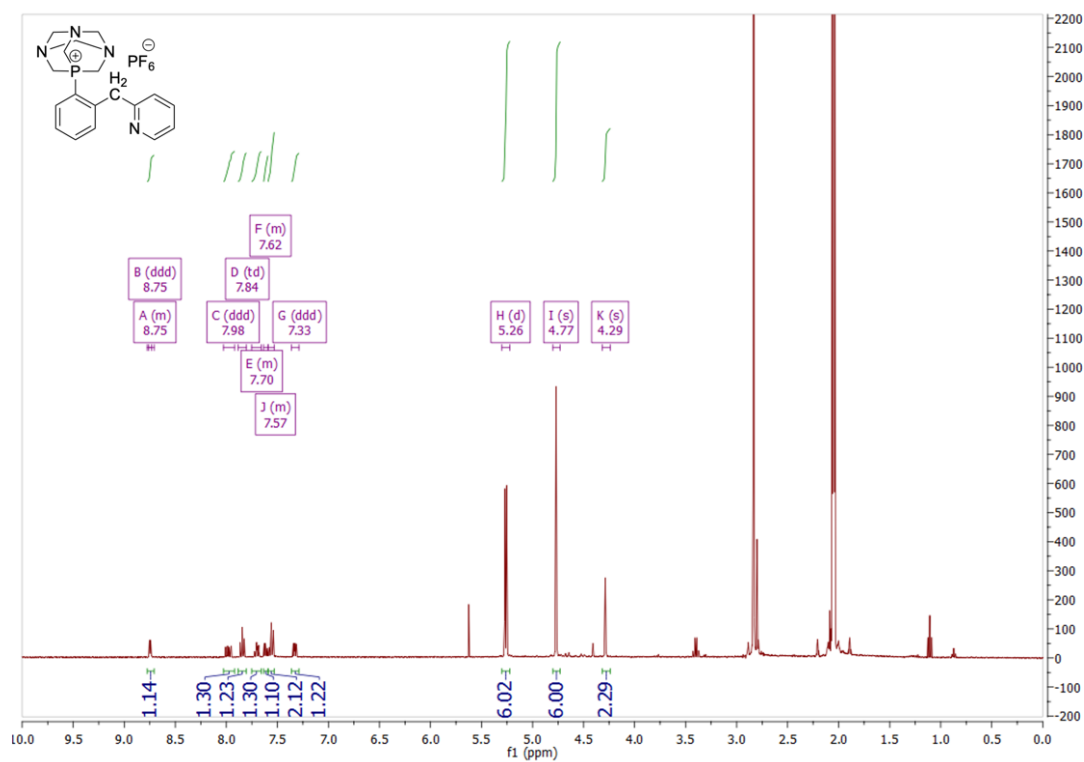


Figure S33 - ^1H NMR spectrum of **2** in acetone- d_6 . Figure modified from ref 341. Copyright 2020, John Wiley and Sons <https://creativecommons.org/licenses/by/4.0/>.³⁴¹

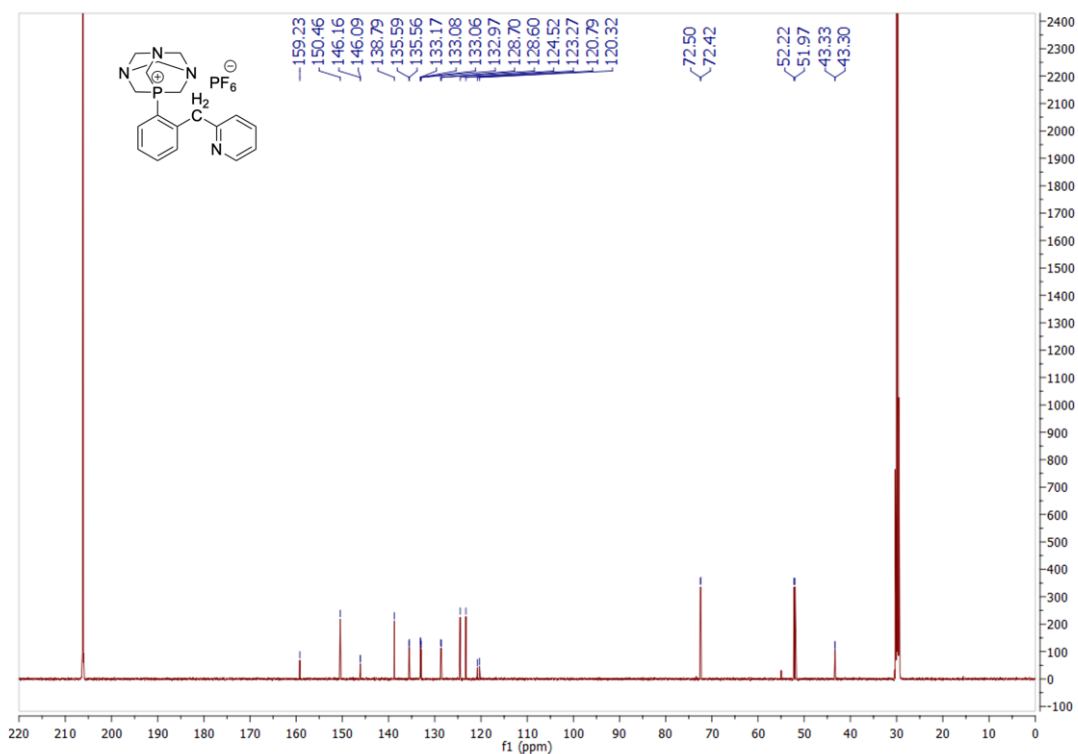


Figure S34 - $^{13}\text{C}\{^1\text{H}\}$ NMR spectrum of **2** in acetone- d_6 . Figure modified from ref 341. Copyright 2020, John Wiley and Sons <https://creativecommons.org/licenses/by/4.0/>.³⁴¹

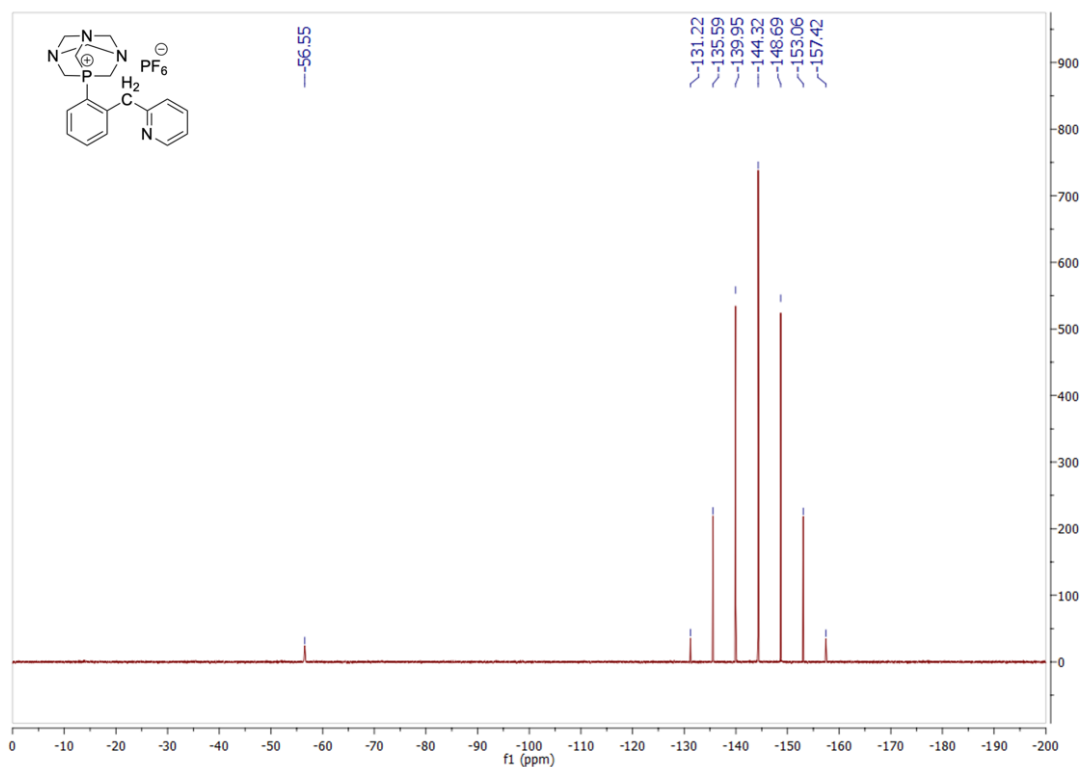


Figure S35 - $^{31}\text{P}\{^1\text{H}\}$ NMR spectrum of **2** in acetone- d_6 . Figure modified from ref 341. Copyright 2020, John Wiley and Sons <https://creativecommons.org/licenses/by/4.0/>.³⁴¹

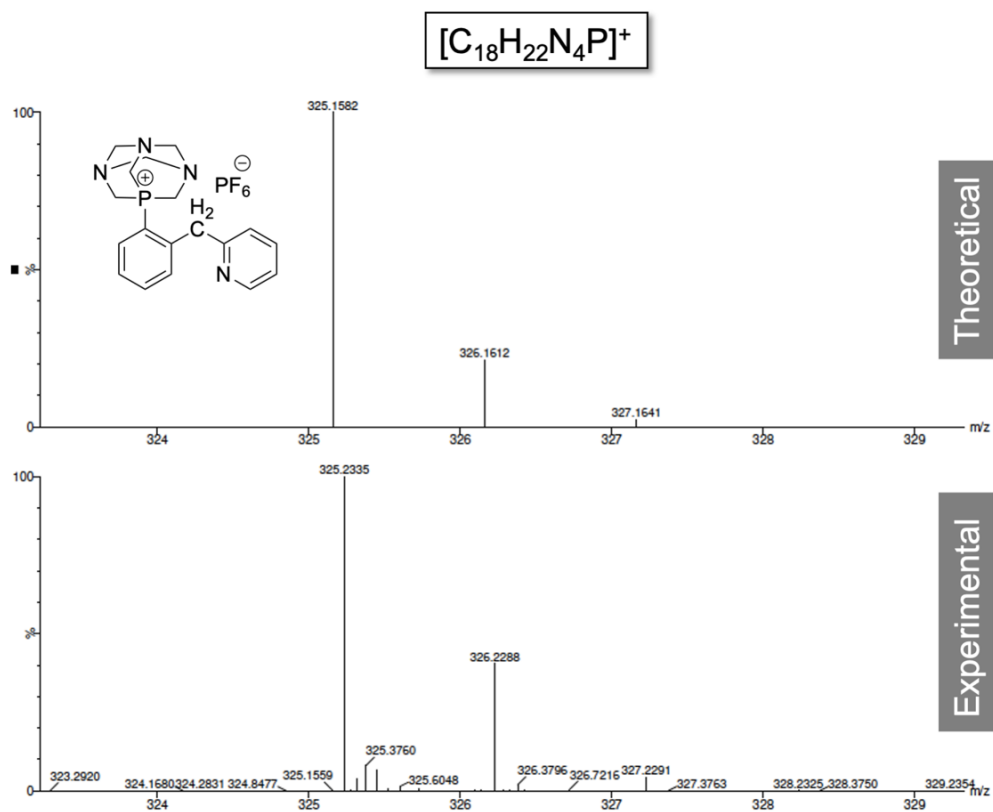


Figure S36 - HR-ESI-MS theoretical (top) and experimental (below) spectra of **2**.³⁴¹

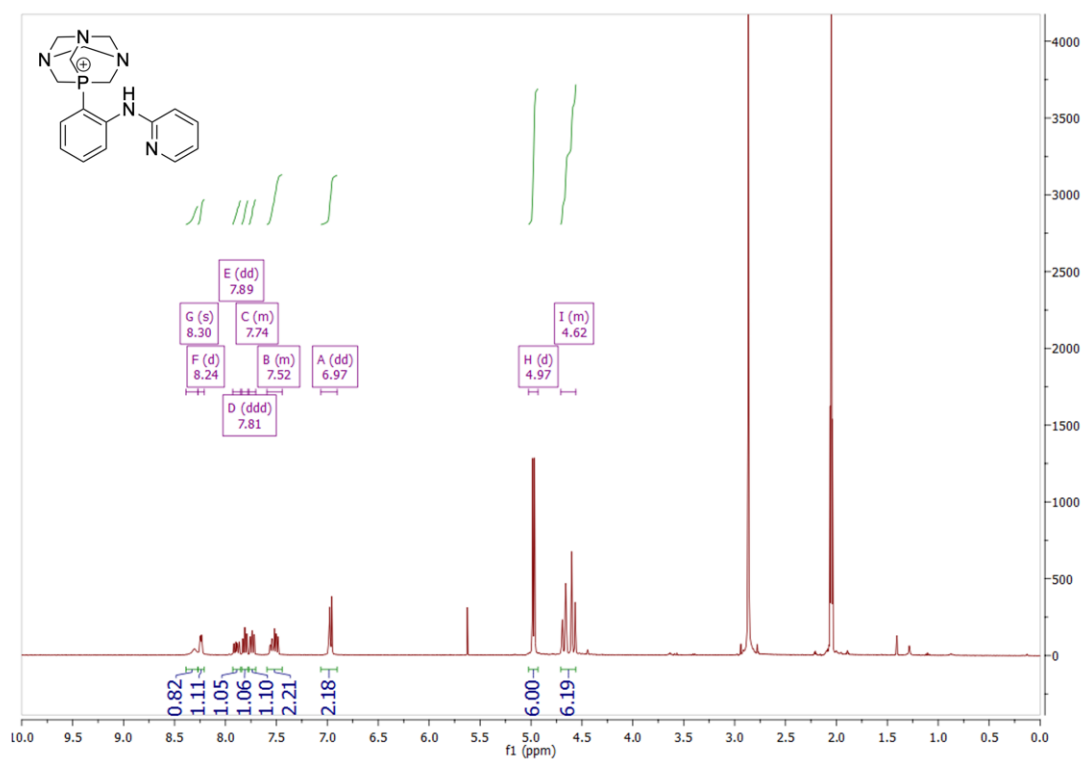


Figure S37 - ^1H NMR spectrum of **3** in acetone- d_6 . Figure modified from ref 341. Copyright 2020, John Wiley and Sons <https://creativecommons.org/licenses/by/4.0/>.³⁴¹

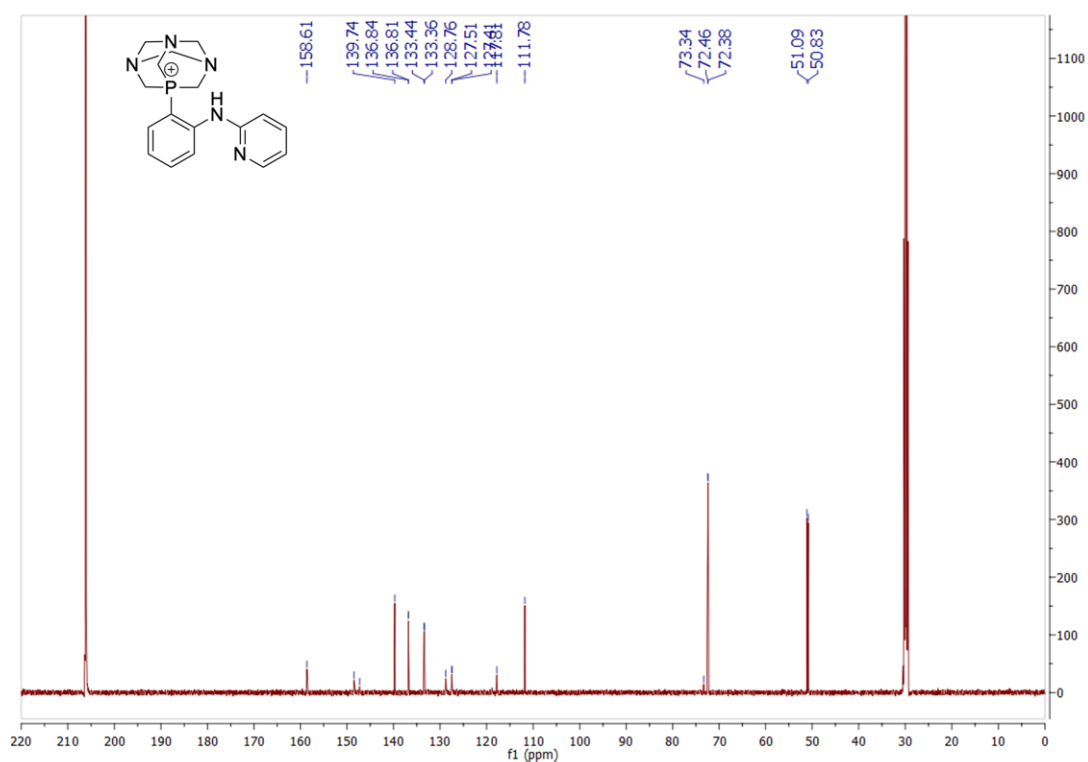


Figure S38 - $^{13}\text{C}\{^1\text{H}\}$ NMR spectrum of **3** in acetone- d_6 . Figure modified from ref 341. Copyright 2020, John Wiley and Sons <https://creativecommons.org/licenses/by/4.0/>.³⁴¹

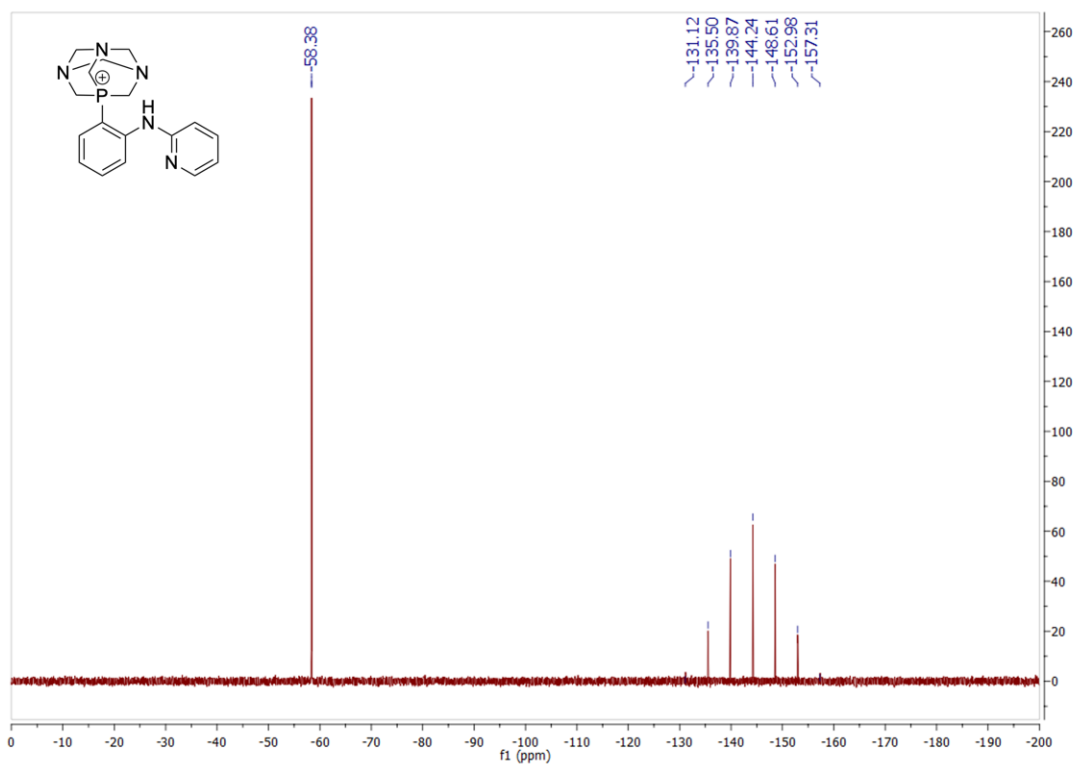


Figure S39 - $^{31}\text{P}\{^1\text{H}\}$ NMR spectrum of **3** in acetone- d_6 . Figure modified from ref 341. Copyright 2020, John Wiley and Sons <https://creativecommons.org/licenses/by/4.0/>.³⁴¹

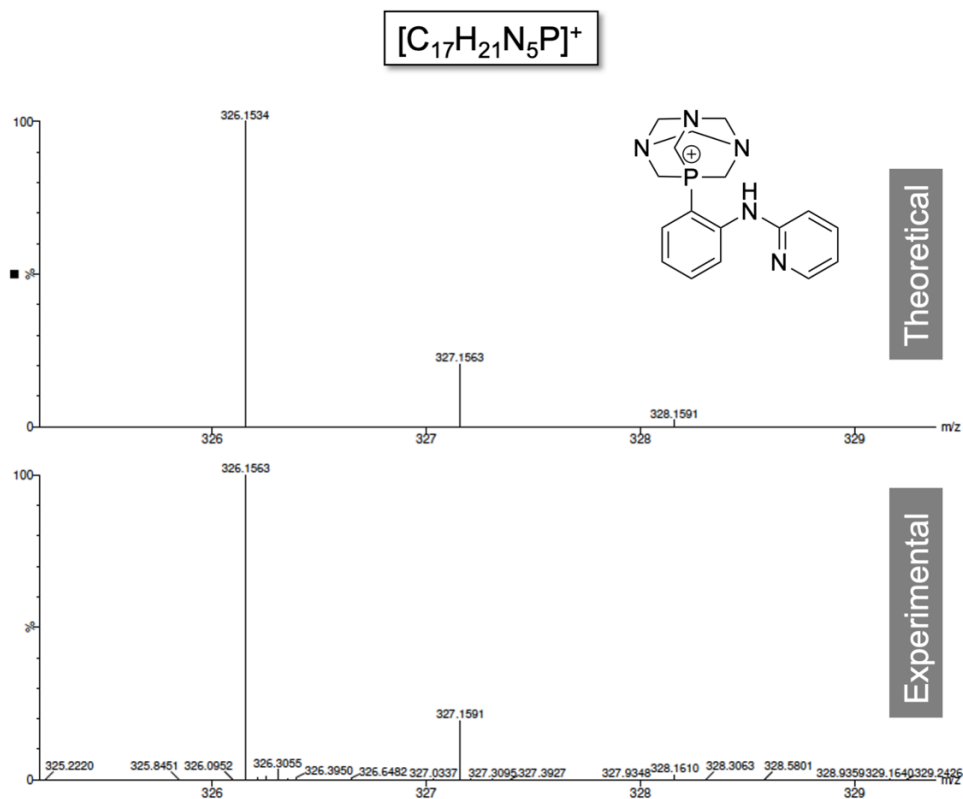


Figure S40 - HR-ESI-MS theoretical (top) and experimental (below) spectra of **3**.³⁴¹

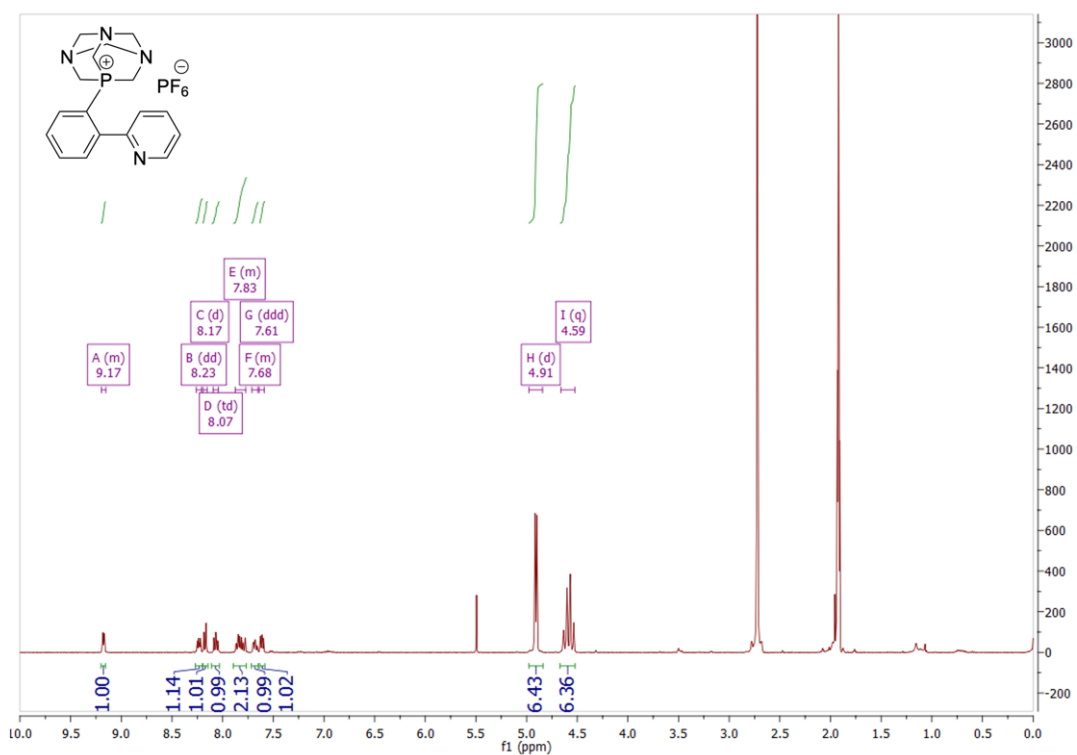


Figure S41 - ^1H NMR spectrum of 4 in acetone- d_6 . Figure modified from ref 341. Copyright 2020, John Wiley and Sons <https://creativecommons.org/licenses/by/4.0/>.³⁴¹

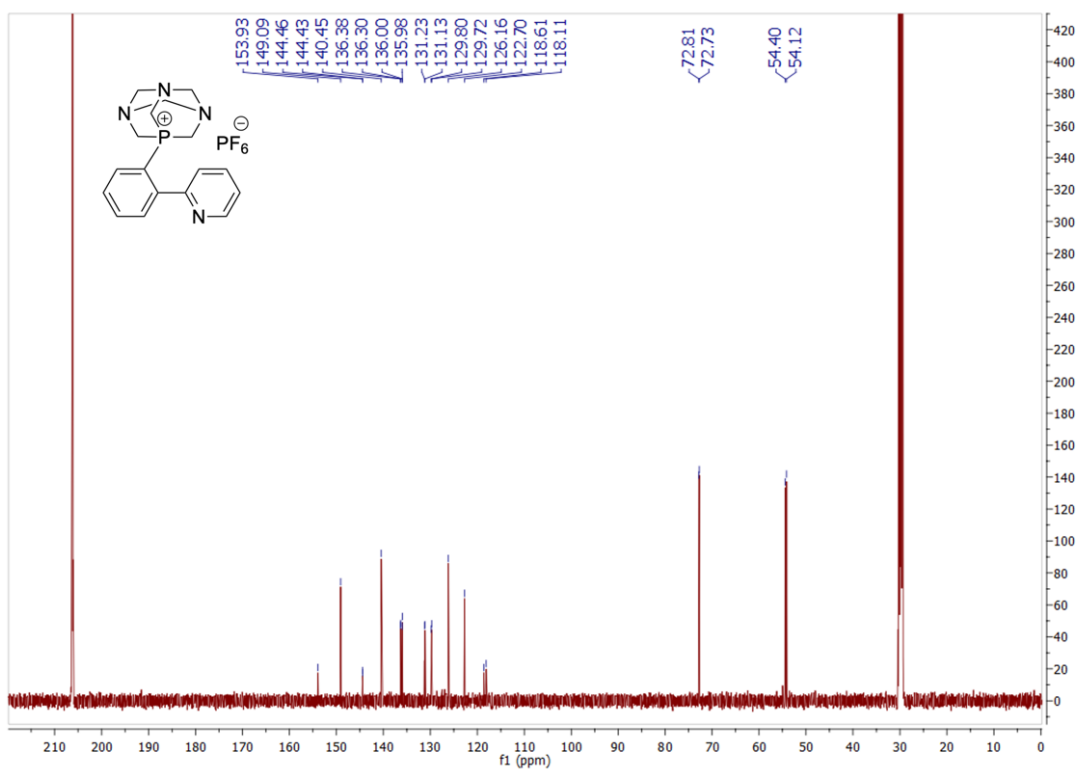


Figure S42 - $^{13}\text{C}\{^1\text{H}\}$ NMR spectrum of 4 in acetone- d_6 . Figure modified from ref 341. Copyright 2020, John Wiley and Sons <https://creativecommons.org/licenses/by/4.0/>.³⁴¹

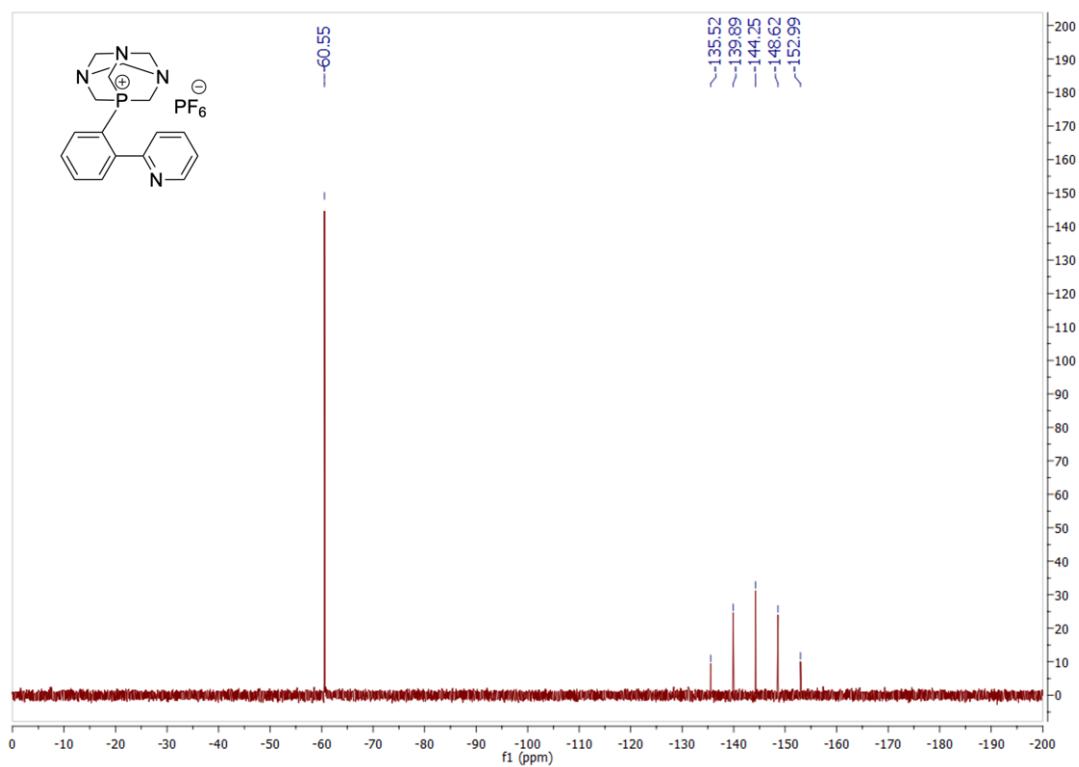


Figure S43 - $^{31}\text{P}\{^1\text{H}\}$ NMR spectrum of **4** in acetone- d_6 . Figure modified from ref 341. Copyright 2020, John Wiley and Sons <https://creativecommons.org/licenses/by/4.0/>.³⁴¹

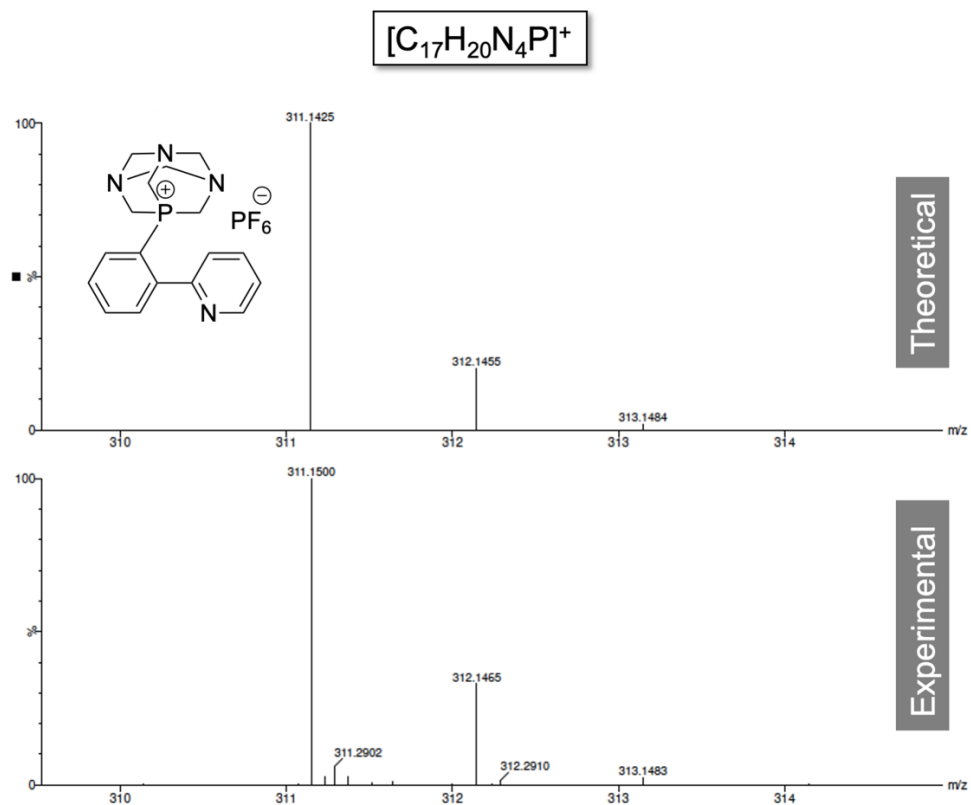


Figure S44 - HR-ESI-MS theoretical (top) and experimental (below) spectra of **4**.³⁴¹

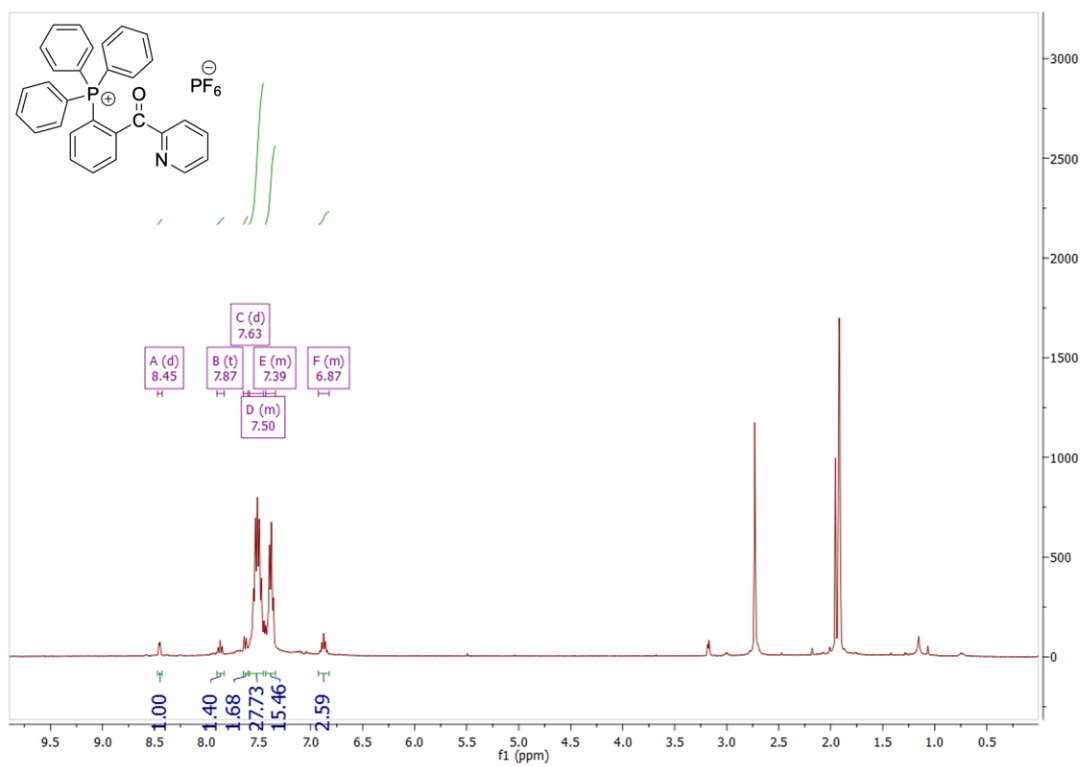


Figure S49 - ¹H NMR spectrum of **5** in acetone-d₆.³⁴¹

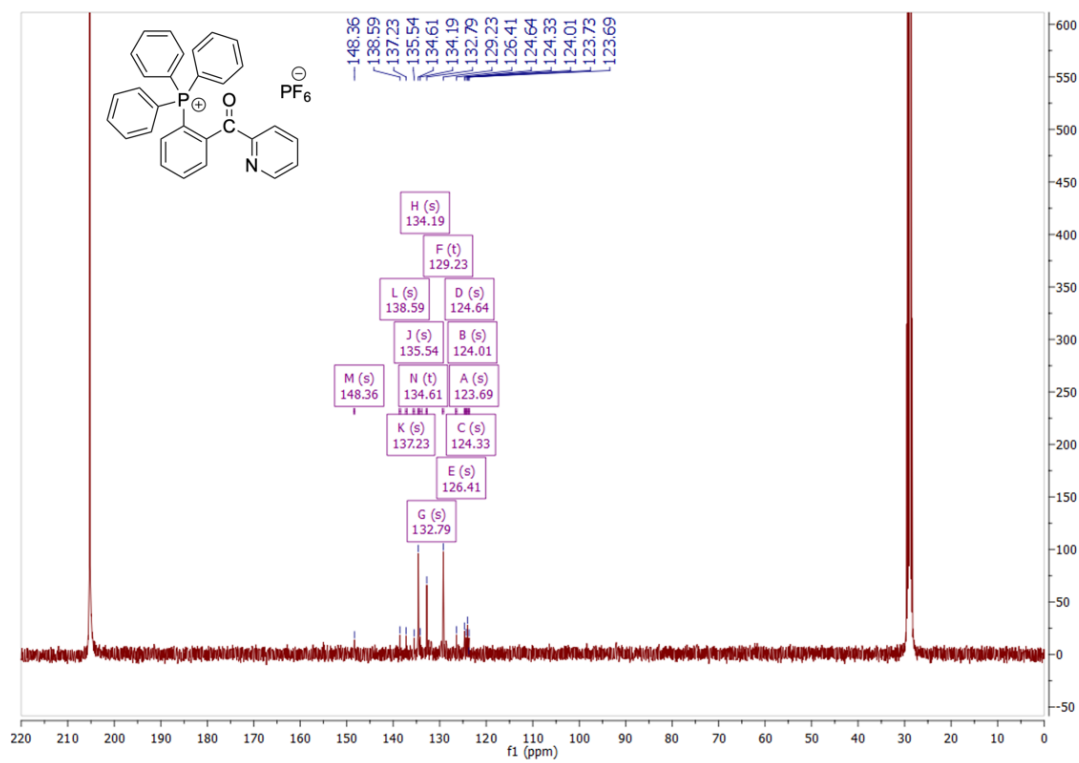


Figure S50 - ¹³C{¹H} NMR spectrum of **5** in acetone-d₆.³⁴¹

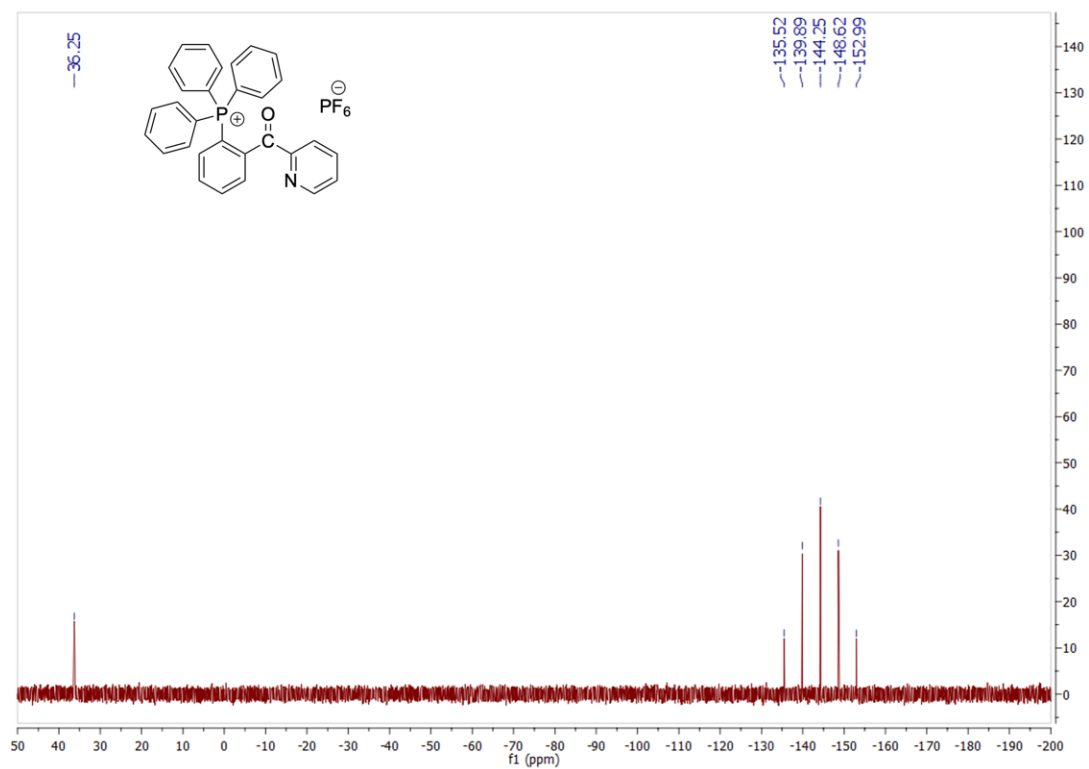


Figure S51 - $^{31}\text{P}\{^1\text{H}\}$ NMR spectrum of **5** in acetone- d_6 .³⁴¹

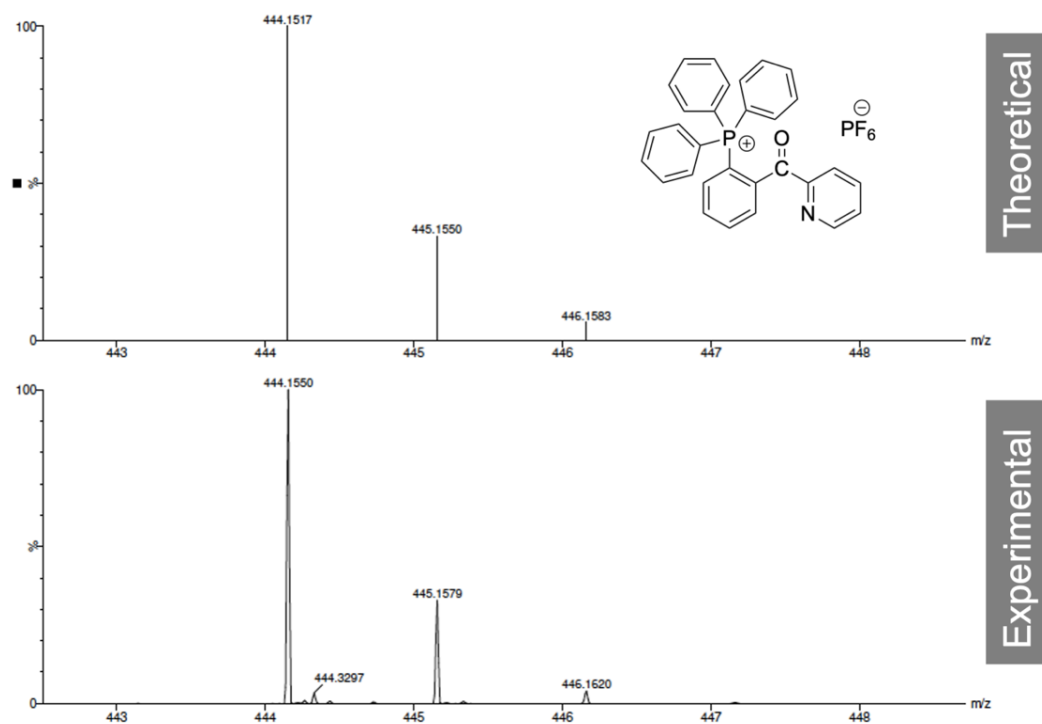


Figure S52 - HR-ESI-MS theoretical (top) and experimental (below) spectra of **5**.³⁴¹

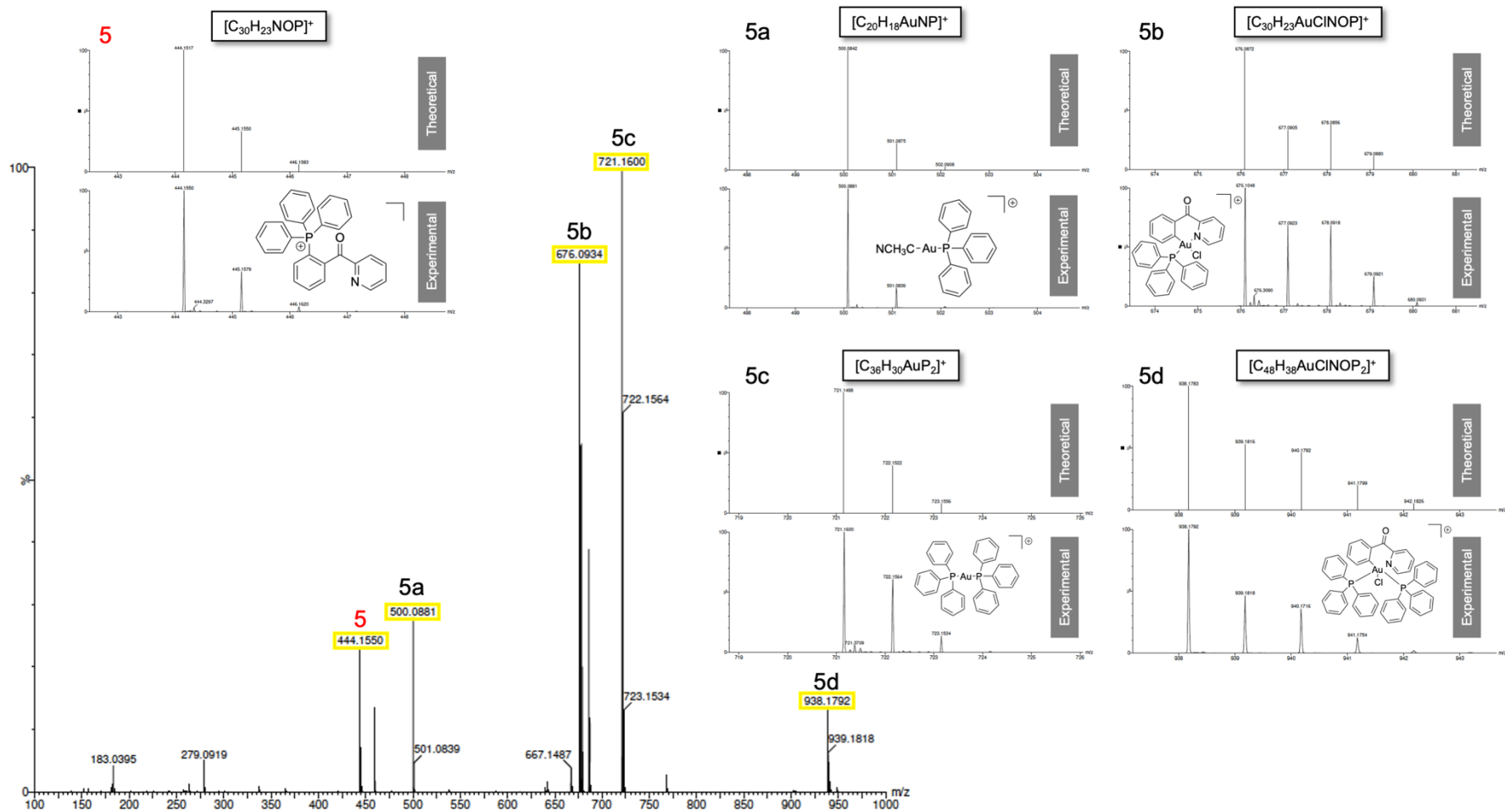


Figure S53 - HR-ESI-MS spectrum of **5** and other species (**5a-d**) formed during the reaction of $[\text{Au}(\text{C}^\text{O})\text{Cl}_2]$ with triphenylphosphine. Inserts show simulated (top) and experimental (bottom) spectra of **5** and **5a-d**. Figure modified from ref 341. Copyright 2020, John Wiley and Sons <https://creativecommons.org/licenses/by/4.0/>.³⁴¹

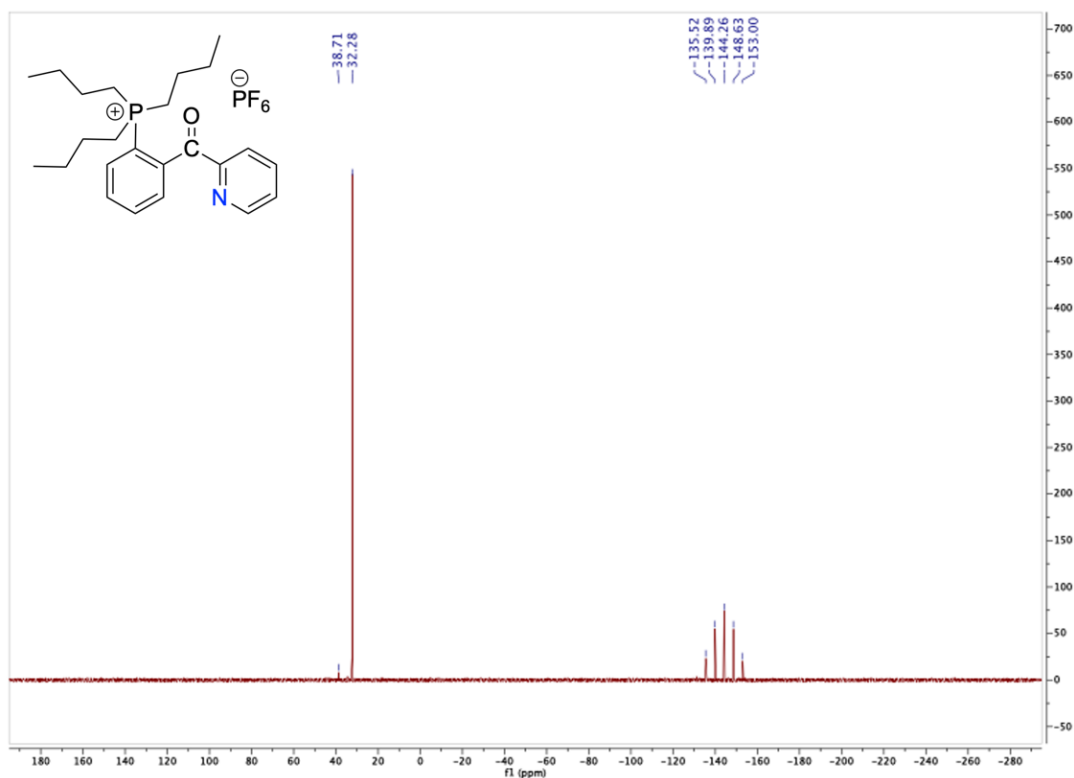


Figure S54 - ³¹P{¹H} NMR spectrum of **6** in acetone-d₆.³⁴¹

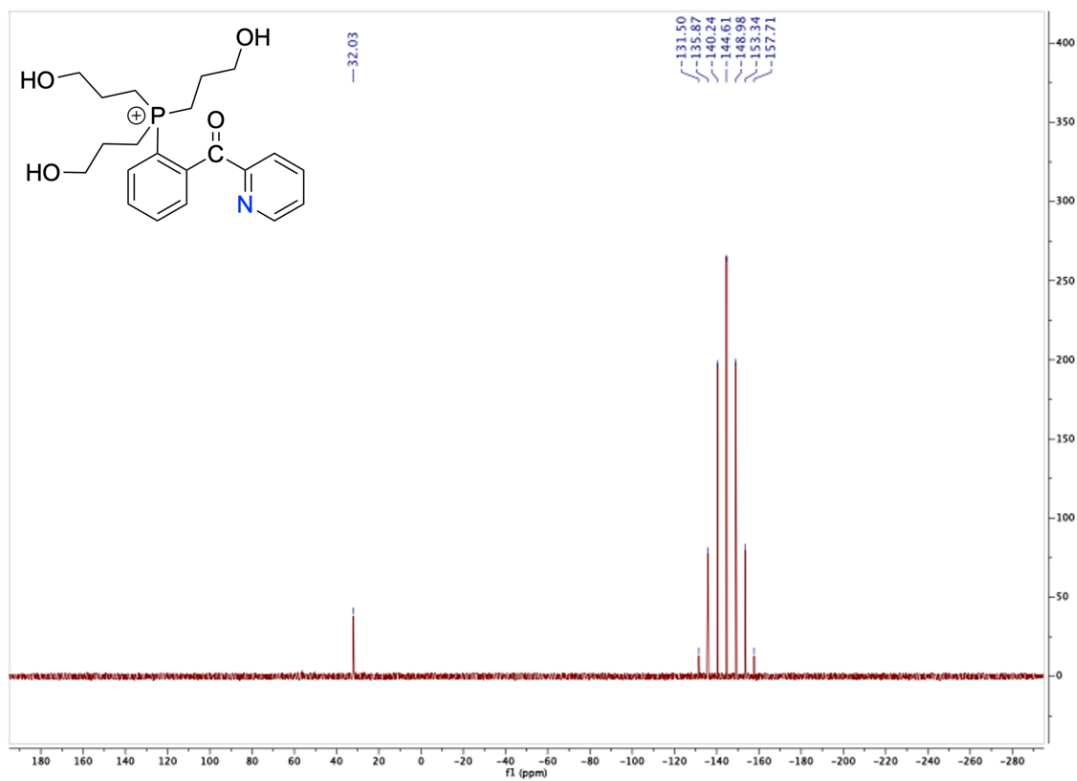


Figure S55 - ³¹P{¹H} NMR spectrum of **7** in acetone-d₆.³⁴¹

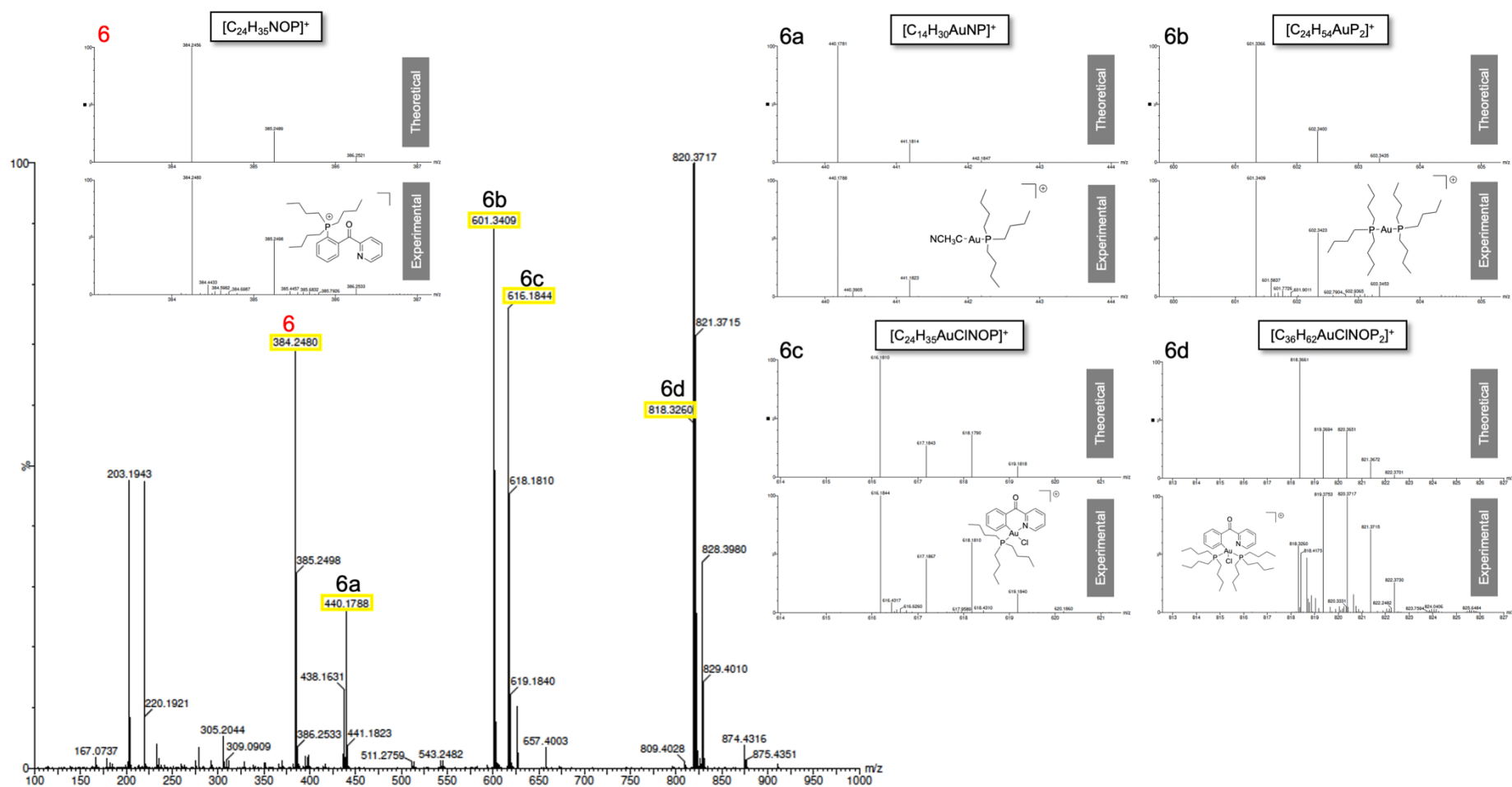


Figure S56 - HR-ESI-MS spectrum of **6** and other species (**6a-d**) formed during the reaction of $[Au(C^O)N]Cl_2$ with tri-*n*-butylphosphine. Inserts show simulated (top) and experimental (bottom) spectra of **6** and **6a-d**. Figure modified from ref 341. Copyright 2020, John Wiley and Sons <https://creativecommons.org/licenses/by/4.0/>.³⁴¹

Supplementary Material: Chapter 7

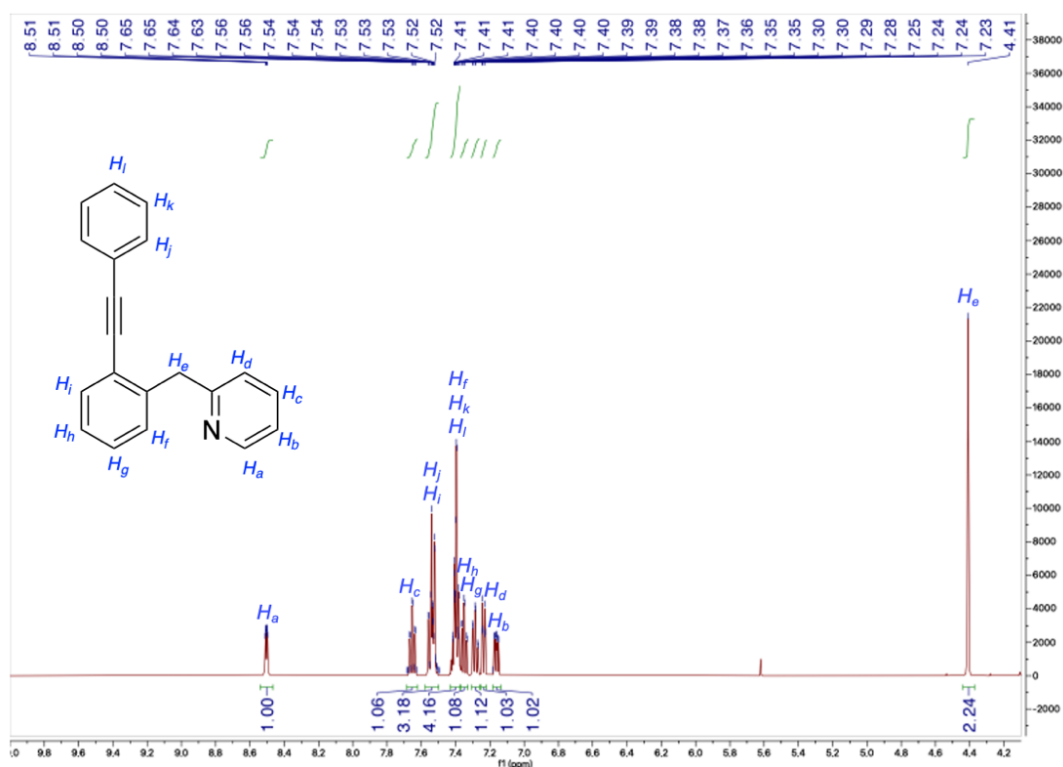


Figure S58 - ^1H NMR of **P** in $\text{acetone-}d_6$. Figure from ref 373. Copyright 2021, John Wiley and Sons <https://creativecommons.org/licenses/by/4.0/>.³⁷³

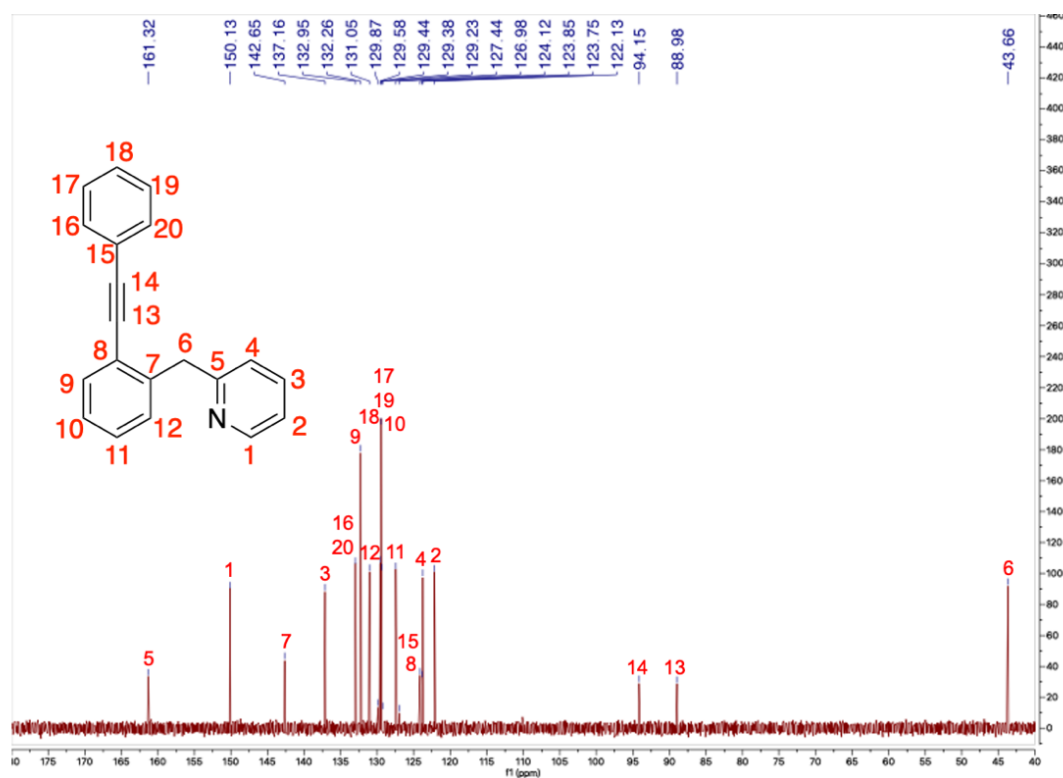


Figure S59 - $^{13}\text{C}\{^1\text{H}\}$ NMR of **P** in $\text{acetone-}d_6$. Figure from ref 373. Copyright 2021, John Wiley and Sons <https://creativecommons.org/licenses/by/4.0/>.³⁷³

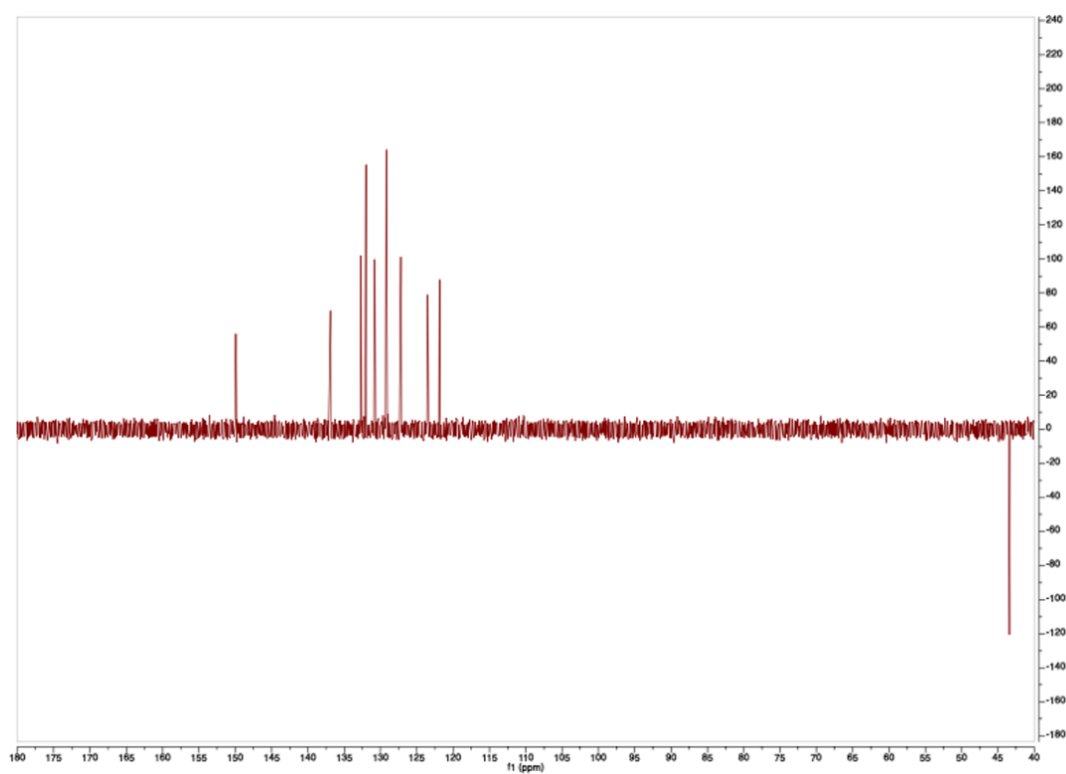


Figure S60 - ^{13}C DEPT NMR of **P** in acetone- d_6 . Figure from ref 373. Copyright 2021, John Wiley and Sons <https://creativecommons.org/licenses/by/4.0/>.³⁷³

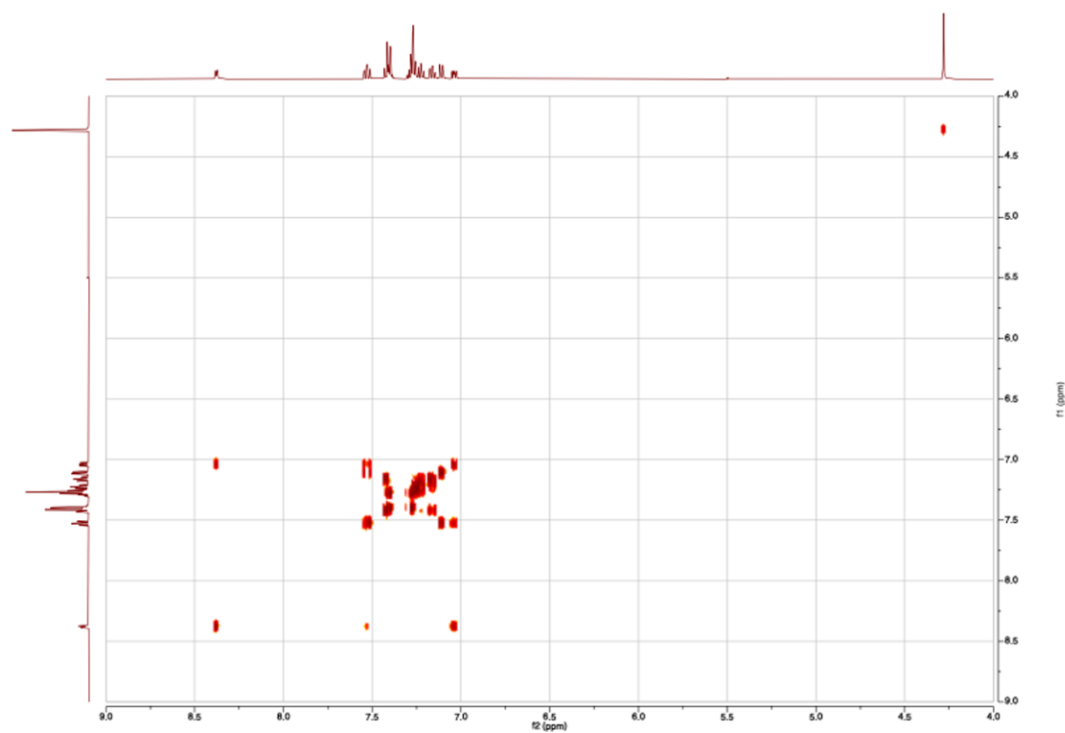


Figure S61 - ^1H - ^1H COSY NMR of **P** in acetone- d_6 . Figure from ref 373. Copyright 2021, John Wiley and Sons <https://creativecommons.org/licenses/by/4.0/>.³⁷³

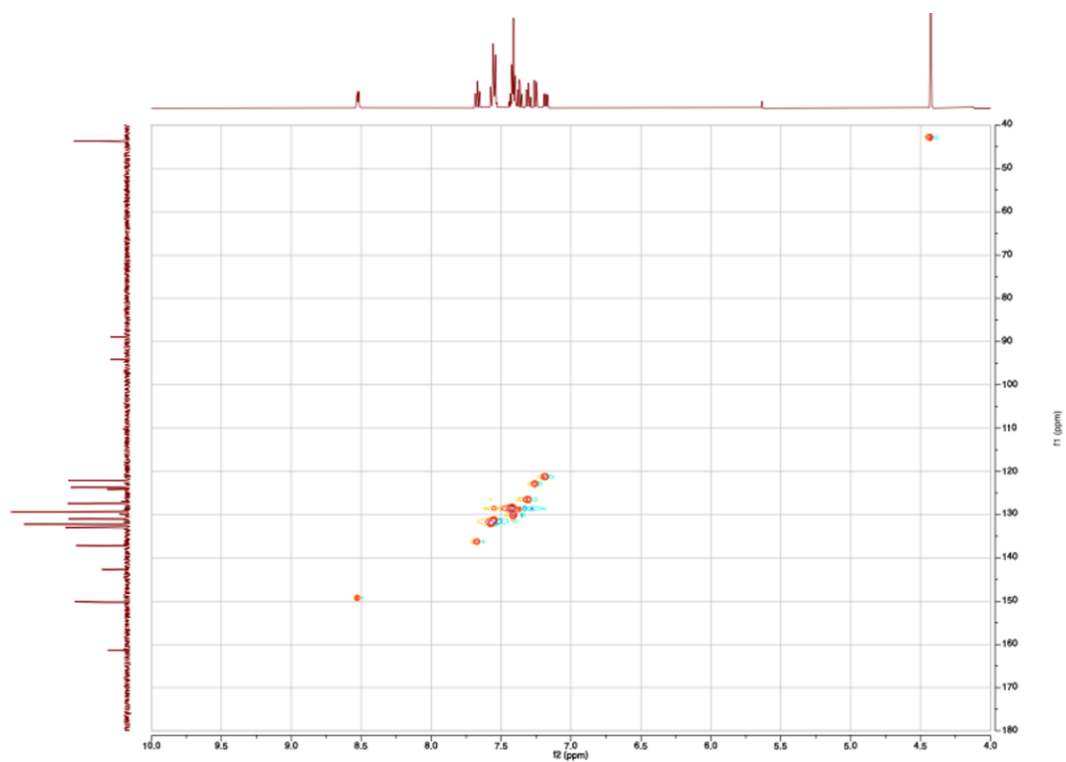


Figure S62 - ^1H - ^{13}C HSQC NMR of **P** in acetone- d_6 . Figure from ref 373. Copyright 2021, John Wiley and Sons <https://creativecommons.org/licenses/by/4.0/>.³⁷³

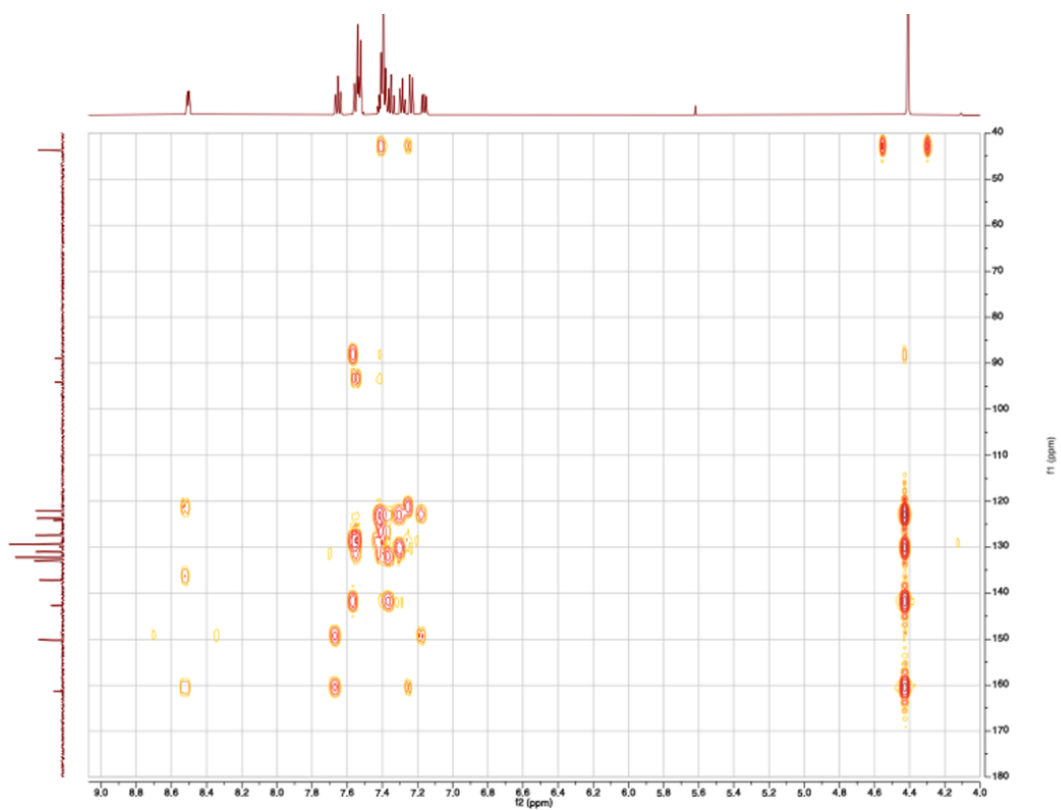


Figure S63 - ^1H - ^{13}C HMBC NMR of **P** in acetone- d_6 . Figure from ref 373. Copyright 2021, John Wiley and Sons <https://creativecommons.org/licenses/by/4.0/>.³⁷³

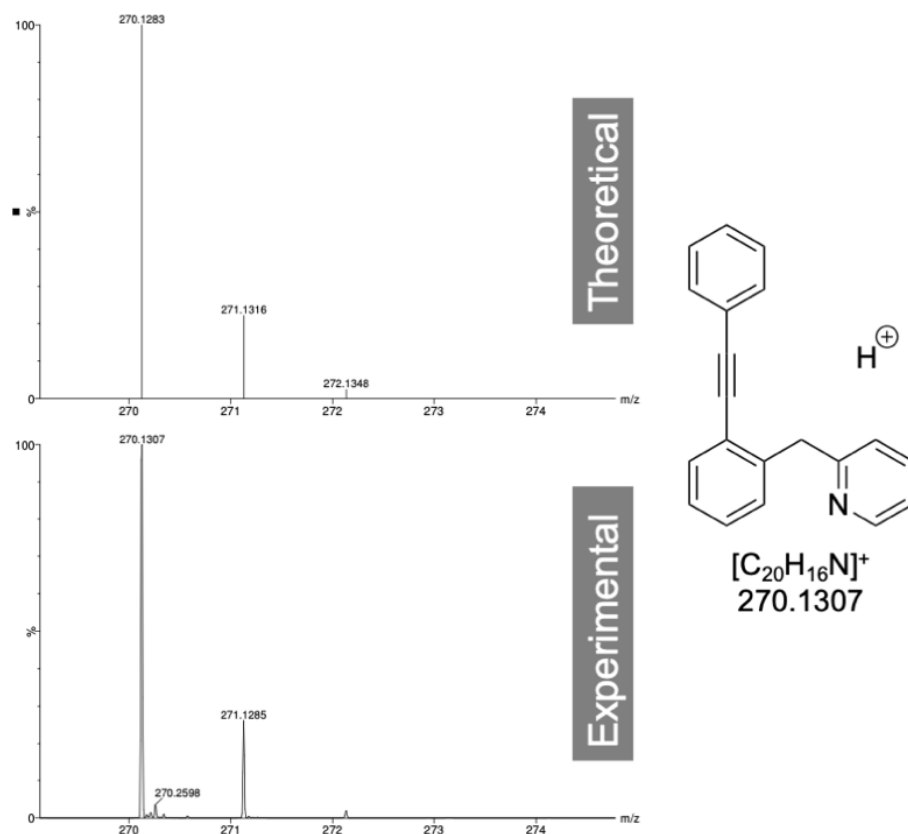


Figure S64 - HR-ESI-MS simulated (top) and experimental (below) spectra of **P**. Figure from ref 373. Copyright 2021, John Wiley and Sons <https://creativecommons.org/licenses/by/4.0/>.³⁷³

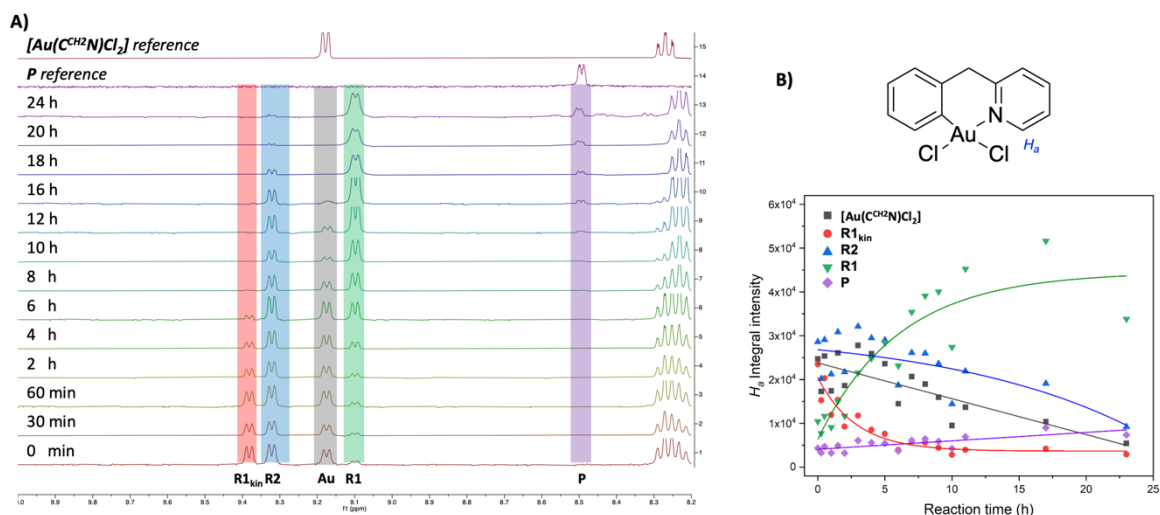


Figure S65 - **A**) ^1H NMR spectra (between 8.2 and 10 ppm) of the reaction between $[\text{Au}(\text{C}^{\text{CH}_2\text{N}})\text{Cl}_2]$ (1 eq.) and AgPhCC (2 eq.) in $\text{DMSO-}d_6$ followed over 24 h at r.t.. The spectrum of the starting material $[\text{Au}(\text{C}^{\text{CH}_2\text{N}})\text{Cl}_2]$ and of the final purified product **P** are reported as reference. **B**) Structure of $[\text{Au}(\text{C}^{\text{CH}_2\text{N}})\text{Cl}_2]$ highlighting the proton ortho to the pyridyl N (H_a), and evolution of the intensities of the integrals of H_a chemical shifts over 24 h. Fitting lines have been included as a visual aid to follow the trend over the selected time window. Figure modified from ref 373. Copyright 2021, John Wiley and Sons <https://creativecommons.org/licenses/by/4.0/>.³⁷³

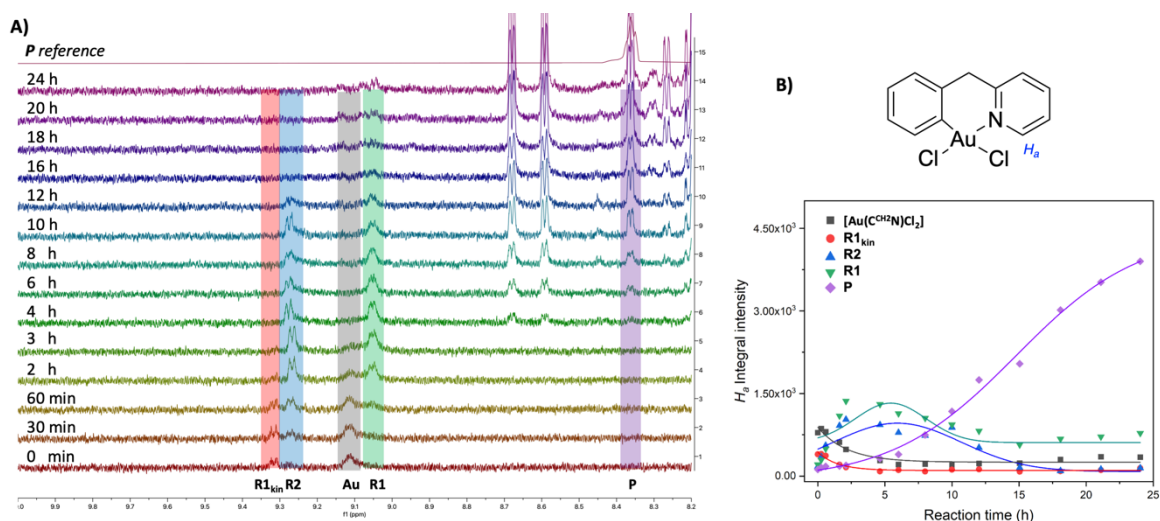


Figure S66 - **A)** ^1H NMR spectra (between 8.2 and 10 ppm) of the reaction between $[\text{Au}(\text{C}^{\text{H}_2\text{N}})\text{Cl}_2]$ (1 eq.) and AgPhCC (2 eq.) in MeOH- d_4 followed over 24 h at r.t.. The spectrum of the final purified product **P** is reported as reference. The reference spectrum for $[\text{Au}(\text{C}^{\text{H}_2\text{N}})\text{Cl}_2]$ cannot be reported due to poor solubility in this solvent. **B)** Structure of $[\text{Au}(\text{C}^{\text{H}_2\text{N}})\text{Cl}_2]$ highlighting the proton ortho to the pyridyl N (H_a), and evolution of the intensities of the integrals of H_a chemical shifts over 24 h. Fitting lines have been included as a visual aid to follow the trend over the selected time window. Figure modified from ref 373. Copyright 2021, John Wiley and Sons <https://creativecommons.org/licenses/by/4.0/>.³⁷³

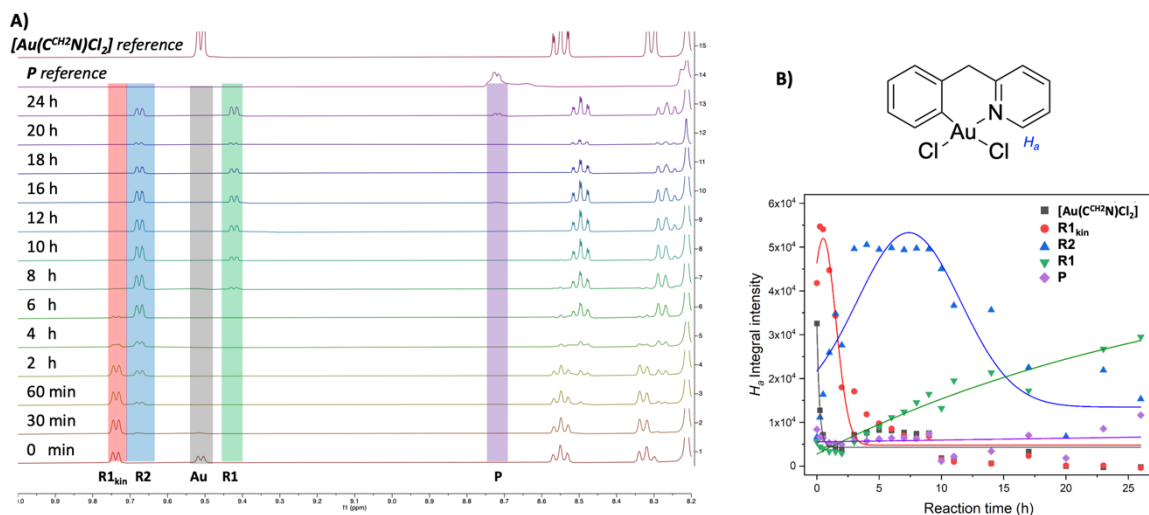


Figure S67 - **A)** ^1H NMR spectra (between 8.2 and 10 ppm) of the reaction between $[\text{Au}(\text{C}^{\text{H}_2\text{N}})\text{Cl}_2]$ (1 eq.) and AgPhCC (2 eq.) in DMF- d_7 followed over 24 h at r.t.. The spectrum of the starting material $[\text{Au}(\text{C}^{\text{H}_2\text{N}})\text{Cl}_2]$ and of the final purified product **P** are reported as reference. **B)** Structure of $[\text{Au}(\text{C}^{\text{H}_2\text{N}})\text{Cl}_2]$ highlighting the proton ortho to the pyridyl N (H_a), and evolution of the intensities of the integrals of H_a chemical shifts over 24 h. Fitting lines have been included as a visual aid to follow the trend over the selected time window. Figure modified from ref 373. Copyright 2021, John Wiley and Sons <https://creativecommons.org/licenses/by/4.0/>.³⁷³

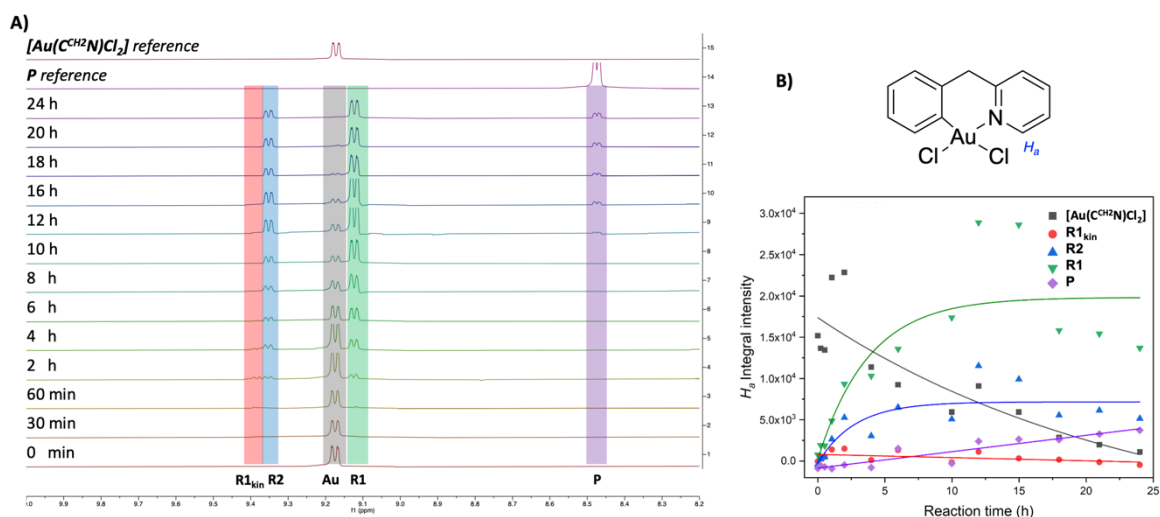


Figure S68 - **A)** ^1H NMR spectra (between 8.2 and 10 ppm) of the reaction between $[\text{Au}(\text{C}^{\text{CH}_2\text{N}})\text{Cl}_2]$ (1 eq.) and AgPhCC (2 eq.) in MeCN-d_3 followed over 24 h at r.t.. The spectrum of the starting material $[\text{Au}(\text{C}^{\text{CH}_2\text{N}})\text{Cl}_2]$ and of the final purified product **P** are reported as reference. **B)** Structure of $[\text{Au}(\text{C}^{\text{CH}_2\text{N}})\text{Cl}_2]$ highlighting the proton ortho to the pyridyl N (H_a), and evolution of the intensities of the integrals of H_a chemical shifts over 24 h. Fitting lines have been included as a visual aid to follow the trend over the selected time window. Figure modified from ref 373. Copyright 2021, John Wiley and Sons <https://creativecommons.org/licenses/by/4.0/>.³⁷³

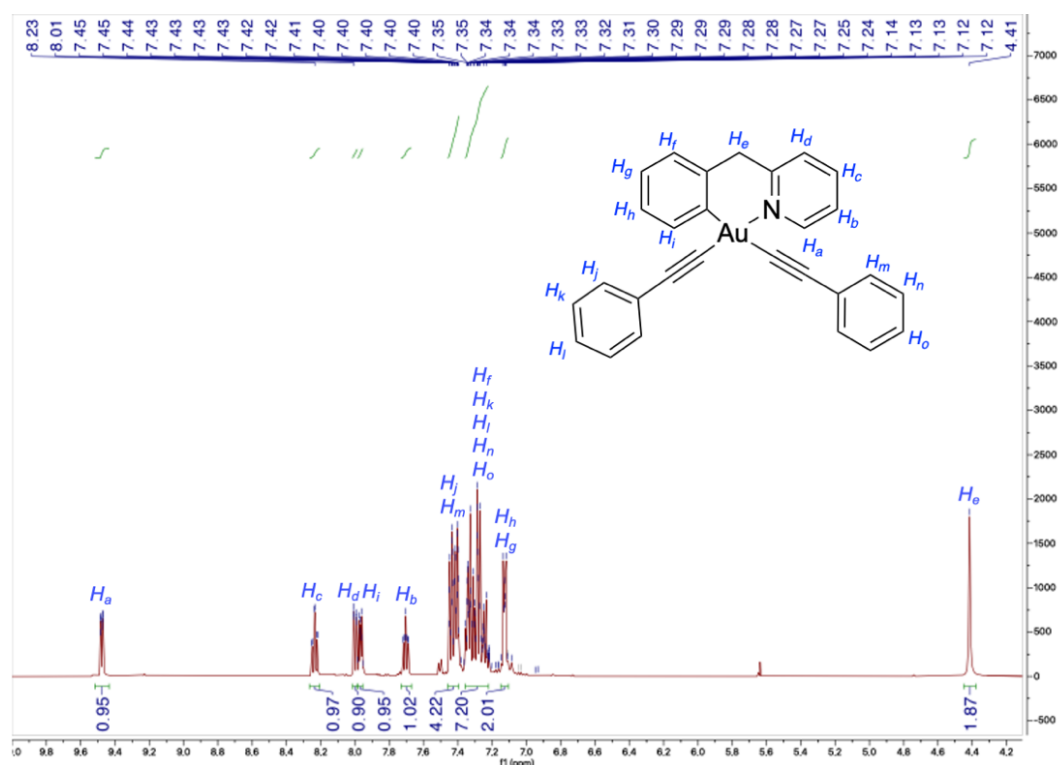


Figure S69 - ^1H NMR of **R2** in acetone- d_6 . Figure from ref 373. Copyright 2021, John Wiley and Sons <https://creativecommons.org/licenses/by/4.0/>.³⁷³

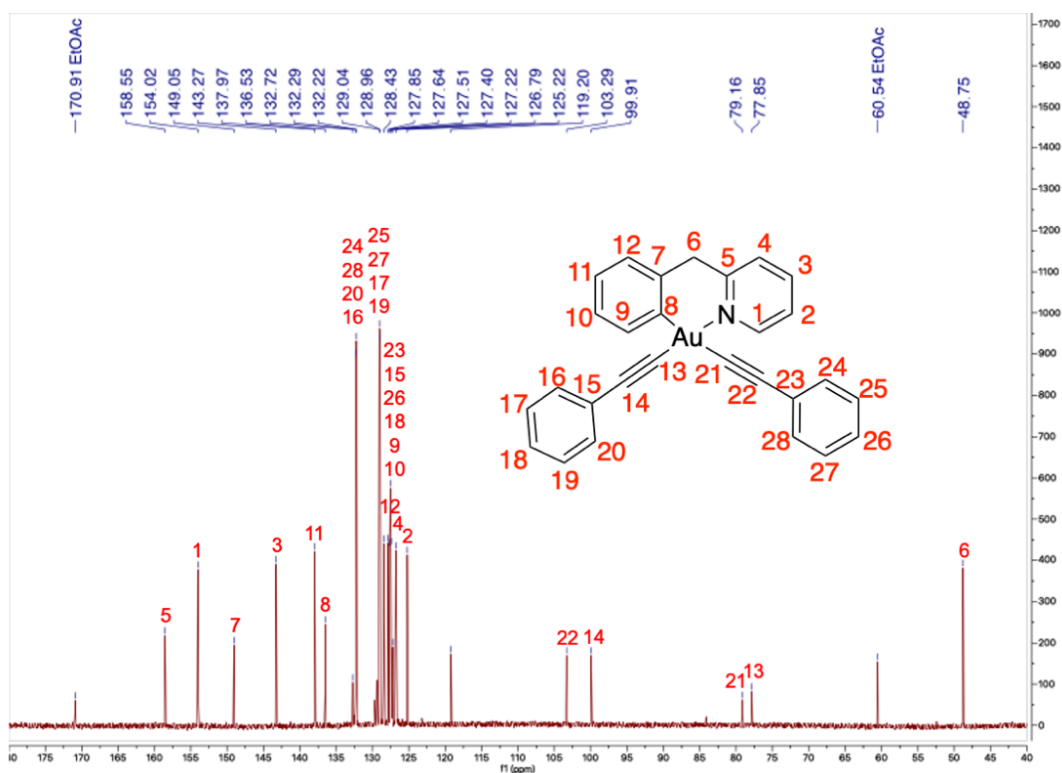


Figure S70 - $^{13}\text{C}\{^1\text{H}\}$ NMR of **R2** in acetone- d_6 . Figure from ref 373. Copyright 2021, John Wiley and Sons <https://creativecommons.org/licenses/by/4.0/>.³⁷³

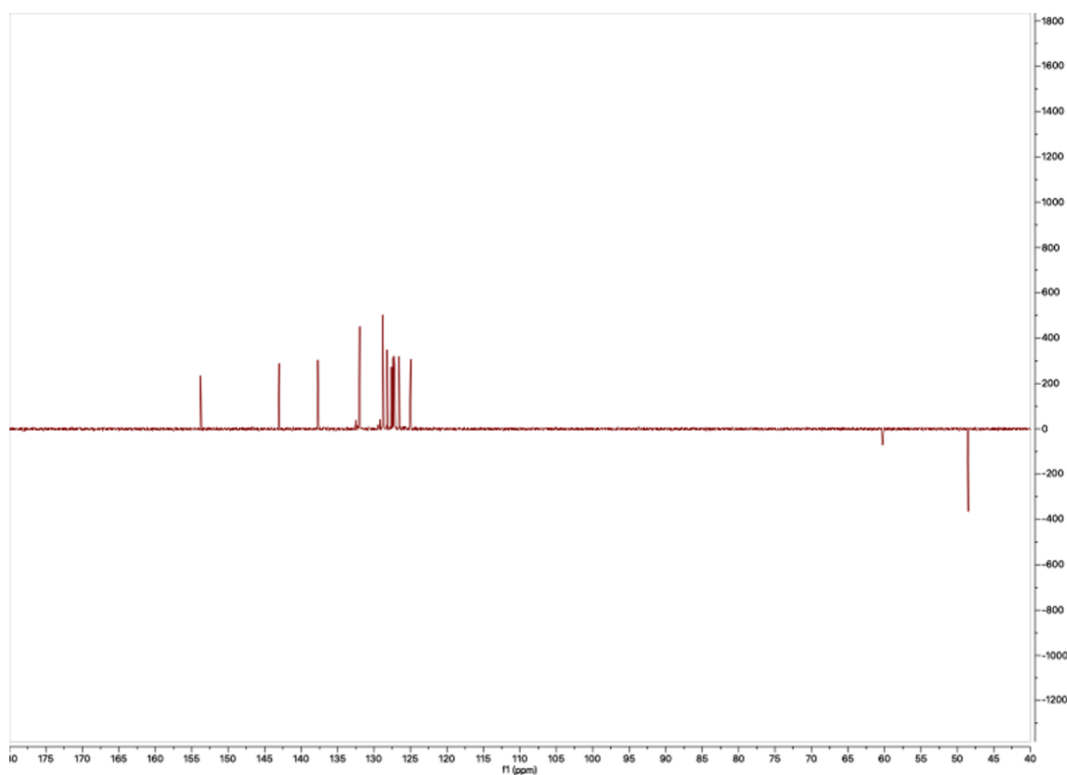


Figure S71 - ^{13}C DEPT NMR of **R2** in acetone- d_6 . Figure from ref 373. Copyright 2021, John Wiley and Sons <https://creativecommons.org/licenses/by/4.0/>.³⁷³

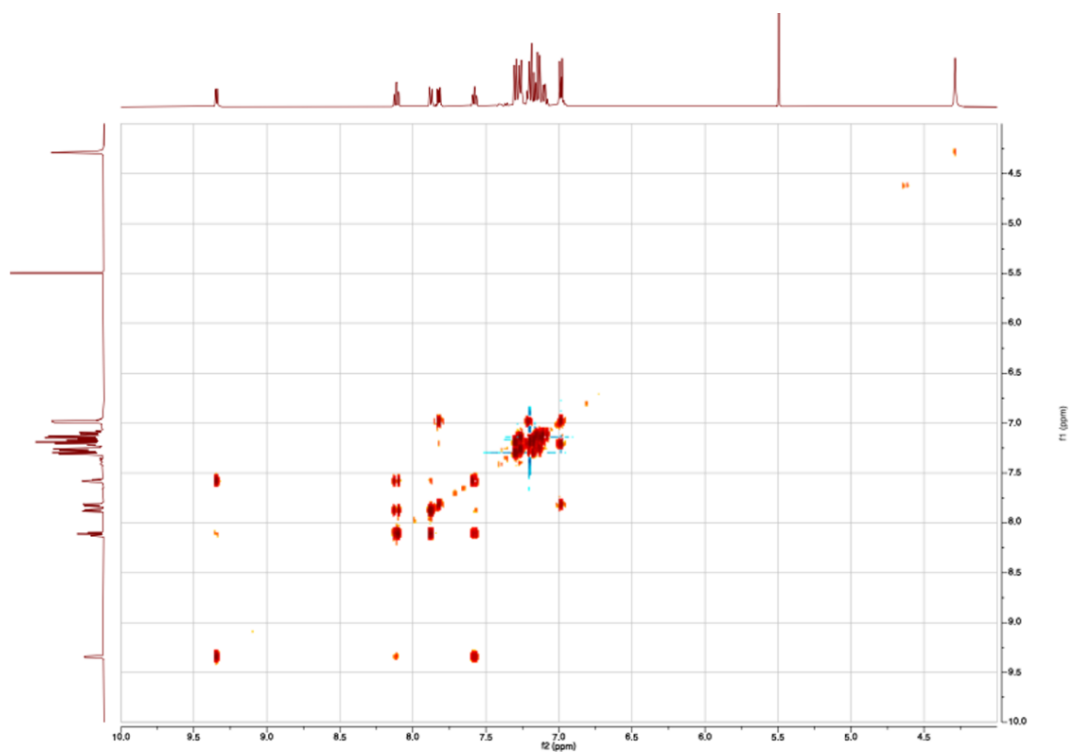


Figure S72 - ^1H - ^1H COSY NMR of **R2** in acetone- d_6 . Figure from ref 373. Copyright 2021, John Wiley and Sons <https://creativecommons.org/licenses/by/4.0/>.³⁷³

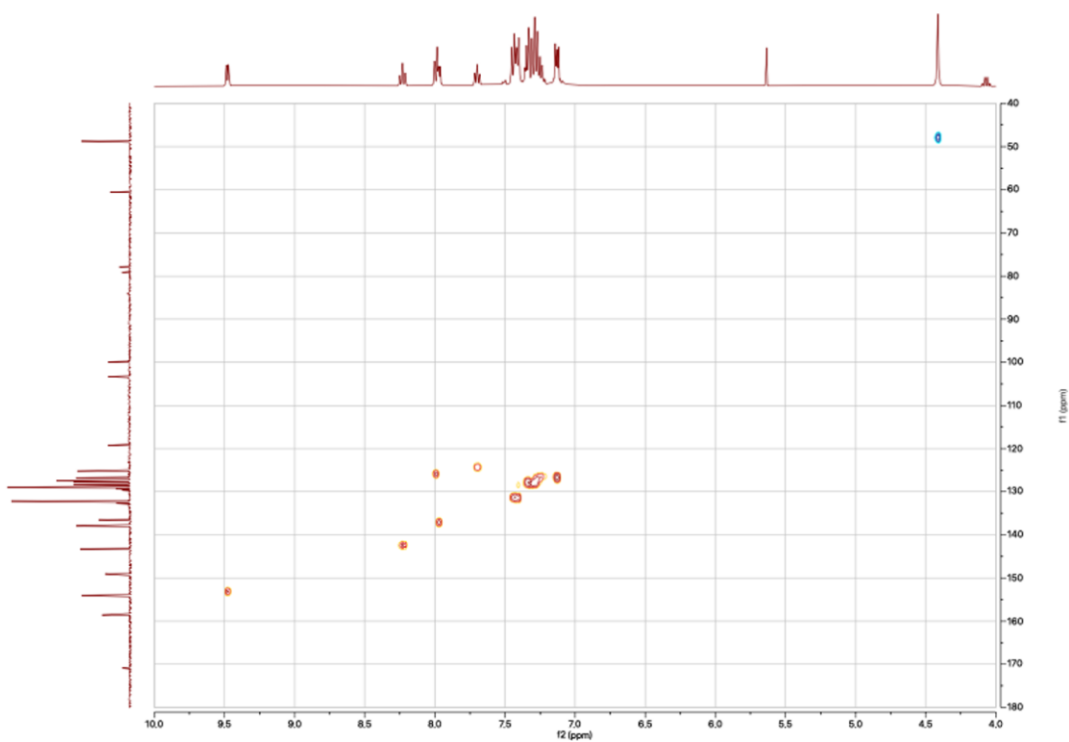


Figure S73 - ^1H - ^{13}C HSQC NMR of **R2** in acetone- d_6 . Figure from ref 373. Copyright 2021, John Wiley and Sons <https://creativecommons.org/licenses/by/4.0/>.³⁷³

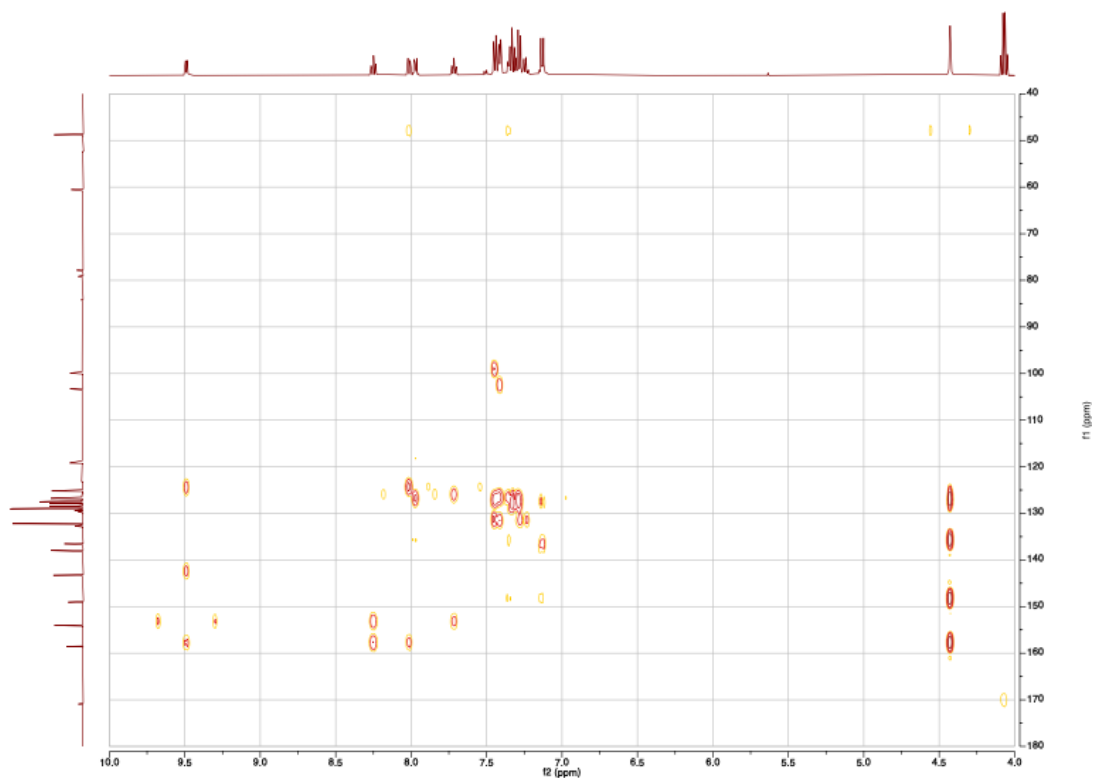


Figure S74 - ^1H - ^{13}C HMBC NMR spectrum of **R2** in acetone- d_6 .³⁷³

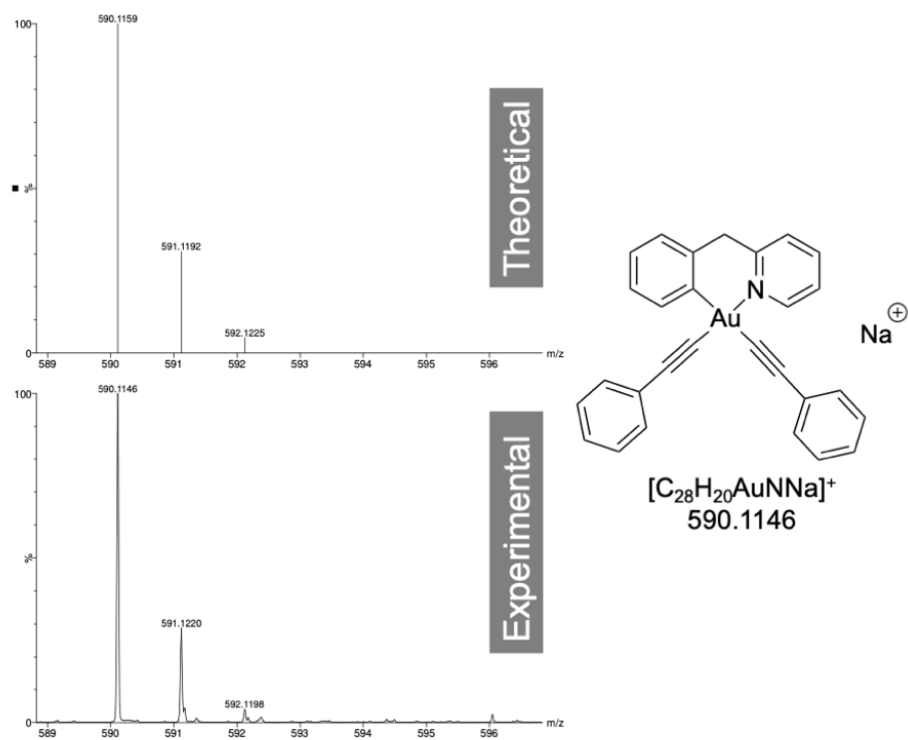


Figure S75 - HR-ESI-MS simulated (top) and experimental (below) spectra of **R2**. Figure from ref 373. Copyright 2021, John Wiley and Sons <https://creativecommons.org/licenses/by/4.0/>.³⁷³

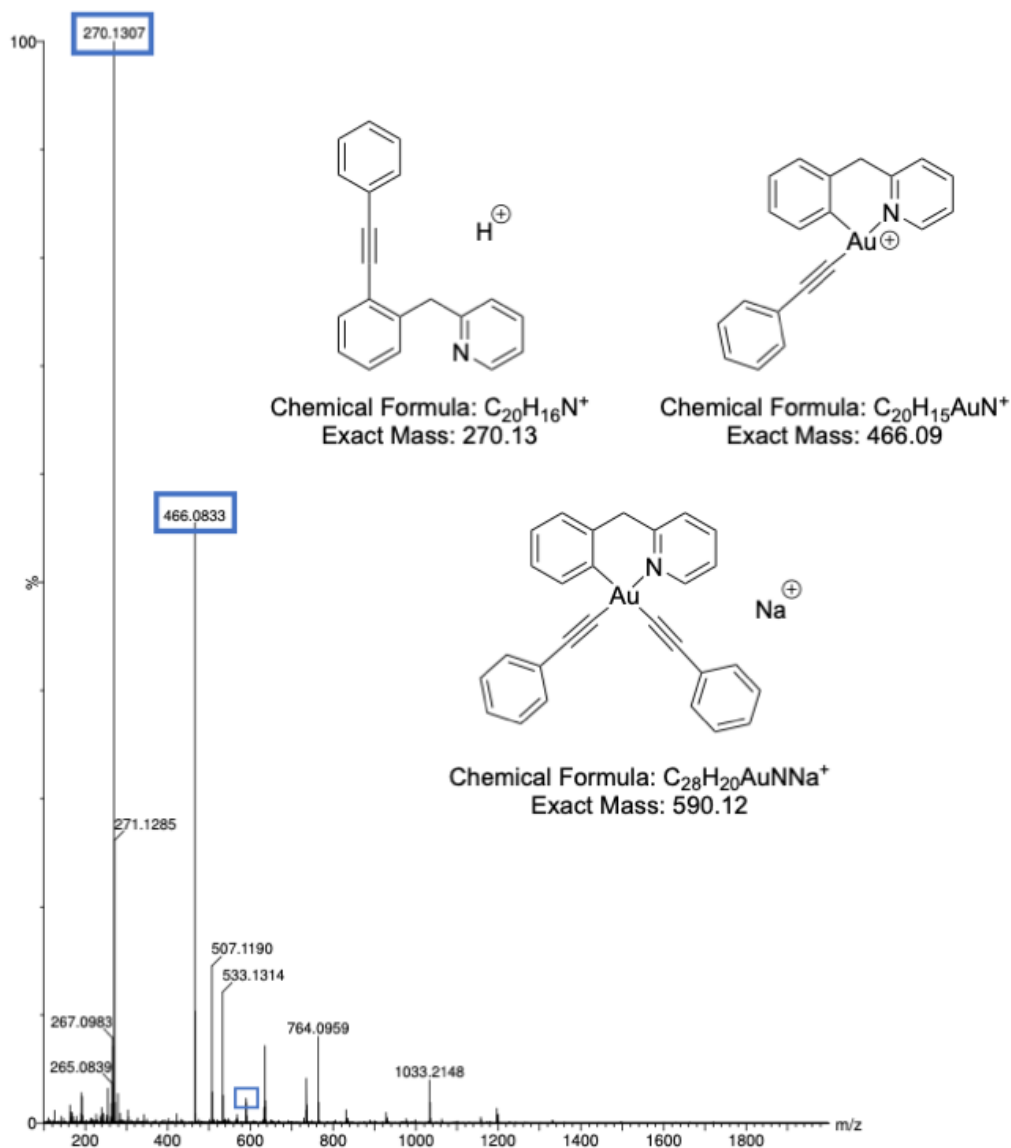


Figure S76 - HR-ESI-MS of crude obtained by reacting $[Au(C^{CH_2}N)Cl_2]$ with AgPhCC in a 1:3 ratio in acetone (25 mL). Figure from ref 373. Copyright 2021, John Wiley and Sons <https://creativecommons.org/licenses/by/4.0/>.³⁷³

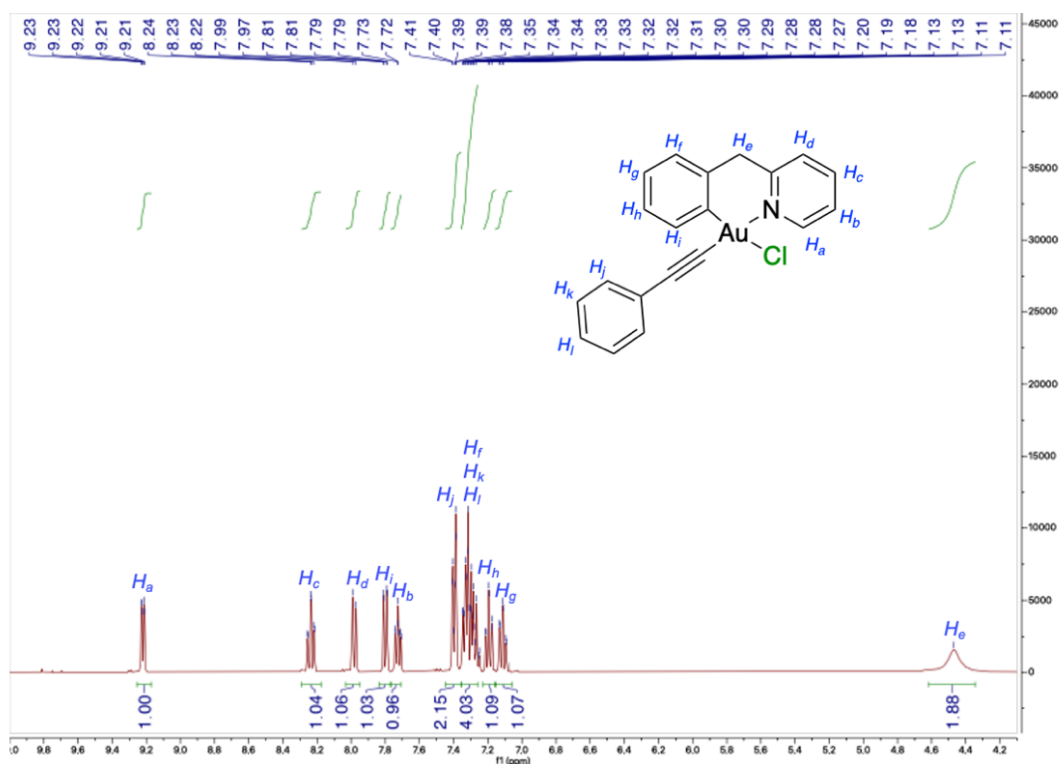


Figure S77 - ^1H NMR spectrum of **R1** in acetone- d_6 . Figure from ref 373. Copyright 2021, John Wiley and Sons <https://creativecommons.org/licenses/by/4.0/>.³⁷³

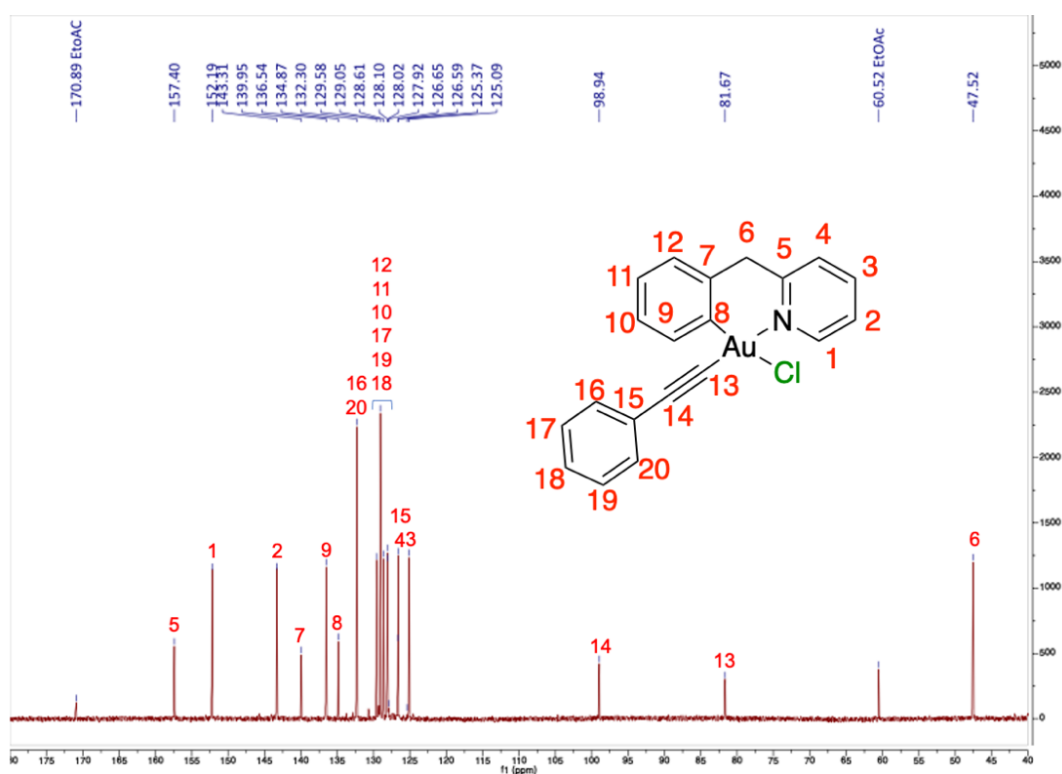


Figure S78 - $^{13}\text{C}\{^1\text{H}\}$ NMR spectrum of **R1** in acetone- d_6 . Figure from ref 373. Copyright 2021, John Wiley and Sons <https://creativecommons.org/licenses/by/4.0/>.³⁷³

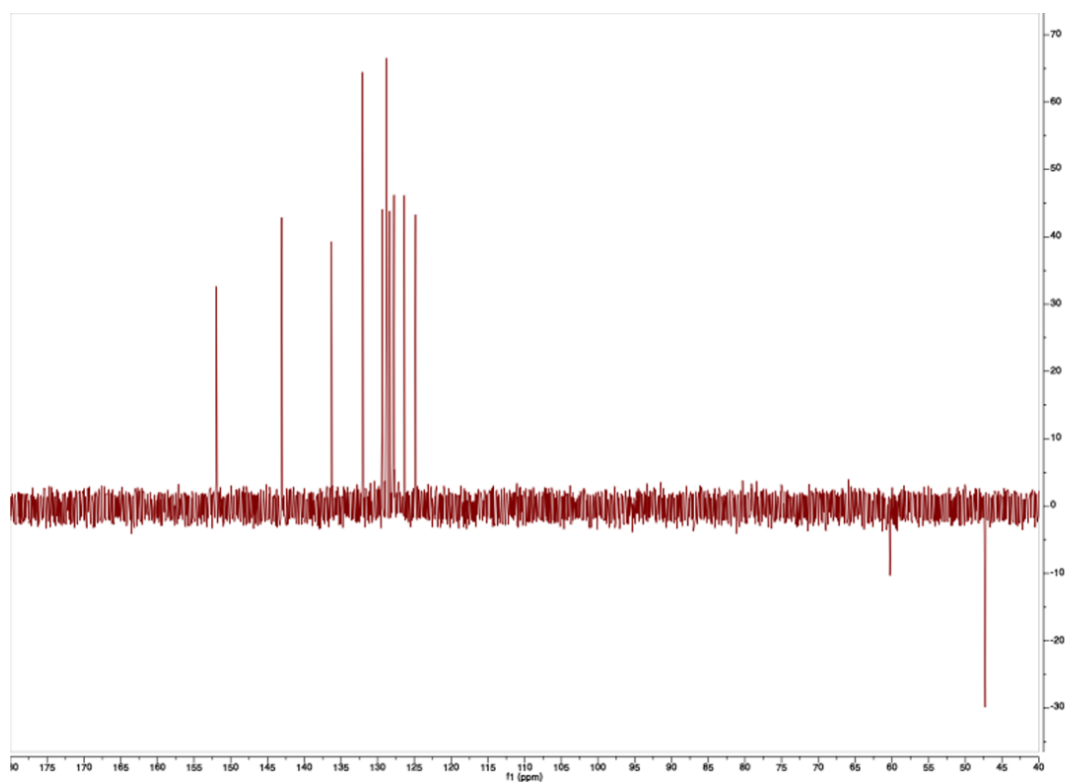


Figure S79 - ^{13}C DEPT NMR spectrum of **R1** in acetone- d_6 . Figure from ref 373. Copyright 2021, John Wiley and Sons <https://creativecommons.org/licenses/by/4.0/>.³⁷³

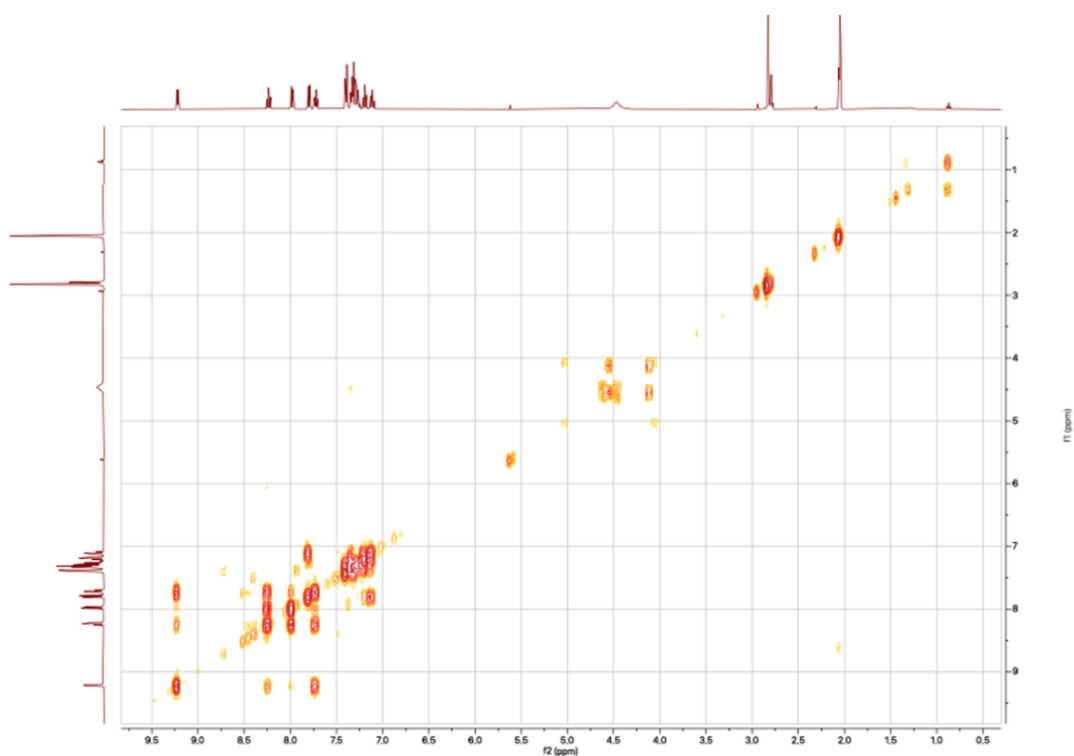


Figure S80 - ^1H - ^1H COSY NMR spectrum of **R1** in acetone- d_6 . Figure from ref 373. Copyright 2021, John Wiley and Sons <https://creativecommons.org/licenses/by/4.0/>.³⁷³

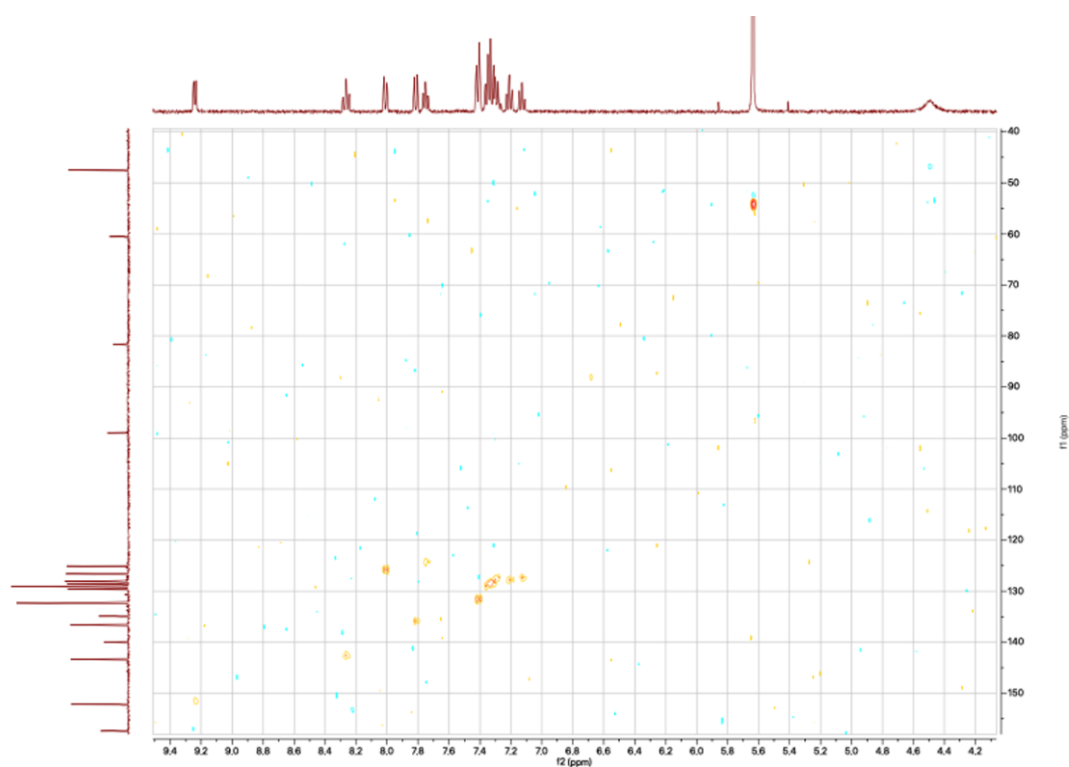


Figure S81 - ^1H - ^{13}C HSQC NMR spectrum of **R1** in acetone- d_6 . Figure from ref 373. Copyright 2021, John Wiley and Sons <https://creativecommons.org/licenses/by/4.0/>.³⁷³

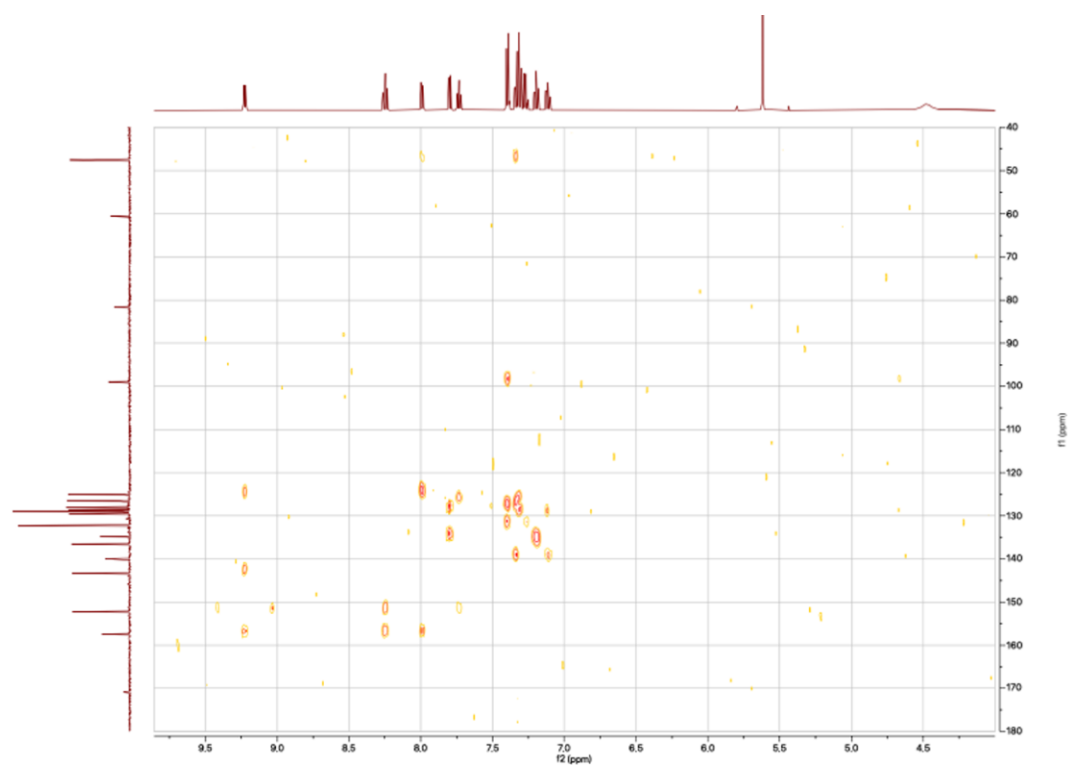


Figure S82 - ^1H - ^{13}C HMBC NMR spectrum of **R1** in acetone- d_6 . Figure from ref 373. Copyright 2021, John Wiley and Sons <https://creativecommons.org/licenses/by/4.0/>.³⁷³

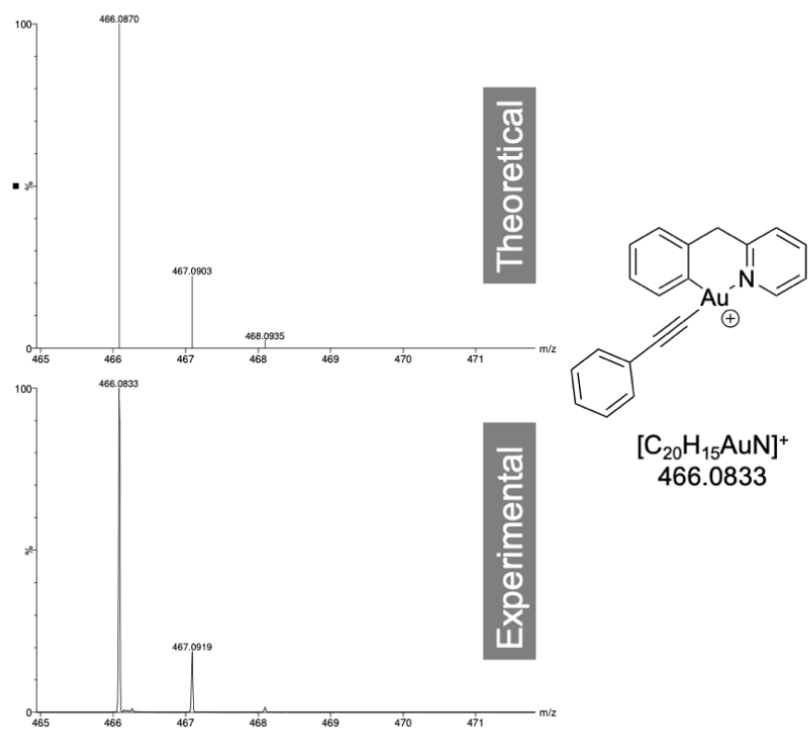


Figure S83 - HR-ESI-MS simulated (top) and experimental (below) spectra of **R1**. Figure from ref 373. Copyright 2021, John Wiley and Sons <https://creativecommons.org/licenses/by/4.0/>.³⁷³

Supplementary Material: Chapter 8

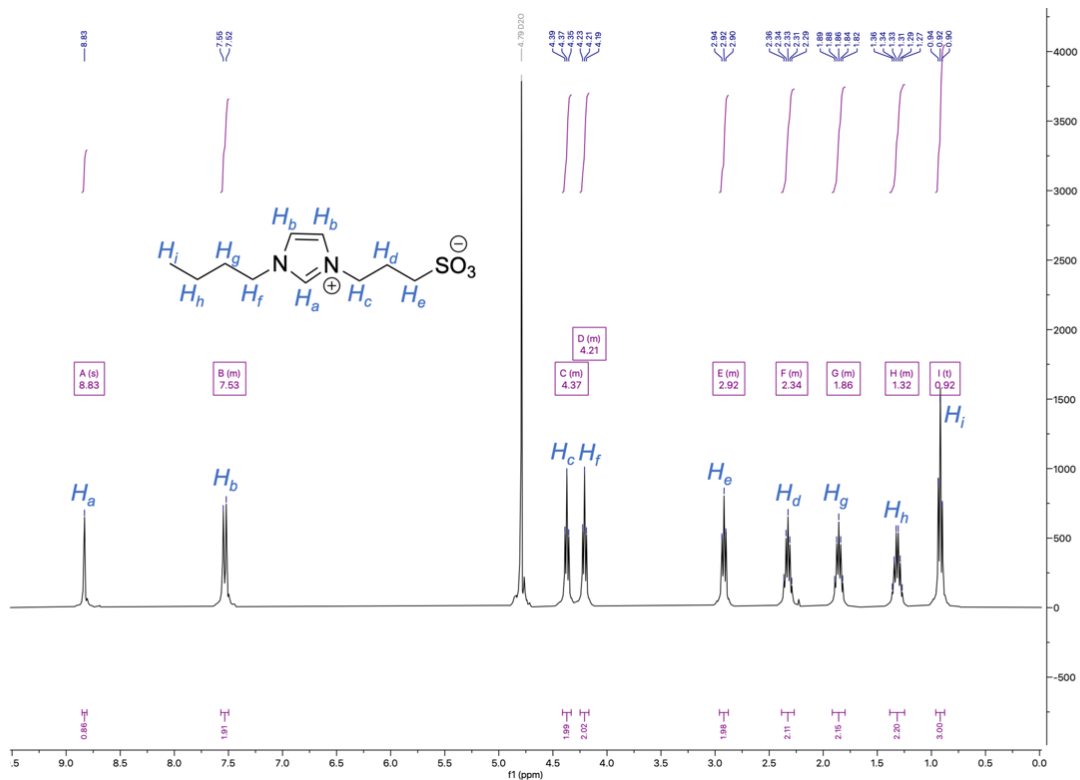


Figure S84 - ^1H NMR of **NHC-1** in D_2O .



Figure S85 - $^{13}\text{C}\{^1\text{H}\}$ NMR of **NHC-1** in D_2O .

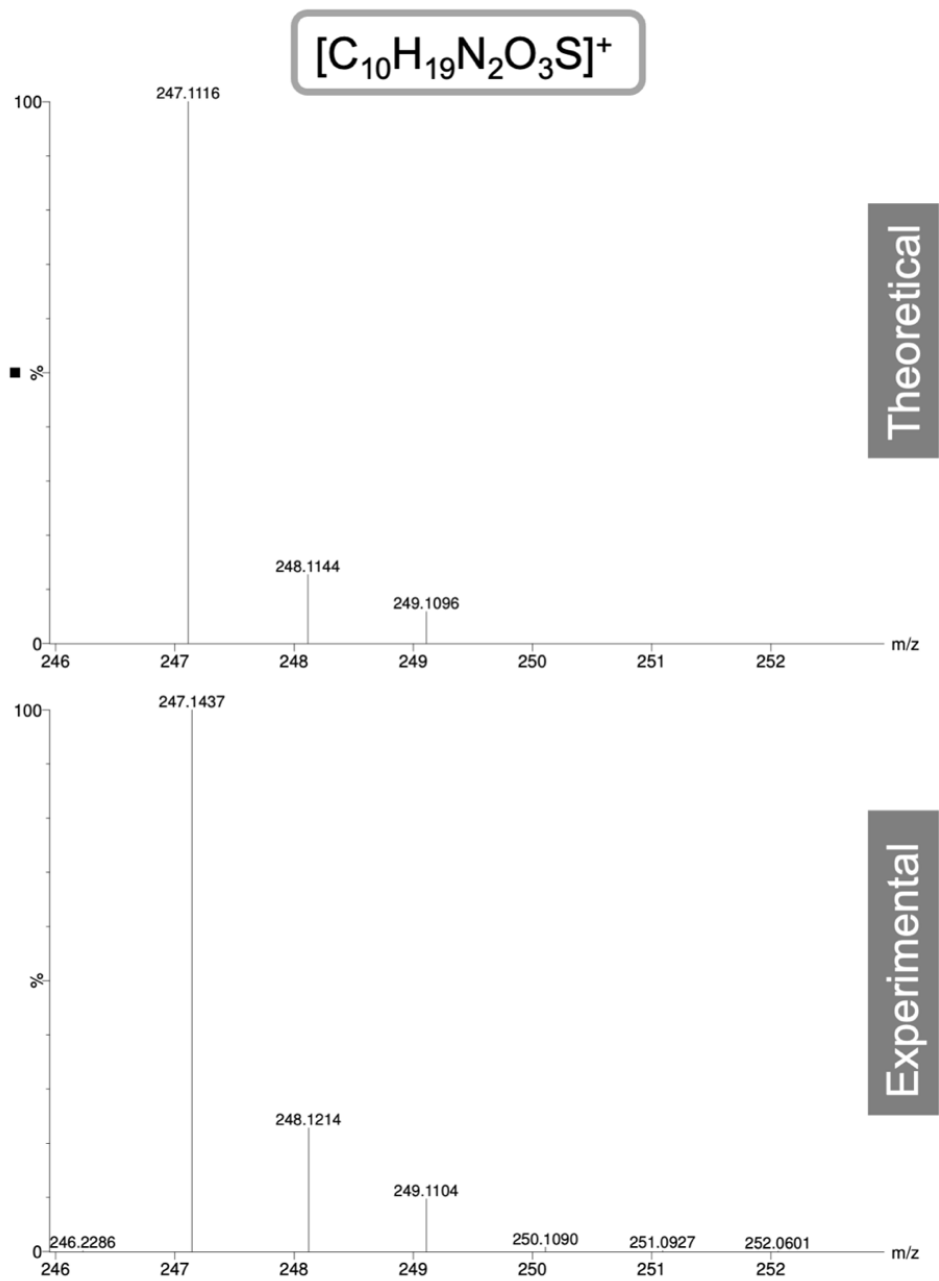


Figure S86 - HR-ESI-MS simulated (top) and experimental (below) spectra of **NHC-1**.

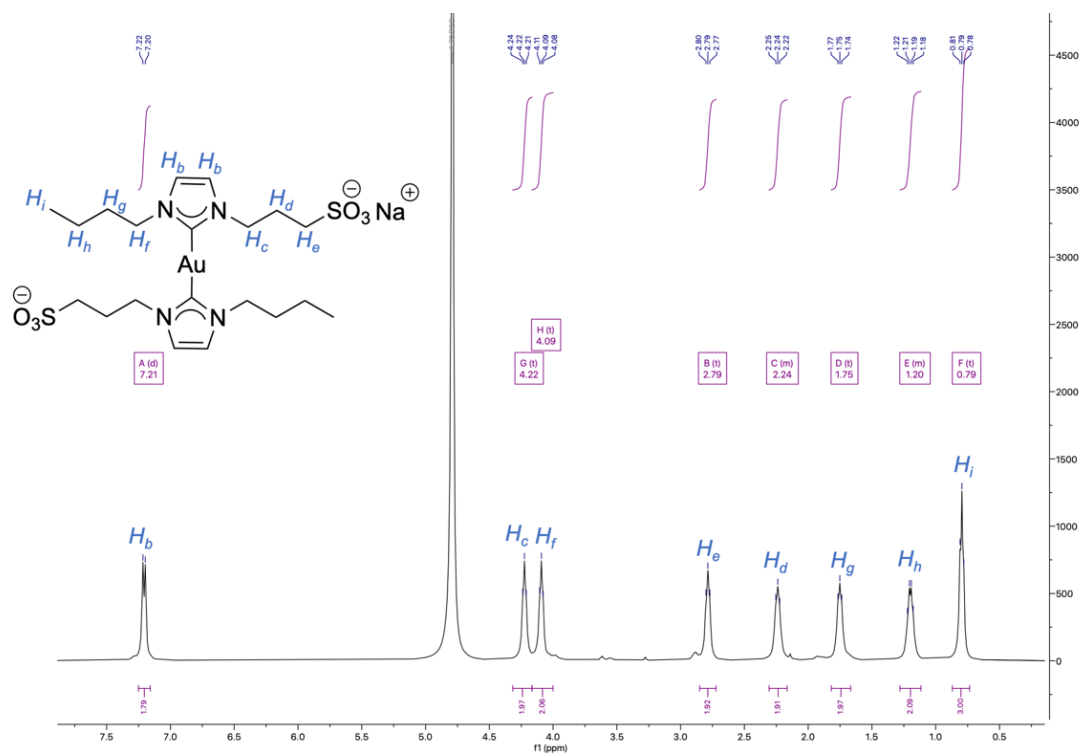


Figure S87 - ^1H NMR of AuNHC-1 in D_2O .

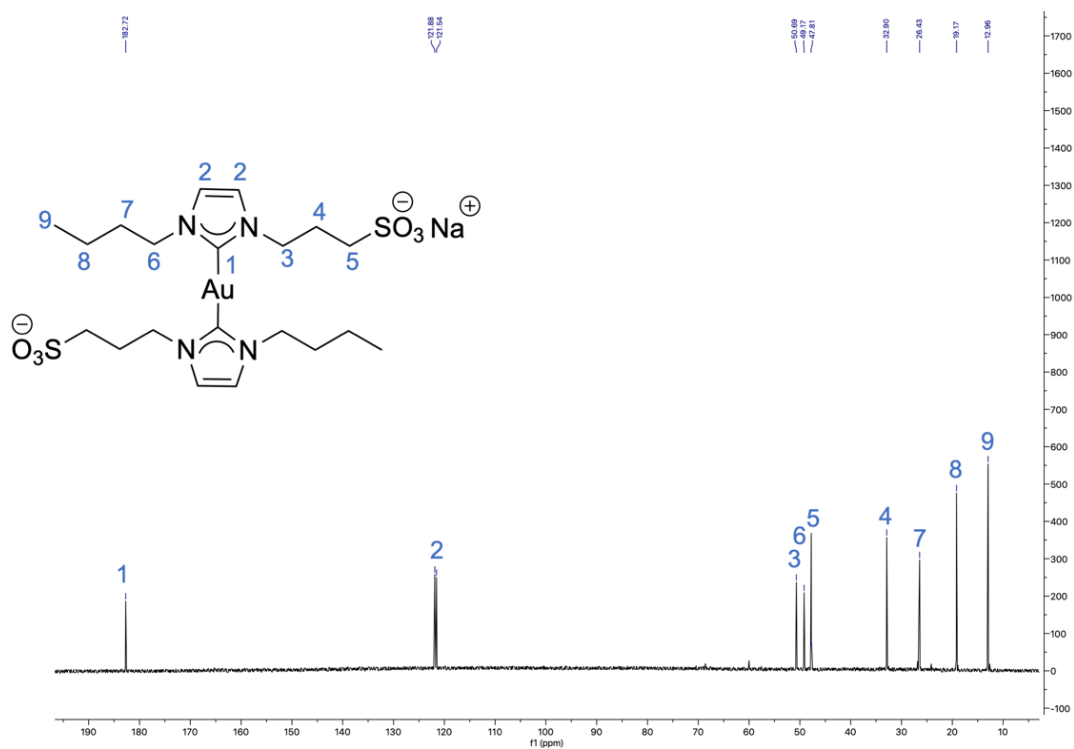


Figure S88 - $^{13}\text{C}\{^1\text{H}\}$ NMR of AuNHC-1 in D_2O .

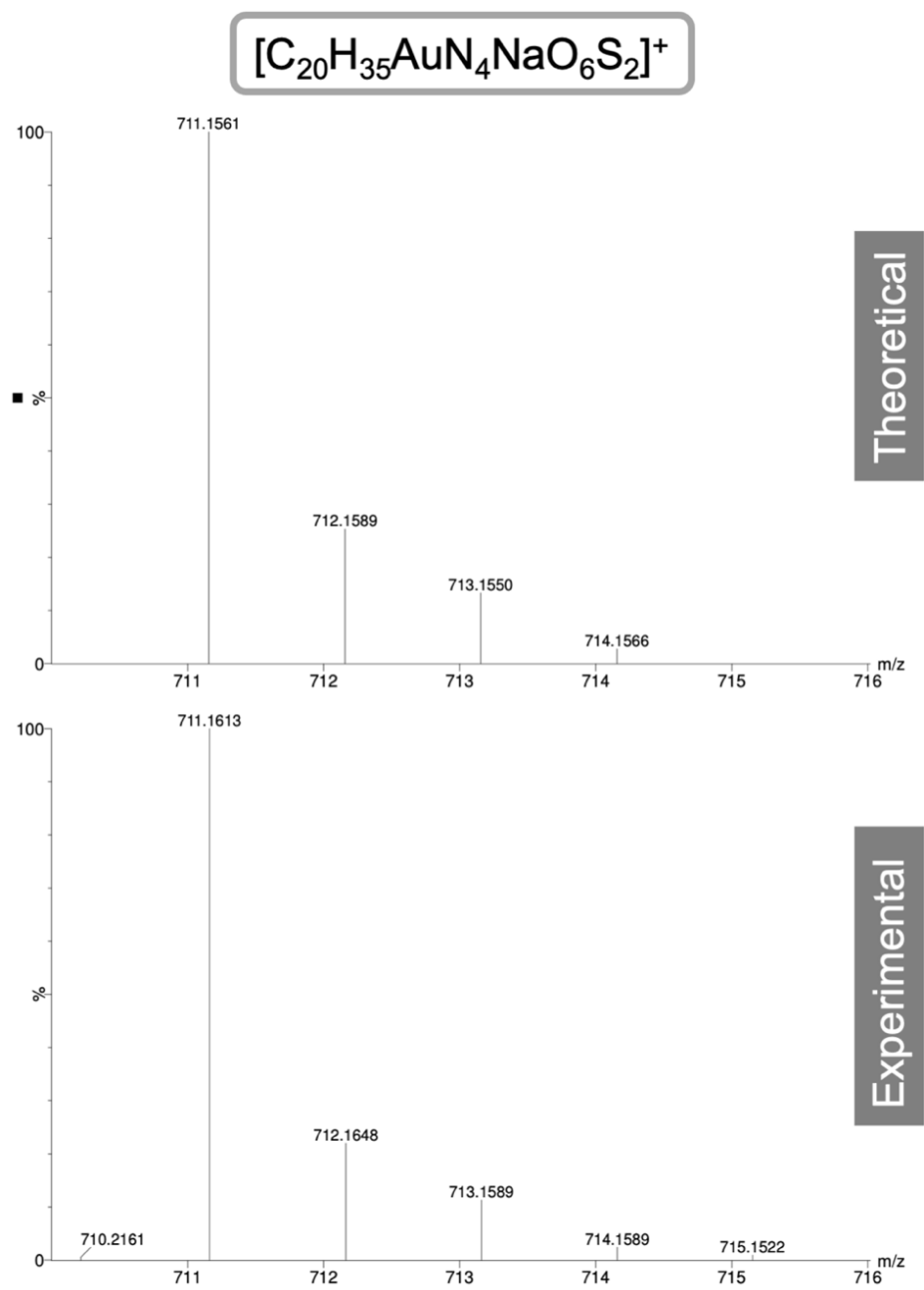


Figure S89 - HR-ESI-MS simulated (top) and experimental (below) spectra of **AuNHC-1**.

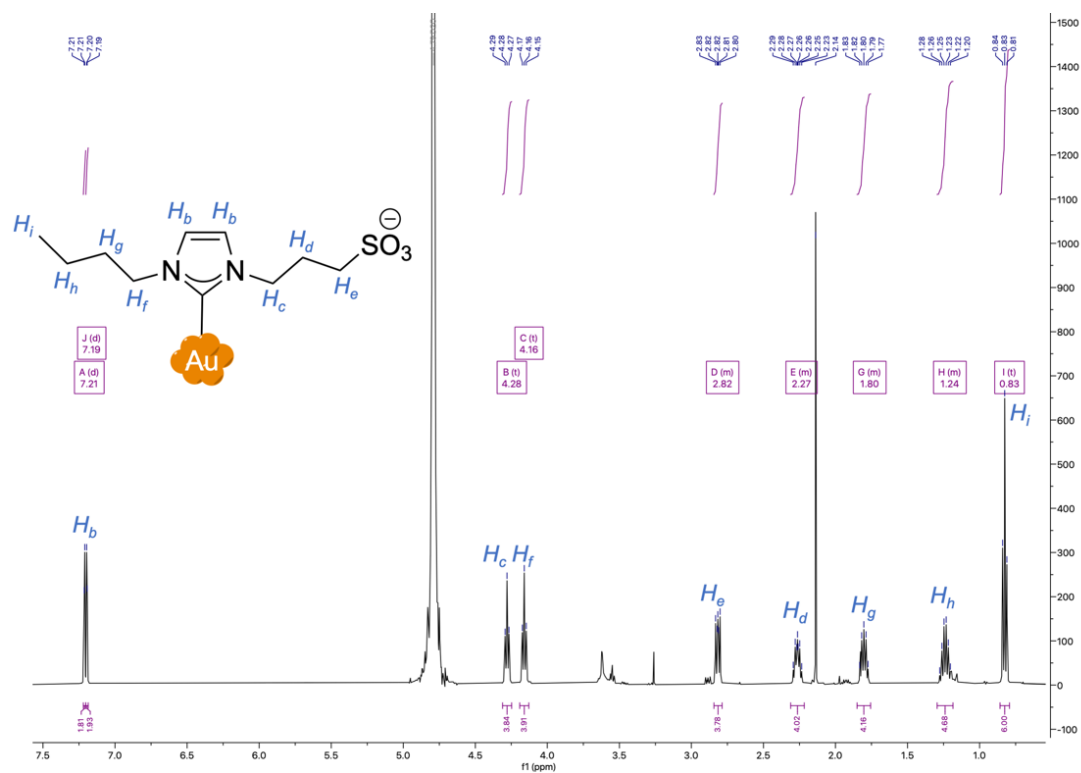


Figure S90 - 1H NMR of AuNP-1 in D_2O .

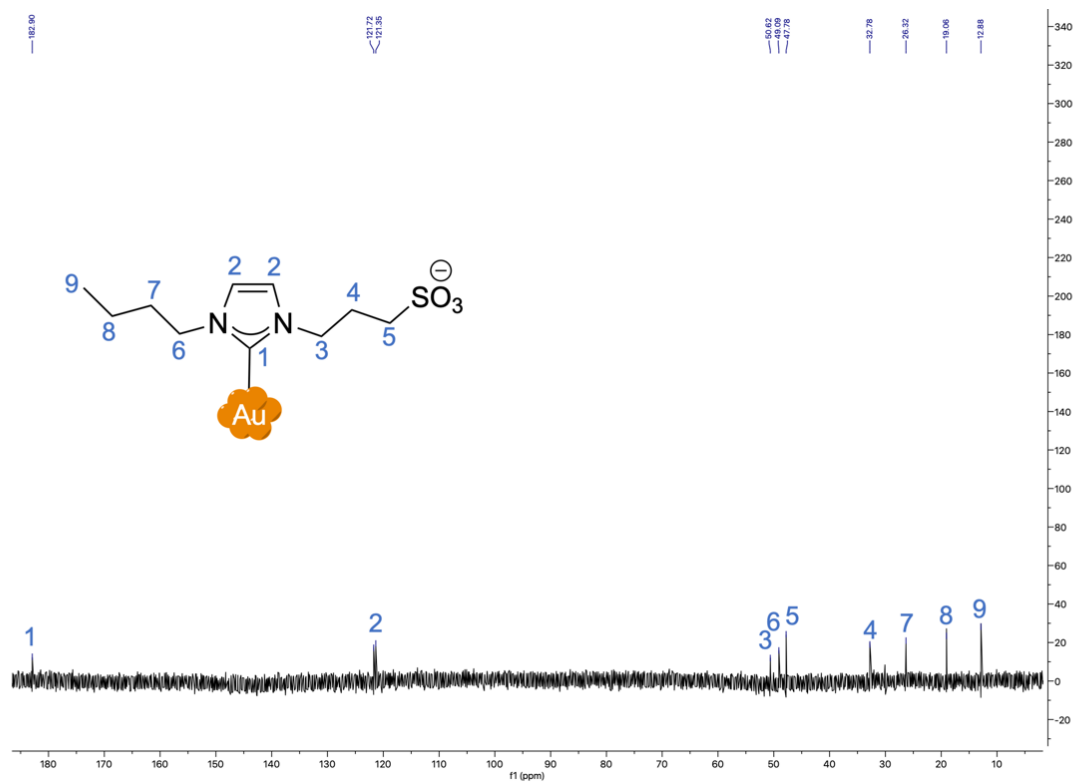


Figure S91 - $^{13}C\{^1H\}$ NMR of AuNP-1 in D_2O .

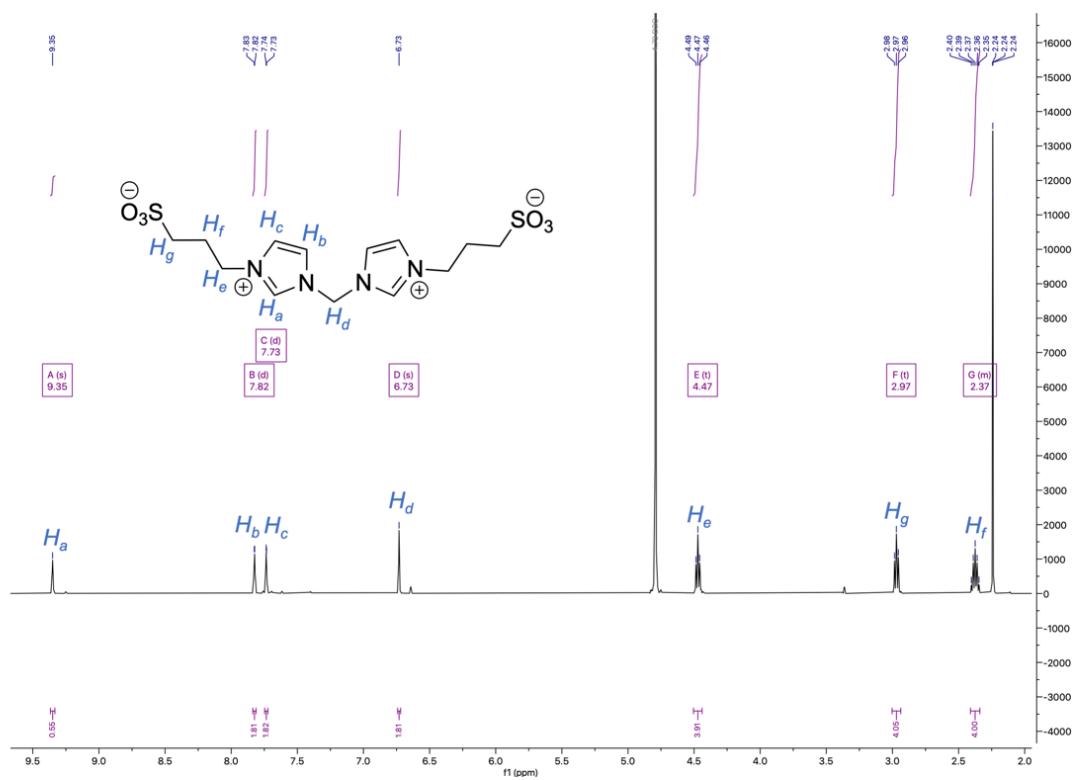


Figure S92 - ^1H NMR of **NHC-2** in D_2O .

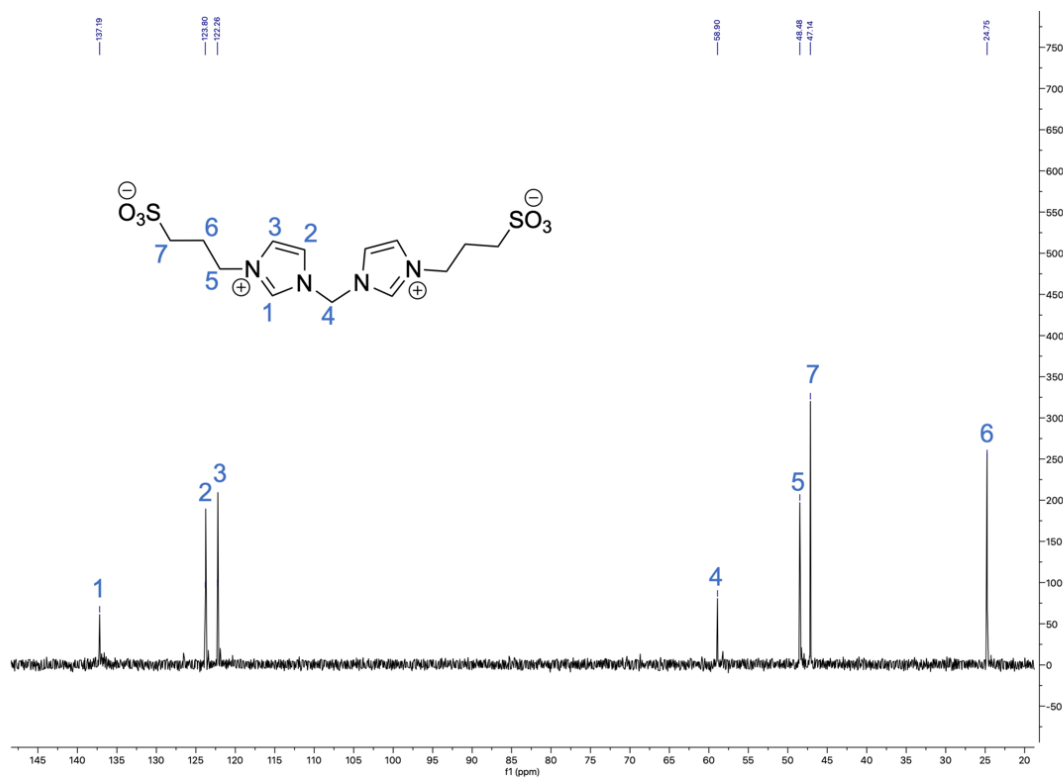


Figure S93 - $^{13}\text{C}\{^1\text{H}\}$ NMR of **NHC-2** in D_2O .

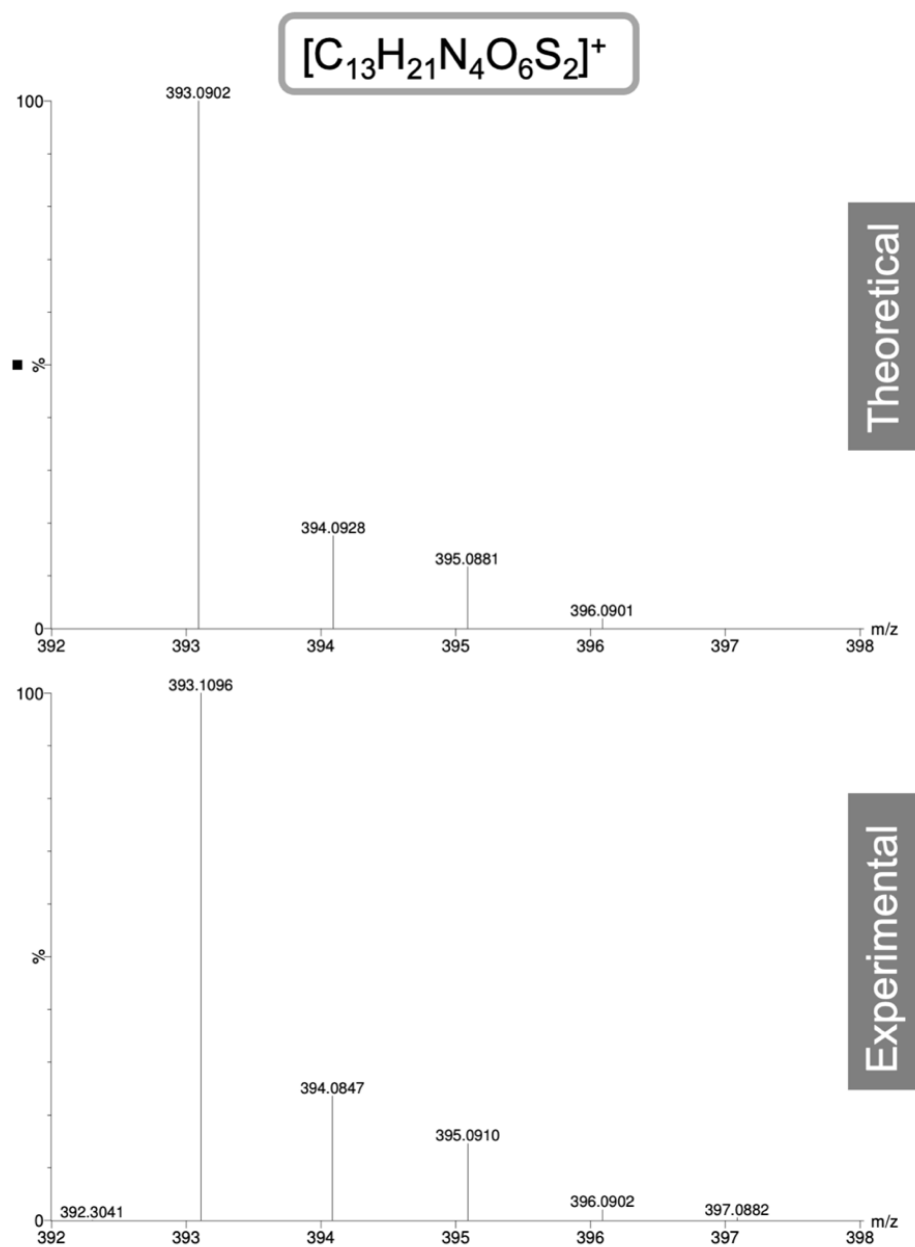


Figure S94 - HR-ESI-MS simulated (top) and experimental (below) spectra of **NHC-2**.

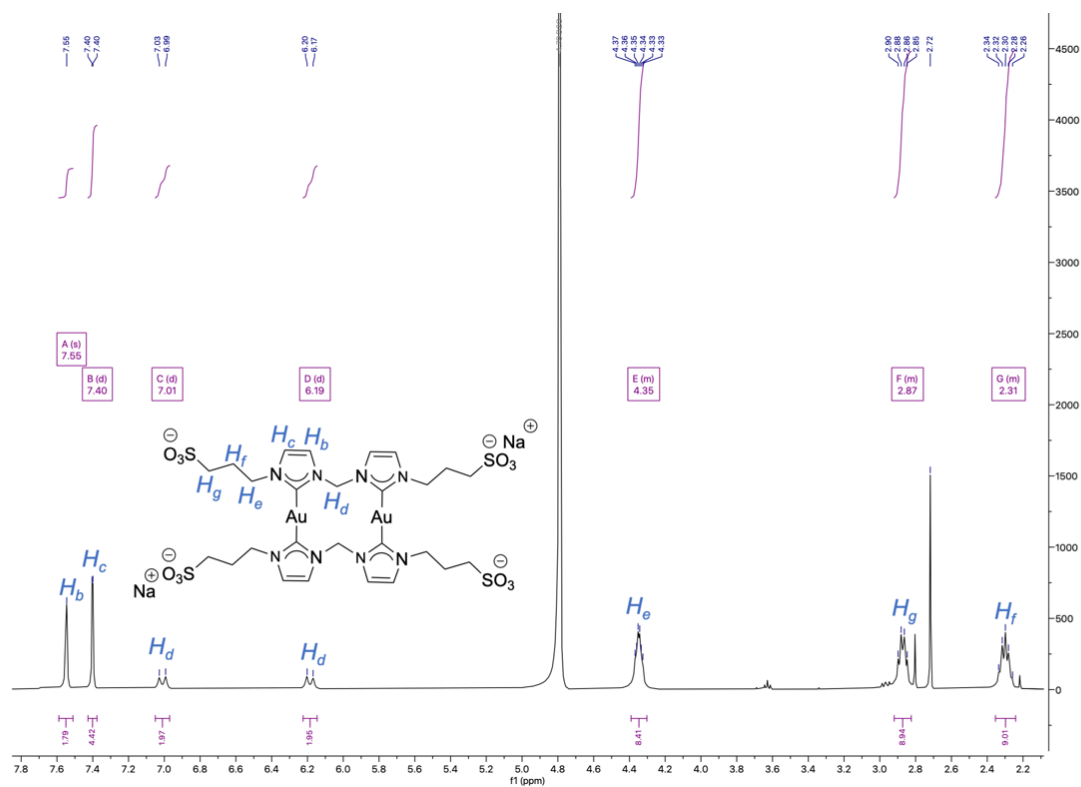


Figure S95 - ^1H NMR of AuNHC-2 in D_2O .

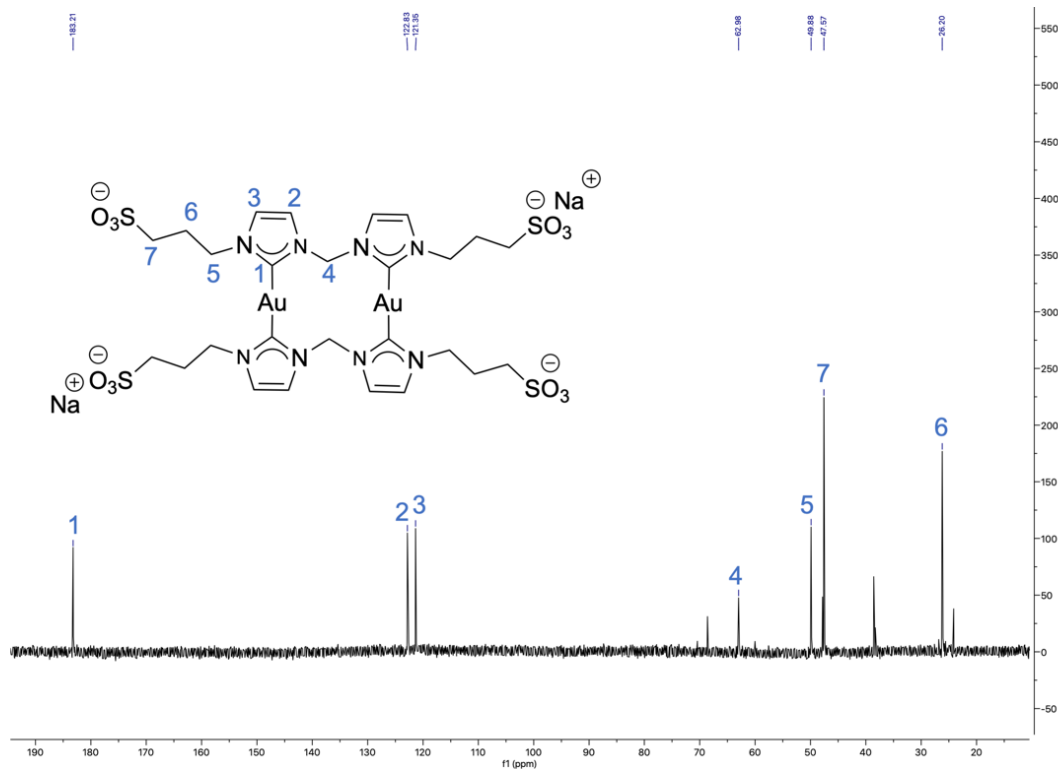


Figure S96 - $^{13}\text{C}\{^1\text{H}\}$ NMR of AuNHC-2 in D_2O .

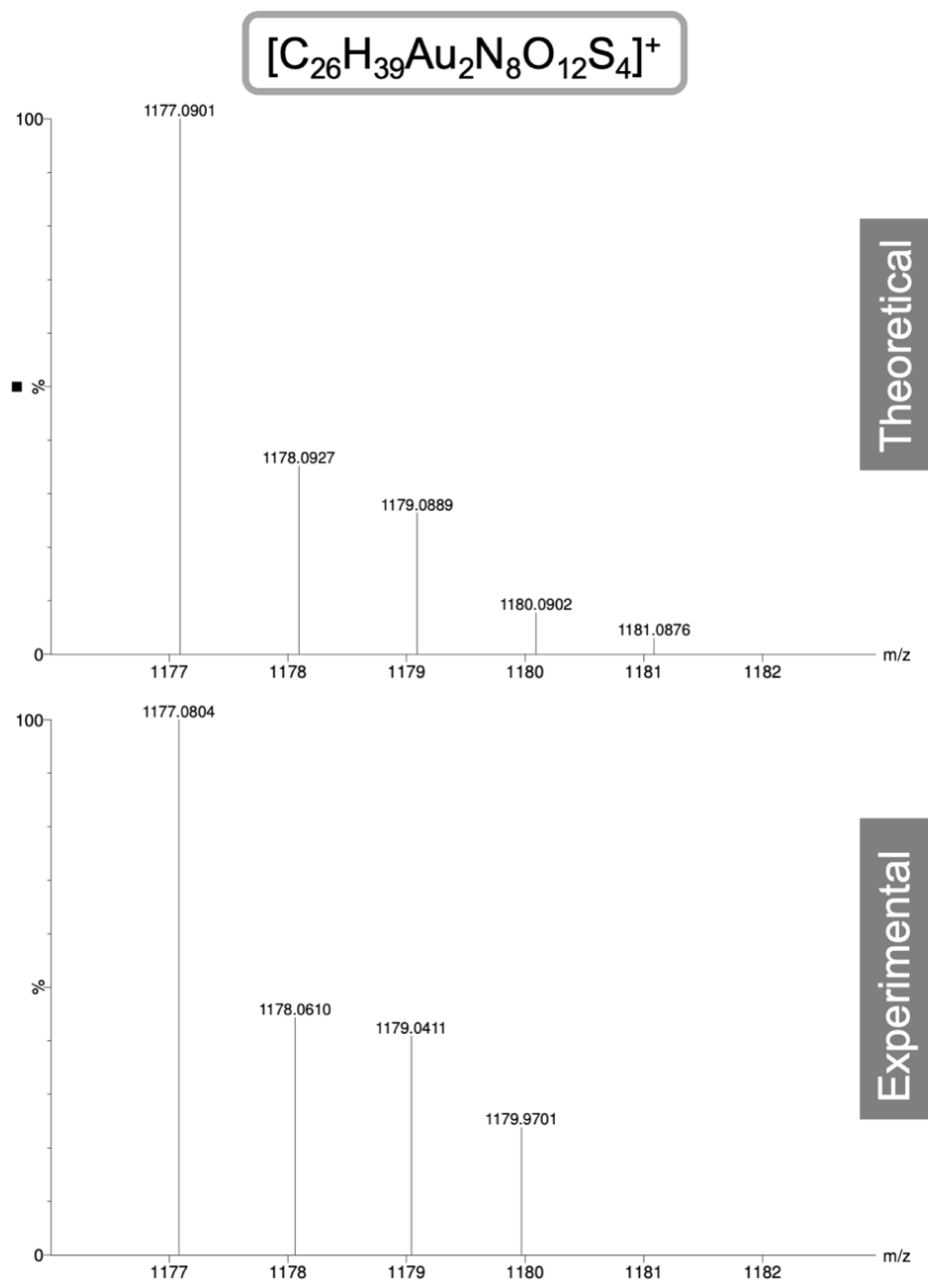
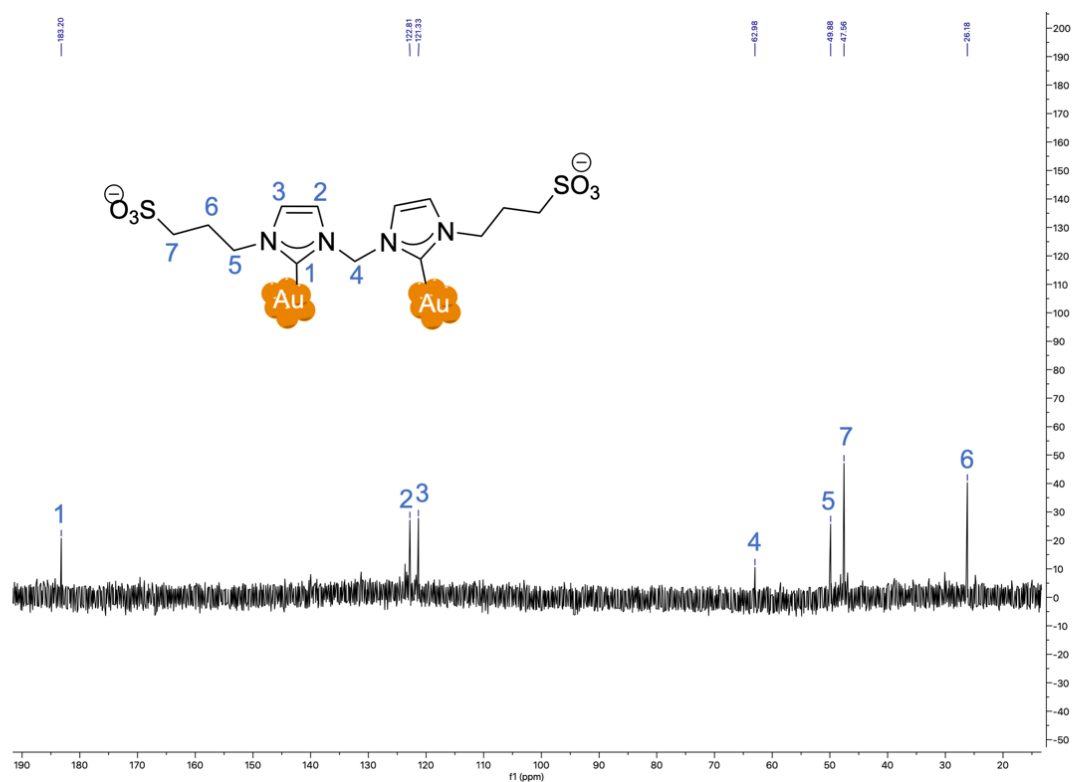
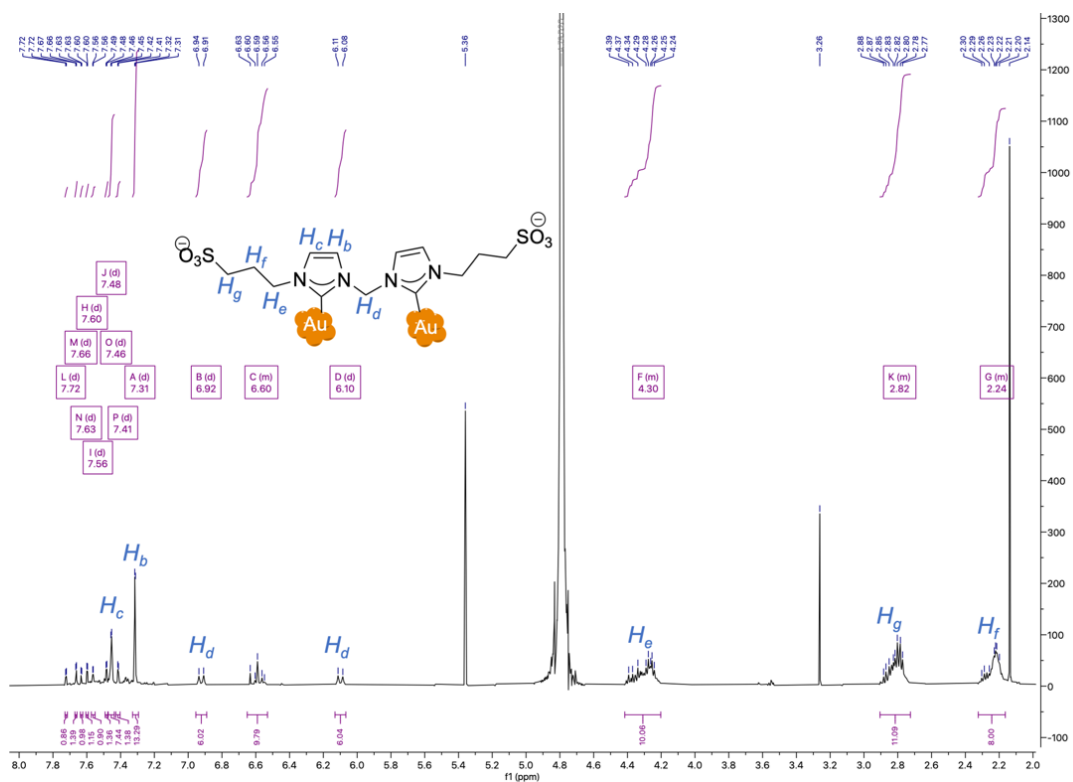


Figure S97 - HR-ESI-MS simulated (top) and experimental (below) spectra of **AuNHC-2**.



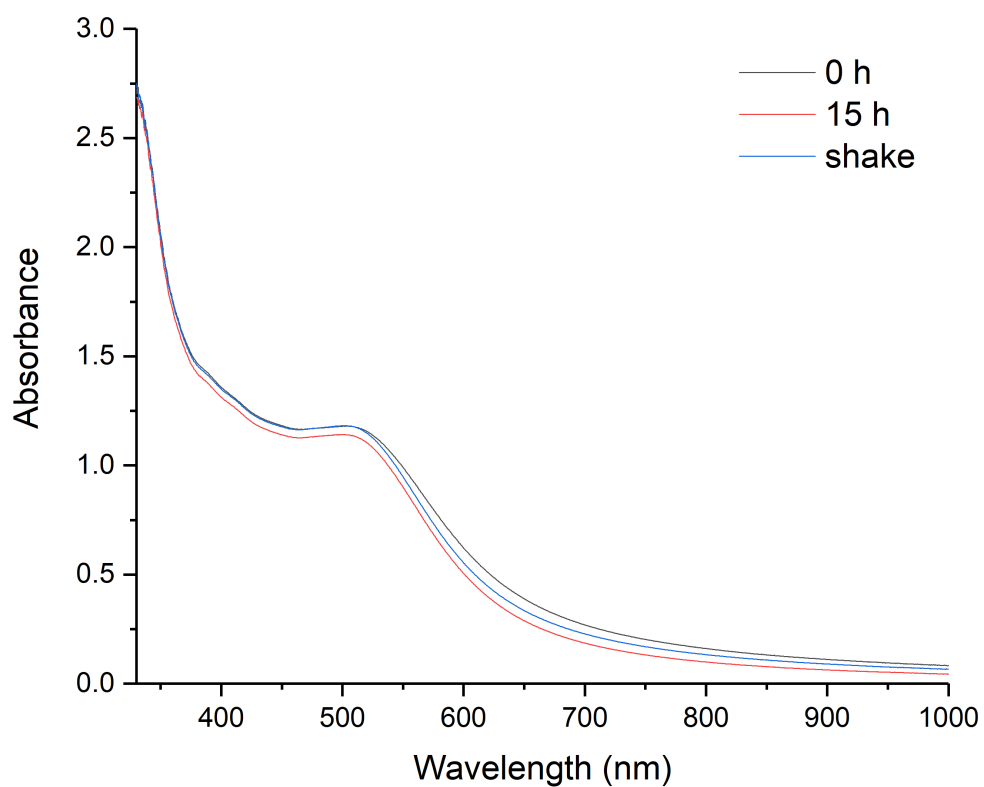


Figure S100 - UV-Vis Spectra of **AuNP-1** in MilliQ water at 0 h, 15 h and at 15 h after the shake.

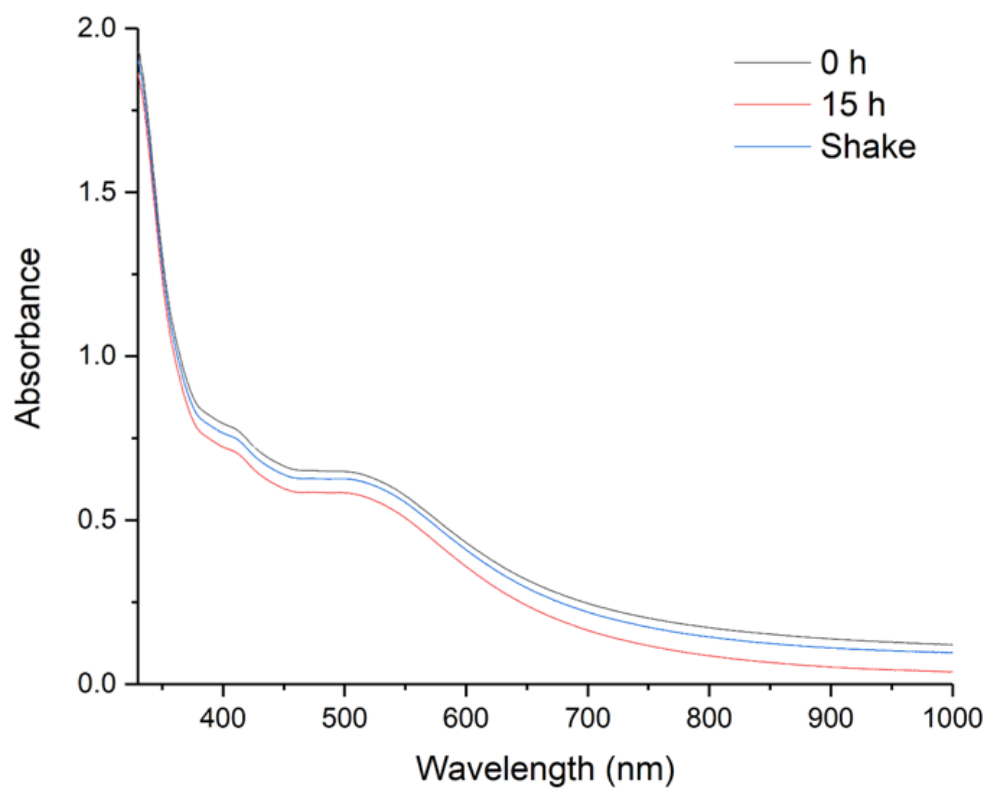


Figure S101 - UV-Vis Spectra of **AuNP-1** in PBS 1x at 0 h, 15 h and at 15 h after the shake.

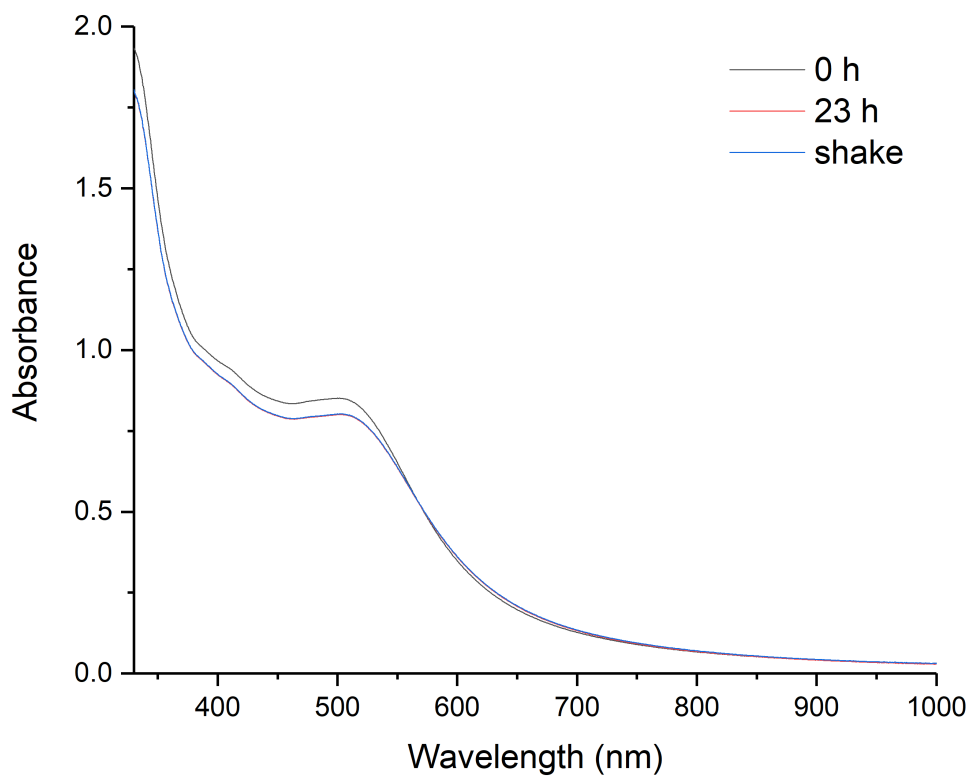


Figure S102 - UV-Vis Spectra of **AuNP-1** in PBS 1x with GSH (2 mM) at 0 h, 23 h and at 23 h after the shake.

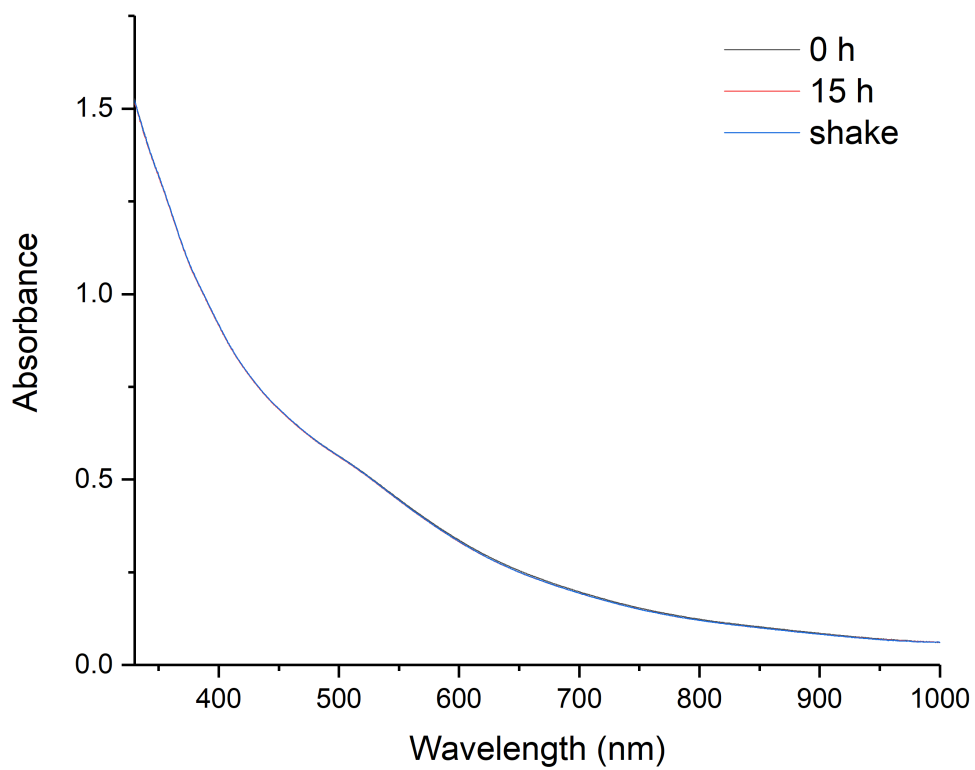


Figure S103 - UV-Vis Spectra of **AuNP-2** in MilliQ water at 0 h, 15 h and at 15 h after the shake.

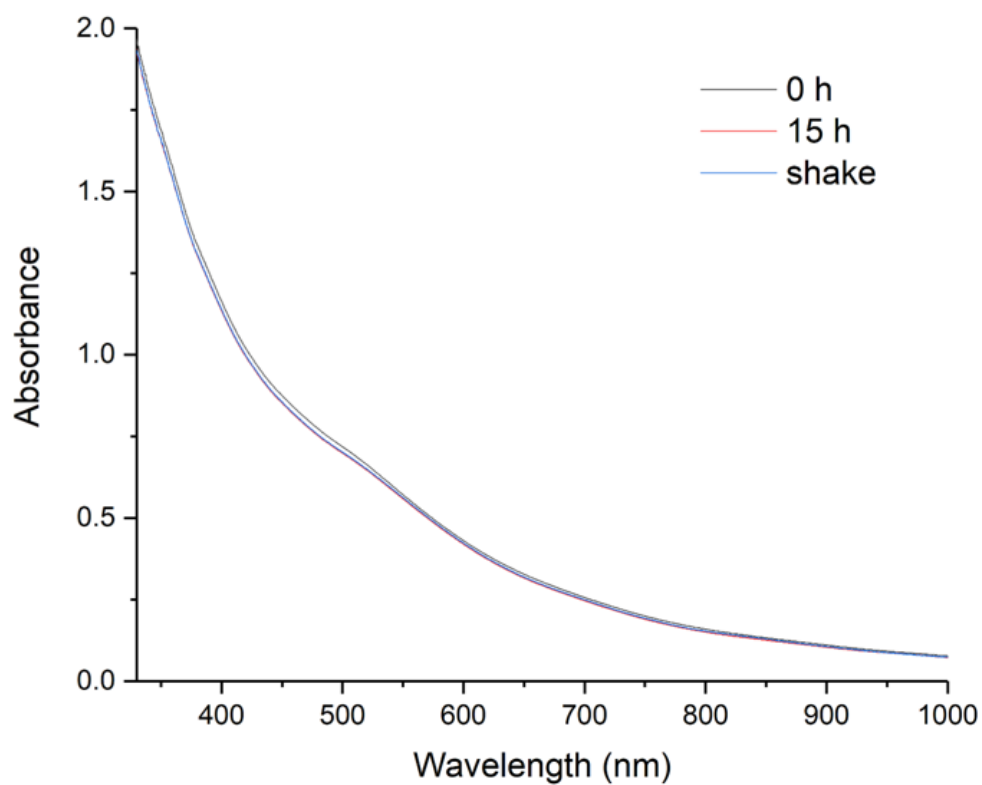


Figure S104 - UV-Vis Spectra of **AuNP-2** in PBS 1x at 0 h, 15 h and at 15 h after the shake.

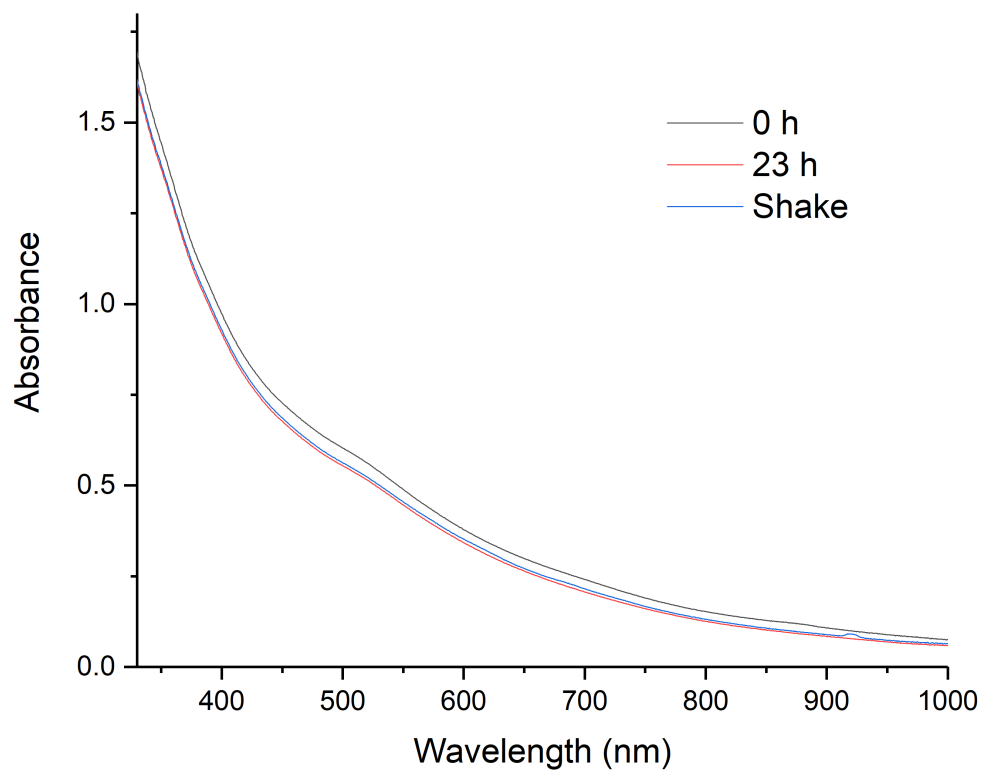


Figure S105 - UV-Vis Spectra of **AuNP-2** in PBS 1x with GSH (2 mM) at 0 h, 23 h and at 23 h after the shake.

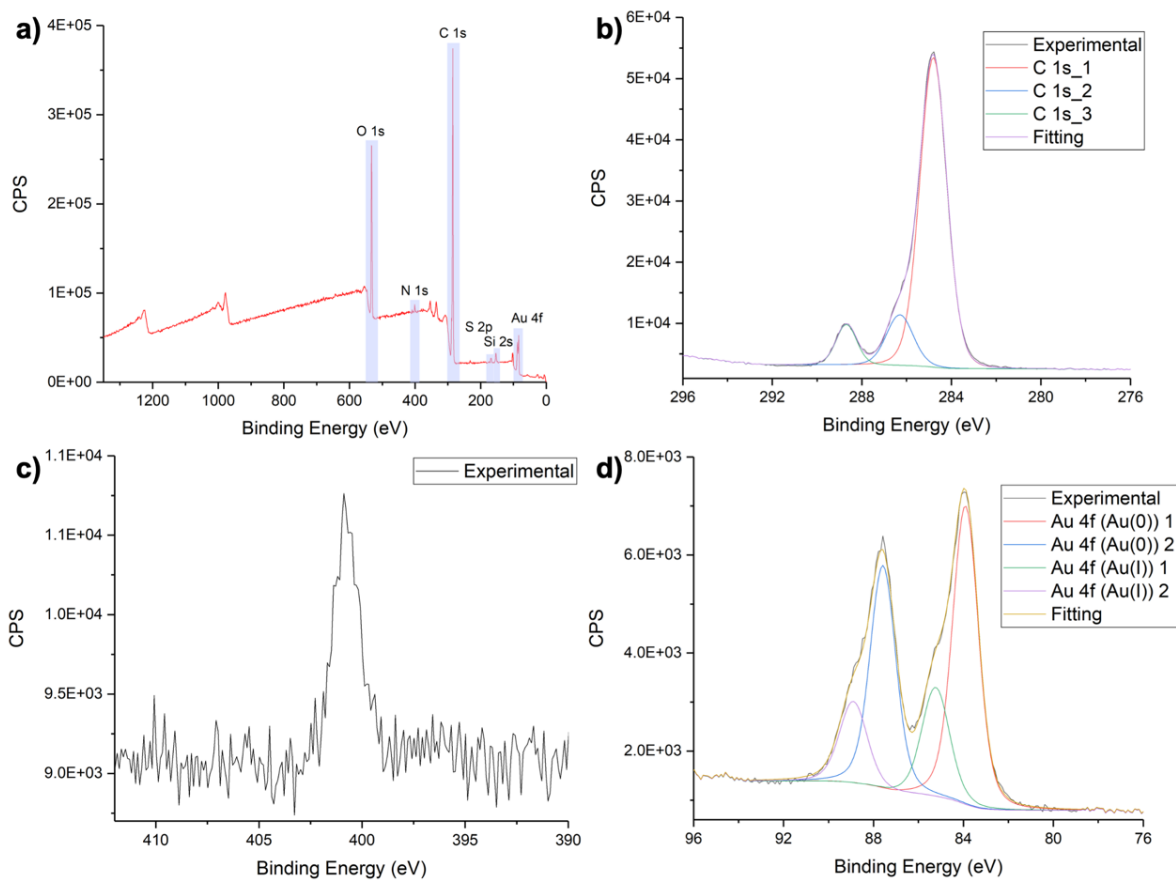


Figure S106 - XPS Spectra for **AuNP-1**: **a)** survey spectrum, **b)** experimental spectra and fitting of C 1s with deconvolution of the peaks, **c)** experimental spectrum of N 1s and **d)** experimental spectra and fitting of Au 4f with deconvolution of the peaks.

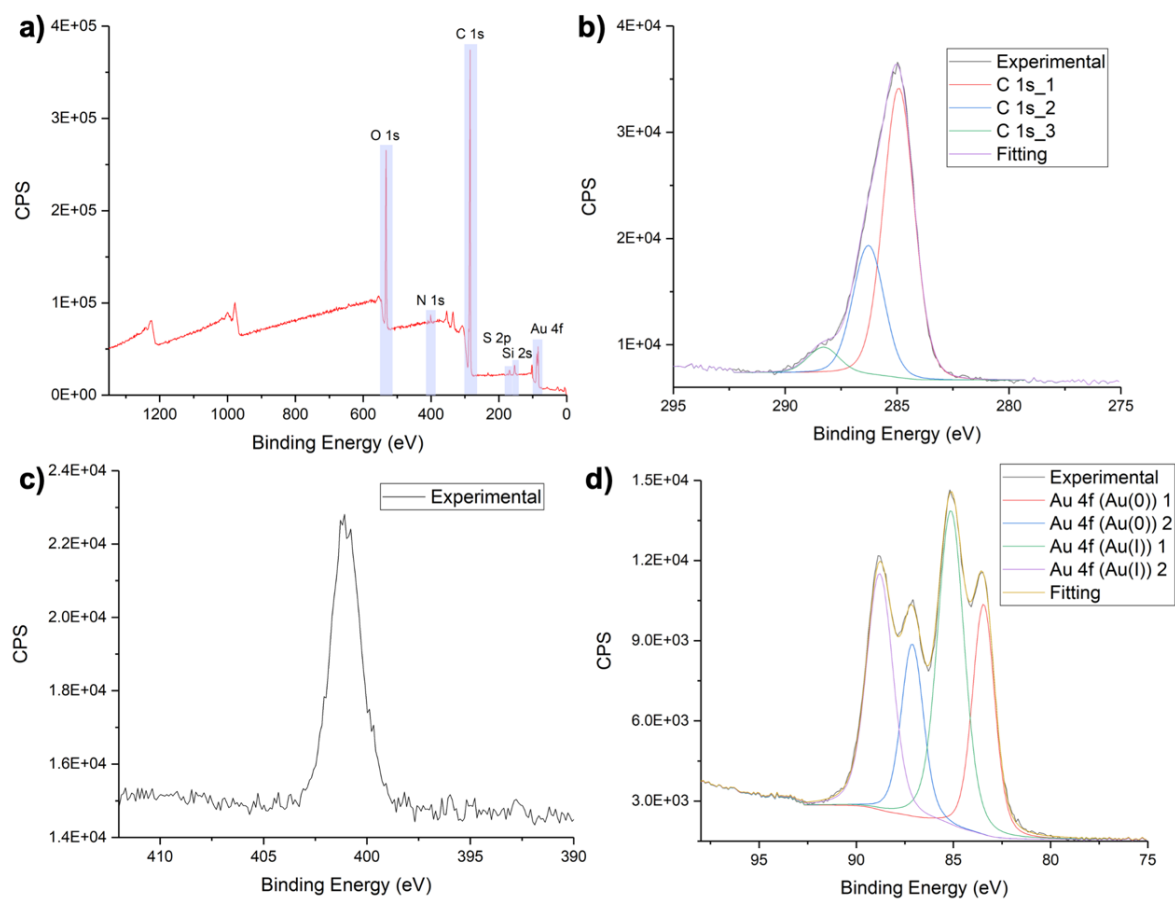


Figure S107 - XPS Spectra for **AuNP-2**: **a)** survey spectrum, **b)** experimental spectra and fitting of C 1s with deconvolution of the peaks, **c)** experimental spectrum of N 1s and **d)** experimental spectra and fitting of Au 4f with deconvolution of the peaks.

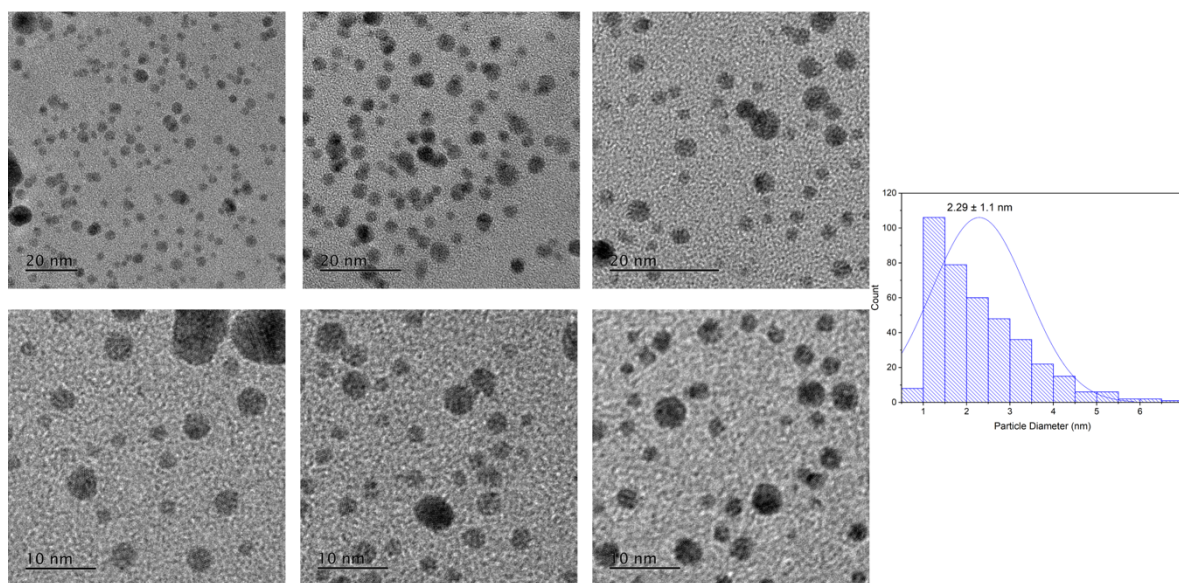


Figure S108 - TEM Images of **AuNP-1** at different magnifications which were used to obtain the particle size distribution histogram.

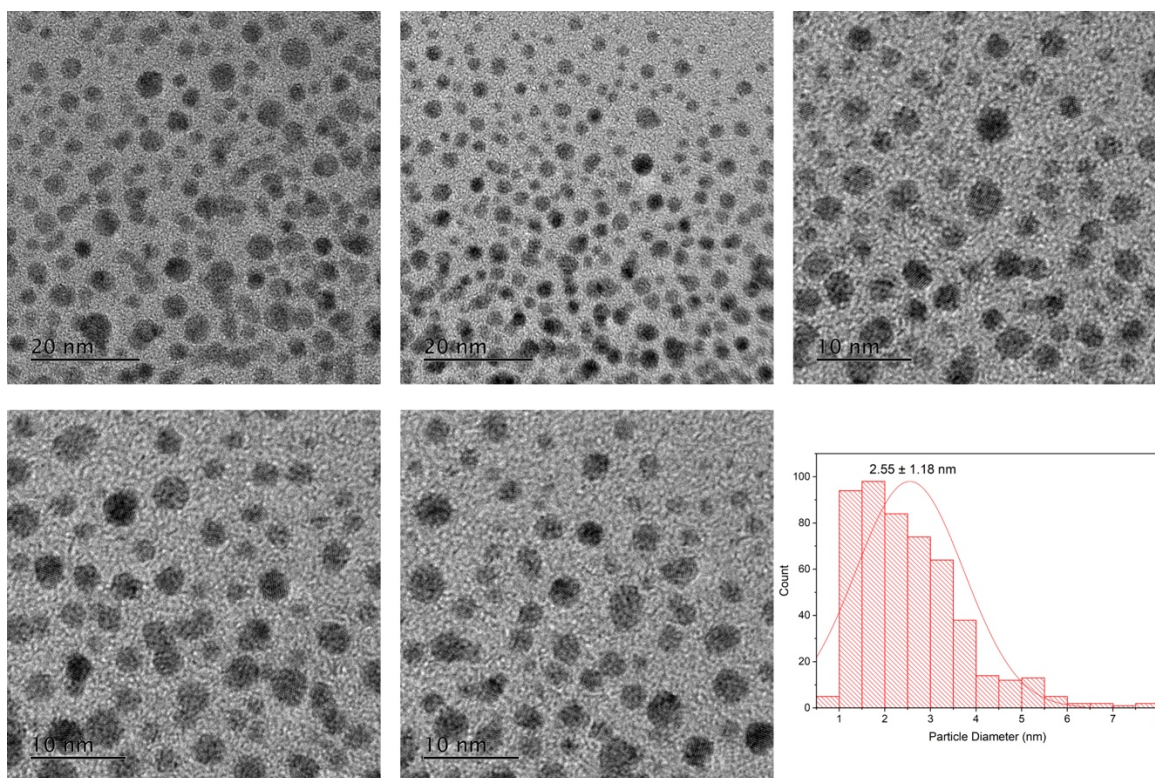


Figure S109 - TEM Images of **AuNP-2** at different magnifications which were used to obtain the particle size distribution histogram.

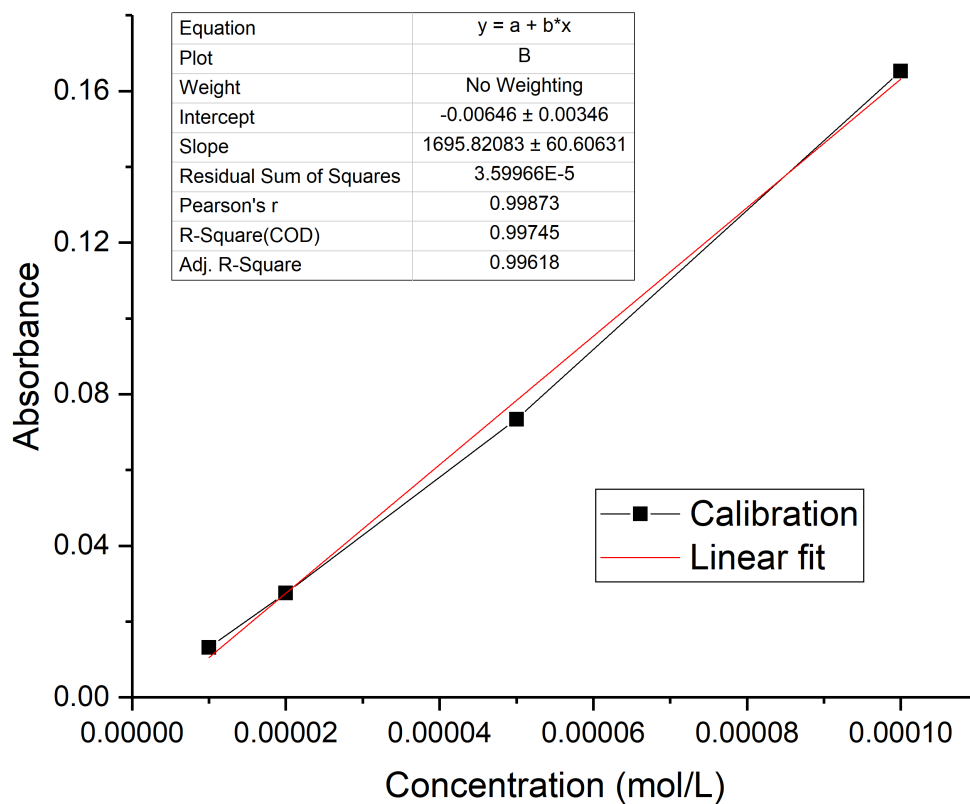


Figure S110 - Calibration plot for 3-nitrophenol.

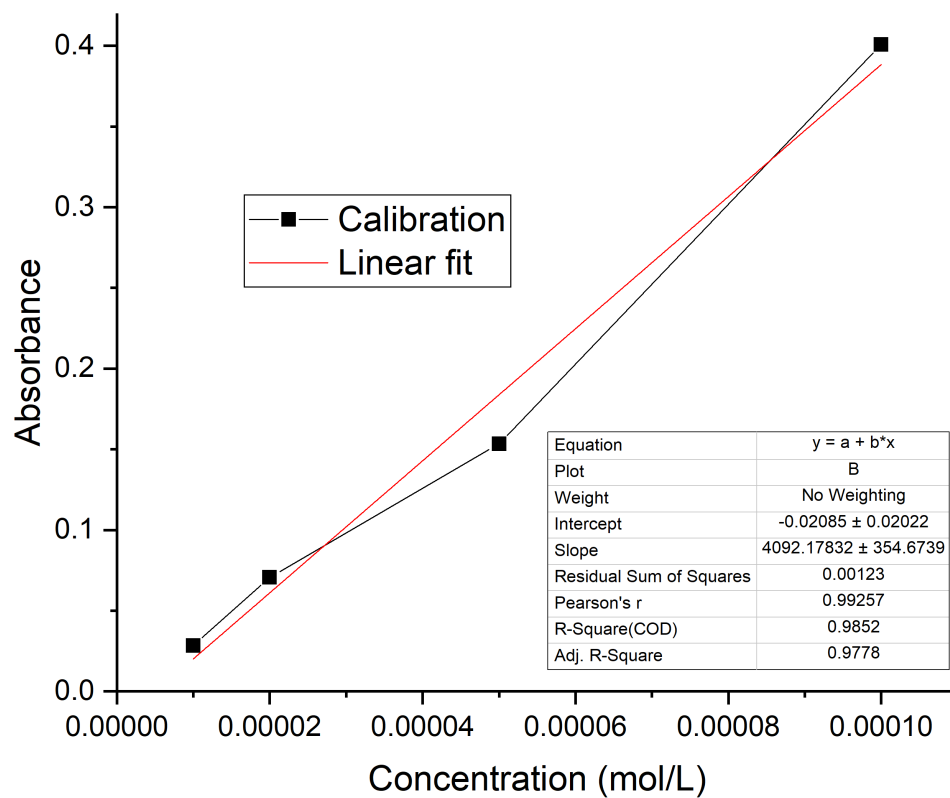


Figure S111 - Calibration plot for 2-nitrophenol.

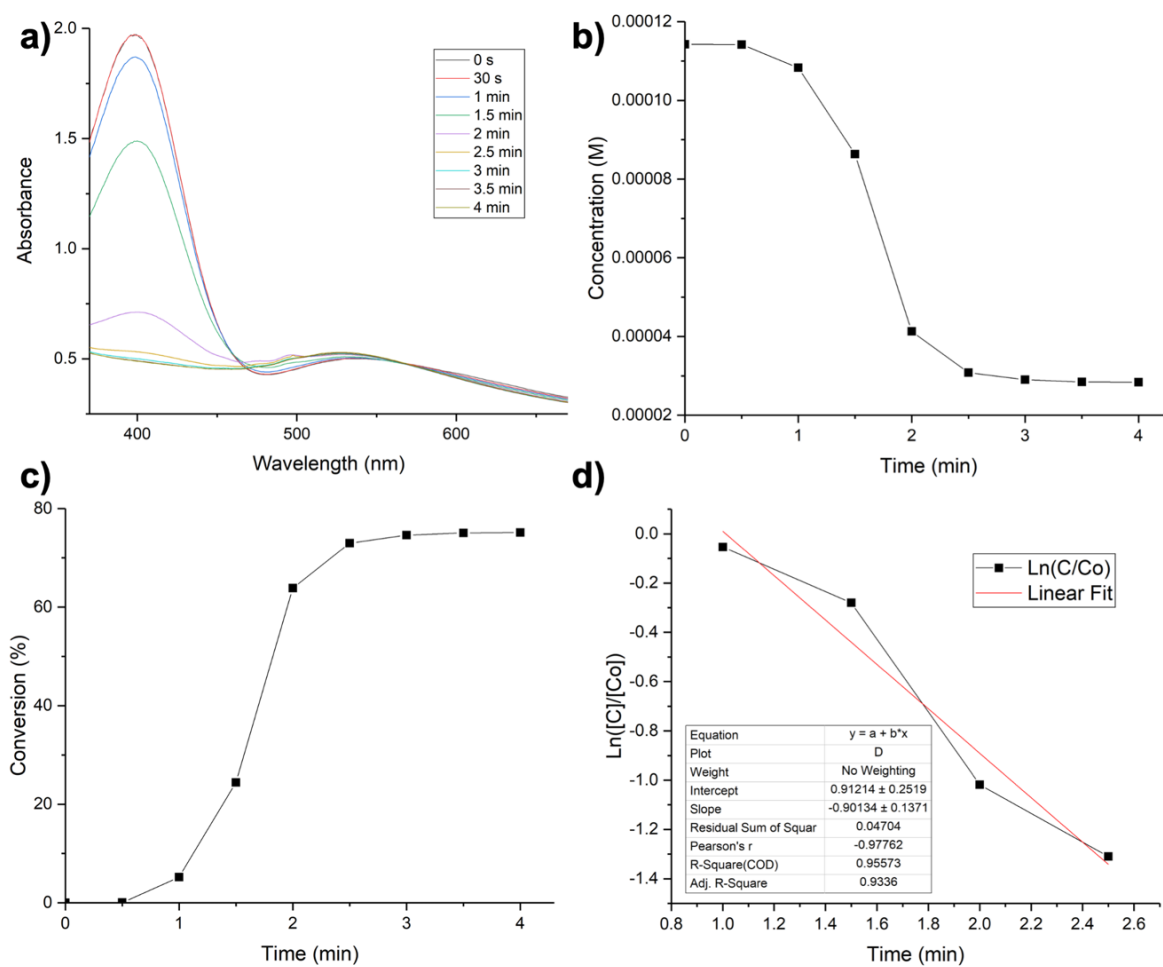


Figure S112 - **a)** UV-Vis kinetic study for the reduction of 4-nitrophenol into 4-aminophenol catalysed by **AuNP-1** (0.8 mg), **b)** plots of concentration; **c)** conversion vs. time at 400 cm^{-1} for the nitrophenol reduction, **d)** $\ln([C]/[Co])$ vs. time to calculate the rate constant.

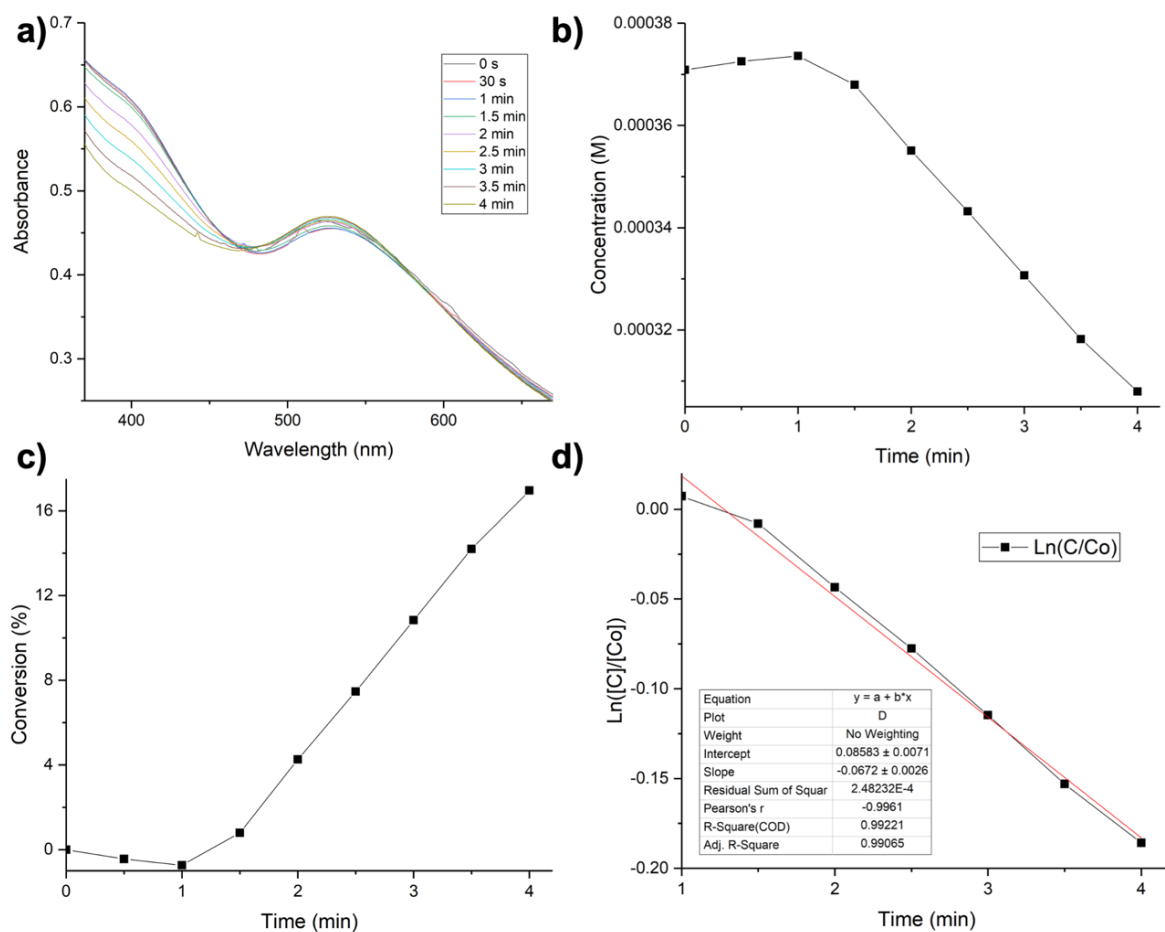


Figure S113 - a) UV-Vis kinetic study for the reduction of 3-nitrophenol into 3-aminophenol catalysed by AuNP-1 (0.6 mg), b) plots of concentration; c) conversion vs. time at 384 cm^{-1} for the nitrophenol reduction, d) $\ln([C]/[Co])$ vs. time to calculate the rate constant.

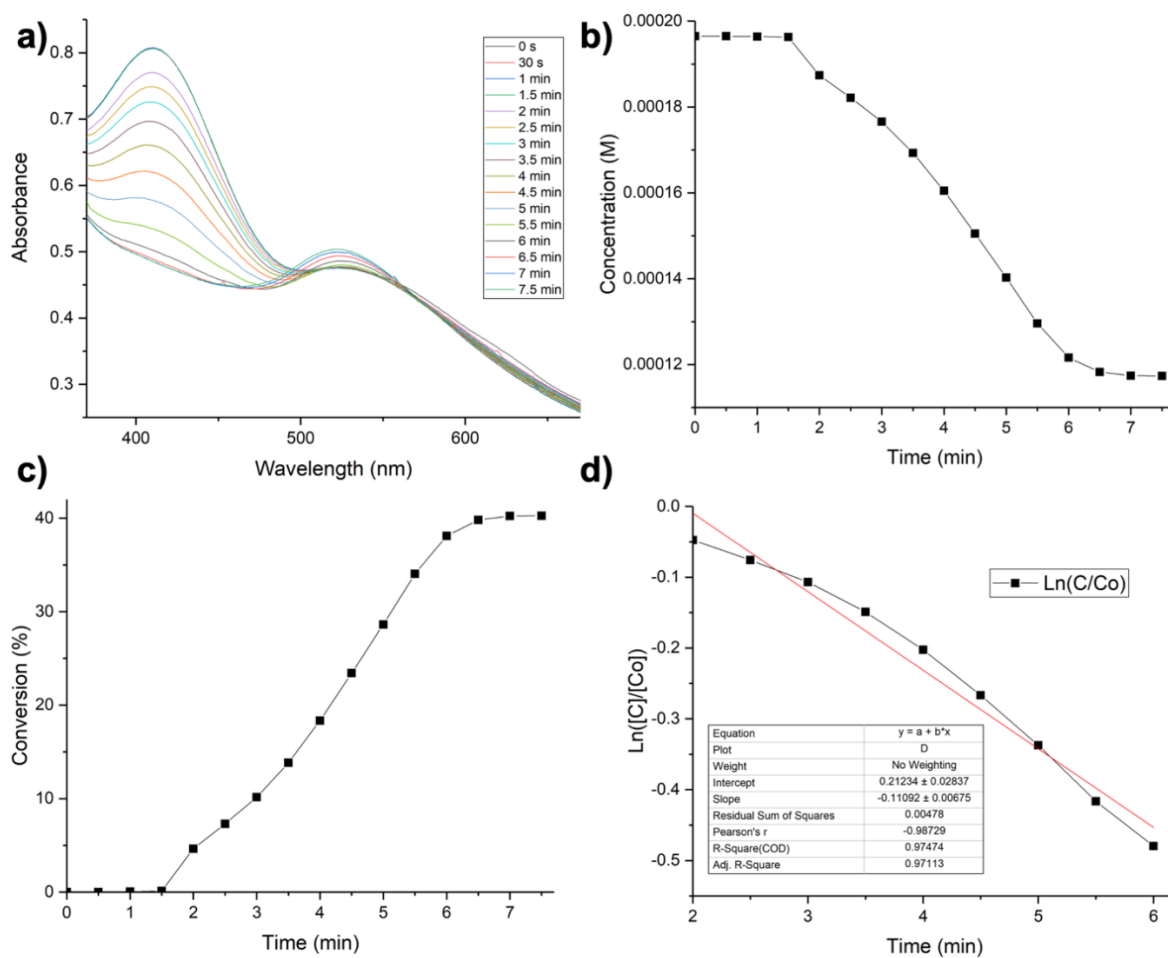


Figure S114 - **a)** UV-Vis kinetic study for the reduction of 2-nitrophenol into 2-aminophenol catalysed by **AuNP-1** (0.5 mg), **b)** plots of concentration; **c)** conversion vs. time at 415 cm^{-1} for the nitrophenol reduction, **d)** $\ln([C]/[Co])$ vs. time to calculate the rate constant.

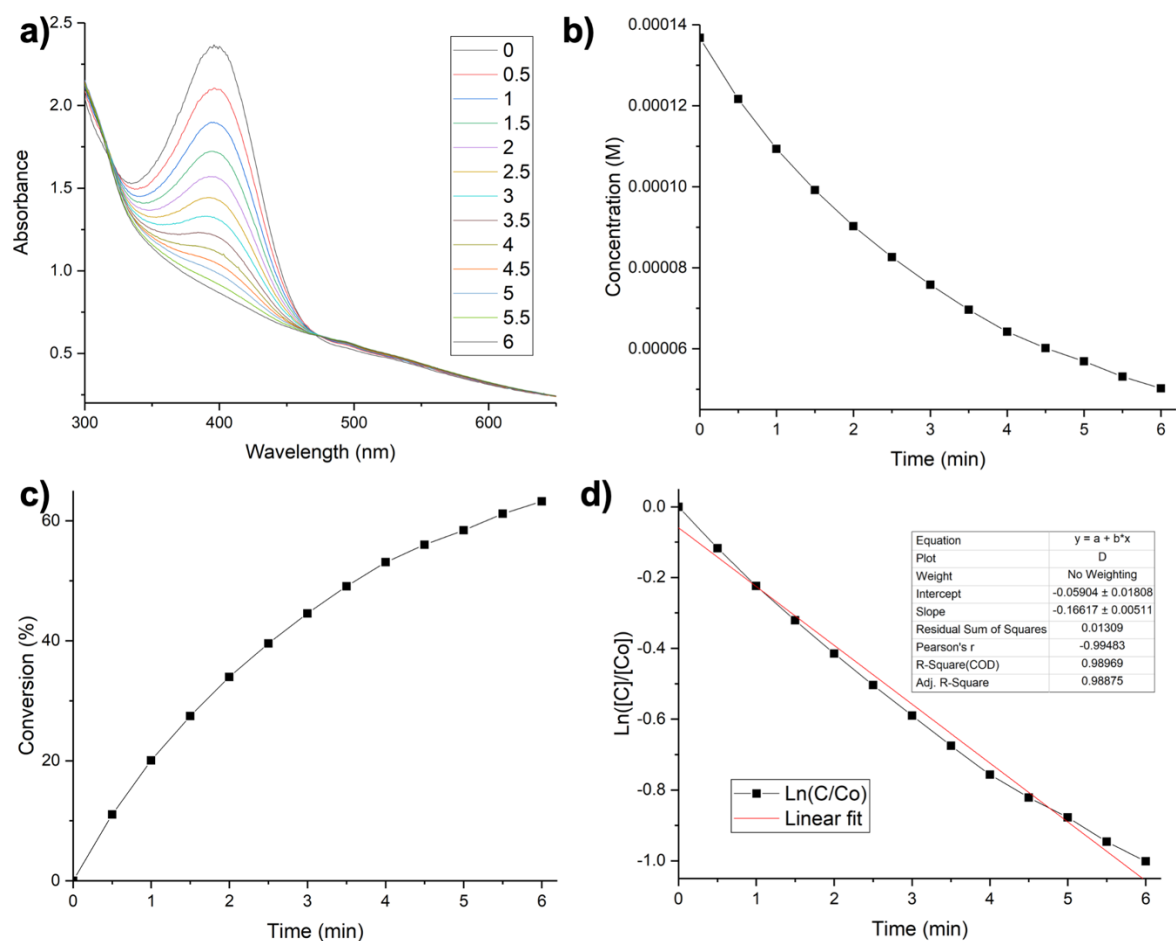


Figure S115 - **a)** UV-Vis kinetic study for the reduction of 4-nitrophenol into 4-aminophenol catalysed by **AuNP-2** (0.5 mg), **b)** plots of concentration; **c)** conversion vs. time at 400 cm^{-1} for the nitrophenol reduction, **d)** $\ln([C]/[Co])$ vs. time to calculate the rate constant.

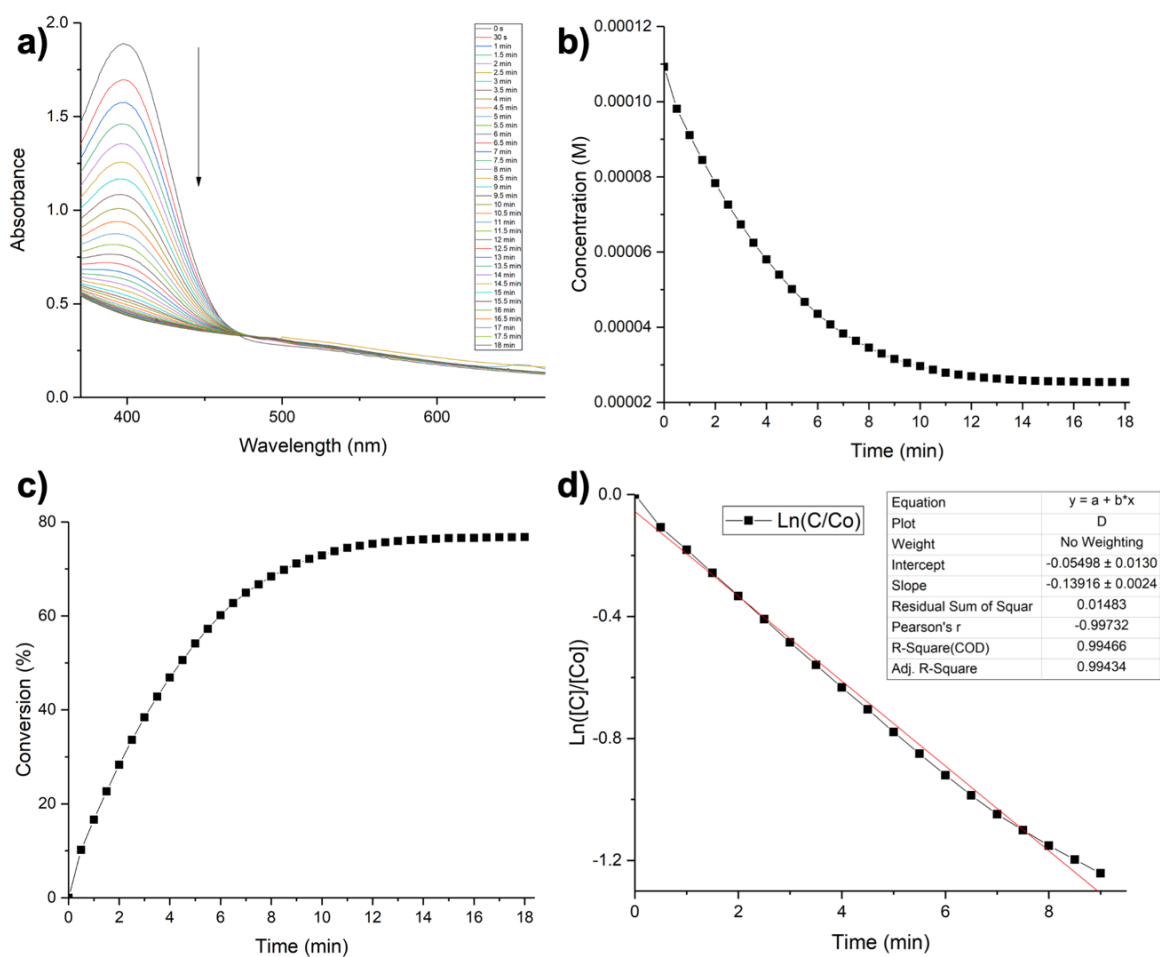


Figure S116 - a) UV-Vis kinetic study for the reduction of 4-nitrophenol into 4-aminophenol catalysed by AuNP-2 (0.6 mg), b) plots of concentration; c) conversion vs. time at 400 cm^{-1} for the nitrophenol reduction, d) $\ln([C]/[Co])$ vs. time to calculate the rate constant.

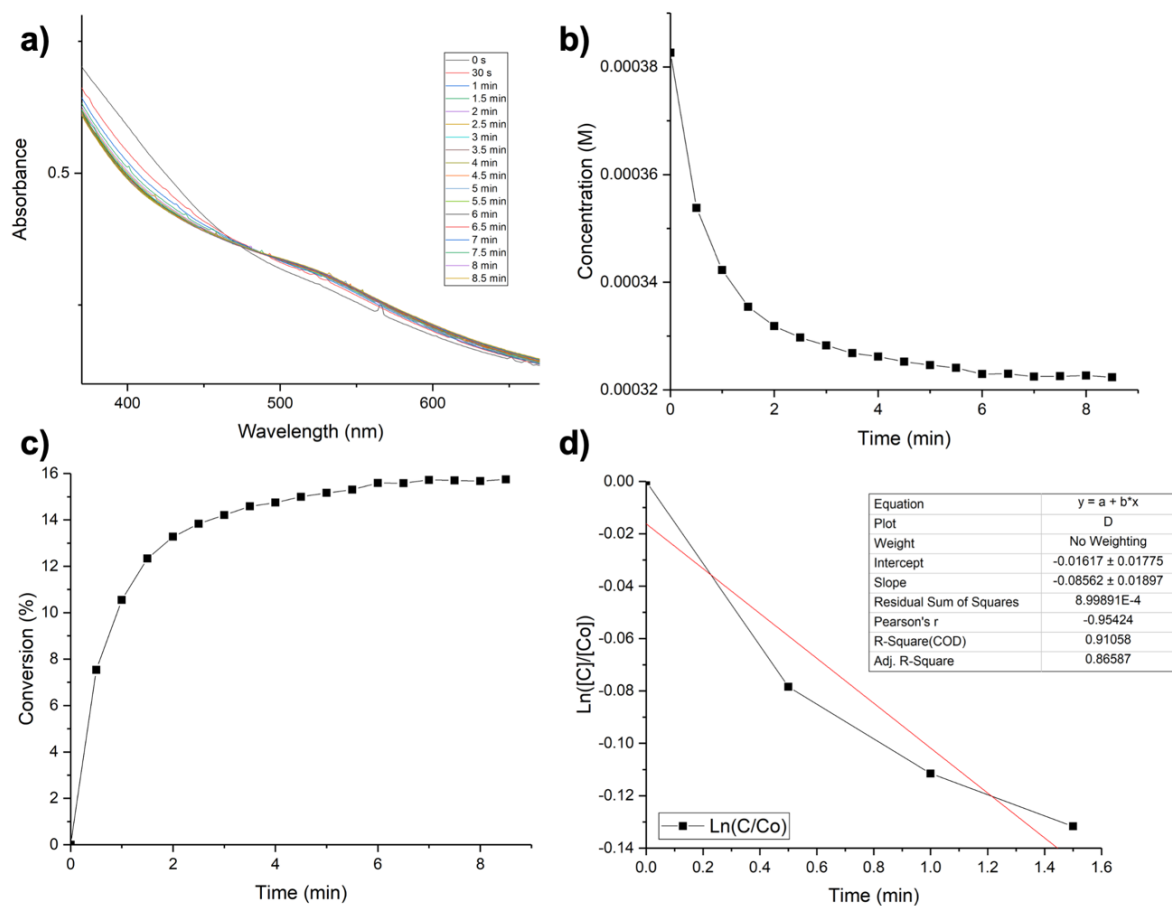


Figure S117 - **a)** UV-Vis kinetic study for the reduction of 3-nitrophenol into 3-aminophenol catalysed by **AuNP-2** (0.5 mg), **b)** plots of concentration; **c)** conversion vs. time at 384 cm^{-1} for the nitrophenol reduction, **d)** $\ln([C]/[Co])$ vs. time to calculate the rate constant.

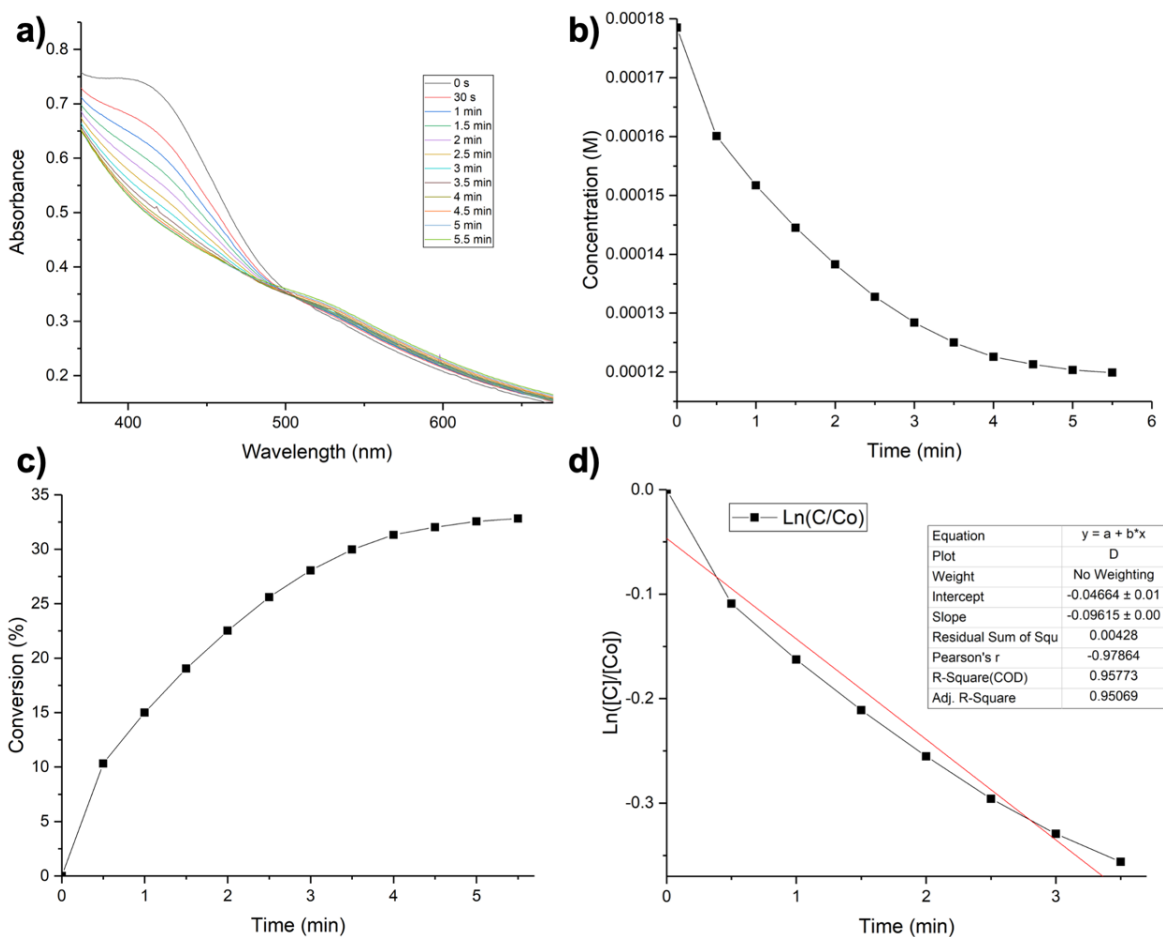


Figure S118 - a) UV-Vis kinetic study for the reduction of 2-nitrophenol into 2-aminophenol catalysed by AuNP-2 (0.5 mg), b) plots of concentration; c) conversion vs. time at 415 cm^{-1} for the nitrophenol reduction, d) $\text{Ln}([C]/[Co])$ vs. time to calculate the rate constant.

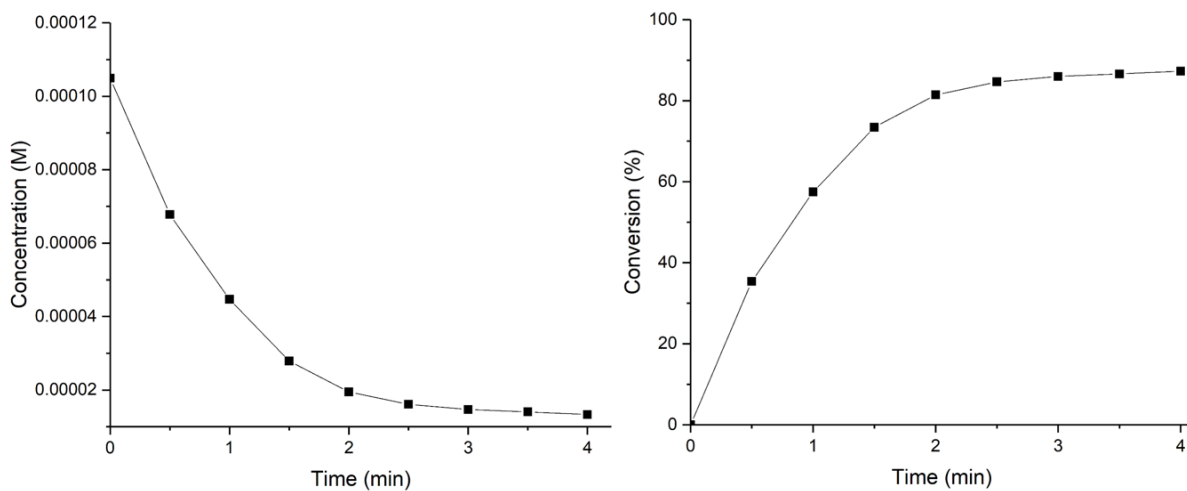


Figure S119 - Plots of concentration (left) and conversion (right) vs. time for the reduction of 4-nitrophenol reduction catalysed by AuNP-1 after pre-treatment with NaBH_4 .

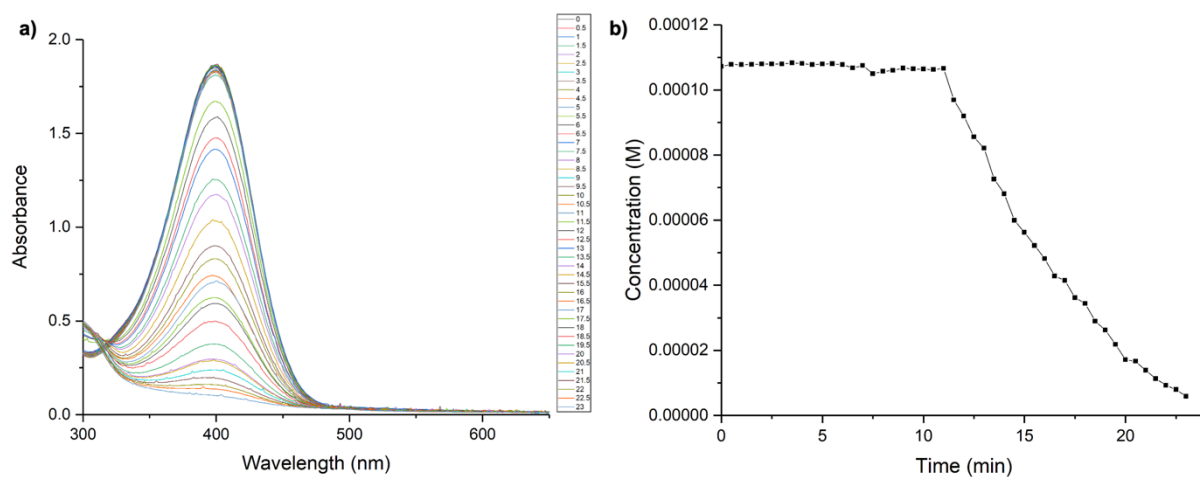


Figure S120 - a) UV-Vis kinetic study for the reduction of 4-nitrophenol with used AuNP-1, b) plot of concentration vs. time.

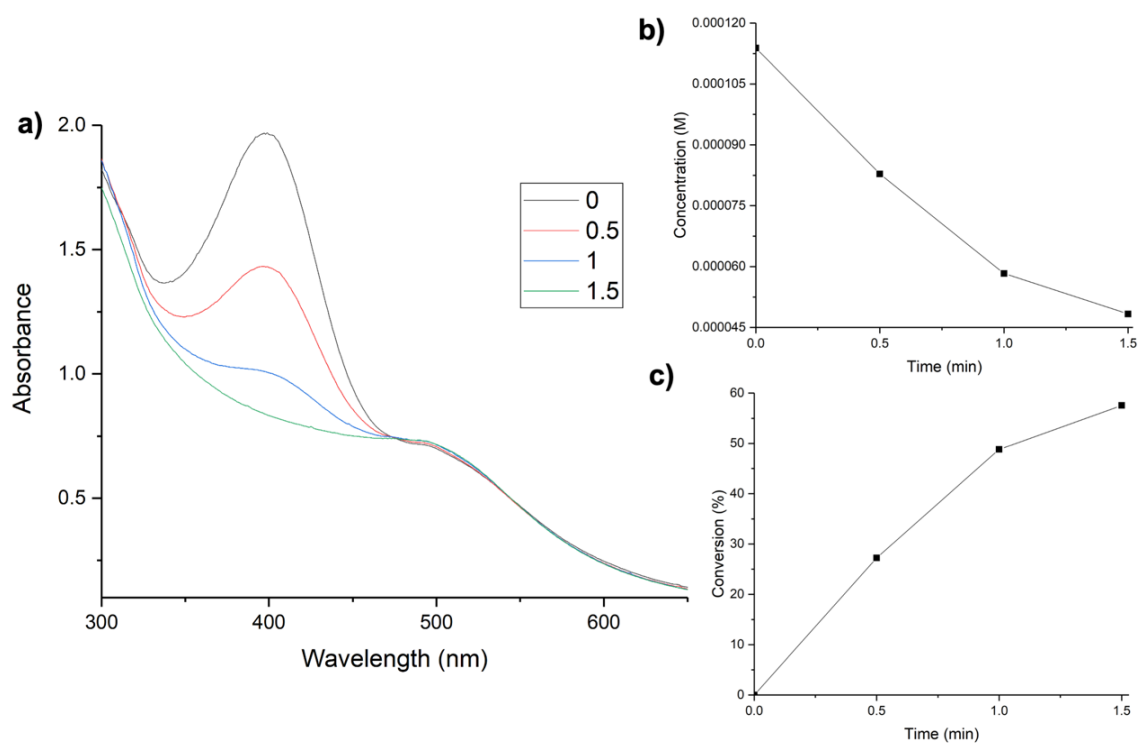


Figure S121 - a) UV-Vis kinetic study for the reduction of 4-nitrophenol with used AuNP-2, b) plots of concentration and c) conversion vs. time.

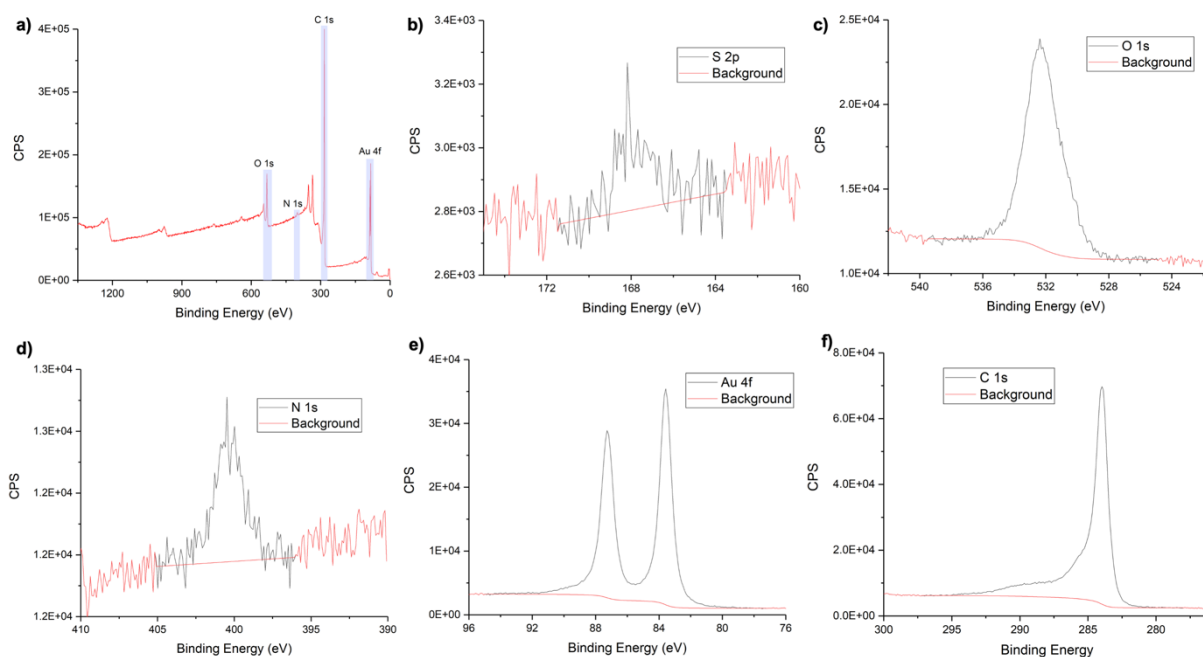


Figure S122 - XPS Spectra for **AuNP-1/C**: a) survey spectrum; experimental spectra and background of b) S 2p, c) O 1s, d) N 1s, e) Au 4f and f) C 1s.

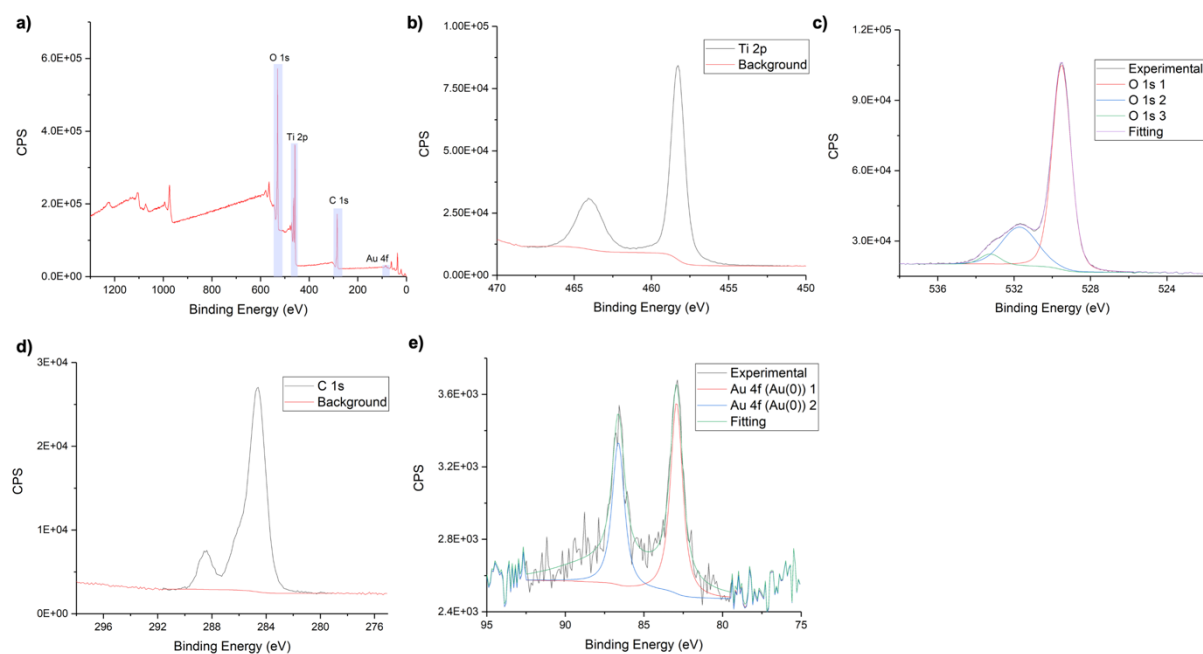


Figure S123 - XPS Spectra for **AuNP-1/TiO₂**: a) survey spectrum, b) experimental spectra and background of Ti 2p, c) experimental spectra and fitting of O 1s with deconvolution of the peaks, d) experimental spectra and background of C 1s and e) experimental spectra and fitting of Au 4f with deconvolution of the peaks.

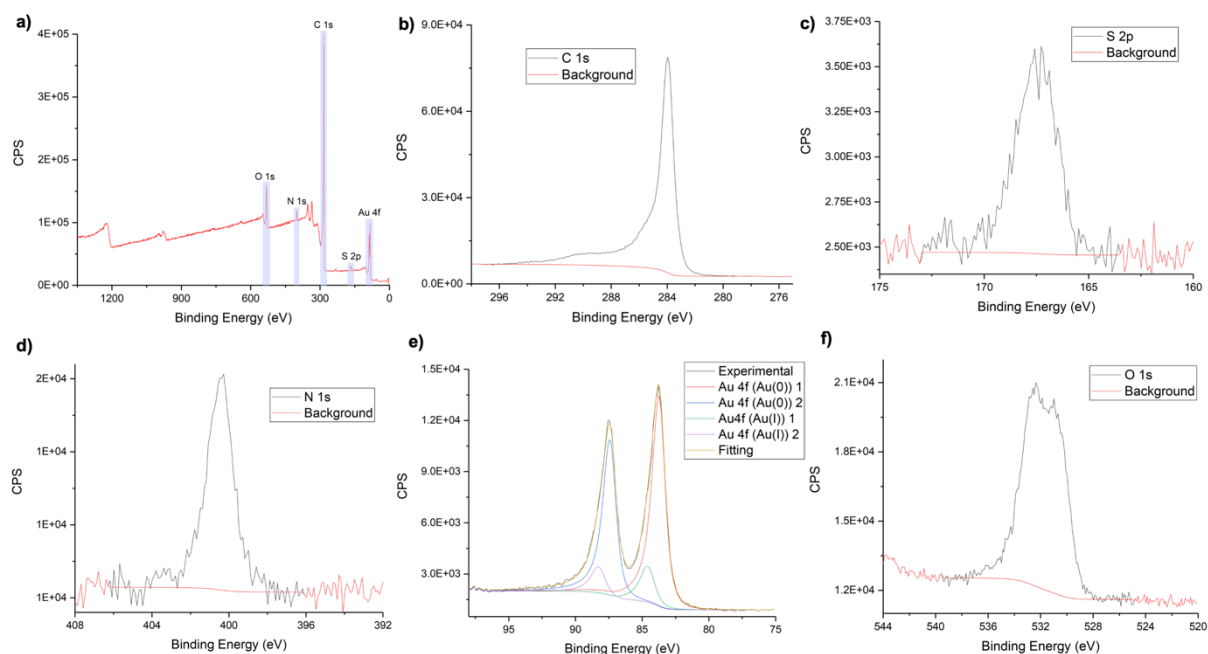


Figure S124 - XPS Spectra for **AuNP-2/C**: **a)** survey spectrum, **b)** experimental spectra and background of C 1s, **c)** experimental spectra and background of S 2p, **d)** experimental spectra and background of N 1s, **e)** experimental spectra and fitting of Au 4f with deconvolution of the peaks and **f)** experimental spectra and background of O 1s.

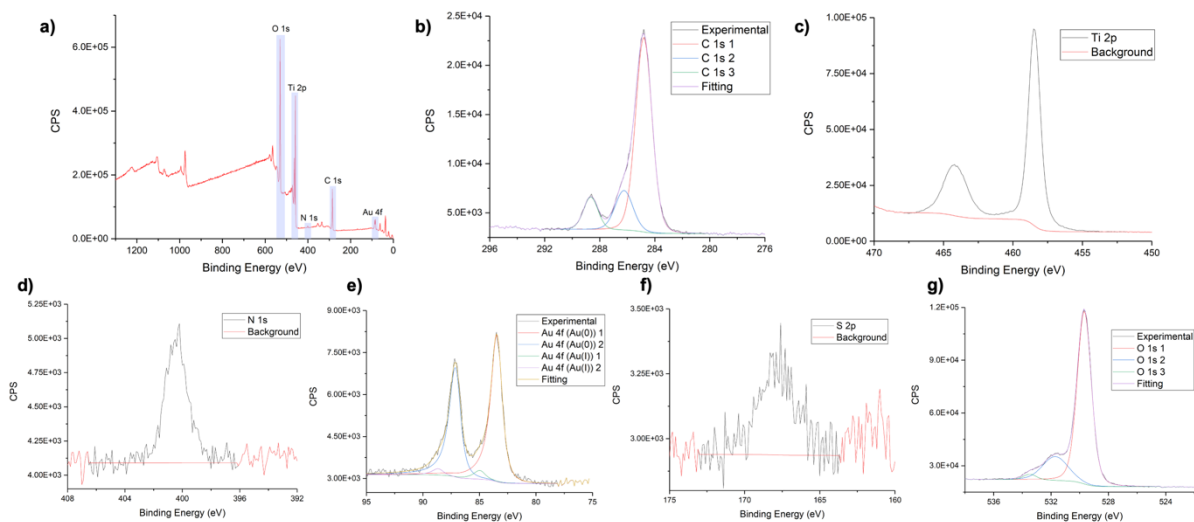


Figure S125 - XPS Spectra for **AuNP-2/TiO₂**: **a)** survey spectrum, **b)** experimental spectra and fitting of C 1s with deconvolution of the peaks, **c)** experimental spectra and background of Ti 2p, **d)** experimental spectra and background of N 1s, **e)** experimental spectra and fitting of Au 4f with deconvolution of the peaks, **f)** experimental spectra and background of S 2p and **g)** experimental spectra and fitting of O 1s with deconvolution of the peaks.

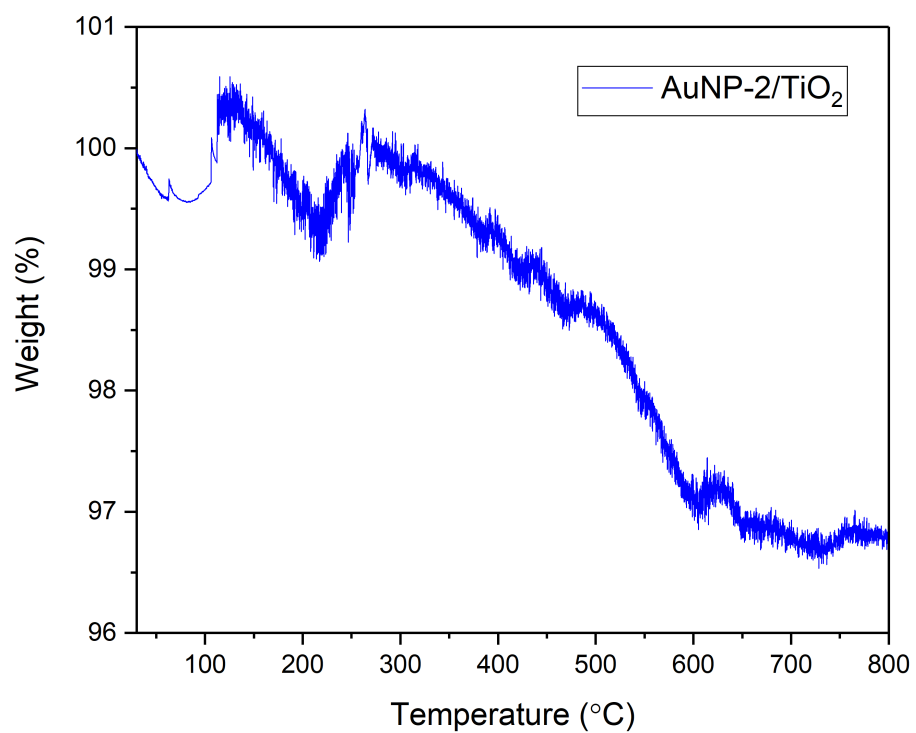


Figure S126 - TG curve of **AuNP-2/TiO₂**.

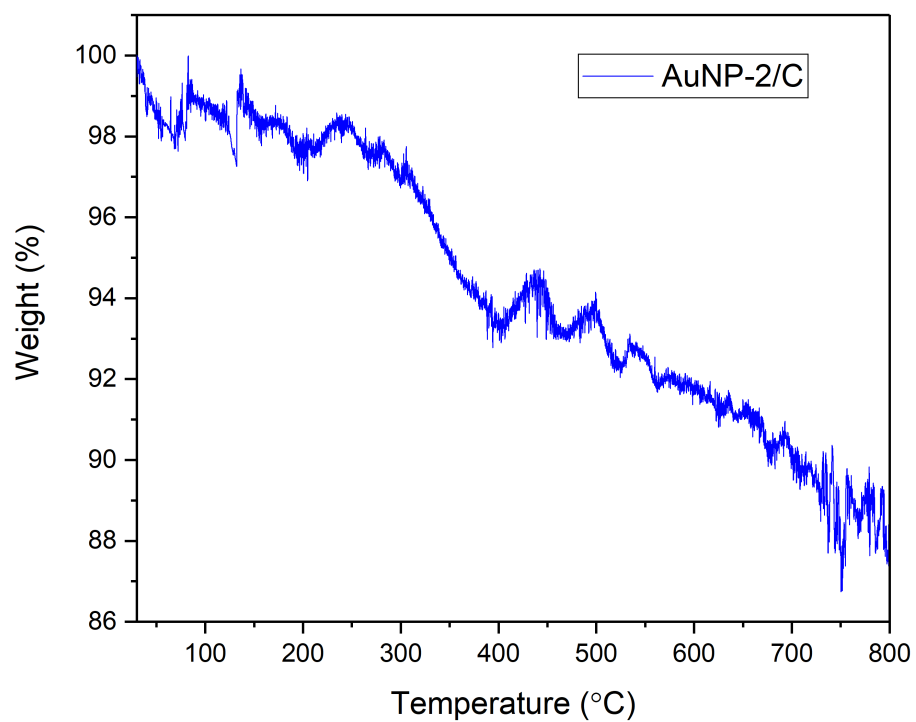


Figure S127 - TG curve of **AuNP-2/C**.

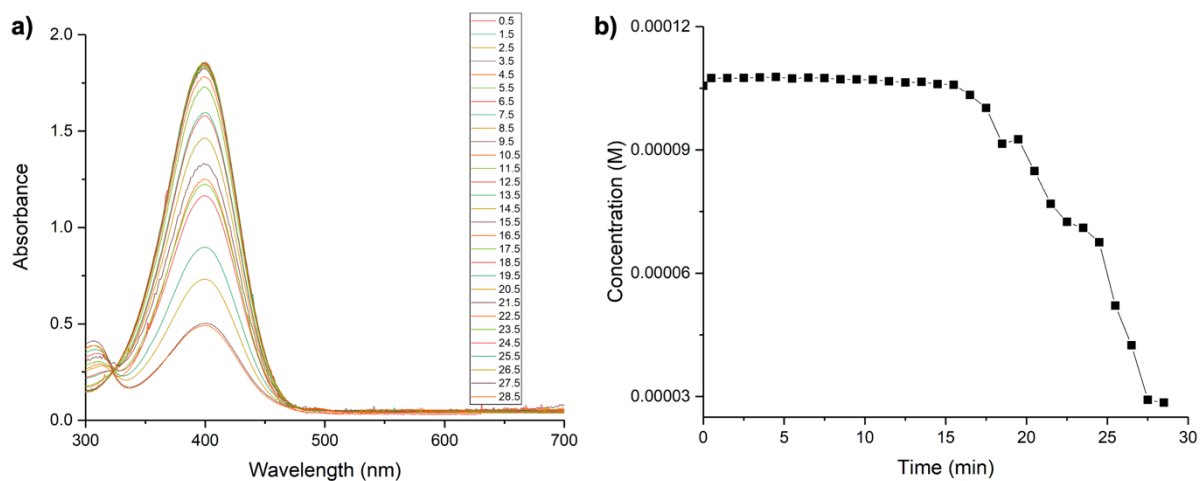


Figure S128 - a) UV-Vis kinetic study for the reduction of 4-nitrophenol with AuNP-1/TiO₂, b) plot of concentration vs. time.

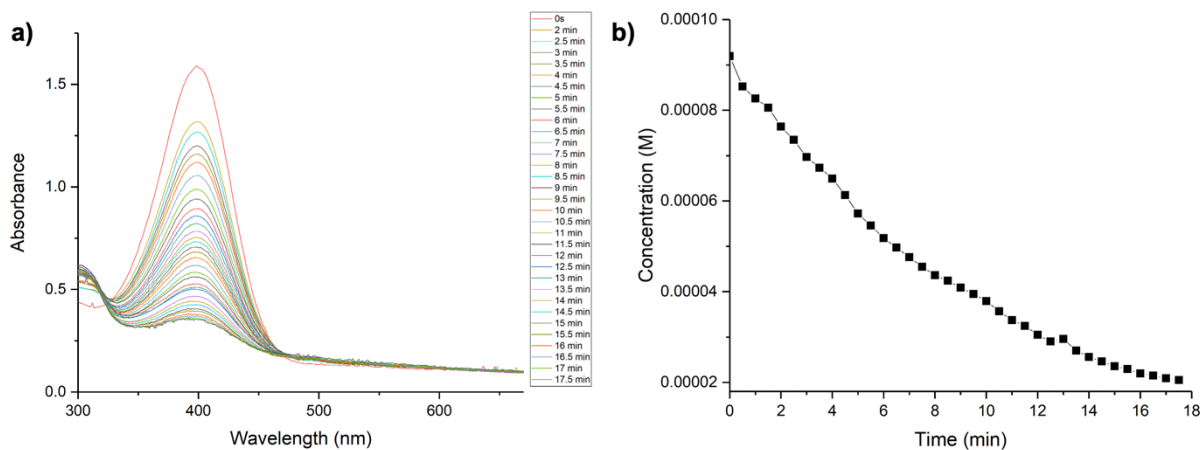


Figure S129 - a) UV-Vis kinetic study for the reduction of 4-nitrophenol with AuNP-2/TiO₂, b) plot of concentration vs. time.

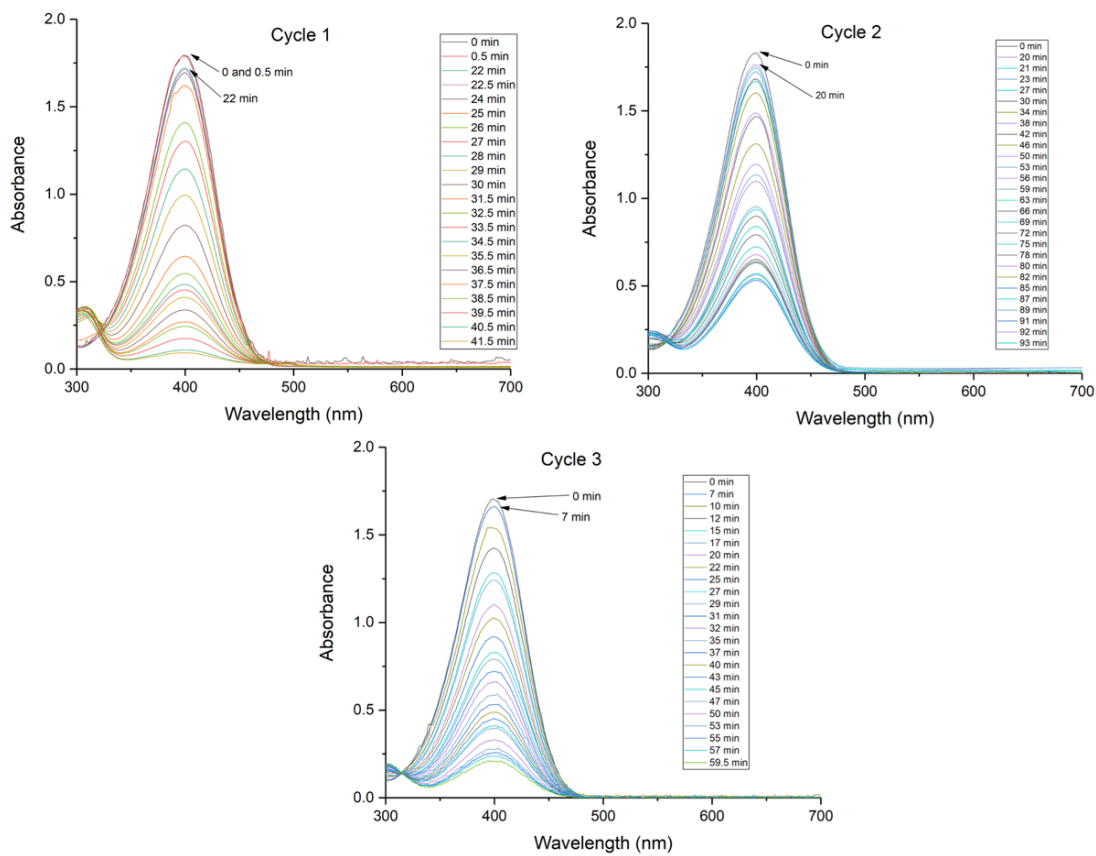


Figure S130 - UV-Vis kinetic study for the reduction of 4-nitrophenol with **AuNP-1/TiO₂** over three cycles.

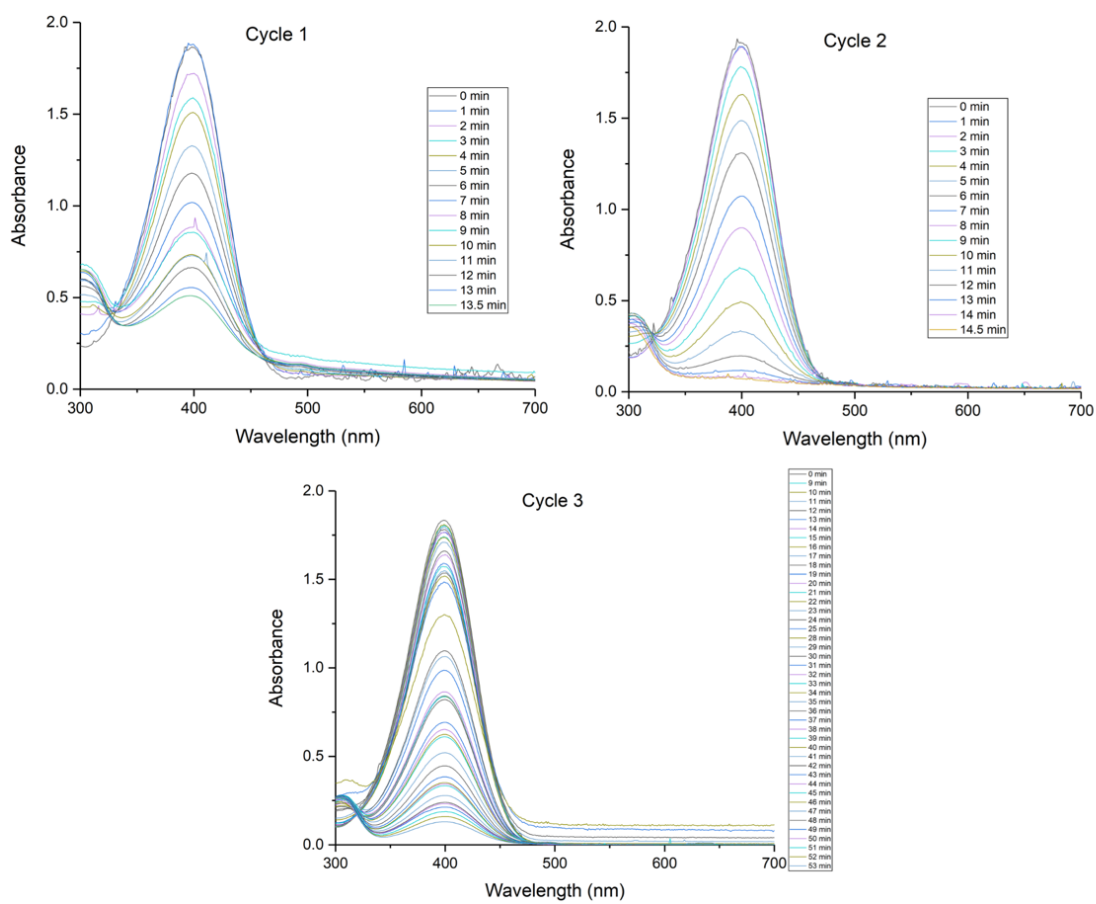


Figure S131 - UV-Vis kinetic study for the reduction of 4-nitrophenol with **AuNP-2/TiO₂** over three cycles.

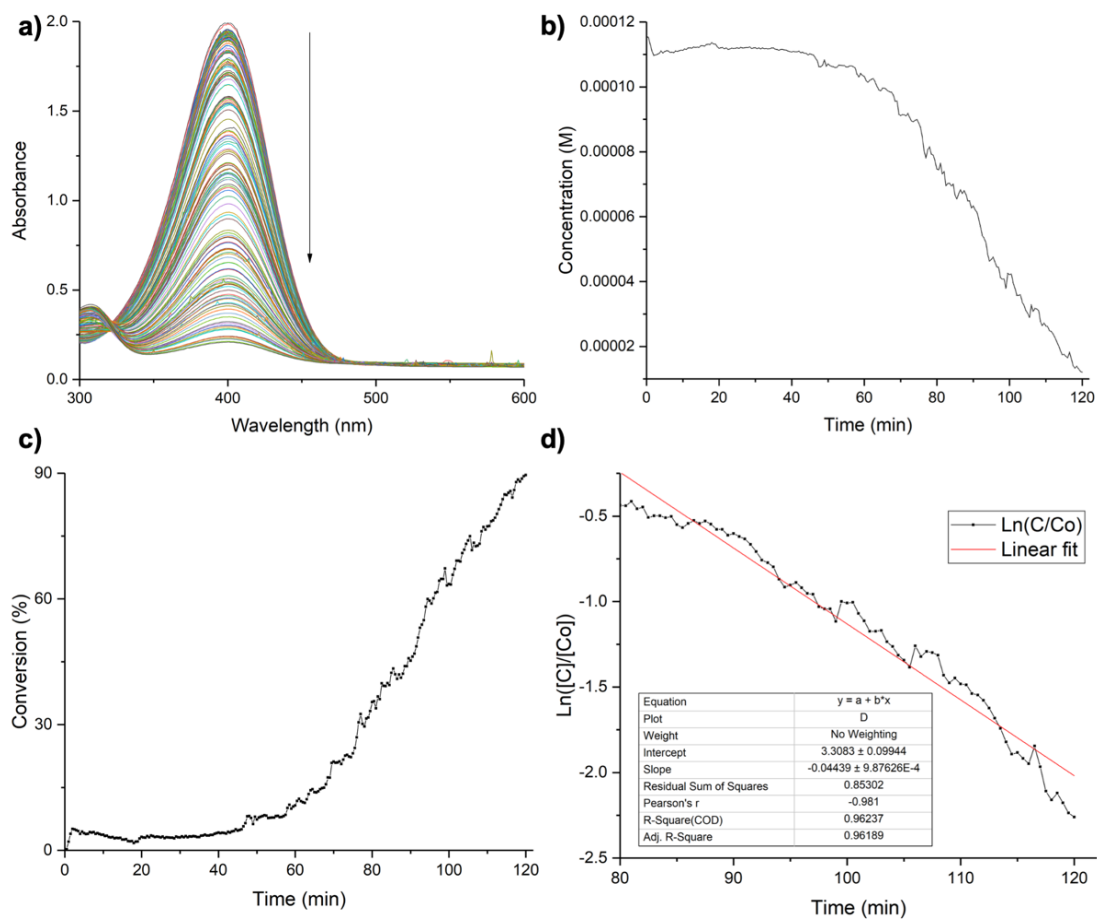


Figure S132 - **a)** UV-Vis kinetic study for the reduction of 4-nitrophenol with **AuNP-1/TiO₂** after **NaBH₄** pre-treatment, **b)** Plots of concentration vs. time, **c)** conversion vs. time and **d)** $\ln([C]/[Co])$ vs. time to calculate the rate constant.

References

1. Ndagi, U., Mhlongo, N. & Soliman, M. E. Metal complexes in cancer therapy - an update from drug design perspective. *Drug Des. Devel. Ther.* **11**, 599–616 (2017).
2. Rosenberg, B., van Camp, L. & Krigas, T. Inhibition of Cell Division in *Escherichia coli* by Electrolysis Products from a Platinum Electrode. *Nature* **205**, 698–699 (1965).
3. Reedijk, J. Metal-ligand exchange kinetics in platinum and ruthenium complexes: Significance for effectiveness as anticancer drugs. *Platin. Met. Rev.* **52**, 2–11 (2008).
4. Culy, C. R., Clemett, D. & Wiseman, L. R. Oxaliplatin: A review of its pharmacological properties and clinical efficacy in metastatic colorectal cancer and its potential in other malignancies. *Drugs* **60**, 895–924 (2000).
5. Gasser, G., Ott, I. & Metzler-Nolte, N. Organometallic anticancer compounds. *J. Med. Chem.* **54**, 3–25 (2011).
6. McNeill, J. H., Yuen, V. G., Hoveyda, H. R. & Orvig, C. Bis(maltolato)oxovanadium(IV) Is a Potent Insulin Mimic. *J. Med. Chem.* **35**, 1489–1491 (1992).
7. Berman, J. D., Waddel, D. & Hanson, B. D. Biochemical mechanisms of the antileishmanial activity of sodium stibogluconate. *Antimicrob. Agents Chemother.* **27**, 916–920 (1985).
8. Higby, G. J. Gold in medicine - A review of its use in the west before 1900. *Gold Bull.* **15**, 130–140 (1982).
9. Zou, T., Lum, C. T., Lok, C. N., Zhang, J. J. & Che, C. M. Chemical biology of anticancer gold(III) and gold(I) complexes. *Chem. Soc. Rev.* **44**, 8786–8801 (2015).
10. Sutton, B. M. Gold compounds for rheumatoid arthritis. *Gold Bull.* **19**, 15–16 (1986).
11. Sadler, P. J. & Sue, R. E. The Chemistry of Gold Drugs. *Met. Based. Drugs* **1**, 107–144 (1994).
12. Forestier, J. Rheumatoid arthritis and its treatment by gold salts. *J. Lab. Clin. Med.* **20**, 827–840 (1935).
13. Sutton, B. M., MCGusty, E., Walz, D. T. & Dimartino, M. J. Oral Gold. Antiarthritic Properties of Alkylphosphinegold Coordination Complexes. *J. Med. Chem.* **15**, 1095–1098 (1972).
14. Simon, T. M., Kunishima, D. H., Vibert, G. J. & Lorber, A. Inhibitory effects of a new oral gold compound on hela cells. *Cancer* **44**, 1965–1975 (1979).
15. Mirabelli, C. K. *et al.* Evaluation of the in Vivo Antitumor Activity and in Vitro Cytotoxic Properties of Auranofin, a Coordinated Gold Compound, in Murine Tumor Models. *Cancer Res.* **45**, 32–39 (1985).
16. Mirabelli, C. K. *et al.* Correlation of the in Vitro Cytotoxic and in Vivo Antitumor Activities of Gold(I) Coordination Complexes. *J. Med. Chem.* **29**, 218–223 (1986).

17. Milacic, V., Fregona, D. & Dou, Q. P. Gold complexes as prospective metal-based anticancer drugs. *Histol Histopathol* **23**, 101–108 (2008).
18. Liu, N. *et al.* Clinically used antirheumatic agent auranofin is a proteasomal deubiquitinase inhibitor and inhibits tumor growth. *Oncotarget* **5**, 5453–5471 (2014).
19. Chen, X. *et al.* Anti-rheumatic agent auranofin induced apoptosis in chronic myeloid leukemia cells resistant to imatinib through both Bcr/Abl-dependent and -independent mechanisms. *Oncotarget* **5**, 9118–9132 (2014).
20. Park, S. J. & Kim, I. S. The role of p38 MAPK activation in auranofin-induced apoptosis of human promyelocytic leukaemia HL-60 cells. *Br. J. Pharmacol.* **146**, 506–513 (2005).
21. Bindoli, A. *et al.* Thioredoxin reductase: A target for gold compounds acting as potential anticancer drugs. *Coord. Chem. Rev.* **253**, 1692–1707 (2009).
22. Mustacich, D. & Powis, G. Thioredoxin reductase. *Biochem. J.* **346**, 1–8 (2000).
23. Gromer, S., Arscott, L. D., Williams, C. H., Schirmer, R. H. & Becker, K. Human Placenta Thioredoxin Reductase. *J. Biol. Chem.* **273**, 20096–20101 (1998).
24. Carlos Lima, J. & Rodriguez, L. Phosphine-Gold(I) Compounds as Anticancer Agents: General Description and Mechanisms of Action. *Anticancer. Agents Med. Chem.* **11**, 921–928 (2012).
25. Berners-Price, S. J. *et al.* In Vivo Antitumor Activity and in Vitro Cytotoxic Properties of Bis[1,2-bis(diphenylphosphino)ethane]gold(I) Chloride. *Cancer Res.* **46**, 5486–5493 (1986).
26. Berners-Price, S. J. & Filipovska, A. Gold compounds as therapeutic agents for human diseases. *Metallomics* **3**, 863–873 (2011).
27. McKeage, M. J. *et al.* Role of lipophilicity in determining cellular uptake and antitumour activity of gold phosphine complexes. *Cancer Chemother. Pharmacol.* **46**, 343–350 (2000).
28. Liu, J. J. *et al.* In vitro antitumour and hepatotoxicity profiles of Au(I) and Ag(I) bidentate pyridyl phosphine complexes and relationships to cellular uptake. *J. Inorg. Biochem.* **102**, 303–310 (2008).
29. Humphreys, A. S. *et al.* Gold(I) chloride adducts of 1,3-bis(di-2-pyridylphosphino)propane: Synthesis, structural studies and antitumour activity. *Dalt. Trans.* 4943–4950 (2007). doi:10.1039/b705008a
30. Rackham, O., Nichols, S. J., Leedman, P. J., Berners-Price, S. J. & Filipovska, A. A gold(I) phosphine complex selectively induces apoptosis in breast cancer cells: Implications for anticancer therapeutics targeted to mitochondria. *Biochem. Pharmacol.* **74**, 992–1002 (2007).
31. Caruso, F., Rossi, M., Tanski, J., Pettinari, C. & Marchetti, F. Antitumor activity of the mixed phosphine gold species chlorotriphenylphosphine-1,3-bis(diphenylphosphino)propanegold(I). *J. Med. Chem.* **46**, 1737–1742 (2003).
32. Caruso, F. *et al.* Mitochondria are primary targets in apoptosis induced by the mixed phosphine gold species chlorotriphenylphosphine-1,3-bis(diphenylphosphino)propanegold(I) in melanoma cell lines. *Biochem.*

Pharmacol. **73**, 773–781 (2007).

33. Caruso, F. *et al.* Chemical behavior and in vitro activity of mixed phosphine gold(I) compounds on melanoma cell lines. *J. Med. Chem.* **51**, 1584–1591 (2008).
34. Pillarsetty, N. *et al.* In vitro and in vivo antitumor properties of tetrakis((trishydroxymethyl)phosphine)gold(I) chloride. *J. Med. Chem.* **46**, 1130–1132 (2003).
35. Tian, S., Siu, F. M., Kui, S. C. F., Lok, C. N. & Che, C. M. Anticancer gold(i)-phosphine complexes as potent autophagy-inducing agents. *Chem. Commun.* **47**, 9318–9320 (2011).
36. Fernández-Gallardo, J. *et al.* Heterometallic titanium-gold complexes inhibit renal cancer cells in vitro and in vivo. *Chem. Sci.* **6**, 5269–5283 (2015).
37. Mora, M., Gimeno, M. C. & Visbal, R. Recent advances in gold-NHC complexes with biological properties. *Chem. Soc. Rev.* **48**, 447–462 (2019).
38. Barnard, P. J., Baker, M. V., Berners-Price, S. J., Skelton, B. W. & White, A. H. Dinuclear gold(I) complexes of bridging bidentate carbene ligands: Synthesis, structure and spectroscopic characterisation. *Dalt. Trans.* **7**, 1038–1047 (2004).
39. Barnard, P. J., Baker, M. V., Berners-Price, S. J. & Day, D. A. Mitochondrial permeability transition induced by dinuclear gold(I)-carbene complexes: Potential new antimitochondrial antitumour agents. *J. Inorg. Biochem.* **98**, 1642–1647 (2004).
40. Lopez, J. & Tait, S. W. G. Mitochondrial apoptosis: Killing cancer using the enemy within. *Br. J. Cancer* **112**, 957–962 (2015).
41. Barnard, P. J. & Berners-Price, S. J. Targeting the mitochondrial cell death pathway with gold compounds. *Coord. Chem. Rev.* **251**, 1889–1902 (2007).
42. Rigobello, M. P., Scutari, G., Boscolo, R. & Bindoli, A. Induction of mitochondrial permeability transition by auranofin, a Gold(I)-phosphine derivative. *Br. J. Pharmacol.* **136**, 1162–1168 (2002).
43. Baker, M. V. *et al.* Cationic, linear Au(I) N-heterocyclic carbene complexes: Synthesis, structure and anti-mitochondrial activity. *Dalt. Trans.* **6**, 3708–3715 (2006).
44. Hickey, J. L. *et al.* Mitochondria-targeted chemotherapeutics: The rational design of gold(I) N-heterocyclic carbene complexes that are selectively toxic to cancer cells and target protein selenols in preference to thiols. *J. Am. Chem. Soc.* **130**, 12570–12571 (2008).
45. Rubbiani, R. *et al.* Benzimidazol-2-ylidene gold(I) complexes are thioredoxin reductase inhibitors with multiple antitumor properties. *J. Med. Chem.* **53**, 8608–8618 (2010).
46. Rubbiani, R. *et al.* Comparative in vitro evaluation of N-heterocyclic carbene gold(I) complexes of the benzimidazolylidene type. *J. Med. Chem.* **54**, 8646–8657 (2011).
47. Pratesi, A. *et al.* Structural Characterization of a Gold/Serum Albumin Complex. *Inorg. Chem.* **58**, 10616–10619 (2019).

48. Rubbiani, R., Salassa, L., De Almeida, A., Casini, A. & Ott, I. Cytotoxic gold(I) N-heterocyclic carbene complexes with phosphane ligands as potent enzyme inhibitors. *ChemMedChem* **9**, 1205–1210 (2014).
49. Mendes, F. *et al.* Metal-based inhibition of poly(ADP-ribose) polymerase—the guardian angel of DNA. *J. Med. Chem.* **54**, 2196–2206 (2011).
50. Tangutoori, S., Baldwin, P. & Sridhar, S. PARP inhibitors: A new era of targeted therapy. *Maturitas* **81**, 5–9 (2015).
51. Mui, Y. F. *et al.* Titanocene-Gold Complexes Containing N-Heterocyclic Carbene Ligands Inhibit Growth of Prostate, Renal, and Colon Cancers in Vitro. *Organometallics* **35**, 1218–1227 (2016).
52. Niu, W., Chen, X., Tan, W. & Veige, A. S. N-Heterocyclic Carbene–Gold(I) Complexes Conjugated to a Leukemia-Specific DNA Aptamer for Targeted Drug Delivery. *Angew. Chem. Int. Ed.* **55**, 8889–8893 (2016); *Angew. Chem.* **128**, 9035–9039 (2016).
53. Zou, T. *et al.* A binuclear gold(I) complex with mixed bridging diphosphine and bis(N-heterocyclic carbene) ligands shows favorable thiol reactivity and inhibits tumor growth and angiogenesis in vivo. *Angew. Chem. Int. Ed.* **53**, 5810–5814 (2014); *Angew. Chem.* **126**, 5920–5924 (2014).
54. Arola, A. & Vilar, R. Stabilisation of G-Quadruplex DNA by Small Molecules. *Curr. Top. Med. Chem.* **8**, 1405–1415 (2008).
55. Bazzicalupi, C. *et al.* Determinants for Tight and Selective Binding of a Medicinal Dicarbene Gold(I) Complex to a Telomeric DNA G-Quadruplex: a Joint ESI MS and XRD Investigation. *Angew. Chem. Int. Ed.* **55**, 4256–4259 (2016); *Angew. Chem.* **128**, 4328–4331 (2016).
56. Wragg, D. *et al.* On the Mechanism of Gold/NHC Compounds Binding to DNA G-Quadruplexes: Combined Metadynamics and Biophysical Methods. *Angew. Chem. Int. Ed.* **57**, 14524–14528 (2018); *Angew. Chem.* **130**, 14732–14736 (2018).
57. Bertrand, B. *et al.* Caffeine-Based Gold(I) N-Heterocyclic Carbenes as Possible Anticancer Agents: Synthesis and Biological Properties. *Inorg. Chem.* **53**, 2296–2303 (2014).
58. Humphrey, W., Dalke, A. & Schulten, K. VMD: Visual molecular dynamics. *J. Mol. Graph.* **14**, 33–38 (1996).
59. Schmidt, C. & Casini, A. Organometallic Chemistry of Gold-Based Drugs. in *Reference Module in Chemistry, Molecular Sciences and Chemical Engineering* 1–17 (Elsevier Ltd., 2021). doi:10.1016/b978-0-12-820206-7.00032-9
60. Schuh, E. *et al.* Synthesis and biological studies of some gold(I) complexes containing functionalised alkynes. *Dalt. Trans.* 10841–10845 (2009). doi:10.1039/b912898k
61. Chui, C. H. *et al.* Antitumor activity of diethynylfluorene derivatives of gold(I). *Bioorganic Med. Chem.* **17**, 7872–7877 (2009).
62. Nishikawa, M., Hashida, M. & Takakura, Y. Catalase delivery for inhibiting ROS-mediated tissue injury and tumor metastasis. *Adv. Drug Deliv. Rev.* **61**, 319–326 (2009).

63. Vergara, E. *et al.* Antiproliferative activity of gold(I) alkyne complexes containing water-soluble phosphane ligands. *Organometallics* **29**, 2596–2603 (2010).
64. Sánchez-de-Diego, C. *et al.* The anticancer effect related to disturbances in redox balance on Caco-2 cells caused by an alkynyl gold(I) complex. *J. Inorg. Biochem.* **166**, 108–121 (2017).
65. Mármol, I. *et al.* Alkynyl gold(I) complex triggers necroptosis via ROS generation in colorectal carcinoma cells. *J. Inorg. Biochem.* **176**, 123–133 (2017).
66. García-Moreno, E., Gascón, S., Rodríguez-Yoldi, M. J., Cerrada, E. & Laguna, M. S -Propargylthiopyridine phosphane derivatives as anticancer agents: Characterization and antitumor activity. *Organometallics* **32**, 3710–3720 (2013).
67. Marzano, C., Pellei, M., Tisato, F. & Santini, C. Copper Complexes as Anticancer Agents. *Anticancer. Agents Med. Chem.* **9**, 185–211 (2012).
68. Meyer, A. *et al.* On the biological properties of alkynyl phosphine gold(I) complexes. *Angew. Chem. Int. Ed.* **51**, 8895–8899 (2012); *Angew. Chem.* **124**, 9025-9030 (2012).
69. Estrada-Ortiz, N. *et al.* Anticancer Gold N-Heterocyclic Carbene Complexes: A Comparative in vitro and ex vivo Study. *ChemMedChem* **12**, 1429–1435 (2017).
70. Meier-Menches, S. M. *et al.* Comparative biological evaluation and G-quadruplex interaction studies of two new families of organometallic gold(I) complexes featuring N-heterocyclic carbene and alkynyl ligands. *J. Inorg. Biochem.* **202**, 110844 (2020).
71. Oberkofler, J. *et al.* Exploring the Reactivity and Biological Effects of Heteroleptic N-Heterocyclic Carbene Gold(I)-Alkynyl Complexes. *Eur. J. Inorg. Chem.* 1040–1051 (2020). doi:10.1002/ejic.201901043
72. Che, C. M. *et al.* Gold(III) porphyrins as a new class of anticancer drugs: Cytotoxicity, DNA binding and induction of apoptosis in human cervix epitheloid cancer cells. *Chem. Commun.* **3**, 1718–1719 (2003).
73. Lum, C. T. *et al.* Gold(III) compound is a novel chemocytotoxic agent for hepatocellular carcinoma. *Int. J. Cancer* **118**, 1527–1538 (2006).
74. To, Y. F. *et al.* Gold(III) porphyrin complex is more potent than cisplatin in inhibiting growth of nasopharyngeal carcinoma in vitro and in vivo. *Int. J. Cancer* **124**, 1971–1979 (2009).
75. Tu, S. *et al.* Gold (III) porphyrin complexes induce apoptosis and cell cycle arrest and inhibit tumor growth in colon cancer. *Cancer* **115**, 4459–4469 (2009).
76. Li, W. *et al.* Inhibition of Akt sensitises neuroblastoma cells to gold(III) porphyrin 1a, a novel antitumour drug induced apoptosis and growth inhibition. *Br. J. Cancer* **101**, 342–349 (2009).
77. Lum, C. T. *et al.* Gold(III) porphyrin 1a inhibited nasopharyngeal carcinoma metastasis in vivo and inhibited cell migration and invasion in vitro. *Cancer Lett.* **294**, 159–166 (2010).
78. Lum, C. T. *et al.* Gold(III) porphyrin 1a prolongs the survival of melanoma-bearing mice and inhibits angiogenesis. *Acta Oncol. (Madr).* **50**, 719–726 (2011).

79. Lum, C. T., Wong, A. S. T., Lin, M. C. M., Che, C. M. & Sun, R. W. Y. A gold(III) porphyrin complex as an anti-cancer candidate to inhibit growth of cancer-stem cells. *Chem. Commun.* **49**, 4364–4366 (2013).
80. Lum, C. T., Wai-Yin Sun, R., Zou, T. & Che, C. M. Gold(III) complexes inhibit growth of cisplatin-resistant ovarian cancer in association with upregulation of proapoptotic PMS2 gene. *Chem. Sci.* **5**, 1579–1584 (2014).
81. Chow, K. H. M. *et al.* A gold(III) porphyrin complex with antitumor properties targets the Wnt/ β -catenin pathway. *Cancer Res.* **70**, 329–337 (2010).
82. Hu, D. *et al.* Anticancer Gold(III) Porphyrins Target Mitochondrial Chaperone Hsp60. *Angew. Chem. Int. Ed.* **55**, 1387–1391 (2016); *Angew. Chem.* **128**, 1409–1413 (2016).
83. Tong, K. C. *et al.* An anticancer gold(III)-activated porphyrin scaffold that covalently modifies protein cysteine thiols. *PNAS* **117**, 1321–1329 (2020).
84. Sun, R. W. Y. *et al.* Stable anticancer gold(III)-porphyrin complexes: Effects of porphyrin structure. *Chem. Eur. J.* **16**, 3097–3113 (2010).
85. Garber, K. Drugging the Wnt pathway: problems and progress. *J. Natl. Cancer Inst.* **101**, 548–550 (2009).
86. Wiechmann, K. *et al.* Mitochondrial Chaperonin HSP60 Is the Apoptosis-Related Target for Myrtilone. *Cell Chem. Biol.* **24**, 614–623 (2017).
87. Nardis, S., Mandoj, F., Stefanelli, M. & Paolesse, R. Metal complexes of corrole. *Coord. Chem. Rev.* **388**, 360–405 (2019).
88. Teo, R. D. *et al.* A cytotoxic and cytostatic gold(III) corrole. *Chem. Commun.* **50**, 13789–13792 (2014).
89. Agadjanian, H. *et al.* Specific delivery of corroles to cells via noncovalent conjugates with viral proteins. *Pharm. Res.* **23**, 367–377 (2006).
90. Messori, L. *et al.* Gold(III) Complexes as Potential Antitumor Agents: Solution Chemistry and Cytotoxic Properties of Some Selected Gold(III) Compounds. *J. Med. Chem.* **43**, 3541–3548 (2000).
91. Verkman, A. S., Anderson, M. O. & Papadopoulos, M. C. Aquaporins: important but elusive drug targets. *Nat. Rev. Drug Discov.* **13**, 259–77 (2014).
92. Martins, A. P. *et al.* Targeting aquaporin function: Potent inhibition of aquaglyceroporin-3 by a gold-based compound. *PLoS One* **7**, e37435 (2012).
93. Martins, A. P. *et al.* Aquaporin inhibition by gold(III) compounds: New insights. *ChemMedChem* **8**, 1086–1092 (2013).
94. Graziani, V. *et al.* A Multi-Level Theoretical Study to Disclose the Binding Mechanisms of Gold(III)–Bipyridyl Compounds as Selective Aquaglyceroporin Inhibitors. *Chem. Eur. J.* **23**, 13802–13813 (2017).
95. Casini, A. *et al.* Structural and solution chemistry, antiproliferative effects, and DNA and protein binding properties of a series of dinuclear gold(III) compounds with bipyridyl ligands. *J. Med. Chem.* **49**, 5524–5531 (2006).
96. Casini, A. *et al.* Chemistry, antiproliferative properties, tumor selectivity, and

- molecular mechanisms of novel gold(III) compounds for cancer treatment: A systematic study. *J. Biol. Inorg. Chem.* **14**, 1139–1149 (2009).
97. Zou, T., Lum, C. T., Chui, S. S.-Y. & Che, C.-M. Gold(III) Complexes Containing N-Heterocyclic Carbene Ligands: Thiol “Switch-on” Fluorescent Probes and Anti-Cancer Agents. *Angew. Chem. Int. Ed.* **52**, 2930–2933 (2013); *Angew. Chem.* **125**, 3002–3005 (2013).
 98. Shimida, H., Takahashi, K., Funakoshi, T. & Kojuma, S. Protective effects of dithiocarbamates against toxicity of cis-diamminedichloroplatinum in mice. *Biol. Pharm. Bull.* **16**, 368–371 (1993).
 99. Ronconi, L. *et al.* Gold dithiocarbamate derivatives as potential antineoplastic agents: Design, spectroscopic properties, and in vitro antitumor activity. *Inorg. Chem.* **44**, 1867–1881 (2005).
 100. Crawford, L. J., Walker, B. & Irvine, A. E. Proteasome inhibitors in cancer therapy. *J. Cell Commun. Signal.* **5**, 101–110 (2011).
 101. Milacic, V. *et al.* A novel anticancer gold(III) dithiocarbamate compound inhibits the activity of a purified 20S proteasome and 26S proteasome in human breast cancer cell cultures and xenografts. *Cancer Res.* **66**, 10478–10486 (2006).
 102. Saggiaro, D. *et al.* Gold(III)-Dithiocarbamate Complexes Induce Cancer Cell Death Triggered by Thioredoxin Redox System Inhibition and Activation of ERK Pathway. *Chem. Biol.* **14**, 1128–1139 (2007).
 103. Cattaruzza, L. *et al.* Antitumor activity of gold(III)-dithiocarbamate derivatives on prostate cancer cells and xenografts. *Int. J. Cancer* **128**, 206–215 (2011).
 104. Marzano, C. *et al.* Gold(III)-dithiocarbamate anticancer agents: Activity, toxicology and histopathological studies in rodents. *Int. J. Cancer* **129**, 487–496 (2011).
 105. Albrecht, M. Cyclometalation using d-block transition metals: Fundamental aspects and recent trends. *Chem. Rev.* **110**, 576–623 (2010).
 106. Jürgens, S., Kühn, F. E. & Casini, A. Cyclometalated Complexes of Platinum and Gold with Biological Properties: State-of-the-Art and Future Perspectives. *Curr. Med. Chem.* **25**, 437–461 (2017).
 107. Bertrand, B. & Casini, A. A golden future in medicinal inorganic chemistry: The promise of anticancer gold organometallic compounds. *Dalt. Trans.* **43**, 4209–4219 (2014).
 108. Parish, R. V. *et al.* Chemical and Biological Studies of Dichloro(2-((dimethylamino)methyl)phenyl)gold(III). *Inorg. Chem.* **35**, 1659–1666 (1996).
 109. Buckley, R. G. *et al.* Antitumor properties of some 2-[(dimethylamino)methyl]phenylgold(III) complexes. *J. Med. Chem.* **39**, 5208–5214 (1996).
 110. Fricker, S. P. *et al.* Metal compounds for the treatment of parasitic diseases. *J. Inorg. Biochem.* **102**, 1839–1845 (2008).
 111. Zhu, Y. *et al.* Inhibition of the cathepsin cysteine proteases B and K by square-planar cycloaurated gold(III) compounds and investigation of their anti-cancer activity. *J. Inorg. Biochem.* **105**, 754–762 (2011).

112. Bertrand, B. *et al.* Exploring the potential of gold(III) cyclometallated compounds as cytotoxic agents: variations on the C^N theme. *Dalt. Trans.* **44**, 11911–11918 (2015).
113. Spreckelmeyer, S. *et al.* On the toxicity and transport mechanisms of cisplatin in kidney tissues in comparison to a gold-based cytotoxic agent. *Metallomics* **9**, 1786–1795 (2017).
114. Fan, D., Yang, C. T., Ranford, J. D., Lee, P. F. & Vittal, J. J. Chemical and biological studies of the dichloro(2-phenylpyridine) gold(III) complex and its derivatives. *Dalt. Trans.* **1**, 2680–2685 (2003).
115. Fan, D., Yang, C. T., Ranford, J. D., Vittal, J. J. & Foo Lee, P. Synthesis, characterization, and biological activities of 2-phenylpyridine gold(III) complexes with thiolate ligands. *J. Chem. Soc. Dalt. Trans.* **3**, 3376–3381 (2003).
116. Zhang, J. J., Sun, R. W. Y. & Che, C. M. A dual cytotoxic and anti-angiogenic water-soluble gold(III) complex induces endoplasmic reticulum damage in HeLa cells. *Chem. Commun.* **48**, 3388–3390 (2012).
117. Zhang, J. J., Ng, K. M., Lok, C. N., Sun, R. W. Y. & Che, C. M. Deubiquitinases as potential anti-cancer targets for gold(III) complexes. *Chem. Commun.* **49**, 5153–5155 (2013).
118. Rubbiani, R. *et al.* Anticancer profile of a series of gold(III) (2-phenyl)pyridine complexes. *ChemMedChem* **9**, 2781–2790 (2014).
119. Shaik, N. *et al.* Synthesis of apoptosis-inducing iminophosphorane organogold(III) complexes and study of their interactions with biomolecular targets. *Inorg. Chem.* **48**, 1577–1587 (2009).
120. Wong, K. H., Cheung, K. K., Chan, M. C. W. & Che, C. M. Application of 2,6-diphenylpyridine as a tridentate [C^NΛC] dianionic ligand in organogold(III) chemistry. Structural and spectroscopic properties of mono- and binuclear transmetalated gold(III) complexes. *Organometallics* **17**, 3505–3511 (1998).
121. Li, C. K. L., Sun, R. W. Y., Kui, S. C. F., Zhu, N. & Che, C. M. Anticancer cyclometalated [AuIII_m(C^NΛC)_mL]ⁿ⁺ compounds: Synthesis and cytotoxic properties. *Chem. Eur. J.* **12**, 5253–5266 (2006).
122. Sun, R. W. Y. *et al.* A dinuclear cyclometalated gold(III)-phosphine complex targeting thioredoxin reductase inhibits hepatocellular carcinoma in vivo. *Chem. Sci.* **4**, 1979–1988 (2013).
123. Yan, J. J. *et al.* Cyclometalated gold(III) complexes with N-heterocyclic carbene ligands as topoisomerase I poisons. *Chem. Commun.* **46**, 3893–3895 (2010).
124. Fung, S. K. *et al.* Cyclometalated Gold(III) Complexes Containing N-Heterocyclic Carbene Ligands Engage Multiple Anti-Cancer Molecular Targets. *Angew. Chem. Int. Ed.* **56**, 3892–3896 (2017); *Angew. Chem.* **129**, 3950–3954 (2017).
125. Tsai, J. L. L., Chan, A. O. Y. & Che, C. M. A luminescent cyclometalated gold(III)-avidin conjugate with a long-lived emissive excited state that binds to proteins and DNA and possesses anti-proliferation capacity. *Chem. Commun.* **51**, 8547–8550 (2015).
126. Fernandez-Cestau, J. *et al.* Synthesis and luminescence modulation of pyrazine-based gold(III) pincer complexes. *Chem. Commun.* **51**, 16629–16632 (2015).

127. Bertrand, B. *et al.* Cytotoxicity of Pyrazine-Based Cyclometalated (C^NNpz^C)Au(III) Carbene Complexes: Impact of the Nature of the Ancillary Ligand on the Biological Properties. *Inorg. Chem.* **56**, 5728–5740 (2017).
128. Wade, M., Li, Y. C. & Wahl, G. M. MDM2, MDMX and p53 in oncogenesis and cancer therapy. *Nat. Rev. Cancer* **13**, 83–96 (2013).
129. Bertrand, B., O'Connell, M. A., Waller, Z. A. E. & Bochmann, M. A Gold(III) Pincer Ligand Scaffold for the Synthesis of Binuclear and Bioconjugated Complexes: Synthesis and Anticancer Potential. *Chem. Eur. J.* **24**, 3613–3622 (2018).
130. Marcon, G. *et al.* Gold(III) complexes with bipyridyl ligands: Solution chemistry, cytotoxicity, and DNA binding properties. *J. Med. Chem.* **45**, 1672–1677 (2002).
131. Messori, L. *et al.* Solution chemistry and cytotoxic properties of novel organogold(III) compounds. *Bioorganic Med. Chem.* **12**, 6039–6043 (2004).
132. Pia Rigobello, M. *et al.* Gold complexes inhibit mitochondrial thioredoxin reductase: Consequences on mitochondrial functions. *J. Inorg. Biochem.* **98**, 1634–1641 (2004).
133. Marcon, G., Messori, L., Orioli, P., Cinellu, M. A. & Minghetti, G. Reactions of gold(III) complexes with serum albumin. *Eur. J. Biochem.* **270**, 4655–4661 (2003).
134. Gabbiani, C. *et al.* Protein metalation by metal-based drugs: Reactions of cytotoxic gold compounds with cytochrome c and lysozyme. *J. Biol. Inorg. Chem.* **17**, 1293–1302 (2012).
135. Coronello, M. *et al.* Mechanisms of cytotoxicity of selected organogold(III) compounds. *J. Med. Chem.* **48**, 6761–6765 (2005).
136. Gabbiani, C. *et al.* Medicinal gold compounds form tight adducts with the copper chaperone Atox-1: Biological and pharmacological implications. *Chem. Commun.* **48**, 11623–11625 (2012).
137. Micale, N. *et al.* Selected cytotoxic gold compounds cause significant inhibition of 20S proteasome catalytic activities. *J. Inorg. Biochem.* **141**, 79–82 (2014).
138. Bondžić, A. M. *et al.* Na/K-ATPase as a target for anticancer metal based drugs: insights into molecular interactions with selected gold(III) complexes. *Metallomics* **9**, 292–300 (2017).
139. Gabbiani, C. *et al.* Thioredoxin reductase, an emerging target for anticancer metallodrugs. Enzyme inhibition by cytotoxic gold(III) compounds studied with combined mass spectrometry and biochemical assays. *Medchemcomm* **2**, 50–54 (2011).
140. Meier, S. M., Gerner, C., Keppler, B. K., Cinellu, M. A. & Casini, A. Mass Spectrometry Uncovers Molecular Reactivities of Coordination and Organometallic Gold(III) Drug Candidates in Competitive Experiments That Correlate with Their Biological Effects. *Inorg. Chem.* **55**, 4248–4259 (2016).
141. Gabbiani, C. *et al.* Mechanistic studies on two dinuclear organogold(III) compounds showing appreciable antiproliferative properties and a high redox stability. *Metallomics* **3**, 1318–1323 (2011).
142. Gratteri, P. *et al.* Interactions of selected gold(III) complexes with DNA G

- quadruplexes. *Dalt. Trans.* **44**, 3633–3639 (2015).
143. Carboni, S. *et al.* New Variations on the Theme of Gold(III) CANAN Cyclometalated Complexes as Anticancer Agents: Synthesis and Biological Characterization. *Inorg. Chem.* **57**, 14852–14865 (2018).
 144. Yang, M., Li, J. & Chen, P. R. Transition metal-mediated bioorthogonal protein chemistry in living cells. *Chem. Soc. Rev.* **43**, 6511–6526 (2014).
 145. Hang, H. C., Yu, C., Kato, D. L. & Bertozzi, C. R. A metabolic labeling approach toward proteomic analysis of mucin-type O-linked glycosylation. *Proc. Natl. Acad. Sci.* **100**, 14846–14851 (2003).
 146. Chankeshwara, S. V., Indrigo, E. & Bradley, M. Palladium-mediated chemistry in living cells. *Curr. Opin. Chem. Biol.* **21**, 128–135 (2014).
 147. Martínez-Calvo, M. & Mascareñas, J. L. Organometallic catalysis in biological media and living settings. *Coord. Chem. Rev.* **359**, 57–79 (2018).
 148. Sasmal, P. K., Streu, C. N. & Meggers, E. Metal complex catalysis in living biological systems. *Chem. Commun.* **49**, 1581–1587 (2013).
 149. Qin, L. H., Hu, W. & Long, Y. Q. Bioorthogonal chemistry: Optimization and application updates during 2013–2017. *Tetrahedron Lett.* **59**, 2214–2228 (2018).
 150. Yusop, R. M., Unciti-Broceta, A., Johansson, E. M. V, Sánchez-Martín, R. M. & Bradley, M. Palladium-mediated intracellular chemistry. *Nat. Chem.* **3**, 239–243 (2011).
 151. Cook, J. D., Penner-Hahn, J. E. & Stemmler, T. L. Structure and Dynamics of Metalloproteins in Live Cells. *Methods Cell Biol.* **90**, 199–216 (2008).
 152. Ngo, A. H., Bose, S. & Do, L. H. Intracellular Chemistry: Integrating Molecular Inorganic Catalysts with Living Systems. *Chem. Eur. J.* **24**, 10584–10594 (2018).
 153. Rostovtsev, V. V., Green, L. G., Fokin, V. V. & Sharpless, K. B. A Stepwise Huisgen Cycloaddition Process: Copper(I)-Catalyzed Regioselective ‘Ligation’ of Azides and Terminal Alkynes. *Angew. Chem. Int. Ed.* **41**, 2596–2599 (2002); *Angew. Chem.* **114**, 2708–2711 (2002).
 154. Tornøe, C. W., Christensen, C. & Meldal, M. Peptidotriazoles on solid phase: [1,2,3]-Triazoles by regiospecific copper(I)-catalyzed 1,3-dipolar cycloadditions of terminal alkynes to azides. *J. Org. Chem.* **67**, 3057–3064 (2002).
 155. Sletten, E. M. & Bertozzi, C. R. Bioorthogonal chemistry: Fishing for selectivity in a sea of functionality. *Angew. Chem. Int. Ed.* **48**, 6974–6998 (2009); *Angew. Chem.* **121**, 7108–7133 (2009).
 156. Wang, Q. *et al.* Bioconjugation by copper(I)-catalyzed azide-alkyne [3 + 2] cycloaddition. *J. Am. Chem. Soc.* **125**, 3192–3193 (2003).
 157. Speers, A. E., Adam, G. C. & Cravatt, B. F. Activity-based protein profiling in vivo using a copper(I)-catalyzed azide-alkyne [3 + 2] cycloaddition. *J. Am. Chem. Soc.* **125**, 4686–4687 (2003).
 158. Link, A. J. & Tirrell, D. A. Cell surface labeling of *Escherichia coli* via copper(I)-catalyzed [3+2] cycloaddition. *J. Am. Chem. Soc.* **125**, 11164–11165 (2003).

159. Streu, C. & Meggers, E. Ruthenium-induced allylcarbamate cleavage in living cells. *Angew. Chem. Int. Ed.* **45**, 5645–5648 (2006); *Angew. Chem.* **118**, 5773–5776 (2006).
160. Soldevila-Barreda, J. J. & Metzler-Nolte, N. Intracellular catalysis with selected metal complexes and metallic nanoparticles: Advances toward the development of catalytic metallodrugs. *Chem. Rev.* **119**, 829–869 (2019).
161. Völker, T., Dempwolff, F., Graumann, P. L. & Meggers, E. Progress towards bioorthogonal catalysis with organometallic compounds. *Angew. Chem. Int. Ed.* **53**, 10536–10540 (2014); *Angew. Chem.* **126**, 10705–10710 (2014).
162. Spicer, C. D., Triemer, T. & Davis, B. G. Palladium-mediated cell-surface labeling. *J. Am. Chem. Soc.* **134**, 800–803 (2012).
163. Indrigo, E., Clavadetscher, J., Chankeshwara, S. V., Lilienkamp, A. & Bradley, M. Palladium-mediated in situ synthesis of an anticancer agent. *Chem. Commun.* **52**, 14212–14214 (2016).
164. Clavadetscher, J., Indrigo, E., Chankeshwara, S. V., Lilienkamp, A. & Bradley, M. In-Cell Dual Drug Synthesis by Cancer-Targeting Palladium Catalysts. *Angew. Chem. Int. Ed.* **56**, 6864–6868 (2017); *Angew. Chem.* **129**, 6968–6972 (2017).
165. Li, N., Lim, R. K. V., Edwardraja, S. & Lin, Q. Copper-free sonogashira cross-coupling for functionalization of alkyne-encoded proteins in aqueous medium and in bacterial cells. *J. Am. Chem. Soc.* **133**, 15316–15319 (2011).
166. Lim, R. K. V., Li, N., Ramil, C. P. & Lin, Q. Fast and sequence-specific palladium-mediated cross-coupling reaction identified from phage display. *ACS Chem. Biol.* **9**, 2139–2148 (2014).
167. Li, N., Ramil, C. P., Lim, R. K. V. & Lin, Q. A genetically encoded alkyne directs palladium-mediated protein labeling on live mammalian cell surface. *ACS Chem. Biol.* **10**, 379–384 (2015).
168. Miller, M. A. *et al.* Nano-palladium is a cellular catalyst for in vivo chemistry. *Nat. Commun.* **8**, DOI: 10.1038/ncomms15906 (2017).
169. Martínez-Calvo, M. *et al.* Intracellular Deprotection Reactions Mediated by Palladium Complexes Equipped with Designed Phosphine Ligands. *ACS Catal.* **8**, 6055–6061 (2018).
170. Indrigo, E. *et al.* Intracellular delivery of a catalytic organometallic complex. *Chem. Commun.* **53**, 6712–6715 (2017).
171. Li, J. *et al.* Palladium-triggered deprotection chemistry for protein activation in living cells. *Nat. Chem.* **6**, 352–361 (2014).
172. Wang, J. *et al.* Chemical remodeling of cell-surface sialic acids through a palladium-triggered bioorthogonal elimination reaction. *Angew. Chem. Int. Ed.* **54**, 5364–5368 (2015); *Angew. Chem.* **127**, 5454–5458 (2015).
173. Weiss, J. T. *et al.* Extracellular palladium-catalysed dealkylation of 5-fluoro-1-propargyl-uracil as a bioorthogonally activated prodrug approach. *Nat. Commun.* **5**, DOI: 10.1038/ncomms4277 (2014).
174. Corma, A., Leyva-Pérez, A. & Sabater, M. J. Gold-catalyzed carbon-heteroatom

- bond-forming reactions. *Chem. Rev.* **111**, 1657–1712 (2011).
175. Joost, M., Amgoune, A. & Bourissou, D. Reactivity of Gold Complexes towards Elementary Organometallic Reactions. *Angew. Chem. Int. Ed.* **54**, 15022–15045 (2015); *Angew. Chem.* **127**, 15234–15258 (2015).
 176. Arcadi, A. Alternative Synthetic Methods through New Developments in Catalysis by Gold. *Chem. Rev.* **108**, 3266–3325 (2008).
 177. Halliday, C. J. V. & Lynam, J. M. Gold-alkynyls in catalysis: Alkyne activation, gold cumulenes and nuclearity. *Dalt. Trans.* **45**, 12611–12626 (2016).
 178. Thomas, S. R. & Casini, A. Gold compounds for catalysis and metal-mediated transformations in biological systems. *Curr. Opin. Chem. Biol.* **55**, 103–110 (2020).
 179. Jung Jou, M. *et al.* Highly selective fluorescent probe for Au³⁺ based on cyclization of propargylamide. *Chem. Commun.* 7218–7220 (2009). doi:10.1039/b917832e
 180. Beccalli, E. M., Borsini, E., Broggin, G., Palmisano, G. & Sottocornola, S. Intramolecular Pd(II)-Catalyzed Cyclization of Propargylamides: Straightforward Synthesis of 5-Oxazolecarbaldehydes. *J. Org. Chem.* **73**, 4746–4749 (2008).
 181. Yang, Y., Lee, S. & Tae, J. A Gold(III) Ion-Selective Fluorescent Probe and Its Application to Bioimaging. *Org. Lett.* **11**, 5610–5613 (2009).
 182. Wang, J. B., Wu, Q. Q., Min, Y. Z., Liu, Y. Z. & Song, Q. H. A novel fluorescent probe for Au(III)/Au(I) ions based on an intramolecular hydroamination of a Bodipy derivative and its application to bioimaging. *Chem. Commun.* **48**, 744–746 (2012).
 183. Seo, H. *et al.* Ground-state elevation approach to suppress side reactions in gold-sensing systems based on alkyne activation. *Org. Lett.* **16**, 1374–1377 (2014).
 184. Seo, H. *et al.* A reaction-based sensing scheme for gold species: Introduction of a (2-ethynyl)benzoate reactive moiety. *Org. Lett.* **14**, 5062–5065 (2012).
 185. Fan, J., Hu, M., Zhan, P. & Peng, X. Energy transfer cassettes based on organic fluorophores: Construction and applications in ratiometric sensing. *Chem. Soc. Rev.* **42**, 29–43 (2013).
 186. Do, J. H., Kim, H. N., Yoon, J., Kim, J. S. & Kim, H. A Rationally Designed Fluorescence Turn-On Probe for the Gold(III) Ion. *Org. Lett.* **12**, 932–934 (2010).
 187. Tsubokura, K. *et al.* In Vivo Gold Complex Catalysis within Live Mice. *Angew. Chem. Int. Ed.* **56**, 3579–3584 (2017); *Angew. Chem.* **129**, 3633–3638 (2017).
 188. Latypova, L. *et al.* Sequential Double “Clicks” toward Structurally Well-Defined Heterogeneous N-Glycoclusters: The Importance of Cluster Heterogeneity on Pattern Recognition In Vivo. *Adv. Sci.* **4**, 1600394 (2017).
 189. Ogura, A. *et al.* Visualizing Trimming Dependence of Biodistribution and Kinetics with Homo- and Heterogeneous N-Glycoclusters on Fluorescent Albumin. *Sci. Rep.* **6**, 21797 (2016).
 190. Tanaka, K. Chemically synthesized glycoconjugates on proteins: Effects of multivalency and glycoform: In vivo. *Org. Biomol. Chem.* **14**, 7597–7794 (2016).

191. Garg, A. *et al.* Elucidation of the Binding Mechanism of Coumarin Derivatives with Human Serum Albumin. *PLoS One* **8**, e63805 (2013).
192. Lin, Y., Vong, K., Matsuoka, K. & Tanaka, K. 2-Benzoylpyridine Ligand Complexation with Gold Critical for Propargyl Ester-Based Protein Labeling. *Chem. Eur. J.* **24**, 10595–10600 (2018).
193. Bisseret, P., Abdelkafi, H. & Blanchard, N. Aryl transition metal chemical warheads for protein bioconjugation. *Chem. Sci.* **9**, 5132–5144 (2018).
194. Vinogradova, E. V., Zhang, C., Spokoyny, A. M., Pentelute, B. L. & Buchwald, S. L. Organometallic palladium reagents for cysteine bioconjugation. *Nature* **526**, 687–691 (2015).
195. Kung, K. K. Y. *et al.* Cyclometalated gold(III) complexes for chemoselective cysteine modification via ligand controlled C—S bond-forming reductive elimination. *Chem. Commun.* **50**, 11899–11902 (2014).
196. Messina, M. S. *et al.* Organometallic Gold(III) Reagents for Cysteine Arylation. *J. Am. Chem. Soc.* **140**, 7065–7069 (2018).
197. de Paiva, R. E. F. *et al.* Gold-Catalyzed C—S Aryl-Group Transfer in Zinc Finger Proteins. *Angew. Chem. Int. Ed.* **57**, 9305–9309 (2018); *Angew. Chem.* **130**, 9449–9453 (2018).
198. Tong, K. C. *et al.* An anticancer gold(III)-activated porphyrin scaffold that covalently modifies protein cysteine thiols. *Proc. Natl. Acad. Sci. U. S. A.* **117**, 1321–1329 (2020).
199. Ko, H. M. *et al.* Selective modification of alkyne-linked peptides and proteins by cyclometalated gold(III) (C^N) complex-mediated alkynylation. *Bioorg. Med. Chem.* **28**, 115375 (2020).
200. Patil, N. T. *et al.* Exploiting the higher alkynophilicity of Au-species: Development of a highly selective fluorescent probe for gold ions. *Chem. Commun.* **48**, 11229–11231 (2012).
201. Vidal, C., Tomás-Gamasa, M., Destito, P., López, F. & Mascareñas, J. L. Concurrent and orthogonal gold(I) and ruthenium(II) catalysis inside living cells. *Nat. Commun.* **9**, 1913 (2018).
202. Pérez-López, A. M. *et al.* Gold-Triggered Uncaging Chemistry in Living Systems. *Angew. Chem. Int. Ed.* **56**, 12548–12552 (2017); *Angew. Chem.* **129**, 12722–12726 (2017).
203. Rubio-Ruiz, B., Pérez-López, A. M., Sebastián, V. & Unciti-Broceta, A. A minimally-masked inactive prodrug of panobinostat that is bioorthogonally activated by gold chemistry. *Bioorg. Med. Chem.* **41**, 116217 (2021).
204. Garnock-Jones, K. P. Panobinostat: First global approval. *Drugs* **75**, 695–704 (2015).
205. Dreaden, E. C., Alkilany, A. M., Huang, X., Murphy, C. J. & El-Sayed, M. A. The golden age: Gold nanoparticles for biomedicine. *Chem. Soc. Rev.* **41**, 2740–2779 (2012).
206. Elahi, N., Kamali, M. & Baghersad, M. H. Recent biomedical applications of gold

nanoparticles: A review. *Talanta* **184**, 537–556 (2018).

207. Serpell, C. J., Cookson, J. & Beer, P. D. N-Functionalised Imidazoles as Stabilisers for Metal Nanoparticles in Catalysis and Anion Binding. *ChemistryOpen* **9**, 683–690 (2020).
208. Falahati, M. *et al.* Gold nanomaterials as key suppliers in biological and chemical sensing, catalysis, and medicine. *Biochim. Biophys. Acta. Gen. Subj.* **1864**, 129435 (2020).
209. Hutter, E. & Fendler, J. H. Exploitation of localized surface plasmon resonance. *Adv. Mater.* **16**, 1685–1706 (2004).
210. Yang, X., Yang, M., Pang, B., Vara, M. & Xia, Y. Gold Nanomaterials at Work in Biomedicine. *Chem. Rev.* **115**, 10410–10488 (2015).
211. Lis, D. & Cecchet, F. Localized surface plasmon resonances in nanostructures to enhance nonlinear vibrational spectroscopies: Towards an astonishing molecular sensitivity. *Beilstein J. Nanotechnol.* **5**, 2275–2292 (2014).
212. Pan, M. *et al.* Noble Metal Nanostructured Materials for Chemical and Biosensing Systems. *Nanomaterials* **10**, 209 (2020).
213. Edwards, P. P. & Thomas, J. M. Gold in a metallic divided state - From Faraday to present-day nanoscience. *Angew. Chem. Int. Ed.* **46**, 5480–5486 (2007); *Angew. Chem.* **119**, 5576–5582 (2007).
214. Murphy, C. J. *et al.* Gold Nanoparticles in Biology: Beyond Toxicity to Cellular Imaging. *Acc. Chem. Res.* **41**, 1721–1730 (2008).
215. Jain, P. K., Huang, X., El-Sayed, I. H. & El-Sayed, M. A. Noble metals on the nanoscale: Optical and photothermal properties and some applications in imaging, sensing, biology, and medicine. *Acc. Chem. Res.* **41**, 1578–1586 (2008).
216. Amiens, C., Ciuculescu-Pradines, D. & Philippot, K. Controlled metal nanostructures: Fertile ground for coordination chemists. *Coord. Chem. Rev.* **308**, 409–432 (2016).
217. Brust, M., Walker, M., Bethell, D., Schiffrin, D. J. & Whyman, R. Synthesis of Thiol-derivatised Gold Nanoparticles in a Two-phase Liquid-Liquid System. *J. Chem. Soc., Chem. Commun.* 801–802 (1994).
218. Maye, M. M., Chun, S. C., Han, L., Rabinovich, D. & Zhong, C. J. Novel spherical assembly of gold nanoparticles mediated by a tetradentate thioether. *J. Am. Chem. Soc.* **124**, 4958–4959 (2002).
219. Peterle, T., Ringler, P. & Mayor, M. Gold nanoparticles stabilized by acetylene-functionalized multidentate thioether ligands: building blocks for nanoparticle superstructures. *Adv. Funct. Mater.* **19**, 3497–3506 (2009).
220. Sharma, R. *et al.* NMR characterization of ligand binding and exchange dynamics in triphenylphosphine-capped gold nanoparticles. *J. Phys. Chem. C* **113**, 16387–16393 (2009).
221. Cushing, B. L., Kolesnichenko, V. L. & O'Connor, C. J. Recent advances in the liquid-phase syntheses of inorganic nanoparticles. *Chem. Rev.* **104**, 3893–3946 (2004).

222. Heuer-Jungemann, A. *et al.* The role of ligands in the chemical synthesis and applications of inorganic nanoparticles. *Chem. Rev.* **119**, 4819–4880 (2019).
223. Smith, C. A. *et al.* N-Heterocyclic Carbenes in Materials Chemistry. *Chem. Rev.* **119**, 4986–5056 (2019).
224. Ling, X., Schaeffer, N., Roland, S. & Pileni, M. P. Nanocrystals: Why do silver and gold n-heterocyclic carbene precursors behave differently? *Langmuir* **29**, 12647–12656 (2013).
225. Roland, S., Ling, X. & Pileni, M. P. N-Heterocyclic Carbene Ligands for Au Nanocrystal Stabilization and Three-Dimensional Self-Assembly. *Langmuir* **32**, 7683–7696 (2016).
226. Ling, X., Roland, S. & Pileni, M. P. Supracrystals of N-heterocyclic carbene-coated Au nanocrystals. *Chem. Mater.* **27**, 414–423 (2015).
227. Narouz, M. R. *et al.* N-heterocyclic carbene-functionalized magic-number gold nanoclusters. *Nat. Chem.* **11**, 419–425 (2019).
228. Salorinne, K. *et al.* Synthesis and Properties of an Au₆ Cluster Supported by a Mixed N-Heterocyclic Carbene-Thiolate ligand. *Chem. Commun.* **56**, 6102–6105 (2020).
229. Nigra, M. M. *et al.* Accessible gold clusters using calix[4]arene N-heterocyclic carbene and phosphine ligands. *Dalt. Trans.* **42**, 12762–12771 (2013).
230. Zhukhovitskiy, A. V., Mavros, M. G., Van Voorhis, T. & Johnson, J. A. Addressable carbene anchors for gold surfaces. *J. Am. Chem. Soc.* **135**, 7418–7421 (2013).
231. Crudden, C. M. *et al.* Ultra stable self-assembled monolayers of N-heterocyclic carbenes on gold. *Nat. Chem.* **6**, 409–553 (2014).
232. Crudden, C. M. *et al.* Simple direct formation of self-assembled N-heterocyclic carbene monolayers on gold and their application in biosensing. *Nat. Commun.* **7**, DOI: 10.1038/ncomms12654 (2016).
233. Wang, G. *et al.* Ballbot-type motion of N-heterocyclic carbenes on gold surfaces. *Nat. Chem.* **9**, 152–156 (2017).
234. Li, Z. *et al.* Carboxymethylated Dextran-Modified N-Heterocyclic Carbene Self-Assembled Monolayers on Gold for Use in Surface Plasmon Resonance Biosensing. *ACS Appl. Mater. Interfaces* **9**, 39223–39234 (2017).
235. Li, Z. *et al.* Self-Assembled N-Heterocyclic Carbene-Based Carboxymethylated Dextran Monolayers on Gold as a Tunable Platform for Designing Affinity-Capture Biosensor Surfaces. *ACS Appl. Mater. Interfaces* **10**, 17560–17570 (2018).
236. Arduengo, A. J., Harlow, R. L. & Kline, M. A Stable Crystalline Carbene. *J. Am. Chem. Soc.* **113**, 361–363 (1991).
237. Hopkinson, M. N., Richter, C., Schedler, M. & Glorius, F. An overview of N-heterocyclic carbenes. *Nature* **510**, 485–496 (2014).
238. Nelson, D. J. & Nolan, S. P. Quantifying and understanding the electronic properties of N-heterocyclic carbenes. *Chem. Soc. Rev.* **42**, 6723–6753 (2013).

239. Herrmann, W. A., Elison, M., Fischer, J., Kocher, C. & Artus, G. R. J. Metal Complexes of N-heterocyclic Carbenes - A New Structural Principle for Catalysts in Homogeneous Catalysis. *Angew. Chem. Int. Ed. Engl.* **34**, 2371–2374 (1995); *Angew. Chem.* **107**, 2602–2605 (1995).
240. Marion, N. *et al.* Au-catalyzed cycloisomerization of 1,5-enynes bearing a propargylic acetate: Formation of unexpected bicyclo[3.1.0]hexene. *Chem. Commun.* 2048–2050 (2006). doi:10.1039/b602839j
241. Ramón, R. S., Marion, N. & Nolan, S. P. Gold Activation of Nitriles: Catalytic Hydration to Amides. *Chem. Eur. J.* **15**, 8695–8697 (2009).
242. Boogaerts, I. I. F. & Nolan, S. P. Carboxylation of C-H bonds using N-heterocyclic carbene gold(I) complexes. *J. Am. Chem. Soc.* **132**, 8858–8859 (2010).
243. Hurst, E. C., Wilson, K., Fairlamb, I. J. S. & Chechik, V. N-Heterocyclic carbene coated metal nanoparticles. *New J. Chem.* **33**, 1837–1840 (2009).
244. Vignolle, J. & Tilley, T. D. N-Heterocyclic carbene-stabilized gold nanoparticles and their assembly into 3D superlattices. *Chem. Commun.* **46**, 7230–7232 (2009).
245. Song, S. G. *et al.* N-heterocyclic carbene-based conducting polymer-gold nanoparticle hybrids and their catalytic application. *Macromolecules* **47**, 6566–6571 (2014).
246. Park, D. H., Kim, M. S. & Joo, J. Hybrid nanostructures using p-conjugated polymers and nanoscale metals: Synthesis, characteristics, and optoelectronic applications. *Chem. Soc. Rev.* **39**, 2439–2452 (2010).
247. Richter, C., Schaepe, K., Glorius, F. & Ravoo, B. J. Tailor-made N-heterocyclic carbenes for nanoparticle stabilization. *Chem. Commun.* **50**, 3204–3207 (2014).
248. Rodríguez-Castillo, M. *et al.* Reactivity of gold nanoparticles towards N-heterocyclic carbenes. *J. Chem. Soc. Dalt. Trans.* **43**, 5978–5982 (2014).
249. Rodríguez-Castillo, M. *et al.* Experimental and Theoretical Study of the Reactivity of Gold Nanoparticles Towards Benzimidazole-2-ylidene Ligands. *Chem. Eur. J.* **22**, 10446–10458 (2016).
250. Sousa, A. A. *et al.* Synthesis, characterization, and direct intracellular imaging of ultrasmall and uniform glutathione-coated gold nanoparticles. *Small* **8**, 2277–2286 (2012).
251. Wu, X. *et al.* Ultrasmall near-infrared gold nanoclusters for tumor fluorescence imaging in vivo. *Nanoscale* **2**, 2244–2249 (2010).
252. Crespo, J. *et al.* Ultrasmall NHC-coated gold nanoparticles obtained through solvent free thermolysis of organometallic Au(I) complexes. *Dalt. Trans.* **43**, 15713–15718 (2014).
253. Cao, Z. *et al.* A Molecular Surface Functionalization Approach to Tuning Nanoparticle Electrocatalysts for Carbon Dioxide Reduction. *J. Am. Chem. Soc.* **138**, 8120–8125 (2016).
254. Narouz, M. R., Li, C. H., Nazemi, A. & Crudden, C. M. Amphiphilic N-Heterocyclic Carbene-Stabilized Gold Nanoparticles and Their Self-Assembly in Polar Solvents. *Langmuir* **33**, 14211–14219 (2017).

255. Nie, Z., Petukhova, A. & Kumacheva, E. Properties and emerging applications of self-assembled structures made from inorganic nanoparticles. *Nat. Nanotechnol.* **5**, 15–25 (2010).
256. Nie, Z. *et al.* Self-assembly of metal-polymer analogues of amphiphilic triblock copolymers. *Nat. Mater.* **6**, 609–614 (2007).
257. Deneke, S. M. & Fanburg, B. L. Regulation of cellular glutathione. *Am. Physiol. Soc.* **257**, L163–L173 (1989).
258. Man, R. W. Y. *et al.* Ultra Stable Gold Nanoparticles Modified by Bidentate N-Heterocyclic Carbene Ligands. *J. Am. Chem. Soc.* **140**, 1576–1579 (2018).
259. Young, A. J., Serpell, C. J., Chin, J. M. & Reithofer, M. R. Optically active histidin-2-ylidene stabilised gold nanoparticles. *Chem. Commun.* **53**, 12426–12429 (2017).
260. Ye, R. *et al.* Supported Au Nanoparticles with N-Heterocyclic Carbene Ligands as Active and Stable Heterogeneous Catalysts for Lactonization. *J. Am. Chem. Soc.* **140**, 4144–4149 (2018).
261. Shu, X. Z. *et al.* Silica-Supported Cationic Gold(I) Complexes as Heterogeneous Catalysts for Regio- and Enantioselective Lactonization Reactions. *J. Am. Chem. Soc.* **137**, 7083–7086 (2015).
262. Lomelí-Rosales, D. A. *et al.* Synthesis of neutral and cationic NHC-Au complexes as nanoparticle precursors. *Polyhedron* **182**, 114476 (2020).
263. MacLeod, M. J. & Johnson, J. A. PEGylated N-Heterocyclic Carbene Anchors Designed to Stabilize Gold Nanoparticles in Biologically Relevant Media. *J. Am. Chem. Soc.* **137**, 7974–7977 (2015).
264. Ferry, A. *et al.* Negatively Charged N-Heterocyclic Carbene-Stabilized Pd and Au Nanoparticles and Efficient Catalysis in Water. *ACS Catal.* **5**, 5414–5420 (2015).
265. Reynoso-Esparza, M. A. *et al.* Synthesis and characterization of Au(I) and Au(III) complexes containing N-heterocyclic ligands derived from amino acids. *Polyhedron* **81**, 564–571 (2014).
266. Monti, G. A. *et al.* Gold nanoparticles stabilized with sulphonated imidazolium salts in water and reverse micelles. *R. Soc. Open Sci.* **4**, 170481 (2017).
267. Monti, G. A., Correa, N. M., Falcone, R. D., Silbestri, G. F. & Moyano, F. Gold Nanoparticles Stabilized by Sulfonated-Imidazolium Salts as Promising Catalyst in Water. *ChemistrySelect* **4**, 13496–13502 (2019).
268. Monti, G. A., Correa, N. M., Falcone, R. D., Silbestri, G. F. & Moyano, F. Water-soluble gold nanoparticles: recyclable catalysts for the reduction of aromatic nitro compounds in water. *RSC Adv.* **10**, 15065–15071 (2020).
269. DeJesus, J. F. *et al.* A Benchtop Method for Appending Protic Functional Groups to N-Heterocyclic Carbene Protected Gold Nanoparticles. *Angew. Chem. Int. Ed.* **59**, 7585–7590 (2020); *Angew. Chem.* **132**, 7655–7660 (2020).
270. Hoshyar, N., Gray, S., Han, H. & Bao, G. The effect of nanoparticle size on in vivo pharmacokinetics and cellular interaction. *Nanomedicine* **11**, 673–692 (2016).

271. Fernández, G., Bernardo, L., Villanueva, A. & Pleixats, R. Gold nanoparticles stabilized by PEG-tagged imidazolium salts as recyclable catalysts for the synthesis of propargylamines and the cycloisomerization of γ -alkynoic acids. *New J. Chem.* **44**, 6130–6141 (2020).
272. Aminabad, N. S., Farshbaf, M. & Akbarzadeh, A. Recent Advances of Gold Nanoparticles in Biomedical Applications: State of the Art. *Cell Biochem. Biophys.* **77**, 123–137 (2019).
273. Sherman, A. I. & Ter-Pogossian, M. Lymph-node concentration of radioactive colloidal gold following interstitial injection. *Cancer* **6**, 1238–1240 (1953).
274. Her, S., Jaffray, D. A. & Allen, C. Gold nanoparticles for applications in cancer radiotherapy: Mechanisms and recent advancements. *Adv. Drug Deliv. Rev.* **109**, 84–101 (2017).
275. Dreaden, E. C., Austin, L. A., MacKey, M. A. & El-Sayed, M. A. Size matters: Gold nanoparticles in targeted cancer drug delivery. *Ther. Deliv.* **3**, 457–478 (2012).
276. Saha, K., Agasti, S. S., Kim, C., Li, X. & Rotello, V. M. Gold nanoparticles in chemical and biological sensing. *Chem. Rev.* **112**, 2739–2779 (2012).
277. Farooq, M. U. *et al.* Gold Nanoparticles-enabled Efficient Dual Delivery of Anticancer Therapeutics to HeLa Cells. *Sci. Rep.* **8**, 2907 (2018).
278. Maeda, H. Tumor-selective delivery of macromolecular drugs via the EPR effect: Background and future prospects. *Bioconjug. Chem.* **21**, 797–802 (2010).
279. Ghosh, P., Han, G., De, M., Kim, C. K. & Rotello, V. M. Gold nanoparticles in delivery applications. *Adv. Drug Deliv. Rev.* **60**, 1307–1315 (2008).
280. Brown, S. D. *et al.* Gold nanoparticles for the improved anticancer drug delivery of the active component of oxaliplatin. *J. Am. Chem. Soc.* **132**, 4678–4684 (2010).
281. Verma, A., Simard, J. M., Worrall, J. W. E. & Rotello, V. M. Tunable reactivation of nanoparticle-inhibited β -galactosidase by glutathione at intracellular concentrations. *J. Am. Chem. Soc.* **126**, 13987–13991 (2004).
282. Haume, K. *et al.* Gold nanoparticles for cancer radiotherapy: a review. *Cancer Nanotechnol.* **7**, 8 (2016).
283. Regulla, D. F., Hieber, L. B. & Seidenbusch, M. Physical and Biological Interface Dose Effects in Tissue due to X-Ray-Induced Release of Secondary Radiation from Metallic Gold Surfaces. *Radiat. Res.* **150**, 92–100 (1998).
284. Herold, D. M., Das, I. J., Stobbe, C. C., Iyer, R. V. & Chapman, J. D. Gold microspheres: A selective technique for producing biologically effective dose enhancement. *Int. J. Radiat. Biol.* **76**, 1357–1364 (2000).
285. Hainfeld, J. F., Slatkin, D. N. & Smilowitz, H. M. The use of gold nanoparticles to enhance radiotherapy in mice. *Phys. Med. Biol.* **49**, N309–N315 (2004).
286. Huang, X. & El-Sayed, M. A. Plasmonic photo-thermal therapy (PPTT). *Alexandria J. Med.* **47**, 1–9 (2011).
287. Huang, X., El-Sayed, I. H., Qian, W. & El-Sayed, M. A. Cancer cell imaging and photothermal therapy in the near-infrared region by using gold nanorods. *J. Am. Chem. Soc.* **128**, 2115–2120 (2006).

288. Jain, P. K., Lee, K. S., El-Sayed, I. H. & El-Sayed, M. A. Calculated absorption and scattering properties of gold nanoparticles of different size, shape, and composition: Applications in biological imaging and biomedicine. *J. Phys. Chem. B* **110**, 7238–7248 (2006).
289. Valluru, K. S. & Willmann, J. K. Clinical photoacoustic imaging of cancer. *Ultrasonography* **35**, 267–280 (2016).
290. Yang, X., Stein, E. W., Ashkenazi, S. & Wang, L. V. Nanoparticles for photoacoustic imaging. *WIREs Nanomed Nanobiotechnol* **1**, 360–368 (2009).
291. Li, W. & Chen, X. Gold nanoparticles for photoacoustic imaging. *Nanomedicine* **10**, 299–320 (2015).
292. Eghtedari, M. *et al.* High sensitivity of in vivo detection of gold nanorods using a laser optoacoustic imaging system. *Nano Lett.* **7**, 1914–1918 (2007).
293. Eghtedari, M. *et al.* Functionalized gold nanorods for molecular optoacoustic imaging. *Proc. SPIE* **6437**, 64370G1-9 (2007).
294. Cole, L. E., Ross, R. D., Tilley, J. M., Vargo-Gogola, T. & Roeder, R. K. Gold nanoparticles as contrast agents in X-ray imaging and computed tomography. *Nanomedicine* **10**, 321–341 (2015).
295. Reuveni, T., Motiei, M., Romman, Z., Popovtzer, A. & Popovtzer, R. Targeted gold nanoparticles enable molecular CT imaging of cancer: an in vivo study. *Int. J. Nanomedicine* **6**, 2859–2864 (2011).
296. Salorinne, K. *et al.* Water-Soluble N-Heterocyclic Carbene-Protected Gold Nanoparticles: Size-Controlled Synthesis, Stability, and Optical Properties. *Angew. Chem. Int. Ed.* **56**, 6198–6202 (2017); *Angew. Chem.* **129**, 6294–6298 (2017).
297. MacLeod, M. J. *et al.* Robust gold nanorods stabilized by bidentate N-heterocyclic-carbene–thiolate ligands. *Nat. Chem.* **11**, 57–63 (2019).
298. Chen, H., Shao, L., Li, Q. & Wang, J. Gold nanorods and their plasmonic properties. *Chem. Soc. Rev.* **42**, 2679–2724 (2013).
299. Wenzel, M. N. *et al.* Selective targeting of PARP-1 zinc finger recognition domains with Au(III) organometallics. *Chem. Commun.* **54**, 611–614 (2018).
300. Gunnoo, S. B. & Madder, A. Chemical Protein Modification through Cysteine. *ChemBioChem* **17**, 529–553 (2016).
301. Yang, M., Li, J. & Chen, P. R. Transition metal-mediated bioorthogonal protein chemistry in living cells. *Chem. Soc. Rev.* **43**, 6511–6526 (2014).
302. Jbara, M., Maity, S. K. & Brik, A. Palladium in the Chemical Synthesis and Modification of Proteins. *Angew. Chem. Int. Ed.* **56**, 10644–10655 (2017); *Angew. Chem.* **129**, 10780–10792 (2017).
303. Chalker, J. M., Bernardes, G. J. L., Lin, Y. A. & Davis, B. G. Chemical modification of proteins at cysteine: Opportunities in chemistry and biology. *Chem. Asian J.* **4**, 630–640 (2009).
304. Abbehausen, C. Zinc finger domains as therapeutic targets for metal-based

compounds-an update. *Metallomics* **11**, 15–28 (2019).

305. Wenzel, M. N. *et al.* Cyclometalated Au(III) Complexes for Cysteine Arylation in Zinc Finger Protein Domains: Towards Controlled Reductive Elimination. *Chem. Eur. J.* **25**, 7628–7634 (2019).
306. Franzman, M. A. & Barrios, A. M. Spectroscopic Evidence for the Formation of Goldfingers. *Inorg. Chem.* **47**, 3928–3930 (2008).
307. Serra, J., Parella, T. & Ribas, X. Au(III)-aryl intermediates in oxidant-free C-N and C-O cross-coupling catalysis. *Chem. Sci.* **8**, 946–952 (2017).
308. Thomas, S. R. *et al.* Exploring the Chemoselectivity towards Cysteine Arylation by Cyclometallated Au(III) Compounds: New Mechanistic Insights. *ChemBioChem* **21**, 3071–3076 (2020).
309. Carboni, S. *et al.* New Variations on the Theme of Gold(III) C₂N₂ Cyclometalated Complexes as Anticancer Agents: Synthesis and Biological Characterization. *Inorg. Chem.* **57**, 14852–14865 (2018).
310. Korneeva, E. N., Ovchinnikov, M. V. & Kostić, N. M. Peptide hydrolysis promoted by polynuclear and organometallic complexes of palladium(II) and platinum(II). *Inorganica Chim. Acta* **243**, 9–13 (1996).
311. Forman, H. J., Zhang, H. & Rinna, A. Glutathione: Overview of its protective roles, measurement, and biosynthesis. *Mol. Asp. Med.* **30**, 1–12 (2009).
312. Hughes, J., Kosterlitz, H. W. & Smith, T. W. The Distribution of Methionine-Enkephalin and Leucine-Enkephalin in the Brain and Peripheral Tissues. *Br. J. Pharmacol.* **61**, 639–647 (1977).
313. Lee, R. F. S., Menin, L., Patiny, L., Ortiz, D. & Dyson, P. J. Versatile Tool for the Analysis of Metal-Protein Interactions Reveals the Promiscuity of Metallodrug-Protein Interactions. *Anal. Chem.* **89**, 11985–11989 (2017).
314. Biemann, K. Nomenclature for Peptide Fragment Ions (Positive Ions). *Methods Enzymol.* **193**, 886–887 (1990).
315. Meier, S. M., Tsybin, Y. O., Dyson, P. J., Keppler, B. K. & Hartinger, C. G. Fragmentation methods on the balance: Unambiguous top-down mass spectrometric characterization of oxaliplatin-ubiquitin binding sites. *Anal. Bioanal. Chem.* **402**, 2655–2662 (2012).
316. Zanon, P. R. A., Lewald, L. & Hacker, S. M. Isotopically Labeled Desthiobiotin Azide (isoDTB) Tags Enable Global Profiling of the Bacterial Cysteinome. *Angew. Chem. Int. Ed.* **59**, 2829–2836 (2020); *Angew. Chem.* **132**, 2851–2858 (2020).
317. Nonoyama, M., Nakajima, K. & Nonoyama, K. Direct cycloauration of 2-anilinopyridine (Hanp) with tetrachloroaurate(III) and the X-ray crystal structure of [AuCl₂(anp)]. *Polyhedron* **16**, 4039–4044 (1997).
318. Constable, E. C. & Leese, T. A. Cycloaurated derivatives of 2-phenylpyridine. *J. Organomet. Chem.* **363**, 419–424 (1989).
319. Fuchita, Y. *et al.* Cycloauration of 2-substituted pyridine derivatives. Synthesis, structure and reactivity of six-membered cycloaurated complexes of 2-anilino-, 2-phenoxy- and 2-(phenylsulfanyl)-pyridine. *J. Chem. Soc. Dalt. Trans.* 4095–4100 (1998). doi:10.1039/a807108j

320. Ma, X., Liu, Q., Jia, X., Su, C. & Xu, Q. Efficient synthesis of unsymmetrical heteroaryl thioethers and chalcogenides by alkali hydroxide-mediated SNAr reactions of heteroaryl halides and dichalcogenides. *RSC Adv.* **6**, 56930–56935 (2016).
321. Laskay, A., Garino, C., Tsybin, Y. O., Salassa, L. & Casini, A. Gold finger formation studied by high-resolution mass spectrometry and in silico methods. *Chem. Commun.* **51**, 1612–1615 (2015).
322. Teles, J. H., Brode, S. & Chabanas, M. Cationic Gold(I) Complexes: Highly Efficient Catalysts for the Addition of Alcohols to Alkynes. *Angew. Chem. Int. Ed.* **37**, 1415–1418 (1998); *Angew. Chem.* **110**, 1475–1478 (1998).
323. Hashmi, A. S. K. Homogeneous catalysis by gold. *Gold Bull.* **37**, 51–65 (2004).
324. Gorin, D. J. & Toste, F. D. Relativistic effects in homogeneous gold catalysis. *Nature* **446**, 395–403 (2007).
325. Pflästerer, D. & Hashmi, A. S. K. Gold catalysis in total synthesis - Recent achievements. *Chem. Soc. Rev.* **45**, 1331–1367 (2016).
326. Qiana, D. & Zhang, J. Gold-catalyzed cyclopropanation reactions using a carbenoid precursor toolbox. *Chem. Soc. Rev.* **44**, 677–698 (2015).
327. Obradors, C. & Echavarren, A. M. Gold-catalyzed rearrangements and beyond. *Acc. Chem. Res.* **47**, 902–912 (2014).
328. Obradors, C. & Echavarren, A. M. Intriguing mechanistic labyrinths in gold(i) catalysis. *Chem. Commun.* **50**, 16–28 (2014).
329. Fürstner, A. Gold and platinum catalysis—a convenient tool for generating molecular complexity. *Chem. Soc. Rev.* **38**, 3208–3221 (2009).
330. Nijamudheen, A. & Datta, A. Gold Catalyzed Cross-Coupling Reactions: An Overview of Design Strategies, Mechanistic Studies, and Applications. *Chem. Eur. J.* **26**, 1442–1487 (2020).
331. Kumar, R. & Nevado, C. Cyclometalated Gold(III) Complexes: Synthesis, Reactivity, and Physicochemical Properties. *Angew. Chem. Int. Ed.* **56**, 1994–2015 (2017); *Angew. Chem.* **129**, 2024–2046 (2017).
332. Queffélec, C., Petit, M., Janvier, P., Knight, D. A. & Bujoli, B. Surface modification using phosphonic acids and esters. *Chem. Rev.* **112**, 3777–3807 (2012).
333. Kollár, L. & Keglevich, G. P-heterocycles as ligands in homogeneous catalytic reactions. *Chem. Rev.* **110**, 4257–4302 (2010).
334. Moonen, K., Laureyn, I. & Stevens, C. V. Synthetic methods for azaheterocyclic phosphonates and their biological activity. *Chem. Rev.* **104**, 6177–6215 (2004).
335. Zhao, D. & Wang, R. Recent developments in metal catalyzed asymmetric addition of phosphorus nucleophiles. *Chem. Soc. Rev.* **41**, 2095–2108 (2012).
336. Feng, C. G., Ye, M., Xiao, K. J., Li, S. & Yu, J. Q. Pd(II)-catalyzed phosphorylation of aryl C-H bonds. *J. Am. Chem. Soc.* **135**, 9322–9325 (2013).
337. Yang, J., Chen, T. & Han, L. B. C-P bond-forming reactions via C-O/P-h cross-

- coupling catalyzed by nickel. *J. Am. Chem. Soc.* **137**, 1782–1785 (2015).
338. Kumaraswamy, G., Rao, G. V. & RamaKrishna, G. Stereocontrolled copper iodide catalyzed phosphorus-carbon bond formation: An efficient synthesis of scalemic tertiary phosphineboranes. *Synlett* **2**, 1122–1124 (2006).
339. Kawai, H., Wolf, W. J., Dipasquale, A. G., Winston, M. S. & Toste, F. D. Phosphonium Formation by Facile Carbon-Phosphorus Reductive Elimination from Gold(III). *J. Am. Chem. Soc.* **138**, 587–593 (2016).
340. He, Y., Wu, H. & Toste, F. D. A dual catalytic strategy for carbon-phosphorus cross-coupling via gold and photoredox catalysis. *Chem. Sci.* **6**, 1194–1198 (2015).
341. Bonsignore, R. *et al.* Carbon-Phosphorus Coupling from C[∧]N Cyclometalated Au(III) Complexes. *Chem. Eur. J.* **26**, 4226–4231 (2020).
342. Díaz-Torres, R. & Alvarez, S. Coordinating ability of anions and solvents towards transition metals and lanthanides. *Dalt. Trans.* **40**, 10311–10315 (2011).
343. Batsanov, S. S. Van der Waals radii of elements. *Inorg. Mater.* **37**, 871–885 (2001).
344. Firth, K. F., Möbus, J. & Stephan, D. W. A pendant phosphorus Lewis acid: Route to a palladium-benzoyl derived phosphorane. *Chem. Commun.* **52**, 13967–13970 (2016).
345. Shilov, A. E. & Shul'pin, G. B. Activation of C-H bonds by metal complexes. *Chem. Rev.* **97**, 2879–2932 (1997).
346. Kovács, G., Rossin, A., Gonsalvi, L., Lledós, A. & Peruzzini, M. Comparative DFT analysis of ligand and solvent effects on the mechanism of H₂ activation in water mediated by half-sandwich complexes [Cp'Ru(PTA)₂Cl] (Cp' = C₅H₅, C₅Me₅; PTA = 1,3,5-triaza-7-phosphaadamantane). *Organometallics* **29**, 5121–5131 (2010).
347. Bickelhaupt, F. M. & Houk, K. N. Analyzing Reaction Rates with the Distortion/Interaction-Activation Strain Model. *Angew. Chem. Int. Ed.* **56**, 10070–10086 (2017); *Angew. Chem.* **129**, 10204–10221 (2017).
348. Wolters, L. P. & Bickelhaupt, F. M. The activation strain model and molecular orbital theory. *Wiley Interdiscip. Rev. Comput. Mol. Sci.* **5**, 324–343 (2015).
349. Tebby, J. C. *Handbook of Phosphorus-31 Nuclear Magnetic Resonance Data*. (CRC Press, 1990).
350. Blons, C. *et al.* Formation of a peri-Bridged Phosphonio-Naphthalene by Cu-Mediated Phosphine-Aryl Coupling. *Chem. Eur. J.* **24**, 11922–11925 (2018).
351. Gelman, D., Jiang, L. & Buchwald, S. L. Copper-catalyzed C-P bond construction via direct coupling of secondary phosphines and phosphites with aryl and vinyl halides. *Org. Lett.* **5**, 2315–2318 (2003).
352. Schwan, A. L. Palladium catalyzed cross-coupling reactions for phosphorus-carbon bond formation. *Chem. Soc. Rev.* **33**, 218–224 (2004).
353. Chan, V. S., Stewart, I. C., Bergman, R. G. & Dean Toste, F. Asymmetric catalytic synthesis of P-stereogenic phosphines via a nucleophilic ruthenium phosphide

- complex. *J. Am. Chem. Soc.* **128**, 2786–2787 (2006).
354. Yu, H., Yang, H., Shi, E. & Tang, W. Development and Clinical Application of Phosphorus-Containing Drugs. *Med. Drug Discov.* **8**, 100063 (2020).
355. Shiotani, A. & Schmidbaur, H. Organogold-chemie IX. Versuche zur Oxydativen Addition an Organogold-Komplexen. *J. Organomet. Chem.* **37**, 24–26 (1972).
356. Tamaki, A. & Kochi, J. K. Catalytic mechanism involving oxidative addition in the coupling of alkylgold(I) with alkyl halides. *J. Organomet. Chem.* **40**, 81–84 (1972).
357. Tamaki, A., Magennis, S. A. & Kochi, J. K. Catalysis by Gold. Alkyl Isomerization, Cis-Trans Rearrangement, and Reductive Elimination of Alkylgold(III) Complexes. *J. Am. Chem. Soc.* **96**, 6140–6148 (1974).
358. Shaw III, C. F., Lundeen, J. W. & Tobias, R. S. Complex bis(tertiaryphosphine)dimethylgold(III) cations: phosphine exchange and reductive elimination of ethane. *J. Organomet. Chem.* **51**, 365–374 (1973).
359. Wolf, W. J., Winston, M. S. & Toste, F. D. Exceptionally fast carbon-carbon bond reductive elimination from gold(III). *Nat. Chem.* **6**, 159–164 (2014).
360. Peng, H. *et al.* Gold-catalyzed oxidative cross-coupling of terminal alkynes: Selective synthesis of unsymmetrical 1,3-diynes. *J. Am. Chem. Soc.* **136**, 13174–13177 (2014).
361. Leyva-Pérez, A., Doménech-Carbó, A. & Corma, A. Unique distal size selectivity with a digold catalyst during alkyne homocoupling. *Nat. Commun.* **6**, DOI: 10.1038/ncomms7703 (2015).
362. Leyva-Pérez, A., Doménech, A., Al-Resayes, S. I. & Corma, A. Gold redox catalytic cycles for the oxidative coupling of alkynes. *ACS Catal.* **2**, 121–126 (2012).
363. Kaphan, D. M., Levin, M. D., Bergman, R. G., Raymond, K. N. & Toste, F. D. A supramolecular microenvironment strategy for transition metal catalysis. *Science (80-.)*. **350**, 1235–1238 (2015).
364. Hofer, M. & Nevado, C. Cross-coupling of arene-gold(III) complexes. *Tetrahedron* **69**, 5751–5757 (2013).
365. Zhang, G., Peng, Y., Cui, L. & Zhang, L. Gold-Catalyzed Homogeneous Oxidative Cross-Coupling Reactions. *Angew. Chem. Int. Ed.* **48**, 3112–3115 (2009); *Angew. Chem.* **121**, 3158–3161 (2009).
366. Nijamudheen, A. & Datta, A. Gold-Catalyzed Cross-Coupling Reactions: An Overview of Design Strategies, Mechanistic Studies, and Applications. *Chem. Eur. J.* **26**, 1442–1487 (2020).
367. Hofer, M., Gomez-Bengoa, E. & Nevado, C. A neutral Gold(III)-Boron transmetalation. *Organometallics* **33**, 1328–1332 (2014).
368. Kang, K. *et al.* C(sp²)-C(sp²) Reductive Elimination from Well-Defined Diarylgold(III) Complexes. *Organometallics* **36**, 4727–4740 (2017).
369. Vicente, J., Bermúdez, M. D., Escribano, J., Carrillo, M. P. & Jones, P. G. Synthesis of Intermediates in the C-H Activation of Acetone with 2-

Phenylazophenylgold(III) Complexes and in the C-C Coupling of Aryl Groups from Diarylgold(III) Complexes. Crystal and Molecular Structures of $[\text{Au}\{\text{C}_6\text{H}_3(\text{N}=\text{NC}_6\text{H}_4\text{Me}-4')-2\text{-Me}-5\}(\text{acac}-\text{C})\text{Cl}]$ (ac. *J. Chem. Soc., Dalt. Trans.* 3083–3089 (1990).

370. Wu, Q. *et al.* Stoichiometric to catalytic reactivity of the aryl cycloaurated species with arylboronic acids: Insight into the mechanism of gold-catalyzed oxidative C(sp²)-H arylation. *Chem. Sci.* **6**, 288–293 (2015).
371. Rocchigiani, L., Fernandez-Cestau, J., Budzelaar, P. H. M. & Bochmann, M. Reductive Elimination Leading to C–C Bond Formation in Gold(III) Complexes: A Mechanistic and Computational Study. *Chem. Eur. J.* **24**, 8893–8903 (2018).
372. Lauterbach, T., Livendahl, M., Rosellón, A., Espinet, P. & Echavarren, A. M. Unlikelihood of Pd-free gold(I)-catalyzed sonogashira coupling reactions. *Org. Lett.* **12**, 3006–3009 (2010).
373. Bonsignore, R. *et al.* C–C Cross-Couplings from a Cyclometalated Au(III) C^N Complex: Mechanistic Insights and Synthetic Developments. *Chem. Eur. J.* **27**, 14322–14334 (2021).
374. Quagliano, J. V. & Schubert, L. The trans effect in complex inorganic compounds. *Chem. Rev.* **50**, 201–260 (1952).
375. Reineke, M. H., Sampson, M. D., Rheingold, A. L. & Kubiak, C. P. Synthesis and structural studies of Nickel(0) tetracarbene complexes with the introduction of a new four-coordinate geometric index, τ_4 . *Inorg. Chem.* **54**, 3211–3217 (2015).
376. Yang, L., Powell, D. R. & Houser, R. P. Structural variation in copper(I) complexes with pyridylmethylamide ligands: Structural analysis with a new four-coordinate geometry index, τ_4 . *Dalt. Trans.* 955–964 (2007).
377. Fuchita, Y., Ieda, H., Tsunemune, Y., Kinoshita-Nagaoka, J. & Kawano, H. Synthesis, structure and reactivity of a new six-membered cycloaurated complex of 2-benzoylpyridine $[\text{AuCl}_2(\text{pcp}-\text{C}_1, \text{N})]$ [pcp = 2-(2-pyridylcarbonyl)phenyl]. Comparison with the cycloaurated complex derived from 2-benzylpyridine. *J. Chem. Soc. Dalt. Trans.* **2**, 791–796 (1998).
378. Deng, J. R. *et al.* Photosensitizer-free visible light-mediated gold-catalysed cis-difunctionalization of silyl-substituted alkynes. *Chem. Sci.* **8**, 7537–7544 (2017).
379. Proietti Silvestri, I. *et al.* Copper(i)-catalyzed cycloaddition of silver acetylides and azides: Incorporation of volatile acetylenes into the triazole core. *Org. Biomol. Chem.* **9**, 6082–6088 (2011).
380. Thomas, S. R. & Casini, A. N-Heterocyclic carbenes as “smart” gold nanoparticle stabilizers: State-of-the art and perspectives for biomedical applications. *J. Organomet. Chem.* **938**, 121743 (2021).
381. Engel, S., Fritz, E. C. & Ravoo, B. J. New trends in the functionalization of metallic gold: From organosulfur ligands to N-heterocyclic carbenes. *Chem. Soc. Rev.* **46**, 2057–2075 (2017).
382. Tegeder, P. *et al.* N-Heterocyclic Carbene-Modified Au–Pd Alloy Nanoparticles and Their Application as Biomimetic and Heterogeneous Catalysts. *Chem. Eur. J.* **24**, 18682–18688 (2018).
383. Lopez-Sanchez, J. A. *et al.* Reactivity studies of Au-Pd supported nanoparticles

- for catalytic applications. *Appl. Catal. A Gen.* **391**, 400–406 (2011).
384. Young, A. J., Eisen, C., Rubio, G. M. D. M., Chin, J. M. & Reithofer, M. R. pH responsive histidin-2-ylidene stabilized gold nanoparticles. *J. Inorg. Biochem.* **199**, 110707 (2019).
385. Karaca, Ö. *et al.* Characterization of Hydrophilic Gold(I) N-Heterocyclic Carbene (NHC) Complexes as Potent TrxR Inhibitors Using Biochemical and Mass Spectrometric Approaches. *Inorg. Chem.* **56**, 14237–14250 (2017).
386. Prajapati, D., Schulzke, C., Kindermann, M. K. & Kapdi, A. R. Selective palladium-catalysed arylation of 2,6-dibromopyridine using N-heterocyclic carbene ligands. *RSC Adv.* **5**, 53073–53085 (2015).
387. Papini, G., Pellei, M., Lobbia, G. G., Burini, A. & Santini, C. Sulfonate- or carboxylate-functionalized N-heterocyclic bis-carbene ligands and related water soluble silver complexes. *Dalt. Trans.* 6985–6990 (2009).
388. Almássy, A., Nagy, C. E., Bényei, A. C. & Joó, F. Novel sulfonated N-heterocyclic carbene gold(I) complexes: Homogeneous gold catalysis for the hydration of terminal alkynes in aqueous media. *Organometallics* **29**, 2484–2490 (2010).
389. Villa, A. *et al.* Characterisation of gold catalysts. *Chem. Soc. Rev.* **45**, 4953–4994 (2016).
390. Khan, S. A. *et al.* Fourier Transform Infrared Spectroscopy: Fundamentals and Application in Functional Groups and Nanomaterials Characterization. in *Handbook of Materials Characterization* (ed. Sharma, S. K.) 317–344 (Springer International Publishing, 2018).
391. Rajkumar, T. & Ranga Rao, G. Synthesis and characterization of hybrid molecular material prepared by ionic liquid and silicotungstic acid. *Mater. Chem. Phys.* **112**, 853–857 (2008).
392. Aziz, M. & Ismail, A. F. X-Ray Photoelectron Spectroscopy (XPS). in *Membrane Characterization* 81–93 (Elsevier B.V., 2017).
393. Bridonneau, N. *et al.* N-Heterocyclic carbene-stabilized gold nanoparticles with tunable sizes. *Dalt. Trans.* **47**, 6850–6859 (2018).
394. Young, A. J. *et al.* One-step synthesis and XPS investigations of chiral NHC-Au(0)/Au(I) nanoparticles. *Nanoscale* **11**, 8327–8333 (2019).
395. Sylvestre, J. P. *et al.* Surface chemistry of gold nanoparticles produced by laser ablation in aqueous media. *J. Phys. Chem. B* **108**, 16864–16869 (2004).
396. Saadatkhan, N. *et al.* Experimental methods in chemical engineering: Thermogravimetric analysis—TGA. *Can. J. Chem. Eng.* **98**, 34–43 (2020).
397. de Oliveira, F. M., de Araújo Nascimento, L. R. B., Calado, C. M. S., Meneghetti, M. R. & da Silva, M. G. A. Aqueous-phase catalytic chemical reduction of p-nitrophenol employing soluble gold nanoparticles with different shapes. *Catalysts* **215**, DOI: 10.3390/catal6120215 (2016).
398. Gu, S. *et al.* Kinetic analysis of the catalytic reduction of 4-nitrophenol by metallic nanoparticles. *J. Phys. Chem. C* **118**, 18618–18625 (2014).

399. Wunder, S., Lu, Y., Albrecht, M. & Ballauff, M. Catalytic activity of faceted gold nanoparticles studied by a model reaction: Evidence for substrate-induced surface restructuring. *ACS Catal.* **1**, 908–916 (2011).
400. Wunder, S., Polzer, F., Lu, Y., Mei, Y. & Ballauff, M. Kinetic analysis of catalytic reduction of 4-nitrophenol by metallic nanoparticles immobilized in spherical polyelectrolyte brushes. *J. Phys. Chem. C* **114**, 8814–8820 (2010).
401. Zhou, X., Xu, W., Liu, G., Panda, D. & Chen, P. Size-dependent catalytic activity and dynamics of gold nanoparticles at the single-molecule level. *J. Am. Chem. Soc.* **132**, 138–146 (2010).
402. Ansar, S. M. *et al.* Removal of molecular adsorbates on gold nanoparticles using sodium borohydride in water. *Nano Lett.* **13**, 1226–1229 (2013).
403. Neal, R. D., Hughes, R. A., Sapkota, P., Ptasinska, S. & Neretina, S. Effect of Nanoparticle Ligands on 4-Nitrophenol Reduction: Reaction Rate, Induction Time, and Ligand Desorption. *ACS Catal.* **10**, 10040–10050 (2020).
404. Zhao, P., Li, N. & Astruc, D. State of the art in gold nanoparticle synthesis. *Coord. Chem. Rev.* **257**, 638–665 (2013).
405. Ventura-Espinosa, D., Martín, S. & Mata, J. A. The non-innocent role of graphene in the formation/immobilization of ultra-small gold nanoparticles functionalized with N-heterocyclic carbene ligands. *J. Catal.* **375**, 419–426 (2019).
406. Ventura-Espinosa, D., Martín, S., García, H. & Mata, J. A. Ligand effects in the stabilization of gold nanoparticles anchored on the surface of graphene: Implications in catalysis. *J. Catal.* **394**, 113–120 (2021).
407. Rogers, S., Catlow, R., Gianolio, D., Wells, P. & Dimitratos, N. Supported Metal Nanoparticles with Tailored Catalytic Properties through Sol immobilisation: Applications for the Hydrogenation of Nitrophenols. *Faraday Discuss.* **208**, 443–454 (2018).
408. Prati, L. & Villa, A. Gold Colloids: From Quasi-Homogeneous to Heterogeneous Catalytic Systems. *Acc. Chem. Res.* **47**, 855–863 (2014).
409. Suttiponparnit, K. *et al.* Role of Surface Area, Primary Particle Size, and Crystal Phase on Titanium Dioxide Nanoparticle Dispersion Properties. *Nanoscale Res. Lett.* **6**, DOI: 10.1007/s11671-010-9772-1 (2011).
410. Villa, A., Schiavoni, M. & Prati, L. Material science for the support design: A powerful challenge for catalysis. *Catal. Sci. Technol.* **2**, 673–682 (2012).
411. Pyrz, W. D. & Buttrey, D. J. Particle size determination using TEM: A discussion of image acquisition and analysis for the novice microscopist. *Langmuir* **24**, 11350–11360 (2008).
412. Chen, M. & Goodman, D. W. Catalytically active gold on ordered titania supports. *Chem. Soc. Rev.* **37**, 1860–1870 (2008).
413. Sankar, M. *et al.* Role of the Support in Gold-Containing Nanoparticles as Heterogeneous Catalysts. *Chem. Rev.* **120**, 3890–3938 (2020).
414. Chakraborty, S., Ansar, S. M., Stroud, J. G. & Kitchens, C. L. Comparison of Colloidal versus Supported Gold Nanoparticle Catalysis. *J. Phys. Chem. C* **122**, 7749–7758 (2018).

415. Lin, C., Tao, K., Hua, D., Ma, Z. & Zhou, S. Size effect of gold nanoparticles in catalytic reduction of p-nitrophenol with NaBH₄. *Molecules* **18**, 12609–12620 (2013).
416. Jin, L., Liu, B., Louis, M. E., Li, G. & He, J. Highly Crystalline Mesoporous Titania Loaded with Monodispersed Gold Nanoparticles: Controllable Metal-Support Interaction in Porous Materials. *ACS Appl. Mater. Interfaces* **12**, 9617–9627 (2020).
417. Schneider, C. A., Rasband, W. S. & Eliceiri, K. W. NIH Image to ImageJ: 25 years of image analysis. *Nat. Methods* **9**, 671–675 (2012).
418. Low, A. & Bansal, V. A visual tutorial on the synthesis of gold nanoparticles. *Biomed. Imaging Interv. J.* **6**, e9 (2010).
419. Huang, B., Hu, M. & Toste, F. D. Homogeneous Gold Redox Chemistry: Organometallics, Catalysis, and Beyond. *Trends Chem.* **2**, 707–720 (2020).
420. Rocchigiani, L. & Bochmann, M. Recent Advances in Gold(III) Chemistry: Structure, Bonding, Reactivity, and Role in Homogeneous Catalysis. *Chem. Rev.* **121**, 8364–8451 (2021).
421. Joost, M. *et al.* Facile oxidative addition of aryl iodides to Gold(I) by ligand design: Bending turns on reactivity. *J. Am. Chem. Soc.* **136**, 14654–14657 (2014).
422. Zeineddine, A. *et al.* Rational development of catalytic Au(I)/Au(III) arylation involving mild oxidative addition of aryl halides. *Nat. Commun.* **8**, 565 (2017).
423. Rodriguez, J. *et al.* Catalytic Au(I)/Au(III) arylation with the hemilabile MeDalphos ligand: Unusual selectivity for electron-rich iodoarenes and efficient application to indoles. *Chem. Sci.* **10**, 7183–7192 (2019).
424. Harper, M. J. *et al.* Oxidative Addition, Transmetalation, and Reductive Elimination at a 2,2'-Bipyridyl-Ligated Gold Center. *J. Am. Chem. Soc.* **140**, 4440–4445 (2018).
425. Cadge, J. A., Sparkes, H. A., Bower, J. F. & Russell, C. A. Oxidative Addition of Alkenyl and Alkynyl Iodides to a AuI Complex. *Angew. Chem. Int. Ed.* **59**, 6617–6621 (2020); *Angew. Chem.* **132**, 6679–6683 (2020).
426. Cadge, J. A., Bower, J. & Russell, C. A. A Systematic Study of the Effects of Complex Structure on Aryl Iodide Oxidative Addition at Bipyridyl-Ligated Gold(I) Centers. *Angew. Chem. Int. Ed.* DOI: 10.1002/anie.202108744 (2021).
427. Winston, M. S., Wolf, W. J. & Toste, F. D. Photoinitiated oxidative addition of CF₃I to gold(I) and facile aryl-CF₃ reductive elimination. *J. Am. Chem. Soc.* **136**, 7777–7782 (2014).
428. Trujillo, M. J. *et al.* Using SERS to understand the binding of N-heterocyclic carbenes to gold surfaces. *J. Phys. Chem. Lett.* **9**, 6779–6785 (2018).
429. Dejesus, J. F., Trujillo, M. J., Camden, J. P. & Jenkins, D. M. N-Heterocyclic Carbenes as a Robust Platform for Surface-Enhanced Raman Spectroscopy. *J. Am. Chem. Soc.* **140**, 1247–1250 (2018).